Atomic-resolution Imaging and Spectroscopy of Platinum-alloy Nanoparticles

By

Sagar Prabhudev

A Dissertation

Submitted in partial fulfillment of the requirements for the degree

Doctor of Philosophy

Materials Science and Engineering

McMaster University

April 26, 2017

TITLE: Atomic-resolution Imaging and Spectroscopy of Platinum-alloy Nanoparticles
AUTHOR: Sagar Prabhudev[1]

DOCTORAL DISSERTATION
NUMBER OF PAGES: 327

SUPERVISOR: Dr. Gianluigi A. Botton[2]
AFFILIATION: Department of Materials Science and Engineering, McMaster University

LOCATION: Hamilton, Ontario, Canada — L8S 4M1

[1] prabhus@mcmaster.ca
[2] gbotton@mcmaster.ca

ABSTRACT

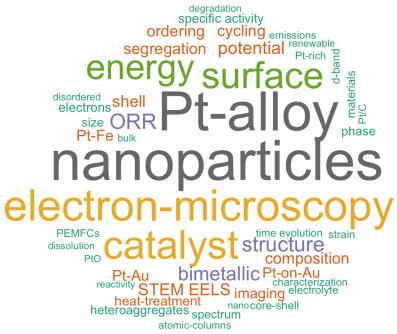

The work presented in this thesis centers on the application of aberration-corrected transmission electron microscopy (TEM) to study Platinum-alloy (Pt-alloy) nanoparticle systems, in particular the platinum–iron (Pt–Fe) and platinum–gold (Pt–Au) nanoparticles. Additionally, few other complementary structures based on Pt thin films and nanowires are also characterized. These materials are studied in the context of their catalytic application towards the oxygen reduction reaction (ORR) in polymer electrolyte membrane fuel cells (PEMFCs).

Here we report on the detailed investigation of many structural and compositional aspects of these catalyst nanoparticles, such as lattice strain, the surface and bulk atomic-structure, the surface/bulk chemical composition, surface segregation, and atomic ordering. In some cases (e.g., Pt–Fe and Pt–Au studies), we have even looked beyond the traditional characterization approaches. For instance, instead of observing the particle structures before and after a particular treatment (e.g., heating and degradation tests), we have captured the dynamics of structural evolution over the entire course of such treatments.

Notable findings pertaining to individual material systems are summarized as follows:

A detailed microscopic investigation of the as-synthesized Pt–Fe nanoparticles revealed that the Pt and Fe atoms are arranged in a random and inhomogeneous fashion. A further characterization of these particles after a routine heat-treatment procedure indicated that the particle surfaces could be covered in a iron-rich outer shell, which is not ideal for the catalytic performance. We show that a simple electrochemical procedure can be used to clean the catalyst surfaces. Inspection of such Pt–Fe particles post-cleaning revealed that the core of the particle is composed of an ordered Pt–Fe alloy (i.e., arrangement of Pt and Fe atoms in an ordered fashion), and the shell is Pt-rich. The routine electrochemical tests on these unique Pt–Fe particles indicated a superior and durable catalyst performance with respect to PEMFCs.

The experiments connected to Pt-on-Au heteroaggregates involved synthesizing them with different Pt feed ratios, heating them inside the microscope (and also other gaseous atmospheres), and importantly, monitoring their structural and compositional changes

during the heat-treatments. We find that depending on the initial particle composition and the heating environment, the Pt-on-Au heteroaggregates transform into either a homogeneous or a inhomogeneous alloy structure. Both these alloy forms are known to exhibit very different catalytic properties.

The catalyst structures investigated under the category *complementary structures* included: Pt-alloy thin film catalysts, Pt-nanotubular skeletons, and Bismuth-decorated Pt nanowires. Each of these catalyst systems were found to exhibit superious catalyst performances compared to state-of-the-art Pt catalysts. A detailed microscopic investigation elucidated the atomic arrangement and composition in the surface, the near-surface and the bulk regions of these structures. This information was useful in interpreting their catalytic performances, which opened new perspectives towards further optimization of such complex catalyst structures.

ACKNOWLEDGEMENTS

I take this opportunity to express my deepest gratitude to all the people who have made my graduate experience at McMaster pleasurable.

Without a second thought, it is to my supervisor Gianluigi Botton that I owe the most. He has allowed me to think and explore science to the fullest possible level. At no point in my PhD was there a single obstacle from his side to execute my research ideas. Thanks Gianluigi for your exceptional mentorship. The lessons I learnt in these years, I will certainly carry them forward.

One other person to whom I am truly indebted is Matthieu Bugnet. From being the one to train me on the microscope, and to the one I collaborated the most, Matthieu has become one of my dearest friends. Thanks for all the memories Matthieu. I hope our paths do cross again someday.

I have had the good fortune of working with an extraordinary bunch of people within the group. Thanks to some earliest members Mickey, Steffi, Guozhen, Sharzhad, Andrew and David. Special thanks to Sam, Lidia, Edson and Hanshuo for always being there when I most needed. Thanks to some latest members - Cory, Michael, Isobel and Alex for exposing me to new research problems, and the accompanying philosophical discussions.

To my supervisory committee members, Leyla Soleymani and Gillian Goward, thank you for the healthy criticisms concerning my work, guidance, and insight. To the faculty and staff members from the materials department - Joey Kish, Jeff Hoyt, Jane Mah, Danielle, Diana and Nanci, thank you for easing my way through a number of administrative hurdles. To the staff members of the CCEM – Glynis de Sylveira, Andy Duft, Andreas Korinek and others, thank you for the technical support around the laboratory.

I have had the opportunity to collaborate with a number of national and international groups. To my collaborators - David Mitlin (Alberta), Drew Higgins (Stanford), Yang Shao-Horn (MIT), XueHai Tan (New Jersey), Ben Zahiri (AFCC), Rongyue Wang (Argonne), David Fermin (Bristol), Jo Humphrey (Bristol), Holger Kleinke (Waterloo), Nader Farahi (Waterloo), thanks for involving me in your cutting-edge research problems. Spe-

cial thanks to Christina Bock (NRC), who in addition to collaborating with me on a number of projects also expanded my knowledge in electrochemistry.

I am grateful to the Carpe-FC network for funding my doctoral research. Special thanks to the McMaster School of Graduate Studies for providing additional funding in the form of scholarships and awards, and the Microscopy Society of Canada for awarding travel bursaries to attend many international conferences.

Special thanks to professors K. T. Jacob and Baldev Raj in India for encouraging me to pursue graduate studies. Thanks to my brother and to all my dearest friends from India and abroad for their unflinching support and concern.

Last but not least, to my girlfriend Oznur Kaynak, thank you for all the healthy distractions, emotional support, and care.

To my parents,
Sunanda and Prabhudev

A NOTE TO THE READER

The present thesis is organized as follows:

Chapter 1 provides an overview of the present day energy challenge, which is to replace the fossil-fuels based energy technologies with alternative low-carbon emitting technologies. Of particular focus to the present thesis is the automotive sector, where polymer electrolyte membrane fuel cells (PEMFCs) are a promising technology that can replace fossil-fuel powered internal combustion engines. For a detailed review of the energy challenge and the different low-carbon energy technologies (based on nuclear, solar, wind, hydrogen and carbon sequestration), the reader is directed to Appendix F and Appendix G. Due to length constraints, these elaborated reviews were curtailed into their present form in Chapter 1.

Chapter 2 focusses entirely on PEMFCs, providing a detailed account of their basic construction, operating principles, the relevant chemical reactions and the technical challenges which restrict their widespread commercialization. It is in this chapter that we also introduce the pressing need for the development of PEMFC electrocatalysts.

Chapter 3 covers many fundamental concepts concerning PEMFC catalysts, such as: (a) the nature of the fuel cell reactions that these catalysts aim to activate, (b) the ways in which the catalyst structures can be fine-tuned in order to achieving improved catalytic performances, (c) the effect of alloying platinum (Pt) on its surface reactivity, (d) different forms of alloying Pt, (e) degradation of catalysts and the related mechanisms, (f) methods available to evaluate the performance and durability of catalysts, and (g) different structural characterization techniques available to investigate the catalyst structure.

Chapter 4 reviews recent progress in the development of different Pt-alloy nanoparticle catalysts for PEMFCs.

Chapter 5 provides the necessary background to scanning transmission electron microscopy (STEM) and its associated techniques that are use to carry out the experiments reported in the thesis.

Chapter 6 discusses the series of STEM characterization works carried out on the Pt–Fe alloy nanoparticles.

Chapter 7 discusses the detailed STEM characterization of Pt–Au alloy heteroaggregate nanoparticles.

Appendix H provides a statement on the choice of above two material systems used for the main thesis work.

Chapter 8 provides a synposis of the experimental works presented in the thesis.

Chapter 9 outlines some future works targeting the reader who wishes to contribute to the efforts taking place in this field.

Appendix D provides a summary of the works we carried out on other complementary structures that were based on thin films and nanowires.

Appendices: Appendix A, Appendix E, Appendix B and Appendix C provide clarifications to some specific concept or a method that is described in the main text. For instance, the Appendix A provides a general description of the electron diffraction phenomenon at an aperture, which is an important concept to achieving the best resolution in the electron microscopes. The reader is linked to these appendices at appropriate locations within the main text.

PUBLICATIONS

Selected list of peer-reviewed publications produced during the course of this thesis.

- **S. Prabhudev**, M. Bugnet, C. Bock, G. A. Botton. Strained Lattice with Persistent Atomic Order in Pt_3Fe_2 Intermetallic Core-Shell Nanocatalysts. *ACS Nano.* 7 (2013): 6103-6110.

- **S. Prabhudev**, M. Bugnet, G.Z. Zhu, C. Bock, and G. A. Botton. Surface Segregation of Fe in Pt–Fe Alloy Nanoparticles: Its Precedence and Effect on the Ordered–Phase Evolution during Thermal Annealing. *ChemCatChem.* 7(22) (2015): 3655-3664.

- G. Z. Zhu, **S. Prabhudev**, J. Yang, C. M. Gabardo, G. A. Botton, and L. Soleymani. *In situ* Liquid Cell TEM Study of Morphological Evolution and Degradation of Pt–Fe Nanocatalysts During Potential Cycling. *The Journal of Physical Chemistry C.* 118(38) (2014) 22111-22119. *Equal contribution with the first author.*

- **S. Prabhudev**, C. Bock and G. A. Botton. Recent progress in the development of Pt-alloy nanocatalysts. *Review article – under review in RSC Energy & Environmental Science.*

- **S. Prabhudev**, C. Chiang, M. Chatzidakis, D. Rossouw, G. A. Botton. Monitoring ordered phase transformation of Pt-Au nanoparticles with *in situ* TEM annealing. (2017) *(in communication)*

- M. Chatzidakis, **S. Prabhudev**, P. Saidi, C. Chiang, J. Hoyt, G. A. Botton. Bulk immiscibility at the edge of the nanoscale. *in communication*

- R. Wang, D. C. Higgins, **S. Prabhudev**, D. U. Lee, J.Y Choi, M. A. Hoque, G. A. Botton, and Z. Chen. Synthesis and structural evolution of Pt nanotubular skeletons: revealing the source of the instability of nanostructured electrocatalysts. *Journal of Materials Chemistry A.* 3 (2015) 12663-12671

- R. Wang, D. C. Higgins, D. U. Lee, **S. Prabhudev**, F. Hassan, V. Chabot, G. Lui, G. A. Botton, Z. Chen. Biomimetic design of monolithic fuel cell electrodes with hierarchical structures. *Nano Energy.* 20 (2016) 57-67.

- X. Tan, **S. Prabhudev**, A. Kohandehghan, D. Karpuzov, G. A. Botton, and D. Mitlin. Pt–Au–Co Alloy Electrocatalysts Demonstrating Enhanced Activity and Durability toward the Oxygen Reduction Reaction. *ACS Catalysis.* 5(3) (2015) 1513-1524.

- J. Humphrey, **S. Prabhudev**, M. Bugnet, G. A. Botton and D. Fermin. Alloyed materials for electrochemical reduction of carbon-dioxide to acetate. (2016) *(in communication)*

CONTENTS

LIST OF FIGURES

LIST OF TABLES

ACRONYMS

ABF Annular Bright Field

BF Bright Field

CV Cyclic Volammetry /Cyclic Voltammogram

DFT Density Functional Theory

EELS Electron Energy Loss Spectroscopy

ECSA Electrochemical Surface Area

FC Fuel Cells

HOR Hydrogen Oxidation Reaction

HAADF High Angle Annular Dark Field

ORR Oxygen Reduction Reaction

PEMFC Polymer Electrolyte Membrane Fuel Cells

Pt–Fe Platinum–Iron

Pt–Au Platinum–Gold

Pt@Au Platinum on Gold

RDE Rotating Disk Electrode

STEM Scanning Transmission Electron Microscopy

TEM Transmission Electron Microscopy

Part I

CONTEXT

1

THE FUTURE LOW-CARBON ENERGY TECHNOLOGIES

Presently, the carbon-dioxide (CO_2) concentration in the Earth's atmosphere is rising at an alarming rate, and according to the International Energy Agency (IEA), the energy sector is the biggest contributor to emissions of all the different anthropogenic activities on the planet [1]. As per the year 2005 basis, the energy sector shared over 95 % of the total anthropogenic emissions globally.

Figure 1.1 compares emissions from different fuel sources within the energy sector. As can be seen, the combustion of fossil fuels (oil, coal and natural gas) remains the primary source of CO_2 emissions, and it has continued to remain so, for over many decades (See Appendix F for a detailed review of the aspects of global energy demand, and its environmental implications).

By the year 2100, the CO_2 concentration in the atmosphere is expected to increase to about 936 *ppm* [2], which is roughly a 234 % increase from the CO_2 concentration maintained over the last 1000 years [3]. The rising CO_2 concentration at such an alarming rate will have serious implications on the climate [2–4]. CO_2 is one of the major greenhouse gases that is able to trap heat within the atmosphere, and thereby, keep the surface of the Earth warm – a phenomenon popularly known as the 'greenhouse effect' [5, 6]. The rising CO_2 concentration will intensify the greenhouse effect, thus leading to further warming of the earth, and the accompanying changes to the planet's climatic system (see Appendix F for details). According to the UN Intergovernmental Panel on Climate Change (IPCC), the global surface temperature change by the end of 2100 is likely to exceed 2 °C relative to its previous average from 1850 to 1900 [2].

Realising the above implications of rising CO_2 emissions, the international community has finally agreed to act. Since the Kyoto Protocol in 2008 and up until the most recent Paris Agreement in 2015, multiple agreements have been signed to secure an international commitment for reducing the CO_2 emissions. Because the anthropogenic emissions of CO_2 result primarily from the combustion of fossil fuels, energy consumption is at the center of the climate change debate. Pledges have been made to move towards a low-carbon energy system *without* altering the rising global needs of energy

[6]. As a primary course of action, alternative fuel sources and energy carriers that are renewable, efficient and less CO_2 producing are being promoted. In order to meet this objective, three general approaches are available, namely (a) the use of nuclear power, (b) carbon capture and storage (CCS), and (c) the use of renewable energy based on solar, wind, and Hydrogen sources [7]. Mass adoption of these technologies, however, is faced with numerous challenges concerning the energy generation, energy conversion, storage and cost-effectiveness of the technology. A detailed review of these low-carbon energy technologies, their cross-cutting opportunities, and the related energy conversion technologies is summarized in Appendix G. Of particular interest to the present thesis are hydrogen based energy systems, which are reviewed in a more detailed manner, and then compared to the similar options offered by solar and wind based technologies.

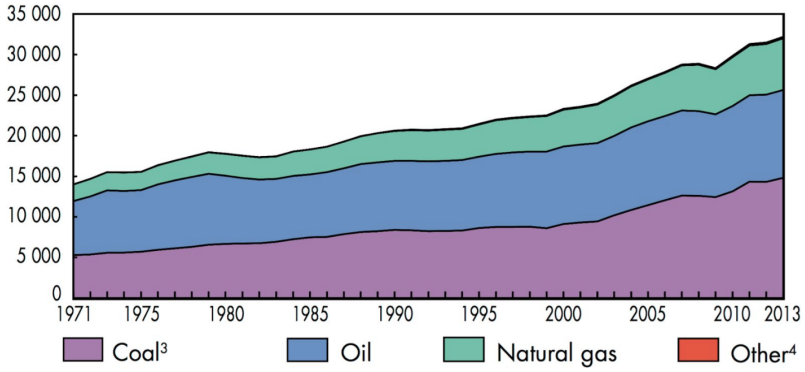

Figure 1.1: Global CO_2 emissions (Mt) from 1971 to 2013 by fuel. source: [1]

With regard to the automotive sector, the polymer electrolyte membrane fuel cells (PEMFCs) are a very promising energy conversion technology for use in the passenger vehicles. These are hydrogen-based electrochemical devices, which can convert the chemical energy stored in H_2 into electricity with negligible amounts of CO_2 emissions.[1] They operate at low temperatures (80 °C), provide high power density, and can vary their output quickly, which make them well suited for the automotive market as an alternative to present day internal combustion engines [8]. According to the international energy agency (IEA), deployment of even 25 % share of fuel cell electric vehicles (FCEVs) by 2050 can contribute up to 10 % of all cumulative transport-related emission reductions required to move from an extreme climate-change scenario to milder one [9]. Remarkable developments are already in progress, e.g., within a span of five years (2008–2013) the global market for fuel cells grew by almost 400 % [10], the manufacturing cost of fuel

[1]Conditional to the use of hydrogen that is produced from the water electrolysis process. See Section G.3.3.4 for a detailed discussion.

cell electric vehicles has decreased by a staggering 90 % since 2005 [11], and the PEMFC technology is regarded as one of the key sustainable energy systems by many countries [9]. Unfortunately, a widespread commercialization of PEMFCs is still not realized, requiring significant reduction in the cost (from $ 3000/kW to $ 30/kW), and sufficient improvements to the durability. This presents numerous materials research challenges, requiring further optimization of the electrode materials, electrolyte membranes and the catalysts used in these devices, which we discuss in the following chapter.

2

POLYMER ELECTROLYTE MEMBRANE FUEL CELLS

Polymer electrolyte membrane fuel cells (PEMFCs) are electrochemical devices which can convert the chemical energy stored in hydrogen and oxygen, into electricity. They are well known for their high energy conversion efficiency (reaching up to 60 %), effective utilization of hydrogen, environmental friendliness (zero CO_2 emissions), and a silent low temperature operation (85 °C – 105 °C) [12, 13]. With these attractive characteristics PEMFCs show great promise to impact a wide range of areas including, automotive [14, 15], stationary [15, 16] and portable power generation [17] sectors. The best utilization of PEMFCs, however, is in the automotive sector when used to develop fuel cell electric vehicles (FCEVs). PEMFCs are well suited for FCEVs as they can provide continuous electrical energy supply at high power density, high efficiency and at low temperatures [14]. Additionally, a transition from the conventional internal combustion vehicles to FCEVs can have a marked impact on the climate change mitigation efforts, as the transportation sector is the second largest source of global CO_2 emissions, over three quarters of which is contributed by road transport automobiles alone [18]. In the subsequent sections, we discuss PEMFCs specifically within the context of such automotive applications.

Despite many advantages of PEMFCs noted above, they have not yet seen a widespread commercialization. This is primarily because of their high cost and poor durability [19–23]. These barriers present various materials research challenges related to optimization of electrode materials, electrolyte membranes and the catalysts, which are all used in fuel cells [23, 24]. The present overview sheds light upon these important aspects of PEMFCs, by first introducing the key components and basic operation, followed by a discussion on various barriers for commercialization, and finally highlighting areas where the fundamental materials research is most needed.

2.1 BASIC FUEL CELL SETUP

Figure 2.1 illustrates the basic setup and key components of a typical PEMFC. Each cell comprises of two electrodes (an anode and the cathode) that are connected in an external circuit, and an electrolyte separating them. The electrodes are exposed to gas flow using 'gas diffusion layers' (GDLs), which supply the electrodes with required fuel (hydrogen) and oxidant (oxygen) for the chemical reaction. Together, this assembly of two electrodes, their respective GDLs and the electrolyte form a 'membrane electrode assembly' (MEA) [25].

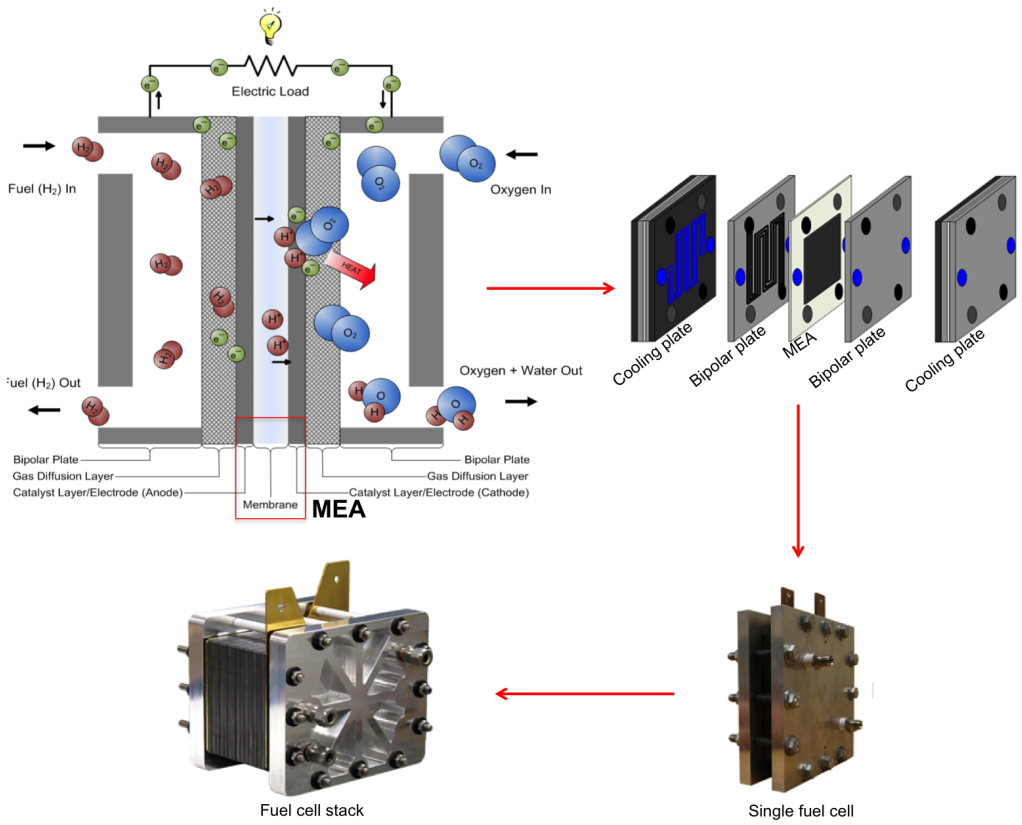

Figure 2.1: Schematic representation of a typical PEMFC and its key components. sources: [26, 27]

2.2 WORKING PRINCIPLE

Gaseous hydrogen flows through channels in the bipolar plates (Figure 2.1) and through the GDL to the anode, where a catalyst splits hydrogen molecules into protons and electrons. Thus, the fuel cell anodic reaction is an 'oxidation reaction of hydrogen' (HOR), given by:

$$\boxed{H_2 \longrightarrow 2\,H^+ + 2\,e^-} \tag{2.1}$$

Protons liberated at the anode enter the electrolyte, and are transported to the cathode. Electrons generated are directed to follow an external circuit to the cathode, through a load or an automotive engine etc. . . for delivering the required external work.

At the cathode, oxygen is introduced through bipolar plates and the GDLs. Oxygen molecules react with incoming electrons and protons on a catalyst surface, forming water and some heat (since the reaction is exothermic). Thus, the fuel cell cathodic reaction is a reduction reaction of oxygen (ORR), given by:

$$\boxed{O_2 + 4\,e^- \longrightarrow 2\,O_2^-} \tag{2.2}$$

The overall reaction in a PEMFC is then given by:

$$\boxed{H_2 + 1/2\,O_2 \longrightarrow H_2O} \tag{2.3}$$

2.3 INDIVIDUAL CELLS VERSUS A STACK OF CELLS

The Gibbs free energy change (ΔG) of the PEMFC reaction noted above (Equation 2.3) is about -237 kJ/mol (negative sign indicates that the energy is released).[1] In other words, for the reaction combining H_2 and $1/2\,O_2$ in PEMFCs, about -237 kJ/mol of chemical energy is being converted into electrical energy.

[1] Calculated from the Enthalpy (ΔH) = -286 KJ/mol, and the Entropy (ΔS) = -163.42 J values of the overall reaction, and then applying $\Delta G = \Delta H - T\Delta S$. Where, T = 298 K.

The Gibbs free energy change of chemical reaction is related to the equilibrium voltage of the cell (E^o) by the Nernst equation:

$$\boxed{\Delta G = -nFE^o} \tag{2.4}$$

where n is the number of electrons transferred in the reaction, and F is Faraday's constant (96485 C/mol).

For the reaction (3.3) taking place in PEMFCs, ΔG = -237 kJ/mol and n = 2. Thus, the equilibrium cell voltage (E^o) under standard temperature and pressure conditions (25 °C, 1 atm.) can be calculated to be 1.229 V.

Under the typical operating conditions, however, each individual MEA produces a voltage less than 1 V [23], which is barely enough to power even the simplest applications (e.g., the ordinary flashlight bulbs are designed to work with minimum 3 V). To produce a practical output voltage, PEMFCs are generally manufactured as a stack of MEAs, each sandwiched between two bipolar plates (Figure 2.1). The bipolar plates, which may be made of either metal, carbon or composites, carry out multiple functions such as introducing fuel and oxidant into the MEAs, providing electrical conduction between the cells and allowing the coolant to flow [28]. Sometimes the entire stack itself is referred to as a fuel cell. Depending on the application, the stack may contain tens to hundreds of cells layered together. This scalability makes fuel cells suited for a variety of small and large scale applications, including laptops (20-50 W), home appliances (1-5 kW), automotives (50-125 kW) and central power generation (1-200 MW) [29].

2.4 ELECTROLYTE AND ELECTRODE MATERIALS

2.4.1 *Electrolyte membrane*

The electrolyte in PEMFCs is typically a polymeric membrane (hence the name 'polymer electrolyte membrane fuel cell') of about 10 – 100 μm thick, which conducts protons from the anode to the cathodic chamber and also provides mechanical stability to the MEA. Desirable membrane properties include high ionic conductivity, prevention of any electron conduction, and precention of the fuel/oxidant crossover between the two electrodes. The membrane must also remain chemically stable in the presence of OH- and OOH- radicals, and thermally stable within the range of operating temperatures. Membrane

resistance for conduction also becomes important with thicker membranes. In general, thinner membranes have lower resistance but the gas crossover can be high.

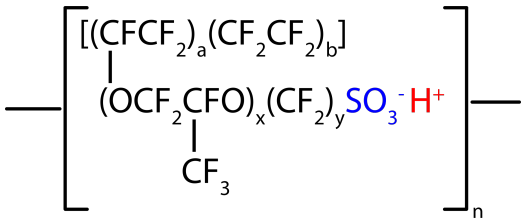

Figure 2.2: Chemical structure of Nafion.

Most current membranes are based on perfluorosulfonic acid (PFSA); *Nafion*^{TM} developed by *DuPont* is particularly very popular [30]. Chemically, Nafion (see Figure 2.2) has the backbone structure of PTFE (polytetrafluoroethylene/Teflon) that provides the membrane with mechanical strength, and the sulfonic acid groups provide charge sites for proton transport. Most studies propose that the ionic conduction in the membrane is assisted by formation of water filled domains which build into an interconnected network of ion conductive channels. To explain the transport of protons, two mechanisms have been proposed. In the 'hopping mechanism' protons hop from one sulfonic group to the other, whereas in the 'vehicular transport mechanism' protons diffuse as hydrated protons through the ion conductive water filled domains. Since both mechanisms require hydrated state of the membrane, the upper limit of PEMFC operating temperature is usually dictated by the humidification needs of the membrane [12]. In addition to Nafion, other perfluorinated polymer membranes are also available, such as Asahi (Asahi Chemical Industry), Neosepta-F (Tokuyama) and Gore-Select (Gore and Associates Inc.).

2.4.2 *Electrode*

Both anode and cathode in PEMFCs have a similar bulk material structure. As illustrated in Figure 2.3*(a, b)*, each electrode is composed of a catalyst layer and a gas diffusion layer, linked side-by-side. The catalyst layer is where the reactions take place and is usually very thin (10 µm thick). The gas diffusion layer is typically a sheet of carbon cloth (~150 µm thick) whose fibers provide a porous structure enabling supply of reactant gases to the catalyst layer [31].

The catalyst layer is composed of catalysts, an electronic conductor and an ionic conductor [35] (see Figure 2.3*(c)*). To ensure supply of reactant gases to the reactant site

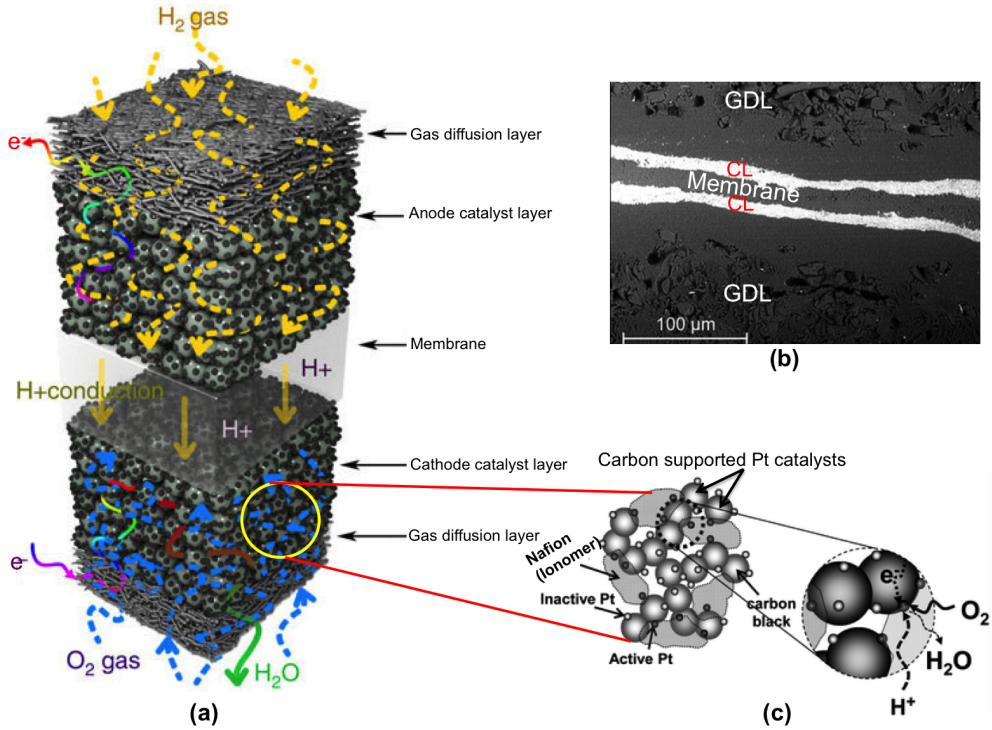

Figure 2.3: Schematic representations of PEMFC electrode structure (a) [32], and the triple-phase region (c) [33]. (c), Microscopic image of an MEA. [34]

(i.e., the catalyst surface) the catalyst layer must have a porous structure. Platinum based nanoparticles supported on high surface area carbon (HSAC) microparticles are commonly used as catalysts, usually abbreviated as Pt/C or Pt-alloy/C. The carbon support also serves as the electronic conductor, conducting electrons to/from the catalyst site. Ionic conductivity is provided by an ionomeric film (dried Nafion solution) that forms a proton conductive network within the entire catalyst layer and has an ionic connection with the membrane.

A good electrode is one in which the supported catalyst particles are in direct contact with the ionomer film Figure 2.3*(c)* and are also exposed to the porous media (i.e., supply of reactant gases). In addition, the catalyst layer must be sufficiently hydrophobic to prevent pores from flooding, particularly at the cathode where water is produced.

The catalyst layers are usually prepared by first making a 'catalyst ink' which is then cast directly onto the membrane, followed by pressing of the GDL (carbon cloth) on top of the catalyst layer [25, 31]. Such catalyst layers are called the 'catalyst coated mem-

branes' or (CCMs). In an alternative method, the catalyst ink is coated directly onto a GDL first, followed by pressing onto the membrane. Such catalyst layers are called 'catalyst coated gas diffusion electrodes' (CCGDL). For both these methods, the catalyst ink is prepared by dispersing supported catalysts in water and isopropanol, along with Nafion solution. Additionally, if the catalyst layer is needed to be made hydrophobic, polytetrafluoroethylene (PTFE) is also introduced along with the Nafion solution.

2.5 ENERGY CONVERSION EFFICIENCY

In order to compare fuel cells with other energy conversion systems such as heat engines (e.g., internal combustion engines (ICEs) or steam turbines), an evaluation of their 'thermodynamic efficiency' (also called the 'theoretical efficiency') is required.

In heat engines, the combustion of hydrocarbons is an exothermic reaction, and the heat generated results in expansion of formed gases. The expanding gases can either move a piston (as in the ICEs), or generate steam to drive turbines (as in the steam turbines), thus producing mechanical work. This mechanical energy can then be converted into electrical energy using rotary generators.

The maximum efficiency for heat engines is given by 'Carnot efficiency' (η_{eff}):

$$\boxed{\eta_{eff} = W/-\Delta H = T_1 - T_2/T_1} \tag{2.5}$$

where W is the reversible work done, ΔH is the enthalpy change of the reaction, T_2 is the temperature of the heat sink and T_1 is the temperature of the heat source. For even the most efficient engines (steam turbines: T_2 = 323 K and T_1 = 673 K), the Carnot efficiencies do not surpass 50-53% [12].

In PEMFCs, the electrical energy is produced from the Gibbs free energy change of reaction (ΔG = -237 kJ/mol), and the energy input is the enthalpy of reaction (ΔH = -286 kJ/mol). Therefore, if all the Gibbs free energy change can be converted into electricity, the thermodynamic fuel cell efficiency under standard temperature and pressure conditions is given by:

$$\boxed{\eta_{theoretical} = \Delta G/\Delta H = 83\%} \tag{2.6}$$

In practice however, fuel cells operate at a much lower efficiency than the theoretical value. This practical fuel cell efficiency is termed as 'electrochemical efficiency', which provides picture of a fuel cell's performance, and allow to compare it against that of the other cells. The 'electrochemical efficiency' of a PEMFC with measured cell voltage 'E' is given by:

$$\boxed{\eta_{electrochemical} = -nFE/\Delta G} \tag{2.7}$$

According to the US Department of Energy (DOE), current fuel cell designs provide an electrochemical efficiency between 40-60 % [29], which is still high compared to typical efficiencies provided by the internal combustion engines (~25 %).

2.6 FUEL CELL OPERATION AND VOLTAGE LOSSES

Although fuel cells boast an equilibrium cell voltage (E^o) of 1.229 V (calculated from Equation 2.4 as above), the observed cell voltages (E) are much lower than the equilibrium value, decreasingly so when the current drawn from the cell is high. A plot of measured cell voltage versus the current density (current drawn per MEA area, A/cm^2) for a typical PEMFC is shown in Figure 2.4. This plot is often referred to as the 'polarization curve'.

As can be seen, even under the open circuit condition when no current is drawn from the cell, the measured voltage (called the 'open circuit potential' (OCP)) deviates from the equilibrium value. This deviation is due to imperfect separation of gases by the membrane and a finite electronic resistance in the cell [23]. Typical OCP for PEMFCs is between 0.6 – 0.9 V.

When current is drawn from the cell, the voltage drops even further than the OCP. This deviation from the equilibrium value is called the overpotential, denoted by η ($\eta = E^o - E$). Based on the nature of the voltage drop with the increasing current, three regions in the polarization curve can be identified, namely the activation polarization, ohmic polarization and mass-transport polarization.

Activation polarization is observed at the onset where the current just begins to be drawn from the cell. The voltage drop in this region, called the 'activation overpotential', is considerably high, and varies sharply with the increasing current. Even for practical currents of just 0.1 A/cm^2, the cell voltage (E) drops by about 370 mV [23]. Activation

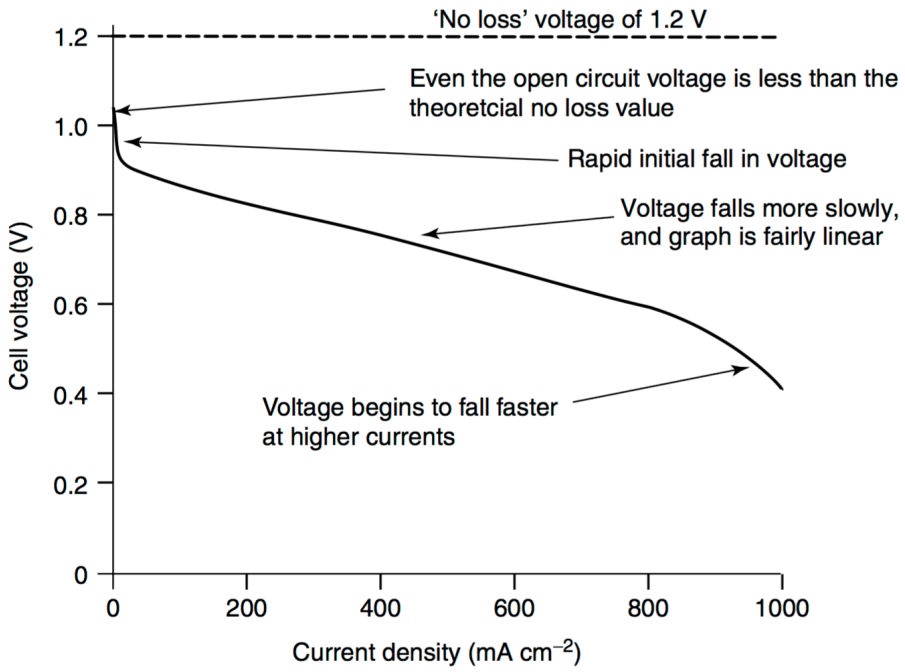

Figure 2.4: Polarization curve plotted for a typical PEMFC. source: [36]

overpotential is attributed to the slow kinetics of electrode reactions, hence it is also referred to as the 'kinetic losses'.

Ohmic polarization corresponds to the region where voltage drops linearly with the increasing currents. Overpotential in this region (called the 'ohmic overpotential') is attributed to the material and interfacial resistances, either in the membrane, cell connections or the bipolar plates.

Mass-transport polarization corresponds to the region at high current densities where the voltage falls off dramatically. Overpotential in this region (called the 'mass-transport overpotential') is due to the fact that the electrode reactions are proceeding at a much faster rate compared to the rate at which the reactants are supplied to the catalyst surface.

Figure 2.5 illustrates a qualitative comparison of these voltage losses, reported by Debe [23]. The blue curve is the typical polarization curve, similar to one shown in Figure 2.4. The cell resistance (R) was measured and multiplied with the current density (i) to obtain the 'ohmic overpotential' (iR-losses). The iR-losses were then added to the polarization

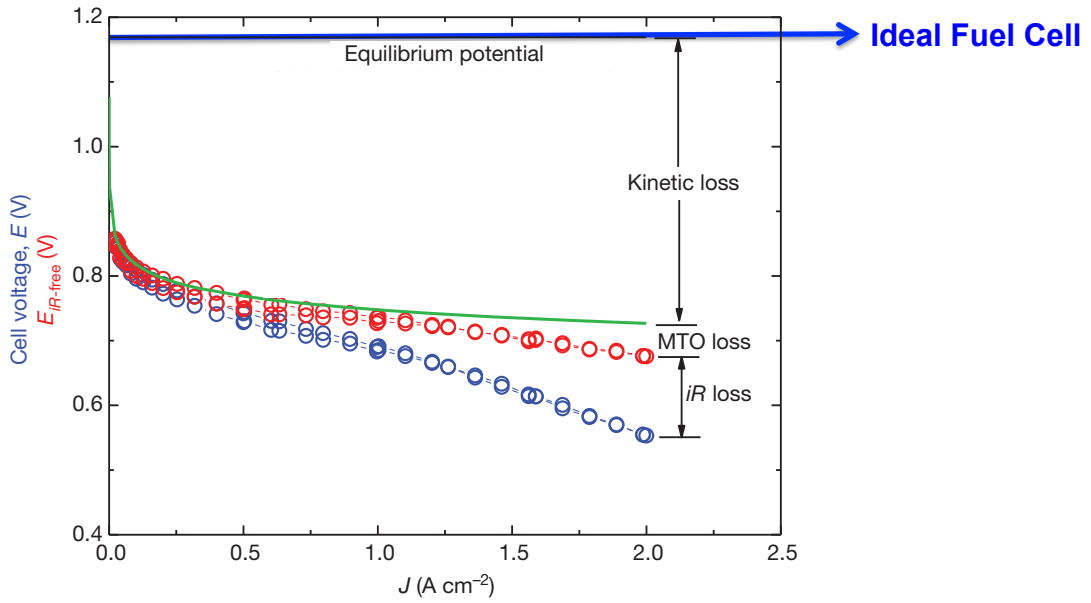

Figure 2.5: Polarization curve of a PEMFC employing Pt/C catalyst and the estimated trends for different voltage losses. source: [23]

curve (blue symbols) to get the iR-free curve, which is shown as the red curve. Thus, the iR-free curve is a combination of activation and mass transport overpotentials only.

The green curve in Figure 2.5 is the polarization curve reflecting activation overpotential only. Also called the ideal kinetic line, the green curve has been calculated using theoretical formulations of electrode kinetics. For more details, the reader is referred to [23]. Thus, the remaining difference between the ideal kinetic line and the iR-free curve represents the total mass-transport overpotential. When the three overpotentials are compared within the range of practical current densities (between 0.1-2.5 A/cm² as in Figure 2.5), it can be seen that the activation overpotential is the largest of all the voltage losses in PEMFCs.

In order to make PEMFCs practically viable, all the three sources of overpotentials need to be mitigated. Ohmic and mass-transport overpotentials are less challenging to minimize than the activation overpotential. Material and interfacial resistances are the primary sources of ohmic overpotential, and they can be minimized by appropriate choice of membrane and the GDLs. Mass-transport overpotential is due to limited supply of reactants to the catalyst surface during reaction, and can be mitigated with the use of pure reactant feeds, increased gas pressures and optimized catalyst layers. Many current

MEA designs are in fact well optimized to minimize both ohmic and mass-transport overpotentials [23]. Since activation overpotential is the largest of the all voltage losses in PEMFCs, its mitigation is a crucial, but also very challenging task. Activation overpotential is caused by the slow kinetics of electrode reactions. Although the reaction rates can be increased with the use of catalysts, the challenge here is that even with an order of magnitude improvement in the electrode kinetics, only modest voltage gains between 60-70 mV can be achieved [23]. With the progress in catalyst development so far, voltage gains of only about tens of mVs has been possible.

2.7 COMPARING KINETIC LOSSES DUE TO ANODIC AND CATHODIC REACTIONS

To mitigate activation overpotential, it is important to first identify the slowest of the two electrode reactions (HOR and ORR).

The kinetics of such redox reactions are best described by the 'Butler-Volmer equation', where the current density (j) is expressed as:

$$\boxed{j = j_o\,(e^{\alpha A F \eta / RT} - e^{\alpha C F \eta / RT})} \tag{2.8}$$

Here, j_o is the exchange current density (i.e., current that flows at equilibrium), αA and αC are the transfer coefficients for the anodic and cathodic reactions, respectively, and η is the overpotential (E^o- E) driving the reaction. These electrochemical quantities are discussed at detail in Section 3.4. For present discussion, the relationship between current density (j) and overpotential (η) can be noted.

Although current density (j) depends on both the kinetics of the charge transfer at the electrode, as well as the mass transport, Equation 2.8 is applicable only when the charge transfer kinetics is the rate limiting step. The mass transfer hindrance has been already treated as a voltage loss in the 'mass transport overpotential' term.

A current density versus potential plot for both anodic (HOR) and cathodic (ORR) reactions is shown in Figure 2.6a. These plots were obtained for electrodes using Pt catalysts supported on carbon (Pt/C).

$U_a(j)$ and $U_c(j)$ are the anodic and cathodic potentials, and $U_{o,a}$ and $_{o,c}$ are their respective equilibrium potentials.

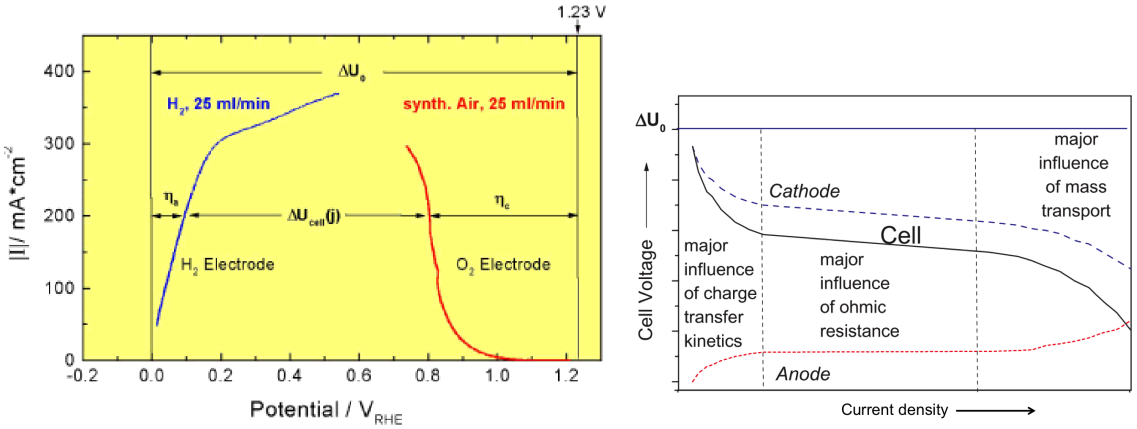

(a) Plot of current density *vs.* potential for HOR and ORR. (b) Overlay of anodic/cathodic current density *vs.* potential plots on the fuel cell polarization curve.

Figure 2.6: Comparing the kinetics of PEMFC anodic (HOR) and cathodic (ORR) reactions. source: [12]

Overpotentials at both the electrodes (η_a and η_c) can then be calculated as:

$$\boxed{\begin{aligned} \eta_a &= U_a(j) - U_{o,a} \\ \eta_c &= U_c(j) - U_{o,c} \end{aligned}} \tag{2.9}$$

Note that $U_{o,c}$ = 1.229 V, and since a reversible hydrogen electrode (RHE) is used as the reference, $U_{o,a}$ = 0 V.[2]

It can be seen from Figure 2.6a that the overpotentials are significantly higher at the cathode compared to the anode. This suggests that the kinetics of oxygen reduction reaction (ORR) is much slower than that of the hydrogen oxidation reaction (HOR), even with the use of Pt/C catalysts. Estimated reaction rate constant for the HOR is about 10 *cm/s* and that of ORR is between 10^{-6}–10^{-9} *cm/s*. This indicates that the ORR is about seven orders of magnitude slower than that of the HOR [23].

Since the cell voltage ($\Delta U_{cell}(j)$ or E) is the difference between its anodic and cathodic potentials ($U_a(j)$ and $U_c(j)$), it can be written in terms of overpotentials (η_a, η_c) as:

$$\boxed{\Delta U_{cell}(j) = U_a(j) - U_c(j) = \Delta U_o - (\eta_a + \eta_c)} \tag{2.10}$$

[2] E^o in Equation 2.4 = $U_{o,c} - U_{o,a}$ = 1.229 − 0 = 1.229 V

Where ΔU_o (or E^o) is the equilibrium cell voltage, equal to 1.229 V.

Since $\eta_c \gg \eta_a$, Equation 2.10 indicates that the reduction in cathodic overpotential (η_c) will have a larger impact toward increasing the cell voltage compared to reduction in anodic overpotential (η_a). This is further clear from Figure 2.6b where the current density versus potential plots for both anode and cathode is overlaid on the fuel cell polarization curve. It is for this reason that greater focus is laid towards developing catalysts for the ORR than the HOR.

To summarise this section, the sluggish kinetics of the oxygen reduction reaction (ORR) at the cathode is the major source of voltage losses in PEMFCs. Development of suitable ORR catalysts with activities higher than Pt/C is imperative, and requires a mechanistic understanding of the ORR. Different mechanisms have been proposed to explain the ORR kinetics, such as associative and dissociative mechanisms, these are reviewed in Section 3.1. Subsequently in Chapter 4, various catalyst development strategies are discussed, including alloying Pt/C nanoparticles with less expensive metals, developing unique supports, and deliberate modifications to the nanostructure, composition and the electronic structure of catalysts.

2.8 BARRIERS FOR COMMERCIALIZATION AND TECHNICAL TARGETS

Although PEMFCs have reached commercialization in smaller markets, such as back-up power and materials handling applications [37], the ultimate success will be when a full scale deployment of PEMFCs in the automotive sector is made possible. While not ignoring the challenges associated with hydrogen supply and processing (Section G.3.3), the two major barriers for fuel cell commercialization in the automotive market are high cost and poor durability [19–23]. Among the many components of PEMFCs that can be contributing to these issues, catalysts facilitating the electrode reactions remain the biggest contributors. Thus, only technical challenges and targets concerning the catalysts are highlighted in the subsequent discussions. Challenges posed by other PEMFC components, while important for the commercialization of fuel cells, are beyond the scope of the present overview. The reader is referred to following articles for a comprehensive review of these components and the challenges associated: [28, 38, 39].

QUANTITY	CURRENT STATUS	SET TARGET FOR 2020
Pt loading (mg_{Pt}/cm^2 electrode area)	0.15	0.125
Mass activity (A/mg_{Pt}@ 0.9 V)	0.47 – 0.67	0.44
Activity losses (mass activity) (%)	37	40
Loss in performance (mV)	10	30 (@ 1.5 A/cm^2)
Non-PGM catalytic activity per volume of supported catalyst	60	300 (@ 1.5 A/cm^2)

Table 2.1: Current status and future set targets of some important PEMFC catalyst related quantities. source: [40]

2.8.1 *Barriers to commercialization from electrode catalysts*

The fuel cell catalyst systems are evaluated based on their performance, cost and durability. An ideal catalyst system is the one that satisfies all these considerations simultaneously, providing high current densities and durability at low Pt loadings [23]. Table 2.1 lists several targets set by the Fuel Cell Technical Team (FCTT) in this regard [40]. The FCTT is a multi-stakeholder group comprising of US Department of Energy (DOE) and several major automotive manufacturers. Evaluation of performance, cost and durability across several catalyst systems indicate that although many catalysts seem to meet one or more set targets, they are still not able to satisfy all the requirements simultaneously [23]. These challenges are summarized as follows.

2.8.1.1 *Catalyst performance*

Among the two fuel cell electrode reactions, ORR at the cathode is the slowest reaction, slower by about seven orders of magnitude compared to the anodic HOR. Thus, the enhancement of the reaction rates of ORR with the use of catalysts is at the focal point of fuel cell catalyst research. Unfortunately, even with the use of Pt/C, the kinetics of ORR are still slow. Catalyst performances is usually compared in terms of specific activities, which is defined as the current density delivered per catalyst surface area (A per $cm^2{}_{Pt}$) measured at 900 mV [41]. Measured specific activities of various catalyst systems indicate that although several catalysts meet the DOE set target (0.7 mA per $cm^2{}_{Pt}$), they may not satisfy one or all the other requirements, namely low catalyst cost and durability [23].

2.8.1.2 *Catalyst cost*

Assuming that all the sources of overpotentials (activation, ohmic and mass transport polarizations) are fully mitigated, fuel cells would still need to compete against the cost and durability offered by other technologies, mainly the internal combustion engines. At 500,000 units per year production volume, the fuel cell drive trains cost at least ten times more than the internal combustion engines. High catalyst cost in PEMFCs is the main challenge here, since almost half of the fuel cell stack cost is due to catalyst cost alone [42]. Presently, both HOR and ORR rely on platinum-based catalysts. Since Pt metal is very expensive (~ $ 32/g_{Pt}), consequently the overall catalyst cost remains high.

As per the DOE target, the overall Pt loading per cm^2 area of an MEA should not exceed 0.125 mg_{Pt}(anode: 0.025 mg_{Pt}/cm^2, cathode: 0.1 mg_{Pt}/cm^2). Strategies to reduce cost by limiting the cathodic loadings to 0.1 mg_{Pt}/cm^2, without loss of performance or durability, is the subject of most catalyst research today. Enhancing the performance of ORR catalysts on the basis of platinum mass (called the mass activity A/g_{Pt}) is particularly recommended. For fuel cell commercialization, mass activities of at least 0.44 $A/mg_{Pt}$is targeted.

2.8.1.3 *Catalytic durability*

In addition to performance and cost, the catalysts face major concerns over their durability [43–45]. The fuel cell environment is intrinsically very corrosive to these catalysts, with a high humidity, acidic environment, and hundreds of thousands of transient potential cycles during their lifetimes. This presents challenges to material durability and performance. Four mechanisms for catalytic performance degradation have been identified, these are (1) dissolution and/or agglomeration of platinum and other metals, (2) detachment of catalysts from the support, (3) the corrosion of carbon support, and (4) poisoning by species such as CO, CO_2, H_2O_2, NO_x and SO_x. Due to these degradation pathways, most current catalyst designs are still short of the 5000 hour durability target (at a power density of 8.0 kW/g_{Pt}) that is required to compete against the IC engines [20, 23]. Therefore, it is extremely desirable to develop ORR catalysts that can provide long term stability even under the corrosive operating conditions of the fuel cell, while not sacrificing their catalytic performance and maintaining a minimal loading of Pt.

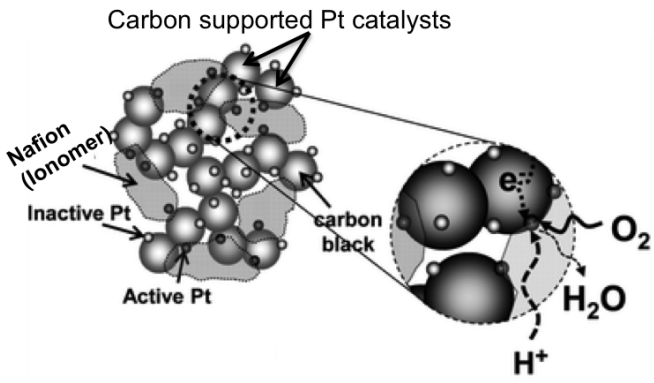

Figure 2.7: Schematic representation of a triple-phase region within the cathode microstructure. [33].

2.8.1.4 *Catalyst utilization*

In addition to barriers such as poor performance, high cost and low durability, PEMFCs suffer from poor utilization of catalyst surfaces in the electrode structure [23, 31, 46]. This requires maximizing the formation of a 'three phase boundaries' (TPBs) in the electrodes (Figure 2.7), whereby (1) the reaction site (i.e., the catalyst surface) is exposed to the pores in catalyst layer that transport gaseous reactants, and the catalyst particle is in direct contact with (2) an electronic conductor and (3) an ionic conductor, to ensure that the electrons and protons are supplied to or taken away from the reaction site. Electronic conductivity is usually provided by the carbon support onto which the catalyst particles are attached. Proton conductivity is provided by the ionomeric networks. Formation of TPBs ensures that the reaction site (i.e., the catalyst surface) is in sufficient supply of all the reactants required, and clear of any products formed.

Optimization of electrode structure is limited by the difficulty of the characterization of ionomer distribution. This is because the ionomer is extremely radiation sensitive to the probes commonly used to study these materials, such as the electron beam and X-ray spectro-microscopic techniques [47]. Additionally, the ionomer is a weak scatter of both the probes, which makes it difficult to image. Fortunately, recent advancements in the areas of low-dose electron imaging and soft x-ray based scanning transmission x-ray microscopy (STXM) limit the radiation damage caused [47, 48], allowing for a detailed visualization of the chemical structure of PEMFC catalyst layers [49–52]. Based on these developments better optimization of the electrode structures to allow for sufficient catalyst utilization can be expected in the near future.

2.9 PERSPECTIVE

In summary, while PEMFCs are a very promising energy conversion technology whose deployment, particularly in the automotive sector, can bring substantial reductions to global CO_2 emissions, their widespread commercialization is hindered by barriers such as high cost and poor durability. Currently, PEMFCs are very expensive and suffer significant voltage losses during their life-times. Even the state-of-the-art fuel cells operate with only 0.6 - 0.8 V, while the equilibrium cell voltage is about 1.2 V. The biggest contributor to the voltage losses is the sluggish kinetics of the cathodic reaction, called the oxygen reduction reaction (ORR). Most PEMFCs rely on Pt or Pt-based catalysts to accelerate this reaction. Since Pt is expensive, the overall fuel cell cost remains significantly high, a problem which will only be exacerbated over time given that Pt is also a scarce resource. Additionally, the fuel cell environment is corrosive to catalysts and this imposes severe durability constraints. Therefore, fundamental research towards ORR catalyst development is imperative, dictated by performance, cost and durability considerations which all need to be satisfied simultaneously. This requires a mechanistic understanding of the ORR kinetics and the catalyst degradation pathways which are both discussed in the following chapter.

Part II

BACKGROUND

3

CONCEPTS IN DEVELOPMENT OF CATALYSTS FOR THE ORR

The previous chapter discussed the construction and operation of polymer electrolyte membrane fuel cells. More importantly, it highlighted that the development of suitable catalysts for the cathodic reaction (i.e., the oxygen reduction reaction (ORR)) is central to commercialization of PEMFCs. This requires fundamental research dictated by three important considerations- the catalytic performance, cost and durability. In the present chapter, we review the relevant background connected to understanding the kinetics of the ORR (Section 3.1), the available strategies to improve the ORR activity of Pt catalyst surface (e.g., alloying, modification to the surface-structure...) (Section 3.2), the different catalyst degradation mechanisms (e.g., ripening, coalescence, dissolution ...) (Section 3.3), and finally, the different characterization methods available to evaluate the performances of catalysts (Section 3.4), and also to investigate their structures (Section 3.5). Subsequently, in the next chapter a comprehensive review of over hundred different Pt-alloy nanocatalyst designs is presented.

3.1 KINETICS OF THE OXYGEN REDUCTION REACTION

In general, the electrochemical oxygen reduction reaction (ORR) is a complex process involving many intermediates and the transfer of one or more electrons. These depend on the electrode material, catalyst, and the electrolytes used [53]. For instance, Table 3.1 lists the typical ORR processes in both acidic and alkaline aqueous electrolytes, along with their standard electrode potentials and the number of electrons transferred [54]. Depending on the application, either of $1e^-$, $2e^-$or $4e^-$reduction pathways are preferred. For instance, in the case of PEMFCs a $4e^-$pathway is preferred, since the product formed is simply water. However, in the production of hydrogen peroxide on an industrial scale, a $2e^-$reduction pathway would be preferred.

ELECTROLYTE	ELECTRODE POTENTIAL (V)	ORR REACTIONS
Acidic (aq.)	1.229	$O_2 + 4H^+ + 4e^- \longrightarrow H_2O$
	0.70	$O_2 + 2H^+ + 2e^- \longrightarrow H_2O_2$
	1.76	$H_2O_2 + 2H^+ + 2e^- \longrightarrow 2\,H_2O$
Alkaline (aq.)	0.401	$O_2 + H_2O + 4e^- \longrightarrow 4OH^-$
	-0.065	$O_2 + H_2O + 2e^- \longrightarrow HO_2^- + OH^-$
	0.867	$HO_2^- + H_2O + 2e^- \longrightarrow 3\,OH^-$

Table 3.1: Different electrochemical ORR reactions and their electrode potentials. source: [54]

3.1.1 *ORR Mechanism on a pure Pt surface*

Oxygen reduction reaction on a Pt surface has been extensively studied from two different viewpoints – the heterogeneous catalysis (surface-ORR) viewpoint, and the electrocatalysis (electrochemical-ORR) viewpoint [54–62]. The distinction lies in the nature of the interface between the O_2 reactant and the Pt surface.

The surface-ORR involves adsorption of gas-phase O_2 onto the Pt catalyst surface, (i.e., gas-solid interface), whereas the electrochemical-ORR involves O_2 adsorption from an electrolyte onto the Pt electrode catalyst (i.e., liquid-solid interface). Although proposed mechanisms for both surface-ORR and electrochemical-ORR are analogous to one another, the calculated energy barriers and the rate limiting steps (i.e., the slowest reaction step) often differ. In the following discussions, emphasis is laid towards understanding the electrochemical-ORR, but some concepts derived from the surface-ORR is also utilized. Of particular use are the density functional theory (DFT) based calculations, called the *d*-band model [63–65], which relates the surface reactivity of metals to their electronic structure and strain.

Two mechanisms have been proposed for the electrochemical-ORR on Pt, namely the *dissociative mechanism* and the *associative mechanism*. It is important to note, however, that the ORR can be even more complex, as many different mechanistic pathways may be in play even on the idealized surfaces (e.g., Pt(111)). The operating environment in fuel cells with varying temperatures, pressures, pH and the electrode potential can further redirect the ORR mechanism in many other pathways [61]. To make the matters worse, the electrode surface may not be pure, but remain surface-oxidised in the potential range of ORR in PEMFCs [65] (discussed in Section 3.1.4). Nonetheless, the proposed mechanisms still

provide a basic understanding of the ORR. The two mechanisms are summarized in Figure 3.1, and are discussed as follows.

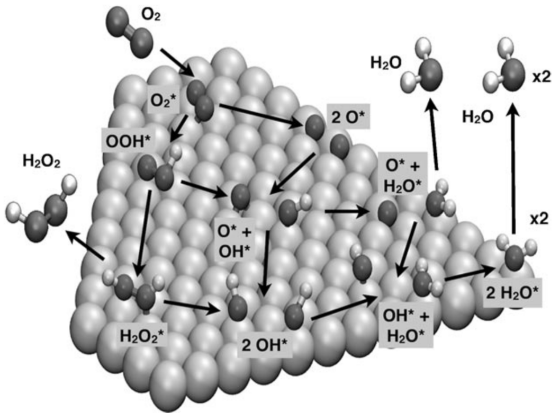

Figure 3.1: Schematic representation of the proposed ORR mechanisms on a Pt(111) surface. source: [62]

3.1.1.1 *Dissociative mechanism*

In the dissociative ORR mechanism, gaseous O_2 molecule chemisorbs onto a catalyst surface, forming two atomic oxygens from the dissociation of O-O bond. For an idealized Pt (111) surface, Keith *et al* [62] have proposed three different binding sites: bridge, fcc, and tilted, as illustrated in Figure 3.2. Of these the bridge site where the O-O bond lies along the bridge position between two surface Pt atoms is reportedly the most preferred site for adsorption.

$$O_2(g) + * \longrightarrow 2O^* \tag{3.1a}$$
$$O^* + H^+ + e^- \longrightarrow OH^* \quad \times 2 \tag{3.1b}$$
$$OH^* + H^+ + e^- \longrightarrow H_2O^* \quad \times 2 \tag{3.1c}$$
$$H_2O^* \longrightarrow H_2O(l) + * \quad \times 2 \tag{3.1d}$$

After the dissociation of O-O bond, the oxygen atoms (represented as O^*) covalently bind to the surface atoms of the catalyst substrate. Here the notation * indicates adsorption to a site located on the catalyst surface. Each of these atomic oxygens then react

with an incoming proton, and an electron, to form an oxygenated intermediate (OH^*). Finally, each OH^* intermediates thus formed, react with another proton and an electron, forming a H_2O^*. The H_2O^* then leaves the catalyst surface as a water molecule, which is the final reaction product according to the dissociative mechanism.

Overall, the dissociative ORR mechanism is a $4e^-$ reduction pathway. Also, since the O-O bond is broken (step(1.1a)), formation of hydrogen peroxide (H_2O_2) is restricted.

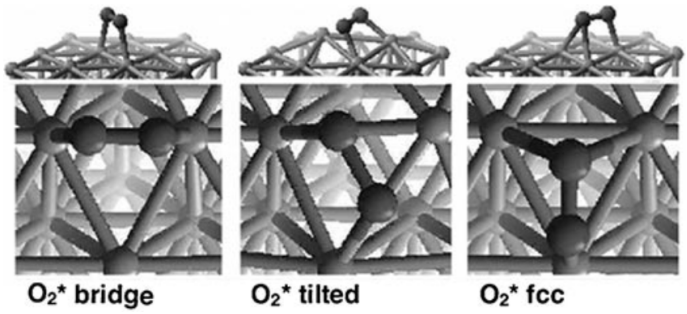

Figure 3.2: Schematic side-view (upper) and top-view (lower) representations of O_2dissociation at different binding sites on Pt(111) surface. source: [62]

3.1.1.2 *Associative mechanism*

In the associative ORR mechanism, a gaseous O_2 molecule chemisorbs onto a catalyst surface without the dissociation of O-O bond, represented as $O_2{}^*$. Similar to dissociative adsorption discussed earlier, the $O_2{}^*$ can be adsorbed at different sites (bridge, tilted or fcc). However, it is still unclear as to which of these sites is the most preferred, particularly under the operating conditions of a fuel cell.

$$O_2(g) + * \longrightarrow O_2^* \tag{3.2a}$$
$$O_2^* + H^+ + e^- \longrightarrow OOH^* \tag{3.2b}$$

The adsorbed $O_2{}^*$ intermediate reacts with an incoming proton and an electron, forming another intermediate (OOH^*), which is still adsorbed onto the catalyst site. In the subsequent steps, depending on whether or not the O-O maybe broken the formation of H_2O_2may or may not be possible. These two scenarios are discussed separately as the 1^{st} and 2^{nd} associative mechanisms.

In the 1st associative mechanism, the OOH^* intermediate further reacts with another proton and an electron. At this point, the O-O bond is broken, forming two intermediates O^* and H_2O^*. In the subsequent steps, O^* reacts with two protons and two electrons to form H_2O^*. Both the H_2O^* intermediates leave the catalyst surface as two water independent water molecules. Overall, this mechanism is a $2e^-$reduction pathway and does not form H_2O_2. These reaction steps are summarized as follows:

$$OOH^* + H^+ + e^- \longrightarrow H_2O + O^* \tag{3.3a}$$
$$O^* + H^+ + e^- + H_2O \longrightarrow OH^* + H_2O \tag{3.3b}$$
$$OH^* + H_2O^* + H^+ + e^- \longrightarrow 2H_2O(l) + * \tag{3.3c}$$

In the 2nd associative mechanism, the OOH^* intermediate further reacts with another proton and an electron, forming $H_2O_2{}^*$. The $H_2O_2{}^*$ can either be further reduced to H_2O, or be remain as the final product. These steps are summarized as follows:

$$OOH^* + H^+ + e^- \longrightarrow H_2O_2^* \tag{3.4a}$$
$$\tag{3.4b}$$
$$H_2O_2^* \longrightarrow H_2O_2 + * \tag{3.4c}$$
$$\tag{3.4d}$$
$$H_2O_2^* \longrightarrow 2\,OH^* \tag{3.4e}$$
$$OH^* + H^+ + e^- \longrightarrow H_2O^* \quad x\,2 \tag{3.4f}$$
$$H_2O^* \longrightarrow H_2O(l) + * \quad x\,2 \tag{3.4g}$$

3.1.1.3 *Rate-limiting step*

Both dissociative and associative mechanisms indicate that the ORR consists of multiple elementary reactions involving both electron transfer (e.g., redox process), as well as chemical steps (e.g., adsorption). Each of these elementary reaction steps has its own reaction rate, and an associated electrochemical current. This makes the deduction of overall ORR reaction rate a very complicated process. The problem is simplified by considering only the slow reaction steps (also called the 'rate-limiting steps') as pseudo-elementary

steps for kinetic modeling [61, 62]. In the discussions below, general approach to identify rate-limiting steps is first presented, followed by their kinetic modeling and formulations.

The rate-limiting steps for a given mechanism can be identified by plotting a potential free energy diagram for the reaction (i.e., 'ΔG (eV)' *vs* 'Reaction coordinate'). Several studies have used this approach to identify rate-limiting steps for associative and dissociative mechanisms, in both heterogenous gas-phase and electrochemical environments [61, 62, 65]. In this overview, potential free energy diagram for only the 1st associative mechanism is discussed.

Following reaction steps for the ORR is considered:

$$\boxed{\begin{aligned} O_2(g) + 4H^+ + 4e^- \overset{(1)}{\longleftrightarrow} OOH^* + 3H^+ + 3e^- \overset{(2)}{\longleftrightarrow} H_2O(l) + O^* + 2H^+ + 2e^- \\ \overset{(3)}{\longleftrightarrow} H_2O(l) + OH^* + H^+ + e^- \overset{(4)}{\longleftrightarrow} 2H_2O(l) \end{aligned}} \tag{3.5}$$

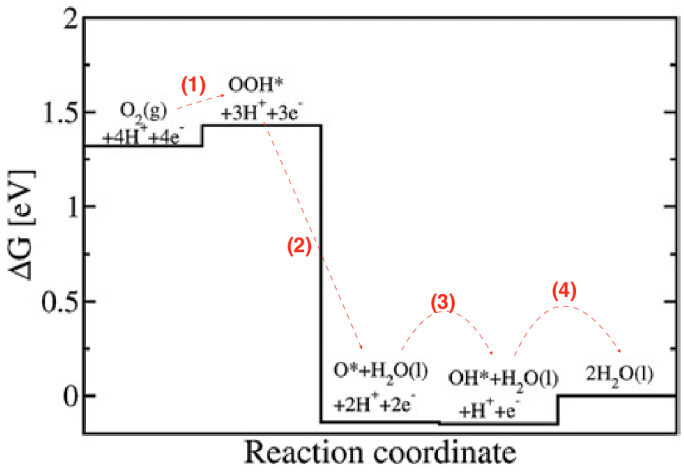

Figure 3.3: Calculated free energy diagram for reaction steps shown in Equation 3.5 assuming a Pt(111) surface at 0.9 V. source: [61]

Figure 3.3 shows the potential free energy diagram for each reaction steps (1) - (4) in Equation 3.5, as calculated by Rossmeisl *et al* [61] using a theoretical model for Pt(111) surface at 0.9 V. The plot illustrates both uphills and downhills in the free energy, the former referring to the difficulty for a particular elementary reaction to occur compared to the latter scenario. As can be seen, there are only two candidates for the rate-limiting step: formation of OOH^* (step(1)) and removal of OH^* (step(4)).

The first uphill corresponds to reaction step (1), wherein the gaseous oxygen is first adsorbed onto the catalyst surface, followed by subsequent protonation of an oxygen atom. This step would be rate-limiting if the oxygen adsorption is too weak, since for the subsequent protonation to occur the oxygen adsorption would be necessary. The second uphill corresponds to the reaction step (4), wherein a second protonation of OH^* occurs, followed by the subsequent desorption of the oxygen containing species (as water molecule). This step would be rate-limiting when the oxygen adsorption is too strong, since the oxygen containing species would then face difficulty in desorbing from the catalyst surface. Therefore, there are two distinct rate-limiting steps which are heavily dependent on the adsorption energy of oxygen to the catalyst surface.

3.1.2 *Relating ORR activity to the binding of the oxygenated intermediates*

The ideal catalyst is the one which finds a middle ground between the reactivities towards both oxygen bond-making and bond-breaking steps (steps(1, 4) in Equation 3.5). This requirement can be tested across different catalyst designs if the oxygen binding energy (ΔE_O) for these surfaces can all be known. The plot used for this purpose is popularly called the 'kinetic volcano', wherein the change in free energy for the ORR is plotted as function of oxygen binding energy (ΔE_O). An illustration comparing two catalysts, the bulk Pt(111) surface and the Pt_3Ni nanoparticles, was conducted by Rossmeisl *et al* [61], as shown in Figure 3.4.

Rossmeisl *et al*'s kinetic volcano in Figure 3.4 is based on the Sabatier principle [64, 65]. As per the Sabatier analysis, the reaction step with the most positive free energy change (ΔG) is the most difficult step along the ORR reaction. This follows from the fact that the rate of a reaction is proportional to exp(-ΔG).

For reaction steps (1)-(4), the Sabatier volcano for ORR is defined as:

$$\boxed{\Delta G(U) = Max[\Delta G_1(\Delta E_O, U), \Delta G_2(\Delta E_O, U), \Delta G_3(\Delta E_O, U), \Delta G_4(\Delta E_O, U)}} \tag{3.6}$$

Where U is the electrode potential, ΔG_{1-4} are the free energy change for the elementary reaction steps (1)-(4), and $\Delta G(U)$ is the most positive change in free energy along the ORR reaction.

To simplify, Rossmeisl *et al*'s analysis considers a special case when U = O, i.e., when $\Delta G = \Delta G_O$. Figure 3.4 shows the plot of ΔG_O as a function of ΔE_O. In agreement with

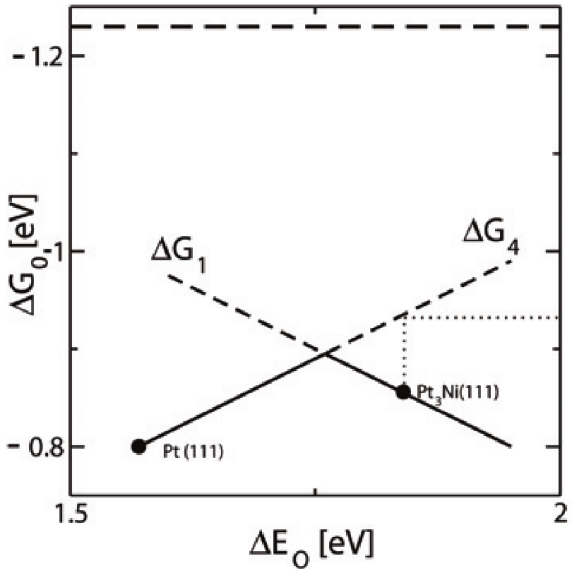

Figure 3.4: Plot of change in free energy (calculated at Potential U = O) as a function of oxygen binding energy $\Delta E_O$for reaction steps listed in Equation 3.5. source: [61]

the earlier analysis in Figure 3.3, it can be seen that it is either ΔG_1 or ΔG_4 that defines ΔG_O. The solid lines in Figure 3.4 mark the boundaries of 'kinetic volcano'. An ideal catalyst is the one positioned at the top of this volcano as it provides optimum binding for both ΔG_1 (formation of OOH^*) and ΔG_4 (removal of OH^*). The top of the volcano is also the position with least overpotential, as evidenced by measuring the distance from the solid volcano to the horizontal dashed line representing zero overpotential. Note also that the adsorption energy of all the intermediates of the ORR is linearly related to the adsorption energy of oxygen, thus ΔE_O is a good descriptor of binding for all the intermediates. Anywhere to the right of the top of volcano would be the region with weaker binding of intermediates, and to the left of this point would be the region where the binding is stronger.

Onto the kinetic volcano in Figure 3.4, the relative ORR activities for Pt(111) and Pt_3Ni catalysts measured as a function of $\Delta E_O$are superimposed.[1] The electrochemically determined activity ratio indicates that Pt_3Ni catalysts accelerate the ORR much faster than Pt(111) catalysts. This can be explained with the Sabatier model, by observing that the Pt_3Ni is much closer to the top of the volcano than Pt(111). In other words, the higher

[1] After converting the measured electrochemical currents into free energy ΔGvalues: 0.80 eV for Pt, 0.93 eV for Pt_3Ni

ORR activity of Pt_3Ni catalysts is a result of the better compromise between the binding to OOH and OH intermediates [61]. In contrast, Pt(111) binds these intermediates relatively more strongly.

Above analyses demonstrate that the theoretical models such as the potential free energy diagram, and the Sabatier kinetic volcano, can provide a good account of the different rate-limiting steps in the proposed ORR mechanisms, and how differently the catalyst surfaces react to them. In the following section, kinetic formulations used to determine the ORR activities of catalysts is discussed. Experimental procedure followed in practice to measure these quantities will be discussed later in Section 3.4.

3.1.3 *Kinetics formulations for the ORR*

For an ORR pseudo-elementary step (or the rate-limiting step) involving n electron transfer ($O + ne^- \Longleftrightarrow R$), the current-overpotential relationship for both forward and backward reactions is given by Butler-Volmer equation [54]:

$$\boxed{I_c = i^o_{O_2}\,(e^{n\alpha_o F\eta_c/RT} - e^{n(1-\alpha_o)F\eta_c/RT})} \tag{3.7}$$

Where, I_c is the ORR current density, $i^o_{O_2}$ is the exchange current density, α_o is the transfer coefficient, η_c is the ORR overpotential, F and R are the faraday and gas constants, T is the temperature.

At large overpotentials (η_c), the current for the backward reaction would be negligible. Thus, Equation 3.7 can be rewritten as:

$$\boxed{I_c = i^o_{O_2}\, e^{n\alpha_o F\eta_c/RT}} \tag{3.8}$$

It is desirable to obtain high current density at low overpotentials.

It is extremely desirable to obtain high current at low overpotential to have the ORR occurring at potentials not too far from the equilibrium. To achieve this, however, the exchange current density ($i^o_{O_2}$) should be large, and the factor ($RT/n\alpha_o F$) should be small. Since R, T and F are all known constants and the n is set for a given reaction pathway, the key parameters dictating the ORR current density are then the exchange current density ($i^o_{O_2}$) and the transfer coefficient (α_o).

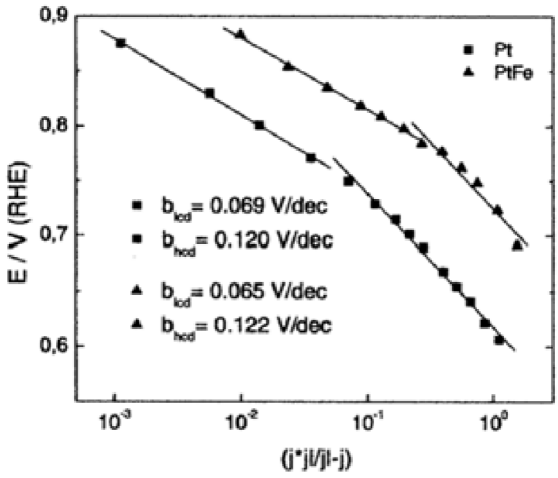

Figure 3.5: Tafel plots for ORR on two different catalysts Pt/C and Pt-Fe/C measured in 0.5 M H_2SO_4.; b_{lcd} and b_{hcd} indicate calculated Tafel slopes at low and high current densities, respectively. source: [54]

Sometimes a 'Tafel plot' is plotted to describe these dependencies. It is a plot of η_c *vs.* $\log(I_c)$ that gives a linear relationship, with slope = $2.303RT/\alpha_o nF$ and intercept = exchange current density ($i^o_{O_2}$). Figure 3.5 shows a typical Tafel plot for two different catalysts (Pt/C and Pt-Fe/C). The larger the Tafel slope is, the faster the overpotential varies with the change in current density. Therefore, for obtaining high currents at low overpotentials, smaller Tafel slope is always preferred, requiring a high transfer coefficient (α_o), and a large exchange current density ($i^o_{O_2}$).

To obtain high currents at low overpotentials, a high transfer coefficient and a large exchange current density is required.

The exchange current density ($i^o_{O_2}$) is an important kinetic parameter for any electrochemical reaction which represents reaction rate at the equilibrium. Under equilibrium, both forward and backward reactions proceed at the same rate, consequently their current densities are both equal, represented as the exchange current density. It is directly proportional to the standard rate constant (K^o), as given by:

$$\boxed{i^o_{O_2} = nFK^oC \qquad (where,\ C = C_O = C_R)} \tag{3.9}$$

Above expression indicates that the magnitude of the exchange current density signifies how fast the reactions can occur. The exchange current density is known to depend on the nature of the electrode surface, for e.g., Table 3.2 lists ORR exchange current densities on different electrode materials [54]. For the same reaction conditions, a pure Pt electrode surface seem to yield higher exchange current densities than a surface-oxidised

ELECTRODE MATERIAL	MEASURED AT	ORR EXCHANGE CURRENT DENSITY (A/cm²)
Pt	Pt/Nafion interface at 30 °C	2.8 x 10^{-7}
PtO/Pt	Pt/Nafion interface at 30 °C	1.7 x 10^{-10}
PtFe/C	0.1 M H_2SO_4 at 60 °C	2.15 x 10^{-7}

Table 3.2: ORR exchange current density for different electrode materials/catalyst surfaces. source: [54]

Pt electrode (PtO/Pt). From Equation 3.9, this means that the ORR kinetics on a pure Pt surface is much faster than a surface-oxidised Pt electrode. This illustrates the important role of electrode surfaces (or catalysts) to alter the ORR kinetics.

Similarly, the exchange current density (*via* the rate constant K^o in Equation 3.9) also depends on the type of the reation (i.e., mechanistic pathway), and the reaction temperature. The estimated rate constants for HOR on a Pt electrode is ~10 cm/s , whereas on the same surface the rate constant for the ORR is ~10^{-9} cm/s.

For a special case where the Pt surface is covered by hydroxyl impurities (OH) and their desorption is rate-limiting, the kinetic current density (I_c) has been proposed to be a function of the Gibbs energy of adsorption (ΔG_{ad}) [66], given by:

$$\boxed{I_c = nFKC(1-\Theta_{ad})^x \exp(-\beta FE/RT)\exp(-\gamma \Delta G_{ad}/RT)} \tag{3.10}$$

Any optimization done to the electrode (catalyst) surface structure (atomic/electronic) for delaying the adsorption of oxygenated intermediates will have a positive impact on the ORR activity

where, $n, F, K, x, \beta, \gamma$ and R are all constants, C is the concentration of molecular oxygen and Θ_{ad} is the fraction of the electrode surface sites covered by hydroxyl (OH) adsorbates. The equation suggests that any optimization done to the electrode surface structure (atomic/electronic) for delaying the adsorption of OH impurities (i.e., make Θ_{ad} smaller) will have a positive impact on the ORR activity (I_c).

Effect of temperature on the reaction kinetics

Both exchange current density and transfer coefficient are temperature dependent quantities. The exchange current density increases with the increasing temperature following Arrhenius equation given by:

$$\boxed{i^o_{O_2} = I^o_{O_2} \exp(-E_a/RT)} \tag{3.11}$$

where $I^o_{O_2}$ is the exchange current density at T = ∞, E_a = energy of activation.

The transfer coefficient (α_o) for a Pt electrode increases linearly with the temperature (T in Kelvin), following the equation:

$$\boxed{\alpha_o = \alpha_o^0 T} \tag{3.12}$$

where α_o^0 is a constant, equal to 0.001678.

From the above two expressions (Equation 3.11 and Equation 3.12), and from the Equation 3.9, it follows that a high ORR current density is expected at higher reaction temperatures. Consequently, the PEMFCs should also perform better at higher operating temperatures. For example, Figure 3.6 shows the measured polarization curves obtained for a fuel cell, at two different temperatures (23 °C and 80 °C). As can be seen, operation at 80 °C provides high current densities at low overpotentials compared to the operation at 23 °C. Unfortunately, the upper limit of the fuel cell operating temperature is usually set by the humidification needs of the membrane. This is beacause, operating at very high temperatures can result in poor ionic conductivity in the membrane from the evaporation of water. To avoid this, most PEMFCs operate within the temperature range of 80 °C – 120 °C.

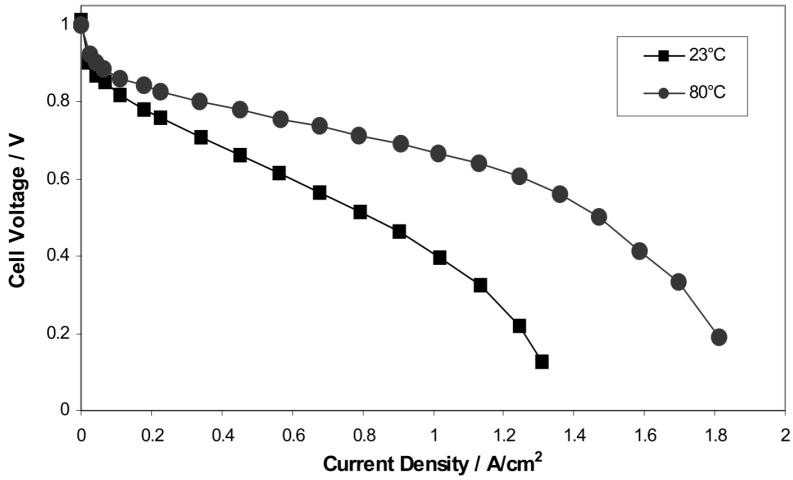

Figure 3.6: Measured polarization curves for a standard PEMFC operating at 23 °C and 80 °C. source: [54]

3.1.4 *Comment on the purity of Pt surface in the ORR potential range*

All the models and calculations discussed so far correspond to ORR on a pure Pt surface, free of any adsorbates and impurities. However, numerous studies have shown that within the potential range of ORR in PEMFC (i.e., 0.9 – 1.23 V), the Pt surface may not be pure, but instead remain surface-oxidised (a phenomenon called as 'Electro-oxidation' [62, 67–70]).

For a polycrystalline bulk Pt surface, Keith *et al* [62] have shown that the formation of adsorbed oxygen as a stable surface species (O^*) occurs in the potential range from 0.85 – 1.1 V. At potentials > 1.2 V, they observed formation of PtO surface compound comprising of Pt^{2+} and O^{2-}. Between 1.1 – 1.2 V, the Pt-O^* converted into PtO through a 'place exchange mechanism'.[2] In the case of Pt nanoparticle catalysts that are routinely used in PEMFCs, the said electro-oxidation is expected to occur at even lower potentials (< 0.85 V).

Allen *et al* and Winograd *et al* have used X-ray photoemission spectroscopy to determine PtO formation in the case of a smooth Pt foil dipped in an acid electrolyte at potentials > 2 V. The proposed general structure for electrooxidised Pt system is Pt | $PtO_{2\ ML}$ | $PtO_{2\ (n\ ML)}$, where 2 ML indicates that the PtO could be limited to ~2 monolayers, and n ML indicates the non-limiting thickness of PtO_2[10].

Pt surfaces may not be pure under the electrochemical environment in PEMFCs. ORR may not be occuring on a pure Pt surface

Figure 3.7 shows the potential diagram reported by Keith *et al* [62] that summarizes the regions where the Pt surface could be electrooxidised (i.e., form of PtO and PtO_2), in relation to the potential range relevant to the ORR. Noticeably, the PtO and PtO_2 onsets overlap with the ORR potential range (i.e., 0.9 – 1.23 V), indicating that the Pt electrode surfaces regardless of bulk or nanostructure could remain covered with a surface oxide layer. Hence, the proposed ORR mechanisms assuming a pure Pt surface may not be representative of the actual ORR taking place. Unfortunately, a much better picture of the electrochemical-ORR is not yet in sight.

[2] The place exchange mechanism refers to the migration of atomic-oxygen from the surface to subsurface positions at electrode potentials relevant to the ORR.

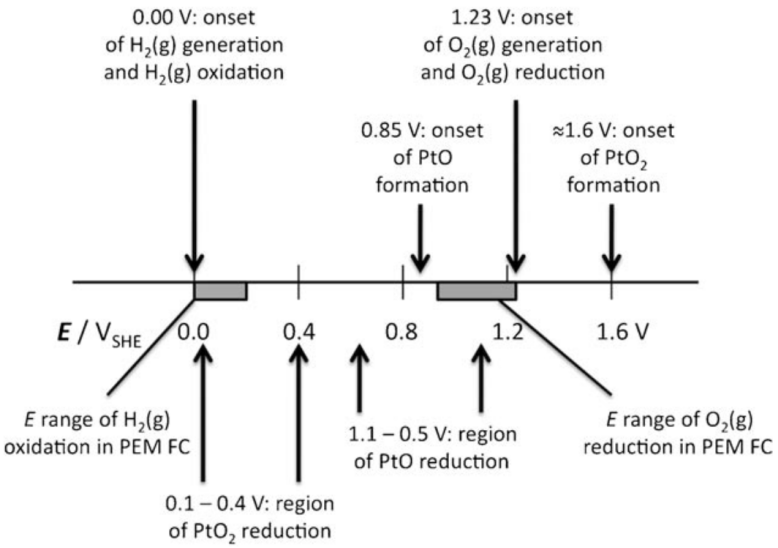

Figure 3.7: Potential diagram illustrating the potentials at which Pt surface can be electrooxidised (i.e., formation of PtO and PtO_2) in relation to the potential ranges for adsorption-desorption of O_2 and H_2 on a Pt surface. source: [62]

3.1.5 *Summary of concepts in the kinetics of ORR*

Although ORR kinetics can be improved by altering both the electrode surface (i.e., the catalyst surface), and the environmental factors (such as temperature), the latter option is more or less restricted in fuel cells. Therefore, finding a suitable electrode surface (or the catalyst) is arguably the only option available for improving the ORR kinetics in fuel cells. The kinetics of ORR has been studied on a variety of electrode surfaces over the years, and typically the Pt surfaces provide better ORR activities compared to most other metal surfaces. Ongoing efforts aim to further optimize the reactivity of Pt electrode surface [23]. Figure 3.8 lists some prominent approaches followed in this respect, which are classified into four broad categories: nanoparticles on low and high aspect ratio supports, unsupported nanoparticles and extended surface area catalysts. Each category is further subdivided based on their geometry, composition and the support material used. Given the scope of present thesis, only efforts pertaining to Pt-alloy nanoparticle designs will be reviewed. For a more comprehensive review of other catalysts designs, the reader is referred to the following articles [71–81], and the references listed particularly in the comprehensive review conduced by Debe [23].

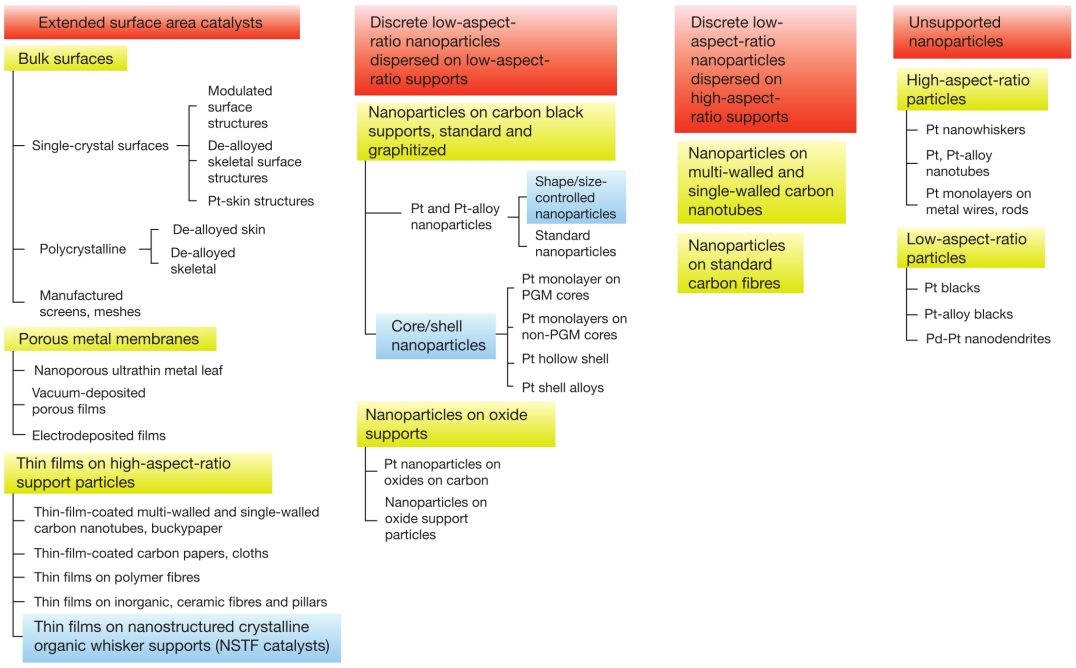

Figure 3.8: Summary of different approaches to optimization of Pt surface for improved ORR catalysis. source: [23]

3.2 FINE-TUNING PT SURFACE REACTIVITY WITH ALLOYING

Pt-alloy nanoparticles are well known for providing exceptional enhancements in the ORR activities compared to a pure Pt nanoparticle (reviewed in detail in Chapter 4). The basic strategy adopted by most Pt-alloy nanocatalyst designs is to fine tune the surface reactivity of Pt, such that the surface is neither too adsorbing nor too desorbing for oxygenated intermediates. Since the oxygen chemisorption on Pt is already very strong (discussed earlier in Figure 3.4), the objective is to further weaken the oxygen chemisorption on Pt. This is achievable by alloying Pt with suitable elements such that the electronic structure is modified [64]. In the following series of sections, this approach is discussed in detail. First, we discuss the factors that determine reactivity of a surface to an adsorbate.

3.2.1 *Factors determining surface reactivity*

In general, the transition metal surfaces are well known to catalysing a number of chemical reactions by bond-making and bond-breaking various atomic- or molecular adsorbates. The *d*-band model based on density functional theory (DFT) provides a semi-quantitative account of chemisorption of different adsorbates on different transition metal surfaces [63, 64, 82] (discussed later in the chapter). From the model calculations carried out over many different adsorbates, and on a variety of surfaces, it is realized that two factors control the reactivity of a surface. These are, (a) the electronic structure of the metal surface (termed as the 'electronic structure effect'), and (b) the atomic-structure of the catalyst surface (termed as the 'geometric effect'). Therefore, in order to fine-tune the reactivity of Pt surfaces, as required for an improved ORR catalysis, their electronic and surface atomic-structures need to be suitably optimized. This requires understanding the electronic states of transition metals (in this case, Pt), and the knowledge of their interactions with the electronic levels of atomic adsorbates (in this case, O_2).

3.2.2 *General remarks concerning metal-adsorbate electronic interaction*

The valence shell in most transition metals is composed of s-, p- and d- electron states. The d-electrons are more localized in comparison to the delocalized free-electron like s- and p-electrons. Consequently, the *d*-band in transition metal surfaces is much narrower compared to the broad s- and p- bands (see Figure 3.9a). During the bond formation, these metal bands interact with the electronic levels of the adatom.

The metal-adsorbate interaction in the transition metals is well described by the Newns-Anderson model. According to this model, the interaction strength between the adatom wave function of a specific electronic level, and the metal states, is denoted by a 'hopping matrix element' (V_{ad}), which is basically a Hamiltonian (H) of the combined system. For example, consider the coupling of a single valence state of an adsorbate adatom ($|a>$) of energy ε_a, with the metal d-electron state ($|d>$) of energy ε_d. The two metal-adsorbate electronic states are coupled by the hopping matrix element, given by:

$$\boxed{V_{ad} = <a|H|d>} \tag{3.13}$$

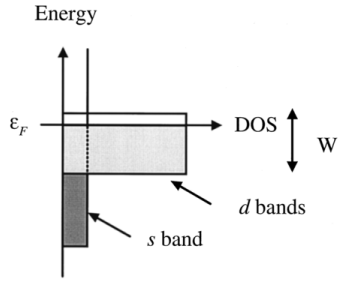

(a) Illustration of the typical density of states of a transition metal: broader *s* band and the narrower *d* band (width W) located around the (ε_F).

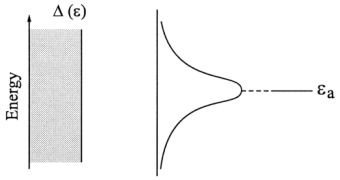

(b) Local density of states at an adsorbate when interacting with broader *s* band.

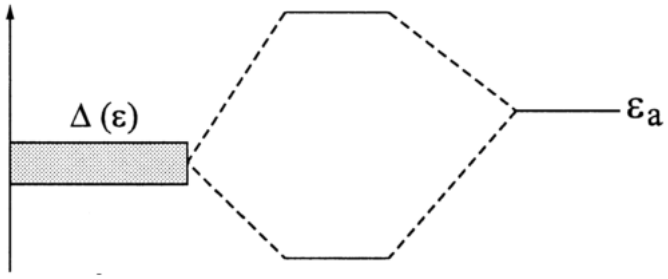

(c) Local density of states at an adsorbate interacting with narrower *d* band.

Figure 3.9: Schematic illustrations of density of states of a typical transition metal with/without adsorbate interaction. source: [63]

If the width of the metal band is much larger than the hopping matrix elements, then the metal-adsorbate interaction results in a broad resonance level of the projected states on the adatom. An example is illustrated in Figure 3.9b. This is usually the case upon interaction with the delocalized s- and p- electronic states. The bottom and the top of the resonance, with respect to the metal and the adatom levels, reflect more bonding and antibonding characters, respectively.

On the other hand, the V_{ad} coupling with much narrower bands, such as the *d*-bands, results in a strong resonance, accompanied by splitting of bonding and antibonding states into new distinct electronic levels, below and above the adatom level (see Figure 3.9c).

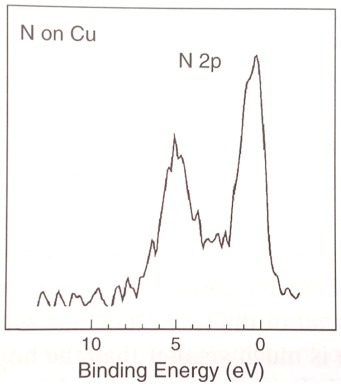

(a) XAS N-K emission spectra for N adsorption on Cu(100) surface.

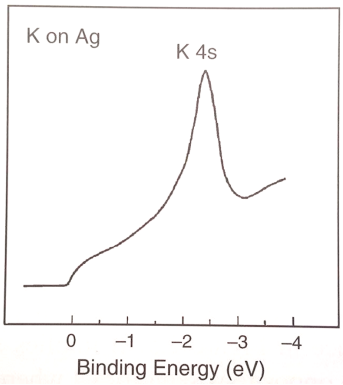

(b) XAS measurement of the projected K-4s states for K adsorbed on Ag(110).

Figure 3.10: Experimental validation of the theoretical view of the metal-adsorbate interactions. source: [63]

Figure 3.10 illustrates the experimental demonstration of these broad/narrow band interactions with adsorbates. X-ray absorption spectroscopy (XAS) measurements of:(1) N adsorbed on Cu(100) surface (Figure 3.10a), and (2) K adsorbed on Ag(110) (Figure 3.10b) are shown. Note that the valence band for Cu is a *d*-band, which is much narrower compared to the Ag sp- bands. Figure 3.10a measures the N-2p density of states, which is the projection of partial p-density of states onto the N-adatom. As can be seen, the atomic level is split into two distinct bonding and antibonding levels, with respect to the Cu *d*-band. This illustrates the case of stronger resonance resulting from the V_{ad} coupling with a narrow metal band (Cu *d*-band here). Figure 3.10b measures the projected K 4s states. Clearly, it is a broad asymmetric resonance which has resulted from the interaction with the delocalized Ag sp- electrons. This is representative of the case when the V_{ad} coupling is with broad metal bands (Ag s- and p- here).

To summarise the above discussion, the interaction of adsorbate electronic levels with the s- and p- states produces a broad resonance, while the interaction with d-states results in strong resonance, accompanied with the formation of two distinct bonding and antibonding states. Based on this foundational principle and with the aid of DFT to calculate electron-DOS, electronic interaction of an adsorbate on different pure- and alloyed-transition metal surfaces can be modeled. This is called as the '*d*-band model', which we discuss in the following section.

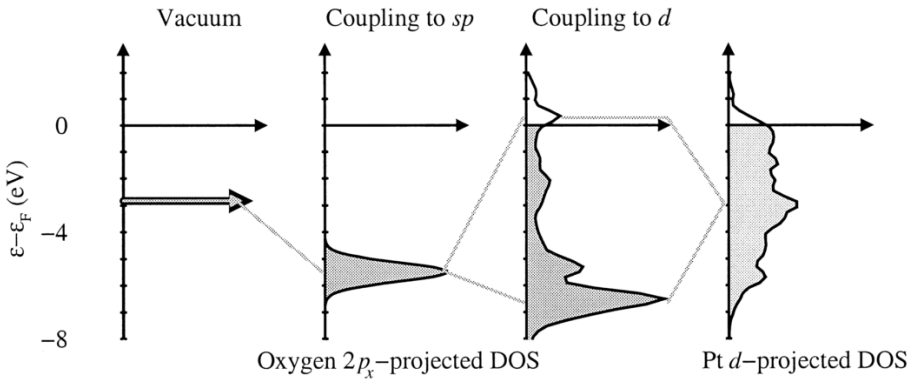

Figure 3.11: Modifications to the local electronic structure of the adsorbate (e.g., O_2) from the interaction with a transition metal surface (e.g., Pt). source: [63]

3.2.3 *Adsorbate on a transition metal: d-band model*

According to the Newns-Anderson view of metal-adsorbate electronic interaction, the interaction of an adatom with metal sp- states leads to broad resonance (large V_{ad} value), while the interaction with metal d- states leads to stronger resonance (small V_{ad}) forming distinct antibonding and bonding levels. Since the valence states of the transition metal surface atoms comprises of s- and d- electron states, the *d*-band model presents formation of a chemical bond as involving, first the coupling between adsorbate atomic-level to the metal s- states, followed by a coupling to the metal d-states. An example is illustrated in Figure 3.11. The adsorbate coupling to the metal s-band results in a broad resonance, and shift in the adsorbate state. Further interaction of this adsorbate state with the narrow metal *d*-states will lead to the formation of bonding and antibonding states.

Thus, the adsorption energy as per the *d*-band model can be written as:

$$\boxed{\Delta E = \Delta E_0 + \Delta E_d} \tag{3.14}$$

Where, ΔE_0 represents the contribution from interaction with the free-electron like sp-states. ΔE_d represents the contribution from interaction with the transition metal *d*-electron states.

The differences between the reactivity of different transition metal surfaces is due to d-bands alone

One assumption made by the '*d*-band model' is to consider ΔE_0 as being independent of the metal. The rationale behind this assumption is that since all the transition metals have a half-filled s- band, and moreover since the band is broad, the differences in

ΔE_0 from one transition metal to the next would be very small [63]. Consequently, it follows from Equation 3.14 that the differences between the reactivity of different transition metals is primarily due to the *d*-bands alone, which is represented by ΔE_d.

The *d*-band model provides a mathematical formulation for the estimation of ΔE_d, which is based on a rigorous treatment of Newns-Anderson model, and a 'chemisorption function' [82]. To present the mathematical procedure is beyond the scope of this overview, the intent here is rather, to develop a semi-quantitative understanding of the trends in surface reactivity for different metals. Ultimately, the *d*-band model spits out two important variables representing the electronic structures of metal and the adsorbate, denoted as $n_d(\varepsilon)$ and $n_a(\varepsilon)$.

$n_a(\varepsilon)$ represents the projection of the density of states on the adsorbate state, or simply called the adsorbate-projected DOS. $n_d(\varepsilon)$ represents the projection of the density of states on the metal state, or simply called the metal-projected DOS. Together $n_a(\varepsilon)$ and $n_d(\varepsilon)$ provides a good account of the electronic interactions between metal and the adsorbate, and when estimated for different transition metals, a comparative picture of their relative reactivities can therefore be established. These aspects are discussed as follows.

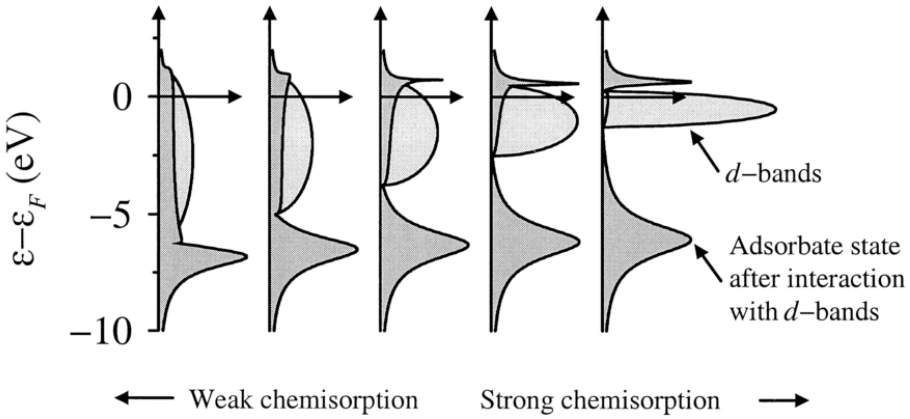

Figure 3.12: Modifications in the local electronic structure at an adsorbate corresponding to interactions with *d*-bands of different positions with respect to the Fermi level. Dark shaded areas indicate adsorbate projected DOS. Light shaded areas indicate metal d-projected DOS before adsorbate interaction. source: [63]

Metal and adsorbate projected density of states: ($n_d(\varepsilon)$ and $n_a(\varepsilon)$)

Figure 3.12 shows a model calculation of the metal- and adsorbate- projected density of states for the case, where a single adsorbate state is coupled with *d*-bands of varying positions with respect to the Fermi level. Since the number of *d* electrons for a given metal

must be conserved, the *d*-band center (ε_d), and the band-width (W), are both coupled. This means that if the band-width is shortened, the *d*-band center must shift up towards the Fermi level in order to compensate for the total number of *d*-electrons, and vice-versa.

As can be seen from Figure 3.12, when the *d*-band is low-lying and broad, i.e., ε_d is farther down from the Fermi level, only a single resonance can be seen at the bottom of the *d*-band. As the ε_d shifts up towards the Fermi level, a distinctive antibonding state appears above the metal *d*-band, in addition to the bonding state present at the bottom of the *d*-band.

Note that the strength of the bond formed (ΔE_d) is a function of the relative occupancies of these bonding and antibonding states. If only the bonding states are filled, the bond formed is stronger, in other words the chemisorption of the adsorbate is stronger. On the other hand, if the antibonding states are also filled, then the bond formed will be considerably weaker.

A downshift of the d-band center with respect to Fermi level results in weakening of the adsorbate chemisorption to the transition metal surface

In Figure 3.12, for the rightmost case when the *d*-band is most narrow, the antibonding state formed is above the Fermi level. Consequently, the bond formed with the adsorbate is strongest. As we start to move left, with the increasing downshift of the *d*-band center, the antibonding states formed start to become filled, consequently the strength of the bond formed gets increasingly weaker. Thus, the *d*-band model arrives at a very powerful conclusion that a downshift of the *d*-band center with respect to the Fermi level results in weakening of the adsorbate chemisorption to the transition metal surface.

3.2.4 *Trends in oxygen chemisorption over different metal surfaces*

Figure 3.13a shows a plot of experimentally determined ORR activity versus the shift in *d*-band center ($\varepsilon_d - \varepsilon_F$) for different catalytically important metal surfaces. This plot is popularly referred to as the 'Volcano plot', analogous to the 'Kinetic volcano' from the plot of free energy change *vs* oxygen binding energies discussed earlier in Section 3.1.2. For the sake of discussion, only the three metals from the extreme positions in the volcano are selected, namely the Gold (at the far left corner), Platinum (close to the top) and Ruthenium (far right corner). Below, we first understand the chemisorption of oxygen on these metals with the help of the *d*-band model, and we then relate the differences in their electronic interaction with oxygen adsorbate to their electrochemically measured ORR activities.

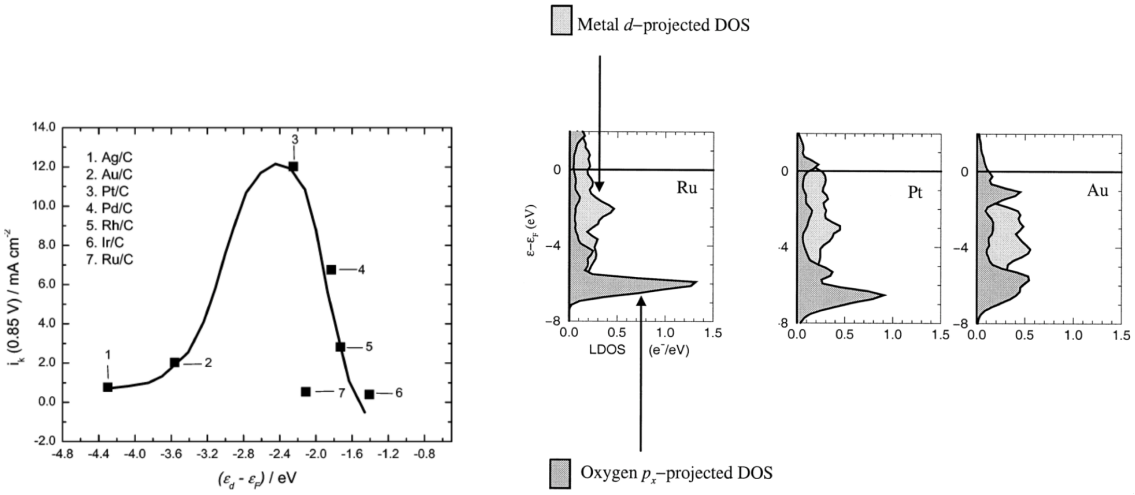

(a) Plot of experimentally determined ORR activity as a function of respective *d*-band centers ($\varepsilon_d - \varepsilon_F$) for notable metal surfaces

(b) Adsorbate- (O_2-p_x) and the metal- (*d*) projected density of states on Ru, Pt and Au metal surfaces.

Figure 3.13: Trends in oxygen chemisorption on different metal surfaces. source: [63]

Considering the case of oxygen chemisorption, Figure 3.13b shows the calculated oxygen p_x-projected DOS for the Au, Pt and Ru metal surfaces. Additionally, the respective metal d-states are also shown in the background. Examining the metal projected d-states in Figure 3.13b, it can be seen that as we move from Au to Ru the *d*-band moves up in energy. This is consistent with their relative positions of the *d*-band centers, following the order Au > Pt > Ru (see Figure 3.13a).

Upon coupling with the sp- electronic levels of oxygen, distinct trends in the occupancy of antibonding states can be observed. For Au, the antibonding states is completely filled, since the Au *d*-band is further below the Fermi level. As we move to Pt and Ru, the antibonding states become depopulated, increasingly so for the Ru metal than Pt. Consequently, the oxygen chemisorption on these surfaces is: strongest on Ru, weakest on Au and optimum on Pt (follows from the *d*-band model Section 3.2.3).

Since an optimum binding of the oxygenated intermediates is what is most preferred for an ORR catalyst (discussed in Section 3.1.2), both Ru and Au are expected to perform poorly towards ORR compared to Pt. In agreement with these model predictions, the measured ORR activity for Pt is the highest compared to most metals (see Figure 3.13a).

This demonstrates the effectiveness of the *d*-band model as a customary tool for screening different metals towards ORR electrocatalysis.

Using the foundational principles discussed above, the effect of alloying on Pt reactivity to oxygen chemisorption can also be understood, which we discuss in the following section.

3.2.5 *Tuning the surface reactivity of Pt with alloying*

As discussed in the preceding section, the oxygen chemisorption on Pt (as with all the transition metals) is heavily dependent on the position of its *d*-band center with respect to the Fermi level. Shifting the *d*-band center further below the Fermi level can weaken its reactivity, and vice-versa. To meet the objective of improving the ORR activity, however, a further weakening of Pt surface reactivity is what is desirable. Therefore, strategies to downshift the Pt *d*-band center are most sought after.

Note that a change in the width of the *d*-band for a fixed *d*-band center should change the number of d-electrons. However, the number of d-electrons for a given metal is fixed [64]. Thus, a change in the bandwidth would be compensated by the shift in the *d*-band center. The *d*-band center shifts up when the bandwidth is shortened, and for the broadening of the band, the *d*-band center shifts down. An illustration for the case of shortening of the *d*-band width is shown in Figure 3.14. Therefore, to weaken reactivity of Pt, the bandwidth (W) must be increased.

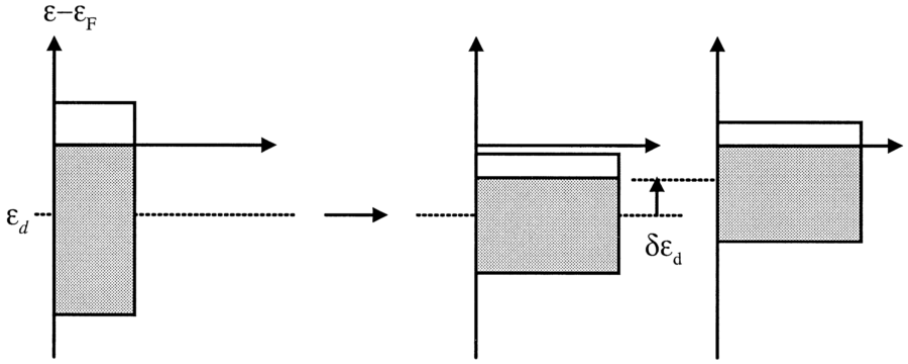

Figure 3.14: Schematic illustration of the effect of shortening the *d*-band width (e.g., by tensile strain) on the position of the *d*-band center. source: [63]

The bandwidth (W) can be altered by two ways. First approach involves, modifying the surface structure, i.e., by increasing or decreasing the number of metal neighbours, N_M, since $W \sim N_M^{0.5}$. Second approach relies on straining the surface layer (i.e., increasing or decreasing the distance, d, between the surface Pt atoms) which modifies the coupling, V_{dd} ($\alpha\ 1/d^5$) of the metal d-states to the neighbours, and the $W \sim |V_{dd}|$ [64, 82]. Former strategy is called the 'geometric effect', the latter is called the 'electronic structure effect'. Although both are mutually interdependent, for the sake of discussion only, these two effects are usually treated as having independent effect on the surface reactivities.

Both effects are discussed below, but more emphasis is laid towards discussing the 'electronic structure effect', which is usually achievable from the compositional variations induced by alloying.

3.2.5.1 *Geometric effect*

For a given transition metal, the d-band width (hence, the d-band center) depends on the coordination number of the metal atoms. The d-band model calculations suggest a direct proportionality, $W \sim N_M^{0.5}$ [82]. Consider for instance the Pt metal surfaces. The coordination number for atoms in a close-packed Pt(111) surface is 9, for those at a step (e.g., (211)) is 7, and at a kink (e.g., (1185)) is as low as 6. Figure 3.15a shows the calculated metal projected density of states for these surfaces. As can be seen, the decreasing coordination number can result in a up-shift of the d-band center, by almost 1 eV, between the Pt-(111) and Pt-kink surfaces.

Figure 3.15b shows the calculated chemisorption energies for CO on these surfaces. It can be seen that the CO-adsorption is much stronger on a Pt-kink surface compared to that on a close packed Pt-(111) surface. In other words, the low-coordinated atoms at the kinks/steps bind the adsorbate stronger than the atoms on flat surfaces.

Similar trends have also been observed for different atomic- and molecular- adsorbates on various metal surfaces [82]. Note that the correlation between the coordination number and the shift in the d-band center is independent of the substrate, this demonstrates the generality of the d-band model. Thus, for a weaker chemisorption of oxygen on Pt, flat Pt-surfaces is preferred over steps/kinks, and among the many different flat Pt-surfaces (Pt-(111), Pt-(100) etc. . .), the surface with higher coordination number is more preferred, e.g. Pt-(111) ($N_M = 9$) over Pt-(100) ($N_M = 8$).

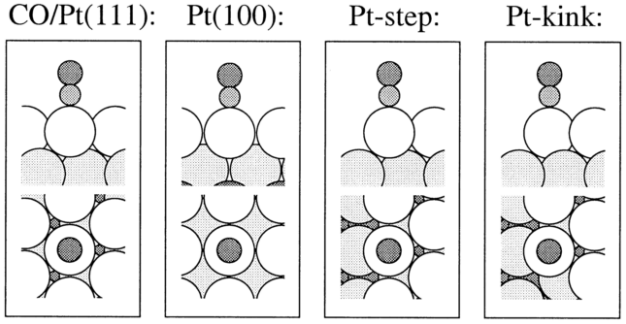

(a) Schematic illustration of a CO molecule chemisorbed on Pt(111), Pt(100), Pt-step and Pt-kink surfaces.

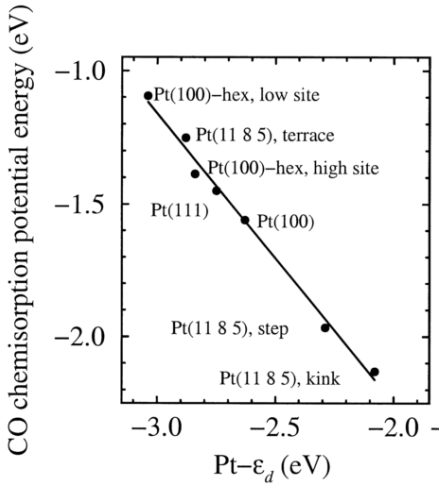

(b) Calculated chemisorption energy for CO on different Pt metal surfaces differing in the co-ordination number.

Figure 3.15: Illustration of the 'geometric effect' on the reactivity of surfaces. source: [63]

3.2.5.2 *Electronic structure effect*

The electronic structure effect originates from the changes to the electronic structure of the metal surface atoms. When a transition metal surface is strained, either compressive (decrease in interatomic distance, d) or tensile (increase in d), the overlap of metal d-states, denoted as V_{ij}, will either increase or decrease near the strained site.

The overlap matrix element for d-orbital interactions of atom i with neighbouring atoms j, V_{ij}, at interatomic distances d_{ij}, is given by the 'tight-binding model' [63] as:

$$V_{ij}(d_{ij}) = (\hbar^2/2\pi m e^-) \sum_{j=1}^{NN} [r_d^i \, r_d^j]^{3/2} / d_{ij}^5 \tag{3.15}$$

Where $r_d^i \; r_d^j$ are element-specific tight-binding constants.

To weaken the chemisorption of Pt, the Pt metal surface needs to be compressively strained

Since the d-band width (W) is related to the matrix element as $W \sim |V_{ij}|$, straining the metal surface will change the bandwidth. As discussed earlier, this change in bandwidth will then be compensated by the up/down shift of d-band center to conserve the number

of *d*-electrons (Figure 3.14). In general, compressive strain results in a downshift of the *d*-band center, while a tensile strain upshifts the *d*-band center. This is commonly termed as the 'strain effect'. Therefore, to weaken the chemisorption of Pt, the Pt metal surface needs to be compressively strained, which can be easily achieved by alloying Pt with suitable metals, and in different structural arrangements, discussed as below.

3.2.5.3 *Different ways of alloying Pt to improve activity*

Preceding section demonstrated that a compressive strain on the Pt metal surface can weaken the chemisorption of oxygen, and is therefore very desirable for an improved ORR electrocatalysis.

In general, introducing strain in a metal can be achieved by alloying (i.e., mixing of dissimilar metals), as dictated by Vegard's law. With respect to Pt, alloying with atoms much smaller than Pt, such as Fe, Co or Ni, introduces a compressive strain in the Pt lattice. The alloying elements can be introduced in three forms: sub-surface alloying, as overlayers and bulk alloying [82]. The effect of alloying on the surface reactivity in each of these cases is different. Ultimately, the practical feasibility of these alloys is dictated by % activity enhancement that is achievable, and also the cost and durability considerations. The three alloying strategies noted above are discussed below, highlighting the effects they have on the surface reactivity. Intention here is to rather point out the different ways in which the Pt electronic structure can be modified from alloying.

In the case of sub-surface alloying (also called 'near surface alloys' or 'skins'), the alloying metal atoms are introduced in the sub-surface regions of the primary metal, sandwiched between the first and second layers. For such sub-surface alloys, the shift in the position of the *d*-band center is attributed to the hybridization between the *d*-states of the surface Pt atoms and the alloy metal atoms in the second layer [82]. The electronic structure modification resulting from such an indirect interaction is termed as the 'ligand effect'.[3]

Another way of compressive alloying is to deposit an overlayer of one metal over the other. In such alloys, in addition to the 'ligand effect' from the sub-surface alloying, there is also the 'strain effect', since the overlayer usually takes the lattice constant of the substrate. Figure 3.16a shows the tabulation of the DFT estimation of the shift in the *d*-band center caused due to different overlayers on various metal surfaces.

[3]The alloying metal atoms are being referred to as the 'ligands' to the surface Pt atoms, which in the case of sub-surface alloying are 'dissimilar', resulting in the 'ligand effect'.

	Fe	Co	Ni	Cu	Ru	Rh	Pd	Ag	Ir	Pt	Au
Fe	**−0.92**	0.05	−0.20	−0.13	−0.29	−0.54	−1.24	−0.83	−0.36	−1.09	−1.42
		0.14	−0.04	−0.05	−0.73	−0.72	−1.32	−1.25	−0.95	−1.48	−2.19
Co	0.01	**−1.17**	−0.28	−0.16	−0.24	−0.58	−1.37	−0.91	−0.36	−1.19	−1.56
	−0.01		−0.20	−0.06	−0.70	−0.95	−1.65	−1.36	−1.09	−1.89	−2.39
Ni	0.09	0.19	**−1.29**	0.19	−0.14	−0.31	−0.97	−0.53	−0.14	−0.80	−1.13
	0.96	0.11		0.12	−0.63	−0.74	−1.32	−1.14	−0.86	−1.53	−2.10
Cu	0.56	0.60	0.27	**−2.67**	0.58	0.32	−0.64	−0.70	0.58	−0.33	−1.09
	0.25	0.38	0.18		−0.22	−0.27	−1.04	−1.21	−0.32	−1.15	−1.96
Ru	0.21	0.26	0.01	0.12	**−1.41**	−0.17	−0.82	−0.27	0.02	−0.62	−0.84
	0.30	0.37	0.29	0.30		−0.12	−0.47	−0.40	−0.13	−0.61	−0.86
Rh	0.24	0.34	0.16	0.44	0.04	**−1.73**	−0.54	0.07	0.17	−0.35	−0.49
	0.31	0.41	0.34	0.22	0.03		−0.39	−0.08	0.03	−0.45	−0.57
Pd	0.37	0.54	0.50	0.94	0.24	0.36	**−1.83**	0.59	0.53	0.19	0.17
	0.36	0.54	0.54	0.80	−0.11	0.25		0.15	0.31	0.04	−0.14
Ag	0.72	0.84	0.67	0.47	0.84	0.86	0.14	**−4.30**	1.14	0.50	−0.15
	0.55	0.74	0.68	0.62	0.50	0.67	0.27		0.80	0.37	−0.21
Ir	0.21	0.27	0.05	0.21	0.09	−0.15	−0.73	−0.13	**−2.11**	−0.56	−0.74
	0.33	0.40	0.33	0.56	−0.01	−0.03	−0.42	−0.09		−0.49	−0.59
Pt	0.33	0.48	0.40	0.72	0.14	0.23	−0.17	0.44	0.38	**−2.25**	−0.05
	0.35	0.53	0.54	0.78	0.12	0.24	0.02	0.19	0.29		−0.08
Au	0.63	0.77	0.63	0.55	0.70	0.75	0.17	0.21	0.98	0.46	**−3.56**
	0.53	0.74	0.71	0.70	0.47	0.67	0.35	0.12	0.79	0.43	

(a) Shift in the *d*-band center caused due to different overlayers. (Vertical axis: host metal, horizontal: overlayer.

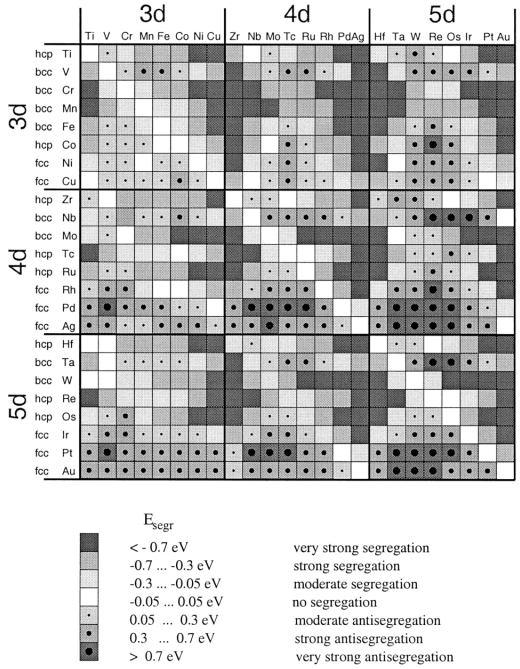

(b) Segregation tendencies of different metals in various bimetallic alloy systems. (Vertical axis: host metal, horizontal: alloy metal.)

Figure 3.16: Illustration of different types of alloying, and the associated electronic structure modifications. source: [63]

Similar electronic effects can also be observed from the 'bulk alloying', which is to form a thermodynamically stable alloy phase by mixing two or more metals at a particular composition. Depending on the number of metals, these bulk alloys can be binary (2), ternary (3), etc.... The effect of alloying in these bulk alloys may be indirect, unless one of the alloy elements segregates to the surface. The segregation tendencies of different metals can be calculated using DFT [63]. As illustrated in Figure 3.16b the calculated segregation tendencies vary from one transition metal to the other. In this case, the effect of alloying can be understood as a combination of 'strain' and the 'ligand' effects. Strain effect would be more dominant when the difference in the lattice parameters of alloying components is large, and the composition of alloying element with the smallest lattice constant is high. The ligand effect is expected to be more dominant when the segregated element forms a thin shell (few monolayers) or a 'skin' (monolayer).

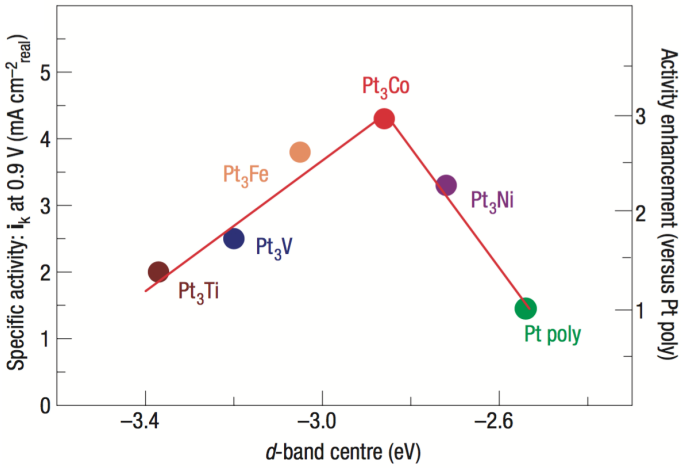

Figure 3.17: Plot of experimentally determined ORR activities for notable 3*d* transition metals as a function of their positions of the *d*-band center with respect to Fermi level. source: [83]

Typically for the ORR in PEMFCs, alloys of Pt with 3*d* transition metals are considered. For e.g., Pt_3Fe, Pt_3Ni, Pt_3Co, PtFe, PtNi, etc.... DFT calculations indicate a greater tendency for the Pt metal to surface-segregate in these alloys. As illustrated in Figure 3.17 for Fe, Co, Ni, V and Ti, the effect of alloying is to downshift the *d*-band center of Pt in the order Pt_3Ti > Pt_3V > Pt_3Fe > Pt_3Co > Pt_3Ni. Consequently, the chemisorption of oxygen on such Pt-alloys is much weaker compared to Pt metal surface.

Also shown on the vertical axis in Figure 3.17 are the measured ORR activities. Evidently, all the Pt-alloys show higher ORR activities compared to Pt-poly surface. Interestingly, despite the highest downshift in the *d*-band center for Pt_3Ti, the activity enhancement of Pt from alloying with Ti is negligibly small. This illustrates that there is a limit beyond which a further downshift in the *d*-band center would be undesirable for the ORR.

Note that the plot shown in Figure 3.17 is a 'volcano plot', similar to the ones discussed previously (Section 3.1.2 and Section 3.1.4). The ideal ORR catalyst is positioned at the top of the volcano, and the corresponding downshift in the *d*-band center would be the optimum for catalysing all the elementary steps involved in the ORR. All the Pt-alloy catalyst designs aim to reach the top of the volcano, and with every major breakthrough, the top of the volcano itself is constantly changing. A comprehensive review of recent progress in the development of different Pt-alloy catalysts is presented in Chapter 4.

3.2.6 *Summary of concepts in fine-tuning Pt surface reactivity*

The *d*-band model and DFT calculations are together, an excellent tool for understanding catalysis on transition metal surfaces, providing reliable semi-quantitative predictions of their surface reactivities towards many atomic- and molecular- adsorbates. Particularly in the development of ORR catalysts, the *d*-band model relates the measured ORR activities for almost any surface (pure or alloy) to its electronic and surface structures. Thus, with suitable optimization of these factors an improved ORR activity can be realized.

Although a pure Pt surface already provides an improved ORR activity compared to most other metal surfaces, the ORR kinetics is still sluggish. DFT calculations show that the chemisorption of oxygen on Pt is strong. Present catalyst developments therefore aim to further weaken the reactivity of Pt. Again, the *d*-band model and DFT calculations are a useful repository for such information. The model calculations suggest that the reactivity of a Pt surface can be weakened either by modifying its surface structure ('geometric effect') and/or by downshifting its *d*-band center ('electronic structure effect'). The *d*-band center of Pt can be shifted further down by inducing a compressive strain on Pt surface, which is achievable with alloying. Typically, 3*d* transition metals are preferred for alloying partly because they are much cheaper compared to other 4*d* and 5*d* transition metals. The *d*-band model calculations show that such Pt-alloys are better optimized for the ORR compared to pure Pt metal surface. Aided by these predictions, there is currently a tremendous research directed towards synthesizing different kinds of Pt-alloy nanoparticles, and testing them to determine ORR reactive under electrochemical environments. These efforts are reviewed in Chapter 4. Since the catalytic durability is also a major consideration in designing these catalysts, common degradation mechanisms affecting the catalyst performance are first reviewed in the following section.

3.3 CATALYST DEGRADATION MECHANISMS

Apart from the performance and cost criteria, one other key factor determining the effectiveness of a ORR catalyst is its durability, i.e. the longevity of catalytic activity under both steady state and voltage-cycling (or load-cycling) conditions [84]. Unfortunately, most current catalyst designs are still short of the 5000 hour durability target (or 10000 continuous potential cycling in CVs, Section 3.4) that is required to compete against the viability of internal combustion engines [23]. This is because, the fuel cell cathode environment is inherently very corrosive with conditions such as high humidity, acidic environment and the hundreds of thousands of transient potential cycles during their lifetimes. As a result, catalysts suffer from severe surface area losses (illustrated in Figure 3.18a), proposed to mainly occur by four degradation mechanisms: (1) Ostwald ripening, (2) Coalescence, (3) dissolution and precipitation in the ionomer/membrane, and (4) detachment of particles from the support [85–87].

Using a range of characterization techniques (diffraction studies, spectroscopy and electron microscopy) many experimental studies have supported the proposed mechanisms listed above, as being responsible for catalyst surface area losses seen in PEMFCs (Pt/C: [85, 87], Pt-alloy/C: [87–91]). Some of these observations include: (1) demonstrating that the surface area loss is dependent on the potential to which the cathode is exposed, severe at high potentials and accelerated by voltage cycling (Figure 3.18a), (2) mass loss of Pt and transition metals from the cathodes (Figure 3.18b), and detection of large Pt or transition-metal crystallites close to the cathode-membrane interface (Figure 3.18b – inset), (3) changes in the size-distributions and morphology (Figure 3.18c), and composition (for Pt-alloys, Figure 3.18d) of catalysts.

The four degradation mechanisms mentioned above are depicted schematically in Figure 3.19, and are discussed as follows.

3.3.1 *Ostwald ripening*

Ostwald ripening is a common phenomenon that occurs during the growth, stabilization and phase transformations of ensembles of atomic- and molecular- clusters with broad size distributions [92]. It involves transportation of atoms or molecules from small clusters onto the larger ones, driven by the reduction in their surface energies. Thus, the larger clusters grow at the expense of smaller ones.

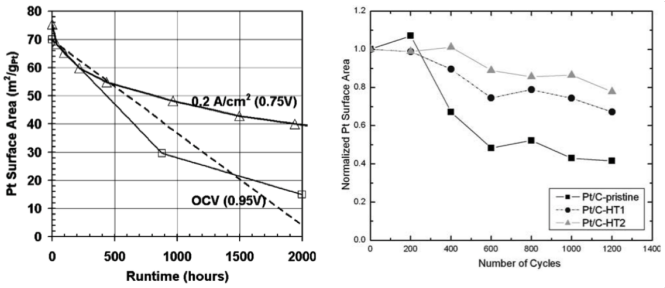

(a) Loss of Pt surface area during MEA operation (left) and potential cycling (right)

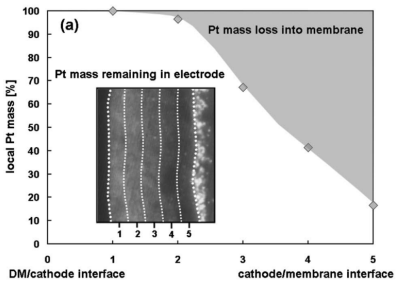

(b) Mass loss across DM - cathode - membrane interface.

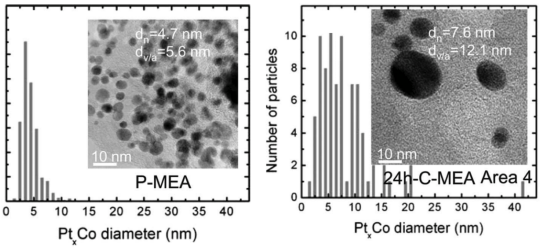

(c) Changes in surface morphology before and after 24-h MEA testing.

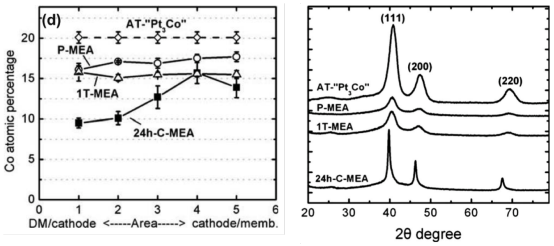

(d) Variation in Co composition in Pt_3Co embedded catalyst layers.

Figure 3.18: Experimental evidences for catalyst degradation. P-MEA: Pristine MEA, 1T-MEA: MEA after 1 fuel cell performance test, 24h-MEA: MEA after 24 hour extensive testing. sources: [85, 86]

In the fuel cell catalyst layers, Ostwald ripening is proposed to involve following three steps [85]: dissolution of surface atoms from the small particles ($Pt \longrightarrow Pt^{x+} + xe^-$), diffusion of soluble species (i.e., Pt^{x+}) into the ionomer phase, and finally, the redeposition of these dissolved species onto the larger particles ($Pt^{x+} + xe^- \longrightarrow Pt$). The entire process is illustrated in Figure 3.19*(a)*.

Usually, an extended tail in the smaller particle size ranges of a size-distribution profile is considered to be a characteristic of the ripening process [93]. The growth rate of particles from ripening can be modeled using classical mean-field theory (also called, Lifshitz-Slyozov-Wagner (LSW) theory) or other molecular theories [93–95]. Since the surface area to volume ratio of smaller clusters is greater than that of larger clusters, decline in the population of small clusters due to ripening, results in the loss of surface area available for catalysis (also called, the electrochemical /electroactive surface area) [85]. Ferreira *et al* [87] have previously shown that the ripening process is likely to be more

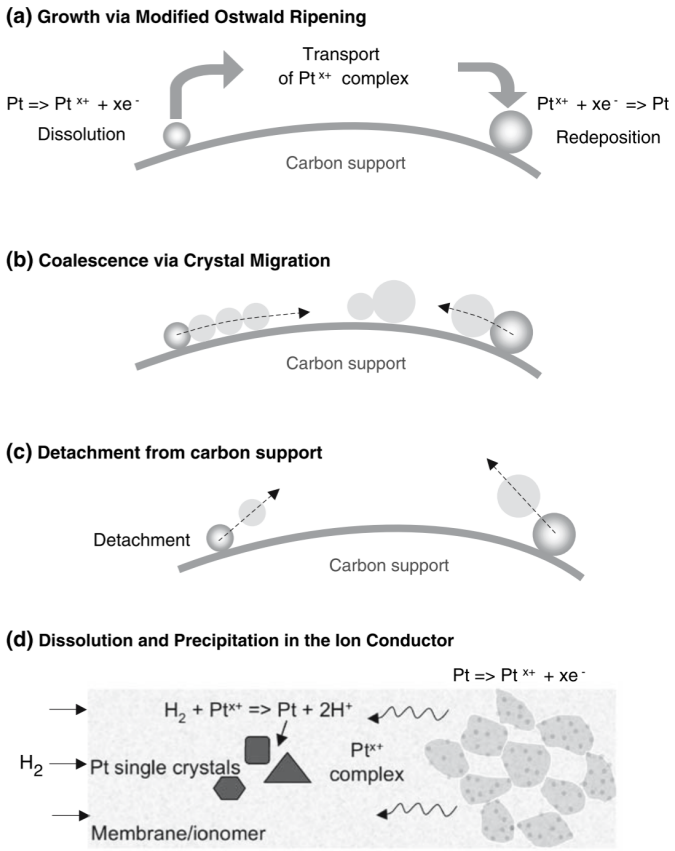

Figure 3.19: Schematic illustrations of different proposed mechanisms for catalyst degradation in PEMFCs. source: [85]

dominant at potentials where the solubility of Pt and the metal species is high, typically $> 0.8\ V$.

3.3.2 *Coalescence*

Coalescence refers to the merging of two or more atomic-/molecular- clusters *via* migration on the support (Figure 3.19*(b)*). It is a common phenomenon in the gas-phase heat treatments of clusters, usually termed as 'sintering' [96, 97]. In the case of fuel cell cathodes, coalescence occurs in the liquid phase, especially at low cell voltages where the solubility of Pt or transition metals is negligible (typically < 0.7 V for Pt) [85]. Various factors may be responsible for coalescence, such as the reduction in the surface energy,

close proximity to other clusters (i.e., high catalyst loading) and the localized corrosion of carbon support, which can all weaken the attachment of catalysts to the substrate, thus resulting in migration of the particle and coalescence with other neighbouring particles. A much closer look at the mobility of particles (specifically, Pt/C catalysts) on the carbon support was taken by Shao-Horn *et al* [85] who found that for a given catalyst loading, the Pt-carbon interactions is more likely to be the dominant factor for particle migration. In their hypothesis, Pt is said to have been 'trapped' at the defect sites such as steps/edges in the carbon structure. The authors expect that a reduction in the 'trapping barrier', for e.g. from the binding of ions in the electrolyte, can then lead to enhanced mobility of particles, consequently resulting in a high rate of coalescence.

3.3.3 *Dissolution and precipitation in the ionomer/membrane*

Many analytical measurements confirm a finite solubility of Pt in the potential range and operating temperatures of PEMFCs [85–87, 98]. In general, the concentration of soluble Pt is found to increase with increasing voltages up to 1.1 V, and then decrease following the formation of a protective PtO_x surface layer [62, 98].

In contrast to Pt, the transition metals easily dissolve in dilute acid electrolytes, as demonstrated by the ion scattering [99] , X-ray diffraction [99, 100] and electron spectromicroscopic studies [89] of many Pt-transition-metal alloy (bulk and nano) catalysts. This creates durability issues for the use of Pt-alloy/C particles as ORR catalysts, since the dissolution of Pt from the surface layers can expose the transition metals lying underneath, resulting in further dissolution of the alloying elements [101].[4] The transition-metal dissolution is usually called as 'leaching' to show equivalence between *ex situ* acid leaching under potentiometric conditions, and *in situ* catalyst aging in PEMFCs [88, 102]. Although detrimental to the catalytic durability, the potentiometric leaching process underpins the development of an entire class of catalysts, called the *dealloyed catalysts*, which are synthesized by voltammetric dealloying (i.e., leaching) of unwanted metal atoms from the regular alloy Pt-alloys [103–105] (see Section 4.2.1 for a detailed discussion).

The dissolved Pt^{x+} and M^{x+} (M: transition metal) in PEMFCs can result in the loss of catalyst surface-area in two forms, first *via* ripening (discussed in Section 3.3.1), and second, by precipitation in the ionomer and the membrane. The precipitation/redeposition process is proposed to involve a chemical reduction in the case of Pt^{x+} ($Pt^{x+} + xe^- \longrightarrow$

[4] see Section 4.2.4 for mechanistic description of leaching in core-shell catalysts.

Pt) species, and in the case of transition metal species M^{x+} an ion-exchange with the ionomer phase [85, 86]. The chemical reduction of Pt^{x+} to Pt is proposed to result from the presence of hydrogen molecules, which in most cases permeate through the proton-conducting membranes from the anode. Ferreira *et al* [87] estimated the flux of Pt^{x+} species dissolving from the platinum particles $N_{Pt^{x+}}$, using a simple Fickian semi-infinite 1D diffusion. The $N_{Pt^{x+}}$ is expressed in terms of the effective diffusion constant of Pt^{x+} in the ionomer phase (D), the equilibrium solubility of Pt^{x+} at a given potential (c), and the thickness of the cathode layer (L), as $N_{Pt^{x+}} \sim Dc/L$.

The precipitated crystallites is usually found close to the cathode-membrane interface, visible as 'Pt bands' (as in Figure 3.18b) or 'transition-metal crystallites'. The exact distance from the interface depends on the partial pressure of oxygen. The higher the oxygen partial pressure, the closer the crystallites are to the cathode-membrane interface. These crystalline precipitates are usually large, on the order of a μm, which indicates that the mass loss of electroactive Pt and transition-metals can be substantial due to dissolution. This is illustrated by (a) Figure 3.18b showing the plot of Pt mass loss across the cathode thickness, and (b) Figure 3.18d showing the plot of variation in the cobalt concentration across the cathode thickness for a cathode using Pt_3Co catalysts. Presence of such large crystallites along the membrane can cause clogging and water management problems [23, 84].

3.3.4 *Detachment of particles from the carbon support*

PEMFCs suffer from corrosion of carbon supports, especially during the start-stop load cycles, and at the cell voltages higher than 1.1 V [106–109]. Although not yet fully understood, the carbon corrosion mechanism is proposed to occur with the aid of disordered boundaries in between the graphitic domains in the carbon, where the catalysts might be nucleating [106, 110]. Water enters into the carbon structure through these defect sites, and at the interphase between the catalyst and carbon, the oxidation of carbon occurs, catalysed by the Pt catalyst surface [111].

$$\boxed{\begin{aligned} Pt + H_2O &\longrightarrow Pt - OH_{ad} + H^+ + e^- \\ C - O_{ad} + Pt - OH_{ad} &\longrightarrow Pt + CO_2 + H^+ + e^- \end{aligned}} \tag{3.16}$$

The extent of carbon corrosion depends on the cell voltage, graphitic nature of carbon, location of catalysts on the carbon and also, the relative humidity in the electrode chamber [85]. Carbon corrosion in PEMFCs can lead to detachment and/or agglomeration of catalysts, loss of graphitic nature of carbon resulting in poor conductivity, loss of ionomer, and increased hydrophilicity in the electrodes. The direct consequence of the detachment and/or agglomeration of catalysts is the mass loss and catalyst surface area loss, contributing to overall loss in the electrochemical activity of the electrodes [112].

Carbon corrosion can be substantially reduced with the use of highly graphitized forms of carbon, such as the high surface area carbon (HSAC) wherein the surface heterogeneity is substantially reduced so as to preferentially anchor the deposited catalysts on the graphitic domains (also called, the 002 basal planes or pi-sites) [113].

3.4 METHODS FOR DETERMINING CATALYTIC ACTIVITIES AND DURABILITY

The ultimate test for the catalyst performance and durability is when they are part of a membrane electrode assembly (MEA) and the polarization curves can be recorded to observe any reduction in the activation overpotential. While testing every catalyst in this manner is important, it can be time-consuming, since the entire MEA needs to be optimized with each catalyst to eliminate mass-transport resistances and other uncertain artifacts. Therefore, the screening process of different ORR catalysts is simplified using an alternative procedure based on the electrochemical rotating disk electrode (RDE) method [41, 114, 115].

In the RDE method, the supported catalysts are deposited on a glassy carbon disc, which can be easily tested in an ordinary electrochemical cell for information on chemical kinetics, concentration, surface area etc. Two quantities are of particular use in the ORR catalyst development, namely the 'kinetic current densities' and the 'electrochemical surface area'. These quantities are used in determining the 'specific activity' and 'mass activity' of the given catalyst system, and by further tracking them over many cycles/runs, the durability of the catalyst system is determined.

In the following sections, the definitions and methods of determining these kinetic quantities are reviewed. First, few general remarks are made on the electrochemical principles behind cyclic voltammetry (CV) (based on reading from [116]). Reader who may be familiar with these techniques is encouraged to begin reading from the next subsection (Section 3.4.2).

3.4.1 *Some general remarks on CV and RDE techniques*

Electrochemistry is a study of chemical response of a system to an electrical stimulation [117]. Normally, the material under an electrical stimulation either loses electrons (oxidation) or gains them (reduction). Understanding such 'redox' reactions, in terms of the variation in the concentrations, the mechanistics, and most importantly the kinetics, provides a better insight into the chemical reactivity of the material to different gas-solid-liquid environments.

Most electrochemical techniques are based on a three-electrode setup, comprising of a working electrode (WE), reference electrode (RE) and a counter electrode (CE) (Fig-

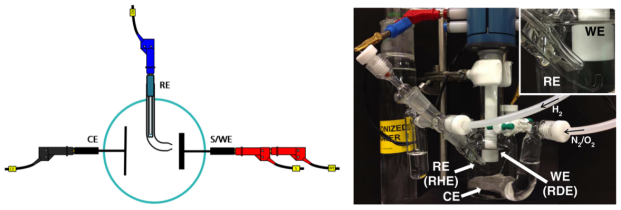

(a) Typical three-electrode electrochemical setup.

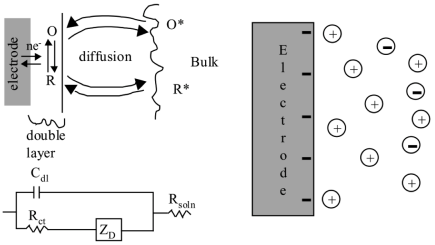

(b) Capacitive and Faradaic processes taking place at the electrode surface.

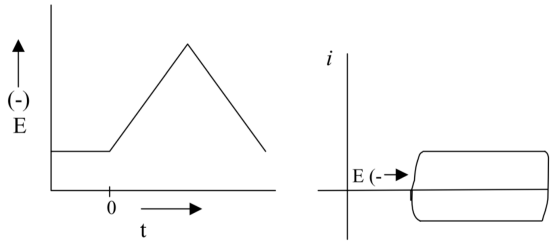

(c) Illustration of a simple CV experiment (left) and profile (right) in the absence of redox couple.

Figure 3.20: Studying redox reactions using a three electrode electrochemical setup. sources: [116]

ure 3.20a). WE is where the reactions of interest take place, therefore typically the 'material of investigation' itself is the WE. A is the geometric area of the WE exposed to the electrolyte. All the three electrodes are connected to a potentiostat for controlling the applied potential of the WE (with respect to RE), as well as measuring its resulting current response. The WE and CE are both in contact with an 'electrolyte' that enables flow of ions between the two electrodes. During an electrochemical measurement, current flows between WE and CE. Since CE should not participate or affect the reaction kinetics at the WE, it is usually made of either Pt or an inert material. The CE also needs to be of a high surface area, thus a mesh structure is usually preferred. The potential of WE is measured with respect to the RE. Commonly used RE is a saturated calomel electrode (SCE).[5] Quantities commonly measured from such an electrochemical setup include, potential (E), current (i), charge (Q) and time (t).

[5]Depending on the experiment, a variety of REs are used. The saturated calomel electrode (SCE) is a simple off the shelf electrode, which is stable and offers long shelf-life. But, one prominent issue with the SCEs is the susceptibility to chloride contamination, which can be detrimental to ORR measurements from the strong adsorption of the chloride on the Pt surface, and in the process alters the ORR activity. Therefore, SCEs are not well suited REs for the ORR measurements.

Of particular relevance to ORR catalyst development is the cyclic voltammetry (CV) technique, wherein the applied potential on the WE is ramped linearly with time (called the voltage scan rate, v) (Figure 3.20c). After reaching a set potential, the potential is ramped in the opposite direction to reach the initial potential. These cycles are repeated as many times as needed, and the voltammograms (i.e., E *vs* i (or i/A) plots) generated for each cycle is called, a cyclic voltammogram (CV).

Figure 3.20b illustrates processes taking place at a simple WE during an electrical stimulation. Two cases exist, in the first scenario no redox species are present in the electrolyte solution (hence, no charge transfer), and in the second, the electrolyte solution contains redox species ($O + ne^- \Longleftrightarrow R$).

Even when there is no charge transfer, a current, called the 'capacitive current', can still be measured. This is because of the formation of an electric 'double-layer' at the electrode-solution interface from the flow of ions (Figure 3.20b). The double-layer behaves like a parallel-plate capacitor,[6] enabling a transient current, i, to flow even when there is no charge transfer. This capacitive current (i) can be calculated as follows:

For a simple parallel-plate capacitor with charge (Q), potential difference (E) and capacitance (C): Q = CE. Thus, i = dQ/dt = C(dE/dt) = Cv (v is the voltage scan rate).

$$\boxed{i = C \times v} \tag{3.17}$$

Figure 3.20c shows the voltage scan rate in a CV and the resulting voltammogram (E *vs* i). As can be seen, a capacitive current flows even in the absence of charge transfer.

In contrast to the capacitive current, the current that flows due to charge transfer at the electrode-solution interface is called the 'Faradaic current'. It depends on two factors, first the kinetics of electron transfer, and second, the ease of mass transport i.e., the rate at which the redox species diffuse to the electrode surface. The Faradaic current (i) as a combination of kinetic current (i_k) and the diffusion-limited current (i_d) can be written as:

$$\boxed{\frac{1}{i} = \frac{1}{i_k} + \frac{1}{i_d}} \tag{3.18}$$

[6]The double layer behaves as a parallel plate capacitor only if the WE surface is smooth. In the case of rough or porous WEs, a non-ideal capacitive behavior is observed.

Using a rotating disk electrode (RDE) during the CV measurements, the diffusion lengths can be controlled by rotating the electrode at suitable angular velocities (ω RPM). The diffusion-limited current (i_d) is related to the rotation (ω) as:

$$\boxed{\frac{1}{i} = \frac{1}{i_k} + \frac{1}{B\omega^{1/2}}} \tag{3.19}$$

Where $B = 0.62\, nFC_o D^{3/2} v^{1/6}$, with number of electrons transferred (n), bulk-concentration of species O (C_o), Diffusivity (D) and the voltage scan rate (v).

If i_k can be estimated, and since all other quantities are known, plotting $1/i$ versus $\omega^{-1/2}$ using Equation 3.19, as in a 'Koutecky-Levich' plot, allows for the determination of the number of electrons (n) transferred during a reaction.

If the reactions are in equilibrium, with both forward and backward reactions progressing at the same rate, the net current flow is zero. The current under this equilibrium condition is given by the Nernstian exchange current density (I_o). On the other hand, if the reactions are not in equilibrium, the kinetic current is given by Butler-Volmer expressions (discussed earlier in Section 3.1.3). Therefore, by measuring the currents using an RDE, appropriate expressions (equilibrium or kinetic) can be used in extracting valuable information on the concentrations, exchange current densities, and rate constants as such.

In contrast to RDE, running just a CV without any electrolyte stirring, will create diffusion-limited currents, making the extraction of kinetic data very difficult. But, the advantage of running CVs is to identify different features (peaks) each arising due to a particular redox reaction taking place at the WE (discussed below).

Features in a CV

Following discussion provides a simple description of the features in a CV by considering the Nernstian behavior (assuming fast kinetics) for the electrode reactions.

When charge transfer kinetics ($O + ne^- \Longleftrightarrow R$) at the electrode-solution interface is rapid, the concentrations of O and R is described by the Nernst equation:

$$\boxed{E = E^o - 0.059\, n \log[R][O]} \tag{3.20}$$

Where E is the applied potential, $E^o$is the OCP and [O], [R] are concentrations of the oxidised species and reduced species at the electrode surface, respectively. As can be seen, increase in the applied potential results in the decrease of O at the electrode surface.

For a rapid charge transfer, the measured current (i) is related to the diffusive flux (J) of the oxidised species (O) from the bulk of the solution to the electrode surface:

$$\boxed{i \propto nFAJ} \tag{3.21}$$

where, n is the number of electrons transferred, A is the electrode area.

According to the Fick's first law, the flux J is given by:

$$\boxed{J = -D\,\frac{(C^* - C_{x=0})}{\Delta x}} \tag{3.22}$$

where, C^* and $C_{x=0}$ are the concentrations of O in the bulk (of the solution) and electrode surface, respectively.

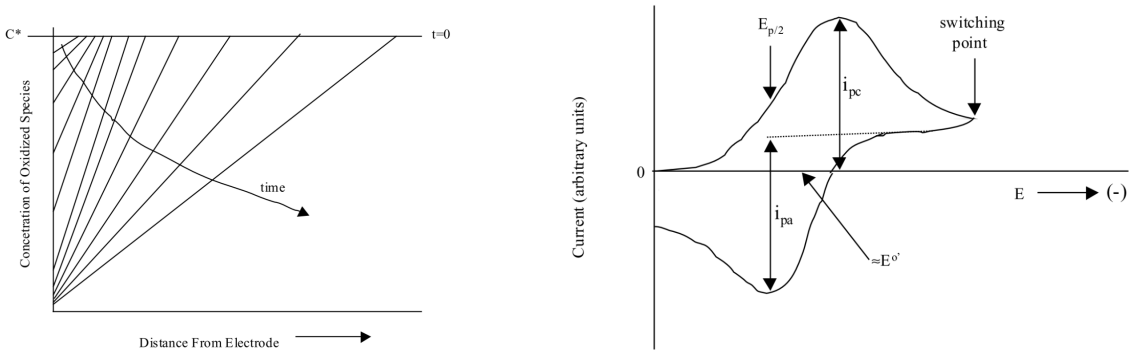

(a) Concentration profiles from the electrode surface to a distance at two different times.

(b) Typical volammogram (E *vs* i) in a CV experiment.

Figure 3.21: Understanding the features appearing in a CV. source: [116]

From the above equation it follows that as the concentration gradient is increased, the diffusive flux increases, and consequently, the measured current also increases.

At the time t = 0, the applied potential E = 0, and there is no concentration gradient since the solution has a uniform concentration of O, i.e. the bulk concentration C^*. As the potential is started to being applied, the concentration of O at the electrode surface starts to deplete. This results in a high concentration gradient $\frac{(C^* - C_{x=0})}{\Delta x}$, consequently high J (Equation 3.22), and a high current i (Equation 3.21).

As we continue to increase the potential this way, the concentration O at the surface will eventually become zero. Simultaneously, the volume in the solution that is depleted of O will increase. As a result, the concentration gradient will begin to decrease (see Figure 3.21a). Consequently, the measured current will begin to decrease. These variations in the measured current with the applied potential is depicted in the upper half of the E *vs* *i* voltammogram shown in Figure 3.21b. Since the applied potentials are all negative, the voltage scan in this direction is called the 'cathodic scan', and the resulting current is called the 'cathodic current'.[7]

As we start to reverse the voltage in the other direction (making it more positive, called the 'anodic scan'), despite the large volume in the solution depleted of O, the surface concentration of O begins to rise. This results in further decrease in the concentration gradient, and consequently the measured current (called the 'anodic current') decreases even further. Finally, a region is reached where the anodic current begins to dominate. With the subsequent increase in the anodic voltage, we begin to go through similar concentration profiles for the reduced species (R), and the anodic current starts to decrease. These variations in the current during the anodic scan is shown in the bottom half of the voltammogram in Figure 3.21b.

The maximum anodic and cathodic currents are called the 'peak anodic current' (i_{pa}) and 'peak cathodic current' (i_{pc}), respectively. For a reversible system, $i_{pa} = i_{pc} =$ peak current, i_p. The potentials at i_{pa} and i_{pc}, are denoted as E_{pa} and E_{pc}, respectively. E_{pa} and E_{pc} are both independent of scan rate (v), whereas the peak currents (i_p) are proportional to v. The OCP is simply estimated as an average of E_{pa} and E_{pc}. For a Nernstian system, the peak current (i_p) is expressed by the *Nicholson and Shain relationship* [118] as:

$$\boxed{i_p = 2.69x10^5\, n^{3/2} A D^{1/2} v^{1/2} C^*} \tag{3.23}$$

In summary, perhaps studying the reaction mechanisms is the most attractive feature of cyclic voltammetry (CV). Each feature appearing in the CV correspond to a specific charge transfer reaction that a redox couple undergoes. Thus, by analysing the peaks appearing in the CV various charge-transfer mechanisms taking place at the WE can be identified. Additionally, by employing a rotating disk electrode (RDE), the diffusion-

[7] Few other terminologies are also used in the literature to indicate anodic *vs* cathodic scan direction, namely: forward scan *vs* backward scan, and positive scan *vs* negative scan, respectively. We can scan negative (backward, cathodic) and have a oxidation current, vice versa.

limited currents can be controlled by the speed of rotation,[8] thereby the required kinetic data can be easily extracted. Application of these concepts in extracting the catalyst surface areas and the kinetic ORR activities is discussed in the following sections (based on much comprehensive review that is provided in the articles [41, 114, 115]). First, the standard electrochemical setup used for these measurements is outlined as below.

3.4.2 *Typical electrochemical setup for studying ORR kinetics*

The electrochemical measurements are typically conducted in a three compartment cell, using a potentiostat for measuring current response to applied voltage. The three compartment cell comprises of a working electrode (WE), counter electrode (CE) and a reference electrode (RE). The WE and CE are both dipped in an electrolyte, typically 0.1 M perchloric acid ($HClO_4$). Usually a platinum mesh is used as the CE, and the reference electrode is a saturated calomel electrode which is separated from the main compartment by an electrolytic bridge. All the potentials are calculated with respect to the measured reversible hydrogen electrode (RHE). The working electrode is prepared by depositing supported catalysts (ultrasonically dispersed in water and ethylene glycol) onto a glassy carbon substrate, which is commonly about 6 *mm* in diameter and polished. Any water content from the deposited catalysts is evaporated by passing an Argon stream. Subsequently, suitable quantity of Nafion solution (on the order of μL) is introduced to attach the catalysts onto the glassy carbon substrate. It is important to limit the thickness of the deposited Nafion film to sub-micrometers. This is essential in order to minimize the diffusion resistance for the flow of oxygen through the Nafion film to reach the catalyst site.

3.4.3 *Procedure for CV and RDE measurements*

First step is to condition the electrochemical setup such that a stable cyclic voltammogram can be recorded. This step is sometimes called 'CV conditioning' in the literature [41, 114, 115]. Firstly, the WE is immersed under an applied potential of 0.05 V in an Argon-saturated electrolyte solution. The potential is then cycled continuously, between

[8] This is the beauty of RDEs. The diffusion layer thickness gets thinner with the increasing rotation rate, resulting in higher currents. Usually, the RDE measurements (depending on the potential relative to the E^o of the reaction) are under mixed or completely mass transport controlled conditions.

0.05 *V* and 1.0 *V* until a stable CV can be recorded. Using the H_{upd} region in the recorded CV, the electrochemical surface area, cm^2/g_{Pt}, can be estimated (see Section 3.4.4). Following CV conditioning and CV recording steps, the RDE is prepared for measuring the ORR activity.

For the ORR, the electrolyte is first bubbled with oxygen at 298 *K*. Measurements are carried out at two temperatures, 298 *K* and 333 *K*. During the experiment, the RDE is rotated at 1600 rotations per minute (RPM) to account for mass-transport considerations. The potential is cycled between 0.05 *V* and 1.0 *V* at the scan rate of 20 *mV/sec* (or 50 *mV/sec*), and the CV is recorded. Exceeding potentials above 1.0 *V* is generally avoided as it can result in corrosion of either the support or the catalyst. With the recorded CV, the specific current density is measured at 0.85 *V* and 0.9 *V*, which is further used to calculate specific and mass activities (see Section 3.4.5). After the measurements, the electrolyte is cooled down to 293 *K* back again, and one final CV is recorded. By comparing this final CV to the one recorded initially any structural changes can be analysed. The entire procedure is repeated for three or more catalyst loadings, as it is important to establish a good usage of catalyst surface independent of the catalyst loading.

3.4.4 *Determining electrochemical surface area*

Electrochemically active surface area (ECSA) is equivalent to the total catalyst surface area available for a reaction per unit mass of Pt, with units cm^2/g_{Pt}. It is an important quantity required to calculating the specific and mass activities of the catalyst (Section 3.4.5). Most commonly the ECSA is calculated from the H_{upd} region in the CV recorded, by estimating the charge that is required to either adsorb or desorb a monolayer of hydrogen on the WE (i.e., catalyst surface). Alternatively, ECSA can also be calculated in a CO-stripping experiment, from the charge it takes to oxidise a pre-adsorbed monolayer of carbon-monoxide (CO). Few other methods are also available, which are based on chronoamperometry and differential electrochemical mass spectrometry techniques [41]. In the current overview, only the commonly used H_{upd} estimation of ECSA is reviewed.

In the H_{upd} estimation of ECSA, first the CVs recorded for a given catalyst system at different loadings of Pt is considered. An example is shown in Figure 3.22a, showing CVs for Pt/C catalyst at three different loadings (3.5 $\mu g/cm^2{}_{geo}$, 7 $\mu g/cm^2{}_{geo}$, 14 $\mu g/cm^2{}_{geo}$). Here $cm^2{}_{geo}$ refers to the geometric area of the WE (the glassy carbon disc).

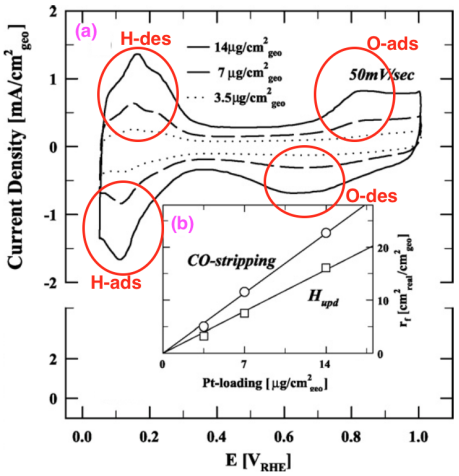

(a) Measured CVs for Pt/C catalyst at three different loadings. Inset: Plot of estimated roughness factor (r_f) as a function of Pt loading.

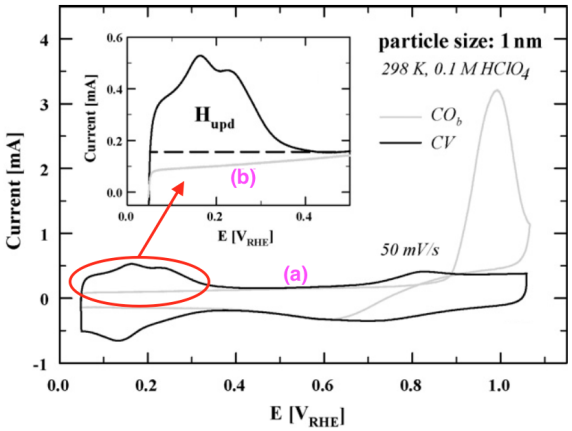

(b) Estimation of charge in the H_{upd} region.

Figure 3.22: Estimation of electrochemical surface area (ECSA) from the recorded cyclic voltammograms. source: [41]

The recorded CVs shown inFigure 3.22a all reproduce major features expected for a Pt electrode (in 0.1 *M* $HClO_4$). These include four regions corresponding to H-adsorption (bottom-left), H-desorption (top-left), O-adsorption (top-right) and O-desorption (bottom-right). The H-adsorption/desorption regions are invariably referred to as the H_{upd} regions (Figure 3.22b).

Q_H is the charge it takes to adsorb/desorb a monolayer of hydrogen on the WE. For the CVs in Figure 3.22, Q_H can be estimated using the area under the CV (i vs E) in the two H_{upd} regions and averaging them. But it is also not uncommon in the literature to only use the H-desorption region to calculate Q_H. Regardless, a correction for the pseudo capacity (resulting from the carbon support) need to be first applied to the double-layer region. This is usually done by assuming a constant double layer capacity, marked by a straight line as shown in Figure 3.22b. Q_H is then calculated from the region above the straight line drawn, using the expression:

$$\boxed{Q_H = (\int i \, dE)/v} \tag{3.24}$$

Here, the $\int i\,dE$ term corresponds to the area of the pseudo-capacity corrected H_{upd} region, and v is the voltage sweep/scan rate used for the experiment.

From the Q_H thus calculated, and with the known value for the charge-density of a bulk Poly-Pt electrode (generally, 195 $\mu g/cm^2{}_{geo}$), the catalyst surface area (A_{real}) (also called, the electroactive surface area) can be calculated using the following expression:

$$\boxed{A_{real}(cm^2_{real}) = Q_H(\mu C)/195(\mu C/cm^2)} \tag{3.25}$$

Subsequently, the roughness factor of the catalyst (r_f) is calculated, which denotes the ratio between the catalyst surface area (A_{real}) and the geometric area of the electrode (A_{geo}).

$$\boxed{r_f = A_{real}/A_{geo} = \frac{Q_H(\mu C)}{195(\mu C/cm^2)\,x\,A_{geo}(cm^2)}} \tag{3.26}$$

The calculations are repeated for all the CVs shown in Figure 3.22a, i.e. for different catalyst loadings (represented by Pt loading (g_{Pt})). The roughness factors calculated is plotted as a function of Pt loading, and as illustrated in Figure 3.22a (*inset*), the plot is approximately linear. The slope of the linear approximation in the r_f *vs* Pt loading plot gives the required electrochemical surface area (ECSA (cm^2/g_{Pt})).

3.4.5 *Determining specific and mass activities*

Specific and mass activities are both measures of the kinetics of the ORR on a given catalyst surface. Faster the kinetics, higher these quantities are, and better the catalyst is. In a typical RDE, the kinetics of the electrode reaction is represented by the kinetic current (i_k), and can be calculated from the measured current (i) using Equation 3.18 ($1/i = 1/i_k + 1/i_d$).

From the RDE measurement we usually get the geometric current density, j ($A/cm^2{}_{geo}$), which is the current (i) over the entire electrode area ($cm^2{}_{geo}$). A typical plot of the geometric current density versus the applied potential is shown in Figure 3.23*(a)* for all the three catalyst samples. Note that only anodic sweep is shown, and the plot is commonly called as the 'ORR polarization curve'. The reader should not confuse this with the 'fuel

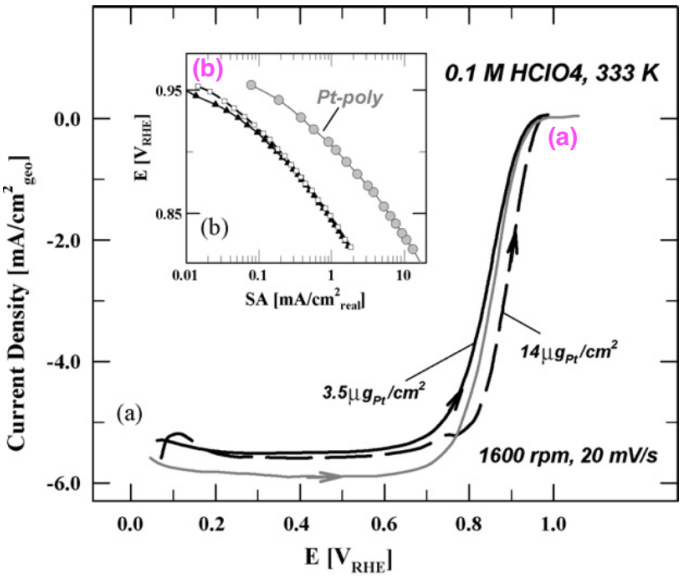

Figure 3.23: Estimation of specific activity of given catalyst from the measured ORR polarization curve. *a*: ORR polarization curves for Pt/C of different loadings. *b*: Plot of potential *vs* current density in the kinetic region (i.e., E *vs* j_k). source: [41]

cell polarization curve' (*j vs E*, where $j = A/cm^2_{MEA}$ and *E* is the cell voltage) discussed earlier in Section 2.6.

In the ORR polarization curve shown in Figure 3.23*(a)*, the diffusion limited current density (j_d) is given by the regime where *j* is more or less constant (5.8 *mA/cm²* for all three samples). Ideally, the diffusion limit current (j_d) is constant, and independent of the potential. The diffusion limiting current is reached when the surface concentration of the reactant (i.e., at the catalyst WE) is zero. The current is now dependent on the geometrical surface area. If the surface concentrations of the reactant is not zero, instead of the geometrical surface area, it is the active catalyst surface area contributes to the current. The kinetic current density ((i_k/cm^2_{geo}) can be extracted in the region where $0.1 \times j_d < j < 0.8 \times j_d$, i.e. the current at the potential of interest is within 10 % and 80 % of the diffusion limited current. For the ORR, this is usually between 0.85 – 0.9 V. Note however that to calculate the ORR activities, we are more interested in the 'specific current density' (j_k), which is the kinetic current (i_k) from over the catalyst surface area (cm^2_{real}).

The specific current density can be calculated from the measured geometric current density, as follows. Specific current density, $j_k = i_k/A_{real}$

Rewriting i_k in terms of i using Equation 3.18, and A_{real} in terms of A_{geo} using Equation 3.26:

$$\boxed{j_k = i_k / A_{real} = \frac{i_d \, x \, i}{i_d - i} \, x \, \frac{1}{r_f \, x \, A_{geo}}} \tag{3.27}$$

Note that i_d, A_{geo}, r_f are all known, and the i is a linear function of E in the kinetic region (0.85 – 0.95 V). Therefore, the specific current density (j_k) can be plotted as a function of E, and the resulting plot is called the 'Tafel plot'. Usually, the specific current density measured at 0.9 V is reported in the literature, this is to avoid parasitic current contributions (such as, capacitive currents) at higher potentials.

Figure 3.23*(b)* illustrates Tafel plots for Pt/C catalyst at two different loadings. It is noticeable that the specific current densities of both the samples are identical, even though their loadings are different. Thus, the specific current density provides a true measure of the reactivity of catalyst surfaces, independent of their loading.

More commonly, the specific current density measured at 0.9 V is called the 'specific activity' of the given catalyst system. For comparison, measured Tafel slope for Poly-Pt is also shown in Figure 3.23*(b)*. As can be seen, the specific activity for Pt/C nanoparticles is higher compared to Poly-Pt electrodes. Therefore, these Pt/C nanoparticles are better ORR catalysts than the Poly-Pt electrodes.

Another closely related measure of catalytic activity is the 'mass activity' (A/g_{Pt}). It is defined as the kinetic current (i_k) for a given mass of platinum (g_{Pt}), and can be calculated from the specific activity (j_k at 0.9 V) using the following expression:

$$\boxed{j_{mass} = j_k x \frac{r_f}{L_{Pt}}} \tag{3.28}$$

where L_{Pt} is the Pt loading (g_{Pt}) per geometric surface area of the electrode (cm^2_{geo})

Since mass activity measures the kinetic current on Pt mass basis, it reflects the cost factor of the given catalyst design. Higher the mass activity, costlier is the catalyst. Therefore, mass activity is of higher significance in the development of economical ORR catalysts.

One major source of error in determining mass activity is the poor utilization of catalysts. Therefore, it is important to validate that the ECSA (or the r_f) is a linear function of the catalyst loading (as in Figure 3.22*(inset)*). Lastly, the reader is cautioned about other

terminologies such as 'ORR activities' or simply 'catalytic activities', which are also used to refer to the measured mass- and specific- activities.

3.5 STRUCTURAL CHARACTERIZATION TECHNIQUES TO INVESTIGATE PT-ALLOY NPS

Fundamental research towards developing electroactive Pt-alloy nanoparticles has already made significant strides over the past decade, this we discuss elaborately in the next chapter (Chapter 4). Unfortunately, no practical ORR catalyst is yet in sight, and therefore, the efforts must continue unabated. Ultimately, the timing and success of such efforts rely on employing suitable structural characterization tools which can probe the structure and chemical composition of nanoparticles down to the atomic-level. Preferably, in their native environments during the synthesis, phase-transformations, potential cycling and MEA operation.

Over the years, many imaging and spectroscopic techniques based on electron microscopy [119–132] and x-ray absorption [133–138] have proven to be particularly useful to carry out such a task. Although few other surface analytical tools such as x-ray photoelectron spectroscopy (XPS) [139, 140], Raman [141], Auger electron spectroscopy [142], low energy electron diffraction (LEED) [143], surface x-ray scattering (SXS) [66] are also in use, e.g. in determining the chemical state of the surface layers and electronic structure calculations, these are commonly known to be more suitable for characterizing bulk specimens, e.g. thin-films, than a batch of nanoparticles. Additionally, finite escape depths of Auger and photoelectrons can further limit the analyses to surface layers only (typically, 1-2 nm) [144].

Similarly, x-ray diffraction is a powerful technique for phase analyses, estimating average 'crystallite size' (sometimes wrongly referred to as the particle size), and comparing the degree of ordering between different samples [145, 146]. But, the information provided is a bulk-average of many particles in the batch, and does not capture the dynamic mechanisms such as ripening, coalescence and dissolution that take place on the atomic- and nano-scale sizes. Not much is discussed on such bulk-average techniques other than to emphasize that a combination of such bulk- techniques with the high spatial resolution techniques (TEM, XAS) yielding local information, would be very ideal.

Following discussions present an overview of different imaging and spectroscopic techniques based on electron microscopy and XAS methods. In the next chapter the techniques used for the thesis work is reviewed in detail, these include an imaging, and a spectroscopic technique primarily based on scanning transmission electron microscopy (STEM).

Electron microscopic techniques

Among the many different electron microscopic techniques, transmission electron microscopy (TEM), electron energy loss spectroscopy (EELS) and the energy dispersive x-ray spectroscopy (EDXS) techniques are the most useful [121, 127]. In TEMs the electron beam generated from a tip is transmitted through the specimen and collected at the other end to obtain useful information. Two TEM imaging modes are particularly very useful, namely the high-resolution TEM (HRTEM) and the scanning TEM (STEM). These differ in the manner in which the electron beam is illuminated on the sample. While HR-TEM illuminates a parallel electron beam on the entire sample, STEM relies on converging the electron beam into a small probe (sometimes of the size of an atom), and raster scanning it on the specimen [147]. In the modern day aberration-corrected TEMs which correct for the spherical and chromatic aberrations in the electron optics, both HR-TEM and STEM approaches provide atomic-resolution. This has led to extensive application of these two techniques to elucidate a variety of aspects of Pt-alloy nanoparticles. To list a few, these include: estimation of particle sizes and size-distribution [148–150], observation of nanoparticle morphology, bulk- and the surface- structures [151–156], estimation of lattice strain [157–161], study of the growth mechanisms [162–166], metal-support interactions [167], order-disorder phase transformations [168–171], insights into coalescence and ripening mechanisms [96, 150, 164, 172, 173], and tracking catalyst degradation [157, 174–179]. Recent advancements in the manufacturing of sophisticated TEM holders for 3D-tomography [180–189], heating [190–193], liquid/gas-cell microscopy [194–203] and further development of dedicated environmental TEMs [204, 205], have further enabled such analyses to be carried out *in situ*, and also in 3D. Finally, to minimize specimen damage from the beam exposure during such long-duration acquisitions, new ways of image acquisition and reconstruction such as compressed sensing are also emerging [206, 207].

In most structural investigations of Pt-alloy nanoparticles, STEM is more common than HR-TEM. This is because the STEM imaging can be very sensitive to the atomic-number (Z) when coupled with a high angle annular dark field detector (HAADF) to detect electrons, usually referred to as HAADF-STEM imaging [147]. Intensities in the HAADF-STEM is proportional to roughly $Z^{1.6}$, thus providing an atomic-number contrast which can be used to extract qualitative and quantitative information about the elemental composition of the sample. Spectroscopic techniques such as EDXS and EELS are capable of providing similar compositional information of the sample, but in a much straight-forward manner [121, 192, 208, 209]. With the use of tomography TEM holders, generation of 3D elemental maps is also now possible [210, 211].

Both EDXS and EELS are based on the excitation of inner-shell electrons of the specimen [212–214]. In EELS, the energy lost by the incident electron in the process is characteristic of a particular element, usually visible as an 'ionization edge' in the electron energy loss spectrum (plot of electron counts *vs.* energy lost). In EDXS, the x-rays generated from the deexcitation process (within about 10-15 secs after the initial excitation) is characteristic of a particular element. Both techniques are complementary, but the real advantage of EELS lies in is its extreme sensitivity to the local electronic structure and bonding environment of the atom under investigation. This information is buried within the fine-structures (ELNES) extending to about 50 eV from the ionization threshold [215]. Detailed analyses of such fine-structures allows for a better understanding of the electronic interactions between oxygen and the Pt surfaces [216–218]. However, such high-resolution EELS (HREELS) analyses are presently limited in the investigations of Pt-alloy nanoparticles, given that the CV-RDE measurements of catalysts occur under a liquid electrolyte environment, and carrying out EELS in liquids can be extremely challenging [201].

X-ray absorption spectroscopy (XAS) based techniques

X-ray absorption spectroscopy (XAS) is analogous to EELS, in here the intensity of a transmitted beam of x-rays is measured as a function of the incident wavelength [219, 220]. Usually, a high-brightness source such as a synchrotron is used to obtain sufficient intensity. Similar to the ionization edges appearing in EELS, the XAS edges occur at an incident energy close to the binding energy of the each atomic-shell. Additionally, the fine-structures seen in the XAS edges can extend from the near-edge region (XANES or NEXAFS) ~5 eV to about 150 eV beyond the ionization threshold (EXAFS). These fine-structures are sensitive to the chemical state of the atom, its interatomic distances from the neighboring atoms and even the subtle geometric distortions disrupting them, e.g. presence of dopants [221, 222]. With such advantages XAS techniques have found valuable applications in the characterization of Pt-alloy catalysts [133–138]. To list a few, these applications include determination of bulk alloy composition and the catalytic behavior [223–226], investigation of atomic-ordering [227, 228], lattice-strain effects [229, 230], estimation of oxidation state [231–234], electronic-structure calculations [235–237], insights into surface-adsorbate electronic interactions [238–241], and tracking catalyst degradation [242–244]. Although x-ray microscopic imaging is also possible by focussing the soft x-rays from the synchrotron onto a spot using zone-plates [245], the resulting spatial resolution (~50 nm) is much lower than that obtained in an electron microscope [246].

Probably the most attractive feature of XAS techniques to fuel cell research is that the x-rays can penetrate through almost any environment - solid/liquid/gases. Thus,

setting up in situ operando MEAs is feasible, and including catalyst nanoparticles, almost any fuel cell component can be characterized in environments that closely mimic those of a working fuel cell [241, 247–250]. Apart from few indirect methods [251–254] (e.g., identical location TEM), such in situ operando type studies is presently not feasible with electron microscopes. Ultimately, the advantages of both electron microscopic- and XAS techniques complement one another in providing useful information about the catalyst particles. For example, to account for the lack of spatial resolution with XAS techniques, same catalysts characterized under XAS can be subsequently imaged under an aberration-corrected TEM (e.g., see recent work by Takao *et al* [255]). On the other hand, to understand the electronic interactions between oxygen and Pt surfaces in the electrochemical (i.e., liquid electrolyte) environments, XAS is still a better option than EELS. In the foreseeable future, inspired by works such as Takao *et al* 's [255], structure characterization of MEAs (and catalysts therein) might evolve into an integrated approach involving both TEM and XAS techniques. For a more comprehensive study of XAS methods and applications in studying fuel cell catalysts, the reader is referred to following excellent reviews [133–139].

3.6 PERSPECTIVE

In summary, the present chapter has covered concepts in developing catalysts for the oxygen reduction reaction (ORR). These included concepts dealing with the kinetics of the ORR, formation of a metal-adsorbate bond in general, and of Pt-O_2in specific, effect of alloying Pt on the surface reactivity towards ORR, theoretical predictions of ORR activities for different Pt-alloy systems, different catalyst degradation mechanisms, methods to quantify and compare the performance and durability of different catalyst systems, and finally an overview of different structural characterization techniques that are available. All these concepts are crucial for improving the ORR activities of catalysts that currently suffer from high cost and poor durability issues, hindering the widespread commercialization of PEMFCs. In the following Chapter recent progress in the development of Pt-alloy nanopoarticle catalysts is reviewed.

4

PROGRESS IN THE DEVELOPMENT OF PT-ALLOY NANOCATALYSTS

Previously in Section 3.2.5 the effective role played by alloying on improved ORR catalysis of Pt surface was discussed. The activity improvement in the Pt-alloys was theoretically attributed to the weakening of the oxygen chemisorption caused due to the modification in the electronic structure of alloyed Pt surface compared to pure Pt. The present chapter reviews recent progress in the development of such Pt-alloy systems, focussing particularly onto those that are synthesized as nanoparticles (Most sections (in parts or full) are currently under peer review in the Royal Society of Chemistry – Energy & Environmental Sciences journal).

Just in the past decade over hundred different alloys of Pt have been synthesized and tested for the ORR activity [23, 73, 256, 257]. Most common are the bimetallic Pt-alloy systems wherein Pt is alloyed with either *3d* transition metals (Pt-M alloys) such as V [258], Co [259], Cr [260], Cu [261], Fe [262], Ni [263], Ti [264], Pb [265], Hg [266], or the Pt-group metals (Pt-PGM alloys) such as Pd [267], Ru [268], Ag [269], Au [270], Ir [271]. The choice of the alloying metal in many cases is guided by the theoretical predictions based on 'd-band model' (Section 3.2.3).

4.1 EFFECT OF ALLOYING BASED ON THE TYPE OF ALLOYING METAL USED

Bimetallic Pt-alloy nanoparticles come in a variety of compositions, range of sizes and unique alloy structures. In particular, Pt alloying with *3d* transition metals Co, Ni, Fe, Cu have been studied extensively [73], given their superior activity enhancements compared to PGMs. Earlier on, Stamenkovic *et al* [83] showed that the activity trend followed the order Pt < Pt_3Ti < Pt_3V < Pt_3Fe < Pt_3Ni < Pt_3Co, corresponding to the changes made to the electronic structure. Since then, significant optimization has taken place to Pt-Fe, Pt-Co and Pt-Ni alloy structures. But, depending on the size, composition and surface-segregating metal, the relative activity trends reported in the literature vary. Most reports,

however, agree to the point that these bimetallic catalysts provide improved specific activities compared to Pt/C, which also comes at a much cheaper cost that is reflected in their higher mass activities over Pt/C.

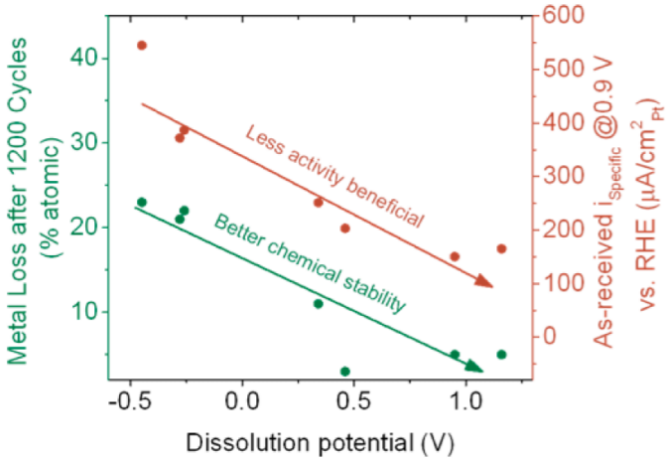

Figure 4.1: Plot of transition metal (M) loss and the measured specific activity of Pt-M as a function of dissolution potential. source:[272]

Despite their improved ORR activities one common problem with the Pt-M bimetallic particles is the dissolution/leaching of transition metals in the corrosive electrochemical environment of fuel cells. For example, a detailed study conducted by Han *et al* [272] showed that the ORR activities are closely connected to the dissolution potentials of the alloying elements. They examined a series of Pt-M bimetallic particles (M = Fe, Co, Ni, Cu, Ru, Pd, Ir) with a nominal ratio of 1:1 for Pt:M. The estimated dissolution potentials for these metals was shown to follow the order PtFe < PtCo < PtNi < PtCu < PtRu < PtPd < PtIr. The lower the dissolution potential, the easier it is for the transition metal to dissolve into the electrolyte. The measured metal loss after 1200 potential cycles, and the initial activities for these seven catalysts are shown in Figure 4.1. As can be seen, the low dissolution potential for a transition metal results in a high ORR activity, but the resulting electrochemical stability is poor.

In contrast to 3*d* transition metals, dissolution is not a major issue for the noble PGMs, such as Pd, Ag, Au and Ir. This is because their dissolution potentials are relatively higher. Problem with Pt-PGM alloy nanoparticles, however, is that the measured ORR activities are usually low, which is ascribed to either stronger or weaker binding of the oxygenated intermediates compared to the optimum. For instance, Pt sites in Pt-Au alloy

nanoparticles bind oxygen more strongly than those in pure-Pt nanoparticles, while those in Pt-Ir and Pt-Ru nanoparticles bind to oxygen more weakly [273].

In order to obtain a highly active as well as electrochemically stable catalyst, a synergy needs to be established between the alloying effects of 3*d* transition metals and the noble PGMs. This underpins the approach followed by many recent efforts to develop 'multimetallic' Pt-alloy catalysts [274–277], combining Pt-MN (where M, N = Fe, Co, Ni, V, Ti, Cr, Sn, Mn, Mo, Pd, Ag, Au, Ir). For example, Lokrakpam *et al* [278] synthesized 1-3 *nm* PtIrCo/C nanoparticles which showed about 3-5 fold increase in the specific activity compared to Pt/C catalysts (depending on the composition). They also found that the rate of ECSA loss was about two times lower than that in the case of commercial Pt/C and Pt_3Co catalysts. At the end of 20000 cycles, the ECSA was found to have decreased from 70 to 25 m^2/g for PtIrCo/C catalysts, while it decreased from 82 to 10 m^2/g for Pt/C and from 49 to 3 m^2/g for Pt_3Co/C. This indicated that the electrochemical stability of ternary PtIrCo/C catalysts was better than that provided by the bimetallic Pt_3Co/C catalysts.

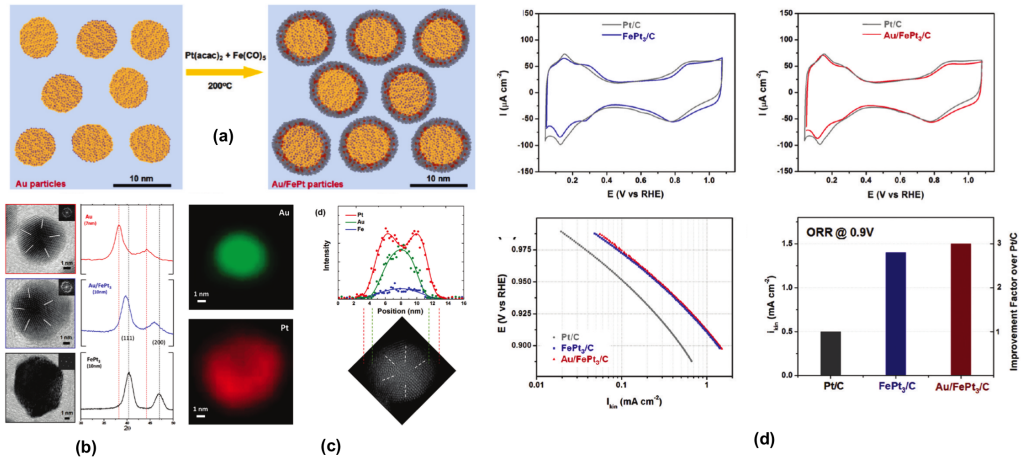

Figure 4.2: Multimetallic Au/FePt catalyst nanoparticles: (a) schematic illustration of synthesis, (b) Comparison of XRD patterns of Pt_3Fe and Au/FePt particles with pure Au, (c) Elemental analyses of Au/FePt particles using STEM-EELS, (d) Measured CV profiles and measured specific activities for bimetallic and multimetallic systems. source:[279]

A similar study was conducted by Wang *et al* [279] on the unique multimetallic Au/FePt nanoparticles (Figure 4.2*(a–c)*) which were synthesized by coating ~1.5 *nm* thick Pt_3Fe layer onto the 7-8 *nm* seed Au particles. Even after about 60000 potential cycles, no significant loss in the ECSA or in the specific activity was observed (Figure 4.2*(d)*). In contrast, the bimetallic Pt_3Fe catalysts without the Au incorporation suffered a major loss in the

specific activity after potential cycling. Observed enhancement in the stability of Au/FePt particles was attributed to the presence of Au in the subsurface layers of Pt, which suppresses the formation of subsurface oxides that is required for the dissolution of Pt from a place exchange mechanism with the electrolyte (i.e., migration of atomic-oxygen from surface to subsurface positions at electrode potentials relevant to the ORR).

4.2 EFFECT OF ALLOYING BASED ON THE TYPE OF ALLOY STRUCTURE

Depending on the nature of mixing of metal atoms, four basic bimetallic Pt-alloy structures exist, namely (1) compositionally homogeneous alloys, (2) compositionally inhomogeneous alloys, (3) core-shell structures, (4) heterostructures, and (5) composite alloy structures. These are schematically depicted in Figure 4.3. Each alloy type is discussed along with suitable examples from the literature, as follows.

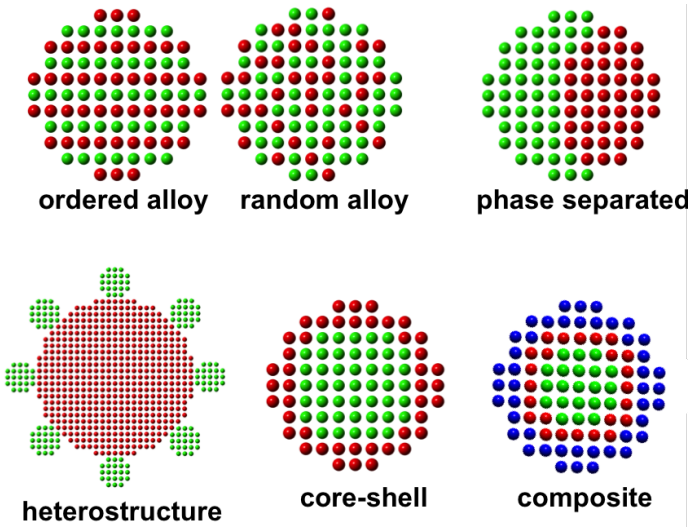

Figure 4.3: Schematic illustrations of different types of bimetallic Pt-alloy nanoparticles structures.

4.2.1 *Compositionally homogeneous alloy nanoparticles*

Compositionally homogeneous alloy structures are composed of atoms of Pt and other alloying elements, arranged either in an ordered fashion (called ordered alloys) or a statistically random order (called random or disordered alloys) (see Figure 4.3).

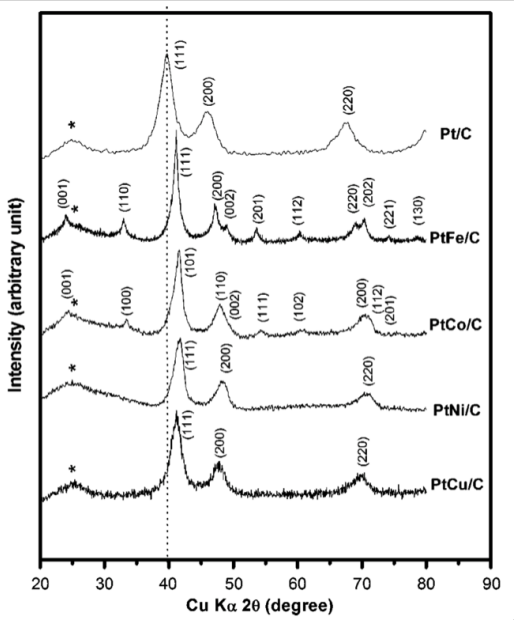

(a) XRD patterns of different heat-treated Pt-alloy NPs.

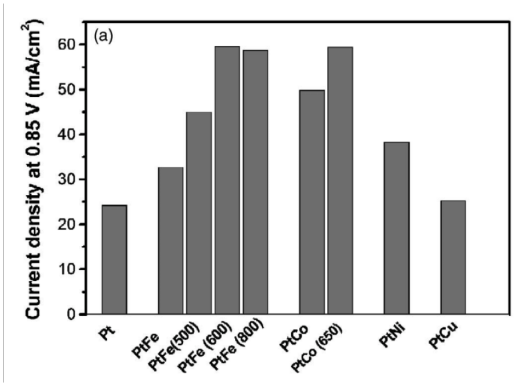

(b) Measured specific activities of different catalysts.

Figure 4.4: Comparison of measured activities of ordered and disordered catalysts. source: [280]

Compared to disordered nanoparticles, synthesizing ordered alloys is generally a more difficult task as it typically requires a post-processing step such as heat treatments to enable diffusion of atoms to rearrange in an ordered manner. For this reason, the reports of disordered alloys are much more common in the literature than the ordered alloy structures. However, the recent trends have begun to reverse [256], ever since Xiong *et al* [280] and many others [281–283] demonstrated that the ordered alloys are more active and also durable, compared to the disordered alloys.

4.2.1.1 *Effect of ordering on catalytic activity*

Different ordered alloy compositions are being explored, such as in the case of Pt-Fe [284–288], Pt-Co [289], Pt-Ni [290, 291], Pt-Cu [292], Pt-Cr [293], Pt-Al [294], Pt-Zn [295, 296] alloy systems. For example, Xiong *et al* synthesized disordered Pt-M (M = Fe, Co, Ni and Cu) catalysts using wet-chemistry, which were then heat-treated for 1 *h* under 90% Ar - 1% H_2atmosphere at 900 °C. X-ray diffraction patterns of the heat-treated samples were obtained as shown in Figure 4.4a. By observing superlattice reflections appearing in the XRD patterns of PtFe ((110) reflection) and PtCo ((100) reflection) samples, Xiong *et al* confirmed that these particles formed an ordered alloy structure upon annealing. Further variations in the annealing temperatures revealed that the ordering maximized around the annealing temperature of 600 °C. Since no such superlattice reflections appeared in the XRD patterns of PtNi and PtCu, they concluded that these particles remained disordered even after the heat treatment. Figure 4.4b shows the measured specific activities for these ordered and disordered catalysts, along with the reference Pt/C catalyst. It can be seen that the ORR activities for the ordered structures are much higher compared to disordered catalysts.

ORR activities of ordered nanoparticles can be higher than that of disordered particles

4.2.1.2 *Effect of ordering on catalytic durability*

Studies have shown that the ordered catalysts are also more durable in the electrochemical environment compared to disordered particles. For example, recently Hodnik *et al* [292] studied the stability of two $PtCu_3$ nanoparticle catalysts, which were prepared carefully such that the only difference between the two structures was their degrees of ordering, one ordered and the other disordered. The ordered structure was confirmed by the superlattice reflections appearing in the XRD patterns, which was absent for the disordered catalysts (Figure 4.5a). Hodnik *et al* found that although, the activity of both catalysts decreased with potential cycling (~500 cycles), the specific activity of the ordered $PtCu_3$ particles were 20-30 % higher than that of the fully disordered particles. The observed stability enhancement was attributed to the better retention of Cu by the ordered alloy structure. In support of this, they estimated the amount of Cu leached by conducting a post-mortem mass spectrometry (ICP-MS) analysis of the electrolyte after various electrochemical treatments. Figure 4.5b shows the specific activity for both ordered and disordered catalysts as a function of the amount of Cu leached. The plot shows that the amount of Cu leached out from the disordered alloy was always higher (~73 % after 500 cycles) than that removed from the ordered alloys (~56 %).

Ordered nanoparticles can be electrochemically more stable to dissolution than the disordered particles

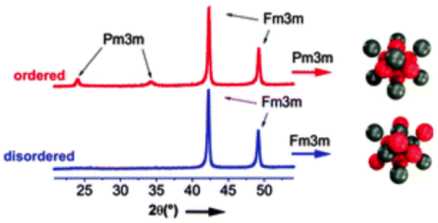

(a) XRD patterns of ordered and disordered $PtCu_3$ structures. [292]

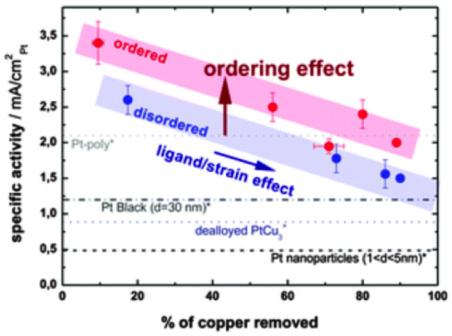

(b) Measured specific activity *vs* amount of Cu leached for ordered and disordered $PtCu_3$ catalysts. [292]

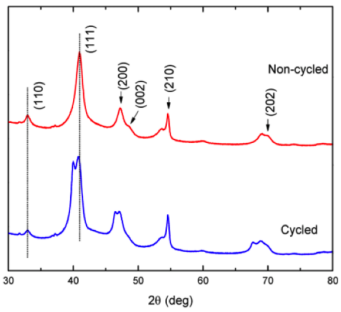

(c) XRD patterns of pristine (non-cycled) and cycled Pt-Fe alloy NPs. [91]

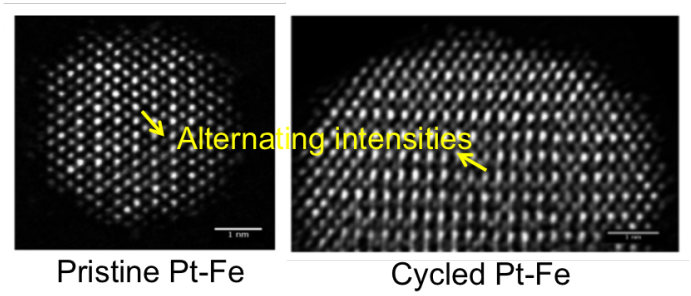

(d) Z-sensitive TEM images of pristine (non-cycled) and cycled Pt-Fe alloy NPs. [91]

Figure 4.5: Comparison of catalytic durabilities of ordered and disordered Pt-alloy nanoparticles. sources: [91, 292]

Stability enhancement was also observed in the case of ordered PtFe alloy nanoparticles encapsulated in a Pt-rich shell by Prabhudev *et al* [91]. In here the specific activity decreased by only about 9 % even after 6000 cycles. XRD patterns of both pristine and the cycled particles (Figure 4.5c) revealed the presence of (110) superlattice reflections, and the Z-sensitive TEM images of the cycled particles revealed alternating intensities characteristic of ordering Figure 4.5d. Both these findings confirmed the retention of ordering in spite of cycling in the case of PtFe alloy nanoparticles.

In relation to Hodnik *et al* 's work, the difference in the electrochemical stabilities of Cu in the ordered and disordered Pt-Cu alloys (more generally, M in Pt-M alloys) was attributed to unequal surface structure, e.g., statistically there are 24 Cu-Cu bonds and

24 Pt-Cu bonds in the ordered phase, while the disordered phase has 27 Cu-Cu, 18 Pt-Cu, and 3 Pt-Pt bonds, both on per unit cell basis. Since Cu has much lower dissolution potential than Pt (0.34 V < 0.7 V), the authors expected that the higher number of stronger Pt-Cu bonds in the ordered phase results in a reduced Cu leaching.

Ultimately, in both studies by Hodnik *et al* and Prabhudev *et al* , retention of transition metals in the ordered alloys retained the electronic-structure effect responsible for preserving the specific activities, in other words, their catalytic durability was extended.

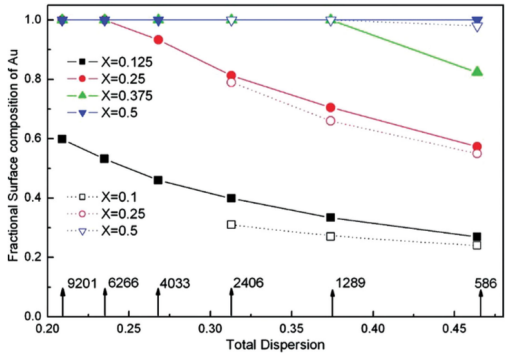

(a) Effect of particle size on the surface-composition of Au-Pt nanoparticles. [297]

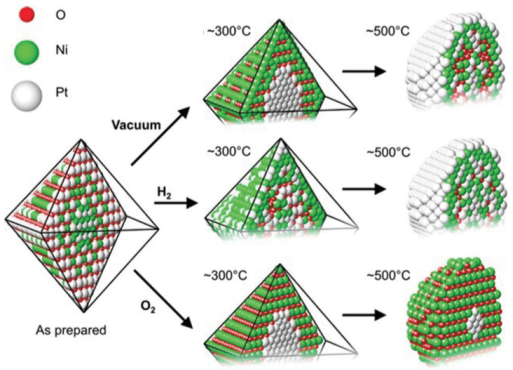

(b) Surface-segregation of Pt-Ni nanoparticles under different atmospheres (vacuum, H_2 and O_2), and different annealing temperatures (300 °C and 500 °C). [298]

Figure 4.6: Effect of heat-treatments on the evolution of a Pt-alloy phase. sources: [297, 298]

4.2.1.3 *Effect of heat treatments*

Heat treatment or annealing is a common procedure carried out to transform the as-synthesized alloys, which are normally disordered, into ordered alloys. During this process, Pt and its alloying elements compete against each other to surface segregate. Although segregation of Pt is highly preferred over the other metals, it may be hindered by various factors such as the particle size, composition and the environment [299]. For example, Lei *et al* [297] investigated the effect of particle size on the surface-composition of Au-Pt nanoparticles with Monte Carlo (MC) simulations (Figure 4.6a). Their findings indicated that at a certain Au-Pt bulk composition, the degree of surface-segregation of Au increases with the increasing nanoparticle sizes. For instance, consider the case of $Au_{0.125}Pt_{0.875}$ (solid black profile in Figure 4.6a) of two different dimensions, 2.46 *nm* and

6.56 *nm*. The total number of atoms in these particles is 586 and 9201, respectively (shown as dispersion on the x-axis). The simulation results (on the y-axis) show that the smaller particle has only 28% Au atoms on the surface, whereas the larger particle has about 60% Au atoms on the surface.

In addition to particle size, segregation also depends on the heat-treatment environment. For example, Ahmadi *et al* [298] studied the surface-segregation of Pt-Ni nanoparticles under different atmospheres (vacuum, H_2 and O_2) and different annealing temperatures (300 °C and 500 °C) (see Figure 4.6b). They found that Ni surface-segregates more-so under the vacuum and oxidising annealing atmospheres than under the reducing H_2 atmosphere. On the other hand, their temperature studies showed that Ni only surface-segregated at relatively low temperatures (T < 475-545 K), at higher temperatures (T > 735 K) they found that it is Pt that surface-segregates.

Most theoretical calculations, however, do not always consider all these factors (size, composition and the environment) simultaneously, and as a consequence, high segregation tendencies for Pt atoms is normally what is predicted for Pt-alloys ([63]). Moreover usually nanoparticles are annealed in batches, i.e. an ensemble of nanoparticles is annealed together as opposed to annealing isolated individual particles. This can result in further deviations from the thermodynamic predictions, as the processes such as ripening and coalescence can constantly change the size and composition of the particles. Additionally, these effects may vary depending on the local chemical environment in the sample, such as the local changes in annealing atmosphere and the substrate orientation with respect to particles. Unfortunately, the *ex situ* approaches (i.e., observing the particles before and after) fail to capture such dynamic processes. Recently, Prabhudev *et al* [300] and Chi *et al* [301] have demonstrated *in situ* structural and compositional tracking Pt-alloy nanoparticles during annealing. Such analyses can be a better alternative to traditional *ex situ* approaches in order to understand the phase-transformation of Pt-alloy nanoparticles. A comprehensive review of surface-segregation phenomenon and the thermodynamic background to nanoparticle transformations can be found in the articles by Liao *et al* [299], Marks *et al* [302].

4.2.1.4 *Voltammetric dealloying*

Since a *3d* transition metal outer shell is not a preferred choice for good ORR electrocatalysis, it has to be removed from the heat-treated Pt-M nanoparticles, which then exposes the underlying electroactive Pt/Pt-alloy surface. This can be achieved by a simple voltam-

metric procedure called 'voltammetric dealloying', which involves continuously cycling the particles between a set potential window [303].

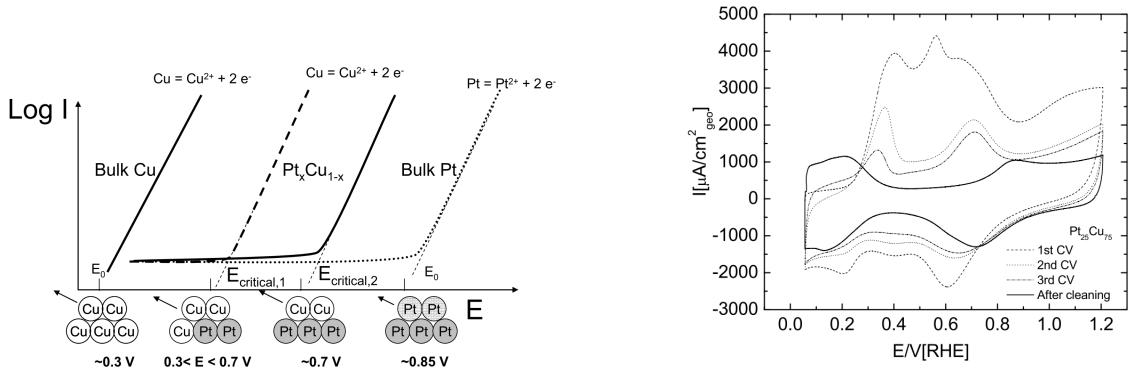

(a) Model estimation of Pt/Cu dissolution potentials for different kinds of surfaces: pure Pt, pure Cu, or a Pt-Cu alloy.

(b) Voltammetric profiles over the course of dealloying.

Figure 4.7: Voltammetric dealloying of Pt-Cu alloy particles. source: [304]

Strasser *et al* [304] showed early on that the Cu species deposited on the surface of Pt-Cu alloy particles could be dissolved ($Cu \longrightarrow Cu^{2+} + 2e^{-}$) when the particles were cycled between 0.06 – 1.2 V. The approach is based on the fact that the dissolution potentials of bulk Cu and monolayer Cu on pure Pt surfaces is about 0.3 V and 0.7 V, respectively. For Cu monolayers on intermediate compositions, such as the Pt-Cu alloy surfaces, the dissolution potentials were estimated to be ranging between these two extreme values (i.e., 0.3 < E < 0.7) (Figure 4.7a). Strasser *et al* obtained the voltammetric profiles for $PtCu_3$ catalyst particles after the 1^{st}, 2^{nd} and the 3^{rd} cycle, and also after fully dealloying, all shown in Figure 4.7b.

In the first CV cycle, no hydrogen adsorption peak is seen (between 0.05 V - 0.3 V), suggesting that initially the particle surface contains very few Pt atoms. In contrast, the profile after fully dealloying shows hydrogen peaks between 0.05 V - 0.3 V that is typical of a Pt surface. The broad anodic peak stretching between 0.25 and 0.85 in the first 3 cycles marks the dissolution of Cu during potential cycling, and its gradual drop in the intensity indicates layer-by-layer leaching of Cu atoms from the surface. Completion of the dealloying process is indicated by the absence of the Cu dissolution peak in the CV curve, as evidenced in the final CV profile. Since the electroactive Pt surface area is recovered in the dealloying process, the resulting ORR activities for such 'dealloyed catalysts'

are usually high. This makes voltammetric dealloying a powerful 'activity enhancing' tool, and is, therefore, widely adopted by most Pt-alloy catalyst systems.

4.2.2 *Compositionally inhomogeneous alloy nanoparticles*

Referring back to the list of different bimetallic alloy types (Figure 4.3), the second alloy type is a compositionally inhomogeneous alloy structure. In here the alloying elements form separate phases within the same structure, separated by a common interface. These structures are sometimes also referred to as the 'phase-separated alloy nanoparticles'.

In comparison to the compositionally homogeneous alloy structures, the reported ORR activities for these structures are much lower. For example, Pt-Au alloys are a commonly discussed system in this aspect as there exists a wide miscibility gap in almost the entire composition range [305]. A miscible PtAu alloy (of random order) is known to form only at low Pt compositions. Fernandez *et al* [306] compared the activities of such Pt-Au catalysts, one random alloy and other phase-separated. They found that the ORR activities of Pt-Au phase separated particles was lower (~2 fold) than that of the random alloys. This was attributed to the poor oxygen binding of Au domains in these particles. Similar studies conducted by Wanjala *et al* [307] indicated higher activities for a phase-segregated Pt-Au shell compared to pure Au shell. The observed improvement was attributed to the incorporation of oxygen-binding Pt domains into the oxophobic Au shell.

4.2.3 *Heterostructured alloy nanoparticles*

The third alloy type is a heterostructure (Figure 4.3) wherein two or more pure metallic nanoparticles/atomic-clusters share one common interface. Commonly reported alloys in this category include Pt@M and M@Pt structures, where M = Au [270, 310], Ag [311], Pd [308], Fe_3O_4 [312]. Here M@Pt refers to the deposition of smaller metal (M) nanoparticles/atomic-clusters onto much larger base nanoparticle Pt, *vice versa* for Pt@M.

Peng *et al* [308] studied the activity of carbon supported Pt@Pd and Pt catalysts. Representative TEM image and elemental mapping of Pt and Pd on a heterostructure is shown in Figure 4.8a. Figure 4.8b*(top panel)* shows the estimated hydroxyl coverage for both catalysts. As can be seen, the incorporation of Pd greatly reduced the fractional adsorption of the hydroxyl species. The effect can be immediately seen in the calculated kinetic

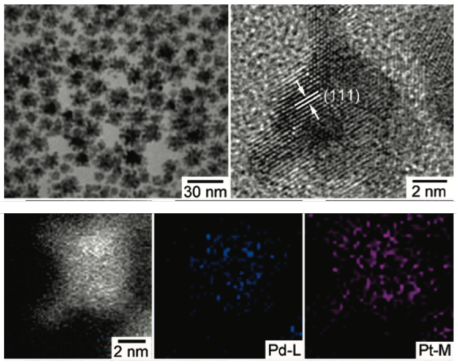

(a) TEM imaging and elemental analyses.

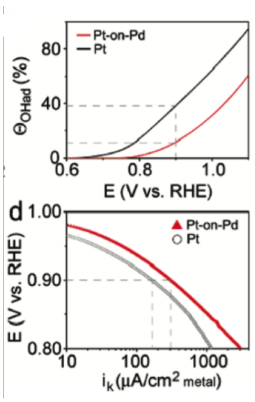

(b) OH coverage (upper) and activity (lower).

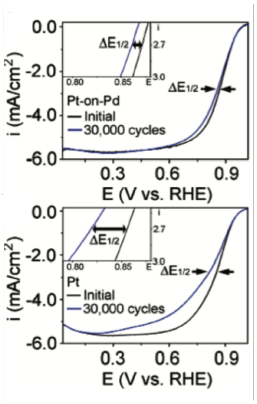

(c) Durability

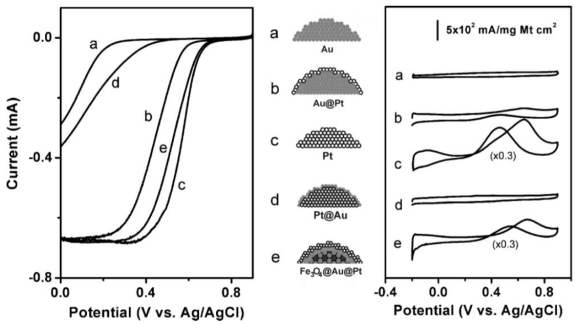

(d) ORR polarization curves.

Figure 4.8: Catalytic performances of heteronanostructures: (a–c), bimetallic; (d), ternary. sources: [308, 309]

current densities (@ 0.9 V) shown in Figure 4.8b*(bottom panel)*, which indicates a much higher ORR activity for the Pt@Pd catalyst compared to the Pt catalyst.

Peng *et al* also studied the long-term stability of these catalysts, over 30000 cycles. The Pt@Pd catalysts suffered only about 12 % of the initial ECSA loss and a small degradation in the half-wave potential (~9 *mV*, Figure 4.8c*(top panel)*). In sharp contrast, Pt catalysts suffered serious ECSA losses (~39 %) and a large degradation in the half-wave potential (~35 *mV*, Figure 4.8c*(bottom panel)*).

As a progression from such bimetallic heterostructures, Luo *et al* [309] formed ternary Pt@Au@Fe_3O_4 heterostructures. They found that the mass activity for Fe_3O_4@Au@Pt catalysts was higher than the bimetallic Pt-Au combinations (Au@Pt and Pt@Au) (see polar-

ization curve given in Figure 4.8d, which was attributed to the synergistic effects of the nanoscale oxide core on the Pt and Au surface sites. This demonstrates the remarkable opportunity for improving the activities of such heterostructures by further fine-tuning.

4.2.4 *Core-shell alloy nanoparticles*

The fourth alloy type is the core-shell alloy structure (Figure 4.3) wherein a monolayer or a few layers of Pt encapsulates the core of lesser expensive metals [313–320]. Depending on the thickness of the Pt-shell, they are also called Pt-skins (two or more atomic-layers thick), or Pt-skeletons (1 atomic-layer thick).

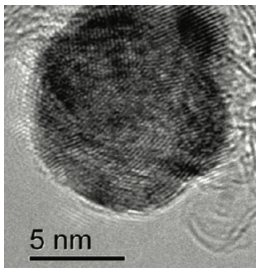

(a) TEM image.

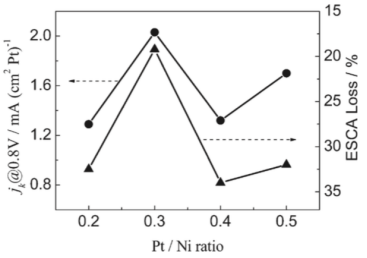

(b) ECSA losses *vs* Pt/Ni ratio.

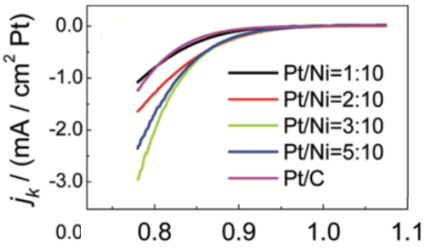

(c) Activity profiles.

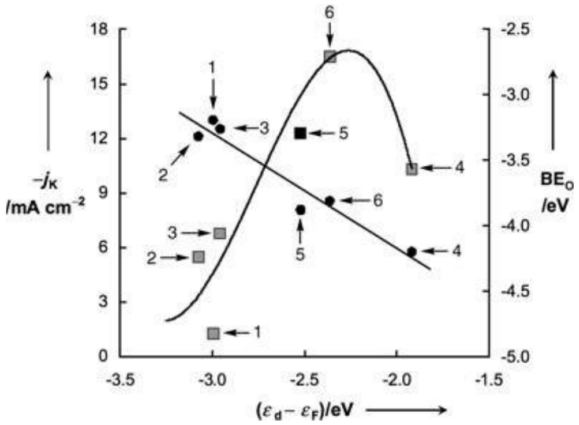

(d) ORR activities *vs* d-band center position for Pt_{ML} on (1) Ru(0001), (2) Ir(111), (3) Rh(111), (4) Au(111), (5) Pt(111) and (6) Pd(111) surfaces.

Figure 4.9: Catalytic performances of core-shell Pt-alloy NPs: Pt-Ni at variable ratio: (a–c), Pt_{ML} on different surfaces (d). sources: [321, 322]

Pt loading in such structures is substantially reduced, and the alloying effect on the Pt-shells particularly in the case of Pt-skeletons can be highly effective. Both these factors contribute to the improvements in the ORR mass and specific activities observed for the core-shell structures. For example, Chen *et al* [321] synthesized a series of Ni(core)-Pt(shell) nanoparticles with different amounts of Pt content deposited on 5 *nm* Ni nanoparticles (Pt/Ni = 0.2, 0.3, 0.4, 0.5). Figure 4.9 summarizes the representative TEM image of such particles (Figure 4.9a), the measured ECSA (Figure 4.9b) and specific activities (Figure 4.9c). All the core-shell catalysts were found to outperform the activity given by Pt/C, the maximum specific activity was given by particles with Pt/Ni ratio of 3:10 (3-4 times higher than Pt/C at 0.85 V). However, among the different compositions a volcano-type relationship in the activities were found (Figure 4.9b). Chen *et al* estimated that the particles with Pt/Ni ratio of 3:10 will have a monolayer Pt-shell. Thus, the activity trend in Figure 4.9b indicates that the monolayer core-shell nanoparticles give the maximum ORR activity, while lower or higher Pt surface coverages evidently result in relatively poorer activities. Adzic *et al* [322] investigated the ORR activity of monolayer Pt-shells on many different metal surfaces such as Au(111), Rh(111), Pd(111), Ir(111) and Ru(0001), and found a volcano-type dependence of the measured ORR activities with the 'd-band centers' (Figure 4.9d). The maximum activity was found for the Pd(111) surface.

Monolayer core-shell nanoparticles gives the maximum ORR activity compared to thicker shells

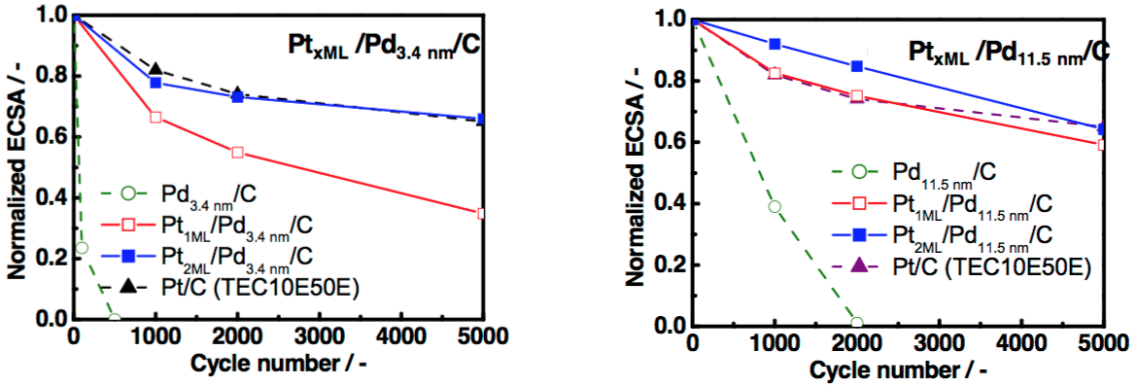

(a) Smaller Pd cores (3.4 *nm*)

(b) Larger Pd cores (11.5 *nm*)

Figure 4.10: ECSA losses in the case of smaller (a) and larger (b) Pd(core)-Pt(shell) nanoparticles. source: [323]

Chen *et al* 's measurement of ECSA profiles in Figure 4.9b showed that the monolayer core-shell particles yielded higher stabilities (i.e., low ECSA losses). However, this is attributed to the large sizes of the Ni cores Chen *et al* had formed. Usually, the opposite stability trend is observed for the smaller core-shell nanoparticles. For example, Inaba

et al [323] synthesized Pd(core)-Pt(shell) nanoparticles of different Pt core sizes, 3.4 *nm* and 11.5 *nm* from a galvanic replacement of the under potentially deposited (UPD) Cu on Pd electrodes with Pt. The measured ECSA profiles are shown in Figure 4.10 for the small (a) and the large Pd (b) core sizes, respectively. For the same Pt-shell thickness, it can be seen that the core-shell particles with larger Pd cores were more durable than the ones with smaller Pd cores. In other words, the larger core-shell nanoparticles were more durable than the smaller ones. This is attributed to the lower dissolution potentials of larger particles compared to smaller ones.

Larger core-shell nanoparticles could be more durable than the smaller ones

4.2.4.1 *Metal dissolution in core-shell structures*

Mechanistically, it is intuitive to think of dissolution in core-shell structures as involving first the dissolution of the atoms in the shell, followed by the dissolution of atoms in the core. However, the coverage of shells are not always complete and moreover, atoms from different facets of the particle can dissolve at different rates (owing to different surface energies). As a result, the metal core can remain exposed to the solution before the shell is even fully dissolved. Depending on their dissolution potential with respect to Pt, some metals in the core can leach out at a much faster rate than the shell, creating structural voids within the core, also called as 'pin holes'.

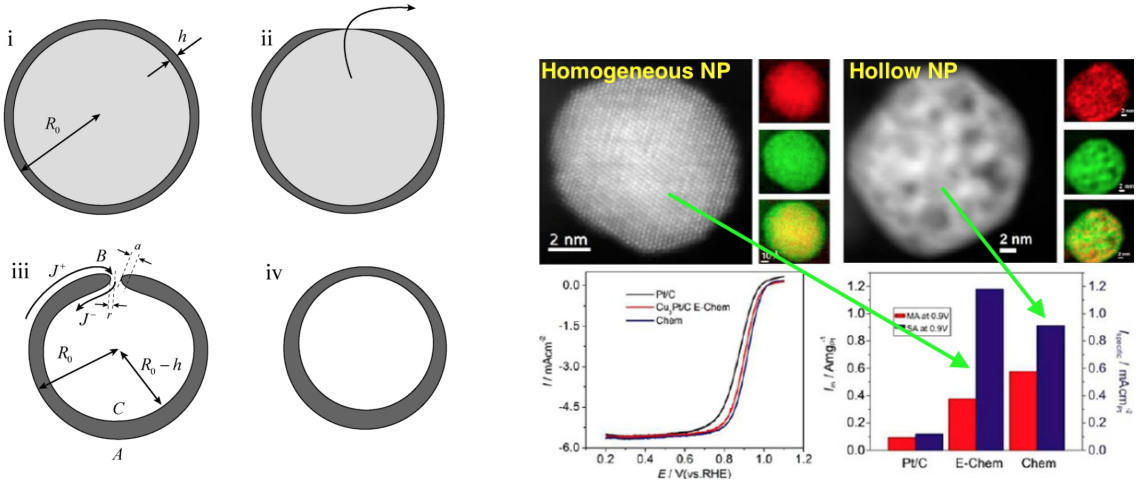

(a) Different stages of the formation of 'pin holes' in core-shell NPs.

(b) Comparison of ORR activities of homogeneous and hollow Pt-Cu NPs.

Figure 4.11: Degradation of core-shell nanoparticles *via* 'pin hole' formation. sources: [324, 325]

Erlebacher *et al* [324] have modeled the 'pinhole' formation in transition-metal core and Pt shell nanoparticles using thermodynamic Gibbs distributions. Their model assumes the surface-diffusion is the major contributor to the dissolution of lesser noble metals, instead of the transport of less noble metals to the surface by bulk-vacancy diffusion. As shown in the series of schematic in Figure 4.11a, a core-shell nanoparticle of radius R_o and shell thickness *h* can expose the core to the acidic environment due to shape fluctuations (i), allowing it to be dissolve away (ii). This results in the formation of a pinhole of radius *r* (iii). Note that a diffusional flux exists from the convex outer surface (A) through the pinhole edge (B) into the inner concave surface (C). Erlebacher *et al* 's calculations showed that for a large radius of curvature of the pinhole, the net flux at the pinhole edge can be positive ($J' > J$), resulting in the closure of the pinhole and the creation of a hollow/spongy nanoparticle.

Wang *et al* [325] have shown that the specific activities of such Pt-Cu hollow nanoparticles are lower compared to $PtCu_3$ homogeneous alloy nanoparticles (Figure 4.11b). This is more likely to be the case for Pd(core)-Pt(shell) structures as Pd is more vulnerable to dissolution than Pt (evident from the ECSA profiles of Pd/C in comparison to Pt/C in Figure 4.10).

One strategy to improve the stability of core-shell nanoparticles is to increase the size of the particles (Figure 4.10). Recently, another strategy is also being explored which is to replace the pure non-noble metal core with a 'mixed alloy cores', such as Pt_3Co, NiN_x, Pd_3Co, Fe_3Pt, Au-Pd. These belong to the class of 'composite alloy structures', discussed in the following section (Section 4.2.5).

4.2.4.2 *Effect of particle size on the activity of core-shell structures*

Larger core-shell particles maybe more active than the smaller ones

In addition to dictating the stability, particle sizes can also dictate the activities in core-shell nanoparticles. For example, Inaba *et al* also measured the specific activities for the same Pd(core)-Pt(shell) catalysts, and have found that the larger Pd core give a higher specific activity compared to smaller Pd cores, Pd(11.4 *nm*): 490 $\mu A/cm^2$ > Pd(3.4 *nm* and 4.8 *nm*): 288-330 $\mu A/cm^2$.

Interestingly, the specific activities of smaller core-shell nanoparticles (Pd core size 3.4 and 4.8 *nm*) was even smaller than that of Pt/C (350 $\mu A/cm^2$). Using DFT calculations, Wang *et al* [326] attributed the activity enhancements seen in the larger particles to the increased surface fraction of atoms on the (111) facets (see Figure 4.12). Particularly, the

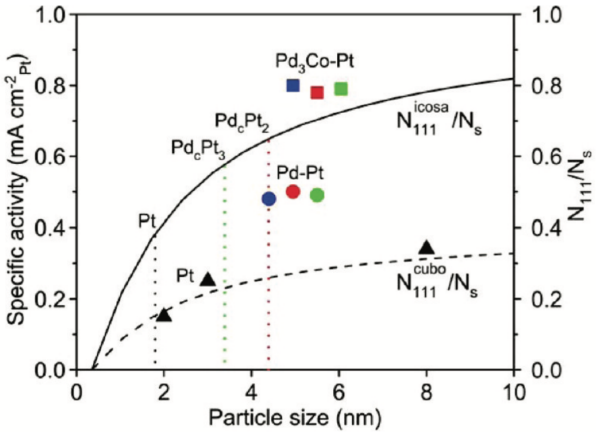

Figure 4.12: Plot of ORR activity and the surface fraction of atoms on the (111) facets as functions of particle size. source: [326]

(111) facet was shown to provide an optimal binding of oxygen compared to other facets (e.g., (100)) and the edge sites.

Overall, such findings on the size-dependency of activity and stability of core-shell nanoparticles explain why larger sized core-shell nanoparticles are preferred over smaller ones.

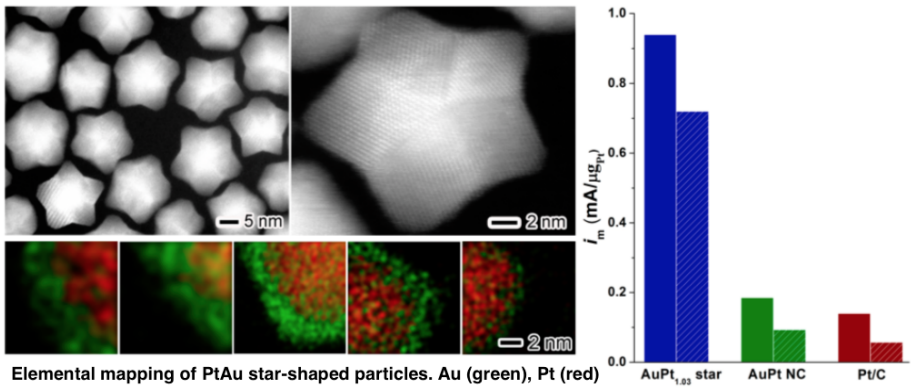

Figure 4.13: Comparing the activities of PtAu star shaped and spherical particles. source: [327]

4.2.4.3 *Effect of particle shape on the activity and stability of core-shell structures*

Wang *et al* 's calculations in Figure 4.12 also illustrate the size-dependency of the fraction of (111)-surface atoms for particles of two different shapes, cuboctahedral and icosahedral. A large difference in the fraction of (111)-surface atoms between the two shapes indicates that the shape-controlled synthesis can be an useful strategy for enhancing ORR activities in core-shell structures.

A recent study by Bian *et al* [327] compared the activities and stabilities of Pt-Au star shaped decahedra core-shell nanoparticles with those of spherical PtAu nanoparticles (Figure 4.13*(Left panel)*). As shown in Figure 4.13*(Right panel)*, the mass and the specific activity of such star shaped particles were both about 5 fold higher than those of PtAu nanoparticles. Additionally, Bian *et al* also conducted accelerated stability tests (ADT) to evaluate the durability. To avoid size-effects from comparing the large PtAu star-shaped decahedra and the small spherical nanoparticles, they instead used Pt icosahedra nanoparticles with the similar size as PtAu star-shaped particles as the reference. They found that the star-shaped particles were highly stable with only ~10 % loss in the initial specific activity after 30000 cycles. In sharp contrast, the Pt icosahedral particles suffered about ~44 % loss in their initial specific activity.

4.2.5 *Composite alloy nanoparticles*

Finally, the fifth alloy type is the emerging class of composite alloy structures (Figure 4.3) wherein the structural features of two or more basic alloy types (four varieties discussed above) are combined to derive synergistic effects. For example, various 'ordered intermetallic core-shell' structures have been reported recently [328, 329]. Here the Pt-shell encapsulates an ordered Pt-alloy. In this way the pure metal character of the core in a core-shell structure is replaced with the alloy character of an ordered alloy structure. Different alloy systems have been explored for the particle core, such as Pt-Fe [91, 330–335], Pt-Co [336], Pt-Cu [337], Pt-Ni [338].

A representative TEM image of a Pt-Co ordered intermetallic core-shell nanoparticle synthesized by Wang *et al* [336] is shown in Figure 4.14a. Since the particular imaging mode is sensitive to atomic-numbers (Z) (Intensity~$Z^{1.6}$), Pt atoms being heavier appear brighter compared to the much lighter Co atoms. Thus, the alternating brighter and darker intensities seen in the core-region correspond to individual atomic-columns of Pt

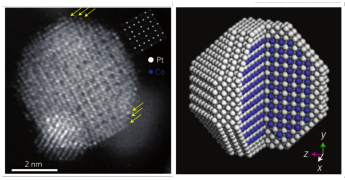

(a) Representative TEM image of a PtCo/C-700 particle.

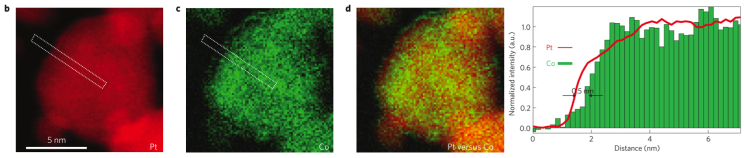

(b) Elemental mapping and line scan over a PtCo/C-700 particle.

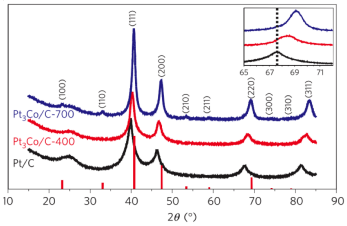

(c) XRD patterns for Pt-Co particles annealed at 400 °C and 700 °C.

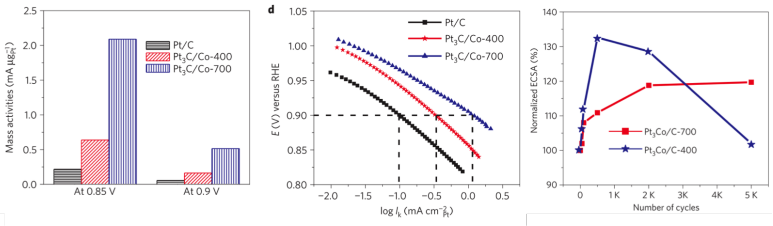

(d) Measured mass activities, Tafel plots (specific activity) and ECSA.

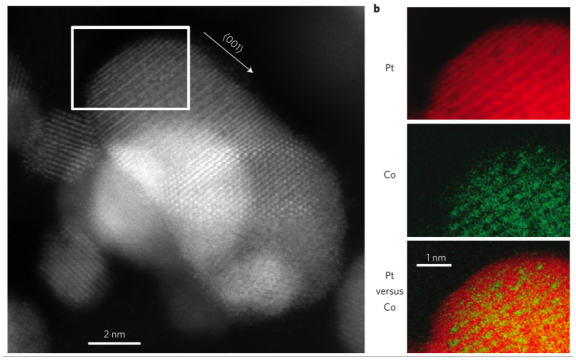

(e) Elemental maps of PtCo/C-700 particles after 5000 cycles.

Figure 4.14: Composite Pt-alloy NPs: case of Pt-Co ordered intermetallic core-shell nanoparticles. Refer to text for details. sources: [336]

and Co, respectively, thus confirming the ordered alloy structure in the particle core. Similarly, the appearance of preferentially brighter intensities in the shell region confirmed the Pt-rich shell. This ordered intermetallic core-shell structure was further supported with Pt and Co compositional profiles across the particle, obtained using electron energy loss spectroscopy (Figure 4.14b).

Wang *et al* studied the activities of these Pt-Co ordered particles, represented as PtCo/C-700, in reference to a disordered particle, represented as PtCo/C-400. The difference between these catalysts was the annealing temperature, 700 °C for PtCo/C-700, and 400 °Cfor PtCo/C-700. Using X-ray diffraction measurements (Figure 4.14c) Wang *et al* showed that the alloy cores in PtCo/C-700 particles were ordered, while the alloy cores in PtCo/C-400 remained disordered. This was clear from the 0.8 % higher lattice contraction and the pronounced appearance of (100) and (110) reflections observed for the PtCo/C-700 sample. The lattice contraction was measured using the Debye-scherrer relationship by noting a shift in the (220) reflection for the two alloy samples with respect to pure Pt. The (220) reflection at $2\theta \sim 69°$ is characteristic of Pt metal, and a shift to higher angles indicates the incorporation of Co into the Pt lattice forming alloy phases.

The measured ECSA and Tafel plots for both alloy samples with respect to Pt/C is shown in Figure 4.14d. The specific activities (i_k at 0.9 V) of PtCo/C-700 was the highest (1.10 mA/cm^2) compared to PtCo/C-700 (0.31 mA/cm^2) and Pt/C (0.09 mA/cm^2). The ordered PtCo/C-700 catalysts were also most durable, evident from their much lower ECSA losses after 5000 cycles in comparison to disordered PtCo/C-400 particles, and a much lower negative shift in the half-wave potential (~10 mV for PtCo/C-700, ~30 mV for PtCo/C-400). The high stability of such composite structures is attributed to the retention of the ordered structure even after 5000 potential cycles (Figure 4.14e shows the TEM image and compositional maps for PtCo/C-700 particles after 5000 cycles). In parallel and occuring simulataneously as Wang *et al* 's work, Prabhudev *et al* have made similar observations in the case of Pt-Fe ordered intermetallic core-shell particles ([91]).

Zhang *et al* [339] studied the effect of alloy composition in Au_xPd_y@Pt composite alloy structures on the ORR activity. Figure 4.15a illustrates the plot of measured ORR activities (in terms of onset potentials of the kinetic regime) for different Au_xPd_y core-alloy compositions as a function of the theoretically determined oxygen binding energies. A volcano-type relationship in the activity trend can be seen, evidencing the highest activity for $Au_{35}Pd_{105}$@Pt, i.e. 75 % Pd. This is in good agreement with the theoretical prediction of the occurrence of optimum binding energy (~1.5 eV) for the 72 % Pd core-alloy (Figure 4.15b).

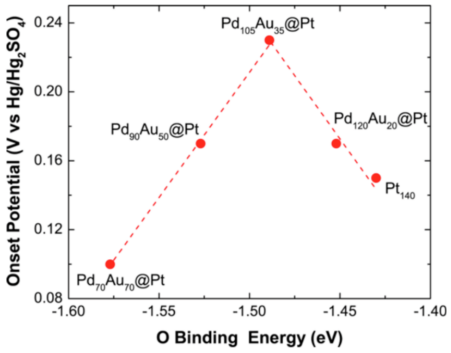

(a) Measured activities (in terms of onset potentials of the kinetic regime) for different Au_xPd_y core-alloy compositions *vs* O_2 BEs.

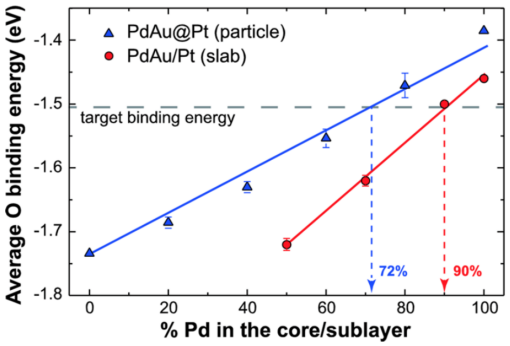

(b) Theoretically determined O_2 BE *vs* % Pd in the sublayer.

Figure 4.15: Effect of alloy composition in Au_xPd_y@Pt composite alloy structures on the ORR activity. source: [339]

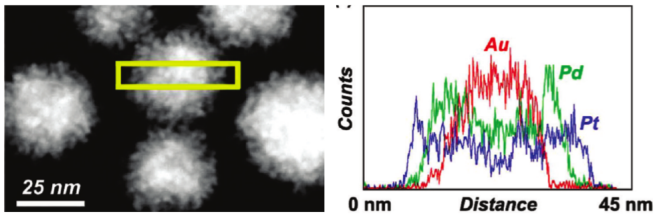

(a) Elemental line profiles evidencing the Au(core)@Pd(inner-shell)@Pt(outer-shell) composite structure.

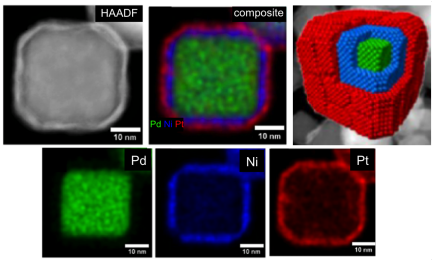

(b) TEM image and elemental maps evidencing the Pd(core)@Ni(inner-shell)@Pt(outer-shell) composite structure.

Figure 4.16: Examples of multi-shell-structured composite Pt-alloy nanoparticles. sources: [340, 341]

Similar synergistic effects has been found when instead of the core, the shell structure is modified. This strategy is the basis of many 'multi-shell-structured' or 'onion-like' nanoparticles [275, 340–343]. For example, Wang *et al* [340] combined the core-shell and heterostructure strategies to synthesize Au@Pd@Pt core-shell composite nanoparticles with Au core, Pd inner shell and nanoporous Pt outer shell. A typical TEM image and Pd, Au, Pt compositional profiles supporting the composite structure is shown in Figure 4.16a. These particles were synthesized by first forming Au@Pd core-shell nanoparticles onto which the Pt clusters were deposited *via* chemical reduction. Wang *et al* compared the activities of these Au@Pd@Pt/C core-shell particles with binary Au@Pt/C core-shell particles. They found about 1.5 times higher activity for the composite alloy structure compared to simple bimetallic core-shells. The enhancement was attributed to the two-step alloying effect on Pt (Pd on Pt, Au on Pt *via* Pd), and the concomitant electronic structure effect reducing the binding energy in Pt. Figure 4.16b illustrates another example where a Ni interlayer is sandwiched between the innermost Pd core and the outer Pt-shell. These examples demonstrate the enormous potential behind the synthesis of such composite alloy structures to further improve the ORR activities and enhance stability.

4.3 RELATIVE STANDING OF DIFFERENT CATALYST SYSTEMS

The above discussion has highlighted many different Pt-alloy catalyst systems and the alloying strategies. Yet, these only represent a small sample of the much larger set of catalyst systems reported in the literature. This is because both the rate of development, and the volume of the reports produced are very large, which is not surprising given that the ORR catalyst development is crucial to the commercialization of PEMFCs. For this reason, most reviews compare the activities and stabilities of only the major catalyst systems reported within a specific span of time (1-5 yr).

In 2012, Debe [23] conducted a comprehensive comparison of major catalyst systems, summarized as shown in Figure 4.17. Composite plots of mass activity versus specific activity measured by both RDE (Figure 4.17a) and MEA (Figure 4.17b) are shown. Debe's two charts indicate that the RDE measured activities tend to be high compared to those measured in a MEA, e.g., specific activity of core-shell monolayer Pt catalysts is > 1 mA/cm^2 in RDE and < 0.5 mA/cm^2 in a MEA. This demonstrates the harshness of the real fuel cell environment wherein the reaction normally occurs on the oxidized catalyst surfaces instead of clean catalyst surfaces that is usually what is achieved under the

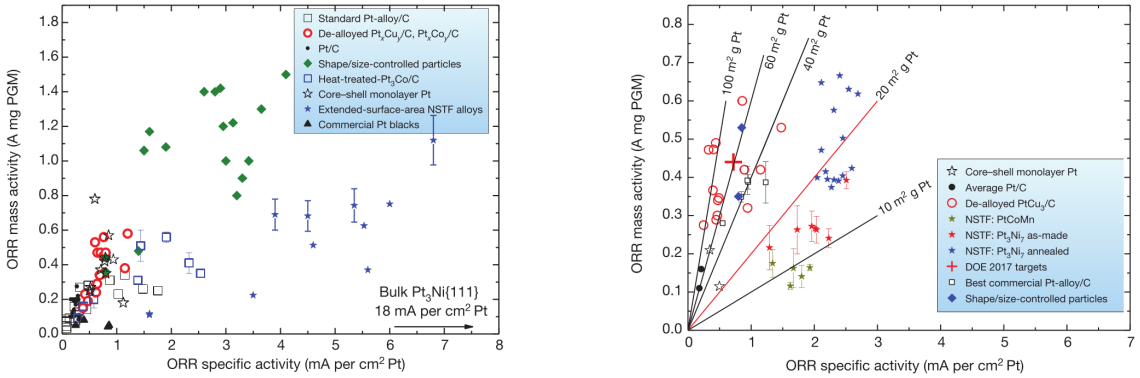

(a) Plot of mass activity *vs* specific activity determined using RDE.

(b) Plot of mass activity *vs* specific activity determined from MEAs.

Figure 4.17: Comparison of kinetic activities of major catalyst systems conducted by Debe [23].

conditions set in a RDE. The MEA chart in Figure 4.17b also provides the activities of standard Pt/C catalysts, and the DOE set target for mass activity (0.44 A/mg$_{Pt}$). These values provide a useful reference for comparing different catalyst systems. As it can be seen in Figure 4.17a, several Pt-alloy/C catalyst systems are able to exceed the activity given by Pt/C catalysts. Similarly, Figure 4.17b shows that the best commercial Pt-alloy catalyst comes very close to the DOE mass activity target in a MEA (Year-2012 basis). However, Debe reports that the durability of the same catalyst fails to meet the DOE set durability target (i.e., 5000 hour continuous MEA operation). By conducting a similar analysis on the other catalysts, Debe concluded that even the highest performing catalyst systems are still not practical as both the mass-activity and the durability requirements are not satisfied simultaneously.

Very recently, Colic and Bandarenka [344] compared the activity trends in the dealloyed Pt-M alloy catalysts (M represents 3*d* -transition metals and lanthanides). They used the atomic-radius of these alloying metals as the semi-empirical descriptor of the strain induced on the Pt-overlayers. In addition to strain, since the activity also depends on the alloy composition, ideally a 3D plot of activity as a function of atomic-radius of the solute and composition would be very descriptive. Colic and Bandarenka's schematic illustration of such a 3D plot is shown in Figure 4.18a (dashed white line connects points of highest activity). This, however, requires a large amount of literature data and normalization of different experimental protocols followed in measuring the activities. Colic and Bandarenka simplified the situation by only plotting the projection of the 2D sur-

face intersecting the highest activity to the activity-atomic radius plain, as shown in Figure 4.18b.

In developing the plot in Figure 4.18b, Colic and Bandarenka extracted the highest activity reported for each alloy system in the literature. To eliminate systematic errors resulting from the comparison of activities measured under different conditions, they calculated 'relative activities' with respect to the activity of the Pt/C benchmarks used by the reports. The white and gray areas in Figure 4.18b mark the regions of stronger and weaker binding of the intermediates with respect to calculated ideal binding.

Colic and Bandarenka obtain two maxima as can be seen in Figure 4.18b, for atoms on either side of Pt (smaller and bigger). Both the trends can be explained from the 'electronic structure effect' discussed earlier in the section, which suggests that a compressive strain on the Pt overlayers resulting from the alloying with smaller solute atoms (to Pt) weakens the chemisorption until an optimum binding is reached (appears close to Pt-Cu). Alloying with atoms much smaller (than Cu) results in binding of the intermediates 'too weakly', consequently leading to decreased activities.

Similar analysis holds even for larger solute atoms (than Pt). Note that although it might be intuitive to think of alloying Pt with larger atoms as inducing tensile strain, studies have shown that the alloying of Pt with lanthanides can result in compressive strain. One possible reason could be that the Pt overlayers may not be epitaxial with the alloy core. Thus, instead of simply a stretch in the Pt-shell in correspondence with the alloy core, a distinct restructuring at the core-shell interface might be happening.

Colic and Bandarenka's comparative plot suggests that the Pt-Cu (among $3d$ metal solutes) and Pt-Y (among lanthanide solutes) nanoparticle catalysts may yield the highest ORR activities, attributed to optimum binding of the intermediate species. However, note that the stabilities of both these catalysts are much lower than the durability target set by DOE. Thus, Colic and Bandarenka's review agrees with Debe's inference that since all the requirements (activity and durability) are not satisfied simultaneously, even the best performing Pt-alloy catalysts are still not practical. Other reviews arrived at a similar conclusion [256, 257].

Apart from providing a clear overview of the strain effects on the activity of different catalyst systems, Colic and Bandarenka's plot is also useful in explaining the anomalous size effects on the activities of different Pt-alloy catalysts. For example, while the activities of Pt and Pt-Y catalysts decrease with the decreasing particle sizes, the activity of Pt-Ni catalysts show an oscillating volcano-type behavior, as illustrated in Figure 4.18c. This

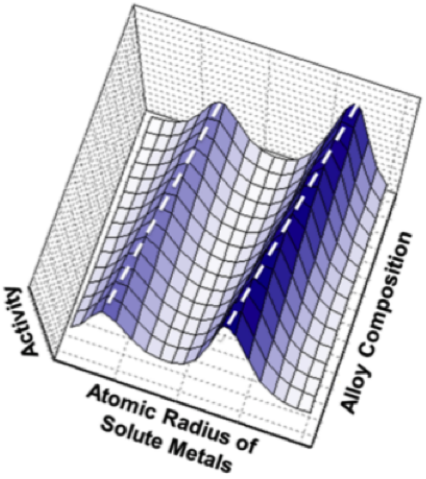

(a) Schematic illustration of a 3D plot of activity as a function of atomic-radius of the solute and composition.

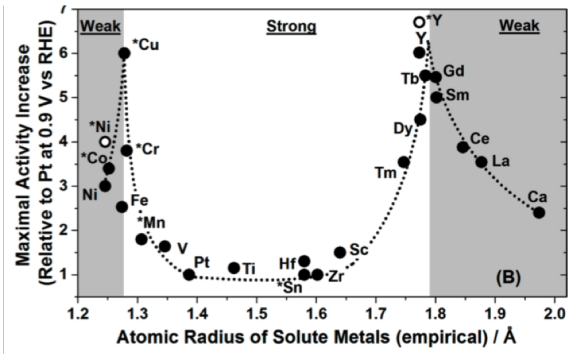

(b) Projection of the 2D surface intersecting the highest activity to the activity-atomic radius plain in (a)

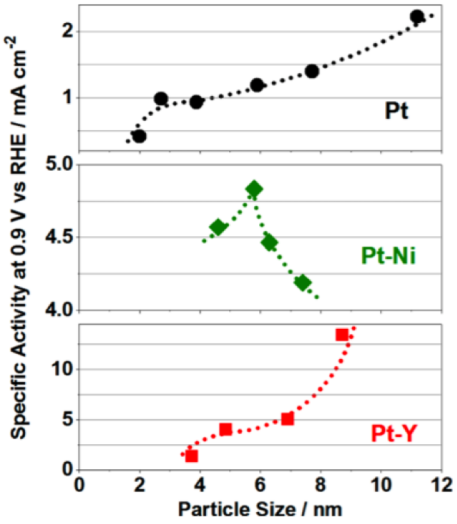

(c) Plot of measured activities of Pt-Ni, Pt-Y and Pt catalysts as a function of particle size.

Figure 4.18: Comparison of calculated activity trends in the dealloyed *Pt-M* alloy catalysts. source [344].

can be explained with the aid of Colic and Bandarenka's plot in Figure 4.18b. Note that a decrease in the particle sizes increases the number of active sites, kinks, steps and edges, which are all stronger binding to oxygen compared to flat surface facets of a larger particle. Thus, decreasing particle sizes results in stronger binding of the intermediates. As one can see from the Figure 4.18b, Pt is already strongly binding. Hence, further decrease in the particle sizes of Pt makes it bind much stronger, and thus decreases the activity. Pt-Y on the other hand, lies on the top of the volcano (larger atomic-radius side) providing optimum binding. Further reduction in the sizes of Pt-Y particles will, therefore, make it strongly binding, and thus the activity is decreased. Pt-Ni catalysts are located in a regime where the binding is 'too weak'. Reducing the sizes of Pt-Ni particles will initially result in stronger binding towards the optimal value, thus activity increases initially. But, once the optimum binding is reached, further reduction in the particle size will only make it more strongly binding, thus decreases the activity.

4.4 PERSPECTIVE

In summary, the present article has provided a comprehensive review of progress in the development of Pt-alloy catalysts for the ORR, and its current status. Great progress has been made over the past decade to fine-tune the electronic structure of Pt surface layer by alloying. Various bimetallic Pt-alloy catalysts have been developed till date. Usually alloying with $3d$ transition metals (M: Fe, Co, Ni, Cu) gives improved ORR activities, while alloying with platinum group metals (PGMs: Pd, Ru, Ag, Au, Ir) provides better stabilities. To benefit from both these advantages, rational design of ternary Pt-M-PGM alloys are also being explored, and in most cases the stabilities of such Pt-M-PGM ternary catalysts are much higher than that of bimetallic Pt-M or Pt-PGM alloy nanoparticles.

Different strategies for the mixing of metals have been developed, classified into five categories as follows: (1) arranging Pt and solute atoms within the nanoparticle structure either in an ordered or disordered manner, (2) forming separate Pt-alloy phases within the same structure, (3) contacting Pt nanoparticles with the nanoparticles/atomic-clusters of other metals at a common interface, (4) forming core-shell structures by encapsulating the core of a lesser expensive metal with either monolayer or a few layers of Pt, (5) combining one or more strategies (1)-(4) in the same nanoparticle structure so as to derive the resulting synergistic effects.

Each strategy aims to control one or more of the many factors determining the activity and the stability of Pt-alloys, including particle size, composition, morphology, surface-segregation, synthesis method, post-treatments. Merits of each strategy were discussed with the aid of recent examples from the literature. Different catalyst systems were highlighted in regards to their structural optimization, mass and specific ORR activities, and the ECSA losses. Comparative analyses of these metrics across different catalyst systems indicate that although several catalysts exceed the activity targets required for the commercialization of PEMFCs, even the best performing catalysts still do not satisfy all the requirements (activities, cost and durability) simultaneously. It can, therefore, be concluded that no one Pt-alloy catalyst system is yet practical to be used in the commercial PEMFCs. Nonetheless, the ORR catalyst development efforts have seen remarkable progress over the past decade, and the efforts must continue unabated.

5

SCANNING TRANSMISSION ELECTRON MICROSCOPY FOR CATALYSIS

Previously in Section 3.5 the importance of structural characterization techniques to ORR catalyst development efforts was pointed out. In particular, the strengths and weaknesses of two prominent techniques, electron microscopy and x-ray absorption spectroscopy, were discussed. Their contributions to understanding the atomic- and chemical- structures of a variety of Pt-alloy catalyst designs were also reviewed. Moving forward, advancements allowing for the visualization of catalysts in their native environments was emphasized.

In the investigation of the Pt-alloy structures discussed in the thesis, the characterization was exclusively carried out using an aberration-corrected scanning transmission electron microscope (STEM), and the associated imaging and spectroscopic techniques (HAADF-STEM and EELS, respectively). The principles, operation and interpretation of various signals related to these techiques, here we discuss in the present chapter.

5.1 CONSTRUCTION AND OPERATION OF A STEM

Figure 5.1 shows the typical ray diagram of a STEM illustrating essential components required for imaging and spectroscopy. These can be categorized into (1) components required to form the smallest possible STEM probe, and (2) components required to detect electrons after the specimen interaction. Components in the first category are placed before the specimen, including an 'electron gun' to generate electrons, 'condenser and objective lenses' to converge the electron beam into a small probe at the sample, 'scan coils' to deflect the electron beam during scanning operation, and an 'objective aperture' to limit the effects of aberrations from lens. Components in the second category are placed after the sample and normally include different electron detectors for imaging, such as bright field (BF), annular bright field (ABF), annular dark field (ADF) and high angle ADF (HAADF) detectors, and for spectroscopy (EELS spectrometer). Depending

on the detector used for imaging, different kinds of STEM images can be produced (e.g., BF-STEM, ABF-STEM, ADF-STEM and HAADF-STEM).

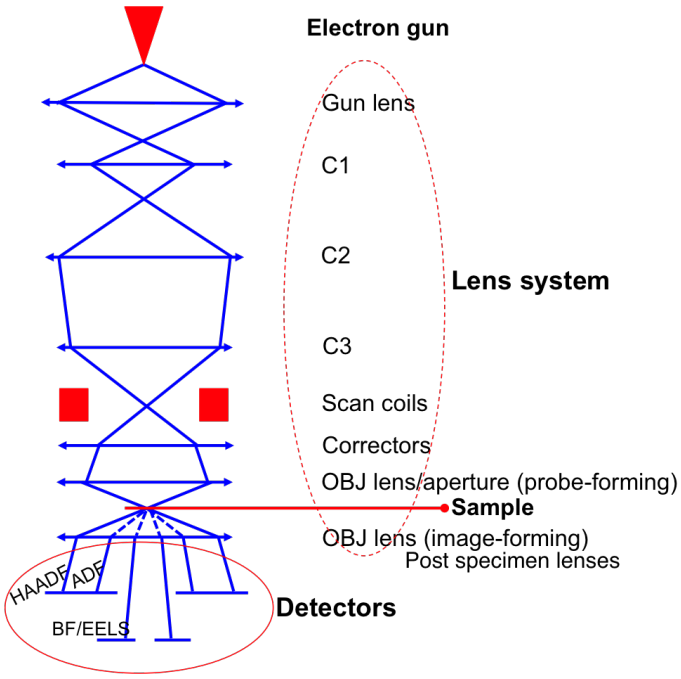

Figure 5.1: Simple ray diagram of a STEM (based on FEI-Titan 80-300 cubed microscope).

The image formation in a STEM is in many ways similar to the more commonly known scanning electron microscopy (SEM) technique. The electron gun generates a beam of electrons which are focused onto a small probe by a series of electron lens systems (condenser and objective lens). The electron probe formed is then scanned over the specimen with the help of scan coils (i.e., by excitation of coils with an applied voltage). The electrons interacting with the specimen are scattered to different angles. Two kinds of interactions can be important,[1] namely (a) elastic scattering, which refers to an electrostatic interaction with the nucleus of the specimen atoms,[2] and (b) inelastic scattering, which refers to the interaction with electrons within specimen atoms. In particular, the elastically scattered electrons are used for imaging, which are collected by different detectors

[1] other interactions include, generation of secondary electrons, back-scattered electrons, X-rays, Auger electrons, and cathodoluminiscence. Detailed description of these processes can be found elsewhere [213].

[2] In addition to this atomic-picture, wave nature of the electrons cannot be ignored. In a crystalline solid, scattered electron waves interfere, peaking at angles characteristic of lattice-spacing of the specimen. Thus, 'diffraction' is another possible elastic scattering event, generating 'diffraction contrast' under certain microscope conditions (see Section 5.3.3).

(BF / ABF / ADF / HAADF) geometrically placed such that the electrons arriving at a particular range of scattering angles can be selectively collected. For example, the 'collection angle' of the BF detector is about 34.8 *mrads*, while that of an HAADF detector is between 120–200 *mrads*. In all the cases, the electron intensity generated on the detector is plotted as a function of probe position to form an image.

Most STEMs are also equipped with an electron energy loss spectrometer which collects the inelastically scattered electrons passing through a central hole in the annular ADF detectors. Inelastic scattering is an 'energy loss' event wherein depending on the interaction with electrons in different shells in the specimen atom (core-levels or valence), the incident electrons exit the specimen at different kinetic energies. The EELS spectrometer collects and separates such inelastically scattered electrons based on their kinetic energies, and plots the intensity (i.e., electron counts) as a function of the energy loss (i.e., initial energy minus the kinetic energy at collection), usually termed as an 'EELS spectrum'. In the modern aberration-corrected STEMs that are equipped with ultra-fast EELS spectrometers, both ADF-STEM imaging and EELS spectrum acquisition can be instantly acquired at a given probe location on the specimen. The approach is usually called as 'spectrum imaging (SI)', and the whole setup allows for the elemental and bonding analysis to be carried out with a spatial resolution down to the atomic-level.

Above description summarizes the image formation and spectroscopic processes taking place inside a STEM. In the following discussions, aim is to generate only a sense of that complexity, but for a comprehensive overview of these techniques the reader is referred the following reviews: [147, 345] for STEM imaging and [212] for EELS. The concepts of STEM imaging is presented in two parts, one discussing the formation of STEM electron probe (Section 5.2), and the second discussing the image formation using different detectors (Section 5.3 and Section 5.4). Section 5.5 describes the correspondence between STEM and HRTEM imaging and shows that the same concepts (of STEMs) can also be used to understand the image formation in HRTEMs. Subsequently in Section 5.6, Section 5.7, Section 5.8, the concepts of STEM-EELS theory, acquisition and interpretation is discussed.

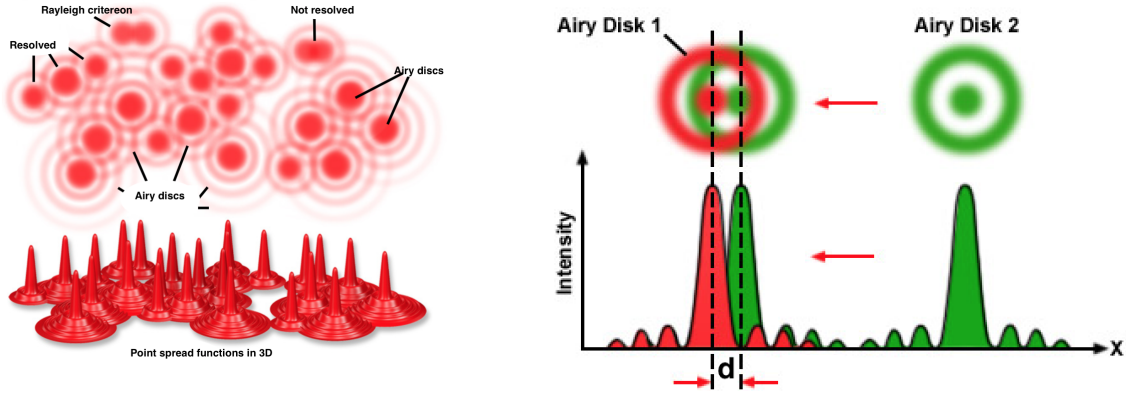

(a) Overlap of Airy discs and resulting 3D point spread functions (PSFs).

(b) Applying Rayleigh critereon on two neighbouring PSFs.

Figure 5.2: Schematic illustrations of overlapping 'Airy discs' on a plane and the Rayleigh critereon for resolution. source: [346]

5.2 FORMATION OF AN ELECTRON PROBE IN A STEM

5.2.1 *Resolving power of a microscope*

The ultimate performance measure of a microscope is its resolving power, given by the point-resolution (r), which is also simply referred to as the 'spatial resolution'. The point-resolution is defined as the shortest distance between the two points on a specimen that can still be distinguished as separate entities. For example, Figure 5.2a illustrates the diffraction of a point source (either light or an electron beam) upon interacting with the specimen, appearing as 'airy discs' at an intermediate plane in the microscope column below the specimen. This plane is usually referred to as the *back focal plane* (BFP) in electron microscopy. Each airy disc visible in the BFP can be seen to have a central bright spot surrounded by many concentric rings. Figure 5.2b shows the vertical projection of the airy discs, called as the 'point spread functions' (PSF). Each PSF has a central maximum in the intensity followed by many subsidiary maxima (1^{st}, 2^{nd}, 3^{rd}, so on), each progressively fainter than the previous. The resolving power of the microscope is then defined as the ability to distinguish between two such closely placed airy discs or PSFs.

Different levels of overlap can be set to define the 'point-resolution' of a microscope and consequently, the criterions for optimal microscope conditions differ. For example, Lord Rayleigh defined the resolution as being when the central maximum of the one PSF falls on the 1st subsidiary maximum of the other PSF (see Figure 5.2b). This is known as the 'Rayleigh criterion'. Under this condition, the minimum separation between any two PSFs is given by d. Values larger than d for a microscope is then regarded as being of poorer resolution.

5.2.2 *Resolution in a STEM*

The spatial resolution in a STEM cannot be any better than the probe formed[3] [246]. Therefore, forming an atomic-scale probe in STEM is crucial obtain atomic-resolution. As with many optical instruments, STEM tries to achieve this by focusing the electron beam with a series of lenses. The final focusing lens is referred to as the 'objective lens', and all other lenses are referred to as 'condenser lenses'. The function of these lenses is to bring enough demagnification in the finite-sized electron source, such that an atomic-scale probe can be formed at the sample. The largest demagnification is caused by the objective lens, which is also the major source of aberrations caused in the entire optical system [147]. In order to limit the blurring caused by such aberrations on the probe, the STEM is usually fitted with a beam limiting 'objective aperture' before the objective lens.[4]

The typical intensity profile of a STEM probe formed is illustrated in Figure 5.3a. The resemblance to PSF from an 'airy disc' is attributed to the diffraction of the electron beam at the edges of the objective aperture. Simply calculating the full-width at half-maximum (FWHM) of the probe-PSF, also referred to as the probe size (d), generally serves as a good measure of the resolution achievable in a STEM. Alternatively, a fast fourier transformation (FFT) of the PSF, commonly called as the 'optical transfer function' (OTF), can also be plotted as a function of spatial frequency. For example, a typical OTF

[3]Use of electron as the probe has its advantages: (a) best resolving power from the extremely small wavelengths achievable, λ), (b) electrons are charged particles so they can be bent as required using electromagnetic lenses (neutrons share similar resolving power with electrons but are difficult to 'shape'). (c) electron interactions with the sample is rich in information from various signals generated (discussed earlier)

[4]Use of this terminology is restricted to electron microscopes with combined TEM-STEM functionality (such as the one used for the present thesis work). In the case of dedicated STEMs, the same aperture would be referred to as the 'condenser aperture'. By the 'principle of reciprocity' (discussed in Section 5.5), the condenser aperture is used in STEM to beam convergence is equivalent to the objective aperture used in HR-TEM to form an image.

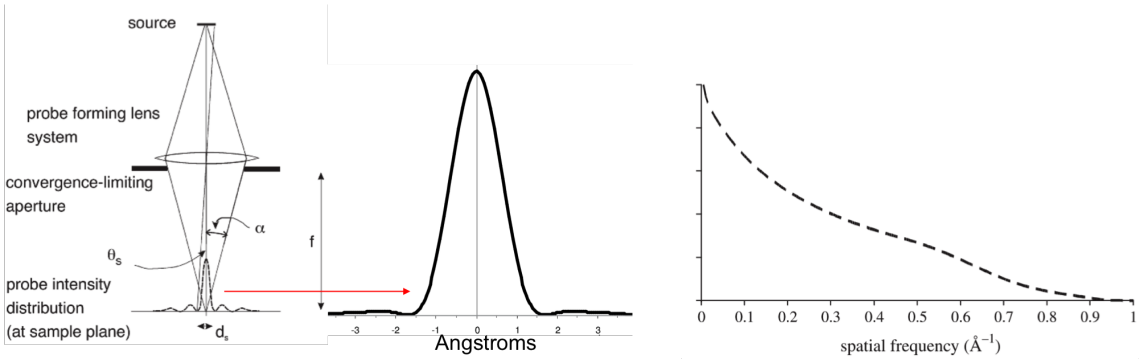

(a) PSF. (b) OTF.

Figure 5.3: Typical point spread function (PSF) and the optical transfer function (OTF) of a STEM probe.

for STEM imaging is shown in Figure 5.3b. As with any ideal lens system, the OTF decreases monotonically as a function of the spatial frequency, and reaches zero at a point defined by the resolution of the microscope. STEM OTF in Figure 5.3b reaches zero at a spatial frequency of about 0.95 ($Å^{-1}$). Therefore, the resolution of the microscope is $1/0.95^{th}$ of an Å, which is about 1.05 Å. Smaller the probe size in STEM, better is the resolution of the microscope.[5]

Note that few other factors such as broadening of the probe inside the specimen [347] and the instabilities in the microscope (from mechanical vibrations, stray magnetic fields, changes in environmental conditions as such) [348] can also affect the 'ultimate resolution' achieved by a STEM, but these factors are not as 'physically limiting' as the formation of STEM probe would be. Moreover, for the modern STEMs which are usually housed in a vibration-free stable environment, the resolution loss is minor. Specimen broadening of the probe, although is a limiting factor particularly for the atomic-scale probes [349], the effect is more serious in the thicker bulk specimens than nanoparticles, and especially when a quantitative analyses of the STEM intensities, e.g. thickness determination [350], is sought.

[5]Note however that the smallest probe is not where the best resolution is usually achieved, but rather at a slightly higher value called 'optimum probe convergence angle', this we discuss in Section 5.2.3. This has to do with the diffraction effects at the aperture (illustrated in Appendix A), which results in a 'disk of confusion' (Δx). The probe convergence angle (α) is related to Δx as $0.61\lambda/\alpha$. Thus, formation of smallest probe means that the Δx is large, which in STEM creates stray intensities in the image that may not be resulting from the specimen.

5.2.3 *Factors determining the formation of smallest probe in STEM*

For a typical STEM probe of size (d) and convergence angle (α) (see Figure 5.3a), the resulting probe current (J) is given by:

$$\boxed{J = \frac{B\pi^2 d^2 \alpha^2}{4}} \tag{5.1}$$

where, B is the brightness of the electron gun.

Equation 5.1 indicates that for a given probe current J, the probe size d can be reduced by (1) using a very high brightness electron gun, and (2) increasing the convergence angle (α) of the probe. The field-emission guns used in the modern STEMs satisfies the first constraint by producing about 1000 times higher brightness than the Tungsten filaments used in the conventional microscopes. Satisfying the second requirement, i.e. to increase the probe convergence angle (α) is what is more challenging (discussed below), and has required over five decades of research in electron optics [351–353].

Recall that the electron source is focussed into a small probe by the demagnifying action of the condenser lenses and objective lens. Additionally, an objective aperture is used to limit the broadening of the beam caused by aberrations in the lens, particularly the objective lens. The challenge to form a small STEM probe is that the formation of large convergence angle is accompanied by large spherical aberrations (C_s) which broaden of the probe diameter by an amount d_{sph}. For small convergence angles, the diffraction of the beam at the objective aperture results in a diffraction error C_{diff} (see Appendix A). Both contributions are related to the probe convergence angle (α), and the electron wavelength (λ) (under Rayleigh criterion conditions) as follows,

$$\boxed{\begin{aligned} d_{sph} &= \frac{1}{2} C_s \alpha^3 \\ d_{diff} &= 0.61 \frac{\lambda}{\alpha} \end{aligned}} \tag{5.2}$$

Thus, for a STEM probe of geometric diameter d, the broadening (Δd) caused is a combination of spherical aberration effects and the diffraction error, given by

$$\boxed{\Delta d = d_{sph} + d_{diff} = \left(0.61 \frac{\lambda}{\alpha}\right) + \left(\frac{1}{2} C_s \alpha^3\right)} \tag{5.3}$$

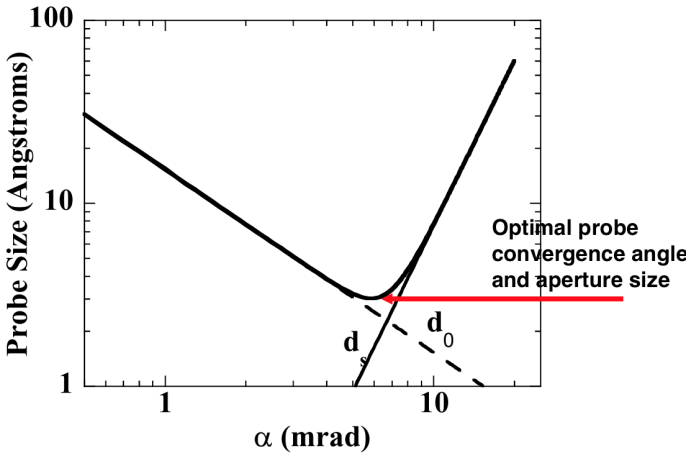

Figure 5.4: Plot of probe size as a function of convergence angle (α). source: David Muller (Cornell)

At low convergence angles the diffraction term dominates, and at high convergence angles the aberration effect dominates. The situation is best described in Figure 5.4 by plotting Δd, d_{sph} and d_{diff} as functions of α. This limitation confines the useful values of the probe convergence angle (α) to a very narrow range. The optimal probe convergence angle (α_o) to form the smallest STEM probe is where the beam broadening Δd is minimum (i.e., $\alpha = \alpha_o$, when $\frac{d(\Delta d)}{d\alpha} = 0$). For Δd given in the Equation 5.3, the α_o is calculated to be $0.63 \left(\frac{\lambda}{C_s}\right)^{\frac{1}{4}}$.

$$\boxed{\alpha_o = 0.63 \left(\frac{\lambda}{C_s}\right)^{\frac{1}{4}}} \tag{5.4}$$

This value α_o is also where the resolution of STEM is at its best. The magnitude of the convergence angle (α) is controlled by the size of the objective aperture (diameter, *D*) used. $\alpha \propto D$ (see Figure 5.3a. This makes 'aperture size' the most important 'physical factor' determining the formation of smallest STEM probe.

Apart from spherical aberration, the electron lenses may also suffer from 'chromatic aberration (C_c)' which can also broaden the STEM probe, consequently reduce the achievable resolution. But, its contribution to the beam broadening Δd is much smaller than the diffraction and spherical aberration effects discussed above [147]. Recently, many microscopes which correct for both C_s and C_c are available in the market today, but it is

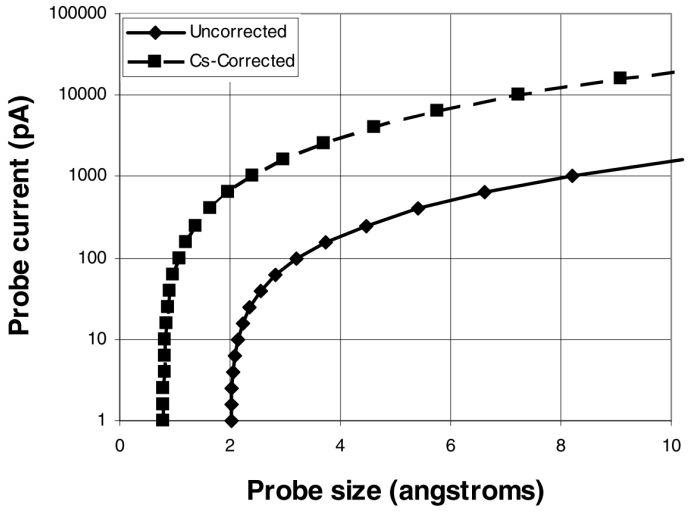

Figure 5.5: Plot of probe current *vs* size in an uncorrected and a C_s corrected microscope. source: [147]

important to note that the C_c-correction is not limiting to achieve atomic-resolution in the STEMs (it would be however for the HRTEMs).

5.2.4 *Benefits of aberration-correction*

For an uncorrected microscope, the coefficient of spherical aberration (C_s) is very large. In such case, Equation 5.4 indicates that the formation of smallest STEM probe is only possible at very small probe convergence angles. For which, use of small objective apertures is required ($\alpha \propto D$). The effect is twofold, first the spatial resolution is significantly reduced (since probe size $d \propto \frac{1}{\alpha}$), and second, the probe current is limited to small values ($J \propto \alpha$, Equation 5.1). In fact, spherical aberration (C_s) was the main resolution-limiting factor until very recently. But, with the advent of aberration-correctors in the electron lens systems (discussed below), most modern STEMs are now C_s-corrected, i.e. the C_s values are much smaller [351–353]. This allows for the use of a larger objective apertures, enabling atomic-scale probes to be formed, and producing high probe currents. Thus, atomic-resolution imaging can be realized in the aberration-corrected STEMs. To have high probe currents is shown to be particularly useful for fast elemental mapping and probing subtle changes in the EELS fine-structures [354]. These effects are best described by the linear regime in the plot of probe current *vs*. probe size shown in Figure 5.5. A

transition from the diffraction-limited regime (probe size is independent of current due to diffraction-effects at the aperture) to the electron source size limited regime (at large currents) is noticeable.

5.2.5 *Electron lenses and the aberration-correctors*

The important role played by aberration-corrected electron lens system (condenser and objective lenses) in forming atomic-scale STEM probes was discussed in the preceding section. Electron lenses are nothing but a series of copper windings around a soft iron core (called the pole-piece), and provided with a hole in the center such that the electrons from the gun can travel through (Figure 5.6). Early on in 1936, Scherzer showed that most 'round electron lenses' suffer from positive spherical and chromatic aberrations (chromatic aberrations are not resolution-limiting in STEMs). But, Scherzer theorized that if similar 'non-round electron lenses' can be made, they can be arranged in a particular order to create negative aberrations, which can then be used to correct for the positive aberrations resulting from the 'round electron lenses'. Although the concept of such 'aberration-correctors' was theorized back in 1947, practical aberration-correctors yielding atomic-resolution in TEMs has been realized only in the past decade or so [351–353].

Electron lenses and their aberration-correctors act based on the 'Lorentz force law' ($F = e \times B$). A strong magnetic field (B) is created in the hole by passing an electric current through the copper windings. This exerts a Lorentz force (F) on the beam of electrons (e) travelling through the hole, which forces the off-axis electrons to spiral back towards the optic axis of the microscope. This focussing action repeated over many condenser lenses (three in FEI-Titan: C1, C2 and C3) and in particular the strong action from the objective lens (fourth lens in FEI-Titan), finally results in sufficient demagnification of the finite-sized electron source to form a probe in the STEMs.

Controlling the parasitic aberrations, such as coma and three-fold astigmatism has been the key to the success of modern aberration-correctors. These aberrations result from many factors such as imperfect machining of corrector-lenses and the round lenses that are being corrected, and their misalignments with one another. Modern corrector designs overcome this challenge by high-precision machining and alignments, providing additional windings, creating multipoles (e.g., quadrapoles, hexapoles, octupoles) within the lenses, and developing computer algorithms to instantly read the source of

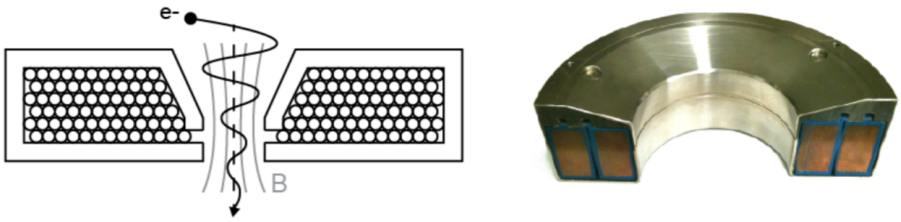

Figure 5.6: Cut section of the condenser lens revealing Cu windings within (right). Current passing through these windings produce a strong magnetic field in the pole piece gap (left). source: [355]

aberrations and alter the multipole power supplies to diagnose. To discuss the optical coupling between the multipolar configurations of the correctors and the round electron lenses is beyond the scope present overview, the reader is referred to following articles for furthering the knowledge on the topic [351–353].

In the microscope used for present thesis, the FEI-Titan STEM, four round lenses (3 condenser lenses and 1 objective lens) is coupled with two sextupole correctors (Figure 5.6*(right panel)*). The correctors were designed and developed by a group of following researchers from CEOS[6]: Haider, Rose, Uhlemann, Kabius and Urban [351]. Additionally, the strongest lens in the microscope, the objective lens, is split into two parts one above the specimen holder and one below (see Figure 5.1). The upper part is referred to as the 'probe-forming (objective) lens', and the lower part is called the 'image-forming (objective) lens', and correctors are used in both cased for minimising the aberrations. Since both the probe forming and image forming objective lenses are corrected, such microscopes are referred to as being 'double-corrected'. Having a corrected image-forming lens is particularly effective in minimising the image delocalization, which results in directly interpretable STEM images.

The gap between the probe and image forming objective lenses is only a few millimeters in FEI-Titan, within which the specimen has to be inserted. This can be of two important consequences, firstly a careful insertion of the specimen holder is critical, secondly, such close proximity between the specimen and the lenses restricts the ability to carry out some *in situ* experiments (e.g., heating or liquid-cell microscopy) for longer periods, wherein despite extreme precautions small amounts of gaseous products is usually generated. Additionally, this may also restrict the use of *in situ* closed-cells that provide gas and liquid environments in a closed environments to a much narrower size-range. In the

[6]Corrected Electron Optical Systems GmBH

later developments of aberration-corrected TEMs [354] this limitation has been overcome by allowing for much wider gap in the objective-lens pole pieces.

5.2.6 *Electron gun*

A typical electron gun in TEMs (or electron microscopes in general) consist of the electron source that generates the electrons, and an accelerating chamber (also called the gun lens) to accelerate the electrons generated. Ultimately, electrons exit the gun with an energy spread (ΔE), defined as the statistical variation in the kinetic energy of the emitted electrons. Larger the energy spread resulting from an electron gun, higher the chromatic aberration effects are, and poorer the spatial- and energy resolutions would be. Thus, sometimes a 'monochromator' is fitted just below the gun to minimise the energy spread produced.

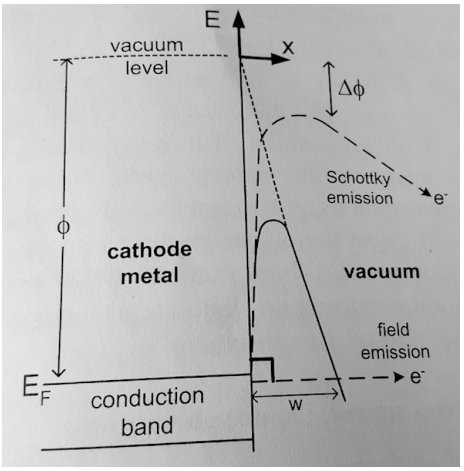

(a) Schematic illustration of the reduced potential barriers in schottky and cold-FEGs.

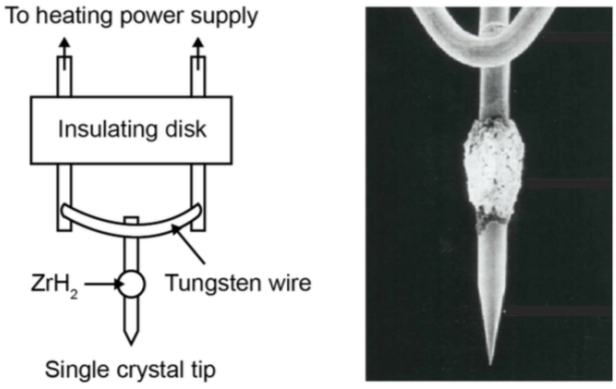

(b) ZrO coated tungsten tip used in the cold-FEGs.

Figure 5.7: Field emission electron gun: principle and an example.

Over the years, many different electron sources have been explored. Most common are the tips/filaments made of tungsten (W), lanthanum boride (LaB_6) and zirconium-dioxide coated tungsten [243]. Electrons are emitted from these sources by three popular methods, thermionic-emission, Schottky field-emission and cold field-emission. In thermionic-emission, the electron source (simply called as cathode) is heated to high temperatures by passing a direct current through the filament. This provides the necessary

ELECTRON EMISSION	MATERIAL	TEMPERATURE (K)	ENERGY SPREAD (eV)
Thermionic	W	2800	1.5-2.5
	LaB_6	1900	1.3-2.5
Schottky	ZrO/W	1800	0.3-0.7
Cold-FEG	W	300	0.3-0.7

Table 5.1: Characteristics of thermionic-, schottky- and FEG based electron guns. source: [243]

energy ($\geqslant \Phi$) for the conduction electrons in the metal to escape into the vacuum (the potential barrier Φ is called the 'work function'). In the Schottky field-emission, in addition to thermal excitation of the cathode (i.e., electron source), an electrostatic field is applied to the cathode surface. The effect is that the potential barrier Φ is lowered by an amount $\Delta\Phi$, which results in higher electron emission current density (by a factor $\Delta\Phi/kT$) compared to thermionic-emission.

In the cold field-emission, there is no thermal excitation of the source, but the surface of the electron source is exposed to sufficiently large electrostatic fields (E). This decreases the width (w) of the potential barrier Φ ($w = \Phi/eE$) (see Figure 5.7a), allowing electrons in the source to escape through the surface potential barrier by quantum-mechanical tunneling. Generally, the required electric field at the surface is of the order of 10^9 V/m. Usually, the electron source in cold-FEGs is thinned down sufficiently (*via* electrolytic etching of W wire) such that the electrons can be emitted from an extremely small area (typically, 10-20 nm in diameter). Such small sized electron-source is ideal for the formation of atomic-scale probes in STEMs as a large demagnification action by the electron lenses would not be not required (in comparison to broader W filaments).[7] Additionally, such W tips in cold-FEGs (and schottky FEGs) can also be coated with zirconium-oxide (ZrO) powder, which is known to lower the work function Φ of the tungsten tip (from 4.5 to 2.7 eV).

Cold-FEGs are called so because no thermal excitation is required and the tip can be operated at room temperatures. Under stable ultra high vacuum conditions (UHV pressure of the order 10-8 Pa), this extends the longevity of the W tip from months to years before replacement.

[7]This requirement, referred to as the 'spatial coherence' is essential for any electron source, irrespective of the nature of electron emission.

Table 5.1 lists different characteristics of electron guns that use different emission processes discussed above. The FEGs give the best performance (lower energy spread, high brightness and longevity) required for the formation of atomic-scale probes in STEM. FEI-Titan used for the thesis employs a cold-FEG with a ZrO coated tungsten tip as the electron source (see Figure 5.7b).

5.3 ELECTRON INTERACTION WITH THE SPECIMEN: SOURCES OF IMAGE CONTRAST

So far we have discussed various physical principles behind the formation of a STEM probe and its resolution limits. Once a small STEM probe can be formed at the sample, the electrons interact with specimen atoms and are subsequently collected by different detectors (BF, ABF, ADF, HAADF) whose contrast highlight different aspects of the material specimen. The interaction between the incident electrons with the specimen atoms could be elastic (coulombic interaction with the nucleus) and inelastic (interaction with other electrons). In particular, the elastic interactions are the important to STEM imaging.

5.3.1 *Atomic-number (Z) contrast*

In the elastic interaction with the specimen, the incident electrons are scattered by relatively large angles (θ) due to coulombic interactions with the nucleus. The resulting angular distribution is best described by calculating the 'scattering cross-section' (σ), or more conveniently, the 'differential scattering cross-section' $d\sigma/d\Omega$ for a given solid angle (Ω). The scattering cross-section at an atom (atomic-number Z) in the specimen is defined as the ratio of the number of electrons scattered (N) with respect to the incident electron flux (J). It is found to be proportional to the atomic-number (Z) of the atom, for e.g. $d\sigma/d\Omega$ and Z are related to each other by $d\sigma/d\Omega = 4Z^2/aq^4$ (q is a scattering vector $\propto \sin(\theta/2)$, $a = \hbar^2/2\pi me^2$), according to Rutherford's model. This suggests that the incident electrons are scattered to much larger angles by the interaction with heavier atoms than the lighter atoms. Thus, by setting the collection angle of the detector (positioned after the specimen) to a particular range of scattering angles, the contrast in the image formed can be made sensitive to the atomic-number, i.e. intensity in the image $I \propto Z^n$. The obtained contrast in the image is called the 'atomic-number contrast' or simply 'Z-contrast', which can be used to identify different atoms, e.g. heavier Pt atom in the vicinity of lighter Fe atoms. Among the different STEM detectors, the collection

range of the HAADF detector is found to be suitable for providing 'Z-contrast', and the intensity in the HAADF-STEM images $I \propto Z^{1.6}$ [147].

5.3.2 *Thickness/mass-thickness contrast*

Note that the 'scattering cross-section' (σ) (with units m^2) describes the scattering process happening at a single atom in the specimen. But the STEM specimen consists of numerous such atoms, all capable of scattering the incoming electrons. Thus, the probability of elastic scattering over an area (m^2) in the specimen can be calculated, given by:
$P(\theta) = N\sigma$, a dimensionless quantity
Where, N is the number of atoms per unit area of the specimen viewed along the direction of the incident beam.

N is also referred to as the 'areal density' of atoms in the specimen. For a sample with n atoms per unit volume, $N = n \times t$, where t is the thickness of the specimen. N can be further expressed in the form of physical density (ρ) as: $n = \rho/A\,u$, where A is the atoms per unit volume, and u is the mass per atom (i.e., atomic mass unit = 1.66×10^{-27} kg).

Thus, the probability of elastic scattering in the specimen, $P(\theta)$, can be rewritten in terms of Z, ρ and t as:

$$\boxed{P(\theta) = nt\sigma = (\rho t)\sigma/A} \tag{5.5}$$

The above expression illustrates that the scattering probability is also dependent on the thickness of the specimen (in addition to Z). The thicker the specimen is, the higher its scattering probability is, and consequently, the larger the intensities formed on the image. This creates a 'thickness contrast' in the images of the specimen. Together, the contrast emerging from both mass (ρ and Z) and thickness (t) dependencies of $P(\theta)$ is referred to as the 'mass-thickness' contrast, which is extremely useful in characterizing non-crystalline materials that do not produce 'diffraction contrast' (discussed below).

It is important to note that the scattering probability ($P(\theta)$) calculated above corresponds to a single-scattering approximation, i.e. one-time scattering of the electrons in the entire specimen. This assumption is valid only for very thin specimens (e.g., nanoparticles < 40 nm), and so is the linearity between the scattering probability ($P(\theta)$) with thickness (t). For much thicker specimens (e.g., bulk materials) the electrons are scattered several times, as indicated by the estimated mean free path (λ_e) for elastic scattering

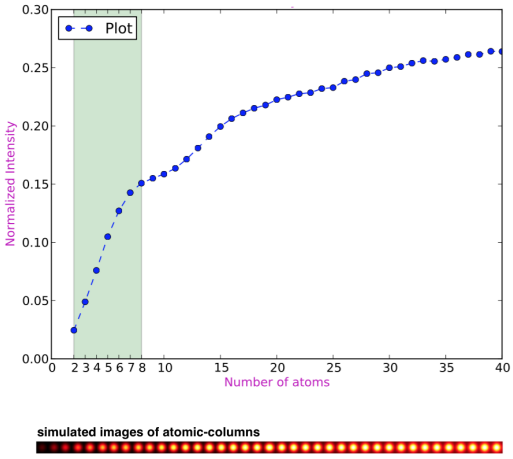

(a) Plot of measured intensity as a function of thickness for a series of Pt atomic-columns. Simulated HAADF images (color-coded) is show in the bottom panel.

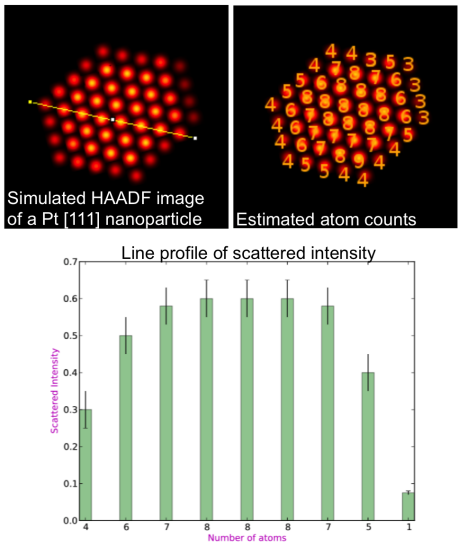

(b) Estimation of number of atoms at every atomic-column of a simulated Pt nanoparticle.

Figure 5.8: Understanding the variation in the scattered intensity (for elastic scattering) with specimen thicknesses.

in the specimen,[8] which is defined as the mean distance between the elastic collisions. Consequently, the single-scattering probability ($P(\theta)$) will actually decrease with the increasing thicknesses. This is illustrated in the image intensity (I) *vs.* thickness plot shown in Figure 5.8a that is calculated for a series of Pt atomic-columns which differ in the number of atoms located along the direction of the incident electron beam[9]. The single-scattering approximation is valid in the linear regime ($I \sim P(\theta) \propto (\rho t)$), but as the thickness increases beyond about 8 atoms, the image intensity starts to loose its linearity. The simulated images for these same atomic-columns are shown in Figure 5.8a*(bottom panel)*. Such information is extremely important for a quantitative estimation of the specimen thicknesses or counting the number of atoms just from the STEM images (e.g., see Figure 5.8b and caption therein). However, a much more reliable method is based on the

[8] Ratio t/λ_e is called as the 'scattering parameter' of the specimen.

[9] Multislice method (described elsewhere Section 6.4.1) was used to simulate the images. The Pt columns were not isolated, but simulated in the form of a supercell. Intensity variations due to phonon scattering and electron channeling were ignored.

inelastically scattered electrons, and the estimation of their scattering probabilities using Poisson statistics is also available for such a task (Section 5.8).

5.3.3 *Diffraction contrast*

In addition to 'mass-thickness' and 'atomic-number' contrasts, the third kind of contrast in some STEM images is the 'diffraction contrast' that is seen particularly in the case of crystalline specimens. For example, in a polycrystalline sample with uniform thickness and composition where the mass-thickness contrast should be absent, the intensity variations in the images can still be observed.

Diffraction contrast emerges from the difference in orientation of the atomic rows and columns with respect to the approaching electron. The situation is similar to the Bragg diffraction seen in the x-rays interacting with the different atomic planes in the specimen. The angle at which the x-rays (wavelength λ) are scattered upon interaction, θ_B, is found to be dependent on the distance between the atomic planes (d), related by $n\lambda = 2d\sin(\theta_B)$. The interplanar distance d is different for different crystal orientations ((111), (100) etc). Consequently, the x-rays interacting with different crystal orientations scatter differently. In the case of electron interactions, the scattering angle θ ($= 2\theta_B$) resulting from the diffraction process is related to the interplanar distance as $\lambda = \theta d$ (small angle approximation: $\sin\theta \sim \theta$). This impacts the scattering probability ($P(\theta)$) as per Equation 5.5, thus a variation in the image intensity emerges corresponding to different crystal orientations, commonly called as the 'diffraction contrast'. Since a particular order in arrangement of atoms is absent in the amorphous specimens, the diffraction-contrast would be very poor, and are therefore characterized based on the mass-thickness contrast.

5.4 IMAGE FORMATION IN A STEM

The elastic scattering process in a given crystalline sample is capable of producing all the three kinds of contrast (atomic-number, thickness- and diffraction-contrast) simultaneously. But the sensitivity of a STEM image to displaying such contrast is ultimately dictated by the detectors used (BF / ADF / HAADF / ABF), and the collection angles that they are set to. To delve into the details of the image formation and associated mathematical relationships is beyond the scope of present overview. But simply put,

what happens after the elastically scattered electrons exit the specimen is typical of any diffraction process, the formation of 'airy discs' or 'diffraction spots' on a screen or a surface placed (in the case of STEM the detector planes).

5.4.1 *Interference with overlapping discs*

For a plane wave illumination (as in HR-TEM), if $\Psi(R)$ is the electron wavefunction at the exit of the specimen, then the intensity of the 'diffraction spots' at the screen placed would be a modulus squared of the fourier transformation of $\Psi(R)$ (FFT($\Psi(R)$) = $\Psi(K)$), given by $I(K) = |\Psi(R)|^2$. However in STEM, the specimen is illuminated not by a plane wave, but by a convergent probe wherein the electrons all arrive at a much broader range of illumination angles. This results in broadening of the 'diffraction spots' that are forming on a screen placed, and appear as large 'discs' that may even overlap against one another. Such a pattern is called the 'convergent electron beam diffraction (CBED)', an example is shown for the case of Si <110> in Figure 5.9.

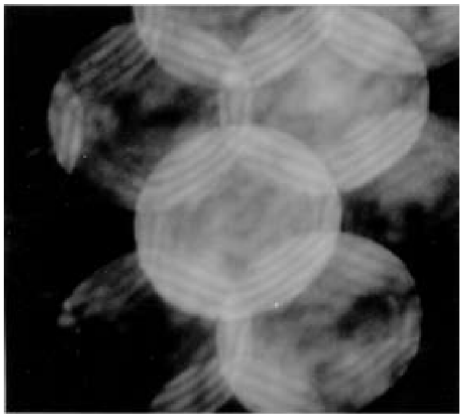

Figure 5.9: CBED pattern of Si <110>. Intereference of fringes in the overlapped areas indicate defocused probe condition from the sample. source: [147]

Different regions in the CBED pattern can be analysed to extract specimen information. For example, the disc overlap regions contain numerous interference fringes, whose position depend on the lens aberrations, probe position and the phase difference between any two diffracted beams. An entire technique called 'Ptychography' is based on measuring the relative positions of such interference fringes [356], which is then inverted in real-space to calculate the wavefunctions of the electrons exiting the surface (i.e., exit-wave function). Such calculations of wavefunctions is otherwise extremely difficult since

the 'phase' of the diffracted beams would be unknown. This uncertainty of phase arises in many instances in TEM electron optics, and is appropriately called as the 'phase problem'.

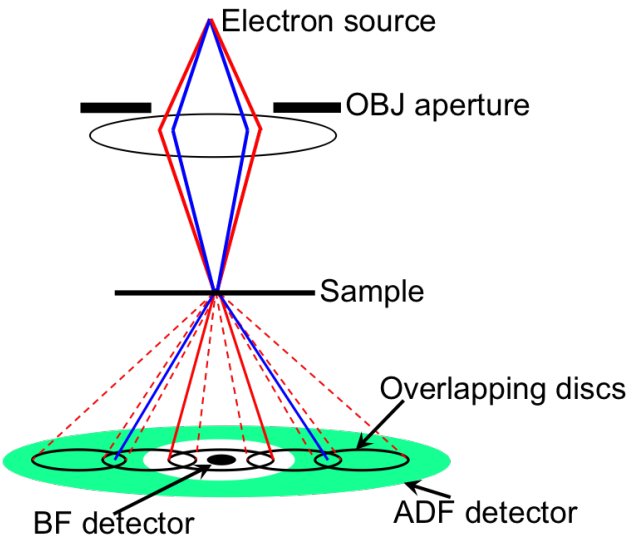

(a) Overlapping discs of electron intensity formed on different STEM detectors.

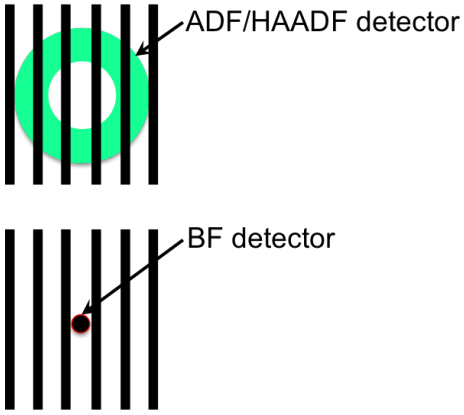

(b) Interference fringes of electron intensity falling on ADF/HAADF detectors (upper), and the BF detector (lower).

Figure 5.10: Imaging in STEM with different detectors.

5.4.2 *Imaging in STEM with different detectors*

Unlike 'Ptychography', STEM-imaging relies on integrating the electron intensities over a region in the CBED pattern, and then plotting the integrated intensity as a function of the probe position to form an image. As mentioned earlier, different STEM detectors are positioned in a diffraction plane either immediately after the sample or in a conjugate plane. Each detector is set to integrate electron intensities over different CBED regions, which is achieved by setting the collection angles of these detectors to different range of values. For example, the BF and HAADF detectors in the FEI-Titan microscope is arranged as shown in Figure 5.10a, and their collection angles is set to range 0–18 *mrads* and 120–180 *mrads*, respectively. Finally, the measured integrated intensity is recorded digitally as a single pixel intensity at each position in the scan, thus forming BF-STEM, ADF-STEM and HAADF-STEM images of the specimen.

Among the different STEM-imaging approaches, the HAADF-STEM imaging is shown to be extremely sensitive to the atomic-number, providing Z-contrast. The image intensity I is found to be proportional to $Z^{1.6}$, which is surprisingly very close to that predicted by Z^2 dependence of the scattering probability in the specimen $P(\theta)$ predicted by Rutherford's model. The Z-contrast capability of HAADF-STEM imaging remains one of its greatest strengths, because of which the HAADF-STEM is by far the most applied STEM imaging techniques to study both structure and composition of materials. When combined with EELS in a technique called STEM-EELS, it becomes a powerful analytical tool to probe the structure, composition and bonding information down to the atomic-level. The HAADF-STEM is not so sensitive to diffraction-contrast, as the scattering angles required to produce it is much lower than the inner collection angle of the HAADF detector, thus pass through the central hole.

One other advantage of ADF/HAADF-STEM imaging is that the contrast in the image is directly interpretable and the transfer function is much simpler, unlike that in the case of BF-STEM (and even ABF-STEM to an extent) which requires tedious image simulations in order to calculate the phase relationship between the scattered electrons (i.e., the exit-wave function). This is attributed to the sustenance/suppression of the phase dependency in the intensity due to detector geometries. A simple illustration is shown in Figure 5.10b, considering an instance where the beam is scattered by a set of planes, and forms interference fringes on the BF and ADF detectors placed below. Since the BF detector is smaller than the fringes formed, the integrated intensity (and the image contrast in BF-STEM images) would be very sensitive to the position of the fringes, which as mentioned earlier, in turn depends on the relative phases of electron scattering from the two atoms. Thus, unless the phase information of the scattered wave functions is known, the contrast in the BF-STEM images cannot be interpreted. This limitation is commonly termed as the 'coherence effect', and the BF-STEM imaging appropriately called as a 'coherent imaging' technique. One example of such 'coherence effects' is the commonly observed contrast reversals with the changes in specimen thickness. On the other hand, the large ADF detector will average over many such fringes, and thus the integrated intensity is not very sensitive to the position of the interference fringes or the relative phases of scattering from the two atoms.

In other words, the coherence effects are lost in the ADF/HAADF-STEM imaging techniques, making them the 'incoherent imaging' techniques, whose image contrast is directly interpretable. Also, since the contribution of the scattered intensities is higher in the integrated intensity collected by the ADF/HAADF detectors, the specimen which is a good scatterer appears brighter while the vacuum (poor scatterer) appears darker in

the images. *Vice-versa*, in the case of BF imaging. It is for this reason that these imaging modes are called the 'dark-field' and 'bright-field' imaging modes.

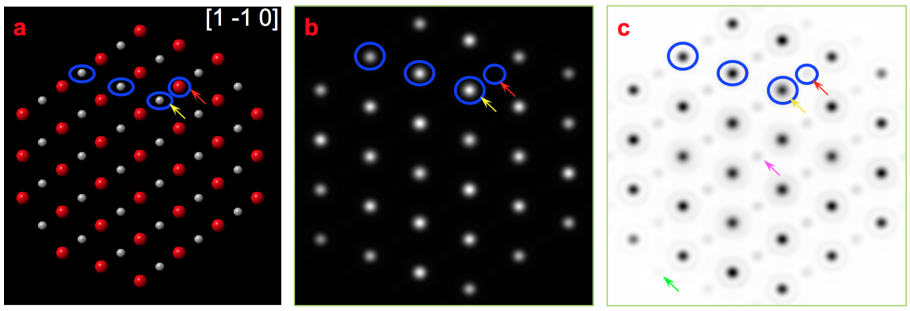

Figure 5.11: Multislice simulated (b) HAADF-STEM and (c) ABF-STEM images of a (a) modeled PtO nanoparticle viewed along $1\bar{1}0$ zone-axis. Yellow and red arrows indicate pure atomic-columns of Pt and O, respectively.

In addition to BF and ADF (including mid-ADF and HAADF) imaging in STEM, one another imaging approach called the 'annular bright field' (ABF) imaging is also available, which has emerged only in the recent past. The technique has emerged to fill in the gap in ADF-STEM imagine where the intensities for lighter elements in the vicinity of much heavier elements was poor enough to be identified [357, 358]. For example, Figure 5.11 illustrates the simulated ADF- and ABF- STEM images of a PtO nanoparticle. Corresponding locations for pure atomic-columns of Pt and O is marked by yellow and red arrows, respectively. As can be seen, in the vicinity of Pt, the O appears with poorer contrast in the HAADF images and is hardly identifiable. In contrast, the presence of O can be easily noticeable in the ABF-STEM image. In practice, the collection angle (β_{ABF}) in the range ($\alpha/2 < \beta_{ABF} < \alpha$) is required for ABF-STEM imaging. This is achievable by either using a dedicated ABF detector, or simply using a beam stop in the BF detector to block out the remaining area, or by increasing the camera length (i.e., distance of the detector from the specimen) to suitable length. ABF-STEM is also found to be 'semi-coherent' where the contrast reversal is only observed with the change in defocus, but not the specimen thickness [357]. Thus, within an optimum defocus range, the ABF-STEM images can still be directly interpretable (see Chapter 9 for more details).

5.4.3 *Working principle of STEM Detectors*

The STEM detectors are all basically discs made of a scintillator material which directs the light (i.e., electron intensity) generated into a photomultiplier tube for recording. BF detector is a circular disc with an angular collection range from zero to a certain Φ, the ADF (mid-ADF and HAADF) and ABF detectors are annular discs collecting within a certain angular range Φ_{min} to Φ_{max}. These collection angles can be varied by decreasing or increasing the camera length ($L \propto 1/\Phi$) of the detector, respectively. This allows for the use of a single annular detector for different imaging modes (ADF, HAADF and ABF). However, such an arrangement would restrict the simultaneous acquisition of a STEM-ABF and STEM-HAADF image if required.

More often the center of the annular detectors is a hole and thus allows for the scattered electrons below its inner collection angle Φ_{min} to pass through, which can be collected to either form a BF image (by a BF detector placed below), or sent to the EELS spectrometer to generate an EELS spectrum (discussed below). The latter option is more common, commonly called STEM-EELS, allows for a simultaneous imaging and spectroscopy at every probe position on the sample. Such opportunities to combine various different modes in the same acquisition is very unique to STEM, and demonstrates an efficient use of the scattered electrons that is possible.

5.5 PRINCIPLE OF RECIPROCITY: CORRESPONDENCE BETWEEN STEM AND HR-TEM

Most concepts of the STEM imaging discussed so far are applicable to understanding image formation in HR-TEM where the illumination is by a parallel beam of electrons as opposed to a small probe in STEM. This is because, the propagation of electron is time reversible for elastic scattering, called the 'principle of reciprocity' [359]. Which means that the alignments in HR-TEM to generate an image is equivalent to that in STEM, but in a reversed order. For example, as illustrated in Figure 5.12, the source plane in STEM is same as the detector plane in HR-TEM. The condenser lenses used to demagnify the source in STEM is same as the projector lens used in HR-TEM to magnify the electron source (necessary for parallel illumination). While the objective lens in STEM focus the beam, the objective lens in HR-TEM collects the scattered electrons from the specimen and focusses them to form an image. Similarly, the so called 'objective aperture' or the

'condenser aperture' is used in STEM to beam convergence, which is equivalent to the 'objective aperture' used in HR-TEM (placed after the objective lens) to form an image.

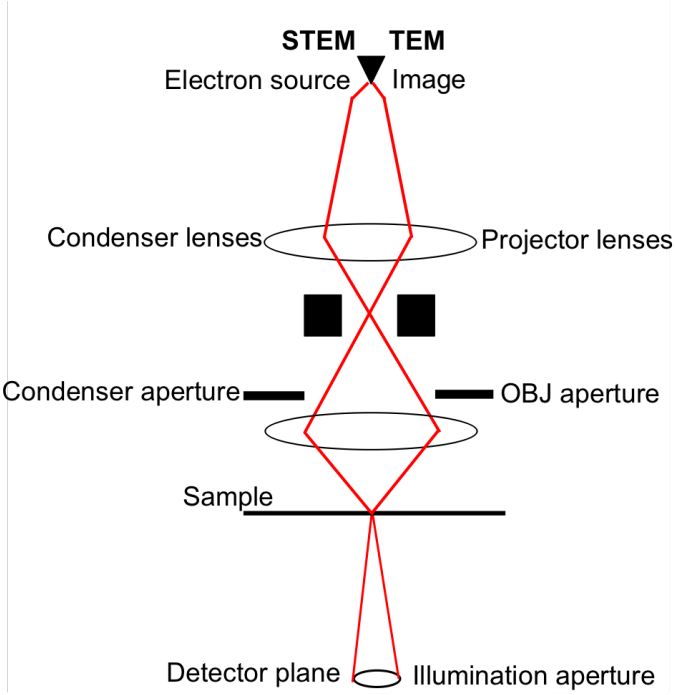

Figure 5.12: Schematic illustration of the principle of reciprocity between STEM and HR-TEM (or a conventional-TEM).

5.6 STEM-EELS SPECTRUM IMAGING

As discussed in the preceding sections, for every probe position on the sample both elastically and inelastically scattered electrons can be collected simultaneously (using the modern ultra-fast spectrometers). While the elastically scattered electrons can be collected by an ADF/HAADF detector to form an image, the inelastically scattered electrons collected can be used to generate an EELS spectrum that carries various features characteristic of the specimen composition and bonding. This combination of ADF/HAADF-STEM imaging and EELS results in the creation of a three-dimensional data cube (Figure 5.13), called a 'spectrum image', wherein the two axes (x and y) correspond to the spatial coordinates on the sample and corresponding to every spatial coordinate (x, y) an EELS spectrum is recorded in the third dimension (z). The entire procedure is called 'STEM-EELS spectrum

imaging' which has become an invaluable tool to probing the structure, composition and bonding aspects of materials.

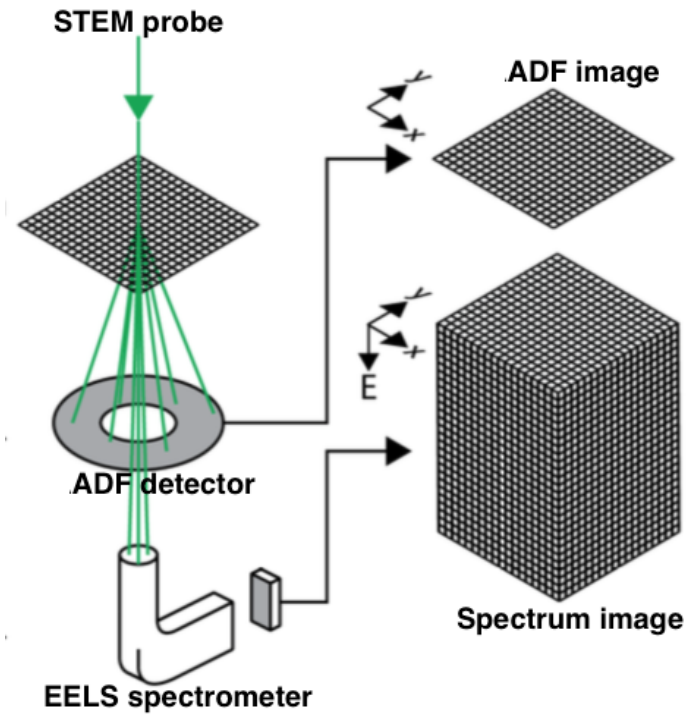

Figure 5.13: Schematic illustration of 'spectrum imaging' in a STEM, which combines ADF/HAADF-imaging with the recording of EELS signal at every probe position on the sample. source: adapted from [355]

5.6.1 *Recording an EELS spectrum*

Depending on the accelerating voltage used in the microscope the kinetic energy of primary electrons incident on the sample is generally between 40 *keV* to 300 *keV*. Many of them undergo inelastic scattering, and in the process, lose certain amount of their initial kinetic energies, and finally reach the EELS spectrometer. The kinetic energies lost in the specimen can be anywhere between few *eV* to few thousands *eV*. Thus, a spectrometer which can detect the smallest differences in their kinetic energies is said to have the best energy resolution.

Figure 5.14 shows the schematic illustration of a typical EELS spectrometer whose function is to collect the inelastically scattered electrons, disperse them based on their kinetic energies, and display the number of electrons collected (i.e., electron intensity) as a function of their energy losses (i.e., the EELS spectrum). The entire process is carried out in four stages, namely (1) electron collection, (2) electron focussing and dispersion, (3) magnification of electron dispersion, and (4) recording and display of EELS spectrum.

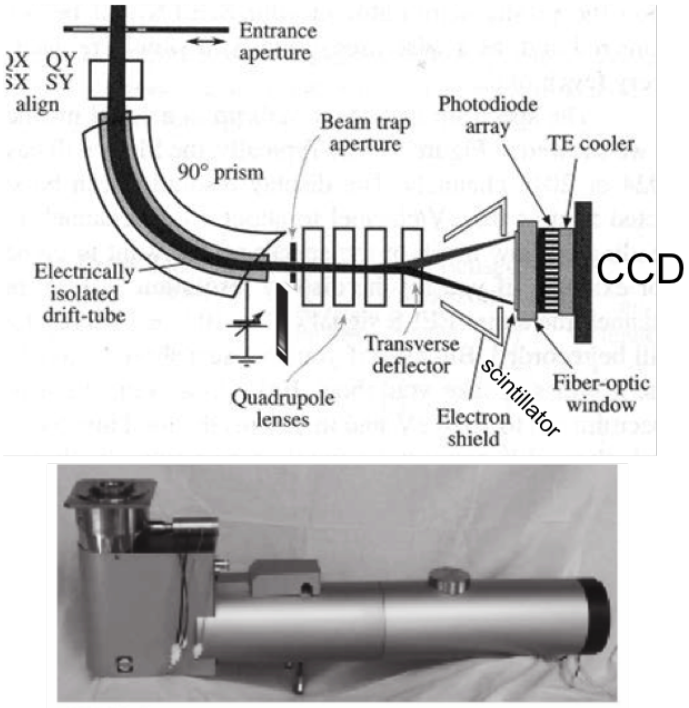

Figure 5.14: Schematic illustration and a photograph showing different components of a typical EELS spectrometer. source: adapted from [213]

Electron collection is achieved by an entrance aperture (2.5 mm or 5 mm in width) placed at the entrance of the spectrometer. Use of such apertures serves two objectives, to cut out the portion of the scattered beam entering that might otherwise cause aberrations, and to increase the electron collection efficiency. The electrons entering the aperture are then focused into a magnetic prism with the help of multipole optical elements (e.g., quadrupole, octupole as such), which further correct for aberrations. Subsequently, the electrons enter a magnetic prism, the heart of a spectrometer, which is basically two parallel faces of an electromagnet applying a uniform magnetic field (B) on the electrons in a direction perpendicular to their travel (velocity, v). This field exerts a force ($F = e\,v\,B$) on the electrons, which provides the necessary centripetal force (mv^2/R) to cause bending

action on the electron path. As a result, the electrons travel along the arc of a circle whose radius R is given by $R = (m/(eB))v$, and exit the magnetic prism at 90° deflection to the initial.

Note that R is dependent on the kinetic energy of the electron (by mass and velocity terms), which means that the inelastically scattered electrons with higher energy losses (i.e., low KE) are deflected by much larger angles than those with smaller energy losses (i.e., low KE). Similarly, the inelastically scattered electrons in general, are deflected to much larger angles compared to the unscattered (direct beam) and the elastically scattered electrons. In this way, the magnetic prism disperses different electrons based on their energy losses. Additionally, the magnetic prism also focuses the electrons, in both axial and radial directions. This brings those electrons of same energy closer together at the exit of the magnetic prism tube.

Both dispersing and focussing actions of the magnetic prism already generates the required EELS spectrum, which is nothing but a plot of the number of electrons for each energy loss value. But, owing to various aberrations (e.g., chromatic) the dispersion created by the prism is generally weak, and requires further magnification (by aberration-correction), which is done so in the state-of-the-art spectrometers with the help of another set of multipole lenses. The magnified spectrum generated is then projected onto a phosphor scintillator which converts the electron intensities into photon intensities (by generating photons from every electron striking ~1000 photons per one 100 *keV* electron). The photon intensities are then captured by the fiber-optic cables which channel them into a charge coupling device (CCD). The CCD converts these photon intensities into electrical signals, and enables storage and display of the recorded EELS spectrum electronically.

The recorded spectrum on a M x N pixel CCD camera is in the form of a 2D array of electron intensities that are arranged in the increasing order of their energy losses (called the 'dispersion direction'). The available CCD pixels, also called the 'channels' are fixed, and thus the dispersion used '*eV*/channel' dictates the maximum energy range that can be acquired in the spectrum. Methods such as 'spectral binning' allow for an extension in the energy range, by merging more spectral data into each channel, however this comes at the cost of the reduction in the energy resolution. The final step is to then integrate the electron intensities of similar energy losses together and plot the measured integrated electron intensity as a function of energy losses, which we call the 'EELS spectrum'. An example of a full EELS spectrum recorded on a CCD is illustrated in Figure 5.15*(top panel)*.

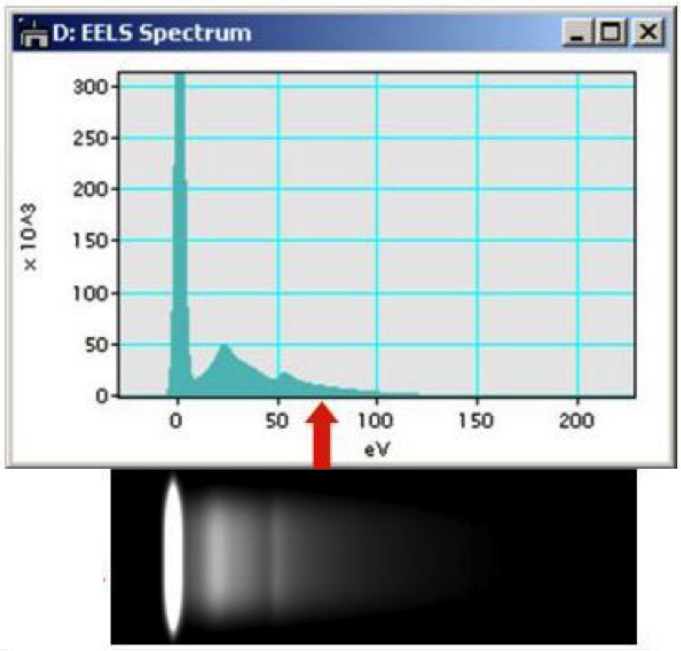

Figure 5.15: Example of recorded electron intensities on a CCD camera (bottom), and the plot of its integrated intensity as a function of energy losses, which we call the 'EELS spectrum' (top). source: adapted from Gatan notes.

5.6.2 *Single-EELS and Dual-EELS capabilities*

The spectrometer used in the FEI-Titan STEM microscope, called the Gatan Image Filter (GIF), uses a state-of-the-art 2048 x 2048 pixel CCD camera with an added camera controller that monitors rapid readout and recording of the EELS spectra (~1000 *spectra/s*) [360]. Additionally, instead of collecting the electron intensities over the entire energy range permitted (0 to 2000 *eV*, i.e., 2000 channels), a variable energy range can be selected (Single-EELS capability). This is implemented in the spectrometer by applying a small voltage to the 'drift tube' that is used to direct the electron path past the magnetic prism, which in turn creates a net downward deflection of the dispersed electrons.

Similarly, two different energy ranges can be selected for simultaneous recording, e.g. one between 0 to 200 *eV* (low energy loss) and another between 600-700 *eV* (high energy loss), this capability is called 'dual-EELS'. This was not possible until recently as the low energy loss region is far more brighter in electron intensity (by about 10^6 times) than the high-energy loss region. To accommodate for this large difference in intensity the

electron optical conditions required for the spectral acquisition of both regions needed to be different (e.g., exposure times), and switching between the two conditions would often result in delayed spectral acquisitions. But, with the recent development of fast 'electrostatic shutters', the beam can be blanked-unblanked in about 1 μs, enabling the spectrometers to record both low and high energy loss spectra, sequentially and under identical electron optical conditions (e.g., STEM probe, detector alignments as such).

5.7 FEATURES IN A TYPICAL EELS SPECTRUM

A typical EELS spectrum (Figure 5.16a) contains an intense zero-loss peak (ZLP) (at 0 *eV*) representing the electrons that either scattered elastically or remained unscattered when interacting with the specimen. Since the width of the ZLP is mainly determined by the energy distribution of the electron source (e.g., wider without a monochromator), measuring its FWHM reflects the microscope limitation for achieving the best energy resolution. Between ZLP to about 50 *eV* in the spectrum, a series of peaks called the low-loss peaks appear, representing the inelastic scattering by outer-shell electrons and the accompanying single-electron inter- and intra- band transitions, and collective excitations.[10]

Beyond 50 *eV* in the spectrum, relatively less intense but distinct peaks can be seen, called as the 'core-loss edges'. These are representative of the inelastic scattering from the inner-shell electrons (Figure 5.16b), and the resulting transition of the inner-shell electron from the deep core levels to the unoccupied states above fermi-level (Figure 5.16c). The onset of the core-loss edges appears at an energy loss which equals to the ionization energy of the inner-shell electron. Thus, every core-loss edges is characteristic of a particular element, and its appearance in the EELS spectrum marks the presence of that element at that particular probe position in the specimen. By scanning the probe over a selected region in the specimen, this allows for elemental mapping showing the elemental distribution in the area. Additionally, since any change in the oxidation state or valence changes in the material would lower or increase (a) the ionization energies, and (b) height of the edges, by tracking these changes in the core-loss edges, the oxidation state of the material can be estimated.

Note that the electron transitions during inelastic scattering to a final state would be very sensitive to the local density of states (LDOS) of the excited atom (see DOS picture

[10]The interband transitions refer to the excitation of valence band electrons to the empty states in the conduction band. The collective oscillation (i.e., a resonance) of many valence electrons is commonly termed as the plasmon excitations.

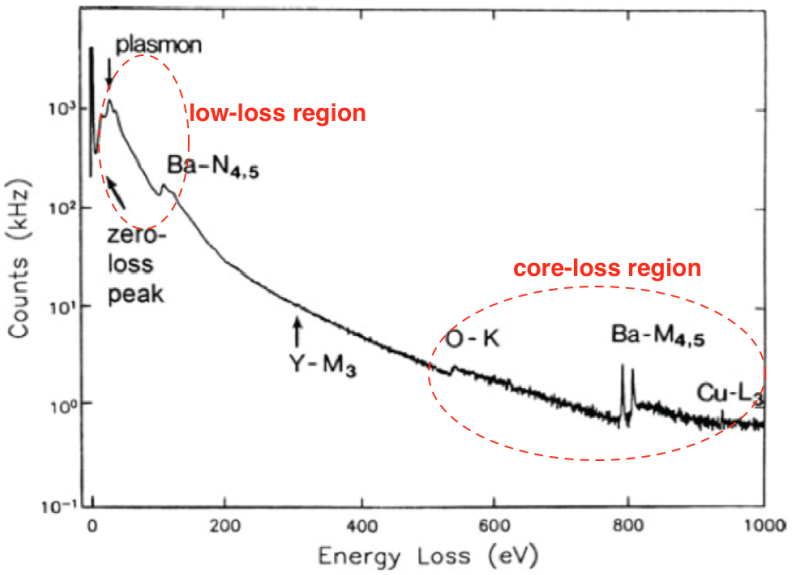

(a) Typical EELS spectrum

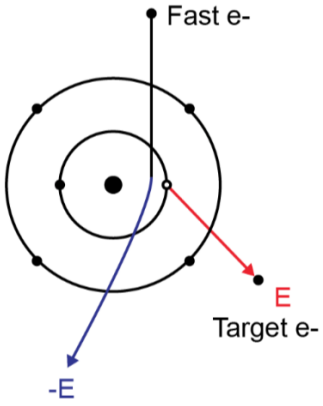

(b) Inelastic scattering event at an inner shell of an atom.

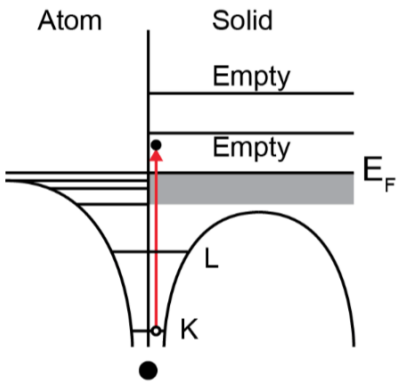

(c) Excitation of an inner shell e^- to an empty state above the Fermi level.

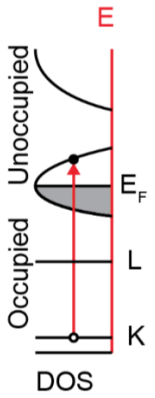

(d) DOS picture of inner shell excitation.

Figure 5.16: Understanding features in a typical EELS spectrum (adapted from [212]), and in particular the core-loss EELS (b, c and d) (adapted from [212]).

of excitation in Figure 5.16d), which is in turn dependent on the bonding and crystallographic environment of the atom. This is represented by the fine structures (ELNES) appearing in the core-loss edges (and also in the low-loss edges) within first few *eV*s after the onset. Any change to alter the electronic structure of the specimen (e.g., doping) will modify the LDOS; consequently the modulations in the ELNES is modified. Therefore, by tracking the changes in the fine structures between two different samples of the same material, its local oxidation state and valence changes can be understood.

5.8 ELEMENTAL MAPPING AND QUANTIFICATION WITH CORE-LOSS EELS SIGNALS

Different features appearing in the EELS spectrum (Section 5.7) can be examined to obtain different aspects of the sample. Use of a particular energy range in the spectrum is ultimately determined by the nature of information sought. In addition, a suite of numerical techniques and software procedures are also available to assist in better signal extraction by background subtraction and noise cancellation. Of particular interest to the characterization of Pt-alloy catalysts are the core-loss edges of Pt and of its different alloying elements, which are used in generating elemental maps over a selected region in the sample. An example is summarized in Figure 5.17 for the case of a Pt-Fe alloy nanoparticle.

Figure 5.17*(a)* is the ADF image showing the region over which the 'spectrum imaging' was carried out. At every pixel, an EELS spectrum in the core-loss region between 500 to 2500 *eV* was recorded, e.g. Figure 5.17*(b)* shows the spectrum summed over pixels located in the core of the particle. The core-loss EELS spectrum reveals two edges corresponding to ionization energies of Fe (708 *eV*) and Pt (2200 *eV*)(step *(1)*). A power law background was fitted to the spectrum, and subtracted, so as to extract only the elemental edges (step *(2)*). The energy-loss intensities for both Pt and Fe was integrated to about 100 *eV* further from their respective ionization thresholds, named I_A and I_B, respectively. Values of I_A and I_B from the entire region is tracked to generate maps (step *(3)*). These maps show the spatial distribution of both elements in the specimen, which can be further color coded (step *(3)*), and overlayed with respect to other elemental maps (step *(5)*).

The elemental concentrations (n_A and n_B, number of atoms present) are proportional to the signal intensities I_A and I_B, given by:

$$\boxed{n_A/n_B = (I_A/I_B)(\sigma_B/\sigma_A)} \tag{5.6}$$

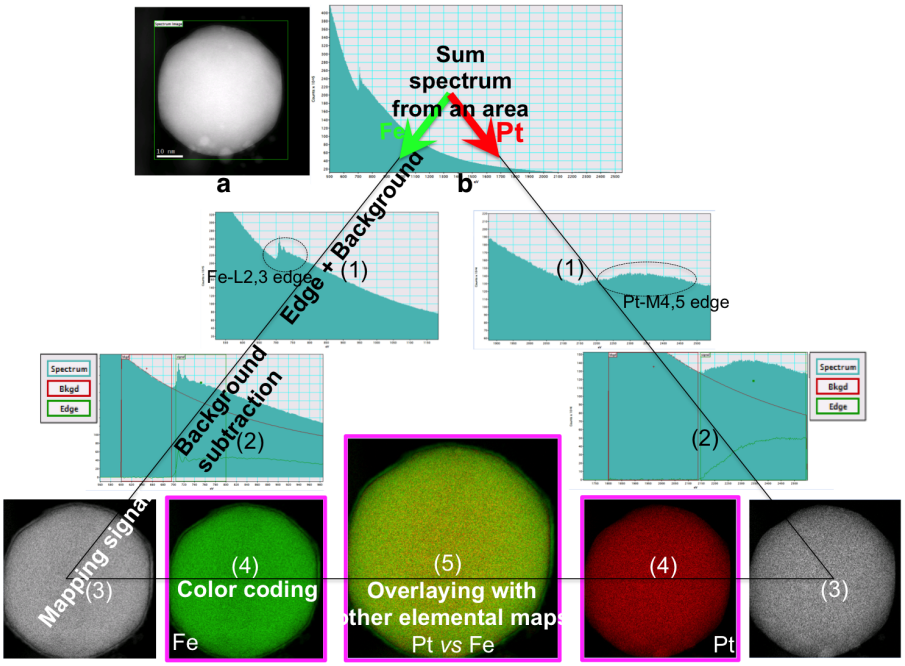

Figure 5.17: Summary of steps involved in elemental mapping with EELS.

Where, σ is the ionization cross-sections (similar to cross-section for elastic scattering) that can be known for a given microscope conditions, element and integration range.

Using Equation 5.6 the relative composition of Fe and Pt can be extracted. For example, the composition in the core region of the particle shown in Figure 5.17 was found to be about 41.4 at.% Pt and 58.6 at.% Fe. Similar analyses on various Pt-alloy nanoparticles can be found in many publications (Chapter 4). However, given that a sophisticated microscope setup is required for carrying out such analyses (aberration-corrected STEM and EELS, and a ultra-fast EELS spectrometer), only a few research groups has been able to produce such elemental maps.

5.9 RECENT DEVELOPMENTS IN *in situ* MICROSCOPY OF NANOPARTICLES

So far we have discussed the principles of STEM imaging and STEM-EELS in an aberration-corrected STEM. As discussed in the introductory section, the applications of HAADF-STEM and STEM-EELS to characterize Pt-alloy PEMFC nanocatalysts span a broad range

from a simple estimation of particle size-distributions to atomic-level imaging and spectroscopy. But, they would be put to most effective use when the catalyst particles can be characterized in their native environments- during synthesis, phase-transformations, potential cycling and MEA operations. In the recent years, significant developments have been made in this direction, particularly with the manufacturing of *in situ* TEM holders where the particles can be heated [190–193, 361], or applied an external voltage [198–203] inside the microscope. In addition, sealed cells ('closed-cells') are also being developed to create a gas or a liquid environment [194–197]. Further combination of these closed-cells and the functional holders can be a great analytical tool. For example, the '*in situ* liquid-cell electrochemical holders' allow for performing electrochemical measurements using a liquid electrolyte inside the microscope. Similarly, *in situ* heating inside a gas-cell allows for studying the adsorption of a gas on the specimen surface (e.g., O_2 on a Pt-alloy surface). These developments are summarized in Figure 5.18.

Although such tools are already available in the market, its adoption to study Pt-alloy nanoparticles is still very limited. For instance, the microscopy of Pt-alloy catalyst particles during *in situ* CV was unprecedented until our first demonstration [202]. Similarly, tracking of a Pt-alloy nanoparticle under annealing with combined HAADF-STEM and STEM-EELS was not attempted [192]. To name a few, the barriers for slow adoption of these *in situ* techniques include, poor spatial and energy resolution in gas/liquid environments owing to plural scattering and high mobility of particles, parasitic reactions from the beam interaction with gas/liquid environments, and the leakage issues in the holder that may be detrimental to microscope stability [203, 365]. Ongoing research in these areas all aim to address these important challenges.

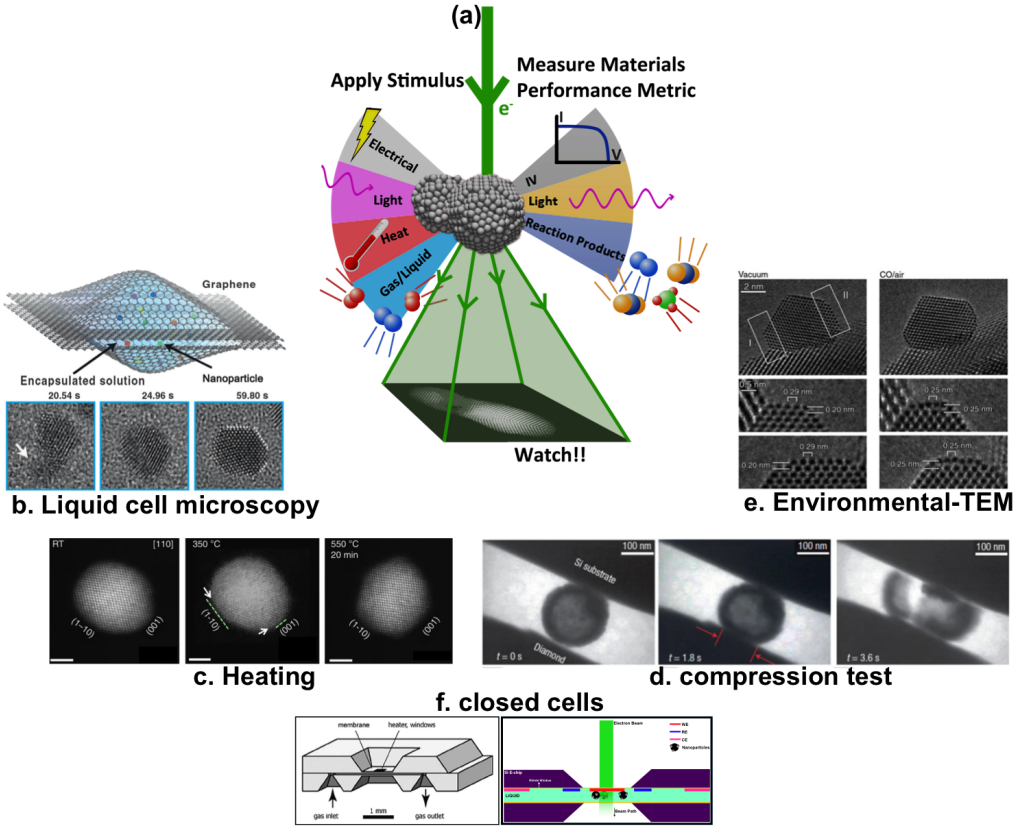

Figure 5.18: Examples of some recent developments in *in situ* microscopy. (a), overview of available techniques (adapted from [362]). (b), Growth process of Pt nanoparticles (adapted from [363]). (c), Surface faceting in Pt-Co particles during heating (adapted from [193]). (d), compression test of a hollow CdS sphere (adapted from [363]). (e), Surface reactivity of $Au@Ce_2$ in gas-phase atmospheres (and vacuum) (adapted from [364]). (f), Illustrations of gas and liquid phase closed-cells (adapted from [202, 362]).

5.10 PERSPECTIVE

Despite tremendous progress in developing electroactive Pt-alloy nanoparticles for PEMFCs, no practical ORR catalyst is yet in sight, thus the efforts must continue unabated. The timing and success of these efforts is closely connected to the structural characterization tools used, the spatial and energy resolution attainable, and the flexibility to characterise *in situ*. Over the years, many imaging and spectroscopic techniques based on electron microscopy and x-ray absorption have proven to be particularly useful to carry out such a task. In particular the high angle annular dark field (HAADF) imaging and electron energy loss spectroscopy (EELS) in an aberration-corrected scanning transmission electron microscope (STEM) are very powerful analytical tools. HAADF-STEM imaging can provide atomic-number (Z) contrast on the atomic-level, which is extensively used to identify the relative distribution of atoms of Pt and its alloying elements in the nanoparticle structure. STEM-EELS can provide spectroscopic informations on the elemental composition, bonding and valence changes. When combined together as in a 'STEM-EELS spectrum imaging' the advantages of both techniques can be derived, which makes it a powerful and complete analytical tool to characterise Pt-alloy nanoparticles. Various *in situ* TEM holders are available (e.g., heating and voltage cycling) that allow for an *in situ* investigation of the particles in a STEM/TEM. Adoption of such tools however is still very limited, requiring on the one hand for the technical barriers to be addressed, and on the other hand for the demonstrative experiments to be attempted.

Part III

RESULTS AND DISCUSSION

6

PLATINUM-IRON ALLOY NANOPARTICLES

Previously in Chapter 2 the need for the development of suitable catalysts for the oxygen reduction reaction (ORR) was discussed. Subsequently, in Chapter 3 the 'alloying' as an effective strategy to improved catalysis on Pt surfaces was presented, which was followed by a detailed review of the recent progress in the development of Pt-alloy nanoparticle catalysts (Chapter 4). Such efforts are imperative for widespread commercialization of the PEMFCs, and as highlighted in Section 3.5, adoption of suitable structural characterization techniques is also crucial, in order to succeed in this effort. The present chapter discusses our findings in regards to the structural and compositional characterization of Pt–Fe alloy nanoparticle system, studied exclusively with the aberration-corrected scanning transmission electron microscopy (STEM, reviewed earlier in Chapter 5). Most sections (either in parts or full) have appeared in the following publications: [91, 202, 300].

6.1 MOTIVATION AND RESEARCH OUTLINE

The Pt–Fe nanoparticles system has gathered a lot of interest, both on the account of its enhanced ORR electrocatalysis [83, 262, 284–288, 366, 367], and also because of the magnetic properties that are deployable in ultrahigh-density information storage [368–372]. The PtFe (L1) ordered phase exhibits a very high uniaxial magnetocrystalline anisotropy along the c direction of the crystal structure. The Pt_3Fe ($L1_2$) phase is shown to deliver an enhanced ORR activity from the compressively strained Pt overlayers that encapsulate ordered alloy cores. Therefore, the chemical synthesis of Pt–Fe alloy nanoparticles in these ordered phases has been extensively studied in the past years. To note a few, the reported novel alloy structures include intermetallic Pt–Fe/Pt core shells [157], Pt–Fe–Cu ternary alloy nanoparticles [262], mono-disperse Ni/FePt core shells [373], and face-centered tetragonal (fct) FePt nanoparticles (see Chapter 2) [374].[1]

[1] The reported specific activities for these structures are about 0.55 mA/cm^2, 0.75 mA/cm^2, 1.95 mA/cm^2, and 3.16 mA/cm^2, respectively.

Collaborators C. Bock *et al* (NRC, Ottawa) synthesized the Pt-Fe catalyst nanoparticles considered in this report using a wet-chemical procedure (discussed below in Section 6.2), which were then evaluated for the ORR performance (Section 6.3). At the time of the first report, these catalysts exhibited the highest activity and extended durability compared to all the other Pt-Fe designs reported in the literature. In the Section 6.4 below, we discuss the findings of a detailed investigation of the structure and compositional aspects of these catalyst particles, studied before and after a series of potential cycling treatments. We found that initially the catalyst particles had a composite alloy structure, composed of an ordered Pt–Fe intermetallic alloy core encapsulated in a typically bilayer thick Pt-rich shell. From a 2-D lattice strain mapping, we find that the bulk strain in the particle was about 3 % (compressive) with respect to pure Pt. Strain at the surface, however, was found to be either more compressive or relaxed relative to this. Over the course of 10000 cycles, we fond that the ordered alloy core remained virtually intact, while the Pt shell suffered a continuous enrichment. With the exception of the relaxation effects at the surface, strain in the bulk of the structure was found to be preserved, which we believe was responsible for the high catalytic durability observed in these catalysts.[2]

As discussed previously in Section 4.2.1, the thermal treatments are a commonly followed pretreatment routine for Pt-alloy catalyst particles. This is because the wet-chemical synthesis yields a disordered alloy structure (face-centered cubic (fcc) A_1 phase in Pt–Fe particles). Many reports indicate that such disordered alloy catalyst particles can be catalytically less durable compared to the ordered particles (discussed in Section 4.2.1). A thermal treatment enables sufficient diffusion of solute and the alloy atoms, required to transform from the disordered A_1 phase into an ordered alloy phase (e.g., $L1_0$ and $L1_2$ equilibrium phases). It is also widely known that the thermal treatments can promote surface segregation of the constituent elements, in addition to the ordering process. In the case of Pt–Fe alloy system, the surface-segregation of Pt is what is commonly reported [83, 367, 375–381]. The preference of Pt over Fe for segregation is ascribed to the larger atomic radius, and also the low surface energies of Pt atoms as compared to Fe. In contrast, both the *ex situ*and *in situ* thermal treatments (i.e., annealing in a furnace *vs.* inside the microscope) of Pt–Fe particles that we conducted, confirmed the surface segregation of Fe. We discuss these results in Section 6.5. Our findings further revealed that the surface segregation of Fe precedes the ordering process, and has a dramatic effect on the local crystallographic arragement of the ordered lattice that is being formed. It is important to point out that the *in situ* approach involved tracking of a single-nanoparticle with both STEM imaging and spectroscopic techniques, which is not

[2] only about 9 % loss in the specific activity despite treating over 10000 potential cycles.

limited to only studying Pt–Fe particles, but rather is an approach useful in studying the phase transformations of many other Pt-alloy catalyst systems.

Finally, as an advancement to the traditional approach of characterizing the catalyst particles before and after cycling, we used the recently developed 'liquid cell electrochemical holders' to monitor the structural evolution of Pt–Fe catalyst particles during the course of potential cycling. We discuss these findings in Section 6.7. The liquid cell holders allow for the simultaneous potential cycling catalysts inside a TEM, the recording of a CV, and the visualization of structural evolution. We believe this can serve as a model study to carryout further investigation of many other catalyst systems. With regards to Pt–Fe particles, we find that the coarsening mechanism is not uniform, both in space and in time scale. The growth rate was found to be site- and potential- dependent. The particles attached to the electrode, and those isolated in the electrolyte, were found to behave differently. This was consistent with the finite element modeling of local current perturbations that we conduced in collaboration with other researchers.

Above findings either in parts or full have appeared in three published articles listed in refs: [91, 202, 300]. A detailed discussion is provided in the following sections, but we first start by describing the procedure used to synthesize the particles studied in this work.

6.2 SYNTHESIS OF PT-FE ALLOY NANOPARTICLES

Collaborators Bock *et al* (NRC, Ottawa) synthesized the Pt-Fe alloy nanoparticles by a wet impregnation of Pt/C nanoparticle precursors with Fe-salt ($Fe(NO_3)_3.9H_2O$ (Alfa Aesar, 99.99 % Fe basis)) [382]. The particles were then supported onto the Vulcan XC-724R carbon microparticles. The steps involved in the synthesis process can be summarized as follows.

First, the Pt/C precursor nanoparticles were synthesized using the *polyol method*. About 0.4652 g of $PtCl_4$ salt (Alfa Aesar, 99.9 % metal basis) was dissolved in about 50 mL of ethylene glycol containing 0.15 M NaOH.[3] The solution was stirred for 1 h at RT, and subsequently heated under a reflux at 160 °C for 3 h. A dark brown colloidal Pt solution was formed in this manner, which was then allowed to cool in air for 1 h. Subsequently, the Pt solution was mixed with about 1.077 g of Vulcan XC-72R (1.077 g) and 1 M HNO_3 (added to stabilize pH). The entire solution was allowed to stir for 24 h. After 24 h,

[3]The pH of the solution was found to determine the resulting particle size.

the Pt/C powder was filtered, extensively washed (in water and ethanol), and then air dried at 80 °C overnight, before finally homogenizing in a glass mortar by grinding. From subsequent TEM characterizations, the extracted powder was confirmed to be Pt nanoparticles deposited on the carbon support (Pt/C).

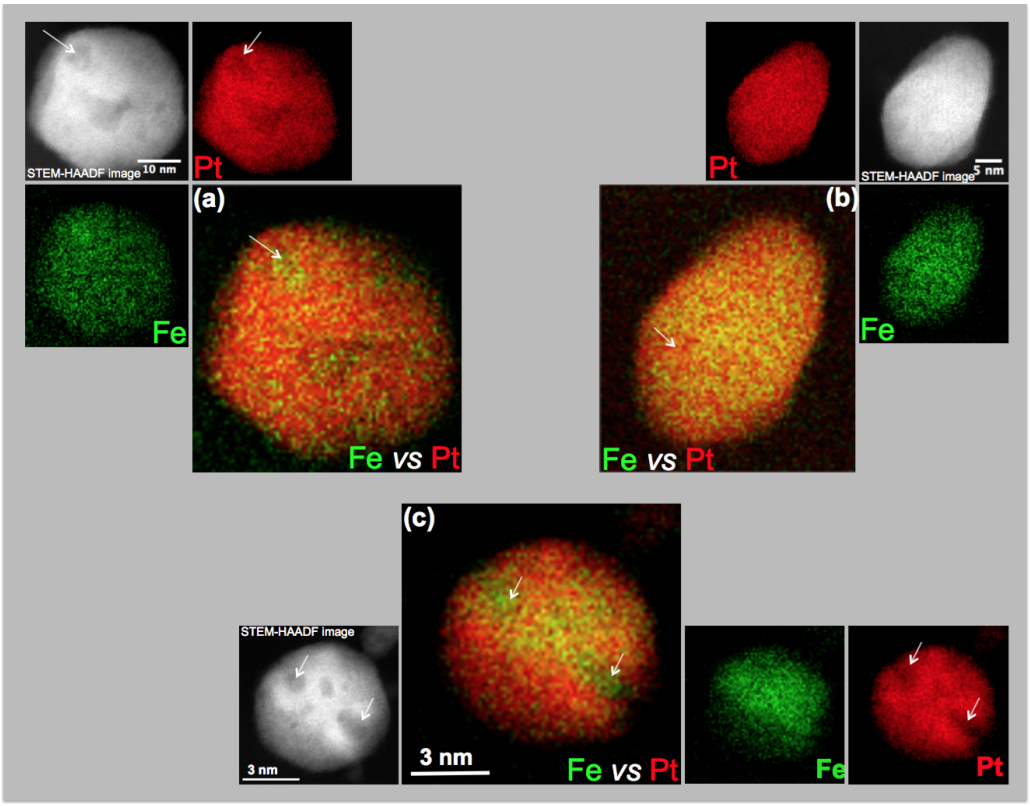

Figure 6.1: A collage of STEM-EELS Pt, Fe and Pt *vs* Fe elemental maps of representative as-synthesized Pt-Fe nanoparticles.

For synthesizing Pt-Fe alloy nanoparticles, about 500 *mg* of Pt/C precursor powder was first ultrasonically dispersed in water.[4] Subsequently, about 0.2072 *g* of Fe-salt ($Fe(NO_3)_3.9H_2O$[5]) was added into the prepared Pt/C suspension.[6] The dissolution of Fe-salt in the Pt/C solution was monitored by constant stirring, and few drops of 1 M HNO_3 was occasionally added so as to maintain the pH at 4. The solution was well stirred for 30 *min* at RT, and subsequently air dried (at 80 °C for 3–4 *h*) to evaporate out water. The dried

[4] 120 *mL* in a 250 *mL* beaker for 1.5 *h*
[5] Alfa Aesar, 99.99 % Fe basis.
[6] Amount of suspension: 0.5 *g* of 20 *wt* %

CATALYST PARTICLES	SPECIFIC ACTIVITY $\mu A/cm^2$	MASS ACTIVITY A/mg_{pt}	ECSA m^2/g_{pt}
Pt/C	170 ± 2	0.11 ± 0.01	60
Pt-Fe(800)(conditioned)(initial)	550 ± 50	0.23 ± 0.05	42
Pt-Fe(800)(conditioned)(6000 cy.)	500 ± 30	0.11 ± 0.03	50
Pt-Fe(800)(conditioned)(10000 cy.)	NA[1]	NA[1]	36

[1] could not be measured due to poor quality of ORR curves after 10000 cycles.

Table 6.1: Measured ECSA, mass and specific activities of Pt-Fe(800)(conditioned) catalyst particles. source: [382]

powders were ground in a glass mortar to homogenize the products. Figure 6.1 shows high-resolution STEM-EELS elemental mapping of these particles. The inhomogeneous distribution of bright and dark intensities in the Pt and Fe maps (see white arrows) indicate structural and compositional inhomogeneities within the particle structure. Thus forward, we refer to the state of such as-synthesized Pt-Fe particles as being 'disordered'.

Subsequent discussions present annealing experiments conducted on the as-synthesized Pt-Fe particles. Unless otherwise noted, the samples were all annealed in a Lindberg Blue tube furnace maintained under a reducing atmosphere (92% Ar / 8% H_2). Particles annealed at 800 °C for 3 *h* would be particularly important, and thus forward, we refer to them as 'Pt-Fe/C(800)' particles.

6.3 ELECTROCHEMICAL ASSESSMENT OF ORR PERFORMANCE

Collaborators Bock *et al* measured the ECSA, mass and specific activities of Pt-Fe(800) catalysts with respect to pure Pt/C(800). However, before any such measurements were made, the Pt-Fe(800) particles were first 'conditioned' under CV by cycling over about 50 voltage cycles.[7] In the subsequent discussions, the conditioned particles are denoted as 'Pt-Fe(800)(conditioned)'. Table 6.1 summarizes the measured ECSA, mass and specific activities of the Pt-Fe(800)(conditioned) particles, measured at 0.9 V, and using the protocol described earlier in Section 3.4.

[7]Note that the CV-conditioning of catalyst particles is more or less, a routine procedure followed to improve the ORR activities, as discussed earlier in Section 4.2.1.4

The measured activities indicate that the Pt-Fe(800)(conditioned) catalysts showed > 3 fold enhancement in the specific activity compared to the state of the art Pt/C catalysts (550 $\mu A/cm^2$ *vs.* 170 $\mu A/cm^2$). Bock *et al* further conducted long term durability tests of the Pt-Fe(800)(conditioned) catalysts over 10000 potential cycles. The measured mass- and specific- activities at the end of 6000^{th} cycle are noted in Table 6.1. The % changes in these values relative to the initial (before cycling), are summarized in the bar chart shown in Figure 6.2. As can be seen, despite treating over 6000 cycles only a negligible decrease in the specific activity is observed (~9.8 % compared to the initial). This indicates that the Pt-Fe(800)(conditioned) catalysts exhibited stable catalytic performance. In contrast, other Pt-Fe alloy nanoparticles synthesized with different Fe concentrations (e.g., 'Pt_3Fe(800)(conditioned)' with 0.0691 *g* Fe salt) had performed relatively poorly [382]. Unlike specific activity, the observed trend in the mass activity indicates a large decrease in the mass activity over cycling. Recall that the mass activity refers to the catalytic performance on the mass basis. In this case, a decrease in the mass activity should not be treated as a sign of low catalytic performance, since Bock *et al* also observed a significant loss in the electrochemical surface area (ECSA) during cycling. One major source of the loss of ECSA (and thus, mass activity) is the loss of catalyst aggregates from the electrode surface, e.g., by dissolution into the electrolyte during cycling.

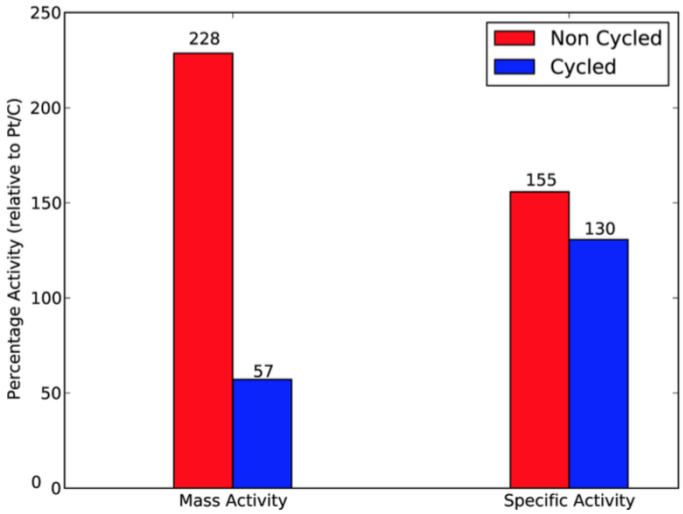

Figure 6.2: Bar chart indicating % change in mass- and specfic- activities of Pt-Fe(800)(conditioned) catalyst particles relative to Pt/C, before and after 6000 electrochemical cycles.

6.4 CORRELATING ENHANCED ACTIVITY AND DURABILITY TO THE NANOPARTICLE STRUCTURE

To understand the structural factors responsible for the observed enhancements seen in the activity and durability, we carried out HAADF-STEM characterization of the pristine 'Pt-Fe(800)(conditioned)' particles, and then compared to particles after 10000 cycles. In particular, we investigated factors such as strain, surface-structure and bulk atomic-structure that determine specific activity. Theseresults are discussed as follows.

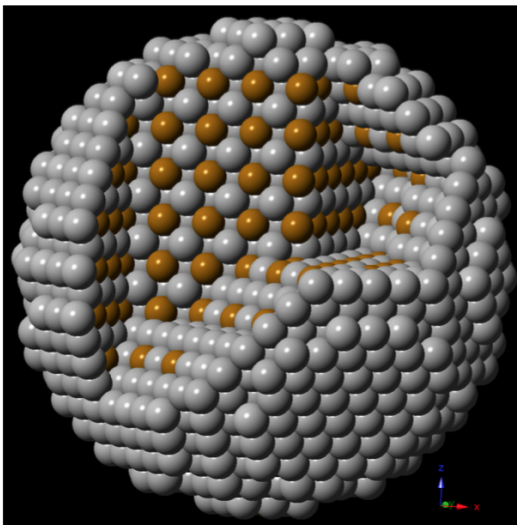

(a) Schematic illustration of a Pt-Fe particle bearing an ordered intermetallic alloy core encapsulated by a Pt-rich shell. Pt and Fe atoms are represented by gray and yellow, respectively.

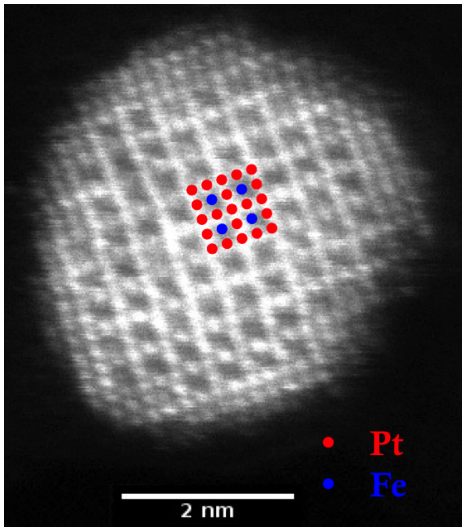

(b) HAADF-STEM image of a representative Pt-Fe(800)(conditioned) particle oriented along 010 zone-axis. Red and blue shapes identify atomic-columns of Pt and Fe, respectively.

Figure 6.3: Structural characterization of a Pt-Fe(800)(conditioned) nanoparticle revealing ordered intermetallic core/Pt-shell structure.

6.4.1 *Investigating catalyst structure with electron microscopy*

Structural and elemental analyses of the 'Pt-Fe(800)(conditioned)' catalyst particles was performed using HAADF-STEM imaging and STEM-EELS, respectively. The HAADF analyses were further supported with multislice image simulations. We find that the 'Pt-

Fe(800)(conditioned)' catalyst particles bear an ordered intermetallic alloy core that is encapsulated in a Pt-rich shell (schematically represented in Figure 6.3a). The findings are discussed in three separate sections as follows.

6.4.1.1 *HAADF-STEM imaging*

Figure 6.3b illustrates atomic resolution HAADF-STEM image of a typical Pt-Fe(800)(conditioned) catalyst particle. The particle is oriented along [010] zone-axis. In this particular orientation, the electron probe is incident on pure atomic-columns of Pt and Fe along the thickness of the projected specimen. The Pt and Fe atomic-columns are visible as 'spheres' in the HAADF-STEM image. Recall from the STEM imaging fundamentals (Section 5.5) that the intensity (I) in a HAADF-STEM image is proportional to the atomic-number of the elements probed ($I \propto Z^{1.7}$). Therefore, the bright atomic-columns in Figure 6.3b can be identified as the heavier Pt ($Z = 72$), and the darker columns can be identified as the (relatively lighter) Fe ($Z = 26$).

A careful inspection of the image intensity in Figure 6.3b reveals that the brighter and darker atomic-columns, i.e. the Pt and Fe atomic-columns, alternate in the core region of the projected particle. This suggests that the core is composed of an 'ordered intermetallic alloy'. In contrast, no such alternating contrast can be seen in the particle 'shell' region, instead the atomic-columns are preferentially brighter, thus indicating that the particle has a 'Pt-rich shell'. Together, these findings indicate that the 'Pt-Fe(800)(conditioned)' catalyst particles have an ordered intermetallic alloy core that is encapsulated in a Pt-rich shell. Thus forward, we refer to this catalyst structure as the 'ordered intermetallic core-shell' (IMCS) structure.

Figure 6.4 shows a montage of various other particles. For those that are oriented along the same zone axis as the the particle in Figure 6.3b, e.g. the particle at the top-left corner), the contrast variations characteristic of the IMCS structure (discussed above) can be observed. Additionally, a careful inspection of the Pt-rich shell in these images reveals that the shell is about 2-3 atomic-layers thick.

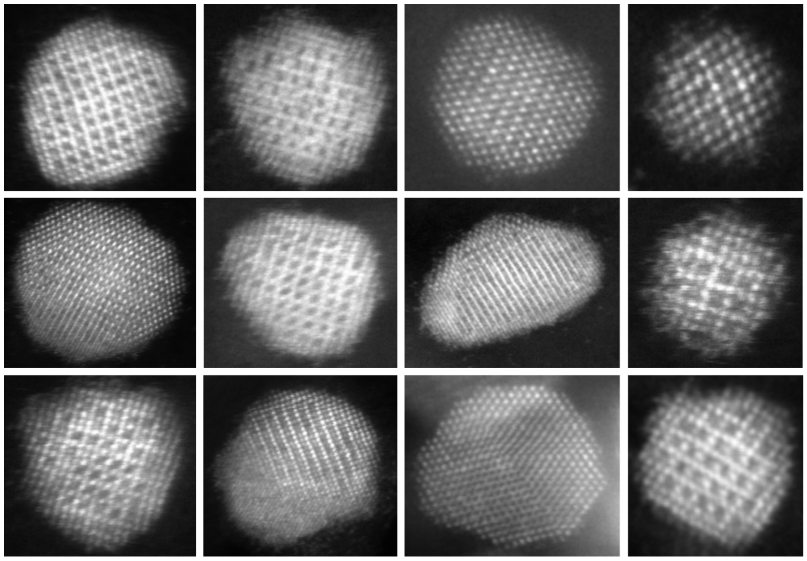

Figure 6.4: Montage showing HAADF-STEM images of many 'Pt-Fe(800)(conditioned)' particles. In most cases, HAADF intensity pattern characteristic of ordered intermetallic alloy core/ Pt-shell structure can be observed in the core- and the shell regions of the particles. In few cases, partial disordering can be observed attributed to heat-treatment effects.

6.4.1.2 *Multislice image simulations*

In support of the HAADF-STEM analyses discussed above, we carried out image simulations based on multislice method.[8] Here we created a 3 *nm* atomic-model of a hypothetical IMCS particle, oriented it along the [010] zone-axis to match with the experiment, and simulated its HAADF-STEM image.

Figure 6.5a show the 2D projection of the atomic-model and the corresponding simulated HAADF-STEM image. The atomic-model was created using the commercial *Crystalmaker* software, and the simulation inputs included the atomic-coordinates obtained from the model, the probe convergence angle, and the collection semi angles of the HAADF detector.

[8]Multislice method is a widely followed approach to simulate electron microscopic images for varying detector angles, microscope parameters and the crystal lattice. Conceptually, the specimen is divided into many thin slices, and the atomic potentials for each individual slice is considered. The incident electron wave function $\psi_{initial}$ is modified under the atomic potential, layer by layer, and finally the electron wave function ψ_{exit} is calculated upon exiting from the surface of the specimen, called the electron exit-wave function. ψ_{exit} can then be used to reconstruct the final image for the given 2D/3D crystal. See [383–385] for an exhaustive review of the algorithm.

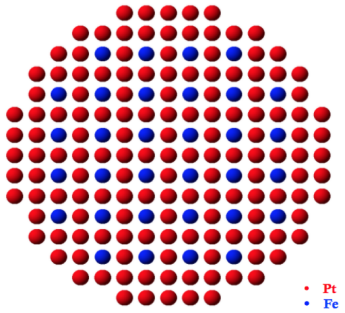

(a) 2D projection of the atomic-model used to simulate.

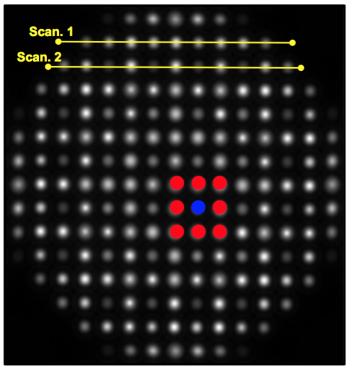

(b) Simulated image.

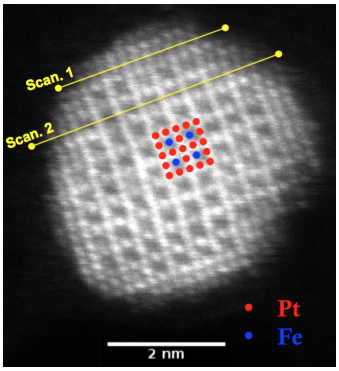

(c) Experimental HAADF STEM image.

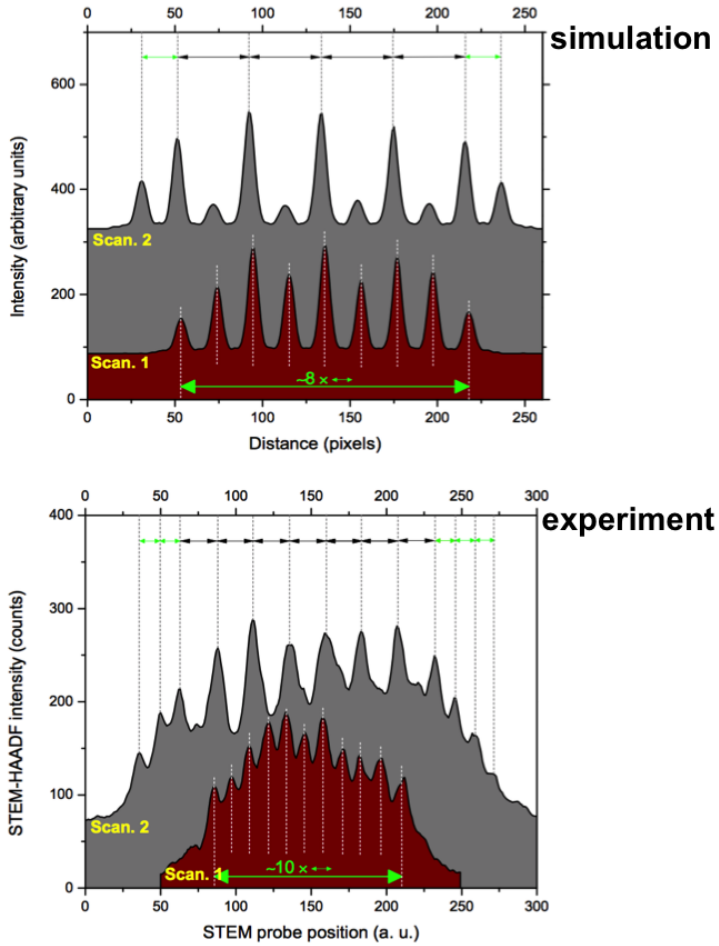

(d) Intensity profiles along the line scans for the simulated (top) and experimental (bottom) images.

Figure 6.5: Multislice image simulation of the Pt-Fe(800)(conditioned) particle structure.

Figure 6.5b and Figure 6.5c show the simulated image and the experimental HAADF-STEM image, respectively. For both images, the intensity profiles were taken along a line scan, one in the shell region (Scan 1), and the other in the core region (Scan 2) of the particles. These are shown in Figure 6.5d (top (simulated), bottom (experimental). By comparing the two, it can be seen that the variation in the HAADF-STEM intensity at the core and shell regions observed for an experimental image is consistent with the simulation result obtained. Scan. 2 (gray) corresponding to the core exhibits an alternating profile, but terminates with a stepped decrease in intensity following a decrease in the number of Pt-atoms at the shell due to the expected thickness variation. The inter-peak distance at the shell measured by Scans. 1 and 2 are self-consistent both for an experimental image and simulation as indicated by the green arrows. This further confirms that a stepped decrease observed at the terminating ends of line scans is due to disordered Pt-rich shell, while the alternating profile corresponds to an ordered core.

It is noticeable from the 2D intensity line profiles shown in Figure 6.5c and Figure 6.5d that the atomic-columns in simulation appear in the form of distinct 'peaks', whereas in the experiment they appear in the form of 'valleys' with significant overlap onto one another. This indicates that the achievable spatial resolution in the experiment was poorer compared to simulation, despite the fact that a sub-angstrom resolution probe was propagated in both the cases. The observed loss in the spatial resolution during the experiment is attributed to scattering or spreading of the electron probe intensity within the specimen. This limitation is usually referred to as 'specimen broadening' in the literature, and it remains one of the major limiting factors for the ultimate spatial resolution in the aberration-corrected STEMs. The seminal work by Dwyer and Etheridge studied the scattering behaviour of small electron probe in silicon [349]. The probe was centered on a specific atomic-column in the specimen, which we call as the column of interest. Dwyer and Etheridge observed that for a given probe size, the probe intensity scattered beyond the column of interest. For e.g., for probes of sizes 2 Å, 4 Å and 0.7 Å, the majority of the total intensity was found to lie beyond 0.2 Å of the column of interest. This effect was particularly more pronounced when the probe size was extremely small. For e.g., for the 0.7 Å probe, the probe intensity on the column of interest was nearly zero at a depth of 80 Åalong the thickness of the specimen. This is attributed to the large convergence angles required to form smaller probes that accompanies larger components of the transverse momentum. Additionally, the effect of specimen broadening on the spatial resolution also depends on the thickness and the orientation of the specimen. The same simulations by Dwyer and Etheridge indicated that for thicknesses greater than 100 Å the contribution from the column of interest to the HAADF signal tends to decrease, while that from

the neighbouring columns tends to increase. When compared to the characteristics of intensity distribution for crystal oriented along [100], the oscillations of intensity in [110] with the depth was found to be more pronounced. The effect of crystal orientation on the specimen broadening is attributed to the decreased nearest-neighbour separation between the columns in [110] (compared to [100]), as a consequence of which a significant overlap between the projected potentials of individual atomic-columns in the specimen is expected.

6.4.1.3 *STEM-EELS elemental mapping*

Elemental mapping of the Pt-Fe(800)(conditioned) catalyst particles was performed using STEM-EELS technique (discussed earlier in Section 5.6). Figure 6.6 shows Pt (red) and Fe (green) maps generated over an edge of a typical Pt-Fe(800)(conditioned) particle. Note that under the STEM-EELS spectrum imaging conditions employed here,[9] an 'atomic-level spectroscopy' has been possible. In other words, the chemical composition of the individual atomic-columns along the projected thickness is being elucidated. From the composite Pt *vs* Fe map shown in Figure 6.6, it can be seen that the Pt and Fe atomic-columns alternate in the core-region of the particle, whereas the shell region is Pt-rich. These observations are both characteristic of an ordered IMCS structure, which is consistent with the HAADF-STEM imaging analyses discussed earlier.

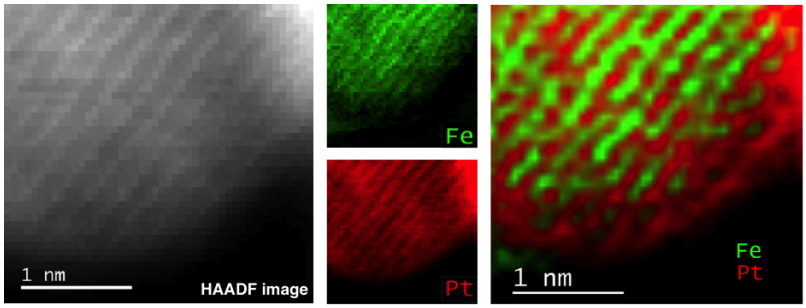

Figure 6.6: STEM-EELS compositional mapping of Pt and Fe over the edge of a Pt-Fe(800)(conditioned) particle.

[9] High tension: 200 kV, EELS spectrum range 450 eV – 2450 eV, Current: 260 pA, Exposure time per pixel: 0.05 secs, Data set size: 46 x 44 pixels

6.4.1.4 *Note on the alloy composition of the particle core*

Previously, Chan and Botton *et al* [386] have performed XRD analyses on the Pt-Fe(800)(conditioned) particles, and inferred that the core alloy structure is possibly in a Pt_3Fe_2 composition ($a = b = 3.865$ Å and $c = 3.769$ Å). However, our subsequent STEM-EELS compositional analyses and the quantification of Pt-$M_{4,5}$ and Fe-$L_{2,3}$ edges revealed a dispersion in the composition across different particles in the batch. For example, as summarized in the Table 6.2 the core alloy composition of a larger nanoparticle (~50 *nm*) was about Pt/Fe = 41/59, whereas that of a smaller nanoparticle (~6 *nm*) was about Pt/Fe = 59/41 (see Table footnote for parameters used for the EELS quantification).[10] Since the Pt-Fe bulk phase diagram suggests only three ordered alloy phases namely Pt_3Fe (75/25), Fe_3Pt (25/75) and PtFe (50/50), the alloy mixtures found in the Pt-Fe(800)(conditioned) particles can thus be simply regarded as 'metastable phases', as opposed to being 'equilibrium phases'.

PARTICLE	At.% Pt	At.% Fe
Pt-Fe(800)(conditioned)(diameter ~ 50 *nm*)	41[1]	58[2]
Pt-Fe(800)(conditioned)(diameter ~ 9 *nm*)	58[3]	41[4]

[1] M edge, signal counts: 678128 ± 1318.8, cross-section: 897.9 ± 179.6 barns
[2] L edge, signal counts: 1199068 ± 3283.9, cross-section: 2500.7 ± 250.1 barns
[3] M edge, signal counts: 3189908 ± 3631.3, cross-section: 1050.5 ± 210.1 barns
[4] L edge, signal counts: 13026533 ± 8295, cross-section: 3030.2 ± 303 barns

Table 6.2: Quantification of Pt and Fe content in the Pt-Fe(800)(conditioned) particles.

A dispersion in the compositions of different Pt–Fe particles can be attributed to the polydispersity in the particle sizes evidenced in the sample. See Figure 6.9b*(red plot)* for the measured size-distribution histogram of over 900 Pt-Fe(800)(conditioned) particles. Many studies have found such size-dependency of particle composition, in the heat-treated samples (Section 4.2.1). This is also consistent with our detailed analyses of the heat-treated particles studies, which we discuss later in Section 6.5.

[10] Beam energy: 300 keV, Collection angle: 34 mrad, Convergence angle: 19.6 mrad. In all the measured compositions, the error estimated was less than 5 %.

6.4.2 *Estimation of lattice strain in the catalyst particles*

As discussed previously, the compressive strain induced on the Pt surface is a determining factor for the ORR activity. In the case of Pt-Fe(800)(conditioned) catalyst particles, a compressive strain on the Pt-rich shell induced by alloy core will be expected. Using the atomically resolved HAADF-STEM images, and a computer-code that we developed in house, we could perform lattice strain mapping over a projected 2D area of the particles. The code developed is applicable to any nanoparticle image, so long as the nanoparticles are atomically-resolved. For the sake of demonstration, an example of a Pt-Fe(800)(conditioned) particle oriented along [110] zone-axis is discussed in the present section (Figure 6.8).

Procedure for estimating strain

Figure 6.7a shows the schematic representation of 2D projected area of a typical Pt-Fe alloy particle oriented along [110] zone-axis. Lattice parameters a and c were obtained from the XRD estimation of the catalyst alloy core composition (a = 3.865 Å, c = 3.769 Å). White and brown spheres visible in Figure 6.7a reveal relative locations of Pt and Fe atomic-columns, respectively. From such an arrangement, a triangular patch bound by three atomic-coordinates (x_i, y_i) (i = 1, 2, 3) is considered. The % strain in this triangular patch for a catalyst particle is calculated, by taking the ratio (η) of the measured area for a catalyst particle with respect to that in a pure Pt.

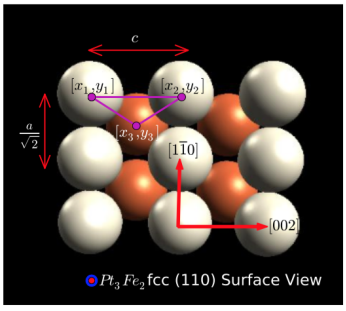

(a) Schematic representation of a 2D projected area of a Pt-Fe alloy particle oriented along 110 zone-axis.

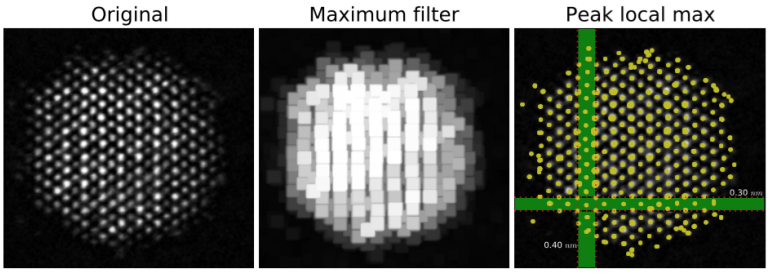

(b) Illustration of steps to accurately locating an atomic-column in HAADF-STEM image.

Figure 6.7: Illustrations of procedure to estimating lattice strain in nanoparticles from HAADF-imaging.

The patch areas for the alloy and pure-Pt cases are represented by 'S_{alloy}' and 'S_{Pt}', respectively, and the ratio $\eta = \frac{S_{alloy}}{S_{Pt}}$.

The % strain along a direction is defined as $\frac{(a-a_{Pt})}{a_{Pt}} x100$, where a and a_{Pt} are lattice parameters for catalyst particle and pure-Pt, respectively. The triangular patch areas (S_{alloy} and S_{Pt}) are related to respective lattice parameters as:

For a pure Pt particle, a = b = c = 3.924 Å. So the triangular patch area S_{Pt} marked in Figure 6.7a would be: $S_{Pt} = \frac{1}{2}(a)(\frac{a}{2x\sqrt{2}}) = 2.72237\,Å^2$

For a catalyst particle, we first estimate the patch area in the core of the particle using the lattice parameters estimated by XRD analyses (a = b = 3.865 Å and c = 3.769 Å). $S_{alloy} = \frac{1}{2}(c)(\frac{a}{2x\sqrt{2}}) = 2.5755\,Å^2$

From the calculated S_{Pt} and S_{alloy}, we can estimate the % strain in a alloy triangular patch using the following expression, referred to as the 'theoretical strain' (Ψ_{theo}).

$$\boxed{\Psi_{theo} = \sqrt{\eta} - 1)\,x\,100 = (\sqrt{\frac{S_{alloy}}{S_{Pt}}} - 1)\,x\,100 = -2.73\%} \tag{6.1}$$

The code written estimates the area of every triangular patch in the experimental HAADF-STEM image (S_i), and its % deviation (μ) from the calculated S_{alloy} is estimated.

$$\boxed{\mu_i = \frac{(S_i - S_{alloy})}{S_{alloy}}\,x\,100} \tag{6.2}$$

The required 'strain Ψ' at every patch in the image is given by:

$$\boxed{\Psi_i = (\sqrt{\frac{S_i}{S_{alloy}}} - 1)\,x\,100 = (\sqrt{(\frac{\mu_i}{100} + 1)} - 1)\,x\,100} \tag{6.3}$$

This indicates that by mapping the calculated μ_i spatially, a 2D lattice strain map can be generated.

As shown in Figure 6.8, the generated strain map is overlaid on the corresponding HAADF-STEM image, and color-coded to indicate different μ_i values. The more negative the μ_i for a triangular patch is, the larger the compressive strain Ψ_i is.

Procedure for measuring the patch area from the HAADF-STEM images
In order to measure the area of the triangular patch in the HAADF-STEM images, the three atomic-coordinates first needed to be precisely identified, for which we followed a series of image processing techniques using *ImageJ*. First, the raw HAADF-STEM images were 2D gaussian filtered, and then, background subtracted. Second, a maximum filter was applied to the background subtracted image using a set mask. The position of the atomic-columns was then obtained as the peak local maximum of all the intensities within this mask area. These steps are illustrated in Figure 6.7b for an particle oriented along [110].

For every set of three atomic-coordinates illustrated in Figure 6.7a and Figure 6.8*(a)*, the area of the triangular patch is given by:

$$S_i\left((x_1,y_1),(x_2,y_2),(x_3,y_3)\right) = \frac{1}{2}\left(x_1y_2 - y_1x_2 + x_2y_3 - y_2x_3 + x_3y_1 - y_3x_1\right) \tag{6.4}$$

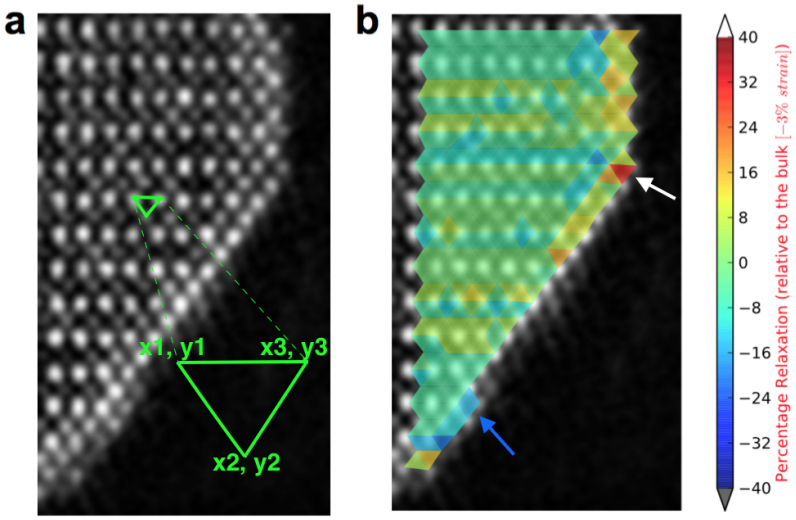

Figure 6.8: Illustration of lattice strain mapping: (a) Gaussian filtered HAADF-STEM image of an edge of a Pt-Fe(800)(conditioned) nanoparticle. (b) 2-D lattice strain mapping over the region shown in (a).

Findings

2D lattice strain map generated for a Pt-Fe(800)(conditioned) particle is shown in Figure 6.8. Close inspection of the color codes in different regions indicates that the strain distribution within the particle is non-uniform. The non-uniformity seems to be stronger in the shell region than the particle core. For example, sites identified by the white arrow seems to be more relaxed compared to the core, whereas the site identified by blue arrow seems to be relatively more compressed. This shows that every site in the shell region is not necessarily strained compressively. Thus, we expect that the strain effect on the observed activity enhancement in the Pt-Fe(800)(conditioned) particle batch is likely from an average effect of all the compressed sites located in the entire catalyst batch. The average strain in a given area can be estimated as an average of the measured Ψ_i (see Equation 6.4) of all the patches within the selected area (i.e., $\Sigma\Psi_i/N$, where N is the no. of patches in the area). Our calculations indicate that the lattice strain in the core is about 3 %, which is in very good agreement with the calculated 'theoretical strain' from the lattice parameters obtained from XRD analyses (2.73 %).

6.4.3 *Monitoring structural evolution of catalysts over cycling*

Structural evolution of Pt-Fe(800)(conditioned) catalyst particles over 10000 cycles was studied using a combination of techniques: low-mag BF-TEM images to understand the size evolution, XRD analyses and HAADF-STEM images to understand the evolution in morphology, phase and atomic-ordering on the bulk (i.e., catalyst batch) level and atomic-level, respectively. Discussed below are our findings revealing that the atomic-ordering is still preserved at the end of 10000 cycles, which explains the exceptional catalytic durability observed in these particles.

6.4.3.1 *Combined BF-TEM, HAADF-STEM, XRD and EDS analyses*

Figure 6.9a shows the representative low-magnification bright-field (BF) TEM images of the non-cycled (left) and cycled (right) catalyst particles, respectively. Using numerous such images for both the samples, sizes of over 1030 particles systematically sampled at various sites on the TEM grid were measured. The resulting size distributions are plotted for the non-cycled and cycled catalyst batches are shown in Figure 6.9b, respectively. Results indicate that the average diameter of the nanoparticles increased by nearly 1 *nm*

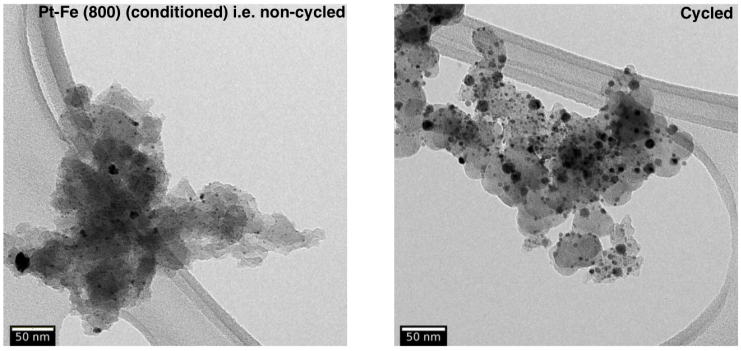

(a) Low-magnification BF-TEM images of Pt-Fe(800)(conditioned) particles before (left) and after (right) potential cycling (10000 cy).

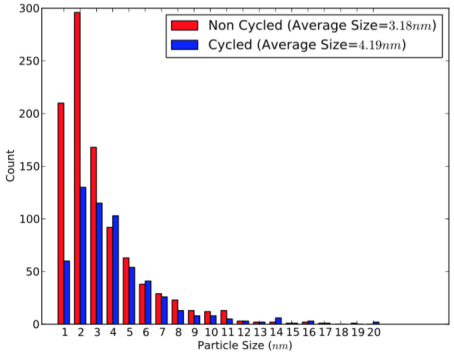

(b) Measured particle size distribution histogram of non-cycled (red) and cycled (blue) samples.

Figure 6.9: Size evolution in the Pt-Fe(800)(conditioned) particles over the course of potential cycling.

upon treating over 10000 cycles, which is further validated by XRD analysis that showed about 1.2 *nm* difference in the crystallite sizes.

It is important to note however that the size enlargement seen in these particles is much smaller compared to that observed in various other Pt-Fe catalyst designs [387]. Such small size enlargements can be attributed to enrichment in the shell thickness, possibly from the redeposition of Pt^{x+} species following a dissolution into the electrolyte *via* Ostwald ripening. This hypothesis is further supported by a much broader distribution (or a longer tail) in the size-distribution of 'cycled batch' compared to the 'non-cycled' (see Figure 6.9b), which is a characteristic of the ripening mechanism (Section 3.3.1). Additionally, an inspection of the shell regions in the HAADF-STEM images of different 'cycled particles', of different sizes (Figure 6.11, discussed later) confirms that the shell thickness is getting thicker as a result of cycling.

Figure 6.10a compares the XRD patterns of non-cycled and cycled catalyst batches. The two small shoulders at 2θ values of 49.2 (due to (002) reflection), and 70.6 (due to (202) reflection), correspond to lattice compression from cubic to a tetragonal ordered PtFe type alloy structure. A leftward shift in the (111) peak toward smaller 2θ values indicates Pt enrichment upon sequential cycling. Most importantly, the presence of the (110) superlattice reflection at around 2θ = 39.77 confirms that the atomic-ordering (in the alloy core) is retained even after 10000 potential cycles. This result is consistent with the atomic-resolution HAADF-STEM images, where the characteristic contrast variation for ordering (alternating bright and dark intensities) is visible even in the cycled particles (e.g., Figure 6.10c). We attribute the catalytic durability observed in these catalysts to this sustenance in the atomic-order, as the retention in the ordered alloy structure implies that the lattice strain effects is preserved, which we know is responsible for the enhanced ORR activity.

A newly developed peak at 2θ = 39.9 in the XRD pattern (Figure 6.10a) of cycled particles suggests evolution of Pt-rich phase, which is further supported by the gradual increase in the Pt/Fe compositional ratio over cycling, obtained from doing EDS point analyses (Figure 6.10b). Since the HAADF-STEM images does not evidence any Pt-rich phase in the particle cores, the XRD and EDS measurements confirm shell enrichment in the particles, preferentially *via* a redeposition of Pt atoms. Further notice from (Figure 6.10b) that the increase in Pt/Fe ratio during the initial 3000 cycles is much steeper than the later cycles. This is possibly because of the presence of relatively higher percentage of smaller particles during these cycles. Consequently, the ripening process results in a higher dissolution of the Pt^{x+} species, which in turn results in a higher rate of Pt

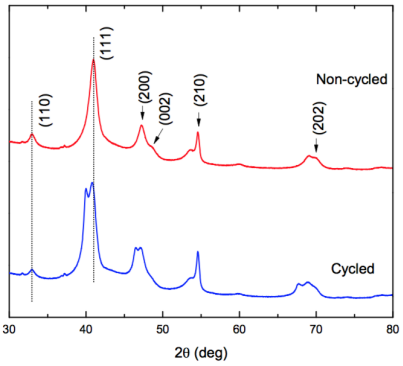

(a) XRD patterns of non-cycled and cycled samples.

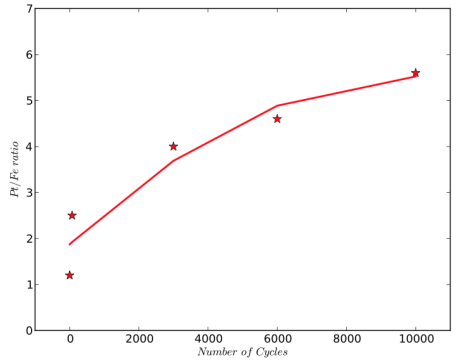

(b) Plot of Pt/Fe ratio obtained from EDS point analysis as a function of cycle number.

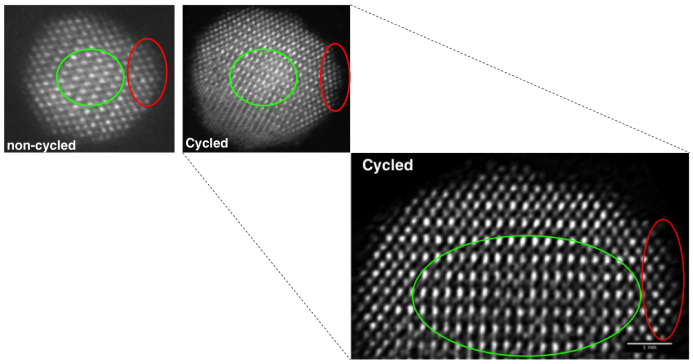

(c) Atomic-resolution HAAD-STEM images of non-cycled and cycled particles. Green circles highlight regions where atomic-columns alternate with bright/dark intensities. Red circles highlight regions where atomic-columns appear preferentially brighter.

Figure 6.10: Evolution of structural ordering and composition in Pt-Fe(800)(conditioned) particles over the course of potential cycling.

redeposition. A relatively less steep increase in the Pt/Fe ratio is expected for the ripening process beyond 3000 cycles, since the dissolution rate of larger particles formed is much slower than the initial smaller particles. Importantly, note that the initial catalyst alloy structure is largely maintained despite cycling (with the exception of thickening of the outer shells). Consequently, the ORR activity of these catalysts is expected to be also preserved to great extent, consistent with the considerably small loss in the activity from over 10000 times cycling (~9 %).

We call the degradation trend discussed above as the 'static core dynamic shell' (SCDS) regime, which is in contrast to the 'dynamic core dynamic shell' (DCDS) regime commonly seen for the disordered *Pt-M* alloy nanoparticles. While the SCDS regime results in a better catalytic durability from the retention of alloy structure, the DCDS degradation regime results in significant decrease in the activity from the loss of alloy structure caused by the dissolution of *M* atoms during cycling.

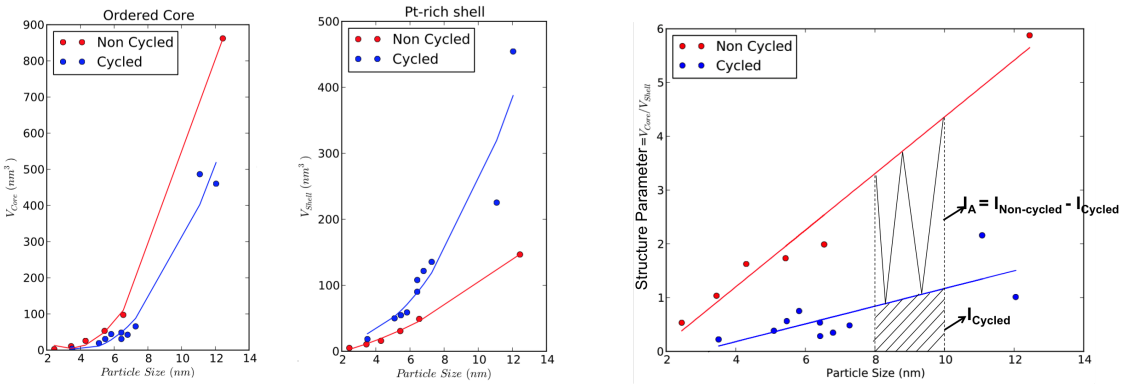

(a) Left: Plot of ordered core volume *vs* particle size. Right: Plot of Pt-rich shell volume *vs* particle size.

(b) Plot of Pt/Fe ratio obtained from EDS point analysis as a function of cycle number.

Figure 6.11: Quantification of changing ordered core and Pt-rich shell volumes over the course of cycling.

6.4.3.2 *Quantitative HAADF-STEM to understand time-evolution of ordering*

In support of the SCDS degradation regime in 'Pt-Fe(800)(conditioned)' catalysts discussed in the previous section, we quantified the time-evolution of ordered alloy core and the Pt-rich shell during cycling, with the help of HAADF-STEM images. The procedure involved, calculating the volume ($V = 1/6\pi d^3$) of the core and the shell regions of many non-cycled and cycled particles. Diameter (d) required to calculate the respec-

tive core and shell volumes was measured from the atomic resolution HAADF-STEM images assuming a spherical 3D volume for the entire particle. An example is illustrated in Figure 6.11a.

Figure 6.11a shows the variation in the estimated core- and the shell- volumes as a function of particle sizes, for both non-cycled and the cycled samples. The plots demonstrate that an average catalyst particle (3.2 to 4.2 *nm* large) retains ordered cores with negligible change in their volumes despite 10000 potential cycles (~2 % change), whereas the volumes of the shell increased by about 50 % upon cycling, indicating shell enrichment. These findings corroborate with the SCDS degradation regime demonstrated earlier. Table 6.3 summarizes the estimated core and shell volumes for an average particle in the non-cycled and cycled batch of particles.[11]

PARTICLES	Size (*nm*)	Pt/Fe ratio[1]	Core volume (nm^3)	Shell volume (nm^3)
Non-cycled	3.19	1.2 ± 0.1	21.51	10.52
Cycled	4.06	4.6 ± 0.5	22.06	18.41

[1] From EDXS point analyses.

Table 6.3: Estimated core and shell volumes for an average particle in the non-cycled and cycled Pt-Fe(800)(conditioned) batch of particles.

6.4.3.3 *The catalyst degradation parameter, and its estimation*

We term the volume ratio of the core to the shell of a catalyst particle as its 'structure parameter'. Figure 6.11b shows the estimated 'structure parameter' for particles in both non-cycled and cycled samples, plotted as function of their sizes. As shown, a linear relationship can be used to describe the 'structure parameter *vs.* particle size' plot. We call the area measured under the fitted line for a set span of particle sizes, as the 'integrated area' ($I_{\text{Non-cycled}}$ and I_{Cycled}) as in Figure 6.11b). We then define an important quantity, the 'catalyst degradation parameter' of a catalyst design, as the ratio of the 'integrated areas'

[11] It is important to note that the corresponding values for the core/shell volume of the average particle is obtained from the intercepts onto the 'fitted' profile of the plots shown in Figure 6.11a. In other words, this represents the selected average core/shell volumes of the selected average particle in the non-cycled and cycled samples.

of the cycled and non-cycled samples calculated within a size-span that is equal to the difference in their average particle sizes (Δr).

$$\text{Catalyst degradation parameter} = \frac{I_{Cycled}}{I_{Non-cycled}}\Big|_{\Delta r} \tag{6.5}$$

By definition, the higher the 'catalyst degradation parameter' for a catalyst design is, the poorer would be its catalytic durability. For the case of 'Pt-Fe(800)(conditioned)' IMCS catalyst particles, the estimated 'catalyst degradation parameter' over the course of 10000 cycles is about *0.27*. This simple method allows for the determination of the 'catalyst degradation parameters' of many other catalyst nanoparticle designs. Once a sizeable set is formed, we propose that the 'catalyst degradation parameter' will serve as an invaluable tool to screen different catalyst designs. For example, catalyst designs beyond a set 'catalyst degradation parameter' threshold can be considered more practical for the ORR. The catalyst design with the smallest 'catalyst degradation parameter' will eventually emerge as the most durable catalyst for the PEMFCs. Although a comparison of mass- and specific- activities is already serving such a task, we believe that the use of 'catalyst degradation parameter' can be much more reliable. This is because the mass- and specific- activities are measures of the surface reactivity, whereas the 'catalyst degradation parameter' is a measure of changes in the surface and bulk atomic-structures. Given these advantages, we propose that the 'catalyst degradation parameter' can be used as the 'design index' of any catalyst design, which is indicative of the structural evolution and durability over the course of potential cycling (or operation in a PEMFC).

6.4.3.4 *2D lattice relaxation mapping to compare surface relaxation in cycled particles*

As demonstrated earlier, the Pt-rich shell thickens during cycling as a result of the redeposition of dissolved Pt^{x+} species from the electrolyte. The relative displacement of atoms in the new surface layers formed may be different from that in the original non-cycled shell. To investigate these changes, we performed a 2D surface relaxation mapping of the non-cycled and cycled particles, as shown in Figure 6.12a, respectively. We generated these maps by following a similar procedure as that discussed earlier in Section 6.4.2. A close inspection of the intensities in these maps reveals that the surface layers in the cycled particle, are rather more relaxed, compared to those in the non-cycled particle. Although some relaxation in the core region can also be seen, these can be attributed to the uncertainty in locating the Fe atomic-columns, whose relative contrast with respect

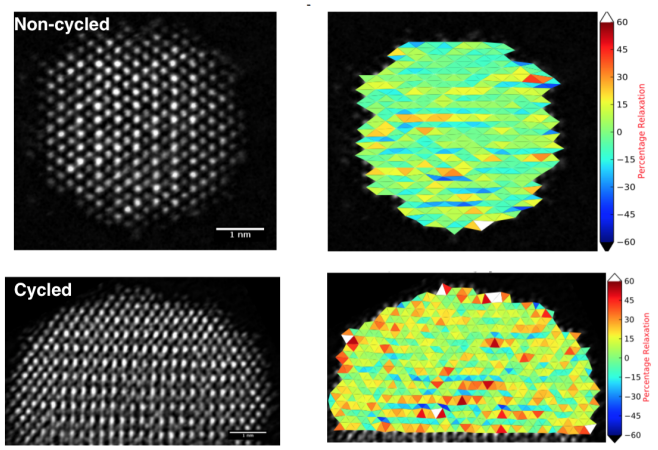

(a) Left: HAADF-STEM images of non-cycled (top) and cycled (bottom) particles. Right: 2-D percentage relaxation mapping of particles shown in (Left).

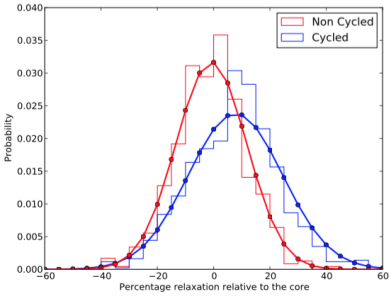

(b) Percentage relaxation distribution plotted from the data obtained at each color segment shown (a)

Figure 6.12: 2D lattice relaxation mapping of non-cycled and cycled particles.

to Pt is expected to be large.[12] Additionally, we plotted a histogram of all the intensities in the map as a function of their relative % difference with respect to an average intensity value in the core. The plotted histograms (after normalization) for both, the non-cycled and the cycled particle is shown in Figure 6.12b. A relatively much broader distribution in the histogram for the cycled particle indicates a much larger surface atomic displacement compared to the non-cycled particle. We think that the surface relaxation resulting from the potential cycling, can be contributing towards the loss in the specific activity of these particles.

6.4.4 *Summary on the evolution of catalyst structure during cycling*

In summary, our characterization work revealed that 'Pt-Fe(800)(conditioned)' catalyst particles were composed of ordered intermetallic alloy cores, which are encapsulated in bilayer thick Pt-rich shells. At the time of reporting, these composite structures were novel, and the reported mass- and specific- activities were the highest among all other Pt-Fe catalyst designs. Our lattice strain measurements revealed overall -3 % compressive strain in the alloy core, and a much higher value at few locations in the shell region. The

[12] due to a combination of mass-thickness effects on HAADF intensity

compressive strain is previously shown to enhance the ORR activities (with respect pure Pt) by lowering the d-band center with respect to the Fermi level.

The 'Pt-Fe(800)(conditioned)' catalysts also showed a high catalytic durability over the course of cycling with only 9 % decrease (from over 6000 cycles). Our BF-TEM and XRD analyses showed a small increase (~1 *nm*) in the particle sizes at the end of 10000 cycles. Such small enlargement in the particle size can be due to enrichment (thickening) of the Pt-rich shell, as confirmed by a combination techniques, including HAADF-STEM, XRD and the EDS. Further analyses using the same techniques also revealed that the original intermetallic core-shell catalyst structure was still retained after cycling, which we believe is responsible for the observed high catalytic durability. Additionally, the surface atoms in the cycled particle were found to be more relaxed with respect to the bulk compared to those in a non-cycled particle, which we believe can contribute to the activity losses in these catalysts. Finally, our findings enabled us to define a parameter called the 'catalyst degradation parameter', which we believe can be useful measure of the catalyst degradation, that can be compared across the different catalyst systems. For the case of Pt-Fe catalyst particles studied in this work the 'catalyst degradation parameter' was estimated to be about *0.27* for treating over 10000 cycles.

6.5 PROBING THE INTERPLAY BETWEEN SEGREGATION AND ORDERING DURING ANNEALING

The previous section presented detailed characterization of the Pt-Fe(800)(conditioned) catalyst nanoparticles to understand their high ORR activities and good durability. In order to further improve these properties an optimization of the catalyst structure is necessary. This requires understanding the structural and compositional evolution of the as-synthesized Pt-Fe nanoparticles during the heat-treatment. Below we present a detailed report of this investigation, conducted using a combination of *ex situ* and *in situ* analyses. For *in situ* analyses, the heat treatment of nanoparticles was conducted inside the microscope, and the selected areas were tracked using HAADF-STEM imaging and STEM-EELS. The *ex situ* involved heat treatment of particles in a furnace, followed by the microscopic characterization of particles, before and after the heat treatment.

6.5.1 *Demonstrating surface-segregation of Fe in the annealed particles*

Figure 6.13*((a1) and (b1))* show HAADF-STEM images of the annealed Pt-Fe particles (i.e., Pt-Fe(800)). In Figure 6.13*(a1)*, the particle core architecture (viewed along [110] zone axis) exhibits alternating bright and dark intensities that is characteristic of atomic-ordering as discussed before. Since HAADF intensity is proportional to $Z^{1.7}$, the bright and dark intensities correspond to atomic columns of Pt and Fe, respectively. This indicates that the particle core transformed into an ordered alloy architecture upon annealing. Note that the particle in Figure 6.13*(b1)* is off a zone axis highlighting this alternating intensity, and therefore, the ordering is not obvious. Below we discuss the STEM-EELS compositional analyses of these annealed particles.

Compositional analyses of the particle in Figure 7.13(a)

Figure 6.13*((a2) and (a3))* show Fe and Pt elemental maps corresponding to the first particle shown in *(a1)*. The Pt-versus-Fe composite map (Figure 6.13*(a4)*) indicates that the particle core is composed of Pt-Fe alloy. It is also visible from a detailed inspection of Figure 6.13*(a4)* that the core is surrounded by two shells, (1) surface-segregated Fe-rich outer shell, and (2) Pt-rich inner shell. These features are better revealed by inspecting the profiles of Pt-$M_{4,5}$ and Fe-$L_{2,3}$ edges taken along a line extending from the core region to the shell, as indicated by the white arrow in Figure 6.13*(a4)*. The extracted Pt and Fe line profiles are shown in the Figure 6.13*(a5)*. From the Fe (green) and Pt (red) profiles

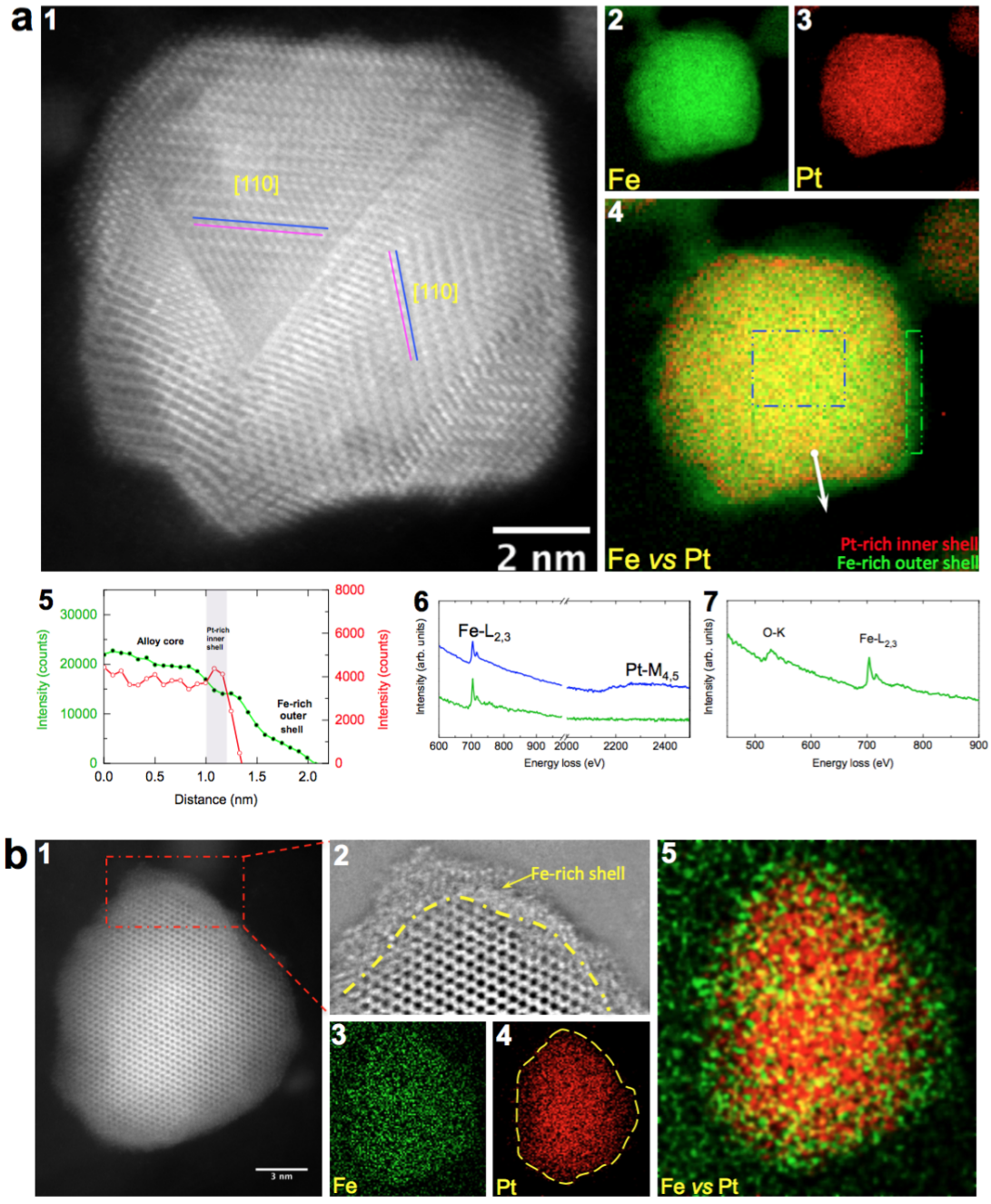

Figure 6.13: 'Atomic-resolution imaging' and spectroscopy of Pt–Fe nanoparticles annealed at 800 °C (1 *h*). (a1, b1) STEM–HAADF images. (a2, b3) 2D EELS map of Fe. (a3, b4) 2D EELS map of Pt. (a4, b5) Composite Fe-versus-Pt maps. (a5) EELS line profiles of Fe L-edge (green) and Pt M-edge (red) taken along the white arrow highlighted in (a4). (a6) EELS spectra integrated over a selected region at the core (dotted blue box) and the shell (dotted green box) in a4. a7) EELS spectra integrated over the dotted green box region in (a4). (b2) Bandpass-filtered image of the region (marked in red) selected from (b1).

between 1.0 and 2.05 *nm* in Figure 6.13*(a5)*, the Fe-rich outer shell (~ 0.7 *nm* thick) and Pt-rich inner shells (~ 0.2 *nm* thick) are clearly evidenced.

Alternatively, Figure 6.13*(a6)* shows the EELS spectra extracted over selected regions in the core and in the Fe-rich shell, respectively. The energy loss values range from 600 eV to 2500 eV such that both Pt-$M_{4,5}$ and Fe-$L_{2,3}$ edges is covered. The regions of spectrum extraction are identified in Figure 6.13*(a4)*, blue box representing a region in the core, and the green box representing a region in the Fe-rich shell. As can be seen, the EELS spectrum extracted from the core evidences both Fe-$L_{2,3}$ (at 708 eV) and Pt-$M_{4,5}$ (at 2206 eV) edges, thus confirming the Pt-Fe alloy structure in the particle core. In contrast, the spectrum extracted from the Fe-rich shell shows only the Fe signature, but bears no evidence of Pt. Further extension of the spectrum to lower energy losses as shown in the Figure 6.13*(a7)* (450 eV to 900 eV) reveals a sharp O-K edge (at 530 eV). These findings indicate that the outermost shell is a Fe-rich (FeO_x) layer.[13] The observed surface oxidation of the Fe-rich shell is attributed to the interaction between the surface-segregating Fe atoms with O_2 present in the annealing atmosphere. Previous studies have shown that the presence of O_2 in a reducing H_2-Ar mixture even in small traces (*ppm* level) can oxidise the surfaces [388]. In summary, above findings demonstrate a composite alloy structure for the Pt-Fe(800) particles, composed of the ordered alloy core that is surrounded by two shells: the inner Pt-rich shell, and the outer Fe-rich shell.

Compositional analyses of the particle in Figure 1 b1

Micrographs in Figure 6.13*((b3) and (b4))* reveal the projected Fe and Pt distribution within the particle described in Figure 6.13*(b1)*. The Pt-versus-Fe composite map Figure 6.13*(b5)* indicates that the Pt-rich alloy core is surrounded by a surface-segregated Fe-rich shell (~ 0.35 *nm* thick). Unlike the particle shown in Figure 6.13*(a4)*, there is no evidence of Pt-rich inner shell in this particle. For a better visibility of the surface-segregated Fe-rich shell, a small region (dotted red lines) in the HAADF-STEM image (Figure 6.13*(b1)*) was bandpass-filtered, the resulting image is shown in Figure 6.13*(b2)*. The filtering was done solely to improve the visibility of the weaker intensities adjacent to the strongly scattering Pt atoms so that the dynamic range of the images allows for the visualization of the existing structure. The segregated Fe-rich shell (region outside the yellow line) surrounding the Pt-rich alloy core is clearly visible in the band-pass filtered image (Figure 6.13*(b2)*).

[13] Note that a further investigation of the exact oxidation state of FeO_x shell is although feasible, it was not central to our present study.

6.5.2 *Investigating the relative occurrence of segregation and ordering*

The previous section demonstrated segregation of Fe and Pt-Fe atomic-ordering as a result of heat-treatment. Irrespective of the element segregating towards the surface, since both ordering and surface-segregation compete for a fixed composition of elements, precedence of one can dramatically influence the other. For example, for a particle with Pt/Fe compositional ratio of 50/50, the precedence of Fe surface-segregation can deplete the core of Fe, thus resulting in the formation of ordered L_{12} (Pt_3Fe) alloy structure, instead of the ordered L_{10} (PtFe) structure. This can significantly decrease the overall specific activity of the catalyst batch, since the necessary strain effects is more pronounced in the L_{10} lattice compared to the L_{12} phase.[14] Such is the impact of the interplay between ordering and segregation. It is therefore crucial to investigate the relative orders of occurrence these two events, in order to be able to take control over the catalyst structures formed from the heat-treatment procedures.

In the case of Pt-Fe particles discussed in this work, using a combination of *ex situ* and *in situ* methods we illustrate below that the surface segregation of Fe precedes the ordering process. The *ex situ* approach involved comparing the nanoparticle structures annealed at 800 °C (presented in Figure 6.3) with those annealed before the disorder-to-order phase-transition temperature (< 500 °C). Although this approach is consistent with most investigations reported in the literature, we believe that the *ex situ* analyses is vastly limited, since the comparison is not made on the same particle. Therefore, we adopted a *in situ* annealing experiment (up to 800 °C), where the same nanoparticle was tracked inside the microscope over the entire course of heat treatment. Both *ex situ* and *in situ* findings are discussed in two separate sections, as follows.

6.5.2.1 *Ex situ analyses*

HAADF-STEM images and STEM-EELS elemental maps shown in Figure 6.14 correspond to particles annealed at 300 °C (1 *h*, 8 % H_2/Ar atmosphere). The annealing temperature was chosen based on the earlier work by Delalande *et al* [389], who showed that the disorder-to-order phase transition in Pt-Fe nanoparticles start to occur at approximately 500 °C. Alongside detailed compositional analyses carried out on one individual

[14] L_{10} compressed along the *c* direction, and exists in a face centered tetragonal (fct) phase, whereas the L_{12} is a FCC phase (a =b = c).

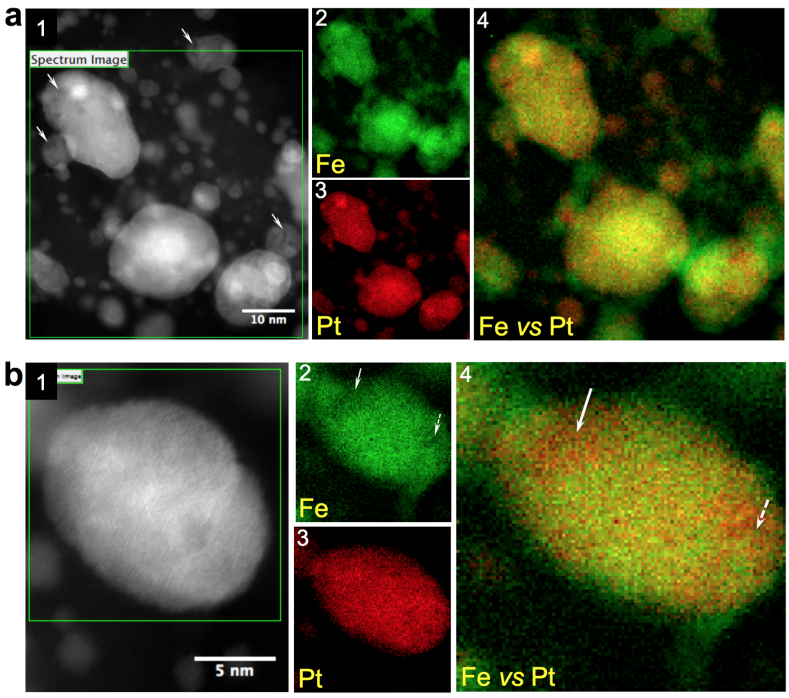

Figure 6.14: Elemental mapping of typical Pt–Fe nanoparticles annealed at 300 °C (1 *h*).

particle (Figure 6.14*(b)*), elemental mapping data from a large area covering a range of particle sizes was also carried out, in order to attain better statistics (Figure 6.14*(a)*).

The white arrows marked in the HAADF-STEM images over the large area (**a(1)**) reveal darker intensities within the particle cores that are apparent as dark patches. Recall that the HAADF-STEM contrast is sensitive to both atomic number and specimen thickness. These dark patches can therefore signify, either a local enrichment in Fe (i.e., compositional inhomogeneity), and/or presence of voids (i.e., structural inhomogeneity) within the particle cores. By inspecting these same areas in the Fe map, a local decrease in the intensity can be seen, which suggests that the observed dark patches in the HAADF-STEM image is due to compositional inhomogeneity.

The compositional inhomogeneity is better revealed from the elemental profiles acquired at high spatial resolution for the particle in Figure 6.14*(b1)*. Corresponding Fe map is shown in the Figure 6.14*(b2)*. The white arrows marked indicates regions with depleted Fe content. The depletion in Fe over this region is compensated by an increase in Pt content, as confirmed by the corresponding Pt (red) versus Fe (green) composite map (white arrows in Figure 6.14*(b4)*). This highlights a compositional inhomogeneity within the particle core.

Above findings indicate that the particle cores remain disordered (i.e., compositionally inhomogeneous) upon a thermal treatment at 300 °C. This is consistent with the predicted disorder-to-order phase-transition temperature (500 °C) by Delalande *et al* [389]. Further close inspection of the particle surfaces in the composite maps for both regions (Figure 6.14*((a4) and (b4))*) clearly indicate that the disordered particle cores are surrounded by Fe-rich shells. Therefore, it can be concluded that the surface segregation of Fe precedes the ordering process.

Importantly, the above *ex situ* analyses involved comparing non-identical particles. It can be argued that the local environments surrounding these particles were dissimilar, and thereby, lead to different segregation behaviors. Such limitations can be overcome by tracking the same nanoparticle, over the course of annealing. In the following section, we illustrate this through an *in situ* annealing experiment.

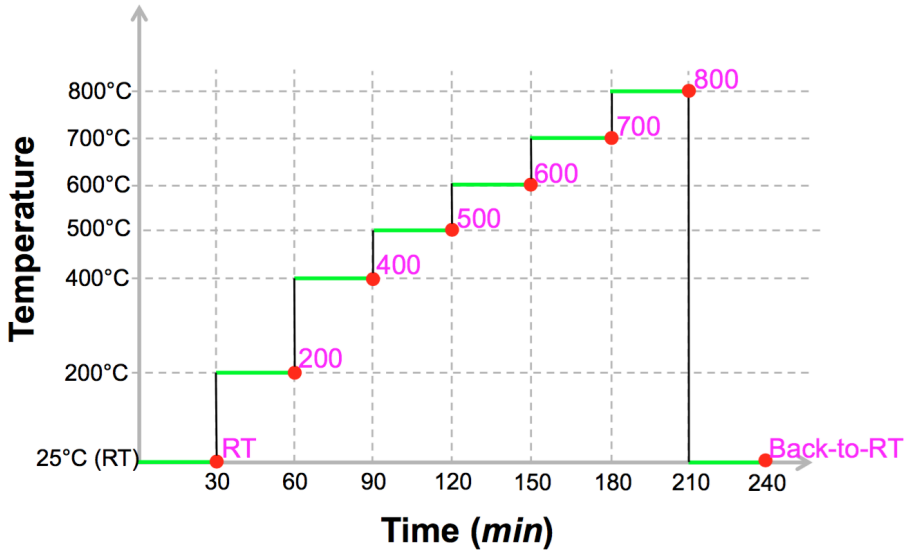

Figure 6.15: Schematic illustration of the *in situ* annealing process carried out.

6.5.2.2 *In situ single-nanoparticle tracking*

The *in situ* heating was performed inside the FEI-STEM microscope, using a microelectromechanical systems (MEMS) based heating holder manufacture by Protochips™.[15] The as-synthesized Pt-Fe nanoparticles were deposited onto the holder. Heat treatment involved an annealing procedure (under vacuum) by holding the sample at 200 °C, 400 °C, 500 °C, 600 °C, 700 °C, until 800 °C for 30 *min* each and, then finally quenching back to the room temperature. The procedure is schematically illustrated in Figure 6.15.

One as-synthesized particle was chosen for the study, and with the help of HAADF-STEM scanning the same nanoparticle was tracked over the course of thermal treatment. At the end of every annealing condition, a HAADF-STEM imaging, combined with STEM-EELS spectrum imaging was performed. The findings are discussed as follows.

Structural and compositional analyses of particles prior to heat-treatment
Figure 6.16*((a) and (b))* show HAADF-STEM images of as-synthesized Pt-Fe particles

[15]The Protochips heating holder design involves a ceramic (SiN_x) thermal e-chip patterned with an array of micron sized holes. These holes are coated with a carbon membrane onto which the nanoparticles were deposited. The temperature of e-chip could be controlled with a separate heating system connected externally. The entire assembly provided a precise temperature control over 1200 °C with super fast heating rates up to 1000 °C per millisecond. More details on the holder and its operation can be found elsewhere [390].

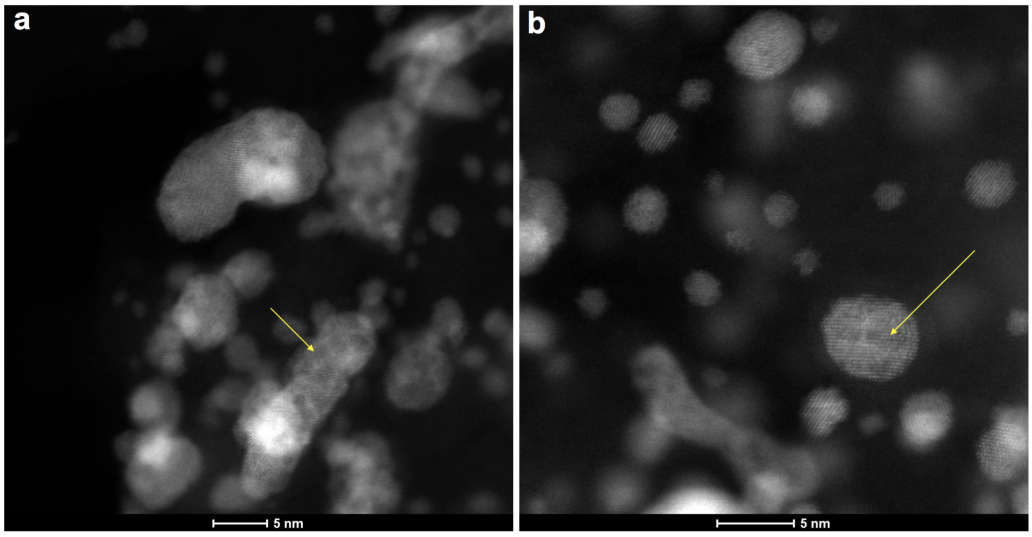

Figure 6.16: HAADF-STEM images of representative as-synthesized Pt-Fe nanoparticles. Arrows highlight regions with relatively darker intensities compared to the neighbouring regions. Scale bars measure 5 *nm*.

prior to the heat treatment. At locations identified by yellow arrows the intensities are much lower compared to the neighbouring areas, apparent as dark patches. As discussed earlier in reference to similar observation in Figure 6.14, such dark patches in HAADF-STEM images suggest a disordered alloy structure (compositional and/or structural inhomogeneities). To confirm that the as-synthesized particles did not already bear a Fe-rich shell, STEM-EELS elemental mapping was performed, discussed earlier in Figure 6.1. Additionally, STEM-EDX analyses on randomly sampled particles (few tens in number) confirmed that the average composition of the as-prepared particles is approximately 67 % ± 5 % and 33 % ± 5 % Fe.

Tracking with HAADF-STEM

Figure 6.17a*(1)* shows HAADF-STEM image of the selected as-synthesized (disordered) particle, about 9 *nm* in diameter. For the sake of discussion this large particle shall be identified as 'particle L'. Series of images shown in Figure 6.17a*(2–8)* illustrate 'particle L' tracked over different annealing conditions. Labels displayed indicate the corresponding annealing condition, for e.g., label 400 in Figure 6.17a*(3)* indicates that the particle was exposed to 200 °C (for 30 *min*) plus 400 °C (for 30 *min*) overall. The reader is encouraged to refer to the table shown in Figure 6.17b, as and when required.

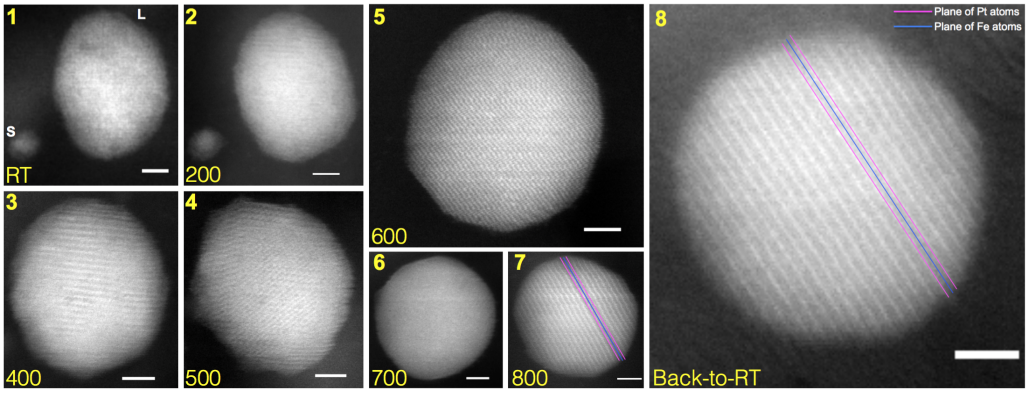

(a) HAADF-STEM images of a Pt-Fe nanoparticle at different stages during the thermal treatment. Labels reflect the annealing condition. Scale bars measure 2 *nm*.

Labels	Overall treatment
RT	RT (30 min)
200	RT (30 min) + 200°C (30 *min*)
400	RT (30 min) + 200°C (30 *min*) + 400°C (30 *min*)
500	RT (30 min) + 200°C (30 *min*) + 400°C (30 *min*) + 500°C (30 *min*)
600	RT (30 min) + 200°C (30 *min*) + 400°C (30 *min*) + 500°C (30 *min*) + 600°C (30 *min*)
700	RT (30 min) + 200°C (30 *min*) + 400°C (30 *min*) + 500°C (30 *min*) + 600°C (30 *min*) + 700°C (30 *min*)
800	RT (30 min) + 200°C (30 *min*) + 400°C (30 *min*) + 500°C (30 *min*) + 600°C (30 *min*) + 700°C (30 *min*) + 800°C (30 *min*)
Back-to-RT	RT (30 min) + 200°C (30 *min*) + 400°C (30 *min*) + 500°C (30 *min*) + 600°C (30 *min*) + 700°C (30 *min*) + 800°C (30 *min*) + Quenched to RT

(b) Description of labels for different annealing conditions.

Figure 6.17: Tracking a single Pt-Fe nanoparticle with HAADF-STEM imaging during thermal treatment.

Tracking with STEM-EELS

Figure 6.18 illustrate STEM-EELS compositional analyses of the 'particle L' at 400, 600, 700, and 800, respectively. In addition to the typical elemental mapping (all the **(1)s'** in Figure 6.18) as before, the line profiles of Fe L-edge (green) and Pt M-edge (red) were also extracted along the blue and yellow scan directions. Blue line scan: all the **(2)s'** in Figure 6.18, Yellow line scan: all the **(3)s'** in Figure 6.18.

In the Figure 6.18a*(3)*, the Fe (green) and Pt (red) profiles reveal the presence of both Fe-rich (green arrow) and Pt-rich (red arrow) regions within the particle. The observed compositional inhomogeneity confirms that the particle L was still disordered at 400 °C. This is consistent with the fact that the overall heat transferred to particle from a treatment at 400 °C is lower than that from a treatment at the predicted disorder-to-order phase-transition temperature, i.e., 500 °C.

Furthermore, the Fe (green) profile in Figure 6.18a*(2)* indicates that the particle surface is enriched in Fe (~0.5 *nm*), as shown by the black arrows. Clearly, this must be the result of surface segregation of Fe as witnessed earlier from the *ex situ* approach (Figure 6.14). However, Fe enrichment at the surface is not seen in Figure 6.18a*(3)*, based on a profile from the same particle, but taken in a different section, in which Pt-rich region (black arrows) can be seen exposed to the surface. Quantification of EELS intensities in these regions revealed a Pt/Fe content (on % basis) of 100.0/0.0 (black arrow on the left) and 75.4/24.6 (black arrow on the right). Hence, it can be concluded that although not complete enough to cover the surface entirely, the surface segregation of Fe began while the particle L still remained disordered. The *in situ* experiment thus demonstrates that surface segregation of Fe precedes the ordering process, which is consistent with the *ex situ* results discussed earlier.

Additionally, close inspection of the particle surface at 600, 700, and 800 °C (black arrows in (2)s' and (3)s' in Figure 6.18b,Figure 6.18c and Figure 6.18d) reveals that the surface was fully covered with Fe-rich shell during later stages of annealing. Further analyses of the particle after quenching (see next subsection) revealed that it existed in a PtFe-$L1_0$ (core) – Fe-rich (shell) alloy structure. This suggests that the disorder-to-order phase transition should have taken place between the treatments at 400 °C and 800 °C. Interestingly, this inference is consistent with the predicted disorder-to-order phase transition (~500 °C) by Delalande *et al* [389].

In summary, above findings suggest a sequence of events taking place during the annealing process listed as follows: 'particle L' is initially disordered, heat-treatments lead to surface segregation of Fe and Pt-Fe atomic-ordering, surface segregation precedes

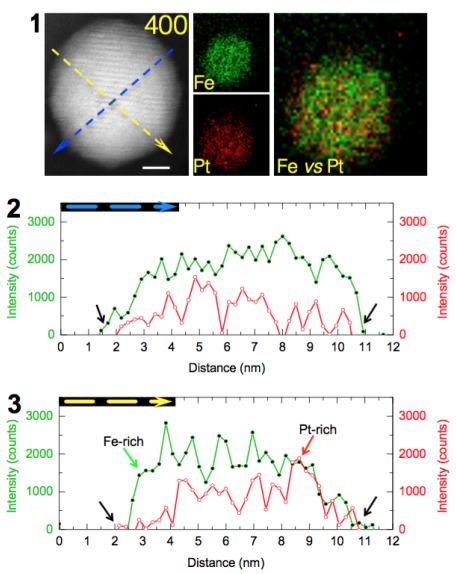

(a) After thermal treatment at 400 °C.

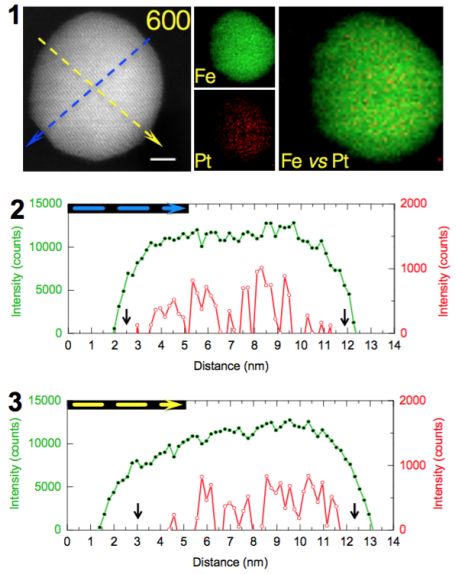

(b) After thermal treatment at 600 °C.

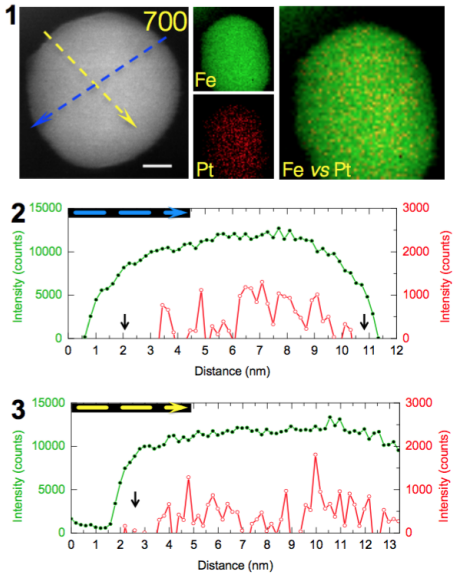

(c) After thermal treatment at 700 °C.

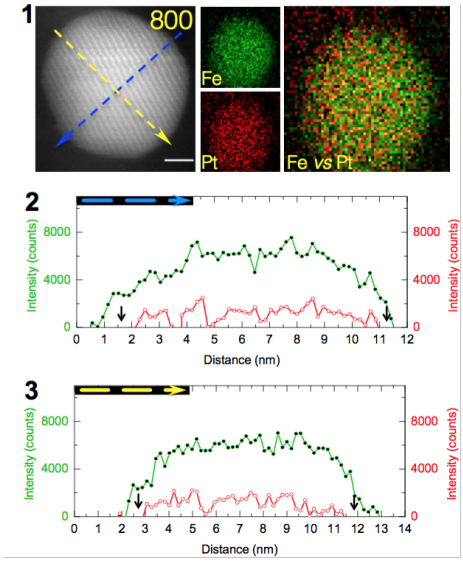

(d) After thermal treatment at 800 °C.

Figure 6.18: Elemental mapping and EELS line profiles across 'particle L' at different stages during the *in situ* thermal treatment.

the ordering process, and lastly, the initially disordered particle finally evolves into a intermetallic core-shell particle with L-1_0 ordered core covered in Fe-rich shell.

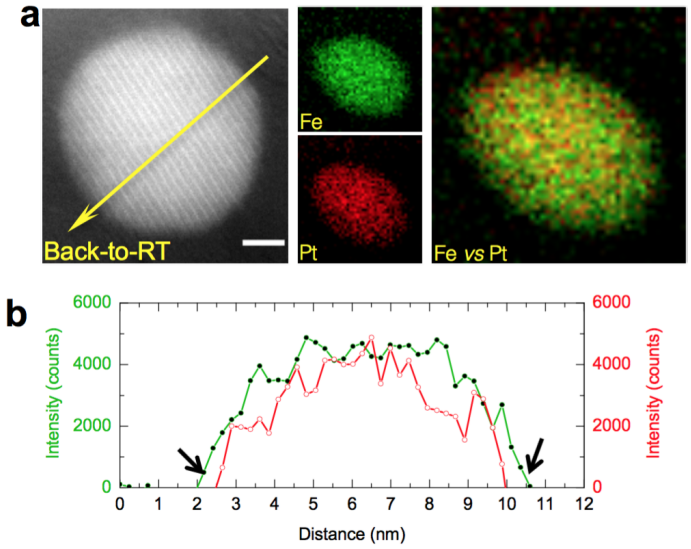

Figure 6.19: Elemental mapping and line profiles of 'particle L' after the *in situ* thermal treatment. (a) HAADF-STEM image and 2 D EELS maps of Fe (green), Pt (red), and the composite Fe *vs* Pt. (b) Line profiles of Fe L-edge (green) and Pt M-edge (red) taken along the yellow scan direction.

Final structure of the tracked single-nanoparticle

Figure 6.19 show Pt and Fe elemental maps and line profiles for the 'particle L' after quenching to the RT. Clearly, the particle core is surrounded by an Fe-rich shell (~0.4 *nm* thick) as revealed by the Fe line profile in Figure 6.19*(b)*(black arrows). After accounting for Fe content in the shell region, it is noticeable from Figure 6.19*(b)* that the EELS intensities of Pt M-edge match very closely with those of Fe L-edge.

On the same particle the EELS intensities were also quantified by using the standard procedure of comparing the cross-section weighted, background subtracted, integrated signals [391]. Table 6.4 lists the quantified Fe and Pt contents on overall particle (58.2 % Fe, 41.8 % Pt), core (56.7 % Fe, 43.3 % Pt), and the shell (93.7 % Fe, 6.3 % Pt) regions. According to these results the composition of the core of the annealed 'particle L' is close to 50:50, which therefore should exist in $L1_0$ ordered phase as dictated by the phase diagram.

Formation of an ordered alloy phase is further supported by the corresponding HAADF-STEM image shown in Figure 6.17a*(8)*, where an alternating bright and dark intensities

is evidenced within the particle (with (001) planes oriented parallel to electron beam). As discussed in many examples, owing to atomic-number contrast in HAADF-STEM, these bright and dark intensities correspond to atomic planes of Pt and Fe, respectively.

REGION SELECTED IN THE SPECTRUM IMAGE	Fe (%)	Pt (%)
Over entire particle	58.2	41.8
Core	56.7	43.3
Shell	93.7	6.3

Table 6.4: Estimated elemental composition in different regions of the *in situ* annealed particle.

6.5.2.3 *Comment on Fe segregation in in-situ vs ex-situ heating*

Figure 6.20 shows the EELS spectra recorded over the Fe-rich shell region of an *in situ* , and an *ex situ* annealed particle (then pink and green spectrum, respectively). Inspection of O K edge in these spectra reveals that the O K edge is present for the *ex situ* case, but absent for the *in situ* case. This suggests that the shell in the *in situ* annealed particle is possibly pure Fe shell, as opposed to the *ex situ* annealed particle where the shell is FeO_x. This is in fact an expected scenario, since the microscope vacuum which was used for the *in situ* annealing experiment contains significantly low O_2 concentration compared to *ex situ* annealing atmosphere. As a result, the surface oxidation is more likely to be the case for *ex situ* annealing experiments. Importantly, it is interesting to note that the surface segregation of Fe occurred irrespective of the annealing atmosphere used (reducing H_2/Ar and vacuum). This is consistent with some recent studies, for e.g., Ahmadi *et al* [298] conducted *ex situ* heat-treatments of $Pt_{0.5}Ni_{0.5}$ nanoparticles in H_2, O_2 and vacuum environments, and observed surface-segregation of Ni in all the three cases.

6.5.3 *Effect of pre-existing Fe-rich shell on the ordering process*

The previous section demonstrated surface segregation of Fe, and its precedence over the ordering process during the annealing of Pt-Fe alloy nanoparticles. Since the pre-existing Fe-rich shell provides a heterogenous boundary to the atoms in the particle core, we surmise that the ordering mechanism in the core can be impacted. This is because the interfacial energies compared to other cases, i.e. absence of a heterogenous boundary, presence of a different heterogeneous boundary, are all different.

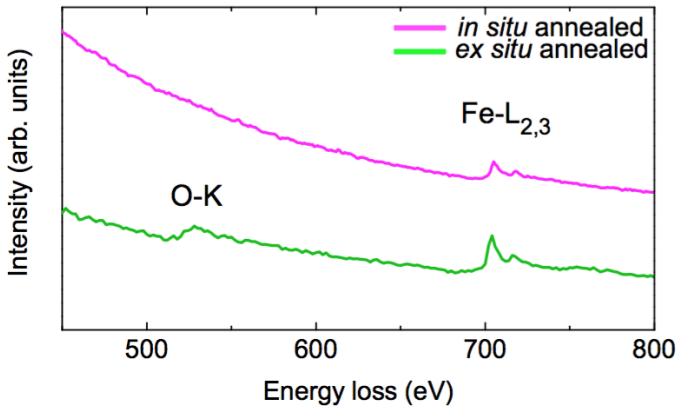

Figure 6.20: Integrated EELS spectra (450-800 eV) over a selected region at the shell of an *in situ* and *ex situ* annealed particle.

Direct observation of the segregation-ordering interplay is extremely difficult given the small time-scales of such events. Thus, we followed an indirect approach, where a particle is quenched in the middle of the ordering process and characterized. The findings and insights obtained are discussed as follows.

Figure 6.21a illustrates HAADF-STEM image of the partially ordered nanoparticle obtained by quenching after 1 *h* annealing at 600 °C *ex situ* (8 % H_2/Ar atmosphere). The nanoparticle is viewed along [110] zone axis. The ordering process is highlighted by the characteristic alternating bright (pink) and dark (blue) intensities, as identified by yellow arrows. As earlier, these bright and dark fringes correspond to atomic columns of Pt and Fe, respectively. However, these alternating bright and dark atomic planes can only be seen as pockets and not homogeneously distributed throughout the particle. This suggests that the ordering process is incomplete.

The dashed red box drawn in Figure 6.21a identifies the order-disorder transition, in which a progressive ordering front is evident on the left half (visible as alternating intensities), and the region onto right half shows no evidence of atomic ordering. The image in Figure 6.21b is a gamma-adjusted STEM–HAADF image corresponding to the image in Figure 6.21a, and a close observation at the particle surface reveals the segregated Fe-rich shell. Noticeably, the atomic ordering starts at the Fe-rich shell and propagates inwards (yellow arrows). Inspection of a neighboring small particle visible in these images also reveals similar characteristics, i.e. Fe-rich shell covering the particle surface, and the initiation of the ordering process at the Fe-rich shell. We interpret these effects as being caused from the pre-existent Fe-rich shell that provides a heterogeneous boundary to the

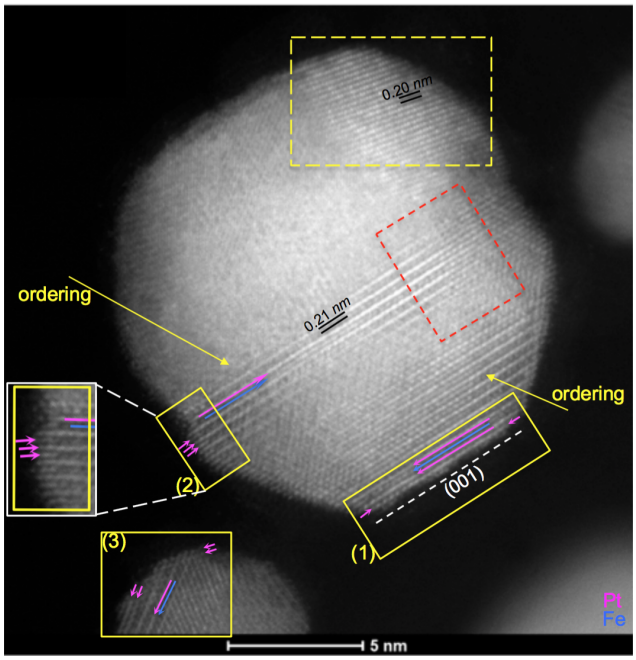

(a) HAADF-STEM image of the particle viewed along 110 zone-axis. Pink and blue lines indicate relatively brighter and darker atomic-columns, respectively.

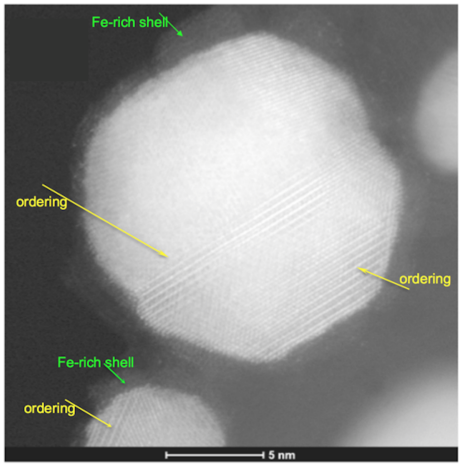

(b) Image obtained after adjusting the dynamic-range in the intensity of (a).

Figure 6.21: Structural investigation of a Pt-Fe nanoparticle annealed at 600 °C.

nanoparticle, such that the formation of nuclei ($L1_0$ or $L1_2$) for ordering is more favored to initiate at the Fe-rich shell than the particle core.

Dashed yellow box in Figure 6.21a identifies a local enrichment in the Pt concentration, as revealed by the bright intensities of the atomic columns with a lattice spacing of 0.20 *nm*. Despite the proximity of this region to the Fe-rich shell, the ordering process is not initiated. This is consistent with the fact that the formation of a Pt-Fe ordered nuclei would be difficult in such an environment where the composition is rich in Pt.

6.5.4 *Crystallographic effects of the segregation process*

HAADF-STEM image for the particle in Figure 6.21 also revealed interesting crystallographic effects caused by the surface-segregation phenomenon.

Consider regions identified as (1), (2) and (3) in Figure 6.21a (yellow box (1)). The pink arrows and lines shown identify atomic-planes appearing with brighter, whereas blue lines identify relatively darker atomic-planes. In the zone-axis that the particle is oriented ([110]), these brighter and darker atomic-planes are composed of Pt and Fe atomic-columns, respectively. Thus, the interior of the particle where the brighter and darker planes is seen to alternate confirm ordering. In contrast, the terminating locations (pink arrows) with preferentially brighter planes confirm Pt segregation. To summarize these findings, the arrangement of any three atomic-planes (1^{st}-2^{nd}-3^{rd}) in the core and the Pt shell regions can be written as Pt-Fe-Pt and Pt-Pt-Pt, respectively. Below we discuss the effect of replacing Fe plane with Pt that is particularly more pronounced particularly for the orientation in Region (2).

First effect of replacing a Fe plane by Pt in the shell is the modification to the Pt-Pt interplanar distances. This is consistent with the fact that the replaced Pt atoms are much larger than the original plane composed of smaller Fe atoms. A reduction in the interplanar distances contributes to higher compressive strain in the Pt shell compared to alloy core, vice-versa. Second effect is the bending of atomic-planes, as we move from the core region to the Pt shell. This is evidenced by comparing the distance between the two planes A and B in the core and shell regions. It can be seen that the A-B separation distance broadens in the shell region, indicating 'bending'. This can be seen as the mechanism whereby the induced strain is relieved from the shell.

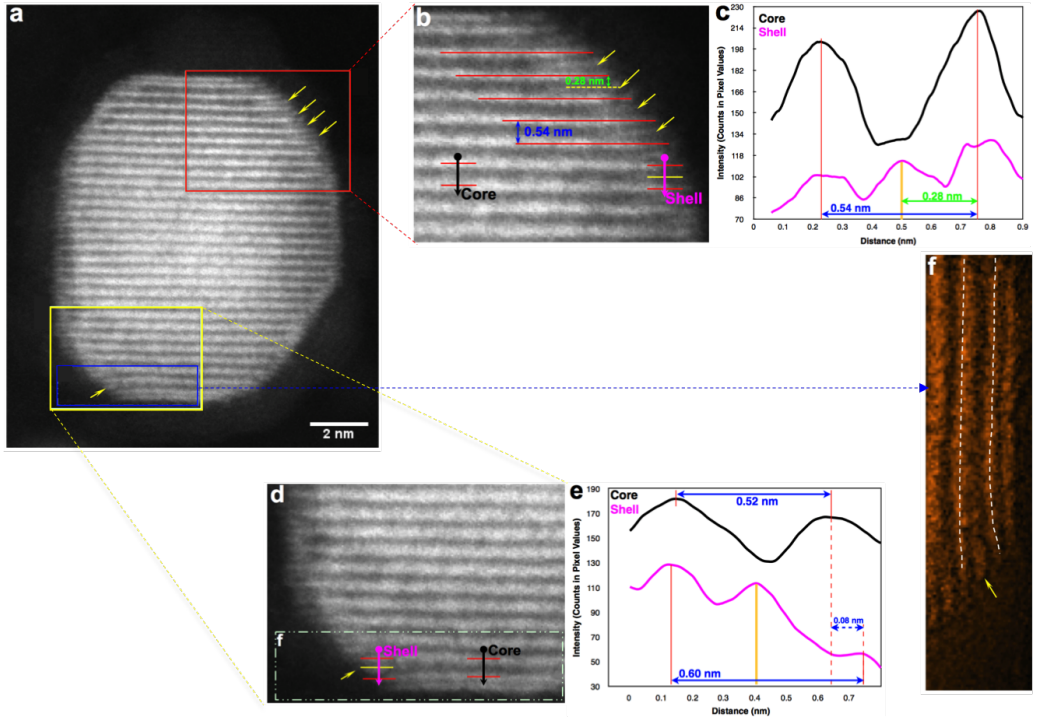

Figure 6.22: Detailed analyses of the crystallographic features of an annealed Pt-Fe particle. (a) HAADF-STEM image identifying three regions, which are individually studied in (b), (d) and (f). (c) and (e), Intensity line profiles.

Further evidences of above two effects is provided by the detailed analyses of interplanar distances for another annealed particle. The findings are summarized in Figure 6.22. The interplanar distances were estimated as the distance between two peaks in the plotted intensity line profiles. Figure 6.22*((c) and (d))* show the intensity profiles obtained from the core/shell planes of a mid-section of the particle (Figure 6.22*(b)*), and far-edge of the particle (Figure 6.22*(d)*). These two regions differ in the fact that in the former case each segregated Pt plane (yellow arrow) is coordinated by additional segregation on either sides, whereas in the latter the segregated Pt plane is coordinated by additional segregation on only on side.

For the mid-section region of the particle: the nearest Pt-Pt distance in the shell region is about 0.28 *nm*, whereas that in the core is 0.54 *nm*. Red lines in Figure 6.22*(b)* indicate Pt atomic-planes that are common to both core and the shell. Comparing their interplanar distances in the core/shell regions does not reveal a significant change. This suggests that the bending of the planes in the mid-section region of the particle was either non-existent or very small (considering measurement error).

In the case of the far-edge region of the particle (Figure 6.22*(d)*), the nearest Pt-Pt distance in the shell region is still lower than that in the core. However, the segregated Pt atoms is separated by different amounts on either sides: slightly more compressed towards the side coordinated with additional Pt segregation. In other words, the Pt plane with no additional segregation to coordinate is more relaxed, which is visible as the 'bending' of the plane in the corresponding HAADF-STEM image shown in Figure 6.22*(f)*. Therefore, we infer that the 'bending effect' of the atomic-plane is stress-relieving mechanisms in these particles imposed by the strain induced from segregation.

In summary, above findings demonstrate two crystallographic effects of segregation: (1) reduction in the interplanar distances in the shell region, and (2) bending of atomic-planes to relieve the induced stress. As discussed in the introductory sections, such local compressive strain can have a positive impact on the catalytic activity exhibited by the structure. Note that in the cases discussed above the segregated Pt shell is still underneath the Fe-rich shell, as evidenced by the gamma-adjusted image in Figure 6.21b for the particles in Figure 6.21a.

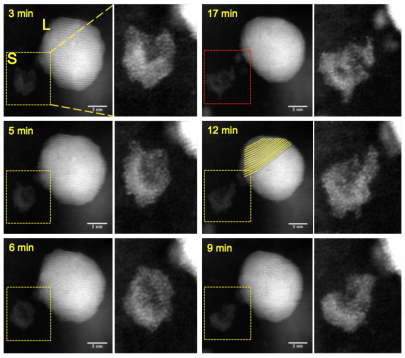

(a) Shrinking of a small particle *via* atom-migration.

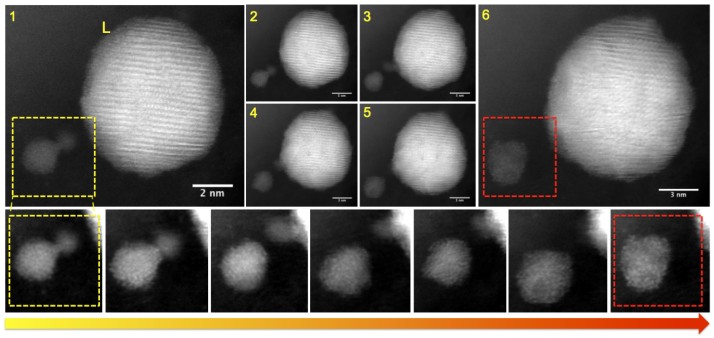

(b) Coalescence of a small cluster with a neighbouring larger nanoparticle.

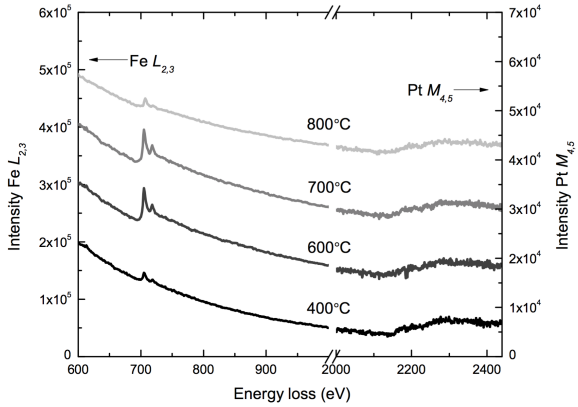

(c) Fe-L and Pt-M edges of particle-L at different annealing conditions. Each spectrum is normalized with respect to the Pt-M and offset along the y-axis for clarity.

Figure 6.23: Time-series of HAADF-STEM images illustrating dynamic mass-transport phenomena during the annealing process.

6.5.5 *Capturing dynamic mass-transport phenomena during annealing*

In addition to single-nanoparticle tracking during the *in situ* annealing experiment, we also performed some time-serial recording of HAADF-STEM images. Two examples are discussed below, where a time-serial image recording evidenced: (1) shrinking of a particle *via* atom-migration, and (2) coalescence of a small cluster with a neighbouring larger nanoparticle.

Figure 6.23a shows a time-series of HAADF-STEM images illustrating two particles, the smaller particle-S and the larger particle-L, residing in close proximity. Inspection of the smaller particle over the course of time reveals shrinking of the particle in size (e.g., compare images at 3^{rd} and 17^{th} mins), which is also accompanied by changes to its structure and morphology. Since the images do not evidence any coalescence effects, we attribute the observed shrinking of the particle to a loss of atoms from the surface and migration, which are both characteristic of the 'ripening mechanism' as discussed earlier (Section 3.3). A similar time-serial recording is shown in Figure 6.23b. The image series illustrate an entire atomic cluster (~1 *nm*) coalescing with a neighbouring larger particle.

As a result of such phenomena (atom-migration and coalescence), a mass transport is established between the particles, which can lead to variations in the size and composition of the particles. For example, Figure 6.23c compares the Fe-L edge intensities obtained for 'particle-L' at different annealing conditions, and a variation in the intensity indicates change in chemical composition of the particle during annealing. Therefore, depending on the amount and composition of the mass-transferred, a situation where the formation of equilibrium phases from annealing cannot be excluded. We propose that the population of equilibrium structures formed from an annealing process can be increased by reducing polydispersity in the particle sizes synthesized.

6.5.6 *Summary on the heat-treatment studies of Pt-Fe particles*

The findings of the detailed heat-treatment studies of Pt-Fe nanoparticles can be summarized as follows. Detailed HAADF-STEM and STEM-EELS analyses during *ex situ* and *in situ* annealing showed that Fe segregates towards the particle surface, and the segregation of Fe can precede the ordering process. The effect of such pre-existent Fe-rich shell on the ordering process was also studied and our findings reveal that the ordering is more favored to initiate at the Fe-rich shell than the particle core. Additionally, the

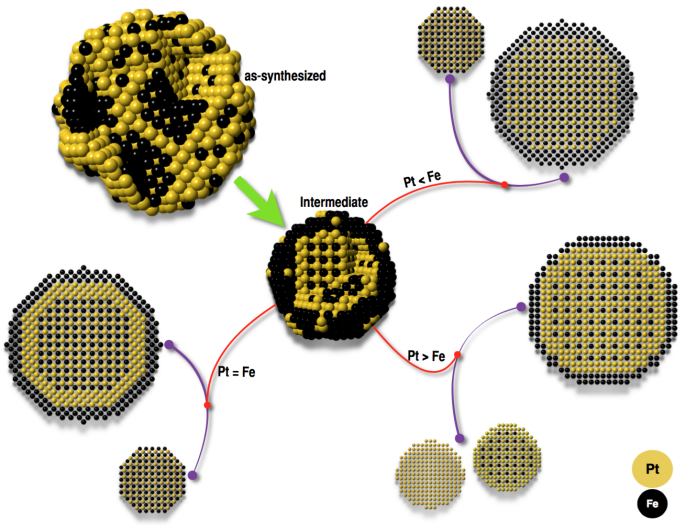

Figure 6.24: Schematic illustration of the different final structures resulting from the annealing of (initially disordered) Pt-Fe alloy nanoparticles.

crystallographic effects of the segregated shell is also studied, more specifically a segregated Pt shell induced compressive strain on the lattice which was being relieved by the bending of atomic-planes. Over the course of these studies unique structures resulting from a typical thermal treatment were elucidated, including particles with (i) Pt-Fe alloy (core)-Pt-rich (inner shell)-Fe-rich (outer shell), (ii) Pt-rich alloy (core)-Fe-rich (shell), and (iii) PtFe-$L1_0$ (core)-Fe-rich (shell) (a schematic illustration of different structures is shown in Figure 6.24). The reported findings open interesting perspectives towards a rational design and a controlled phase evolution of Pt–Fe nanoalloys, ultimately intended for viable applications in ORR electrocatalysis and magnetic storage devices.

6.6 REMOVAL OF FE-RICH SHELL FROM THE CATALYST SURFACE

Previous section demonstrated that the surface layers in annealed particles (Pt-Fe(800)) was a Fe-rich FeO_x, which was shown to be a consequence of Fe surface-segregation accompanying the heat-treatment process. Note that the ORR activity measurements of these particles are measured only *after* conditioning them under multiple voltammetric cycles. The procedure is also referred to as *voltammetric dealloying*. The annealed particles

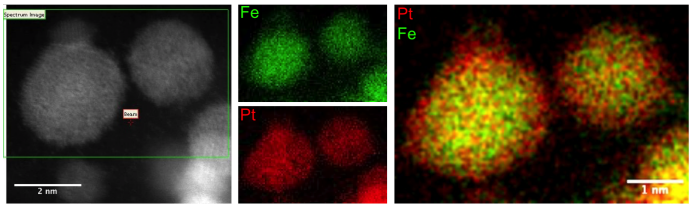

(a) STEM-EELS elemental mapping of Pt-Fe(800) particles after conditioning.

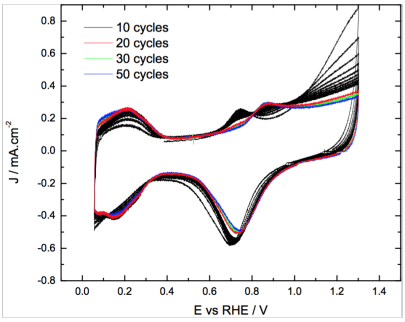

(b) Typical CV data recorded over the conditioning pre-treatment of Pt-Fe alloy nanoparticles.

Figure 6.25: Evidencing removal of Fe-rich shell from the catalyst surface by potential cycling.

studied in this work were 'conditioned' to about 50 potential cycles, a typical CV data over the course of cycling is shown in Figure 6.25b.[16]

Figure 6.25a summarizes the STEM-EELS elemental mapping of Pt-Fe(800)(conditioned) particles (Fe (green), Pt (red) and Pt *vs* Fe composite). Close inspection of the surface layers in the Pt *vs* Fe composite map reveals that the surfaces are Pt-rich, as opposed to being Fe-rich which was the state originally before conditioning. This suggests that the effect of CV conditioning is to leach out the FeO_x layer. This observation is consistent with the CV profiles (Figure 6.25b) where a small oxidation peak in the voltage range 0.6 V to 0.8 V corresponding to Fe dissolution, is more pronounced during the initial 10 cycles, and diminishes gradually with the cycling number, until disappearing completely at the end of 50^{th} cycle.

Note that the sub-surfaces underneath the FeO_x layer in the particles investigated was either a Pt-rich shell or a Pt-Fe alloy (Section 6.5.1). These surfaces are exposed to further leaching once the FeO_x layer is removed completely. Since Pt is relatively more stable to leaching than Fe, further conditioning of Pt-Fe alloy surface can expect to eventually result in the formation of Pt-rich shells. Whereas in the case of Pt-rich surfaces exposed to further conditioning, leaching of Pt atom-by-atom can be expected to result in formation of thinner Pt-rich shells. Both these hypotheses are consistent with the observations made from voltammetric dealloying of over many different Pt-M catalyst systems (Section 4.2.1.4).

[16]The voltammogram was recorded by collaborator Christina Bock (NRC, Ottawa) with similar conditions as that listed in Section 6.3 earlier.

Also, since a Pt-rich shell is favored for ORR catalysis over FeO_x surface, controlling the number of CV cycles would be particularly important. Because, a higher number of cycles can result in thinner Pt-shells and lower number of cycles can result in incomplete FeO_x removal. Fortunately, the effect of cycling on Fe-removal can easily be tracked with the recorded CV profiles, e.g. the Fe oxidation peak almost disappears within first 10 cycles, indicating that the removal Fe-rich shell is almost complete, and further cycling would only result in thinner Pt-shells (for Pt-rich subsurface initially) or formation of Pt-rich shells (for Pt-Fe alloy subsurfaces initially).

In summary, the CV conditioning or voltammetric dealloying of Pt-Fe(800) particles was shown to leach out the Fe-rich shells formed during the thermal treatments. The Pt-Fe(800)(conditioned) particles formed were shown to bear Pt-rich shells, and were shown to earlier to exhibit exceptional ORR activities and durability. This illustrates the beneficial role played by CV conditioning as a surface-cleaning pretreatment.

6.7 MONITORING STRUCTURAL EVOLUTION DURING E-CYCLING WITH LIQUID CELL TEM

Understanding structural evolution of catalyst particles during potential cycling is crucial to developing better ORR catalysts. However, microscopic investigations of catalyst particles is still mostly an *ex situ* type analyses, meaning that the analyses is limited to understanding the initial and final catalyst structures, but not during during the course of cycling. An example of such an analyses was discussed earlier in Section 6.4. Identical location TEM (IL-TEM) based studies emerged as an improvement in this regard by allowing for the study of structural evolution in the same area, before and after a number of cycles [251–254]. However, a real-time observation of the evolution was still not possible. Therefore, correlation between the structural evolution during working condition in the native environment, and the catalytic performance, is not yet fully understood. For example, general processes such as ripening, dissolution and coalescence have been proposed to explain the degradation of catalyst structure during cycling, however, the detailed mechanistic information of these individual processes is still lacking [85–87].

Recently, the liquid cell electrochemical holders have been developed, which allow for the simulataneous potential cycling of catalysts inside a TEM, the recording of CVs, and the visualization of their structural evolution [361]. As a model to further studies on many other catalyst systems, here we applied this technique to studying structural evolution of as-synthesized Pt-Fe nanoparticles during cycling. Attempts to perform EELS analyses was not successful, due to the plural scattering effects from the thick liquid layers. For this reason, only the findings illustrating structural evolution is being discussed here.

The discussions are organized as follows: first the electrochemical setup in the liquid cell holder is described, followed by demonstration of cycling on pure Pt. At this point, the mathematical modeling of current density distribution is also described. Finally, the structural evolution of Pt-Fe catalysts is discussed.

6.7.1 *Electrochemical setup in the liquid cell holder*

Figure 6.26*(a)* shows a schematic illustration of the electrochemical setup in the liquid cell used. The liquid cell is an assembly of two microfabricated chips (*Protochips Inc.*, Poseidon 510) separated by a 500 *nm* silicon-dioxide spacer. Both chips contained 50 *nm*

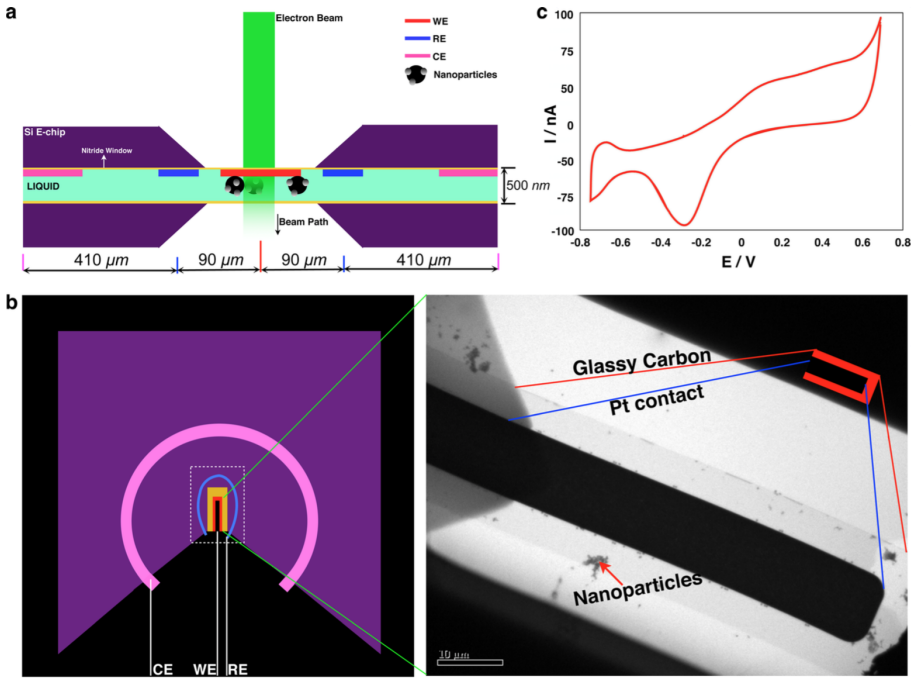

Figure 6.26: Illustration of the *in situ* electrochemical liquid cell TEM holder and working. (a) Representation of the liquid cell. (b) Representation of the upper chip with electrode setup. Inset: TEM image of the carbon working electrode and the Pt nanoparticles. (c) CV recorded using the liquid cell holder with the electron beam turned on.

silicon-nitride (SiN_x) electron transparent window, and the top chip featured miniaturized three electrode electrochemical cell. The liquid cell was positioned into a flow cell holder provided with arrangements for electrolyte flow, and electrical contact with a potentiometer.

The electrochemical setup used for in our experiments included carbon working electrode, and the platinum counter and reference electrodes (Figure 6.26**(b)**). Use of carbon WE was ideal as its weak electron scattering enabled TEM imaging with minimal loss in spatial resolution, and its wider potential window allowed electrochemical measurements to be performed with minimal interference from parasitic reactions.

6.7.2 *Cycling and imaging of pure-Pt particles*

To demonstrate the effectiveness of the experimental setup described above, we performed potential cycling of pure platinum nanoparticles whose voltammetric profiles are well understood. The TEM micrograph in Figure 6.26*(b)* shows the deposited Pt particles located on the carbon working electrode. The CV profiles measured under a 0.1 M H_2SO_4 electrolyte at a scan rate of 100 mV/s is shown in Figure 6.26*(c)*. Importantly, the electron beam was turned on during the recording of the CV profile.

The CV profile obtained from the liquid cell, and under the influence of electron beam, reproduces all the redox signatures that is expected for Pt in acidic solutions. These include: platinum oxidation, platinum oxide reduction, hydrogen adsorption/absorption, and hydrogen desorption. This indicates that the liquid cell setup under beam-ON conditions can be reliably used for electrochemical measurements. However, two major differences can be noted. First, the potential range is shifted as compared to systems with conventional reference electrodes. This is expected from the fact that a platinum pseudo-reference is used in our setup. Second, the CV profile from liquid cell shows a positive slope indicating that there is an ohmic current superimposed on the Faradaic component. This is also expected, as the thin (<1 μm) electrolyte layer can impart large solution resistances (R), resulting in larger IR drop.

6.7.3 *Modeling current density distribution within E-cell*

In order to understand the distribution of current density in the electrode setup, we collaborated with Prof. Soleymani's group (McMaster U) for numerical modeling based on the finite elemental analyses. Recall that the current density is a measure of the rate of electrode reactions (Section 3.4). Thus, we simulated variation in the current density at hypothetical conductive microparticles placed at arbitrary locations on the WE, and at very close proximities, to better mimic the experimental conditions where Pt-Fe particles are deposited on the carbon electrode.

In order to reduce the computational complexity, we first simplified the three electrode setup to a two electrode setup featuring Pt counter electrode and the carbon working electrodes. Secondly, we also replaced the 3D problem by a 2D geometry, ignoring for the sake of simplicity the current density variation in the direction perpendicular to the electrode surface. The software procedures used for simulation is described elsewhere [202], only the findings are summarized as follows.

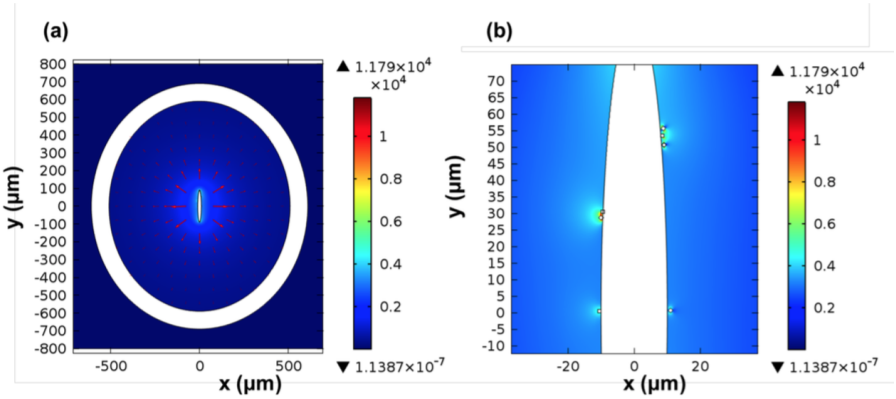

Figure 6.27: Numerical modeling of current density (A/m²) within the electrochemical cell. (a) Plot of current density norm (A/m²) within the acid electrolyte of electrochemical cell; red arrows indicate the current density vector. Inner ellipse represents the working electrode, and outer ring represents the counter electrode. (b) Magnified plot of (a).

Figure 6.27*(a)* demonstrates the magnitude of the calculated current density along with the current direction in the electrochemical cell. An increased current density is observed near the working electrode, which is reduced as we move toward the counter electrode. It should be noted that in the length scale of Figure 6.27*(a)*, we do not observe any spatial current density variation due to the deposited microparticles. However, if we look at

a zoomed-in view of the working electrode (Figure 6.27*(b)*), we observe an increase in current density in the electrode regions with immobilized microparticles. In addition, we see current density hot spots, between particle aggregates. We expect higher electrochemical reaction rates to occur at areas with increased current density. However, due to the highly localized nature of this effect, we do not expect it to influence the electrochemical reaction rates in regions beyond a few micrometers away from the particles.

6.7.4 *Structural evolution of Pt-Fe particles during cycling*

By obtaining a reasonably good picture of liquid cell potential cycling in the TEM, we next moved on to investigating the structural evolution of real Pt-Fe catalyst nanoparticles. Earlier in Section 6.2, these particles were shown to have a compositionally disordered alloy structure. As before, the Pt-Fe particles were supported on vulcan carbon, and then deposited the liquid cell working electrode. In addition, a *Nafion* solution was dispersed to entangle the deposited particles. Additional protocols were adopted based on the conventional cycling of catalysts (Section 3.4), these details can be found elsewhere [202]. A solution of 0.1 M $HClO_4$ was used as the supporting electrolyte in the experiment.

6.7.4.1 *Monitoring structural changes over a set of cycles*

Figure 6.28 shows the morphology of Pt-Fe particles (identified using red arrows) and the corresponding CV profiles for the first 130 potential cycles at a scanning rate of 100 *mV/s*. It should be noted that the presence of the silicon nitride window (100 *nm*), along with the liquid layer (500–1000 *nm*), deteriorates the resolution of the system, which is consistent with previous studies demonstrating a 4 *nm* resolution using a similar *in situ* liquid TEM system.

The CV curves in Figure 6.28*(b)*, recorded at first, 50^{th}, 100^{th} cycles, clearly show dramatic changes in the current voltage characteristics with an increase in cycle number. Because the recorded CV curves represent the behavior of the entire liquid cell beyond the observation area, the differences in curve shape or current magnitude can be attributed to the possible contact changes between the catalysts, electrodes, and electrolyte during the stabilization processes at the beginning of the cycling process. Therefore, it is difficult to identify the current voltage characteristics, which reflect the changes in catalyst

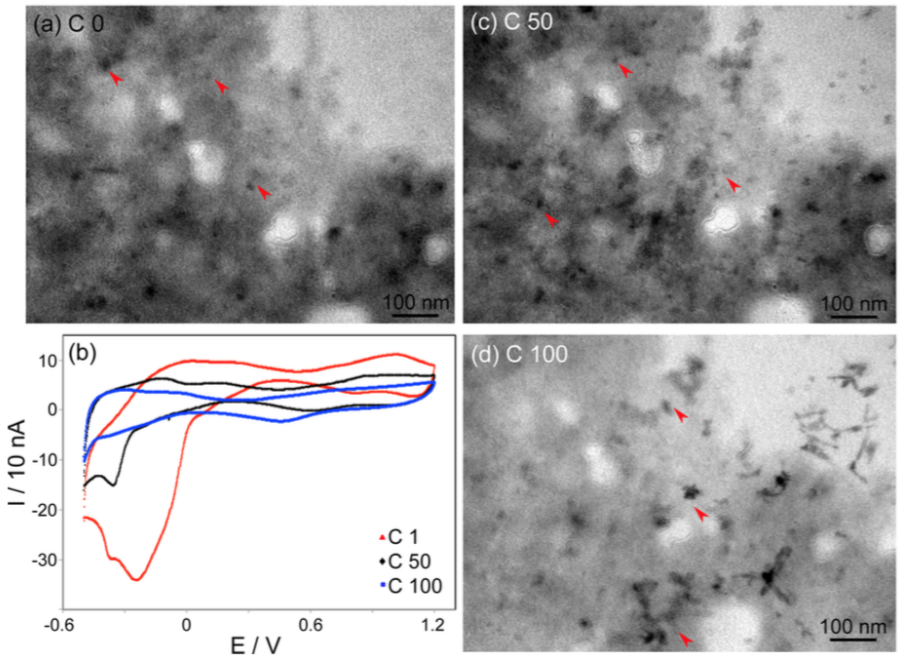

Figure 6.28: Structural evolution of disordered Pt-Fe nanocatalysts during electrochemical cycling under 0.1 M $HClO_4$ electrolyte. Parts (a), (c), and (d) are TEM images, showing the morphology of nanocatalysts (appearing with darker intensities) and their carbon supports in gray, before cycling (a), after 50 cycles (c), and after 100 cycles (d). Some of these nanocatalysts are identified with red arrows. Corresponding CV curves of the 1st, 50th, and 100th cycles are shown in (b).

structures, observed in the corresponding TEM micrographs. These current changes can also be attributed, to a lesser degree, to the electroreduction of residual oxygen present in the solution.

As shown in the TEM micrographs in Figure 6.28*(a, c and d)* during electrochemical cycles shown in Figure 6.28*(b)*, disordered Pt-Fe nanoparticles were dispersed in the supported carbon matrix. As compared to the initial morphology in Figure 6.28*(a)*, these catalyst nanoparticles in Figure 6.28*(c and d)*, particularly those isolated in the electrolyte, have a significant growth tendency during electrochemical cycling. Some large particles seem to be located on the carbon support, which may not necessarily be in contact with the supports, because TEM images are primarily 2D projections of 3D objects. It is important to point out that catalysts do not significantly change after they are exposed under the electron beam without potential cycling for a few minutes.

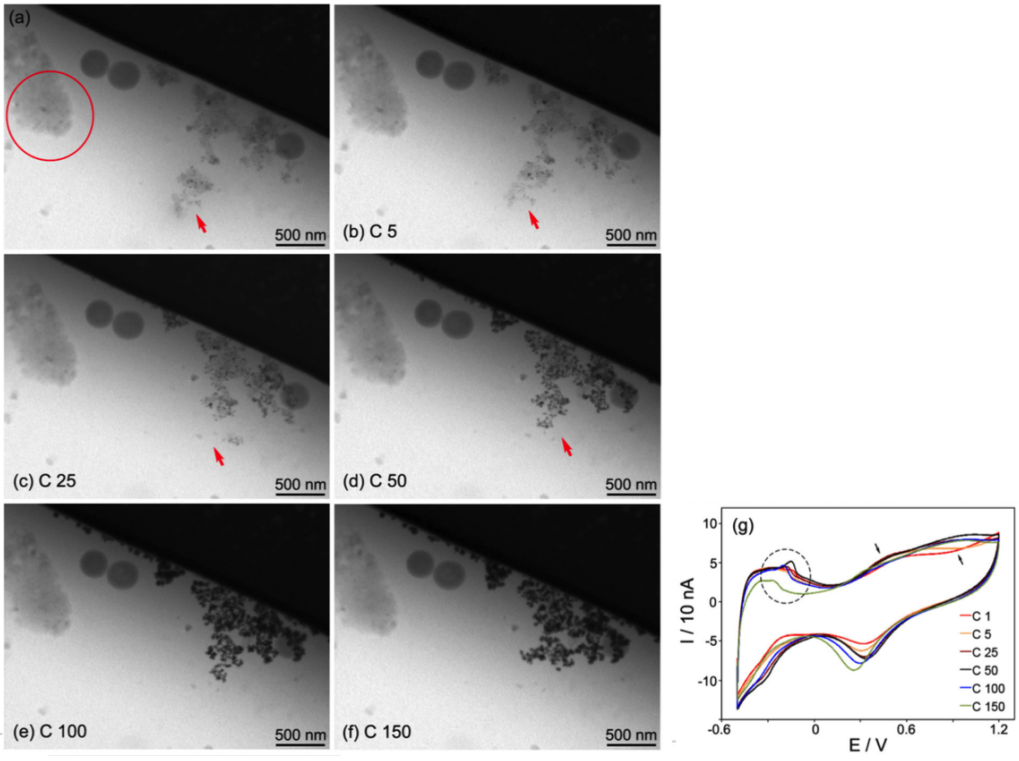

Figure 6.29: Structural evolution of Pt-Fe nanocatalysts at the edge of an observation window. (a)–(f) are the morphology of the same region at additional 0, 5^{th}, 25^{th}, 50^{th}, 100^{th}, and 150^{th} cycles after the first 130 cycles. (g) shows the corresponding CV curves.

In support of the significant growth tendency of particles, TEM images of particles close to the edge of the observation windows was recorded during additional electrochemical cycling afterward, as shown in Figure 6.29*(a—f)*. These nanoparticles which are detached from the working electrode are expected to lose their catalytic activity substantially, showing stronger similarity to those large particles observed at the electrode-membrane interface in PEMFCs. The mass transport mechanism corresponding to the growth of inactive nanocatalysts probably occurs through the dissolution of nanoparticles into the ionomer phase, the movement of soluble metal species under applied electric field, and the attachment of metal species at nucleation sites. Although another mass transport mechanism, the migration of small nanoparticles, cannot be entirely excluded because the spatial resolution of these TEM images is not high enough to resolve nanoparticles with a few nanometer in diameter, it should be noted that nanoparticles have a poor chance to migrate across the Nafion film covering these catalysts.

As shown in Figure 6.29*(a—f)*, the nucleation of nanoparticles can be recognized at different potential cycles, and the growth of nanoparticles does not appear to be in unison. These observations suggest that the reprecipitation processes of Pt in the ionomer phase are not uniform both in time and in space. In addition to that, the corrosion of the carbon support was also detected as indicated by the red arrows in Figure 6.29*(a—d)*. Further, we observe that the carbon corrosion can significantly be accelerated by a relative enhancement in the catalyst loading (carbon with low catalyst loadings is circled in red in Figure 6.29*(a)*. This can be due to these nanoparticles that now act as sites catalyzing the corrosion of carbon substrate underneath.

The corresponding CV curves in Figure 6.29*(g)* for additional 150 potential cycles are relatively stable and show changes in the catalytic structures such as the acid leaching of Fe from Pt-Fe nanocatalysts and the coarsening of nanocatalysts. The sharp feature at -0.2 V, due to the hydrogen desorption at the Pt active sites, increases during 0-50 cycles and then decreases afterward. During the forward sweep, the metal oxidation peak initially occurs at 0.45 V followed by a second peak feature and eventually changes its potential to 0.9 V (see black arrows in Figure 6.29*(g)*). These observations imply an increase in Pt active sites followed by its decrease, possibly due to the formation of Pt-rich surfaces from iron leaching and the domination of nanoparticle coarsening afterward.

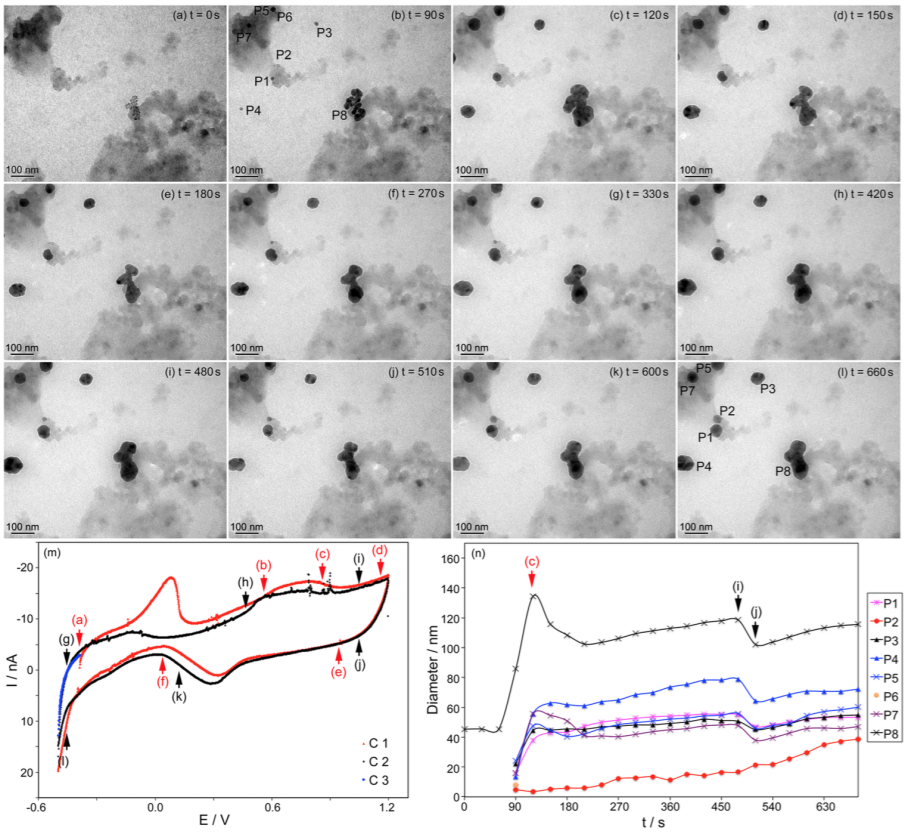

Figure 6.30: Structural evolution of Pt-Fe particles at various stages during one potential cycle. (a)–(l) are the TEM images taken from different stages during electrochemical cycles. The tracked particles labeled by P1–P8 are shown in (b). (m) presents the CV curves corresponding to the different stages for (a)–(l). (n) shows the particle size during cycling. The average diameter was calculated by measuring the area of individual particles under an assumption that these particles have a spherical shape.

6.7.4.2 *Monitoring potential dependent structural changes within a CV cycle*

The growth processes of nanocatalysts can be thoroughly studied during individual cycles and simultaneous TEM observations Figure 6.30 requiring a slow scanning rate (e.g., 10 *mV/s*) to record CV curves. Each micrograph (Figure 6.30*(a—l)*) corresponds to a point and label on the CV curve (Figure 6.30*(m)*). With respect to individual stages during electrochemical cycles, the particle size of tracked particles is calculated and presented in Figure 6.30*(n)*. Nanoparticles do not show detectable changes for the first 60 *s*, equivalent to the forward sweep up to 0.25 V. We find that the abnormal sharp peak appearing in the first CV curve (red) in Figure 6.30*(m)* is not detectable during the second scan (black curve, with forward sweep starting earlier to -0.3 V). We suspect the disappearance of this abnormal peak to be related to the compositional changes of these non-dealloyed nanoparticles *via* elemental leaching in the native electrolyte environment.

Rapid growth of the nanocatalysts occurs at few sites during the forward sweep in the range of 0.55–0.85 V, covering the broad platinum oxidation peak at 0.6–0.8 V. Particles coalesce with the neighboring ones resulting in an irregular structure, which is consistent with our previous report [170]. Subsequently, particles start to dissolve around the highest applied voltage (1.2 V), yet appear to be exhibiting a positive growth trend during the reverse sweep. This general behavior of the particles is repeated during the second scan. As an exception is particle P2, the smallest one in our set of measurements, which continuously grows with different growth rate during cycling within the resolution of our measurements. These observations confirm that the growth rate, either positive or negative, is different for individual particles and varying applied voltages. This effect can be attributed to local changes, for e.g. as predicted by our modeling work, particles positioned at different electrode locations with varying proximity to other particles can experience a different current density (Figure 6.27*(b)*), which would result in growth rates to be site specific. This is observed in the data presented in Figure 6.30*(n)* (for e.g., comparing particle 1 and 8), confirming that the nucleation and growth of nanocatalysts are site-dependent in addition to being potential-dependent.

6.7.5 *Summary on the liquid cell electrochemical study of Pt-Fe particles*

In summary, we applied an *in situ* liquid cell technique in TEM to study the structural evolution and electrochemical responses of Pt–Fe nanocatalysts, simultaneously and in their native electrolyte environment. The coarsening processes of disordered nanocata-

lysts, including the nucleation and the growth, are not uniform, both in space and in time scale. The growth rate is site-dependent, and potential-dependent nanocatalysts were found to exhibit considerably different behaviours when attached to the electrode as opposed to when isolated in the electrolyte consistent with modeling of local current perturbations in proximity of particles. With Pt–Fe nanoalloy system as a candidate material, our current work demonstrates that the characterization of the structural evolution of nanocatalysts *in situ* provides much deeper insights into the catalyst degradation mechanisms as compared to the routine *ex situ* electrochemical studies.

6.8 PERSPECTIVE

In summary, we have characterized Pt–Fe alloy nanoparticles using suitable imaging ad spectroscopic methods based on scanning transmission electron microscopy. The Pt–Fe nanoparticles have gathered a lot of interest, both on the account of enhanced ORR electrocatalysis, and also because of the magnetic properties that are deployable in ultrahigh-density information storage. Using both *ex situ* and *ex situ* approaches, we have obtained insights into a variety of aspects of these materials, such as the surface and bulk atomic-structure, faceting, lattice strain, the surface and bulk composition, and a time-evolution of these structural features before, after and during the durability tests and also the heat-treatment procedures. A detailed summary of insights obtained in each of these investigations is provided in Section 6.4.4, Section 6.5.6, and Section 6.7.5. These provide useful research directions and generate new perspectives for the future development of highly active and less expensive Pt–Fe catalysts, which are crucial for the widespread commercialization of PEMFCs. As discussed earlier in Chapter 4, a detailed review of the different Pt-alloy catalysts indicates that the Pt–Fe is not a particularly superior catalyst system compared to Pt-Co and Pt-Ni nanoalloys. One major issue is the poor electrochemical stability of Pt-Fe alloys due to dissolution of Fe, which is relatively less serious in the case of Pt-Co and Pt-Ni nanoalloys. In such a juncture, we believe that the present work on Pt-Fe nanocatalysts can be regarded as a model study for further investigation of various other Pt-alloy systems using the aberration-corrected TEM techniques.

7

PLATINUM–GOLD HETEROAGGREGATE NANOPARTICLES

Previously in Chapter 6 we discussed the characterization work carried out on the platinum-iron (Pt–Fe) alloy nanoparticles. The present chapter discusses our investigations related to the platinum-gold (Pt–Au) alloy nanoparticle system, studied exclusively with the aberration-corrected STEM in combination with the *in situ* heating stage. Most sections (either in parts or full) have been adapted from the following manuscript that has been communicated to peer-review: [392].

7.1 MOTIVATION AND RESEARCH OUTLINE

Bimetallic Au-Pt alloy nanoparticles are a promising class of materials for ORR electrocatalysis [393–399]. Several examples substantiating this were discussed in the literature review presented earlier in Chapter 4. Additionally, the Au-Pt nanoparticles are also being considered for the catalysis of many other reactions, such as H_2 activation [400], CO oxidation [401–403] and Methanol oxidation [393]. One major advantage here is that the combination of two noble metals allows the nanoparticle alloys to remain stable in many gaseous, liquid and electrochemical environments.

Despite great progress in the development of Au-Pt nanoparticle alloys, a vast majority of the alloys that are reported are limited to heteroaggregates [404–408], core-shells [409, 410] and phase-separated alloy mixtures [393, 411] (See Figure 7.1 for a schematic illustrations of these different alloy types). The formation of solid solution (i.e., random disordered / ordered arrangement of Au and Pt atoms, as in Figure 7.1*(d)*) is considered extremely difficult, owing to reasons discussed as follows.

For a wet-chemical synthesis approach involving the reduction of Au and Pt salts, the difference in the reduction potentials of Au and Pt ions make it challenging to kinetically trap them into a homogeneous alloy structure [412]. For example, Ataee-Esfahani *et al* chemically reduced chloroplatinic acid (H_2PtCl_6) and chloroauric acid ($HAuCl_4$) species in the presence of a surfactant, and found that the particles formed a Au@Pt core-shell

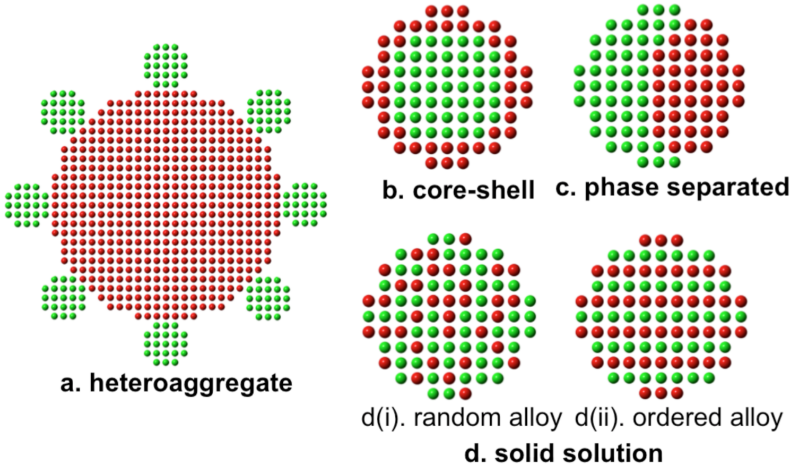

Figure 7.1: Schematic representation of different bimetallic alloy types.

type alloy structure [396]. The authors attribute this to a faster reduction of Au ions compared to Pt ions, which they believe led to the formation of Au seeds, onto which the Pt seeds then deposit.

In the case of solid-state approach of alloying that involves a post-annealing treatment following the synthesis of Au-Pt mixture, the challenge is that the formation of a solid solution is thermodynamically not favoured [413]. Most reports interpret this from the presence of a wide miscibility gap in the Au-Pt phase diagram, over almost in the entire range of composition and temperature. For example, a 50/50 homogenous AuPt alloy is said to be stable only above 1200 °C [414]. This is further supported by many atomistic simulations. For instance, Mariscal *et al* have performed atom dynamics simulations using the embedded atom (EAM) potentials [415]. They found that the formation of core-shell type structure is energetically more favourable than the mixing in the form of an alloy solid solution.

Recent studies have shown that it is much easier to form a solid solution on the nanoscale compared to the bulk, when the structures are synthesized in the form of nanoparticles [393, 416]. For example, Petkov *et al* studied the phase transformations of a range of Pt_xAu_{1-x} nanoparticle compositions (x = 0.77, 0.51, 0.4, 0.2), and found that all the alloys existed in a random alloy solid-solution even when annealed to as high of the temperature as 800 °C [416]. One possible reason for such differences between the bulk and nanoscale phase transformations could be that the solubilities of Au and Pt into the matrix of the other metal are different. For example, Braidy *et al* have shown that the

solubility of Au in the Pt-rich phases for nanoparticles can be higher than the bulk by about 5-10 at.% [417]. Additionally, other effects from size, surface energy and segregation tendencies can also play an important role [417, 418]. The development of such solid solution alloy nanoparticles affords a superior catalytic performance compared to phase separated mixtures, and even some state-of-the-art catalysts (e.g., Pt/C in fuel cells).

It is important to point out, however, that besides above reports that suggest favourability to the formation of solid solution on the nanoscale, many contrasting reports that support phase-separation are also available [418, 419]. For example, Xiao *et al* calculated the heats of formation of Au-Pt nanoparticles for a range of particle sizes and compositions [418]. They suggest that although at very small particle sizes a solid-solution alloy mixture can be favourable (i.e., negative heat of formation), an increase in temperature can induce surface-segregation of Au, from which a solid solution can decompose into a core-shell structure. Such contrasting views illustrate the point that it is still unclear as to which type of alloy, the phase-separated or the solid solution, that is the most favoured during the phase transformation of Au-Pt nanoparticles.

One major limitation to address above critical question is the approach adopted towards the structural characterization of Au-Pt particles. Most reports still rely on *ex situ* type analyses, wherein the structural and compositional evolution of particles is studied before and after the heat-treatments, and never during the course of annealing process (as in the case of *in situ* type analyses). This precludes us from gaining insights into the many dynamic changes related to compositional segregation and ordering processes taking place during annealing.

In the present work, we monitor the Au-Pt phase transformation process using a *in situ* thermal annealing method. For this we consider the as-synthesized Pt-on-Au heteroaggregate particles as a test system, and anneal them inside a transmission electron microscope. Using high angle dark field imaging (HAADF) and electron energy loss spectroscopy (EELS) techniques we monitor both the structural and the compositional changes in these nanoparticles, over the entire course of heat-treatments. In order to understand the effect of chemical composition on the resulting final structures formed, we study the heat-treatment process on two distinct compositions of Pt-on-Au heteroaggregate particles, identified as low-Pt and high-Pt heteroaggregates. Our results indicate that depending on the initial composition of the particles, the formation of both the solid solutions and the phase-separated alloys are possible. We found that the low-Pt heteroaggregates transformed into a phase-separated alloy mixture (discussed in Section 7.6), whereas the high-Pt heteroaggregates formed a solid solution (discussed in

Section 7.5). A detailed analysis of the solid solution further indicates a uniform chemical composition and an ordered atomic-structure, virtually in the entire particle.

In addition to above experiments, we also investigated the melting of Pt clusters deposited on the Au surface during the initial stages of heat-treatment (discussed in Section 7.8). These insights were important in the context of understanding the dynamic homogenization process which eventually lead to the formation of Au-Pt solid solution.

In addition to annealing the heteroaggregates under the microscope vacuum, we also conducted heat-treatments in other atmospheres (e.g., air and N_2). We found that despite annealing the heteroaggregates to about 18 hours at 400 °C in 1 atm. N_2, the particles did not transform into a solid solution, but instead existed as phase-separated alloy mixtures forming two lobes, Pt-rich and Au-rich, separated by one common interface. A series of Molecular Dynamics (MD) and Monte Carlo simulations carried out by our collaborators is also summarized, which illustrate why a flat AuPt phase-seperated interface would be energetically more favored compared to a core-shell type structure (e.g., Pt-rich shell covering the Au-rich lobe). These findings are discussed in Section 7.9.

Below, we first start by introducing the method of synthesis of the initial Pt-on-Au heteroaggregate nanoparticles and then discuss aspects related to their structural characterization (Section 7.4). Subsequently, we describe the heat-treatment procedure in Section 7.4, and then present the experimental findings pertaining to the above listed experiments.

7.2 SYNTHESIS OF PT-ON-AU HETEROAGGREGATE NANOPARTICLES

The synthesis of Pt-on-Au nanoparticles involved a two-step wet-chemical reduction procedure wherein the Au NPs were synthesized first, and then used as seeds for a heterogeneous nucleation of Pt. The procedure is schematically illustrated in Figure 7.2.

Au-NPs were synthesized using the well known 'citrate reduction' technique developed by Frens [420]. For this procedure, 300 *mL* of 10^{-2} wt. % chloroauric acid ($HAuCl_4$) was brought to boiling, into which about 9 *mL* of trisodium citrate (1 *wt.* %) (boiled prior to 100 °C) was added to initiate reduction towards forming Au-NPs. The dark purple solution formed was kept under continued heating for a reaction time of 40 *mins* when it turned into a wine red color indicating the formation of colloidal solution containing Au-NPs.

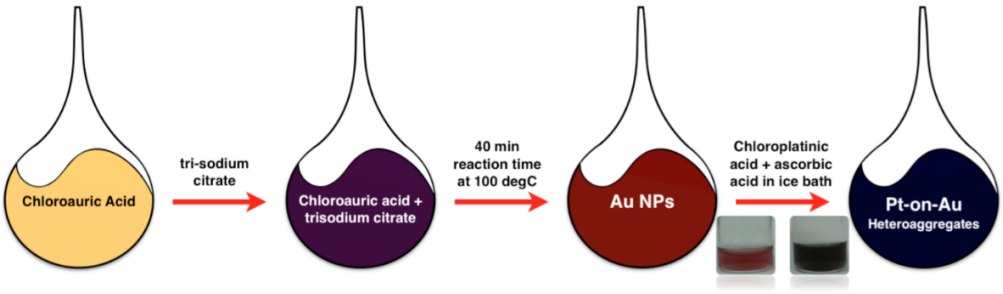

Figure 7.2: Schematic representation of the procedure for synthesizing Au NPs and Pt@Au heteroaggregate nanoparticles.

To coat the Au-NPs with Pt clusters, the procedure developed by Lu *et al* [421] was adopted. About 9.6 *mL* of the colloidal Au-NP solution (cooled to RT) was mixed with 10 *mL* of chloroplatinic acid, H_2PtCl_6 (5 x 10^{-4} *wt.%*) and 6 *mL* of ascorbic acid (1.76 *wt.%*) in an ice bath. The resulting solution was removed from the ice bath after a reaction time of 1.5 *h* when it turned into dark purple color. For the TEM/STEM analyses, the samples were drop cast onto the copper grid coated with lacey carbon.

The above procedure corresponds to the synthesis of low-Pt heteroaggregates. The same procedure was also used in synthesizing the high-Pt heteroaggregates, the difference being the feed ratio of Pt,[1] which was relatively much higher.[2] The acid and reducing agent concentrations noted here are based on a series of preliminary experiments that we conducted in order to understand the effects of changing reducing agent concentrations, the chloroplatinic acid concentration, and the reaction times. These investigative experiments are discussed as follows.

7.2.1 *Effect of changing the reducing agent concentration*

Figure 7.3 illustrates the effect of changing the reducing agent concentration on the sizes of the Au NPs formed. Here, the concentration of Au precursor i.e., chloroauric acid, is kept constant. Three variations in the reducing concentration were considered: 3 *mL*, 9 *mL* and 15 *mL*. The corresponding low-magnification TEM images of the synthesized Au particles are shown in Figure 7.3*(1—3)*, respectively. The measured size distribution is

[1] Calculated as, $[H_2PtCl_6]$ / $[H_2PtCl_6]$ + $[HAuCl_4]$
[2] by about 3 times compared to low-Pt heteroaggregates

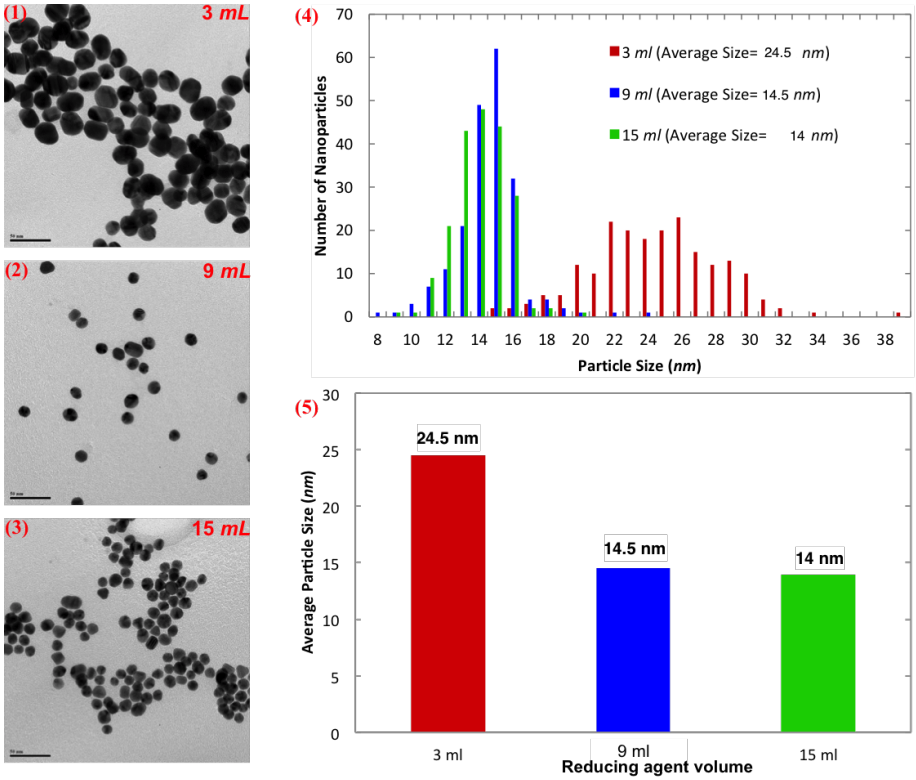

Figure 7.3: Effect of varying the reducing agent concentration on the synthesis of Au NPs. (1)-(3): TEM images. (4) Particle size distribution. (5) Bar chart of Particle size versus reducing agent volume.

displayed in Figure 7.3*(4)*, and the estimated average particle sizes for these three cases is shown in Figure 7.3*(5)*.

As shown in Figure 7.3*(5)*, an increase in the reducing concentration from 3 *mL* to 9 *mL* resulted in the particle size decrease of about 10 *nm*. This is attributed to the resulting decrease in the critical size of the Au nuclei due to the increase in the number of nucleation centers in the solution. However, a further increase in the reducing agent concentration to 15 *mL* did not result in significant change to particle sizes. This is expected, because the concentration of Au species in the solution is fixed, and once consumed in forming Au NPs, a further addition of the reducing agent will not create any more nucleation centers, thus has no effect on the resulting particle size.

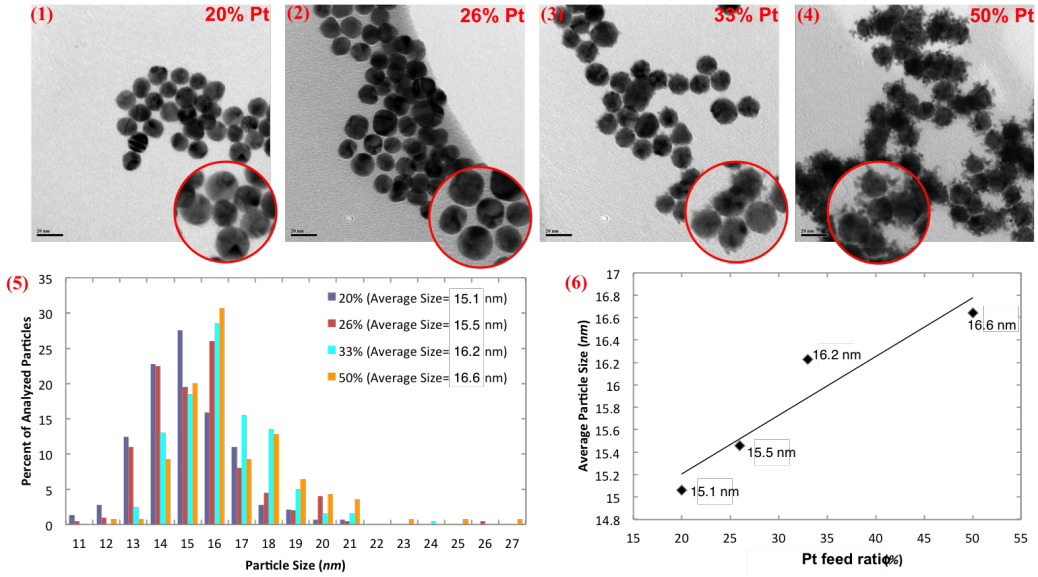

Figure 7.4: Effect of varying the chloroplatinic acid concentration on the synthesis of Pt-on-Au heteroaggregates. (1)-(4): TEM images. (5) Particle size distribution. (6) Particle size versus the Pt feed ratio.

7.2.2 *Effect of changing the chloroplatinic acid concentration*

Figure 7.4 illustrates the effect of incrementally increasing the Pt feed ratios in the order 20 %, 26 %, 33 % and 50 %, on the coverage of Au NP surfaces with the deposited Pt clusters. This can be monitored by observing changes in the heteroaggregate particle sizes calculated relative to pure Au NP.[3]

From the TEM images shown in Figure 7.4*(1—4)*, it is clear that there is no apparent Pt deposition for the Pt feed ratios 20 % and 26 %. With a further increase in the Pt feed ratio, small number of clusters can be seen for 33 % Pt, that multiply significantly with the increase in feed ratio to 50 %. This suggests that there is a critical feed ratio for the formation of Pt clusters on Au. Since the Pt composition on the Pt-on-Au heteroaggregates is proportional to the coverage of Pt clusters during synthesis, the Pt composition in heteroaggregates with 33 % Pt feed ratio is lower than those formed with 50 % Pt feed ratio (Panel (3) *vs* (4)). These structures are identified as low- and high-Pt heteroaggregates, respectively, and were used in the subsequent heat-treatment experiments (discussed under Section 7.5 and Section 7.6, respectively).

[3]The estimated average particle size of pure Au NPs is about ~15 *nm*.

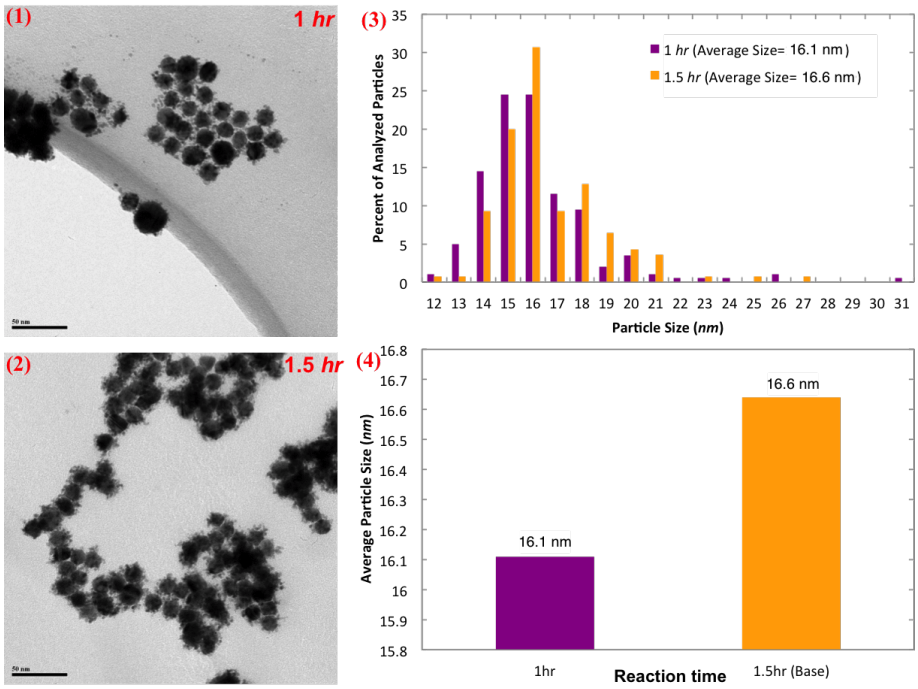

Figure 7.5: Effect of varying the reaction time on the synthesis of Pt-on-Au heteroaggregates. (1) and (2): TEM images. (3) particle size distribution. (4) Bar chart of particle size versus the reaction time.

7.2.3 *Effect of changing the reaction time*

The reaction time (τ) refers to the time required for the deposition of Pt clusters on Au, which includes the time required for reduction, nucleation and the growth processes. Figure 7.5*(1, 2)* show low-magnification TEM images of the particles synthesized with reaction times of 1 *h* and 1.5 *h*, respectively. A close inspection of the heteroaggregate surfaces in these images reveals that a relatively higher surface coverage with Pt clusters is observed for longer reaction time (1.5 *h*). The average particle sizes were estimated using the measured size distributions, and an increase in the particle sizes was observed corresponding to the higher surface coverage in Pt (see Figure 7.5*(3, 4)*).

7.3 CHARACTERIZATION OF AS-SYNTHESIZED PT-ON-AU HETEROAGGREGATES

Figure 7.6a *(i, ii)* show bright-field TEM micrographs of the as-synthesized Au nanoparticles and Pt-on-Au heteroaggregates, respectively. The measured size-distributions of the two samples are shown in Figure 7.6b, and the estimated average particle size for Au NPs is about 14 *nm*, and that for the Pt-on-Au heteroaggregates is about 16.6 *nm*.

7.3.1 *Structural characterization*

Detailed structural characterization of the Au NPs and the Pt-on-Au heteroaggregates was performed using HAADF-STEM imaging, shown in Figure 7.6a*(iv, v)*, respectively. The solid line drawn in Figure 7.6a*(v)* highlights the heteroaggregate structure by revealing the base Au nanoparticle, and the as-deposited Pt clusters. The estimated average size of the as-deposited Pt clusters is about 3.3 *nm*. For better visualization of the structural morphology, we adjusted the dynamic range in intensity of these images with suitable image filtering techniques[4]. From the filtered images shown in Figure 7.6a*(iv, vi)*, the as-synthesized Au nanoparticles appear to be faceted. As shown in Figure 7.6a*(iv)*, the measured lattice parameter (~0.3 *nm*) is consistent with that of bulk-Au along [111] zone-axis.

Figure 7.7 compares the FFTs obtained from the nanoparticle and the cluster regions. As can be noticed, they resemble one another, which suggests an orientation relationship between the two regions. This is consistent with a previous study by Mourdikoudis *et al* [405], which reported an epitaxial growth mode for the clusters deposited on the seed particles.

[4]Two kinds of image filtering techniques are utilized in this work, namely band-pass and Sobel filters. These were both performed using ImageJ software package. Band pass filtering operates in the Fourier space where a mask with a set range of frequencies is applied on the FFT of an image. Frequencies within this range are allowed while the rest are attenuated. The filtered image is obtained by taking inverse FFT after masking. Sobel filters are popular for finding edges within an image. As illustrated in Figure 7.6a*(vi)*, we have made use of this in finding the facet boundaries in a 2D HAADF-STEM image. The Sobel operator performs a 2D spatial gradient measurement of the image, emphasizing regions with high spatial frequencies that correspond to edges. More details on these filtering techniques can be found elsewhere [422].

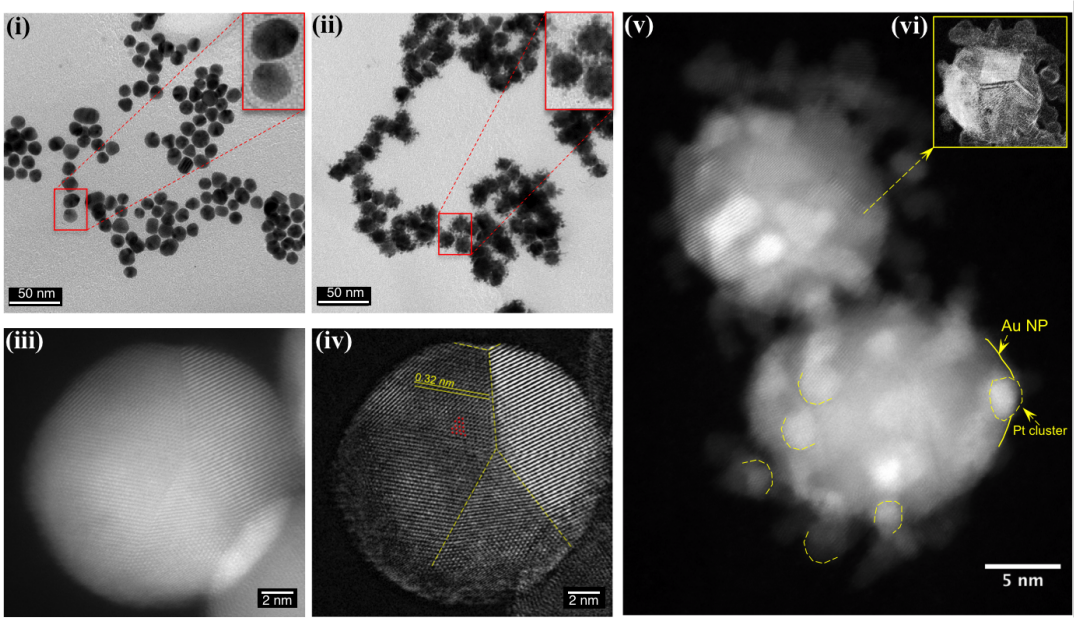

(a) (i, iii) and (ii, iv), TEM and HAADF-STEM images of as-synthesized Au nanoparticles and Pt-on-Au heteroaggregates, respectively. (iv) band-pass filtered image of (iii). (vi) Sobel filtered image of particle (top most) in (v).

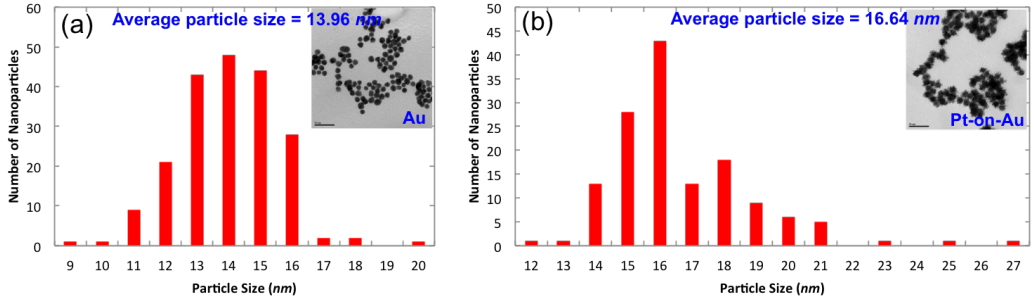

(b) Size distribution measurement of as-synthesized Au nanoparticles (left) and Pt-on-Au heteroaggregates (right).

Figure 7.6: Structural characterization of as-synthesized Au and Pt-on-Au heteroaggregates.

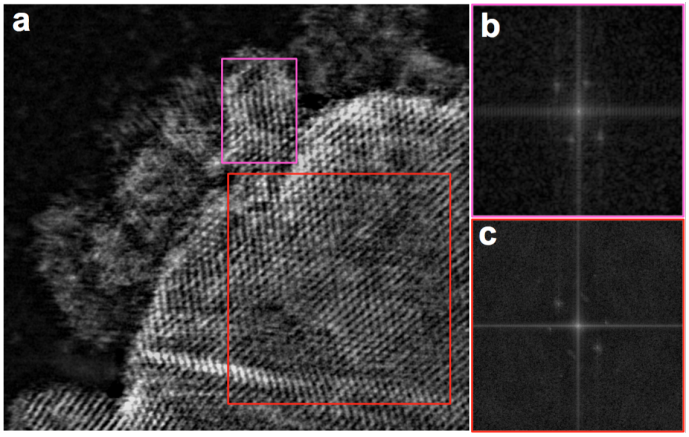

Figure 7.7: Epitaxial growth of Pt clusters on Au. (a) Band-pass filtered HAADF-STEM image of selected region over a Pt-on-Au heteroaggregate. (b) and (c), Fast Fourier Transformation of the regions identified by pink and red boxes in (a), respectively.

7.3.2 *Challenges posed to EELS compositional analyses*

In addition to structural characterization, a detailed compositional analysis was carried out using electron energy loss spectroscopy (EELS). Since the M-4,5 edges of Pt (onset at 2120 eV) and Au (onset at 2206 eV) overlap, this can be very challenging. Figure 7.8 illustrates the challenge involved in separating Pt and Au signals. A small window of about 86 eV is available between the onsets of these edges, which can be used to extract Pt only. Beyond 2206 eV, the Pt and Au signals are mixed. The situation is even more difficult in the case of nanostructures, considering that we require a low electron-dose rate ($D = It/A$; Probe current I, dwell time t, Area A) in order to minimize the beam damage. Typically, the use of low D results in low signal-to-noise ratios, which is not an ideal setting for elemental analyses.

7.3.3 *Use of MLLS fitting and independent component analysis methods*

We overcome the above mentioned challenge by adopting a multiple linear least square (MLLS) fitting procedure to separate the Pt and Au signals. MLLS serves as a great

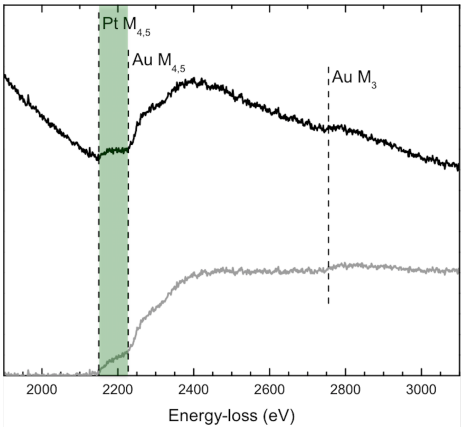

Figure 7.8: Challenge to EELS mapping of Pt and Au in a Pt-Au nanoparticle. Black curve: Typical raw EELS spectrum of Pt-on-Au heteroaggregate. Gray curve: EELS spectrum after background subtraction. Vertical dotted lines: Onsets of Pt-M4,5 and Au M4,5 edges. Green window: Available 86 eV window available for extraction of Pt only. Beyond this, Pt signal is convolved with Au.

tool for separating the overlapping EELS edges of many alloy combinations [212]. The method involves fitting of the total spectral intensity (*F(E)*) to an expression of the form:

$$\boxed{F(E) = AE^{-r} + B_a R_a(E) + B_b R_b(E) + \dots} \tag{7.1}$$

Where, AE^{-r} corresponds to the power-law background preceding the edge of lowest energy loss $R_a(E), R_b(E), \dots$ represent core-loss reference spectra of the elements of interest $B_a, B_b, \dots$ are fit coefficients found by minimizing the differences between the experimental spectra and the model F(E) estimated using Equation 7.1.

In the present work, we input the reference spectra of Au and Pt, $(R_{Au}(E), R_{Pt}(E))$. Thus,

$$\boxed{F(E) = AE^{-r} + B_{Au} R_{Au}(E) + B_{Pt} R_{Pt}(E)} \tag{7.2}$$

We used the MLLS routine that is available in the Gatan Digital Micrograph (DM) software. The Au and Pt reference spectra were collected from pure nanoparticle samples. Once an optimal fitting was achieved, the software returned the fit coefficients (B_{Au}, B_{Pt}). These fitting coefficients were multiplied to their respective reference spectra to obtain the deconvoluted Au $(B_{Au} \times R_{Au}(E))$ and Pt spectra $(B_{Pt} \times R_{Pt}(E))$. The Au and Pt spec-

tra thus obtained, were then used to generate maps (termed MLLS-fitted maps), which illustrate the spatial distribution of the constituent elements.

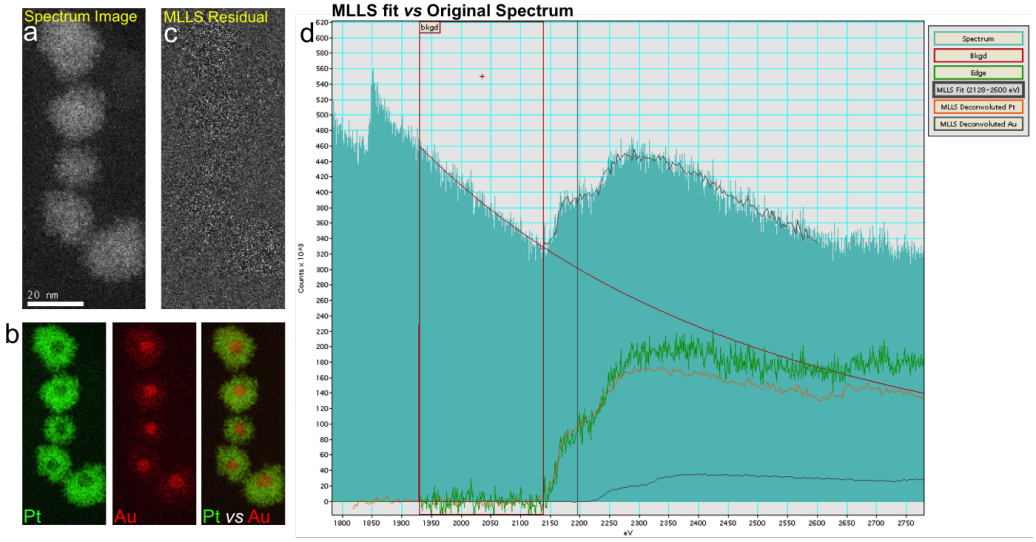

Figure 7.9: Illustrating the good agreement between the MLLS fitting and the raw EELS spectrum that was possible to achieve. (a) Spectrum image of Pt-on-Au heteroaggregates. (b) MLLS fitted compositional maps of Pt (green), Au (red) and Pt *vs* Au composite. (c) MLLS residual image. (d) MLLS fitted spectrum overlayed onto the original spectrum: Background subtracted original spectrum (green) in the range 2100 eV to 2700 eV, MLLS deconvoluted Pt signal (Orange), MLLS deconvoluted Au signal (Gray), MLLS fitted spectrum (Black).

A strong agreement between the original and the fitted spectrum was attainable in our studies. For example, Figure 7.9 illustrates the typical MLLS fitting of an experimental EELS data of a Pt-on-Au heteroaggregate sample. The MLLS generated maps for Pt (green), Au (red) and composite Pt *vs* Au are shown in Figure 7.9*(b)*. Figure 7.9*(c)* shows a 'residual image', calculated as the difference between original and the fitted spectrum at each pixel on the spectrum image. The goodness of the fit is evidenced by the fact that the residual image does not show features resembling the structures seen in the spectrum image (Figure 7.9*(a)*). The goodness of the fit is even more clearer from the good overlay of the MLLS fitted spectrum on the original spectrum (Figure 7.9*(d)*).

Note that the deconvoluted spectra will only be as accurate as the MLLS fit is, and the MLLS fit is only as accurate as the reference spectra. The standard reference spectra, e.g. the EELS Atlas available in the Gatan Digital Micrograph, were not used for our analyses. This is because these reference spectra are obtained for the bulk materials, and

when overlaid on the nanoparticle spectra, a large deviation in the slopes (proportional to specimen thickness) and the fine structures were found. For this reason, we instead used the EELS spectra obtained from pure Au and Pt nanoparticles as the references. Additionally, we also employed independent component analysis (ICA) to validate the maps generated from MLLS. ICA is based on the blind source algorithm within machine learning[5], and is previously shown to be an effective tool for separating mixed micro-analytical signals from nanoheterostructures.

7.3.4 *Compositional analyses*

Figure 7.10*(a, b)* provides a comparison of the MLLS and ICA results of an EELS map obtained from a region enclosing a linear particle ensemble. The region over which the mapping was carried out is shown by the HAADF-STEM image in Figure 7.10*(a(i))*, wherein small clusters can be seen deposited over larger particles. The spatial distributions of Pt and Au are shown in Figure 7.10*(a(iii, iv))*.

In comparison to Figure 7.10*(a(i))*, these maps reveal that the base particles are Au, whereas the small clusters lying on top of Au are Pt, also evident in the Pt-Au composite map in Figure 7.10*(a(v))*. The MLLS results are in good agreement with the ICA results shown in Figure 7.10*(b)*. The dataset is well described just by three independent components, labelled IC#1–3 in Figure 7.10*(b(i))*. IC#1 and #2 bear a strong resemblance to reference EELS edges for Au-M4,5 and Pt-M4,5 respectively, and IC#3 is interpreted as a background signal. Their corresponding spatial maps, shown in Figure 7.10*(b(iii–v))*, indicate that small Pt clusters decorate the surface of the Au nanoparticles, which is in agreement with the MLLS results.

As discussed earlier (Section 7.2), the heteroaggregates of different compositions could be synthesized, by controlling the Au/Pt salt concentrations and reaction times. Figure 7.11 displays the compositional analysis of a Pt-on-Au heterostructure from a different synthesis in which the chloroplatinic acid concentration was increased (by a factor of 3), resulting in a higher concentration of Pt clusters surrounding the base Au nanoparticles. This can be observed in the HAADF-STEM image shown in Figure 7.11*(a)*, and in

[5]ICA involves projecting the spectrum image data, comprised of mixed energy loss signals, onto a set of independent (maximally non-Gaussian) axes [423]. In some cases, the independent components can represent the separate phases present in a heterogeneous material [424, 425]. We performed ICA using the FASTICA algorithm [423], implemented in the Scikit-learn machine learning module for Python [426], conveniently accessed and applied to EELS signals using HyperSpy [427].

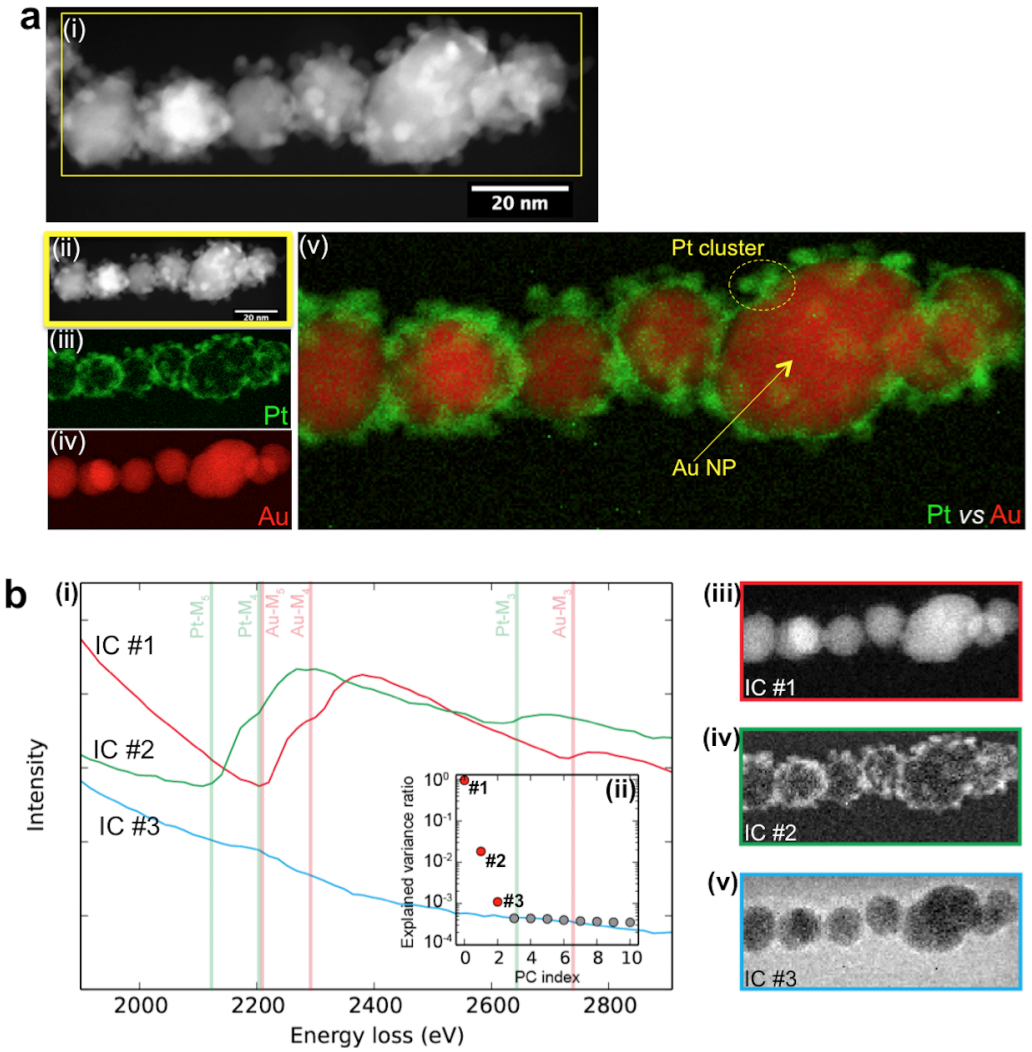

Figure 7.10: EELS compositional analyses of the as-synthesized Pt-on-Au heteroaggregates using: (a) MLLS fitting and (b) Independent Component Analysis. a(i), HAADF-STEM image. a(ii), Region over which the EELS mapping was carried out. a(iii) and a(iv), MLLS fitted EELS maps of Pt (green) and Au (red), respectively. a(v), Composite map of Pt-*vs*-Au. b(ii), Scree plot of the first 10 principal components. b(i) Independent component (IC) spectra of components #1, #2 and #3. b(iii-v), corresponding spatial maps generated. Vertical lines in b(i) indicate onsets for Pt and Au M-4,5 reference edges.

the Pt and Au EELS maps Figure 7.11*(b, c)*, which reveal the aggregation of Pt clusters around base Au nanoparticles, resembling a shell.

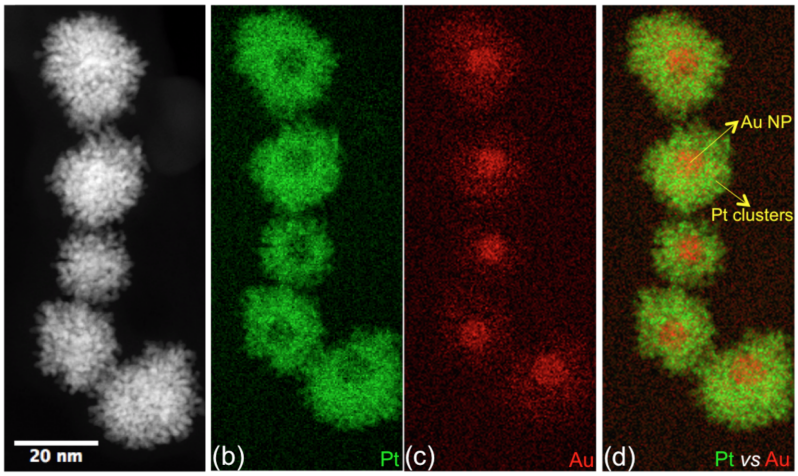

Figure 7.11: High Pt loaded Pt-on-Au heteroaggregates. (a) HAADF-STEM image. (b) and (c) EELS maps of Pt (green) and Au (red), respectively. (e) Composite Pt-versus-Au map.

7.3.5 *Quantification of low- and high-Pt heteroaggregate compositions*

A quantification of the extracted EELS edges (summarized in Table 7.1) for particles in Figure 7.11 yielded a Pt content of 87 %, which is higher compared to the heteroaggregates discussed in Figure 7.10 (23 % Pt). The procedure involved quantification of the weights of MLLS fit coefficients, the detailed procedure is described in Appendix B. Here onwards, we simply call the heteroaggregate-batch in Figure 7.11 as high-Pt heteroaggregates, and those in Figure 7.10 as low-Pt heteroaggregates. In the subsequent sections, we show that the heat-treatment of high-Pt and low-Pt heteroaggregates result in two distinct alloy structures. The high-Pt heteroaggregates transformed into compositionally homogeneous alloy solid-solution (Section 7.5), and the low-Pt heteroaggregates formed phase-separated alloy nanoparticles (Section 7.6).

SAMPLE	At.% Pt	At.% Fe
high-Pt heteroaggregates[1]	87 %	13 %
low-Pt heteroaggregates[1]	23 %	77 %

[1] In both the cases, the estimated error is about 10 %, which is calculated from the uncertainties in the values of Au and Pt cross-sections used in the quantification.

Table 7.1: Quantification of Pt and Au content in the low- and high-Pt heteroaggregate particles.

7.4 HEAT-TREATMENT PROCEDURE

Heat-treatment of both low-Pt and high-Pt heteroaggregates was carried out inside the microscope using a dedicated heating holder manufactured by Protochips[6]. As schematically illustrated in Figure 7.12, the heat-treatment procedure involved holding the sample, initially at RT, for 25 *min* at 200 °C, 400 °C, 600 °C and 800 °C. In total after about ~1.5 hours of heat-treatment, the particles were finally quenched back to RT.

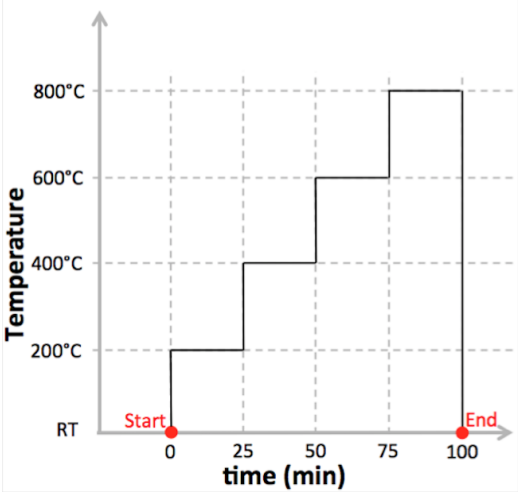

Figure 7.12: Temperature *vs* time plot illustrating the heat treatment process.

[6]Design involves a ceramic (SiN_x) thermal e-chip patterned with an array of micron sized holes. These holes are coated with a carbon membrane onto which the nanoparticles were deposited. The temperature of e-chip could be controlled with a separate heating system connected externally. The entire assembly provided a precise temperature control over 1200 °C with super fast heating rates up to 1000 °C per millisecond. More details on the holder and its operation can be found elsewhere [390].

7.5 HEAT-TREATMENT OF HIGH-PT LOADED HETEROAGGREGATES

Figure 7.13 summarizes the structural and compositional evolution of a selected area of high-Pt heteroaggregates during annealing. These aspects are discussed in two separate sections as follows.

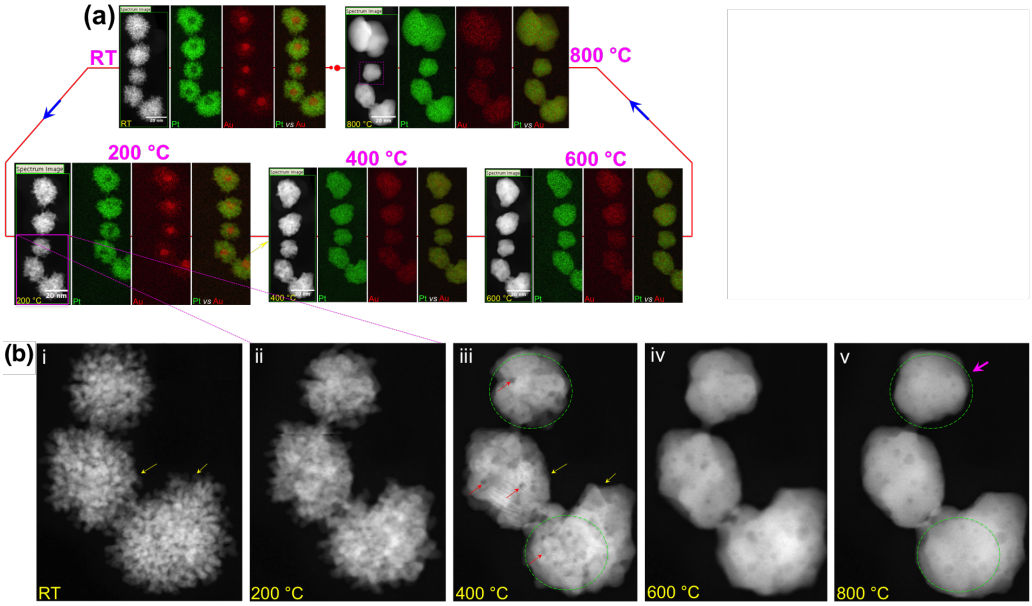

Figure 7.13: Structural evolution of high-Pt loaded Pt-on-Au heteroaggregates during *in situ* TEM annealing. a, Selected area is being tracked over the course of annealing using HAADF-STEM imaging and EELS. Labels indicate holding temperature. b(i–v), magnified HAADF-STEM images.

7.5.1 *Tracking structural changes during annealing*

For better visibility, the HAADF-STEM images are enlarged as shown in Figure 7.13*(b)*. Compared to the initial condition at RT (Figure 7.13*b(i)*), the particle surfaces at the end of heat treatment appear relatively smoother. Figure 7.13 *(b(ii–iv))* illustrate that the surfaces of particles smoothen gradually during annealing, with visible changes taking place within the first 25 minutes of annealing (Figure 7.13*b(ii) vs b(i)*). Furthermore, in the HAADF-STEM image at 400 °C shown in Figure 7.13*(b(iii))*, dark spots within the structures emerge, as identified by the red arrows. Recall that the HAADF-STEM imaging

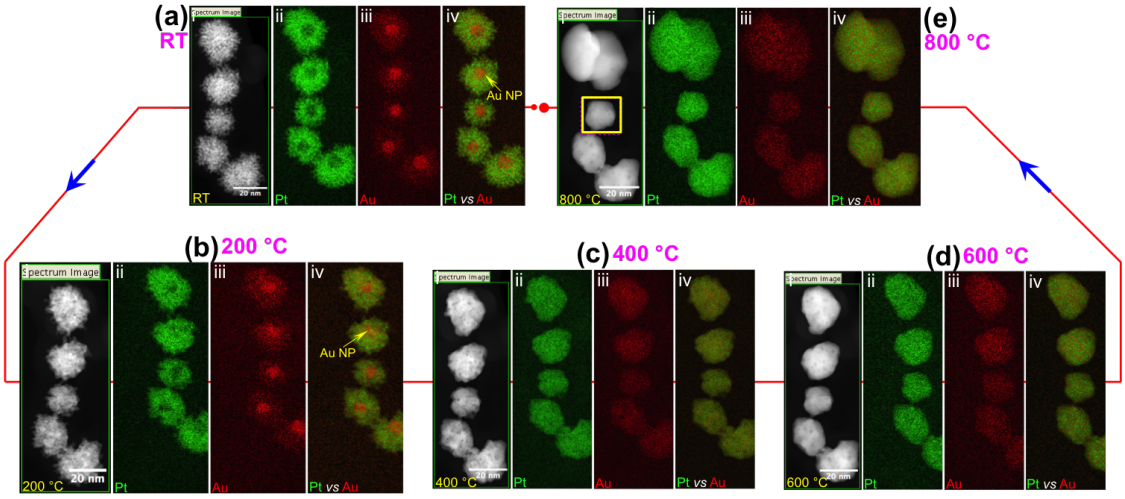

Figure 7.14: Compositional evolution of high-Pt loaded Pt-on-Au heteroaggregates during *in situ* TEM annealing. (a)—(e) Selected area is being tracked over the course of annealing. Labels in pink indicate holding temperature. a(i), b(i), c(i), d(i) and e(i), HAADF-STEM images. a(ii), b(ii), c(ii), d(ii) and e(ii), EELS map of Pt. a(iii), b(iii), c(iii), d(iii) and e(iii), EELS map of Au. a(iv), b(iv), c(iv), d(iv) and e(iv), Composite Pt-versus-Au map.

produces a mass-thickness contrast, with image intensity roughly proportional to $tZ^{1.6}$ (thickness t, atomic number Z). Since the atomic numbers of Pt and Au are close, the observed intensity drop at the highlighted locations in Figure 7.13*(b(iii))* correspond to thickness variations, suggesting the presence of structural inhomogeneities such as voids or defects. By further comparing the highlighted regions (green circles) in Figure 7.13 *(b(iii) and b(iv))*, it is evident that the inhomogeneities gradually disappear over the course of annealing (400 °C *vs* 800 °C), likely from the expected high diffusion rates at the elevated temperatures.

7.5.2 *Tracking compositional changes during annealing*

In addition to the structural changes discussed above, the heat treatment of high-Pt heteroaggregates accompanied interesting compositional changes that eventually led to the formation of Au-Pt solid solution at the end of the anneal.

Figure 7.14*(a—e)* displays a summary of the compositional changes during annealing. The maps coloured in green and red illustrate spatial distribution of Pt and Au,

respectively. For the dataset at RT (Figure 7.14*(a)*), the Pt *vs* Au composite map shown in Figure 7.14*(a(iv))* illustrates Pt clusters encapsulating the base Au nanoparticle. This Pt-on-Au heteroaggregate composition was discussed in detail earlier (in Figure 7.11). A similar elemental distribution of the Pt and Au can be seen even in the Pt *vs* Au composite map shown in Figure 7.14*(b(iv))*, that corresponds to 200 °C annealing condition. This indicates that the heteroaggregate composition is preserved even after 25 *min* heating at 200 °C. However, by comparing the composite map of 200 °C to that of 400 °C (Figure 7.14*b(iv) vs c(iv)*), it can be clearly seen that the heteroaggregate composition is lost upon 25 *min* heating at 400 °C. Further analysis of the Au and Pt maps shown in Figure 7.14*(c(iii, iv))* reveals a relatively uniform distribution of Pt and Au throughout the structure, suggesting an inter-diffusion of Pt and Au atoms. Subsequent heat-treatments at 600 °C and 800 °C does not seem to drastically change the local composition within the particles. This is evident from the similarities between Pt *vs* Au composite maps of 600 °C and 800 °C (Figure 7.14*d(iv) vs e(iv)*), with respect to that of 400 °C (Figure 7.14*c(iv)*). However, it is noticeable from comparing Figure 7.14*d(i) vs e(i)* that the two particles at the top have coalesced during the heat-treatments between 600 °C and 800 °C.

7.5.3 *Detailed analyses of an annealed particle*

The high-resolution structural and compositional data of an individual particle after annealing (emboxed in Figure 7.14*(e(i))* is provided in Figure 7.15a. Individual atomic columns are resolved in the HAADF-STEM image shown in Figure 7.15a*(i)*. From the Pt (green) and Au (red) maps shown, it is evident that both Pt and Au are homogeneously distributed in the projected area of the particle, thus suggesting a compositional homogeneity. This is also indicated in the composite Pt *vs* Au map shown in Figure 7.15a*(vii)*, where no segregation of one particular element is observable in the bulk of the particle. A similar spatial distribution of Pt and Au was observed even with the use of independent component analyses (ICA), as illustrated in Figure 7.15b. Observed homogenous distribution of Au and Pt within the particle thereby confirms that the heat-treated high-Pt heteroaggregate particle has formed a compositionally homogeneous Au-Pt solid solution.

In addition to the observed compositional homogeneity, we also observe a uniform crystal structure in the HAADF-STEM image Figure 7.15a*(i, ii)*. The ordered structure is evidenced by the repeated arrangement of the set of atomic-columns identified in Figure 7.15a*(iii)* along the horizontal direction, virtually in the entire projected region of the

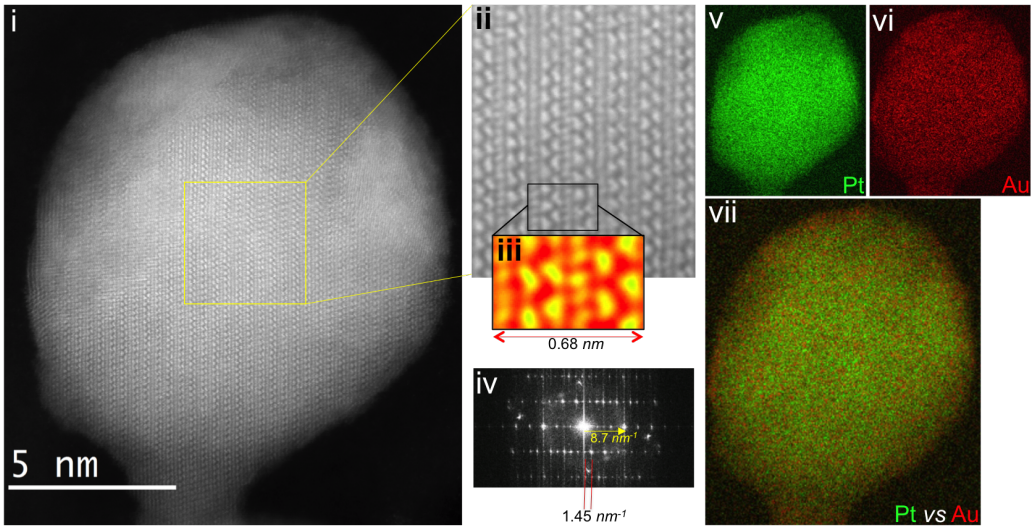

(a) Heat-treated high-Pt heteroaggregate nanoparticle (800 °C annealing condition). (i) HAADF-STEM image. (ii) Magnified image of boxed region in (i). (iii) Repeating unit of the 2D projected lattice in (ii) (color-coding for better visibility). (iv) Diffractogram of (i). (v–vii) EELS maps of Pt, Au and Pt-versus-Au, respectively.

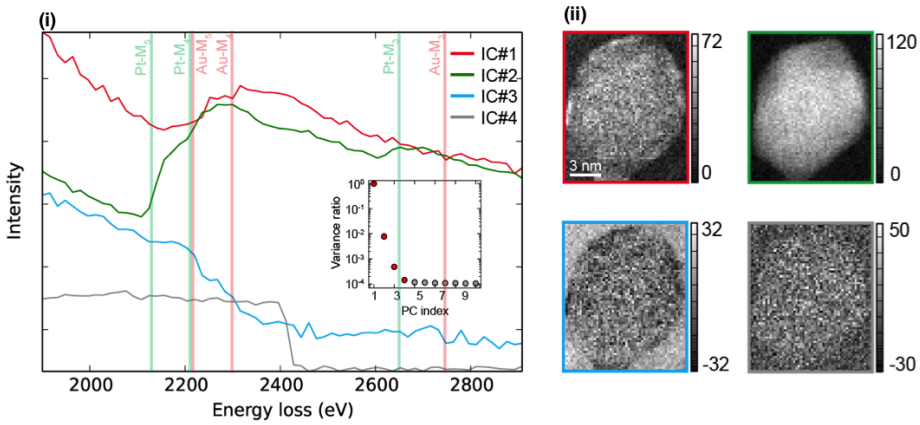

(b) ICA dataset of the ordered single-phase particle in fig.(a). i, Independent component (IC) spectra of components #1, #2, #3 and #4. Vertical lines indicate onsets for Pt and Au M-4,5 and M-3 reference edges. ii, corresponding spatial maps generated.

Figure 7.15: Detailed structural and compositional analyses of an annealed particle.

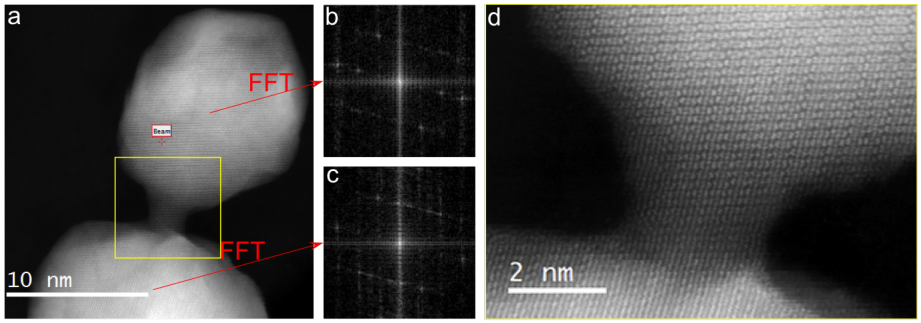

Figure 7.16: Structural similarity between two neighbouring heat-treated high-Pt loaded heteroaggregates. (a) HAADF-STEM image. (b) and (c), FFT of top and bottom particles, respectively. (d) Magnified image of a selected region from (a) identified within yellow box.

particle. The repeating unit shown in Figure 7.15a*(iii)* was identified from the measurement of the shortest spacing of the reflections appearing in the Fourier diffractogram of the particle displayed in Figure 7.15a*(iv)*. Furthermore, the observed ordered structure could also be found in a neighbouring particle, which we confirm from the resemblance in the Fourier diffractograms of the two particles as illustrated in Figure 7.16.

Unfortunately, the crystal structure of the particle could not be confirmed from a crystallographic database search for 87 % Pt composition. To the best of our knowledge, a crystal structure for this composition has not been reported in the literature. In the following section, we discuss some preliminary attempts that we have undertaken to propose a unit cell structure from the projected image of the particle. Nonetheless, above findings clearly show that the high-Pt heteroaggregate particles transformed into a compositionally homogeneous Au-Pt solid solution after the heat-treatment. As mentioned in the introductory remarks, the formation of solid solution is in contrast to the bulk phase diagram, according to which a phase-separated alloy mixture is what is expected from the heat-treatment of 87/23 Pt/Au alloy mixture.

7.5.4 *Preliminary work on phase identification of the annealed particle*

In order to propose the unit-cell structure of the observed particle in Figure 7.18a, the first step is to identify the orientation (i.e., zone-axis) of the particle. One standard procedure to determine the zone-axis of the particle from its diffractogram, is to match the reciprocal lattice spacing of the shortest vectors in the particle diffractogram to that of

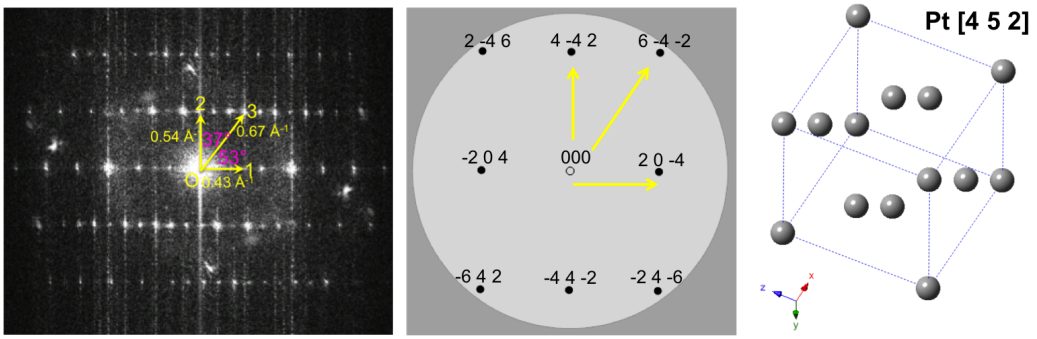

Figure 7.17: Identifying the zone-axis of the annealed high-Pt heteroaggregate particle. (a) Diffraction pattern of the particle shown in Figure 7.15a. (c), unit-cell of Pt crystal oriented along [452] zone-axis. (b) simulated diffractogram of (c).

a reference. Here we consider fcc-Pt crystal (a = 3.97 Å) as the reference, which is reasonable starting point given that the Pt composition in the particle is considerably high (87 %). The procedure to identify the particle orientation involved following steps: (a) identification of three unique directions in the diffractogram with the shortest reciprocal lattice spacings. (b) measurement of the lattice spacings, labeled as 1, 2, and 3 in the order of lattice spacing (shortest to high). (c) measurement of the angles between the three directions, 1-2, 2-3, 1-3. (d) calculation of lattice spacing ratios: 1/2, 2/3, 1/3. (e) scanning through the zone-axes file of fcc-Pt crystal in search of above values noted in (c) and (d).

Figure 7.17*(a)* shows the diffractogram of the particle, with the three shortest reciprocal spacing directions labeled as 1, 2 and 3. Note that only the major reflections are being considered, ignoring the other satellite peaks (e.g., two spots between 2 and 3). Once we have modeled a reasonable structure of the unit cell that is representative of the bulk of the particle, we can then refine it with the inclusion of the satellite reflections that we have presently ignored. The approach taken to identify the noted major reflections (1, 2 and 3) is discussed in Appendix C. It basically involved a detailed analysis of the different sets of reflections in the diffractogram of the particle, and the real space features that they represent.

The measured angles for the three shortest vectors in Figure 7.17*(a)* are: 1-2 = 90°, 2-3 = 53° or 127° (supplementary angle), and 1-3 = 37° or 143° (supplementary angle). The calculated reciprocal lattice spacing ratios for these vectors are: 1/2 = 0.8055, 2/3 = 0.8023, 1/3 = 0.6463. We compared these values with those for all possible zone-axes of the fcc-Pt crystal. The complete zone-axes file for fcc-Pt crystal was obtained from

DIFFRACTOGRAM	Experiment[1]	Reference (Pt-fcc)[2]
Spacing (1, 2 and 3) (in $Å^{-1}$)	0.44, 0.54, 0.67	1.13, 1.51, 1.89
Spacing ratio (1/2, 2/3 and 1/3)	0.81, 0.80, 0.65	0.75, 0.80, 0.60
Angle (1-2, 2-3 and 1-3)	90°, 37°, 53°	90°, 36.7°, 53.3°

[1] Figure 7.17*(a)*
[2] Figure 7.17*(b)*

Table 7.2: A comparison of the reciprocal spacings in the diffractograms of experiment and the Pt reference.

the crystal maker software.[7] The closest match we found was for the particle with an orientation along the [4 5 2] zone-axis.

Figure 7.17*(c)* show the simulated diffractogram for Pt along [4 5 2]. Its corresponding unit-cell is also shown as in Figure 7.17*(c)*. The three reflections 1, 2 and 3 in the experimental diffractogram correspond to reflections $2\,0\,\bar{4}$, $4\,\bar{4}\,2$ and $6\,\bar{4}\,\bar{2}$ in the simulated diffractogram of Pt reference. Table 7.2 summarizes the three angles (1-2, 2-3, 1-3) and the reciprocal lattice spacings for both the experimental and the Pt reference. It can be seen that all the three reflections in the experimental diffractogram are shorter than the Pt reference (by atleast 50 %). In real space, this means that the unit cell for the heat-treated particle is much larger than the pure Pt particle. In fact, this is expected since the heat-treated particle has formed a compositonally homogeneous alloy with Au, and therefore, the inclusion of relatively larger Au atoms in the Pt unit cell should increase the overall unit-cell volume. In the future, the approach would be to refine the Pt unit cell with approporiate inclusions of Au atoms such that the reciprocal lattice spacing in the simulation matches with the experiment.

7.6 HEAT-TREATMENT OF LOW-PT LOADED HETEROAGGREGATES

So far, we have discussed the formation of Au-Pt solid solution from the heat-treatment of high-Pt heteroaggregates. A similar heat-treatment procedure was carried out on the

[7] The zone-axes file is about 484 pages long, therefore, is not being included here. However, upon request, it can be sent to the interested reader.

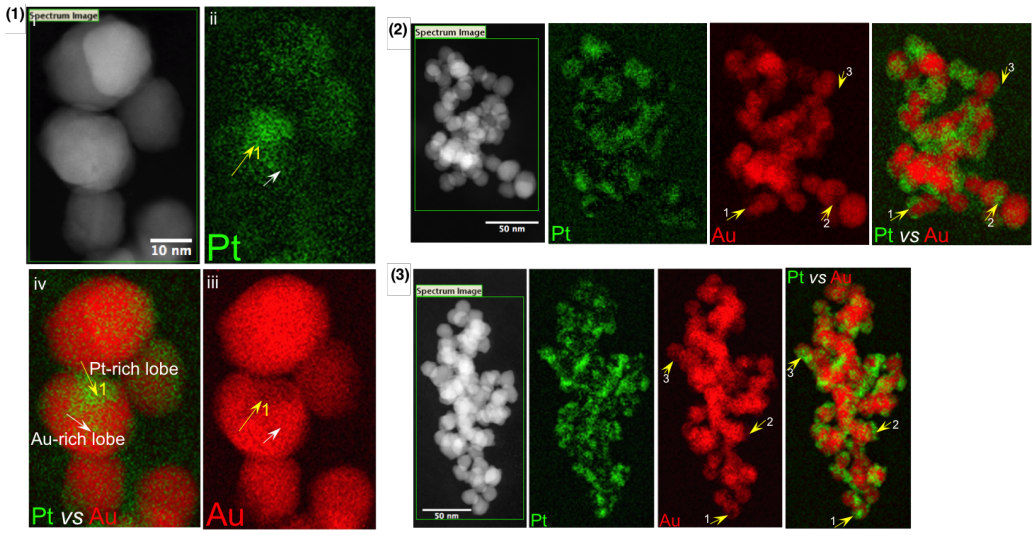

(a) (1–3), Collage of EELS maps and HAADF-STEM images illustrating elemental distribution of the phase-separated Au-Pt particles. Yellow arrows in Pt-*vs*-Au composite maps and pure-Pt maps indicate Pt-rich region. Yellow arrows in the Au maps indicate local depletion in Au content.

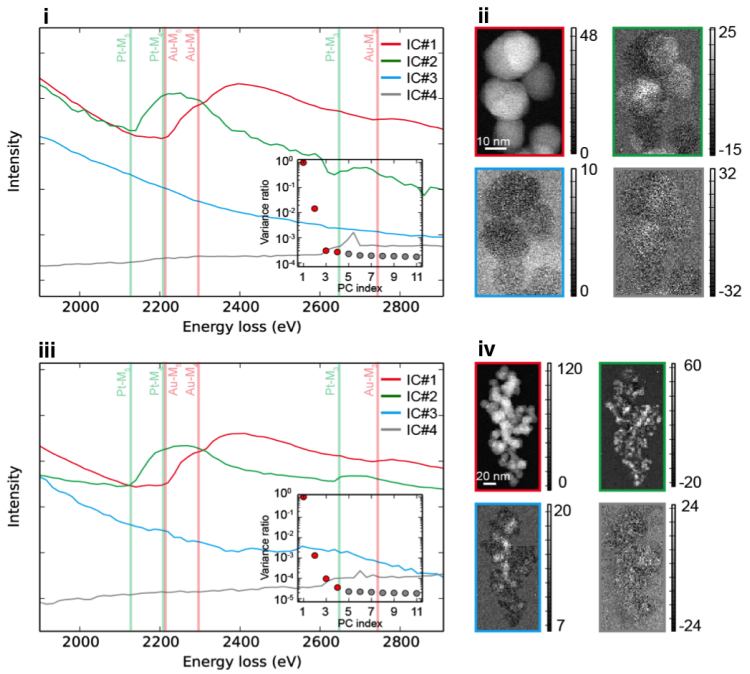

(b) ICA dataset of the phase-separated particles: top (a(i)) and bottom(a(iii). i, Independent component (IC) spectra of components #1, #2, #3 and #4. Vertical lines indicate onsets for Pt and Au M-4,5 and M-3 reference edges. ii, corresponding spatial maps generated.

Figure 7.18: Compositional analyses of phase-separated Pt-Au NPs using: (a) MLLS fitted elemental maps, and (b) ICA data. Thermal history of these particles: Section 8

low-Pt heteroaggregates.[8] In the present section, we discuss the compositional mapping of the structures formed at the end of this heat-treatment. As discussed in detail below, our findings reveal that the annealed nanoparticles from the low-Pt heteroaggregates sample exist in a phase-separated alloy mixture.

Figure 7.18 shows the HAADF-STEM images and EELS elemental maps of over three different regions in the heat-treated low-Pt heteroaggregate sample. Maps in red and green correspond to Au and Pt, respectively. We first consider data shown in Figure 7.18a*(1)*, where the elemental maps are better spatially resolved. The yellow arrow marked on the Au map Figure 7.18a*(1)(iii)* identifies a darker region within the particle (identified as Region-1), compared to its surrounding areas that appear brighter (white arrow). Note that the intensity in EELS compositional maps is proportional to the elemental content. Therefore, the observed drop in the Au intensity at the Region-1, indicates a local depletion in the Au content of the particle. The same location is also identifiable on the Pt map as indicated by the yellow arrow in Figure 7.18a*(1)(ii)*. Evidently, the Pt intensity at Region-1 is higher than that in the rest of the particle. This suggests a local enrichment in Pt at the Region-1. The Au and Pt maps have thus revealed that the Region 1 is Pt-rich, while the rest of the particle is Au-rich. In other words, this means that the particle is composed of two phases, one which is Pt-rich, and the other which is Au-rich. This is much clearer from the composite Pt *vs* Au map shown in Figure 7.18a*(1)(iv)*.

The segregation of Pt and Au is further evidenced by ICA of the EELS spectrum image data enclosing particle clusters shown in Figure 7.18a*(1, 3)*. In both datasets (shown in Figure 7.18b), the separated component spectra, IC#1 and IC#2, strongly resemble reference EELS spectra for Au-M4,5 and Pt-M4,5 respectively, and their inhomogeneous spatial distribution suggests segregation of the two elements within the nanoparticles.

A similar phase separation can be observed in numerous other particles from the same synthesis batch. This is illustrated in the maps shown in Figure 7.18a*(2, 3)* wherein the Pt-rich regions are identified using yellow arrows in the composite Pt *vs* Au maps. Corresponding depletion in the Au content at these same sites are evidenced by the yellow arrows marked on the Au maps.

[8] From RT to 25 *min* heating at following series of temperatures: 200 °C– 400 °C– 600 °C– 800 °C and then quenching back to RT, see Section 7.4 for details.

7.7 SUMMARY OF *in-situ* HEAT-TREATMENT INVESTIGATIONS

In summary, we have observed formation of both solid solution and phase-separated Au-Pt alloy mixtures during in-situ TEM annealing of Pt-on-Au heteroaggregate nanoparticles. A solid solution of Au-Pt was found to result from the heat-treatment of high-Pt heteroaggregates (87 % Pt) to about 800 °C, while the phase separated structure formed from a similar heat-treatment of low-Pt heteroaggregates (23 % Pt). The formation of a solid solution contrasts the wide miscibility gap seen in the equilibrium bulk phase diagram of the Au-Pt system, according to which a phase-separated mixture is expected in almost the entire composition range. It is possible that the solid solution formed is either a metastable structure, or an equilibrium phase resulting from the compression of phase-diagram due to nano-scale phenomena. For example, we observed that the formation of solid solution is accompanied by formation of structural inhomogeneities in the early stages of annealing. Presence of such inhomogeneities in materials can alter the diffusion kinetics of species (e.g., Au in this particular case). Additionally, the coalescence of Pt clusters observed in these particles could also have altered the solubilities (of Au in Pt, vice-versa). Such factors can in turn, alter the enthalpy of mixing, which determines whether or not the formation of a solid solution is favoured during the heat-treatments. To confirm these possible origins, however, dedicated atomistic simulation studies is needed. Currently, there is an over growing interest in employing Au-Pt nanoparticles for CO-tolerance, methanol oxidation and fuel cell oxygen reduction reactions. We believe that the insights developed in the present work open new perspectives for the development of active and stable Au-Pt alloy nanoparticles for use in the aforementioned applications.

7.8 MELTING OF PT CLUSTERS ON AU NANOPARTICLE SURFACE

The present section discusses two separate experiments carried out to understand the gradual melting of the Pt clusters on Au nanoparticle surfaces. The two cases considered involve –(1) melting of isolated Pt clusters without coalescing with other clusters, and (2) melting of two or more Pt clusters coalesced together (i.e., coalesced clusters). By 'melting', here we are referring to the thermally induced spreading of Pt clusters, which are still in a solid phase, on the Au surface. Previously, a similar work by Yu *et al* has referred to this phenomenon (in Pt-on-SiO_2) as 'thermal wetting [428].

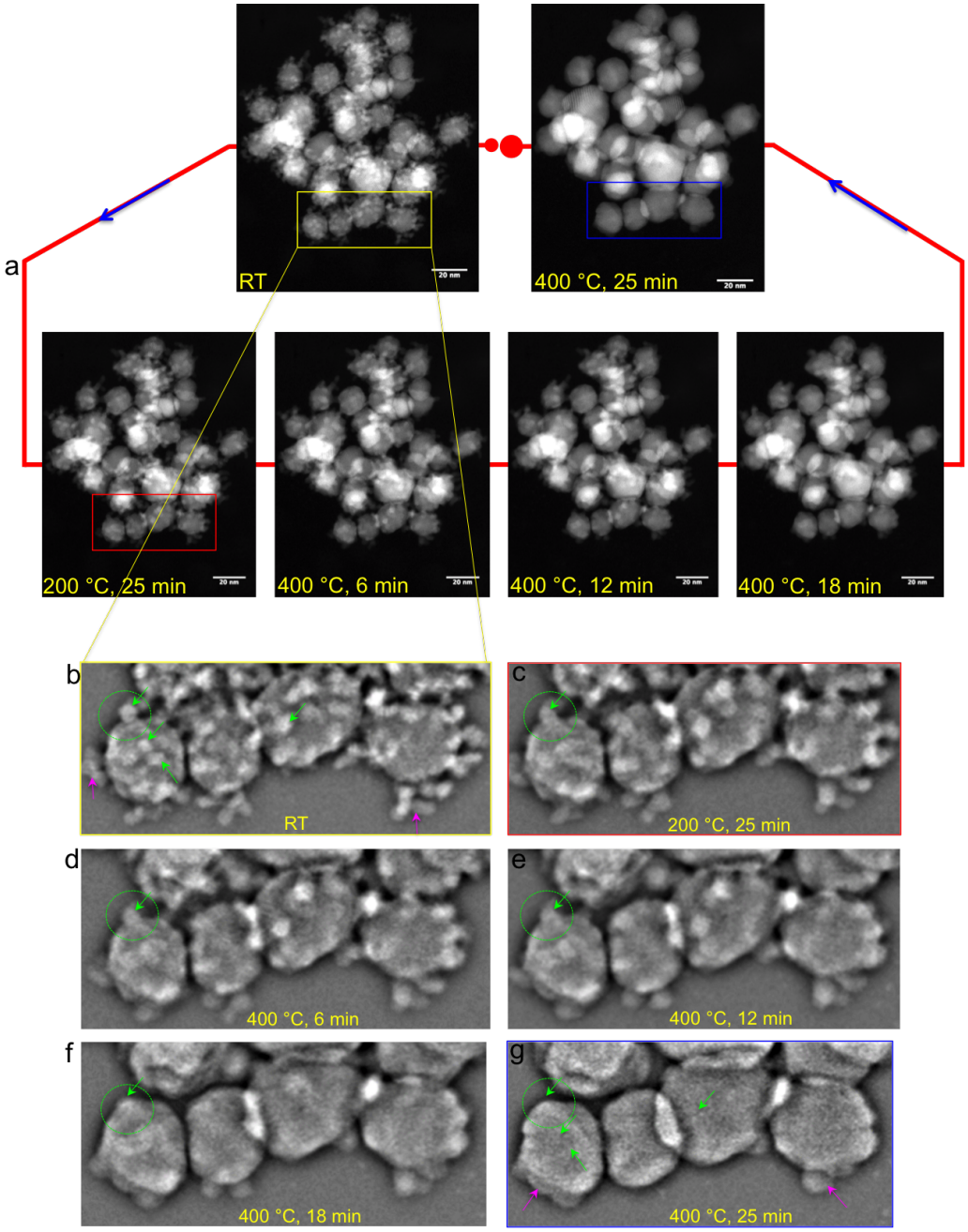

Figure 7.19: Tracking the melting of Pt clusters in low-Pt loaded heteroaggregates. (a) HAADF-STEM images at different annealing conditions (temperature and time indicated by labels in yellow). (b–g) Enlarged images of a selected area at different annealing conditions. Arrows in green and pink identify isolated clusters and coalesced-clusters, respectively. Green circle identifies a particular isolated cluster.

7.8.1 *Melting of isolated Pt clusters*

Figure 7.19*(a)* shows a series of HAADF-STEM images illustrating the structural evolution of a selected area of heteroaggregates during different stages of heat-treatment. To ensure isolation of Pt clusters, these heteroaggregates were synthesized by using low chloroplatinic acid feed concentrations. Earlier experiments had indicated that the Pt melting occur between 200 °C and 400 °C temperature holdings. Therefore, to better investigate the melting process, the images were acquired at additional time steps (6^{th}, 12^{th}, 18^{th} and 25^{th} *mins*), when holding the annealing temperature at 400 °C. For good visibility, a small region in Figure 7.19*(a)* is enlarged as shown in Figure 7.19*(b–g)*. Here, the dynamic range of HAADF-STEM images has been further improved by bandpass filtering (method discussed earlier).

Consider Figure 7.19*(b)*, that corresponds to particles at the RT. As expected for a low loading of Pt clusters, a large number of isolated Pt clusters could be seen, as identified by green arrows. However, few spots where the clusters coalesced together can also be observed, indicated by the pink arrows. Now, consider Figure 7.19*(g)* that corresponds to sample after 25 *min* heating at 400 °C. On comparing the Figure 7.19*(g) and (b)*, it is evident that the isolated particles seen in Figure 7.19*(b)* have disappeared in Figure 7.19*(g)*. In contrast, the coalesced-clusters are still present (see pink arrows in Figure 7.19*(g)*), although the contact angle made with Au is different compared to that in Figure 7.19*(b)*.

To better understand the reason for the observed disappearance of isolated clusters, we tracked one particular cluster, as highlighted by the dotted green circle in these images. By tracking this selected region at different annealing conditions, especially in Figure 7.19*(e–g)*, it can be seen that: (1) the Pt cluster is melting the Au surface, and (2) a complete melting of the cluster is observed by the end of 25 *min* heating at 400 °C, as evident from the absence of the cluster in Figure 7.19*(g)*. Note that the exact time for complete melting (t) might be anywhere between $18\,min < t < 25\,min$. However, the time-steps we used were relatively large[9] to discern this much further.

Figure 7.20 illustrates a collage of many randomly selected areas that were tracked during the heating experiment. Close inspection of the images reveal that the rough-to-smooth transitioning of surfaces has happened by the end of 400 °C heat-treatment, which is consistent with the detailed analyses one such area we discussed in the previous paragraph. From these findings, it is clear that a rough-to-smooth transitioning

[9] every 6 *mins*

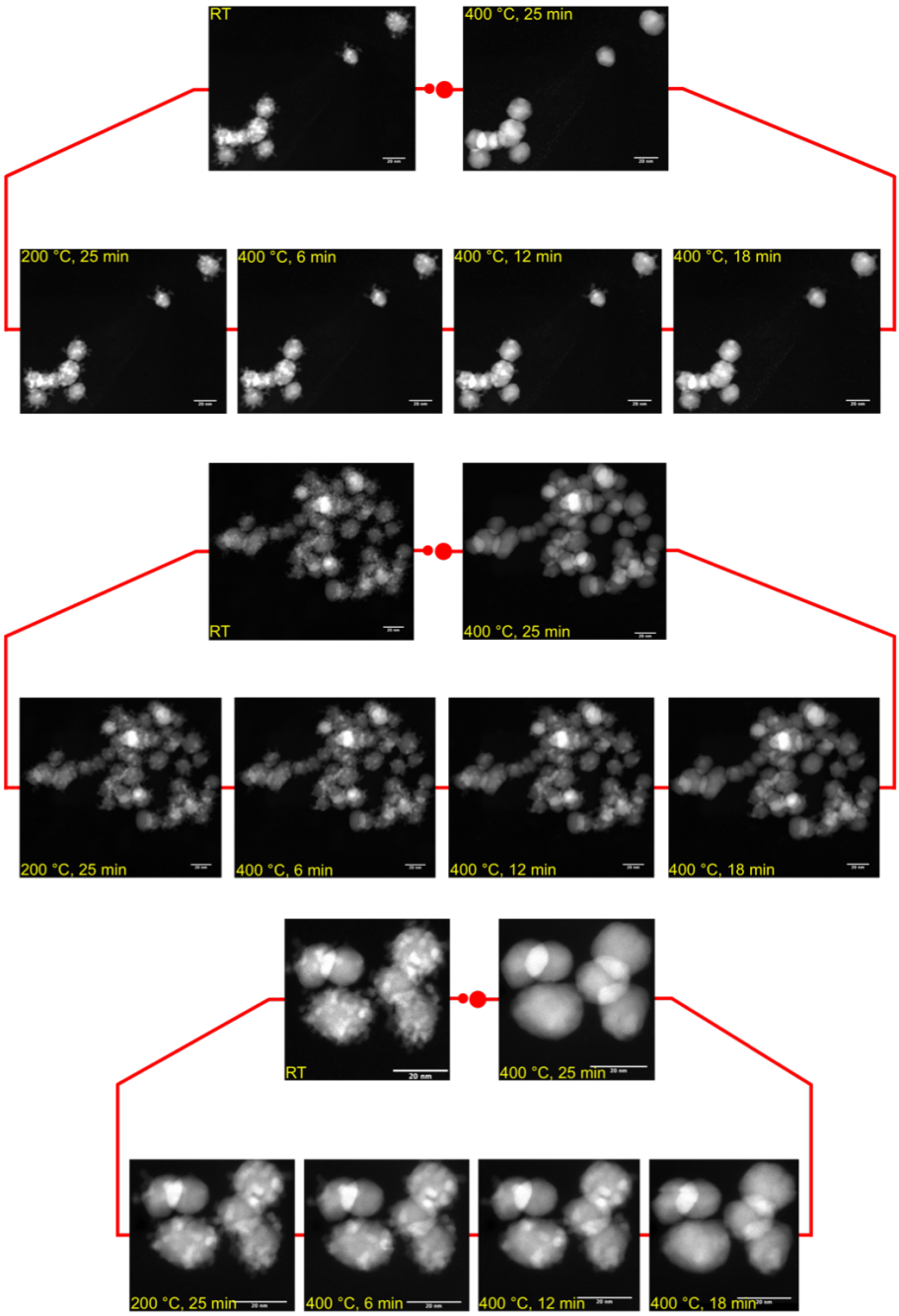

Figure 7.20: Collage of randomly selected areas of low-Pt loaded heteroaggregates tracked during heat-treatment (similar to area discussed in Figure 7.19).

during annealing of heteroaggregates is due to the melting of Pt clusters on Au. Any irregularities, e.g. remaining surface roughness, can be attributed to coalescence effects. For example, the pink arrows in Figure 7.20*(g)* show coalesced-clusters which do not undergo complete melting even after the heat-treatment. We performed another experiment to understand the melting behavior of such coalesced clusters, which we discuss in the following section.

7.8.2 *Melting of coalesced Pt clusters*

The previous section demonstrated that, whereas the isolated Pt clusters show complete melting by the end of 400 °C annealing condition, the coalesced-clusters may not undergo complete melting. To better understand this effect of coalescence on the melting behavior, here we track the melting of three different Pt coalesced-clusters, varying in their degree of coalescence. Annealing conditions beyond 400 °C were also studied to identify whether or not complete melting is possible for coalesced-clusters. The overall heat-treatment procedure involved heating the sample for about 25 *min* at 200 °C, 400 °C, 600 °C and 800 °C, and then finally, quencing back to the RT.

The melting of three different regions - namely Regions 1, 2 and 3, were tracked as shown in Figure 7.21*(a—e)*, identified by circles in green, red and blue respectively. The HAADF-STEM image corresponding to RT shown in Figure 7.21*(a)* reveals different degrees of coalescence in these regions, varying in the order: Region 1 < Region 2 < Region 3. The measured projected areas are roughly in the ratio 1 : 5 : 10 for Region-1 : Region-2 : Region-3. Since $A = \frac{\pi d^2}{4}$, the three regions can be distinguished in terms of their measured projected diameters (*d*), where d_1 = 3.3 *nm*, d_2 = 7.2 *nm* and d_3 = 9.5 *nm*. Consequently, the radius of curvature that these regions form in contact with the Au NP is in the order $R_1 < R_2 < R_3$.

From the series of HAADF-STEM images shown in Figure 7.21*(a—e)*, it is noticeable that the coalesced-clusters undergo a gradual melting on the Au surface. We quantify this by measuring the contact angle (θ) made by the melting cluster with the underlying Au surface, for different annealing conditions. Two approaches were followed in measuring the contact angles: (1) direct measurement of angles using HAADF images as illustrated in Figure 7.21*(f)*, and (2) $\theta/2$ method wherein the measured height (*h*) and width (*d*) of the melting droplet was used to calculate θ, as given by $\frac{\theta}{2} = \tan^{-1}\left(\frac{h}{d}\right)$ (see Figure 7.21*(g)*). One exception had to be made in the case of Region-1. Since the radius

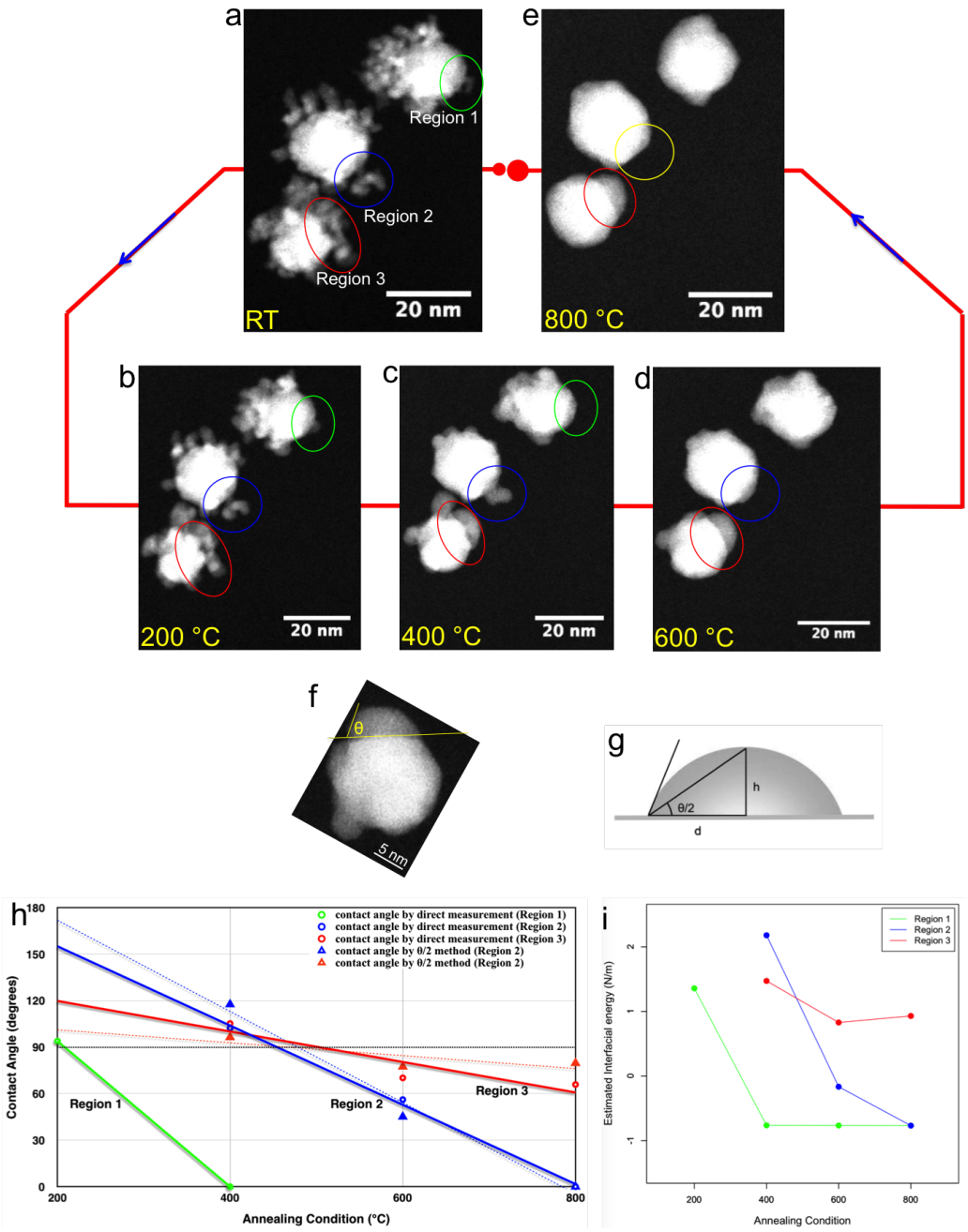

Figure 7.21: Tracking the melting of coalesced-clusters with varying degrees of coalescence. (a)-(e) HAADF-STEM images at different annealing conditions (temperature indicated by labels in yellow). Regions 1, 2 and 3 are identified by circles in green, blue and red, respectively. (f) Example of direct measurement of contact angle from a HAADF-STEM image. (g) Schematic illustration of contact angle calculated from measuring height, h and width, d of the melting cluster. (h) Plot of contact angle *vs* Annealing condition. (i) Plot of estimated interfacial energy between Pt and Au surfaces for Regions-1,2&3, at different annealing conditions.

of curvature formed was very small, the $\left(\frac{h}{d}\right)$ measurement was inaccurate. Hence, only the direct measurement could be reported in this case. The measured contact angles (θ) are summarized as a 'θ *vs* Annealing condition plot' as shown in Figure 7.21*(h)*. The measured contact angles are also tabulated in Table 7.3.

ANNEALING CONDITION	Region-1	Region-2	Region-3
200	[1]93.92°	NA[2]	NA[2]
400	[1]0°	[1]102.3°, [3,4]117.6°	[1]105.3°, [3,5]96.4°
600	[1]0°	[1]56.2°, [3,6]45.1°	[1]70.2°, [3,7]77.4°
800	[1,3]0°	[1,3]0°	[1]65.9°, [3,8]79.7°

[1] direct-measurement from HAADF-STEM images
[2] remain as clusters
[3] measured using *h/d* method
[4] h = 4.0 *nm*; d = 2.4 *nm*
[5] h = 6.2 *nm*; d = 6.0 *nm*
[6] h = 1.9 *nm*; d = 4.65 *nm*
[7] h = 4.7 *nm*; d = 5.88 *nm*
[8] h = 4.4 *nm*; d = 5.24 *nm*

Table 7.3: Contact angle (θ) measured for regions 1, 2 and 3 identified in Figure 7.21.

In Figure 7.21*(g)*, the data points represented by circles indicate θ measured using the direct measurement of angle approach, while those represented by triangles indicate $\theta/2$ method. Fitting the former with a linear function is shown by the solid trend lines, and the dotted lines are plotted for the latter. By comparing these two trend lines, it can be seen that the observed trends following both these approaches, are similar. First, considering the melting of coalesced-cluster in Region-1 (plotted in green), initially the $\theta > 90^{\circ}$ at 200 °C and becomes $\theta = 0^{\circ}$ at 400 °C. This indicates complete melting by the end of 400 °C annealing condition, which is consistent with the earlier observation made in the case of isolated cluster (Section 7.8.1). Note that the average diameter of isolated cluster = 3.2 *nm*, and the calculated projected diameter for Region-1 = 3.3 *nm*. Given this similarity in terms of size, a closeness in their melting behavior is also expected, since the pressure ΔP, which is the driving force for wettiing is inversely proportional to the radius of curvature (R) (i.e., $\Delta P \propto \frac{1}{R}$).

The solid-blue trend line drawn in Figure 7.21*(g)* corresponds to the melting of coalesced-cluster shown in Region-2. In this case, unlike Region-1, the $\theta > 90^{\circ}$ at 400 °C, which

suggests incomplete melting. It can be seen that the coalesced-cluster in Region-2 eventually wets the Au surface completely (i.e., $\theta = 0^{\circ}$) by the end of 800 °C annealing condition. This observation demonstrates that a stronger coalescence can delay complete melting of Pt clusters on Au, compared to isolated clusters without coalescence effects. This is further supported by the melting behavior of Region-3, wherein the degree of coalescence is much stronger than that in Region-2. The solid-red trendline in Figure 7.21*(h)* is the linear fit of the measured contact angles for Region-3. $\theta \neq 0^{\circ}$ even at the end of 800 °C annealing condition, which is in contrast to $\theta = 0^{\circ}$ observed for Region-2. Additionally, the slope (θ/°C) for Region-3 is much lower than that for Region-2, which suggests a sluggish melting kinetics for the coalesced-clusters in Region-3 compared to those in Region-2.

As shown in Figure 7.21*(i)*, we also estimated the interfacial energy between Pt and Au in these regions.[10] The interfacial energy for Region-1 is negative after 400 annealing condition, that for the Region-2 is negative only after the 600 annealing condition, and that for Region-3 is never negative over the entire course of heat-treatment. A previous study by Yu *et al* [428] followed a similar approach to estimate the interfacial energies between Pt clusters deposited on SiO_2 substrate. According to this study, a negative interfacial energy would indicate a stronger interaction between the two mixing components (i.e., Pt and Au here) from the enhanced interdiffusion of metal atoms across the interface. Similarly, other reports have found that the negative interface energy in certain metal-metal systems is accompanied by strong interfacial alloying (from interdiffusion of atoms) and negative heat of mixing [430, 431].

In summary, the above findings have revealed that (1) the coalesced-clusters exhibit delay in melting on the Au surface completely as compared to the isolated clusters. (2) the coalesced-clusters with a smaller radius of curvature exhibit faster melting compared to those with larger curvature. We can think of two possible reasons to explain this observation. First, the driving force ΔP for melting for Region-3 compared to Region-2 is expected to be weaker, since $\Delta P \propto \frac{1}{R}$ (R for Region-3 is greater than Region-2). Second, since the mass of the two clusters are different, the corresponding mass transport properties is also expected to be different: larger the mass of the cluster, longer it takes

[10] The interfacial energy between Pt and Au is given by the Young-Dupre equation: $\gamma_{int} = \gamma_{Au} - \gamma_{Pt}\cos(\theta)$. The interfacial energies of Au and Pt at various annealing temperatures are as follows: Au (in N/m) $\longrightarrow$ 1.2214 (200 °C), 1.2472 (400 °C), 1.2730 (600 °C), 1.2990 (800 °C); Pt (in N/m) $\longrightarrow$ 1.9834 (200 °C), 2.0113 (400 °C), 2.0393 (600 °C), 2.0674 (800 °C). These values were estimated from the reported interfacial energies of these two metals measured at their melting point temperatures (Au: 1.333 N/m, Pt: 2.203 N/m) ([429].

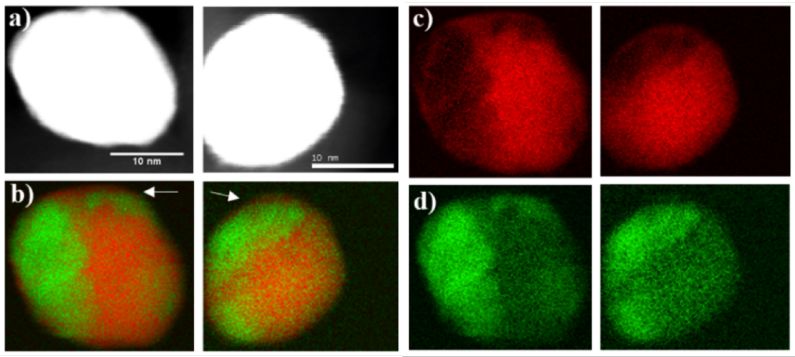

Figure 7.22: Pt, Au and Pt *vs* Au elemental maps of two representative of Pt-on-Au heteroaggregates after 18 hours annealing at 403 °C under 1 atm. N_2 environment. a, HAADF images. b, composite maps. c, Au maps. d, Pt maps. source: [432]

for the entire mass to diffuse, and consequently, longer it takes the cluster to completely wet the Au surface.

7.9 ANNEALING PT-ON-AU HETEROAGGREGATES UNDER OTHER ATMOSPHERES

In addition to annealing the Pt@Au heteroaggregates under the microscope vacuum, the samples were annealed under Air and Nitrogen atmospheres. The work was carried out in association with the then undergraduate research assistant Mike Chatzidakis (now a Masters student in the group) whom I trained and supervised during the summer term. Here I discuss one study carried out under N_2 atmosphere (1 atm.).

The heat treatment was conducted inside a quartz tube furnace at ~400 °C. The Pt-on-Au heteroaggregates were first stabilized on a carbon black (Vulcan Carbon XC-72R) support. This involved three steps, dispersion of as-synthesized heteroaggregates in ethylene glycol, ultrasonication along with carbon black, and finally evaporating the solvent by heating in a N_2 flux at 190 °C.

Several heat treatment experiments were conducted by varying both temperature and the annealing time, but only the 18 *h* annealed Pt-on-Au heteroaggregate sample is discussed here. The conditions were chosen so as to compare the Molecular Dynamics (MD) simulation results (discussed below) to two prior experimental studies conducted by, Braidy [417] in 2006 and Wanjala [416] in 2012. The simulations were carried out by Chatzidakis *et al* and a detailed report can be found elsewhere [432].

Figure 7.22 shows the MLLS fitted STEM-EELS elemental maps of a particles after 18 *h* annealing. It can be seen that the distribution of Pt and Au within the particles is not homogeneous. For example, a Au-rich phase and a smaller Pt-rich 'lobe' is visible as identified by the arrows shown. These findings imply a phase-separated alloy structure, similar to the particles obtained by *in situ* TEM annealing of low-Pt heteroaggregates (Section 7.6). Despite extensive annealing, a compositionally homogeneous alloy could not be formed. Additionally, as identified by the arrow in Figure 7.22, a thin layer of Au is present locally on the Pt-rich lobe surface. The Au segregation in Au-Pt nanoparticles is consistent with many observations in the literature since Au is known to have a lower surface energy than Pt. Using the quantification procedure (described earlier in Section 7.3.5), the compositions of these phase-separated nanoparticles were estimated to be $35.7 \pm 10\%$ Pt (left), and $39 \pm 10\%$ Pt (right). Both compositions fall within the miscibility gap of the bulk binary Pt-Au phase diagram, and thus, the formation of such phase-separated alloy structures is not an apparent contradiction.

To understand the segregation behaviour (i.e., Au segregation on a Pt-lobe) and the phase equilibrium, a set of hybrid Molecular Dynamics (MD) and Monte Carlo simulations were carried out by Chatzidakis *et al* independently. Both single- and multi- phase particles (20 *nm* diameter) were considered and allowed to equilibrate at the experimental temperature of 400 °C (other details on the simulation can be found elsewhere [432]). Figure 7.23 illustrates the morphologies of the Pt-rich phase within the nanoparticle as a function of alloying concentration. At low Pt composition (Pt < 2 %), the nanoparticles exist as a single phase solid solution. Between 2 % Pt and 89 % Pt, a faceted Pt-rich lobe is observed within the nanoparticle. Because of some solubility of Au within the Pt-rich phase, Au is seen to preferentially segregate towards the surface of the Pt-rich phase. Thus, we can infer that the phase equilibrium in these 20 *nm* nanoparticles behaves similar to that of a bulk system, despite having an incredibly small size.

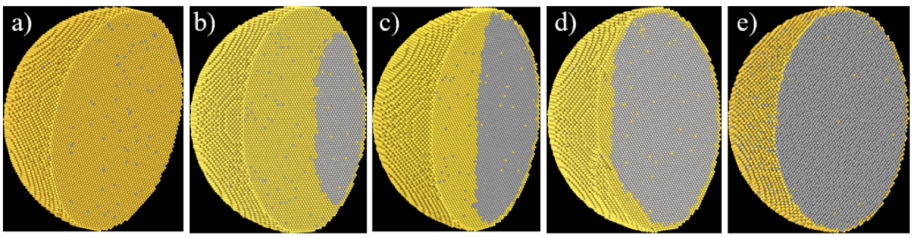

Figure 7.23: Simulated atomic-structures (bisected along (100) plane) of equilibrated Au-Pt nanoparticles varying in initial composition (left to right: $Au_{0.98}Pt_{0.02}$, $Au_{0.75}Pt_{0.25}$, $Au_{0.5}Pt_{0.5}$, $Au_{0.25}Pt_{0.75}$ and $Au_{0.11}Pt_{0.89}$). source: [432]

It is important to note that the Au surface atoms of the phase-separated Pt-Au nanoparticles is not energetically uniform across the entire surface, but depending on the nature of the underlying sub-surface (Au phase or Pt-rich phase), the interfacial free energy for Au segregation (ES) can vary. From the simulations that Chatzidakis *et al* carried out, a higher interfacial free energy for Au segregation was found on a Pt-rich phase compared to pure Au/vacuum interface (40 % greater) [432]. This suggests that the segregated Au layer is destabilized by the presence of Pt-rich lobe underneath it. In contrast, a core-shell structure with spherical Pt phase surrounded by a thick Au shell offers lower interfacial free energy for Au segregation [432]. It is then not immediately obvious as to why a hemispherical lobe structure of the Pt rich phase would be more favorable to form than a core-shell structure.

MD calculations show that the elastic strain energy effects could have led to the observed hemispherical lobe structure of the Pt rich phase. For example, Figure 7.24a shows the stress maps calculated for both lobe and the core-shell structures of the Pt-phase. It can be seen that the lobe structure is a stress-minimized structure, considering the fact that a large volume fraction of the nanoparticle is relaxed. Figure 7.24b compares the total internal energy calculated for both configurations. It can be seen that the total internal energy of a hemispherical lobe structure is much lower than that of a core-shell alloy structure. In other words the lobe structure of Pt-rich phase is the most stable configuration, since the lower the internal energy of a structure the greater is its stability. This explains why despite having an unfavorable interface for Au segregation, the hemispherical lobe structure of the Pt rich phase is energetically more favorable to form than a core-shell structure.

7.10 PERSPECTIVE

In summary, we have monitored the Au-Pt phase transformation process using a *in situ* thermal annealing method. For this we considered the as-synthesized Pt-on-Au heteroaggregate particles as a test system, and annealed them inside a transmission electron microscope. Using high angle dark field imaging (HAADF) and electron energy loss spectroscopy (EELS) techniques we monitored both the structural and the compositional changes in these nanoparticles, over the entire course of heat-treatments. In order to understand the effect of chemical composition on the resulting final structures formed, we studied the heat-treatment process on two distinct compositions of Pt-on-Au heteroaggregate particles, identified as low-Pt and high-Pt heteroaggregates. Our results indicate

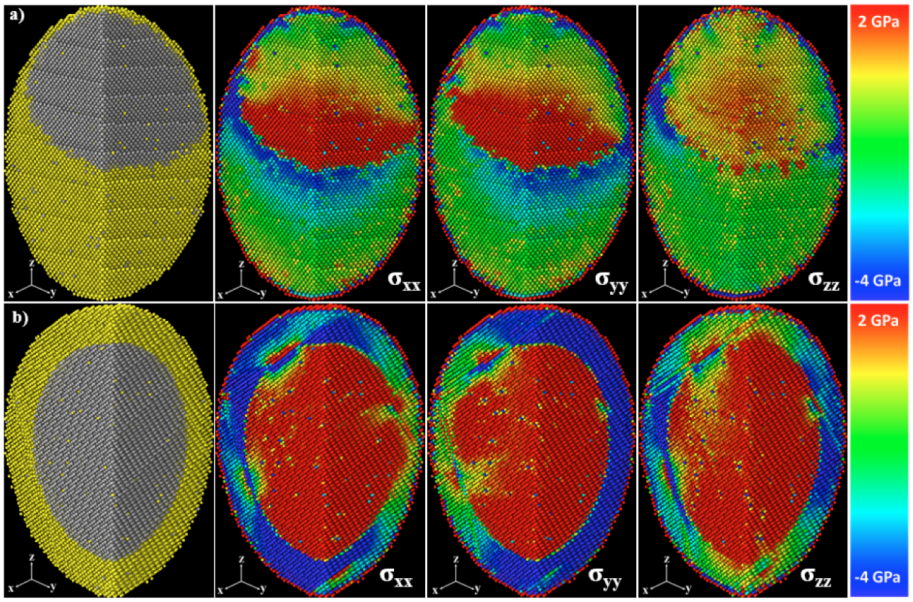

(a) Visualization of the interior of the Au-Pt nanoparticle structures with different morphologies for Pt-rich phase: (a) hemispheric lobe and (b) spherical. Corresponding color-coded stress maps are also shown for different components along different direction vectors.

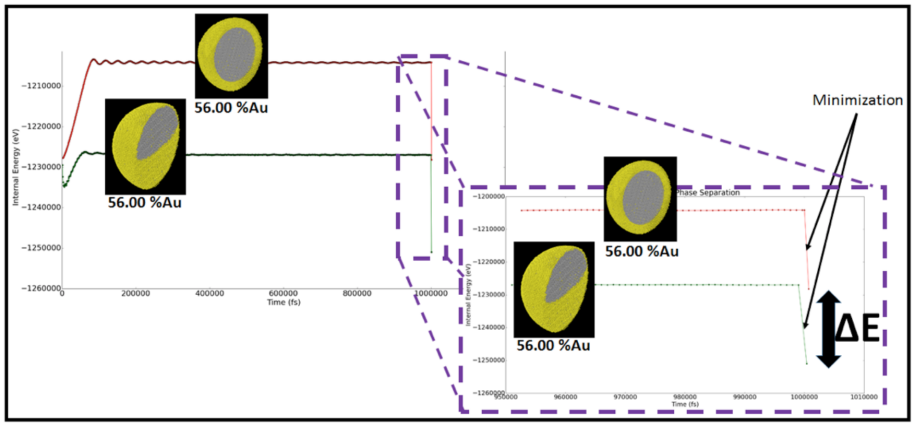

(b) Comparison of internal energies of lobe and spherical morphologies of the Pt-rich phase.

Figure 7.24: Simulations verifying the (b) relative thermodynamic feasibility, and (a) elastic strain energy effects for the formation of two different Pt-rich phase morphologies in the Au-Pt nanoparticles: hemispherical lobe structure and a core-shell structure. source: [432]

that depending on the initial composition of the particles, the formation of both the solid solutions and the phase-separated alloys are possible. We find that the low-Pt heteroaggregates transformed into a phase-separated alloy mixture (discussed in Section 7.6), whereas the high-Pt heteroaggregates formed a solid solution (discussed in Section 7.5). A detailed analysis of the solid solution further indicates a uniform chemical composition and an ordered atomic-structure, virtually in the entire particle. Formation of such Au-Pt alloy nanoparticles in a solid solution alloy is considered extremely challenging.

In addition to annealing the heteroaggregates in vacuum, we also conducted annealing in other atmosheres, such as Air and N_2. We find that the annealing in N_2 environment transformed the heteroaggregates structure into a phase separated alloy, with a hemispherical lobe structure of the Pt rich phase in contact with the Au-rich phase. In collaboration with other researchers, a detailed molecular dynamics simulations of equilibrium structures was also conducted. The results indicate that, despite having an unfavorable interface for Au segregation, the hemispherical lobe structure of the Pt rich phase is energetically more favorable to form, than a core-shell Au-Pt structure.

In addition to above experiments, we investigated the melting of Pt clusters on the Au surface during the annealing of Pt-on-Au heteroaggregate particles. Our results suggest that the coalescence of Pt clusters plays an important role in the kinetics of melting. When coalesced, the coalesced-clusters experienced considerable delay for melting fully on the Au surface compared to the isolated clusters. Furthermore, among the different coalesced-clusters, those with a smaller radius of curvature experienced faster melting compared to those with relatively larger curvatures. This could be due to the differences in the mass transport properties of these clusters, i.e., greater the mass of the coalsced-cluster, longer it takes for it to fully wet the Au surface.

Part IV

SYNOPSIS

8

SYNOPSIS

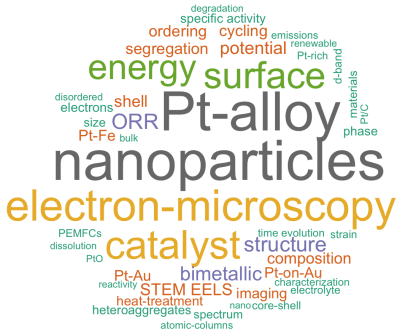

The work presented in this thesis involved application of scanning transmission electron microscopic (STEM) techniques to conduct an atomic-level investigation of the structural and compositional aspects of Pt-alloy nanostructures. Based on the material investigated, the experiments conducted are classified into three main categories, namely the platinum-iron (Pt–Fe) alloy nanoparticles (Chapter 6), the platinum-on-gold (Pt-on-Au) heteroaggregate nanoparticles (Chapter 7), and the other complementary structures involving thin films and nanowires (discussed separately in Appendix D). Detailed technical summary of these individual works can be found in Section 6.8, Section 7.10, and Appendix D. Noted below is a summary of the general insights that we have obtained from these listed works.

A detailed microscopic investigation of the as-synthesized Pt–Fe nanoparticles revealed that the Pt and Fe atoms are arranged in a random and inhomogeneous fashion. A further characterization of these particles after a routine heat-treatment procedure indicated that the particle surfaces could be covered in a iron-rich outer shell, which is not ideal for the catalytic performance. We show that a simple electrochemical procedure can be used to clean the catalyst surfaces. Inspection of such Pt–Fe particles post-cleaning, revealed that the core of the particle is composed of an ordered Pt–Fe alloy (i.e., arrangement of Pt and Fe atoms in an ordered fashion), and the shell is platinum-rich. The routine electrochemical tests on these unique Pt–Fe particles indicated a superior and durable catalyst performance.

The experiments connected to Pt-on-Au heteroaggregates involved synthesizing them with different Pt feed ratios, heating them inside the microscope (and also other gaseous atmospheres), and importantly, monitoring their structural and compositional changes during the heat-treatments. We find that depending on the composition in which we synthesize them, the environment in which we heat them, the Pt-on-Au heteroaggregates transform into either a homogeneous or a inhomogeneous alloy structure. Both these alloy forms are known to exhibit very different catalytic properties. Therefore, an atomic-

level visualization of the entire transformation process allowed us to derive novel insights into their structural formation.

The structures investigated under the category 'complementary structures' (Appendix D) included: thin film catalysts such as Pt–Au–Co alloys, Pt–Ir–Ni alloys, the Pt-nanotubular skeletons, and the Bi-decorated Pt nanowires. Each of these catalyst systems were found to exhibit superious catalyst performances. A detailed microscopic investigation revealed the atomic arrangement and compositions in the surface, near-surface and the bulk regions of these catalyst structures. This information was useful in interpreting their catalytic performances, which generated new perspectives towards further development of these catalysts.

Part V

FUTURE WORK

9

PROPOSED FUTURE WORK

Through series of examples highlighted in the previous chapters (Chapter 6, Chapter 7 and Appendix D), I hope to have convinced the reader that the STEM based imaging and spectroscopy techniques offer a full suite of options to characterize Pt-alloy catalyst structures. Moving forward, similar analyses can be extended to many other PEMFC catalyst systems such as those we reviewed earlier in Chapter 4. Also, suitable *in situ* approaches that we reviewed earlier in Section 4.4 and Section 5.9 can be adopted. Additionally, tools such as compressive sensing methods that promise a minimal beam-damage of materials can also be incorporated into our analytical measurements. From the materials viewpoint, however, one area where STEM techniques can be potentially of great value is the investigation of the surface-oxidation mechanism in the fuel cell working environments.

As discussed earlier in Section 3.1.4, the catalyst nanoparticles in PEMFCs are subjected to conditions that promote surface-oxidation (termed 'electro-oxidation'), such as (1) high oxidation potentials, (2) presence of water, and (3) a direct exposure to gas-phase oxygen [433]. The surface-oxidation of catalyst reduces the available area for further adsorption of fresh incoming oxygen molecules, and consequently decreases the electrocatalytic activity. Experiments attempting to understand Pt electro-oxidation on the nanoscopic size scales have been scarce, partly due to a lack of surface analytical techniques with atomic-resolution capability.

The mass-thickness sensitivity[1] provided by HAADF-STEM is certainly a great tool for studying the catalyst nanoparticles. While this works well for detecting heavy atoms in the matrices of light atoms, the converse[2] is not often easy [89]. For instance, it is extremely difficult to image chemisorbed oxygen atoms against a Pt background, solely with HAADF-STEM imaging. The elastic-scattering cross section of Pt is about 20 times that of oxygen and thus, the electrons scattered by Pt dominate the signal. In a surface-

[1] Intensity as a function of the number of atoms viewed in projection and their atomic-numbers
[2] i.e., detection of light atoms in the matrices of heavy atoms

oxidised Pt nanoparticle of diameter 5 *nm*, only 5 of the projected 25 atoms in an atomic column are oxygen, which is also not favourable to allow the detection of oxygen atoms.

In the recent past, the annular bright field (ABF) imaging has attracted great interest for the visualization of the light elements in the presence of heavier elements [434, 435]. For example, H-atoms in the metal hydrides (YH_2 and VH_2), O-atoms in a $SrTiO_3$ crystal and lithium columns in lithium metal oxides (LiV_2O_4 and $LiCoO_2$) have been visualized [436–439]. In addition to experiments, developments of the required theoretical formulations to interpret the ABF image contrast have also been undertaken [440]. With its optimum sensitivity towards both heavier and lighter elements, the ABF technique can be expected to also serve as an ideal analytical tool for studying the surface-oxidation in Pt/Pt-alloy nanocatalysts. However, to the best of our knowledge, no such research effort has been undertaken so far. In the following section, we highlight the potential to visualize the oxide layer residing on the Pt surface using multislice simulations of the ABF-STEM image. The reader is referred to Appendix E for the detailed version of this work, where we have studied the dynamics of the ABF-contrast with changing defocus and speciment thicknesses, and performed simultaneous ABF-STEM and HAADF-STEM characterization of the real PtO_x sample.

Simulation of ABF-STEM and HAADF-STEM images of surface-oxidised nanoparticles
Figure 9.1 illustrates a case study on two different surface-oxidised Pt nanoparticles: (1) ~3 *nm* Pt-core, ~1 *nm* O-shell, oriented along $1\bar{1}0$ as shown in *Fig. (a)*, and (2) ~9 *nm* Pt-core, ~1 *nm* O-shell, oriented along [111] as shown in *Fig. (c)*. Note that by O-shell, we mean a hypothetical case of pure-oxygen covering the Pt surface. Detailed analyses on the simulated ABF-STEM and HAADF-STEM images are discussed as follows.

Firstly, as shown in Figure 9.1*(a1)*, a 3 *nm* (diameter) pure-Pt nanoparticle was considered with an orientation along $1\bar{1}0$. Onto this, a ~1 *nm* thick surface-oxide shell was created Figure 9.1*(a2)* to form a core-shell type structure Figure 9.1*(a3)*. The corresponding ABF-STEM and HAADF-STEM simulated images are shown in Figure 9.1*(a4, a5)*, respectively. The atomic-columns of Pt appear with brighter and darker intensities in the HAADF-STEM and ABF-STEM images, respectively. The blue circles compare identical atomic-columns in both the images, while the green arrow identifies an O atomic-column at the surface. Clearly, the HAADF-STEM image (Figure 9.1*(a5)*) does not reveal any intensity for surface O atomic-columns. Figure 9.1*(b)* shows a section of the ABF-STEM image simulated for the same particle as displayed in Figure 9.1*(a4)*. Here we have optimized the dynamic range of the display for ensuring better visibility of atomic-columns. As indicated by appropriate labels in Figure 9.1*(a4)*, it is clear that a simultaneous de-

tection of both the projected Pt-core (along $1\bar{1}0$), and the O-shell is possible with the ABF-STEM imaging condition. For instance, at the location indicated by green arrow in Figure 9.1*(b)*, an O atomic-column has now been clearly identified, unlike that in the HAADF-STEM image (Figure 9.1*(a5)*).

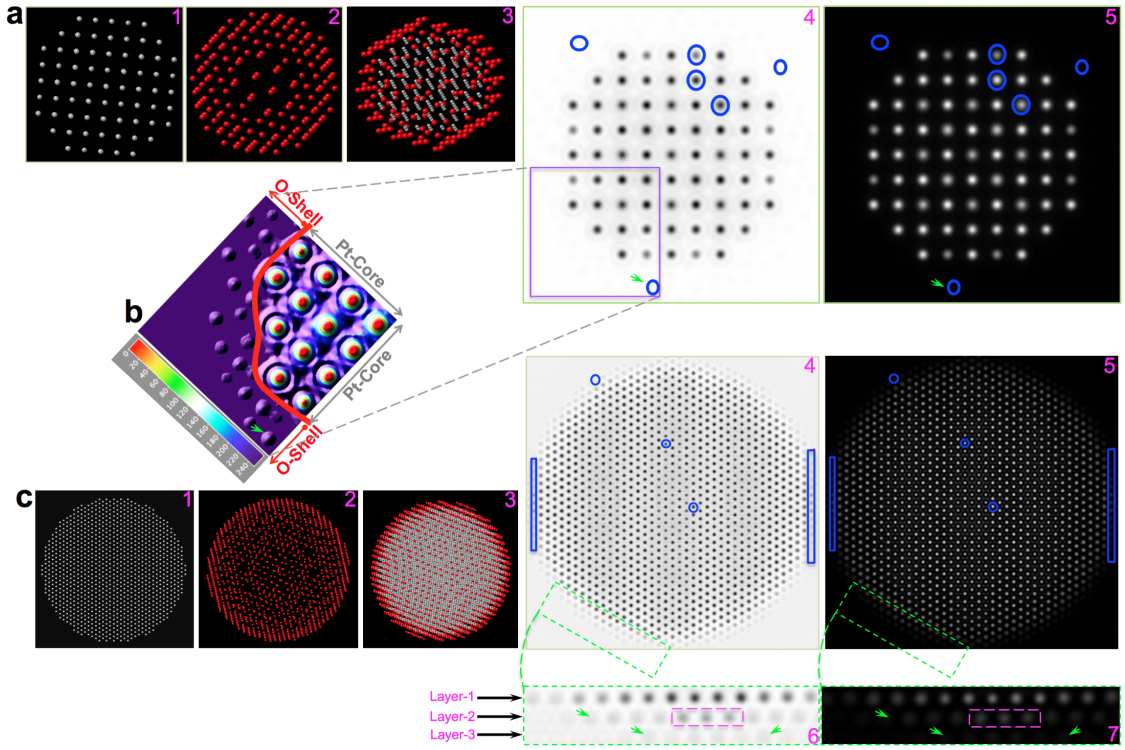

Figure 9.1: ABF-STEM and HAADF-STEM simulations of surface-oxidized Pt nanoparticles. (a) and (c), correspond to data-sets of two different modeled particles of sizes ~ 5 *nm* and 10 *nm*, respectively. a(1) and c(1), Modeled Pt-cores of size 4 *nm* and 9 *nm*. a(2) and c(2), Modeled O- shells of size 1 *nm*. a(3) and c(3), Atomic-models with O-shell overlayed on Pt-core. a(4) and c(4), ABF-STEM image simulations. a(5) and c(5), HAADF-STEM image simulations. b, 2D Surface-plot of the boxed region in a(4). c(6) and c(7), Magnified images of the boxed regions in c(4) and c(5), respectively.

Figure 9.1*(c)* illustrates the simulation results of the second variety of Pt nanoparticle, composed of a ~9 *nm* Pt-core (Figure 9.1*(c1)*) that is covered by ~1 *nm* thick O-shell (Figure 9.1*(c2)*), and oriented along [111]. Here again, by O-shell we mean that a hypothetical shell composed of pure oxygen is covering the Pt particle surface. The orientation along [111] was chosen so that the atomic-columns are composed of a mixture of both Pt and O atoms. The modeled Pt-core and O-shell are overlaid to form a core-shell type structure (Figure 9.1*(a3)*). The corresponding ABF-STEM and HAADF-STEM simulated images are

shown in Figure 9.1*(c4, c5)*, respectively. The blue and green markings identifying identical locations in both the images. To obtain a more detailed comparative picture, the identical regions within the green boxes marked in Figure 9.1*(c4, c5)* are magnified and shown in Figure 9.1*(c6, c7)*, respectively. Noticeably, these images represent the same region, and illustrate ABF-STEM and HAADF-STEM intensities of atomic-columns from the 3 top-most surface layers (in the order 3-2-1, referring to pink labels noted).

The three atomic-columns within the dotted pink boxes marked in Figure 9.1*(c6, c7)* are composed of a mixture of Pt and O atoms; this information is available from the atomic-model created (Figure 9.1*(c1, c2)*).[3] By comparing these three columns in Figure 9.1*(c6, c7)*, it can be seen that the intensities are observed in both the images, confirming that both ABF-STEM and HAADF-STEM techniques can detect a non-pure atomic column (mixing of both Pt and O atoms). Finally, the green arrows in Figure 9.1*(c7)* indicate atomic-columns composed of O atoms solely. A close observation of the intensities at these locations in both the images (Figure 9.1*(c6, c7)*) reveal that the ABF-STEM conditions enabled their detection, whereas the HAADF-STEM did not provide any intensity.

In summary, the two case studies illustrate that the ABF-STEM technique (unlike HAADF-STEM) can identify the presence of O-shell residing on the Pt nanoparticles. As mentioned earlier, such a capability makes the ABF-STEM a right tool to investigate the electro-oxidation problem faced in PEMFCs. A detailed report of the above case study is provided in Appendix E.

[3] It is important to note here that the mixing of Pt and O atoms in the column does not imply a PtO_x shell, since the input to the simulation was an atomic-model composed of a hypothetical pure-oxygen shell. Instead, the mixing of Pt and O atoms in the atomic-column stems from the fact that we are looking at a 2D projection of the actual 3D particle.

Part VI

APPENDIX

A

DIFFRACTION EFFECTS AT AN APERTURE

Objective aperture is fitted to exclude the aberrated beam to probe formation. What happens mechanistically is similar to diffraction of a light beam at a slit, resulting in the formation of an 'airy disk' at a screen placed. A simple situation is illustrated in Figure A.1, where a parallel beam of light is being diffracted by a circular aperture (diameter, D). The angle subtended by the radius of the aperture on the screen can be called as α. The diffracted light forms an airy disc on the screen with a bright spot in the center, accompanied by subsidiary concentric rings. This we call the 'disk of confusion'. The diameter Δx of the 'disk of confusion' exceeds that of the aperture itself. (i.e., $\Delta x \gg D$). For an aperture of much smaller diameter, the diameter of 'disk of confusion' Δx is even higher. Relationship between Δx and α (note that $\alpha \propto D$) is found to be $0.61\,\lambda/\alpha$.

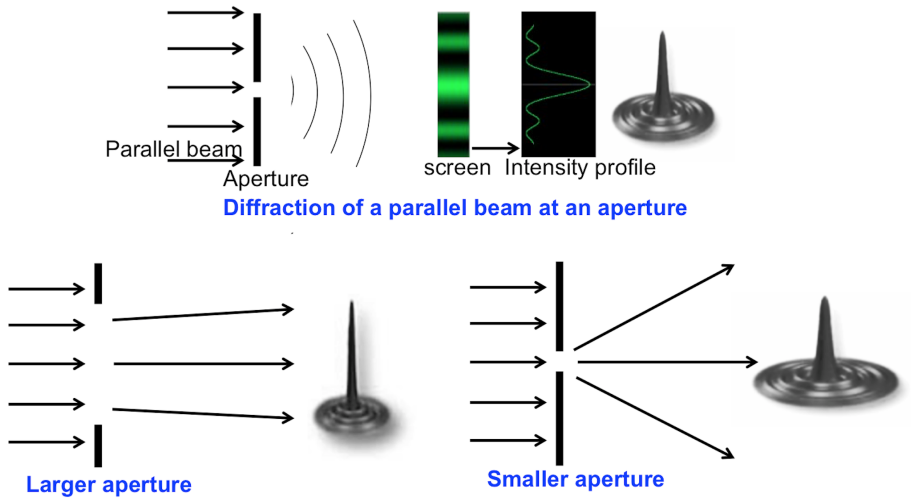

Figure A.1: Illustration of diffraction at a typical aperture, and the comparison of the 'airy discs' formed with a larger, and a much smaller apertures.

In STEM, formation of such 'disk of confusion' creates stray intensities in the image that may not be resulting from the specimen. As a result, the images may not be directly interpretable. This limitation set by the nature is termed as the 'diffraction limitation',

and is particularly more dominant at the smaller aperture sizes, in other words, at small probe convergence angles. In such cases, STEM probe is referred to as the 'diffraction-limited probe' and the quantity Δx is the resulting diffraction error $d_{diff} = 0.61\,\lambda/\alpha$ with respect to a probe unafflicted by such diffraction effects.

B

ESTIMATING AU AND PT COMPOSITIONS IN EELS

In the following discussions, we first describe the general relationships between the EELS intensities and the atomic fraction of a given element in the sample. We then describe the procedure that we adopted to quantify the composition of Au and Pt in the heteroaggregate samples discussed in the thesis (Section 7.3.4). Note that the Au and Pt M-4,5 edges were first deconvolved from the experimental sum spectrum using MLLS fitting (see Section 7.3.3). The estimated composition of both low-Pt and high-Pt heteroaggregate particles is summarized in Table B.1.

General relationship between material composition and EELS signals
I_{Pt} and I_{Au} are the core-loss integrals (integrated within same window Δ). $I_{low-loss}$ is the low-loss intensity integrated up to Δ). The areal density (N, no. of atoms per unit area) is then given by:

$$\boxed{\begin{aligned} I_{Pt} &= N_{Pt}\, I_{low-loss}\, \sigma_{Pt} \\ I_{Au} &= N_{Au}\, I_{low-loss}\, \sigma_{Au} \end{aligned}} \tag{B.1}$$

Where σ is the partial cross-section for energy losses within same range Δ and collection angle.

Then the Pt/Au atomic ratio is given by:

$$\boxed{\frac{N_{Pt}}{N_{Au}} = \left(\frac{I_{Pt}}{I_{Au}}\right) x \left(\frac{\sigma_{Au}}{\sigma_{Pt}}\right)} \tag{B.2}$$

Similarly, the Pt *wt.%* is given by:

$$\boxed{W_{Pt} = \frac{M_{Pt}}{M_{Pt} + \left(M_{Au}\, x\, \frac{N_{Au}}{N_{Pt}}\right)}} \tag{B.3}$$

Where M_{Pt} and M_{Au} are atomic-masses of Pt and Au, respectively.

Since, moles of Pt = $N_{Pt}/N_{Avag.}$ and moles of Au = $N_{Au}/N_{Avag.}$ Molar ratio of Pt/Au = N_{Pt}/N_{Au} Therefore, mole fraction of Pt (X_{Pt}) is given by:

$$\boxed{X_{Pt} = \frac{1}{1 + \left(\frac{N_{Au}}{N_{Pt}}\right)}} \tag{B.4}$$

SAMPLE	At.% Pt	At.% Fe
high-Pt heteroaggregates[1]	87 %	13 %
low-Pt heteroaggregates[2]	23 %	77 %

[1] Au/Pt M-edges, B_{Pt}: 1.32143, B_{Au}: 0.161672, I_{Pt}: 3.59 x 10^6, I_{Pt}: 4.65 x 10^5, σ_{Pt}: 1616 $\pm$ 162, σ_{Au}: 1438 $\pm$ 144, N_{Pt}/N_{Au} = 6.8783

[2] Au/Pt M-edges, B_{Pt}: 6.78824, B_{Au}: 7.73651, I_{Pt}: 5.36 x 10^8, I_{Pt}: 1.46 x 10^9, σ_{Pt}: 1664 $\pm$ 166, σ_{Au}: 1338 $\pm$ 134, N_{Pt}/N_{Au} = 0.2946

Table B.1: Quantification of Pt and Au content in the low- and high-Pt heteroaggregate particles.

Quantification of Au and Pt composition in Pt-on-Au heteroaggregates

As mentioned earlier, the MLLS fitting was carried out to deconvolve individual Pt and Au M-4,5 signals from the experimental EELS spectra of heteroaggregates. The MLLS fit coefficients are denoted as B_{Pt} and B_{Au} for Pt and Au, respectively. To calculate total number of counts (I_{Pt}, I_{Au}) of the deconvolved Pt and Au signals: we first obtain total counts of the Au and Pt reference spectra by integrating over the same energy range (200 eV) ($I_{Pt,ref}, I_{Au,ref}$), followed by multiplication of the obtained counts with the corresponding fit coefficients (B_{Pt} and B_{Au}). That is:

$$\boxed{\begin{aligned} I_{Pt} &= I_{Pt,ref} \times B_{Pt} \\ I_{Au} &= I_{Au,ref} \times B_{Au} \end{aligned}} \tag{B.5}$$

The cross-sections of Au (σ_{Au}) and Pt (σ_{Pt}) were calculated based on *Hartree-Slater model*, available in the Gatan Digital Micrograph software. The cross-section values were obtained for over the same size of the energy window for both Au and Pt. The intensity and the cross-section values calculated from the steps listed above is substituted in

Equation B.2, to obtain the composition of Pt relative to Au (from Equation B.3 and Equation B.4). The compositions of low-Pt and the high-Pt heteroaggregates thus calculated are summarized in Table B.1 (refer to main text for details: Section 7.3.5). In all the cases, the estimated error was about 10 %, which was calculated from the uncertainities in the Au and Pt cross-sections used for quantification.

C

ANALYSIS OF THE DIFFRACTOGRAM OF A PT–AU PARTICLE.

Here we discuss the detailed analyses of the diffractogram of the heat-treated high-Pt heteroaggregate particle presented in Section 7.5.3. The objective is to identify the major reflections in the diffractogram that represent the bulk of the particle structure. The reflections were selected by applying a circular mask to the diffractogram. The corresponding real space image was then recalculated by taking an inverse FFT of the retained reflections in the diffractogram.

As illustrated in Figure C.1*(a)*, we identify three separate components of the diffractogram, labeled as the Groups-1, 2 & 3. The corresponding real space images in each case are also shown (see Figure C.1*(b–e)*). From Figure C.1*(b)*, it can be seen that the Group-1 reflections do not represent the bulk structure of the nanoparticle visible in Figure 7.18, but instead, correspond to small pockets of regions most likely in the surface regions of the nanoparticle. Therefore, for a further analysis of the bulk nanoparticle structure, we subtracted the Group-1 reflections from the full spectrum, which is summarized in Figure C.1*(c)*.

The reflections belonging to the Groups-2&3 are summarized in Figure C.1*(d) and (e)*, respectively. These groups comprise of many reflections that are related in symmetry to the two reflections M and L highlighted in Figure C.1*(a)*. As shown in Figure C.1*(f)*, these groups of reflections appear to fully represent the bulk structure of the nanoparticle when combined together. However, a close inspection of the two power spectra, and also the real space images, in Figure C.1*(f)*, reveals that the Groups-2&3 reflections represent two distinct structural arrangements of atoms. For example, the repetitive column-A identified in the real-space image of Group-2 is absent in that of Group-3 (see Figure C.1*(f)*). In Fourier space, we can quantify this distinction by measuring the angle M2-O-M3 in the power spectrum. As illustrated in Figure C.1*(g)*, the estimated misorientation between the two groups of reflections is about 17°. It is also important to note that the two triangles M2-O-L2 and M3-O-L3 also differ in the *m/l* length ratios (see Figure C.1*(g)*) (1 *vs* 0.75 for Groups-2&3, respectively), which again suggests that the two groups of reflections represent two distinct structural arrangements.

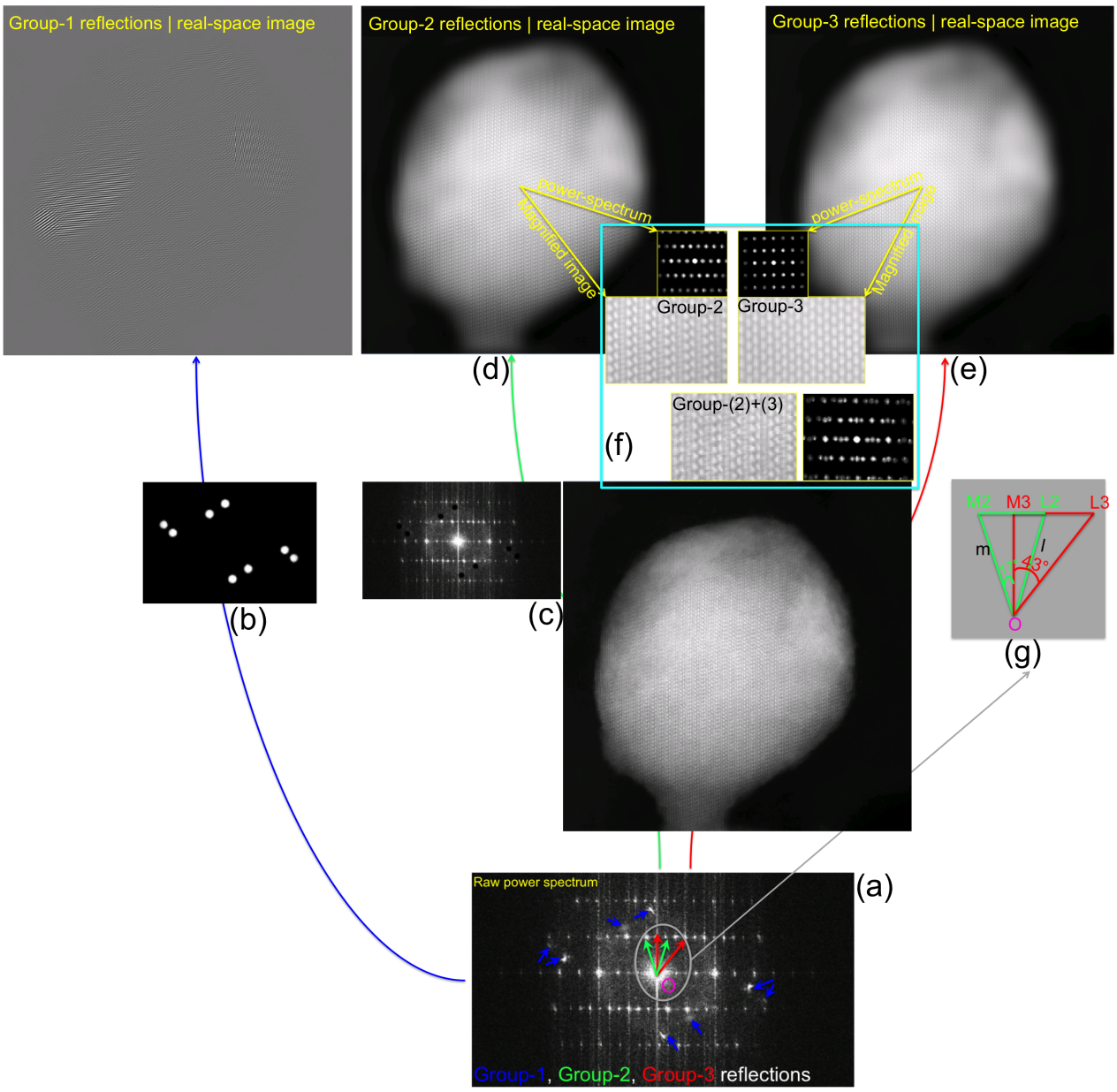

Figure C.1: Detailed analysis of the Fourier diffractogram of the annealed high-Pt heteroaggregate. (a) Raw power spectrum from the particle. (b), (d) and (e), three individual groups of reflections and the associated real-space reconstructed images. (f) comparison of structural features represented by two different groups of reflections. (g) Schematic of the angles between the reflections identified within the circled region in (a).

Above analyses of the power spectrum of the annealed particle suggest that the projected 2D lattice is composed two distinct arrangements of atoms, which are both misoriented as well as distinct in lattice spacing compared to one another. The net effect is the formation of an ordered superlattice along the horizontal direction. Furthermore, the Group-3 reflections appear to fully represent the bulk structure of the nanoparticle. Therefore, matching the reciprocal lattice spacing of Group-3 reflections with the literature can provide a good starting point to identifying the zone-axis, and eventually the crystal structure of the particle. As discussed in Section 7.5.4, we found that the Group-3 reflections closely represent a Pt crystal oriented along 4 5 2 zone-axis. Thus, in the future, additional structural refinements of the Pt unit cell so as to fit the reciprocal lattice spacing of Group-3 reflections would need to be performed.

D

COMPLEMENTARY STRUCTURES

The discussions in Chapter 6 and Chapter 7 presented the characterization work related to Pt–Fe and Pt–Au alloy nanoparticle systems. In addition to these, we also conducted structural and compositional characterization of around four other groups of ORR catalysts, namely the thin film catalyst structures composed of Pt–Au–Co and Pt–Ir–Ni alloys, and the novel Pt-nanotubular skeletons, and Bi-decorated Pt nanowires. These structures were complimentary to the work on 'Pt-alloy nanoparticles' that we focussed in the earlier parts of the thesis discussion. Brief summary of the findings obtained from each of these four complimentary catalyst structures are presented as follows.

D.1 PLATINUM-GOLD-COBALT THIN FILMS

Collaborators Tan and Mitlin (University of Alberta) studied the ORR catalytic performances of Pt-Au-Co and Pt-Ir-Co alloy thin films as a function of Au and Ir substitution [274]. Figure D.1a shows the HAADF-STEM images of a typical area under different magnifications in the microscope. The samples were synthesized by a sputtering technique. In the present discussion, the work carried out on only the Pt-Au-Co alloys is being highlighted.

Figure D.1c illustrates the reported CV profiles and ORR polarization curves for different Pt-Au-Co alloy catalysts. The measured specific activities are summarized in Figure D.1d*(top-panel)*. All the Pt-Au-Co catalysts showed higher activities relative to binary Pt-Co alloy and pure Pt catalysts. The catalytic stability was monitored over the course of 100000 potential cycles (cycled between 0.6 and 1.0 V). Figure D.1d*(bottom-panel)* illustrates the change in the initial specific activities of different catalysts over the course of 100000 cycles. As can be seen, although the Pt-2.5Au-25Co thin film (i.e., 2.5 at. % Pt, 25 at. % Au) showed the highest specific activity of all the Pt-Au-Co alloy catalysts initially (about 5 fold improvement to pure Pt), it suffered the most degradation by the end of 100,000 cycles (70 %). In contrast, the Pt-10Au-25Co thin film showed a relatively

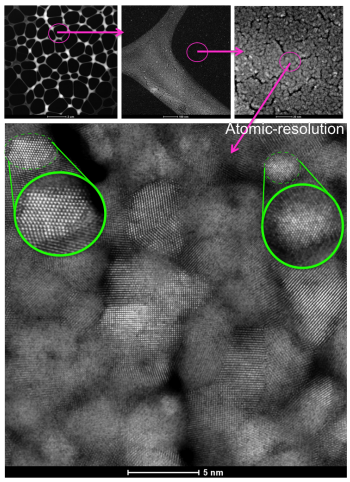

(a) HAADF-STEM image series of catalyst structure at different magnifications (bulk-to-nano).

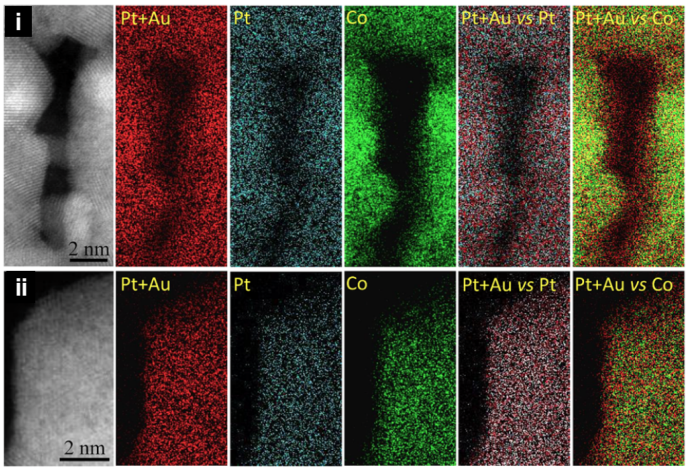

(b) Elemental mapping of an area of Pt-10Au-25Co thin film (i) before and (ii) after potential cycling.

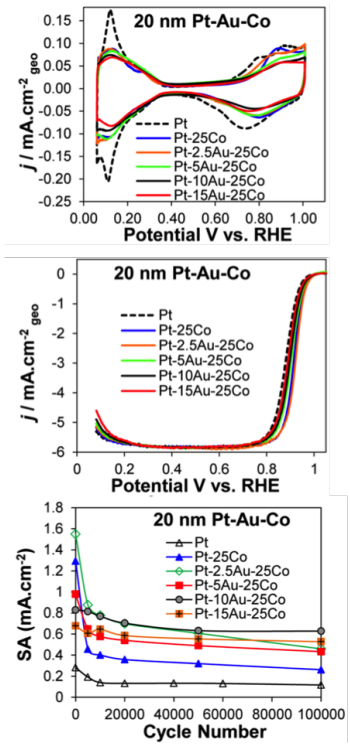

(c) CV profiles and ORR polarization curves for different Pt-Au-Co alloy catalysts.

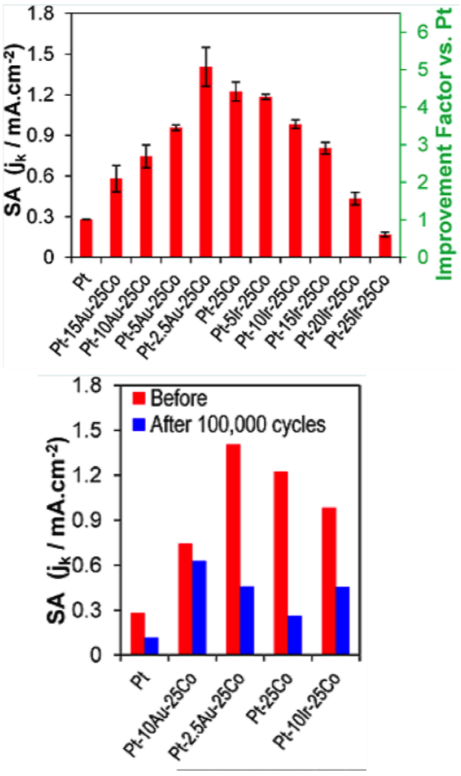

(d) Summary of the measured specific activities for different Pt-Au-Co alloy catalysts (top) before and (bottom) after 100000 potential cycles.

Figure D.1: Atomic-scale characterization of Pt-Au-Co thin films catalysts. source: [274]

lower activity (2.7 fold improvement to pure Pt), but the catalyst stability shown was substantially higher (25 % degradation in initial activity).

The catalyst surface structure of Pt-10Au-25Co alloy was characterized before and after 5000 cycles using HAADF-STEM imaging and EELS elemental mapping. The onsets of core-loss edges of Pt (M-4,5), Au (M-4,5) and Co (L-2,3) are at 2120, 2206, and 779 eV, respectively. Given the difficulty of deconvoluting Pt and Au signals from the EELS (as described in Section 7.3.2), we acquired (Pt + Au) combined, Pt, and Co elemental maps. As may be seen in the map of the as-synthesized alloy (Figure D.1b*(i)*), the material is overall quite homogeneous on the atomic scale. However, there does appear to be a subnanometer thick Pt-Au-rich surface layer in this specimen. On the basis of the EELS elemental maps, the Pt-Au-rich surface layer is about 0.5 nm, which corresponds to two to three atomic layers. Such fine segregation would be driven by the differences in surface segregation energies of Au, Pt, and Co, with the diffusion distances being small enough for it to occur even at ambient temperature. As shown in Figure D.1b*(ii)*, a similar scale Pt-Au-rich surface layer also exists after 5000 potential cycles between 0.6 and 1.0 V. Additionally, many other regions were analysed [274], and a subnanometer thick Pt-Au-rich surface layer could be found in all the cases. These results highlight the structural stability of the Pt-Au-Co alloy surface during the extended electrochemical cycling test conducted.

Compared to binary Pt-25Co catalysts which suffered a significant degradation of about 80 %, the role of Au on the structural/compositional stabilization of ternary Pt-Au-Co alloys is attributed to a 'self-healing' mechanism of Au, which has been previously proposed for PdAu-Pt monolayer core-shell nanoparticles [441]. Driven by the lower surface energy of Au, the segregated Au atoms toward the surface could potentially stabilize the Pt–Au surface layer, which in turn suppresses the dissolution of Co from the ternary core.

D.2 PLATINUM-IRIDIUM-NICKEL THIN FILMS

Collaborators Zahiri and Mitlin (University of Alberta) studied the ORR catalytic performances of Pt-Ni-Ir alloy thin films as a function of Ni and Ir substitution (unpublished). Figure D.2a shows low-magnification TEM images of different Pt-Ir-Ni samples, including pure Pt and binary Pt-Ni and Pt-Ir samples. Figure Figure D.2b illustrate the CV profiles and ORR polarization curves for different binary and ternary catalysts. The mea-

sured mass- and specific- activities is summarized in Figure D.2c*(top-panel)*. As can be seen, with exception to one composition (PtIr/10Ni) all the other ternary Pt-Ir-Ni catalysts performed poorly in comparison to the binary Pt-Ni catalyst. This can be ascribed to the expected high oxygen binding by Ir, which is further evidenced by the observed increasing trend in the specific activity following a decrease in the Ir content in the samples studied.

Figure D.2c*(bottom-panel)* shows the changes in the specific activities of these catalysts after 2500 potential cycles (between 0.6 to 1.2 V). As can be seen, the ternary alloy with the highest Ir content ($PtIr_3Ni$) showed the least degradation among the ternary alloys. We investigated the structure and composition of this particular catalyst ($PtIr_3Ni$), in reference to its counterpart $PtNi_3Ir$, and the binary Pt-Ni catalysts. The findings are discussed as follows.

Figure D.3a illustrates HAADF-STEM images of binary (Pt-Ni, Pt-Ir) and ternary (Pt-Ni-Ir) catalyst thin films at different magnifications. Of particular interest to analyses are the atomic-resolution images, which on comparison does not reveal a characteristic distinction between the atomic-structures these catalysts. Features such as the presence of both low- and high-index facets, network of nanoparticles forming the thin film structure is common to all the catalysts.

Figure D.3b illustrates the Pt, Ni and Pt+Ir elemental maps of Pt-Ni, $PtIr_3Ni$ and $PtNi_3Ir$ samples. Due to overlap between the M-4,5 edges of Pt and Ir, the elemental mapping the Ir in the particle was difficult. The Ni maps reveal a homogeneous distribution of the Ni in all the three catalysts. In addition, comparing the relative distribution of noble metals (Pt + Ir) with respect to Ni in $PtIr_3Ni$ and $PtNi_3Ir$ samples does not evidence a characteristic distinction. This suggests that the one possible reason for the high durability of PtIr3Ni catalysts with respect to $PtNi_3Ir$ is the increased concentration of Ir atoms. The role played by Ir in extending the durability can be similar to that of Au in Pt-Au-Co Pd-Au-Pt particles, where the presence of platinum group metals (Au, Ir) stabilizes the surface layers by suppressing the dissolution of metals with relatively higher dissolution potentials (e.g., Co, Pd and Ni) from the ternary core.

D.3 PT NANOTUBULAR SKELETONS

Using the five-fold twinned Pd nanowires as a template, collaborators Wang, Higgins and Chen (University of Waterloo) synthesized 'Pt nanotubes', which from subsequent

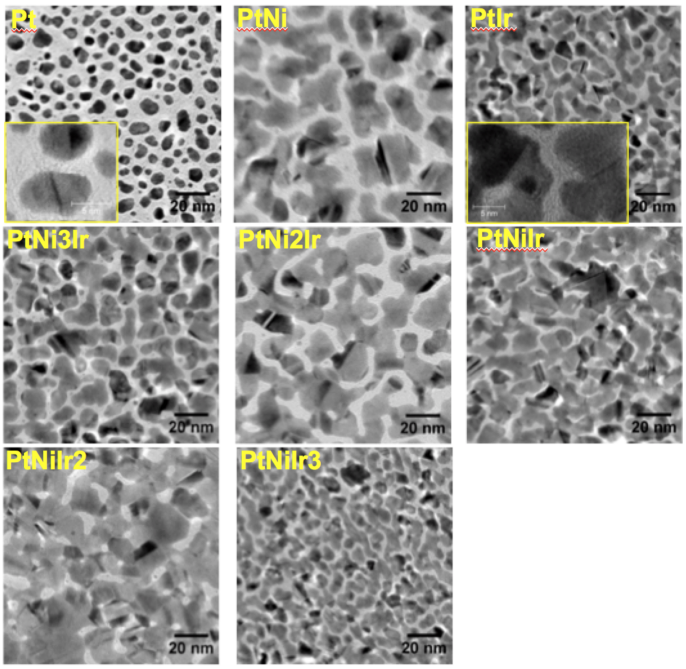

(a) Low-magnification TEM images of different Pt-Ni-Ir catalysts.

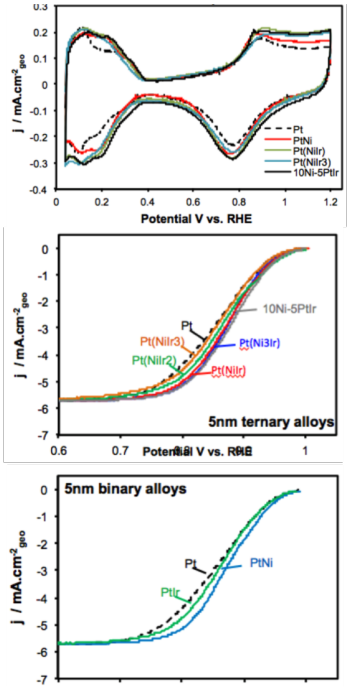

(b) CV profiles and ORR polarization curves for different Pt-Ni-Ir thin film catalysts.

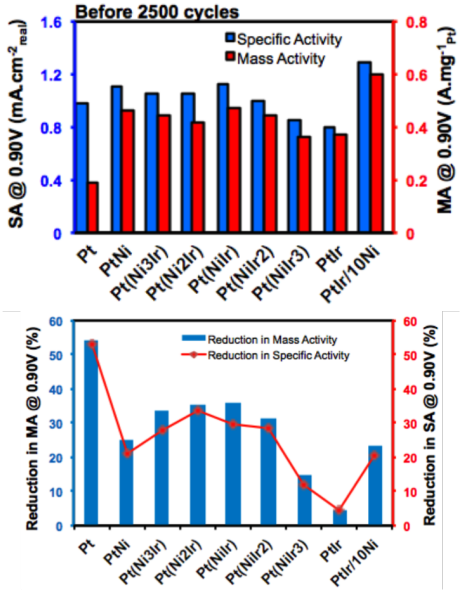

(c) Summary of the measured specific activities for different Pt-Ni-Ir catalysts (top) before cycling, and (bottom) % reduction in their activities after cycling.

Figure D.2: TEM and electrochemical characterization of different Pt-Ir-Ni thin films catalysts. source: Zahiri, Ben and Mitlin, David (unpublished)

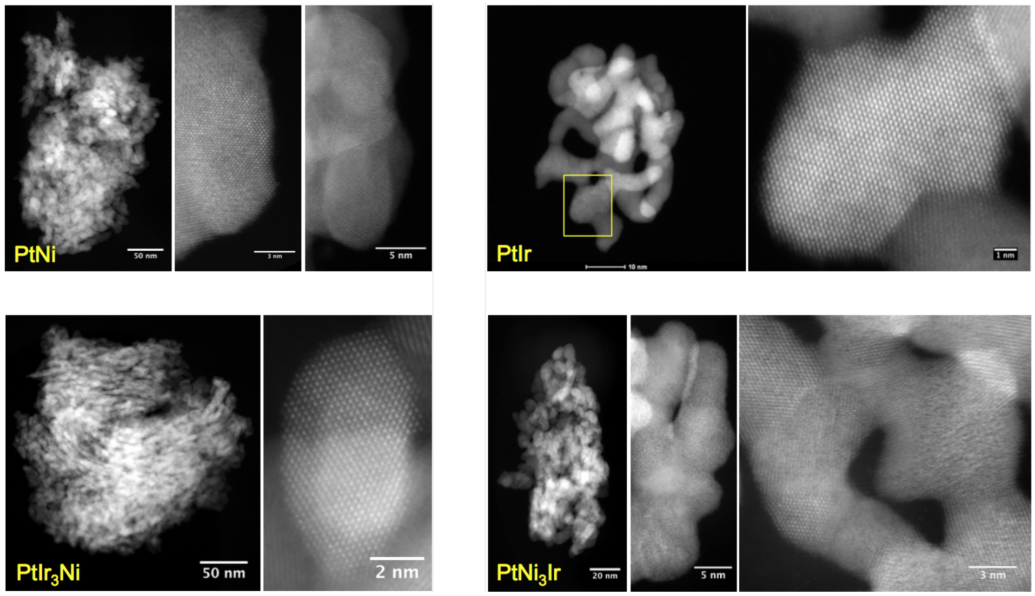

(a) HAADF-STEM imaging.

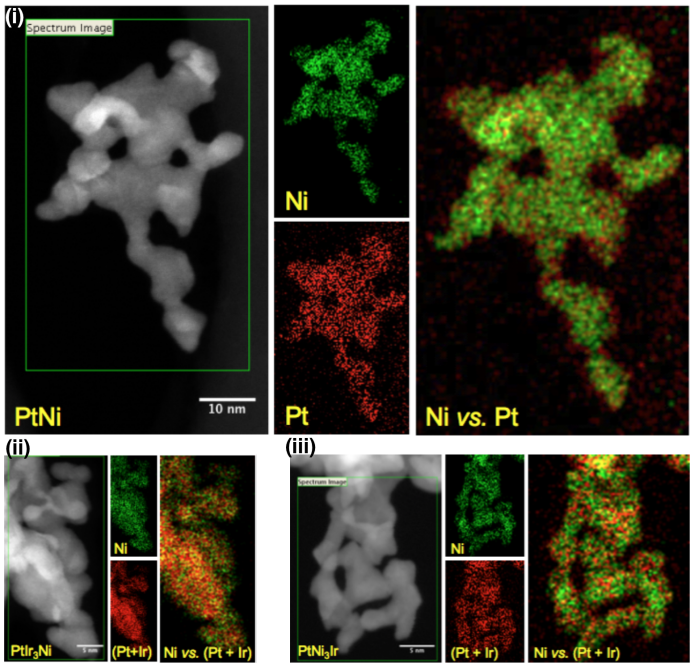

(b) Elemental mapping.

Figure D.3: Atomic-level characterization of Pt-Ir, Pt-Ni, $PtIr_3Ni$ and $PtNi_3Ir$ thin film catalysts.

annealing treatment resulted in the formation of 'Pt nanotubular skeletons' [442]. Wang *et al* studied the ORR catalytic performances and durability of 'Pt nanotube' and 'Pt nanotubular skeleton' catalysts with respect to state of the art Pt/C catalysts. The measured Tafel plot for three catalysts indicate better ORR activity for Pt nanotubular skeletons (see Figure D.4a*(i)*). Monitoring the ECSA losses over the course of 3000 cycles indicates that the Pt nanotubular skeletons is a very durable catalyst compared to others (see Figure D.4a*(ii)*). At the end of 3000 cycles, only 25.7 % of the pristine ECSA was left for the Pt/C catalyst, while 76.0 % and 59.1 % of the initial ECSA remained for 'Pt nanotubular skeletons' and 'Pt nanotubes'.

The catalyst structures before and after the durability tests were investigated by BF-TEM imaging. Figure D.4b illustrates, (i) the initial structures of Pd nanowires, (ii) epitaxial growth of Pt nanoparticles on Pd nanowires, (iii) Pt nanotubes formed by acid leaching of Pd, and finally, (iv) the Pt nanotubular skeletons formed by annealing of Pt nanotubes. The electron-diffraction patterns (inset) reveal that the five-fold twinned structure of the initial Pd nanowires is preserved in both Pt nanotubes as well as Pt nanotubular skeletons. The distinction in Pt nanotubular skeletons is shown by the HR-TEM images as a smoothening of the rough particle surfaces seen in Pt nanotubes from annealing. TEM and HRTEM results show that the smooth surface and continuous lattice fringes along the length of the structure is a characteristic of the Pt nanotubular skeletons.

Detailed inspection of surface-structure of Pt nanotubular skeletons was conducted using HRTEM imaging. The images shown in Figure D.4c reveals a tube like structure composed of individual single crystal ligaments along the length direction, although some unreleased dislocations could also be observed (white arrows). Together with the electron diffraction, these results demonstrated a nanotubular skeleton structure with preserved five-fold twinned structure. Note that the images were band-pass filtered and color-coded to enhance the visibility of lighter contrast features.

Figure D.5 shows the TEM images of three catalysts (Pt nanotube, Pt nanotubular skeleton and Pt/C) after the durability tests (i.e., end of 3000 cycles). The cycled Pt/C catalysts showed severe particle size enlargement compared to pristine particles. This is consistent with the observed large ECSA losses in these particles (about 75 %). On the other hand, the Pt nanotubes and Pt nanotubular skeletons underwent different structural evolutions. As shown in Figure D.5*(ii, iii)*, both catalysts ultimately turned into tubular structures with diamond shape ligaments (knots) that extend continuously along the entire length of the structure. Detailed examination of the surface-structure of Pt nan-

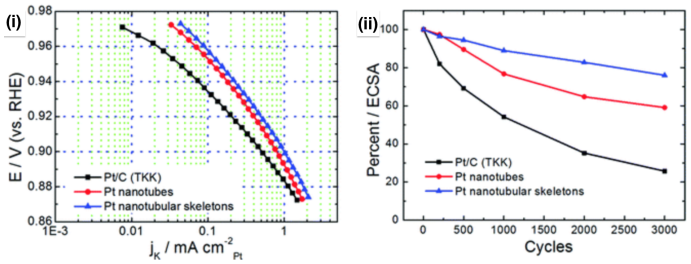

(a) (i): ORR polarization curves. (ii): % ECSA loss over cycling.

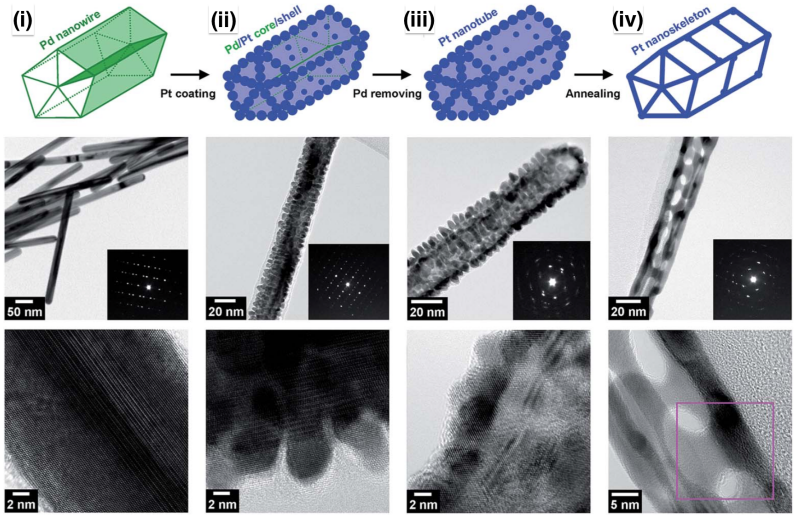

(b) TEM illustrations of different steps to synthesize Pt nanotubular skeletal structures.

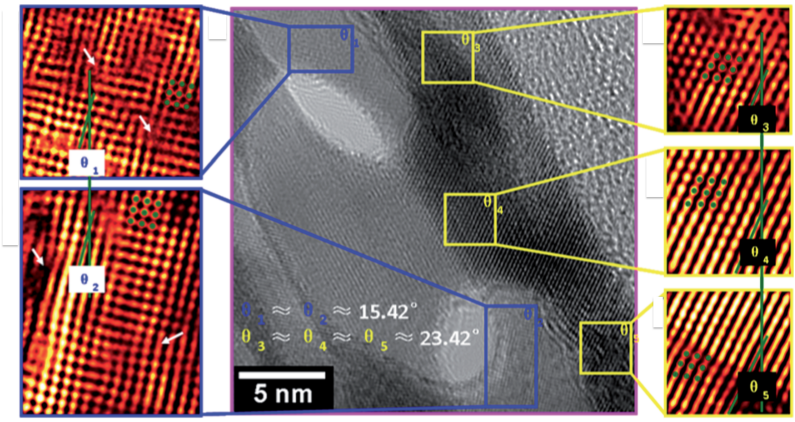

(c) Center: HRTEM image. Color coded images: band-pass filtered to enhance visibility.

Figure D.4: ORR activity measurements of Pt/C, Pt nanotubes and Pt nanotubular skeletons, and the detailed TEM characterization of the nanotubular skeleton catalyst structure. source: [442]

otubular skeletons in Figure D.5*(iii)* reveals that most of the surface is covered by atomic steps composed of high-index facets such as {210}, {310} and {311}. This is believed to be a relatively stable structure resulting from the potential cycling conditions employed that resulted in better durability with only 25 % losses in the ECSA.

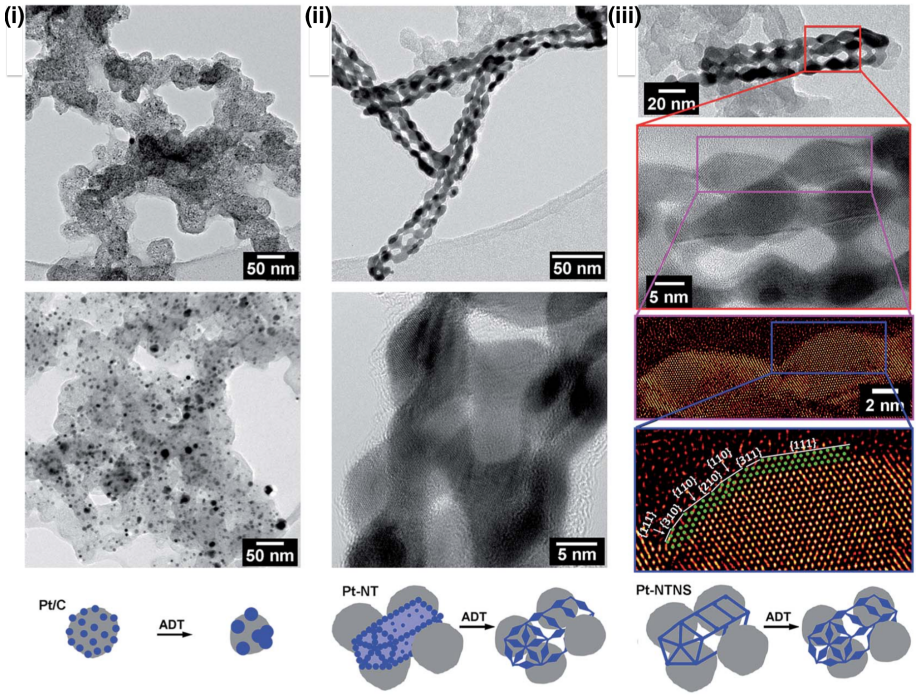

Figure D.5: Structural evolution of Pt nanotubular skeleton catalyst structure. (i) TEM images of Pt/C before and after the acceleration durability test (top and middle). (ii) TEM images of Pt nanotubes after durability testing (top and middle). (iii) TEM images of Pt nanotubular skeletons after testing (top and middle), HRTEM images were band pass filtered and color coded to enhance visibility. source: [442]

Comparing Figure D.4b*(iii)* and Figure D.5*(ii)*, it is obvious that the structural changes in Pt nanotubes is much more dramatic than that seen in Pt nanotubular skeletons. This observation is consistent with the high ECSA losses found for Pt nanotubes (40 %), and can be attributed to the higher concentration of low-coordinated Pt atoms for rough surfaces (as in Pt nanotubes) than smooth surfaces (as in Pt nanotubular skeletons). These low-coordinated Pt atoms dissolve at a faster rate during potential cycling, thus should be avoided in the design of new Pt nanostructural catalysts.

D.4 BISMUTH-DECORATED PT NANOWIRES

Collaborators Wang and Chen from University of Waterloo synthesized a novel monolithic fuel cell electrode mimicking a pine tree [443]. As schematically illustrated in Figure D.6a, the entire electrode structure consisted of several branches of pines. Each individual branch refers to a nanofiber (or carbon nanofilm), and individual pines refers to Bi-decorated Pt nanowires. While the nanofibers provide electron conductivity, the Pt nanowires provide surface area for catalysis. Additionally, the nanofibers were electrospun to form of a carbon net, which ensured good mass transport of reactant gases through many micrometer sized pores. The detailed report can be found in the published article [443]. Below I discuss the HRTEM characterization work carried out to evidence the Pt nanowire structure and the presence of Bi coating.

TEM images of Bi-decorated Pt nanowires at different magnifications is shown in Figure D.6b. Close inspection of the atomic-resolution images reveal a ultra-thin layer of Bi coating covering the surface of Pt nanowires. Additionally, a lack of ordered arrangement of the atomic columns visible suggests a lack of crystallinity in the coated Bi layer. Using EDS spectroscopy, the Bi/Pt atomic ratio was found to be 6:94. A EDS line scan across the surface confirms the presence and distribution of Bi on the surface of Pt nanowires (Figure D.6b*(right-panel)*).

Wang *et al* measured the ORR performance of these electrodes (denoted as C-PtNW-Bi), along with a similar sample but without Bi decoration (C-PtNW), and a standard Pt/C catalyst (GDL-PtB). The measured specific activities is summarized in Figure D.6c, and evidently the Bi-decorated Pt nanowires with an unique architecture (described above) showed a superior activity compared to others.

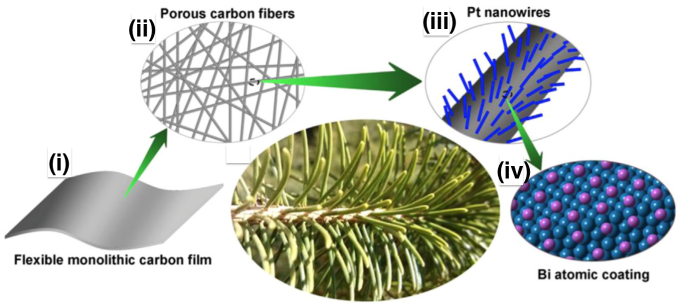

(a) Schematic representation of the synthesis process.

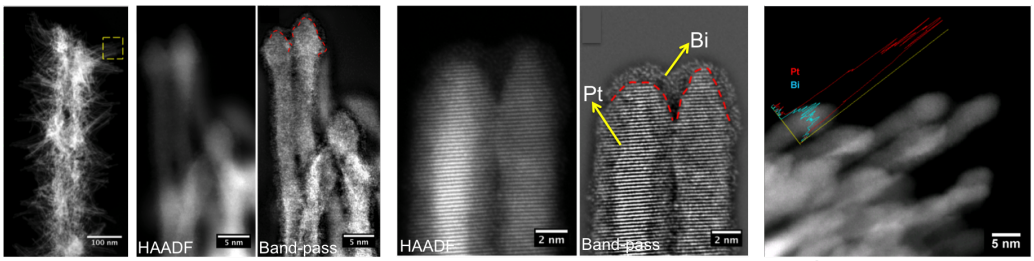

(b) Illustration of Bi-coated surface layer with HAADF-STEM imaging and EDS elemental line scan.

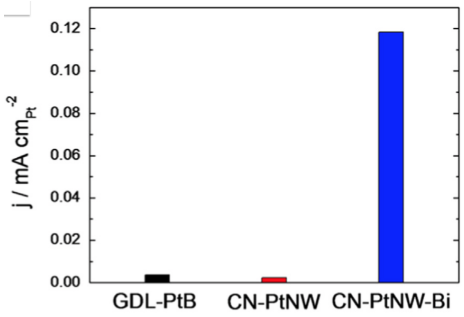

(c) Bar-chart indicating measured specific activities.

Figure D.6: ORR activity measurements, detailed HAADF-STEM imaging and EDS spectroscopy of the synthesized Bi-decorated Pt nanowires. source: [443]

E

INVESTIGATION OF PT SURFACE OXIDATION WITH ABF-STEM

As discussed in the doctoral dissertation (Section 3.1.4), the catalyst nanoparticles in PEMFCs are subjected to conditions that promote surface-oxidation (termed 'electro-oxidation'), such as (1) high oxidation potentials, (2) presence of water, and (3) a direct exposure to gas-phase oxygen [433]. The surface-oxidation of catalyst reduces the available area for further adsorption of fresh incoming oxygen molecules, and consequently decreases the electrocatalytic activity. Experiments attempting to understand Pt electro-oxidation on the nanoscopic size scales have been scarce, partly due to a lack of surface analytical techniques with atomic-resolution capability.

The mass-thickness sensitivity[1] provided by HAADF-STEM is certainly a great tool for studying the catalyst nanoparticles. While this works well for detecting heavy atoms in the matrices of light atoms, the converse is not often easy [89]. For instance, it is extremely difficult to image chemisorbed oxygen atoms against a Pt background, solely with HAADF-STEM imaging. The elastic-scattering cross section of Pt is about 20 times that of oxygen and thus, the electrons scattered by Pt dominate the signal. In a surface-oxidised Pt nanoparticle of diameter 5 *nm*, only 5 of the projected 25 atoms in an atomic column are oxygen, which is also not favourable to allow the detection of oxygen atoms.

In the recent past, the annular bright field (ABF) imaging for detecting low-Z elements has attracted much interest for permitting direct visualization of light elements in the presence of heavier elements [434, 435]. For example, H-atoms in the metal hydrides (YH_2 and VH_2), O-atoms in a $SrTiO_3$ crystal and lithium columns in lithium metal oxides (LiV_2O_4 and $LiCoO_2$) have been seen within heavy element rich environments [436–439]. In addition to experiments, a considerable research have been made in the development of the required theoretical formulations to interpret the ABF image contrast [440]. With its optimum sensitivity towards both heavier and lighter elements, the ABF technique can be expected to also serve as an ideal analytical tool for studying the surface-oxidation in Pt/Pt-alloy nanocatalysts. However, to the best of our knowledge no such research effort

[1] Intensity as a function of the number of atoms viewed in projection and their atomic-numbers

has been undertaken so far. In the following sections I discuss some preliminary work carried out in this direction.

The preliminary analyses is presented thus, Section E.1 and Section E.2 describes the ways in which implementing ABF imaging in a STEM is possible. Section E.3 explore the dynamics of ABF contrast with the varying specimen thickness and defocus with the aid of multislice simulations. Section E.2 discusses the method and parameters used in simulations. Sections Section E.4 and Section E.5 present the simulated ABF images of two case studies: (a) single-crystal PtO nanoparticles, and (b) surface-oxidised Pt nanoparticles, respectively. Finally, the Section E.6 discusses simultaneous acquisition of the ABF-STEM and HAADF-STEM images over a real specimen (PtO_x particles deposited on Poly-Pt substrate).

E.1 DIFFERENT APPROACHES TO ABF IMAGING IN STEM

Figure E.1 shows schematic illustrations of three prominent approaches that can be followed to implement ABF in STEM (termed ABF-STEM imaging). α is the convergence semi-angle of the incident STEM electron probe. β_{inner} and β_{outer} are the inner and the outer collection semi-angles of the annular detectors (ADF, HAADF, ABF). Typically, α = 22 *mrad* for a STEM electron probe that is focussed to sub-angstrom dimensions, while the β_{inner} is about 60 *mrad* and 120 *mrad* for ADF and HAADF detectors, respectively. Since $\beta_{ADF/HAADF,inner} > \alpha$, the collection range of ADF and HAADF detectors lie outside the illumination cone of the focussed electron probe.

Figure E.1*(a)* illustrates ABF-STEM that is implemented with the aid of a dedicated detector. $\beta_{ABF,inner}$ and $\beta_{ABF,outer}$ are the inner and outer collection semi-angles of the ABF detector. $\beta_{HAADF,inner}$ is the inner collection semi-angle of the standard HAADF detector. In STEM, the ABF imaging is implemented by setting its inner detector semi-angle ($\beta_{ABF,inner}$) to a value equal to half of the convergence semi-angle of the incident electron probe (i.e., $\beta_{ABF,inner} = \alpha/2$), while the $\beta_{ABF,outer} = \alpha$. Therefore, the collection range of ABF detector spans within the illumination cone of the focussed electron probe (i.e., $\alpha/2 < \beta_{ABF} < \alpha$) [434–440].

Figure E.1*(b, c)* illustrate alternative approaches to implementing ABF-STEM without the need for a dedicated detector. The first approach shown in Figure E.1*(b)* involves utilizing the traditional bright field (BF) detector, but in conjunction with a beam stop [440]. However, it is important to note that the geometry of beam-stop is constrained so

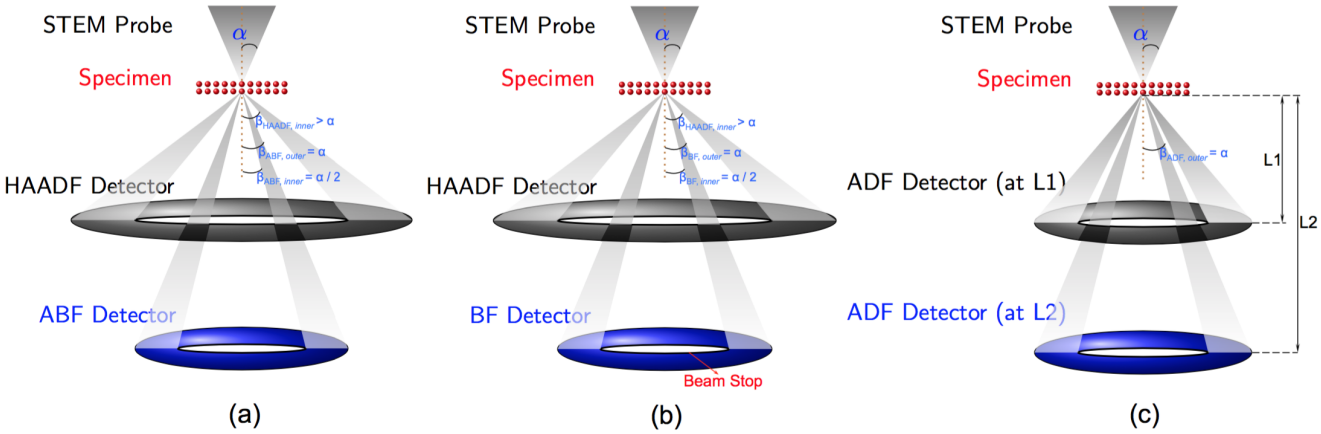

Figure E.1: Schematic illustration of prominent ABF-STEM approaches. (a) using dedicated ABF detector. (b) using BF detector in conjunction with a beam-stop. (c) by increasing the camera length of ADF detector.

as to ensure that the $\alpha/2 < \beta_{BF} < \alpha$. The second approach (Figure E.1*(c)*) is based on the principle that the collection range of the annular detectors can be adjusted by changing the camera length (L) [440]. Herein, a standard annular dark field (ADF) detector is used to collect the scattered electrons and its camera length (L) is increased from L1 to L2 as shown in Figure E.1*(c)*, so as to reach an outer collection semi-angle that is equal to α (i.e., β_{ADF}, outer = α). In such an acquisition, it is even possible to collect the energy loss electrons that are passing through the center hole.

E.2 MULTISLICE SIMULATIONS

In the case of coherent imaging techniques (for instance, BF-TEM), the contrast generated can undergo a reversal with the varying specimen thicknesses and defocus values; hence, the image interpretation is not obvious [147, 383, 384]. To correlate the observed contrast with the crystal structure, it is then necessary to perform image simulations. In this work, we adopt multislice approach to simulate the HAADF-STEM and ABF-STEM images. The HAADF-STEM imaging is well known to be an incoherent image formation technique with no contrast reversal from the changing defocus and specimen thickness. It is the suppression of coherence effects in the case of ABF-STEM that we need examine.

For simulations, an incident electron probe of 300 keV energy with 18 *mrad* convergence semi-angle (α) was considered. The outer and the inner collection semi-angles of the ABF-STEM detector were set to 18 *mrad* and 9 *mrad* respectively. Similarly, the HAADF detectorg geometry was set to $\beta_{HAADF,outer}$ = 180 *mrad* and $\beta_{HAADF,inner}$ = 120 *mrad*. The crystal lattice was modeled using *CrystalMaker* commercial software.

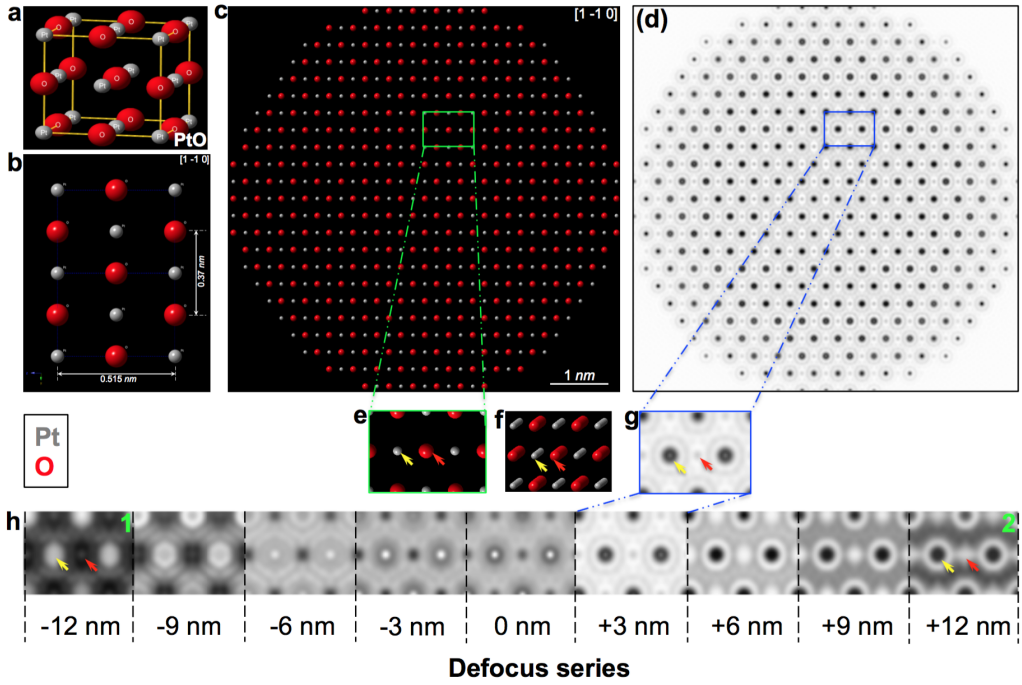

Figure E.2: Dynamics of ABF-STEM image contrast with the changing defocus. (a) PtO FCC unit-cell (a = b = c = 5.15 Å). Pt and O atoms are identified by gray and red spheres, respectively. (b) PtO unit-cell viewed along $1\bar{1}0$ zone-axis. (c) 2D projected image of the modeled PtO nanoparticle (size~6 *nm*) along $1\bar{1}0$ zone-axis. (d) Multislice simulated ABF-STEM image of (c). (e and g), cropped images from the green window marked in (c) and (d), respectively. (f), off-axis tilted view of atomic-columns visible in (e). (h) Simulated ABF-STEM images of (e) at varying defocus values ranging from -12 *nm* to +12 *nm*.

E.3 DYNAMICS OF ABF-STEM CONTRAST WITH CHANGING THICKNESS AND DEFOCUS

Figure E.2 and Figure E.3 illustrate the dynamics of ABF-STEM image contrast with the changing defocus values and specimen thicknesses (discussed below).

Single-crystal platinum oxide (PtO) was used as the candidate material, and its face centered cubic (fcc) unit cell with a = b = c = 5.15 Å is shown in Figure E.2*(a)*. The gray and red spheres indicate Pt and O atoms respectively, and the indicated sizes are based on the corresponding crystal radii of Pt (0.71 Å) and O (1.21 Å). PtO was chosen as a test candidate owing to its simple fcc structure and visibility of O atomic-columns separated out distinctly from the Pt columns along $1\bar{1}0$ at all particle sizes. Figure E.2*(b)* shows the PtO unit-cell oriented along $1\bar{1}0$ zone-axis. With this unit-cell, a nanoparticle of size ~6 *nm* was modeled as illustrated by its 2D projection along $1\bar{1}0$ shown in Figure E.2*(c)*. ABF-STEM images of this particle were simulated at defocus values ranging between -12 *nm* to +12 *nm*. Figure E.2*(d)* shows one such multislice-simulated ABF-STEM image, calculated at a defocus value of +3 *nm*. For better visibility and comparison, an identical region from Figure E.2*(c, d)* is enlarged as shown in Figure E.2*(e, g)*, respectively. The yellow and red arrows in Figure E.2*(e)* indicate the locations of pure Pt and O atomic-columns, respectively. The fact that there was no intermixing of Pt and O atoms within each of these atomic-columns can be confirmed by a off-axis tilting of the region in Figure E.2*(e)*, as shown in Figure E.2*(f)*. Hence, the ABF-STEM image contrast at these locations should correspond to pure atomic-columns of Pt and O, solely.

By comparing Figure E.2*(e, g)*, it can be observed that in ABF-STEM image (defocus +3 *nm*), the atomic-columns corresponding to O (red arrow) appears with a lighter-gray contrast, whereas those of Pt (yellow arrow) appear with darker-gray contrast. This suggests that theoretically the ABF-STEM can offer a direct visualization of O together with Pt.

Panels shown in Figure E.2*(h)* are the ABF-STEM simulated images corresponding to region in *fig. (2e)*, but calculated at different defocus values in the range -12 *nm* to +12 *nm*. By comparing the yellow (Pt column) and red (O column) arrows indicated in panels 1 (defocus -12 *nm*) and 2 (defocus +12 *nm*), it is evident that the contrast has undergone a reversal. While the contrast for O-columns is darker at defocus -12 *nm*, their contrast at defocus +12 *nm* is lighter. Vice-versa, for atomic-columns of Pt. Clearly, this demonstrates that the coherence effects are not suppressed in ABF-STEM, with respect to the changing defocus.

Figure E.3*(a)* provides a quantitative treatment of the observed variation in contrast with defocus, by plotting the ABF-STEM scattered intensities (seen in Figure E.2*(h)*) for Pt and O atomic-columns across varying defocus values. Trends corresponding to Pt and O are represented by dotted blue and red lines, respectively; and the intensity values are normalized such that a value of +1 and 0 indicate brightest and darkest ABF-STEM intensity, respectively. With the changing defocus value from -12 *nm* to +12 *nm*, these trend-lines for both Pt and O highlight the contrast reversal in the ABF-STEM images. Additionally, the difference between the Pt and O ABF-STEM intensity at each defocus value (green line) is useful in calculating the optimal defocus range (ODR) for ABF-STEM imaging.

The ODR refers to that range of defocus values wherein the contrast for a particular atomic-column might suffer a lowering in the intensity (dimness) but not a contrast reversal. With the observed sensitivity of ABF-STEM towards defocus values, the ODR provides a useful window to the microscopist, within which various other microscopic parameters (such as Z-height) can be tuned, and at the same time, obtain images whose contrast can be correlated with the structure, reliably. The ODR extends between the defocus values at the maximum and the zero intensity. From Figure E.3*(a)*, it is clear that the ODR (indicated by the green window) lies between the defocus values of -3 *nm* (intensity = 0.6) and +1.5 *nm* (intensity = 0).

In the above discussion, it was shown that the coherence effects with respect to changing defocus are still not suppressed in ABF-STEM imaging, consistent with earlier reports by Findlay *et al* [438, 440]. It is also equally important to examine the variation in ABF-STEM image contrast with the specimen thickness; because, unlike defocus, the thickness is not a tunable parameter in the hands of a microscopist.

Figure E.3*(b)* illustrates the variation in ABF-STEM contrast at varying thicknesses while the defocus is fixed to 0 *nm*. Simulations were carried out on the modeled crystal slabs (along $1\bar{1}0$) of varying thicknesses. A maximum thickness of 7 *nm* was chosen so as to cover the range of particle sizes intended towards the ORR. The region shown in Figure E.3*(b1)* represents the 2D projected view (along $1\bar{1}0$) of a small area (0.515 *nm* x 0.37 *nm*) extracted from the modeled slabs. With the aid of the dashed blue boxes overlaid in Figure E.3*(b2)*, the same area is being tracked at varying thicknesses. The yellow arrows shown identifies the location of a pure Pt atomic-column, and a careful observation reveals that the ABF-STEM contrast is not reversed with the varying thicknesses (5, 6, and 7 *nm*). Hence, although ABF-STEM is not fully suppressed by the coherence effects in terms of its sensitivity towards defocus values, it shares with HAADF a relative

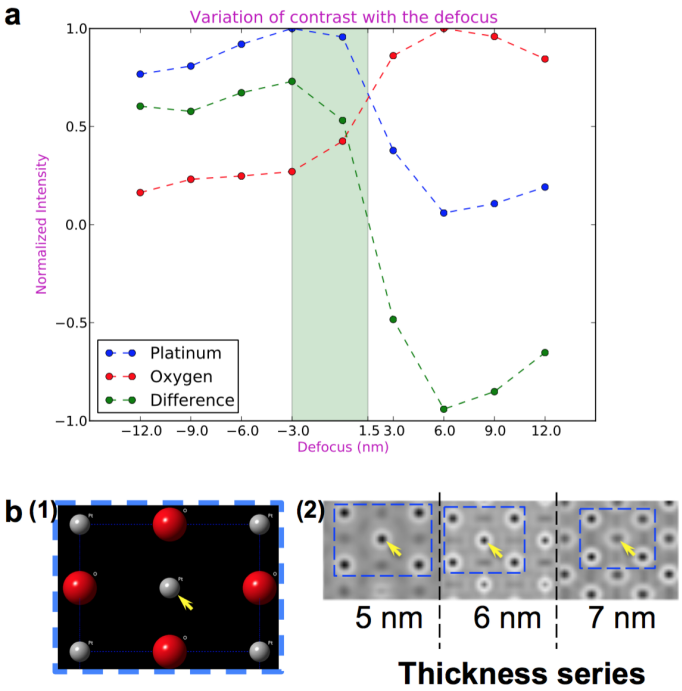

Figure E.3: Dynamics of ABF-STEM image contrast with the changing defocus values and specimen thicknesses. (a) Quantified ABF-STEM intensity plotted as a function of changing defocus values. Trendlines in blue and red correspond to intensities of Pt and O atomic-columns (of constant thickness), respectively. b(1), 2D projected area along $1\bar{1}0$ from the modeled crystal slab. b(2), ABF-STEM simulations at varying slab thicknesses. The dashed blue box in each panel correspond to 2D area shown in b(1). Yellow arrows in b(1) and b(2) identify the location of a pure Pt atomic- column.

insensitivity to particle sizes. This is consistent with the recent work by Findlay *et al* [440] where they studied the dynamics of ABF-STEM contrast on $SrTiO_3$.

The above findings uncover a remarkable benefit of employing ABF-STEM to study surface-oxidation, as opposed to conventional coherent imaging techniques. While operating within the optimal defocus range (ODR) it is possible to detect both Pt and O simultaneously, for a range of particle sizes of catalytic interest. Having realized this unique ability of ABF-STEM imaging, we performed case studies on (1) PtO single-crystal nanoparticles and (2) the surface oxidized Pt nanoparticles, discussed as follows.

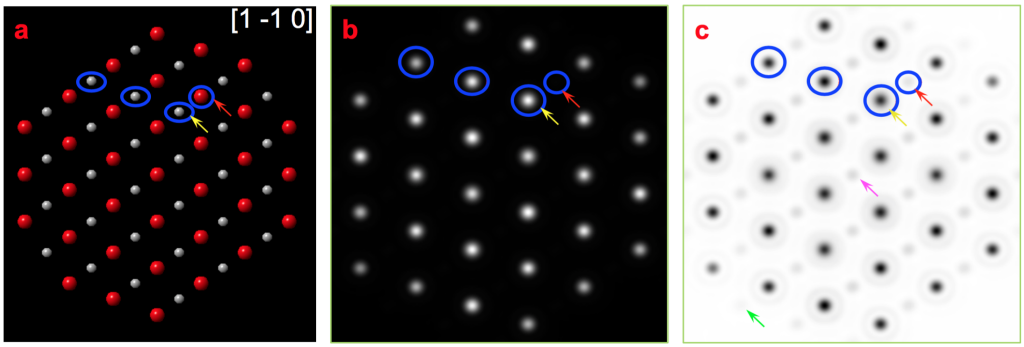

Figure E.4: Multislice simulated HAADF-STEM and ABF-STEM images of a modeled PtO nanoparticle viewed along $1\bar{1}0$ zone-axis. (a) Modeled PtO nanoparticle of size ~ 3 *nm* oriented along $1\bar{1}0$. (b) simulated HAADF-STEM image of (a). (c) simulated ABF-STEM image of (a). Yellow and red arrows indicate pure atomic-columns of Pt and O, respectively. Pink and green arrows in (c) identify an O atomic-column in the core and the shell regions, respectively.

E.4 ABF SIMULATIONS OF SINGLE-CRYSTAL PTO NANOPARTICLE

Figure E.4*(a)* illustrates the modeled PtO nanoparticle (size = 3 *nm*) lattice viewed along $1\bar{1}0$ zone-axis. The corresponding HAADF-STEM and ABF-STEM simulated images are shown in *Figs. (4b, 4c)*. The blue circles in Figure E.3*(a–c)* compare identical locations, and the arrows in yellow and red indicate atomic-columns of Pt and O, respectively. By comparing the red arrows in *Figs. (4b, 4c)*, it is clear that the HAADF-STEM imaging fails to detect the presence of O together with Pt, while the ABF-STEM can be seen to provide a lighter-gray contrast for O atomic-columns. Also, by comparing an O atomic-column at the core (pink arrow in *Fig. (4c)*, 5 atoms thick) and the shell (green arrow in *Fig. (4c)* 2 atoms thick), the intensity can be observed to decrease in proportion with the thickness, demonstrating the thickness-contrast sensitivity of the ABF-STEM technique.

E.5 ABF SIMULATION OF SURFACE-OXIDISED NANOPARTICLES

Figure E.5 illustrates the case study on two variety of Pt nanoparticles composed of - (1) ~3 *nm* Pt-core, ~1 *nm* O-shell, oriented along $1\bar{1}0$ as shown in *Fig. 5(a)*, and (2) ~9 *nm* Pt-core, ~1 *nm* O-shell, oriented along [111] as shown in *Fig. 5(c)*. Detailed analyses on the simulated ABF-STEM and HAADF-STEM results are discussed as follows.

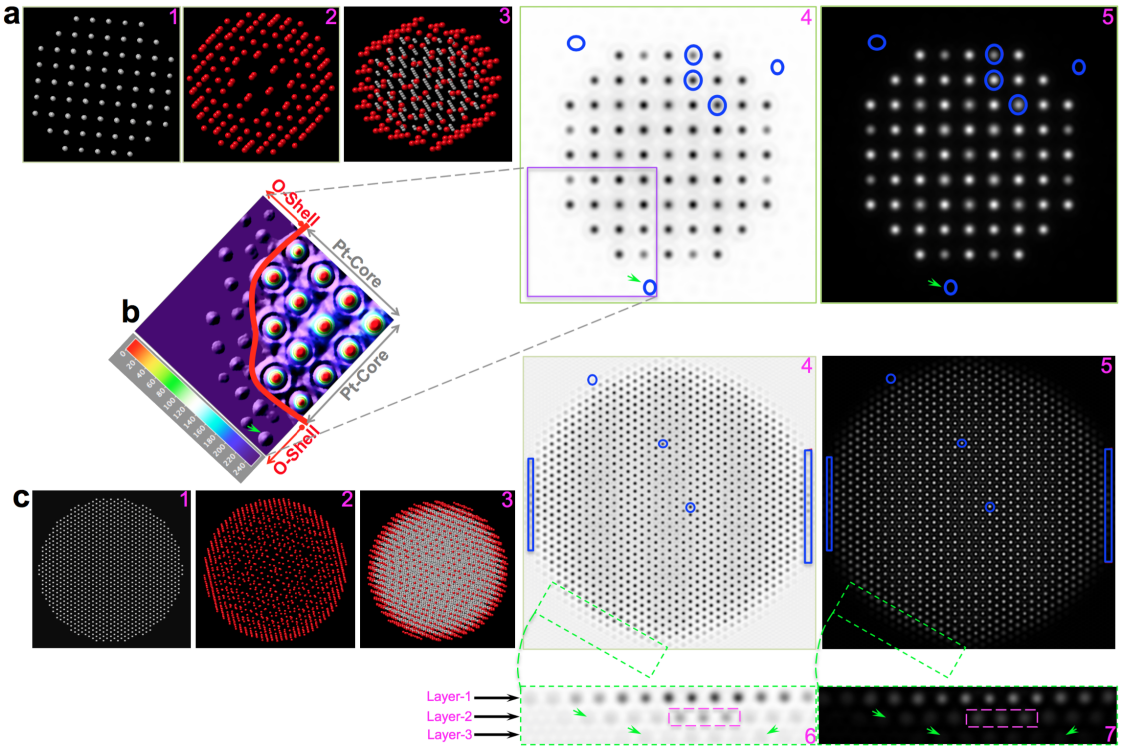

Figure E.5: ABF-STEM and HAADF-STEM simulations of surface-oxidized Pt nanoparticles. (a) and (c), correspond to data-sets of two different modeled particles of sizes ~ 5 *nm* and 10 *nm*, respectively. a(1) and c(1), Modeled Pt-cores of size 4 *nm* and 9 *nm*. a(2) and c(2), Modeled O- shells of size 1 *nm*. a(3) and c(3), Atomic-models with O-shell overlayed on Pt-core. a(4) and c(4), ABF-STEM image simulations. a(5) and c(5), HAADF-STEM image simulations. b, 2D Surface-plot of the boxed region in a(4). c(6) and c(7), Magnified images of the boxed regions in c(4) and c(5), respectively.

Firstly, as shown in *Fig. 5(a1)*, a 3 *nm* (diameter) pure-Pt nanoparticle was considered with an orientation along $1\bar{1}0$. Onto this, ~1 *nm* thick surface-oxide shell was created (*Fig. 5(a2)*) to form a core-shell type structure (*Fig. 5(a3)*). The corresponding ABF-STEM and HAADF-STEM simulated images are shown in *Figs. 5(a4, a5)*, respectively. The atomic-columns of Pt appear with brighter and darker intensities in the HAADF-STEM and ABF-STEM images, respectively. The blue circles compare identical atomic-columns in both the images, while the green arrow identifies an O atomic-column at the surface. Clearly, the HAADF-STEM image (*Fig. 5(a5)*) does not reveal any intensity for surface O atomic-columns. In the case of ABF-STEM image (*Fig. 5(a4)*) however, although the intensities for surface O is certainly detectable, the values are very close to that of background and hence, remains invisible to naked eyes. We overcome this by re-plotting the ABF-STEM

image as a 3D surface-plot (x and y: position, z: intensity) as shown in the *Fig. 5(b)*, for a small region extracted from *Fig. 5(a4)* (within purple box). As indicated by the color bar, the image has been color coded such that the lowest (value: 0) and highest intensities (value: 256) span between red and purple colors, respectively. From a careful reading of the labels marked in *Fig. 5(b)*, it is clear that a simultaneous detection of both the projected Pt-core (along $1\bar{1}0$) and the O-shell is possible with ABF-STEM. For instance, at the location indicated by green arrow in *Fig. 5(b)*, an O atomic-column has now been clearly identified, unlike that in the HAADF-STEM image (*Fig. 5(a5)*).

Figure E.5*(c)* illustrates the simulation results of the second variety of Pt nanoparticle, composed of ~9 *nm* Pt-core (Figure 5c(1)) covered by ~1 *nm* thick O-shell (*Fig. 5(c2)*) and oriented along [111]. The orientation along [111] was chosen so that the atomic-columns are composed of a mixture of both Pt and O atoms; unlike that in $1\bar{1}0$ discussed earlier. The modeled Pt-core and O-shell are overlaid to form a core-shell type structure (*Fig. 5(a3)*). The corresponding ABF-STEM and HAADF-STEM simulated images are shown in *Figs. 5(c4, c5)*, respectively; with the blue and green markings identifying identical locations in both the images. To obtain a more detailed comparative picture, the identical regions within the green boxes marked in *Figs. 5(c4, c5)* are magnified and shown in *Figs. 5(c6, c7)*, respectively. Noticeably, these images represent the same region, and illustrate ABF-STEM and HAADF-STEM intensities of atomic-columns from the 3 top-most surface layers (in the order 3-2-1, referring to pink labels noted).

The three atomic-columns within the dotted pink boxes marked in *Figs. 5(c6, c7)* are composed of a mixture of Pt and O atoms; this information is available from the atomic-model created (Figures 5c(1) and 5c(2)). By comparing these columns in *Figs. 5(c6, c7)*, it can be seen that the intensities are observed in both the images, confirming that both ABF-STEM and HAADF-STEM techniques can detect a non-pure atomic column (mixing of both Pt and O atoms). Finally, the green arrows in *Fig. 5(c7)* indicate atomic-columns composed of O atoms solely. A close observation of the intensities at these locations in both the images (*Figs. 5(c6, c7)*) reveal that ABF-STEM enabled their detection while the HAADF-STEM did not provide any intensity; consistent with the multislice simulation results discussed earlier.

Overall, the case study on two varieties of surface-oxidized particles discussed above suggests that the ABF-STEM technique (unlike HAADF-STEM) can identify the presence of O-shell residing on the Pt nanoparticles. As mentioned earlier, this capability then holds a great potential to investigate the electro-oxidation problem faced in PEMFCs.

E.6 SIMULTANEOUS ABF-STEM AND HAADF-STEM ACQUISITION ON REAL SPECIMEN

In addition to the image simulations, we also undertook the task of performing ABF-STEM on a real specimen. Unfortunately, the synthesis of PtO nanoparticles was extremely challenging, since Pt does not form stable oxide phases. The formation and stability of PtO, PtO_2 and Pt_3O_4 species has been extensively investigated in the past [444]. The standard enthalpies of formation of these phases are reported to be: PtO (-71 kJ/mol), PtO_2 (-134 $\pm$ 42 kJ/mol) and Pt_3O_4 (-268 $\pm$ 100 kJ/mol) [445–449], and consequently, the thermodynamic stability follows the trend PtO < PtO_2 < Pt_3O_4. Seriani *et al* [450] have further shown that the thermal decomposition of PtO_2 phase follows the trend $PtO_2 \longrightarrow Pt_3O_4 \longrightarrow$ Pt. On the nanoscale, the situation could be much worse, due to high surface chemical potentials (due to small sizes), and an enhanced mass-transport (promoted by mechanisms such as Ostwald ripening and coalescence). For instance, the formation of PtO_x species is suggested to accelerate coarsening of Pt nanoparticles during annealing in O_2 atmosphere as opposed to that under a reducing H_2 [96, 451]. Owing to these practical difficulties involved with thermal-based and O_2 plasma exposure syntheses, alternative methods were employed in the present study, for enabling direct visualization of Pt and O with ABF-STEM.

Our approach involved imaging the Pt oxide particles that were grown on a polycrystalline Pt substrate. The oxide was grown under potentiostatic conditions (in aqueous solution) by applying a constant polarization potential, for a controlled time, and a fixed temperature range.[2]

$$\boxed{Pt\,(s) + H_2O\,(l) \longrightarrow Pt^{\delta+}_{surf}\text{—}O^{\delta-}_{chem} + 2H^{+}(aq) + 2e^{-}} \tag{E.1}$$

Greater details on the synthesis is described in a recent work by Furuya *et al* [452], but few key points on the lattice-structure can be noted as follows. As per the literature [452], the grown Pt oxide particles form a quasi-3D lattice comprising of Pt^{2+} and O^{2-}; following an interfacial place exchange mechanism between the electro-adsorbed O (chemisorbed-O, O_{chem}) and the Pt surface atoms (Pt_{surf}) from the Poly-Pt substrate.

$$\boxed{Pt^{\delta+}_{surf}\text{—}O^{\delta-}_{chem} \longrightarrow \left(Pt^{2+}\text{—}O^{2-}\right)_{quasi-3D\,lattice}} \tag{E.2}$$

[2] The synthesis was carried out by collaborators Jerkiewich *et al* from Queens University.

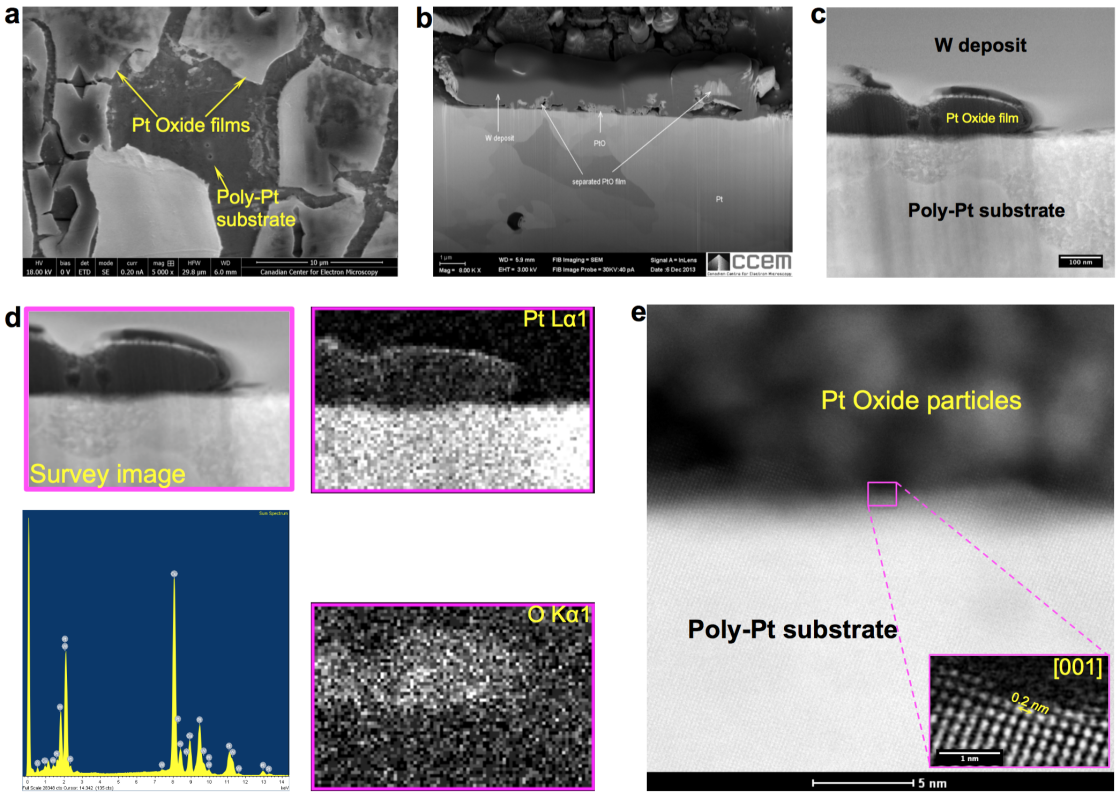

Figure E.6: Pt oxide particles deposited on Poly-Pt substrate. (a) SEM image of the sample illustrating Pt oxide film (brighter contrast) deposited on Poly-Pt (darker contrast) substrate. (b and c) HAADF-STEM images of the FIB'd section revealing Poly-Pt | Pt oxide | W interface, respectively. (d) EDS mapping of Pt-L and O-K line over an area shown in the *survey image*. (e) Atomic-resolution HAADF-STEM image illustrating Pt oxide | Poly-Pt interface. Inset image (band-pass filtered) shows the interphase at an atomic- resolution. Poly-Pt is oriented along 001 zone-axis.

Since the above lattice-structure was comprised of both Pt and O, we thought it to be suitable to perform experimental ABF-STEM imaging on these particles. Figure E.6*(a)* shows an SEM image identifying the Pt oxide films (lighter contrast) on the Poly-Pt substrate (darker contrast). As shown in Figures *6(b)* (low-mag SEM image) and *6(c)* (low-mag HAADF-STEM image), a FIB (focused ion beam) was prepared to analyze the Pt oxide | Poly-Pt substrate interface. HAADF-STEM is a Z-contrast imaging tool with intensities proportional to $Z^{1.7}$. Hence, as evident from *Figs. 6(c)*, the Pt oxide region and Poly-Pt substrate appear with darker and brighter intensities, respectively; suggesting that the Pt oxide region is O-rich. This is further confirmed by the STEM-EDX mapping of Pt (Lα) and O (Kα) profiles over a Pt oxide | Poly-Pt region, as shown in the *Fig. 6(d)*. The HAADF-STEM image illustrated in *Fig. 6(e)* provides an atomic-resolution visualization of the Pt oxide | Poly-Pt region. Atomic-columns with bright intensities (lower half) confirm pure-Pt lattice oriented along [001] zone-axis (see inset figure for clarity, d-spacing = 0.2 *nm*). The upper half corresponds to region with Pt oxide particles appearing with darker intensities and out of focus, expected due to smaller elastic-scattering angles from the O-rich quasi-3D Pt oxide lattice that leads to poor collection of the transmitted electrons by HAADF detector ($\beta_{HAADF,inner}$ = 120 *mrad*).

Figure E.7 illustrates a simultaneous acquisition of the ABF-STEM and the HAADF-STEM images, over an identical location in the Pt oxide lattice and Poly-Pt substrate. The ABF-STEM was performed by implementing the approach described in Figure E.1*(c)* earlier, wherein the camera lengths of the ADF detector could be changed so as to reach an outer collection semi-angle that is equal to (i.e., $\beta_{ADF,outer} = \alpha$). The defocus was kept constant at zero. Upon comparing the ABF-STEM (*Fig. 7(a)*) and HAADF-STEM (*Fig. 7(b)*) images of the Pt substrate (oriented along [001]), it is clear that the pure-Pt atomic-columns appear with bright (in HAADF-STEM) and dark (in ABF-STEM) intensities. Similar imaging over the Pt oxide particles reveals that the O-rich Pt oxide lattice appears with bright and dark intensities in ABF-STEM (*Fig. 7(c)*) and HAADF-STEM (*Fig. 7(d)*) images, respectively. These findings validate with the observed image contrast in the multislice simulations presented earlier (Figure E.4, O and Pt atomic-columns appearing with brighter and darker intensities). Furthermore, unlike HAADF-STEM (*Fig. 7(d)*) wherein the Pt oxide particles appear out of focus, the ABF-STEM (*Fig. 7(c)*) provides a sufficient depth of field, owing to adequate collection of electrons passing through O atomic-columns that are scattered at low-angles. Also noticeable is that the ABF-STEM could keep even the Pt substrate in focus (*Fig. 7(a)*), unlike HAADF-STEM where only Pt substrate was in focus but the Pt oxide particles were completely out of focus. This again, is a unique ability offered by the ABF-STEM technique. Further, the *Fig. 7(e)* is

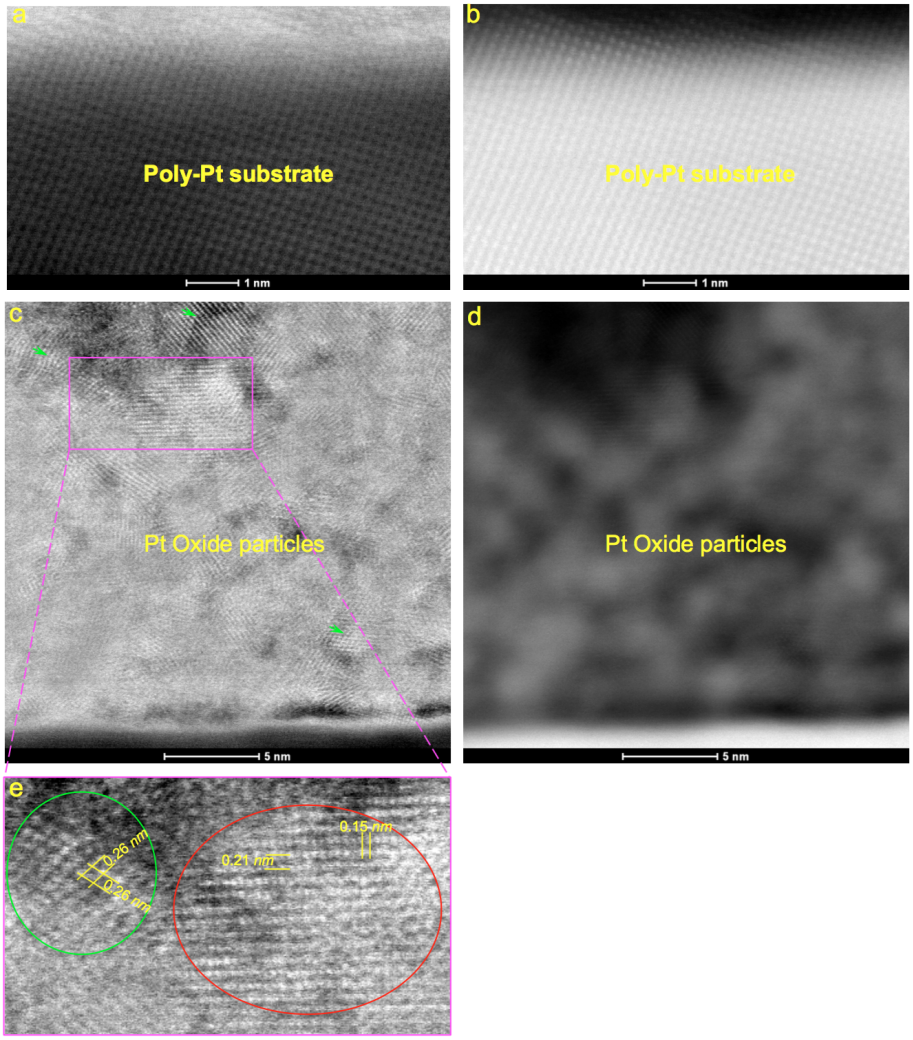

Figure E.7: Simultaneous ABF-STEM and HAADF-STEM imaging of Pt oxide particles and Poly-Pt substrate. (a and c) ABF-STEM images of Pt oxide particles and the Poly-Pt substrate, respectively. (b and d) Corresponding HAADF-STEM images. (e) Magnified image of the boxed region in (c).

a magnified image of the boxed region (highlighted in pink) in *Fig. 7(c)*. The sizes of the atomic-columns in the region encircled in green appear larger compared to the sizes of the atomic-columns within the region encircled in red. As labeled in *Fig. 7(c)*, the measured lattice spacings in these locations are also different; larger for the region encircled in red. These observations suggest that the lattice is composed of dissimilar atoms, possibly an intermix of both O and Pt atoms and in which case, corroborates with the proposed quasi-3D lattice for the Pt oxide particles.

From the green arrows pointed in *Fig. 7(c)*, it can also be seen that the particles were oriented in multiple zone-axes. This made it difficult to tilt onto a suitable zone-axis (such as $1\bar{1}0$) and perform ABF-STEM on pure columns of Pt/O. Note also that within the field of view of *Fig. 7(a)* (Pt substrate) and *Fig. 7(c)* (Pt oxide particles), a range of specimen thicknesses ranging from nanoparticles to bulk material have been imaged with ABF-STEM, and clearly, the contrast is not reversed; corroborating with our earlier inference (from multislice simulations) that ABF-STEM shares an insensitivity towards varying thicknesses with the HAADF-STEM imaging.

E.7 SUMMARY AND OUTLOOK

In summary, the prospects of employing ABF-STEM imaging technique to investigate surface-oxidation of Pt nanocatalysts in fuel cells (also termed, electro-oxidation) is discussed. Our results indicate that the ABF-STEM is relatively insensitive to varying specimen thickness. ABF-STEM contrast is sensitive to changing defocus, which by choosing a suitable defocus range (optimal defocus range (ODR)) can be easily overcome. Using multislice simulations, we discussed the use of ABF imaging to detect oxygen in (a) single-crystal PtO nanoparticles, and (b) surface-oxidized Pt nanoparticles. Our findings show that the chemisorbed O-shell on Pt nanoparticles can be visualized using ABF-STEM unlike HAADF-STEM technique. Using an aberration-corrected TEM, simultaneous acquisition of ABF-STEM and HAADF-STEM images was carried out over a real PtO_x specimen. Although acquisition of ABF images was practically feasible, owing to high beam sensitivity of the specimen the oxygen atoms in the specimen could not be located. In future, we propose to carry out similar analyses on much stable specimens such as some Pt-alloy catalysts with mixed surface structures, e.g. surface oxidised Pd-Pt alloy shell yielding stable PdO sites for ABF analyses.

F

GLOBAL ENERGY DEMAND AND ITS ENVIRONMENTAL IMPLICATIONS

ENERGY can be classified into three broad categories [453]. First, the energy derived from photo-physical/chemical sources that rely either on oxidising some reduced substance (e.g., combustion of fossil fuels), or absorbing sunlight to generate heat and electricity (e.g., solar). Second, the energy derived from nuclear reactions, by either splitting a heavy nucleus or fusing light nuclei. Third, the thermomechanical energy which is derived from geological sources such as wind and water. Typically, the energy generated from the chemical/photophysical reaction is about a fraction of an electron-volt (*eV*), that from a nuclear reaction is on the order of a Mega-electron-volt (*MeV*[1]), and that from a thermomechanical process is few milli-electron-volts (*meV*[1]).[2]

Combustion of fossil fuels is the primary source of global CO_2 emissions. Presently, the fossil fuels are the most consumed energy source in the world. This is best illustrated with the help of an energy flow chart shown in Figure F.1a. Here, the global energy flow is mapped according to sources, transformation processes, and the end uses. In the year 2013, the global energy consumption was about 786992 Peta-Joules (PJ)[3] [454]. Of which, over 80 % has been transformed into heat, electricity, or transportation, by means of fossil fuel combustion[4] [1]. In the process, carbon-dioxide (CO_2) released into the atmosphere was about 31.9 $GtCO_2$ (Giga-tonnes), of which about 98 % was from fossil fuel combustion alone (oil (33 %), coal (46 %), gas (20 %). Realizing this the United Nations (UN) Intergovernmental Panel on Climate Change (IPCC) has ascertained (to 90

[1] 1 *MeV* = 10^6 eVs; 1 *meV* = $(1/1000)^{th}$ eV

[2] per elementary reaction/process basis.

[3] 1 Peta-Joule = 10^{15} Joules. This is equivalent to about 50 megatons of TNT, which is about the same energy as that produced by *Tsar Bomba*, the Hydrogen bomb created and tested by the then Soviet Union in 1961. The *Tsar Bomba* is considered to be the 'single most physically powerful device ever deployed by mankind'.

[4] Contribution to energy supply from other sources: 9 % from nuclear plants, and the remaining 11 % from renewable sources, such as hydro, wind, solar, biofuels, geothermal, wave, and tidal power

% certainty) that the combustion of fossil fuels to produce energy is the primary source of anthropogenic CO_2 emissions [2].

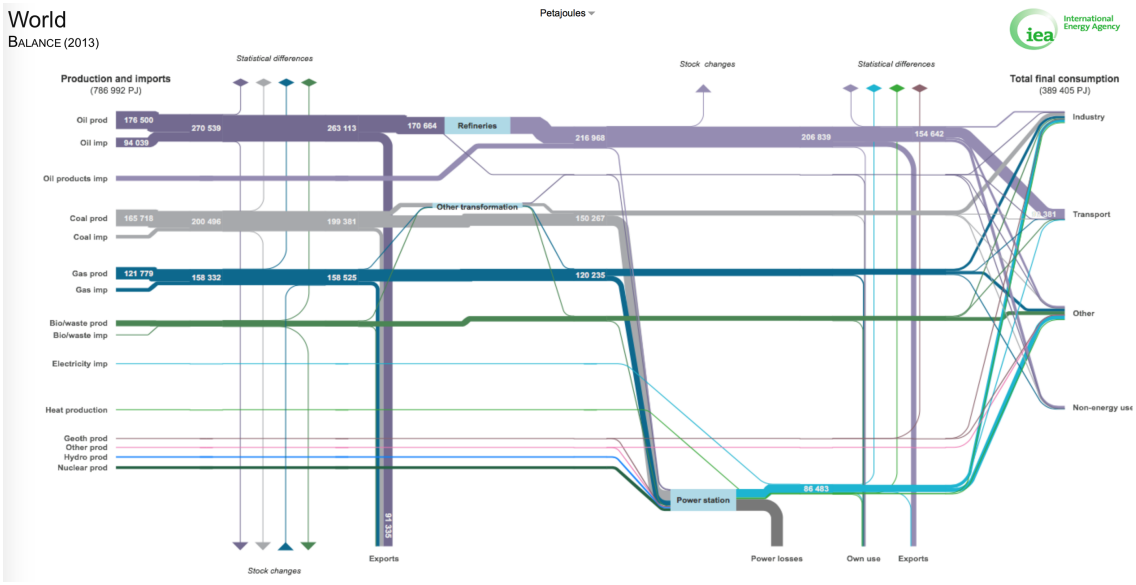

(a) Global energy flow chart for the year 2013. source: [454]

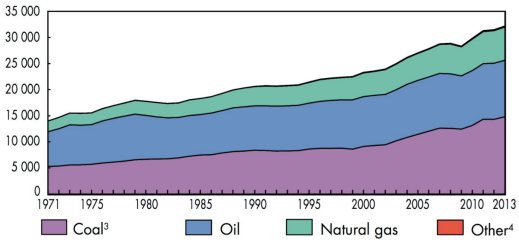

(b) Global CO_2 emissions (Mt) from 1971 to 2013 by fuel. source: [1]

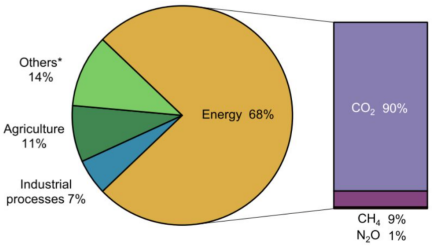

(c) Shares of global anthropogenic greenhouse has emissions (2010). source: [1]

Figure F.1: Combustion of fossil fuels is the primary source of global CO_2 emissions.

Of all the anthropogenic activities the energy sector produces the most CO_2 emission. Figure F.1c shows the contribution of different human activities to greenhouse gas emissions (GHGs[5]), including CO_2. It is evident that of all the different anthropogenic activities (e.g., agriculture, domestic livestock, energy-consuming processes etc. . .), the energy sector is the largest producer of CO_2 emissions (over 95 % of the global anthropogenic emissions).

[5] CO_2, Methane, Nitrous Oxide (N_2O), and few others

Figure F.1b compares the emissions within the energy sector, from different fuel sources. As can be seen, the emissions due to the combustion of fossil fuels remains the highest. More importantly, Figure F.1b also illustrates that the fossil fuel combustion has in fact dominated the total energy-related CO_2 emissions, for over many decades.

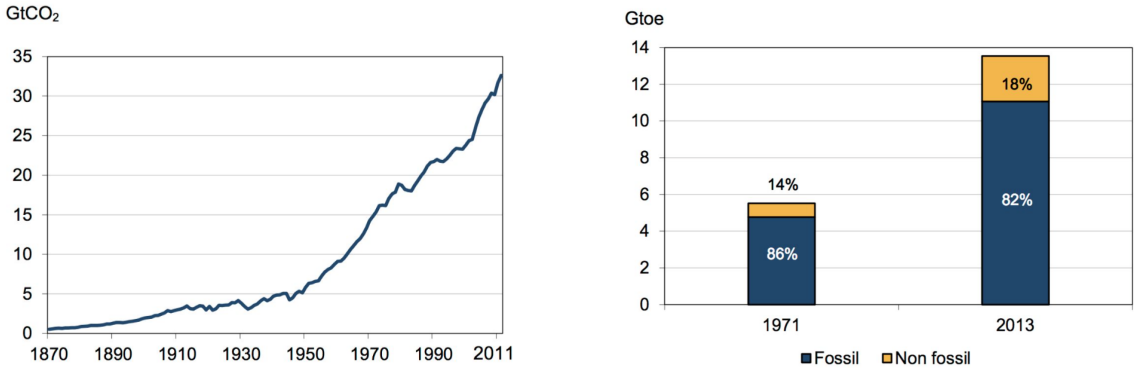

(a) CO_2 emissions from fossil fuels pre- and post-industrial era. source: [3]

(b) World primary energy supply in 1971 and 2013 (toe = tonne of oil equivalent) source: [3].

Figure F.2: Ever-increasing global demand for energy.

Ever-increasing global energy-demand can double the current CO_2 emissions by 2050. Figure F.2a shows the trend in CO_2 emissions due to fossil fuel combustion, in the post industrial era (i.e., mid-19th century onwards). The annual CO_2 emissions has dramatically increased from near zero in 1870, to over 32 $GtCO_2$ in 2013. This is attributed primarily to the industrialization seen particularly in the West, which led to substantial increase in the demand for energy [3]. Figure F.2b shows the global energy supply in 1971 and 2013. Over the span of these 42 years, a rise of about 150 % in the supply was observed to meet the energy demand. Importantly, the % share of the fossil fuels has remained almost the same during this period. Considering that the fossil fuel supply is a scarce commodity, an extrapolation of the present rate of energy consumption indicates that the supply of oil could terminate by 2050, natural gas in 70-100 years, and coal in a couple of centuries [455, 456].

Understanding the energy consumption trends of some of the big emitters in the world, particularly in relation to their socio-economic structures, allows us to predict the future trends in global CO_2 emissions. Figure F.3 shows the trends in CO_2 emission 'per capita' as well as 'per gross domestic product (GDP) per capita (GDP PPP[6])' for the top five emitters in the world, in the year 1990 and 2013. The size of the circle in Figure F.3

[6]PPP refers to the purchasing power parity in that particular country.

indicates total CO_2 emissions from each country, in that year. These indicators establish relationships between the population, the amount of GHGs emitted, and how efficiently sectors in the economy are minimizing emissions while producing goods and services for consumption and export. These aspects we discuss, as follows.

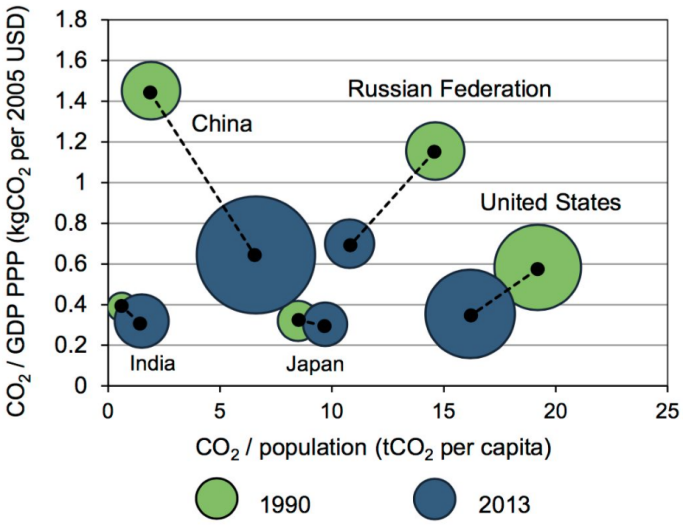

Figure F.3: Energy consumption trends of top CO_2 emitting countries in the world. source: [3]

The United States of America (US) has the highest emissions per capita, despite its smaller population compared to developing nations such as China and India. Furthermore, all the five largest emitters showed reduction in emissions per GDP-PPP, between 1990 and 2013, but is particularly more pronounced in the case of China and the Russian Federation. These improvements are attributable to the more efficiency in the industrial processes, a shift to a more service-based economy, or a reduced production of carbon intensive fuels such as coal. On the other hand, the emissions on the per capita basis showed contrasting trends (see Figure F.3). While the US and the Russian Federation decreased their emissions per capita significantly, China tripled its, and India more than doubled its. This is alarming, especially considering that India and China account for about 36.41 % of total world population. The consequence would be that the global CO_2 emissions will increase substantially [3, 4, 457]. Assuming that the use of fossil fuels is continued at the same rate as present day, the energy-related CO_2 emissions is expected to reach about 60 $GtCO_2$ by the year 2050, which is almost double the present day's emissions [4]. It is therefore, crucial that both China and India reduce their per capita emissions in the coming future. One possible solution here could be to further improve upon the same measures that have helped them reduce their 'emissions per GDP-PPP'.

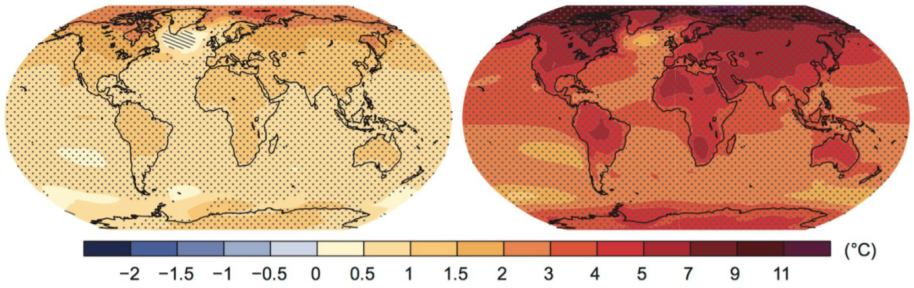

Figure F.4: Predicted change in average surface temperature of earth between 1986-2005 to 2081-2100 based on two scenarios: Mild climate change (Left) and Extreme climate change (Right). source: [2]

Implications of CO_2 emissions on the environment – climate change is inevitable

The rising CO_2 concentration in the Earth's atmosphere at the current alarming rate (Figure F.2a) will have serious implications on the climate [2–4]. CO_2 is one of the major greenhouse gases that is able to trap heat within the atmosphere, thus keeping the surface of the Earth warm, a phenomenon popularly known as 'greenhouse effect' [5, 6]. Over the last 1000 years, the concentration of CO_2 in the atmosphere has remained stable, at roughly 280 parts per million (ppm), maintaining an average temperature on the Earth's surface at about 15 °C [3]. However, with CO_2 concentration expected to increase to about 936 ppm by the year 2100 [2], the greenhouse effect will intensify, trapping more heat and thus further warming the earth, and in the process, altering the planetary climatic system.

The UN Intergovernmental Panel on Climate Change (IPCC) predicts that relative to the average from 1850 to 1900, the global surface temperature change by the end of 2100 is likely to exceed 2 °C [2]. Figure F.4 illustrates the geographic distribution of the change in the Earth's of surface temperature, based on an extreme scenario (termed, RCP 8.5) as well as a relatively less extreme scenario (termed, RCP 2.6). Noticeably, both indicate that the Arctic region will warm more rapidly than the global mean, and mean warming over the land will be larger than that over the ocean. Other expected effects of the climate change include, rise in the sea water levels (up to 1 meter), acidification of water, frequent heat waves and drought, heavy precipitation and increased cyclone activity. While some of these effects entail both beneficial and adverse effects on the environment and socio-economic systems, the adverse effects are likely to dominate in the longer run. Unfortunately, most aspects of climate change will persist for many centuries even if CO_2 emissions are completely stopped as of today [2].

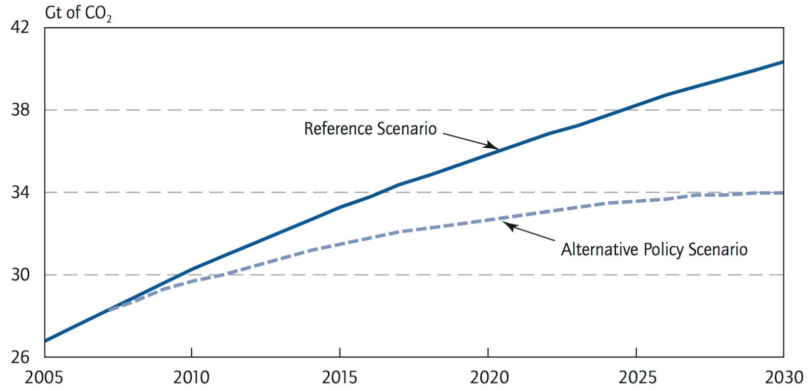

Figure F.5: Projected trends in CO_2 emissions as per two scenarios: Reference scenario: (no implementation of policies) and Alternative scenario (successful implementation of drafted policies). source: [2]

International commitment to developing a low-carbon future

Realising the implications of rising CO_2 emissions noted above, the international community has finally agreed to act. Since the Kyoto Protocol in 2008 up until the most recent Paris Agreement in 2015, multiple agreements have been signed to secure an international commitment for reducing emissions. Because the anthropogenic emissions of carbon dioxide (CO_2) result primarily from the combustion of fossil fuels, energy consumption is at the center of the climate change debate. Pledges have been made to move towards a low-carbon and more efficient energy system, but without altering the rising global needs of energy [6]. As a primary course of action, alternative fuel sources and energy carriers that are renewable/abundant, efficient and less CO_2 producing, are being promoted. Notable candidates in this category include the solar, wind, and Hydrogen based technologies. [7].

Figure F.5 provides a projection of CO_2 emissions from the energy sector up to 2030, following a reference scenario assuming no implementation of policy measures, as well as an alternative scenario wherein the drafted policy measures are implemented. In the reference scenario, CO_2 emissions will continue to rise, growing by about 50 % between 2005 and 2030. If the policy measures are implemented (i.e., in the alternative scenario), the emissions are projected to grow by 27 %, which is almost a reduction by half compared to the reference scenario. This suggests that although the rising emissions and the consequent climate change cannot be prevented, its effects can be delayed, provided the shift to low-carbon and efficient energy systems is executed in a timely and stringent manner.

Currently there is a tremendous research effort directed towards developing low-carbon energy systems, primarily based on solar, wind and hydrogen energy sources/carriers. Mass adoption of these technologies, however, is faced with numerous challenges concerning energy generation, conversion, storage and the cost-effectiveness. An in-depth review of these energy systems for applications other than the transportation sector is beyond the scope of the present work. In Appendix G, a brief overview of solar, wind and hydrogen based energy technologies is discussed, for the specific case of transportation applications. Of particular interest to the present thesis are hydrogen based energy systems, which are reviewed in a more detailed manner, and compared to solar and wind based energy technologies.

G

LOW-CARBON ENERGY TECHNOLOGIES FOR THE FUTURE

The previous chapter (Appendix F) discussed the ever-increasing demand for energy that is derived primarily from the fossil fuel sources, and its arguably irreversible impact on the Earth's climate system. Importantly, the pressing need to develop alternative energy technologies to replace fossil fuels while still sustaining the future energy demands was highlighted. Three general approaches are available to meet this objective: (1) use of nuclear power, (2) carbon capture and storage (CCS), and (3) use of renewable energy. Each of these solutions are overviewed in the following sections, but given the scope of the present thesis, the hydrogen based energy technologies (falling under the category (3)) will be reviewed in a more detailed manner.

G.1 NUCLEAR POWER

Typically, a nuclear fission reaction releases vast amount of energy on the order of few Megawatts by splitting heavy nuclei such as, Uranium. In the process, no CO_2 is emitted. From the standpoint of global warming, nuclear power is therefore an ideal energy source. The problem however is that it would require widespread implementation of the so-called breeder reactors that feed on Uranium [458]. Terrestrial Uranium reserves are sufficient to produce about 100 TW (Tera-Watts) of nuclear power [459]. On the basis of 10 TW produced by conventional fission reactors per year, this means that the Uranium reserves would be exhausted in less than a decade.[1] Moreover, these reactors would have to be built at a very rapid rate by traditional standards. However, the current understanding of radiation effects on the reactor materials is still not mature enough to successfully lead such an effort [460]. In addition, nuclear energy faces serious criticisms over its assurable safety and radioactive waste disposal [461]. Since the disaster in Fukushima (2011), the public fear has only been aggravated [462]. Submitting to these public sentiments, the construction of nuclear plants has reduced drastically in the past few years [453, 463].

[1] On the basis of an annual energy consumption of 786992 Peta-Joules (PJ) every year.

Nuclear Fusion (of light nuclei) is yet another process that in principle, can provide limitless power. The problem however is that the temperatures are high enough for the interacting ions to overcome coulomb repulsion (resulting in a state of 'plasma'). Confining them to obtain a net energy output is still not practically viable [464, 465]. Although magnetic confinement technology is envisaged to be a promising option, the timeline for practicability is much too far in the future [465]. For example, the International Tokamak (Magnetic confinement fusion) Experiment (ITER) is scheduled to demonstrate an energy break-even point in about 35 years, for a few minutes of operational time. At this rate, the fusion process is expected to be viable only in the late 21st century [464].

G.2 CARBON CAPTURE AND STORAGE

In the carbon capture and storage (CCS) process, CO_2 is stripped away from the atmosphere using absorption, adsorption or membrane separation techniques and stored in the underground geological formations (saline aquifers, minerals, ocean beds, exhausted gas fields and mines) as gaseous injections or solid carbonates [466]. For CCS to be viable, any leakage of CO_2 should be restricted to the maximum leakage rate of 1% over a few centuries [467]. Tremendous research is already underway, but extensive modeling, experimentation and validation is still required to ascertain that the leakage rate would be acceptably low over at least five centuries. Estimations suggest that the global reservoirs can store enough CO_2, equivalent to full reduction in the emissions for next 100-150 years. Therefore, if CCS can be validated within the next two decades, the rate of global warming can be considerably delayed, which can also relax the task of developing the alternative energy technologies in hand.

G.3 USE OF RENEWABLE ENERGY

As a third general approach, renewable means of producing electricity using solar, hydrogen and wind is becoming increasingly popular [468]. Development of energy conversion devices such as solar cells and fuel cells to effectively convert renewable energy into useful forms have made remarkable progress. Various reliable ways of storing and transmitting energy are also being explored and optimized in the fields of rechargeable batteries, hydrogen storage and superconductors. In this overview, opportunities and challenges offered by major renewable energy technologies based on solar, wind and

hydrogen are discussed. The present status of other energy technologies based on renewable sources such as biomass, hydropower, geothermal, tidal etc. . . can be found in the following review articles [468–471].

G.3.1 *Solar energy*

The sun is the most obvious source of renewable energy. On a clear sunny day with sun overhead, the radiation falling on a horizontal surface is roughly 1000 Wm^2 [472]. Considering the US as an example, over its total area of 9.86 trillion-m^2 the annual insolation (amount of solar energy falling on a given area) is about 4.67 x 10^4 *quads*.[2] This is well in excess of the total annual energy consumption of the US, which is about 98.6 *quads* [473]. Yet, only about 0.55 *quads* of solar energy is being produced in the US [474]. In fact, the world solar scenario is no different- although the proportion of solar radiation reaching the Earth's surface is about 10000 times the annual global energy consumption [475], the utilization is extremely poor (2001: < 0.1% share in world electricity supply [476]). Therefore, suitable utilization technologies are required to better integrate the solar energy produced into the grid. Prominent applications of solar energy include heating, lighting, electricity generation and even production of other chemical fuels (e.g., hydrogen). The principal disadvantage is the seasonal-diurnal variability in local insolation. Current challenges for widespread commercialization include high cost and low efficiency in its utilization.

G.3.1.1 *Energy conversion technologies for solar energy utilization*

Solar energy utilization requires (1) energy capture and conversion, and (2) storage. Prominent technologies for capturing and conversion of solar energy include photovoltaics (solar energy into electricity), solar thermal technology (solar energy into thermal energy) and photoelectrochemical cells (solar energy into electricity or hydrogen production) [459]. The principal challenge here is to substantially reduce the cost per Watt ($/Watt) of solar electricity delivered.

Photovoltaics (PVs) are highly capital-intensive, with almost all expenditures paid upfront. PVs work on the principle that photons falling on a semiconductor can create electron-hole pairs, and at a junction between two different materials, this effect can set

[2] 1 *quad* = 2.9 x 10^{11} KWh

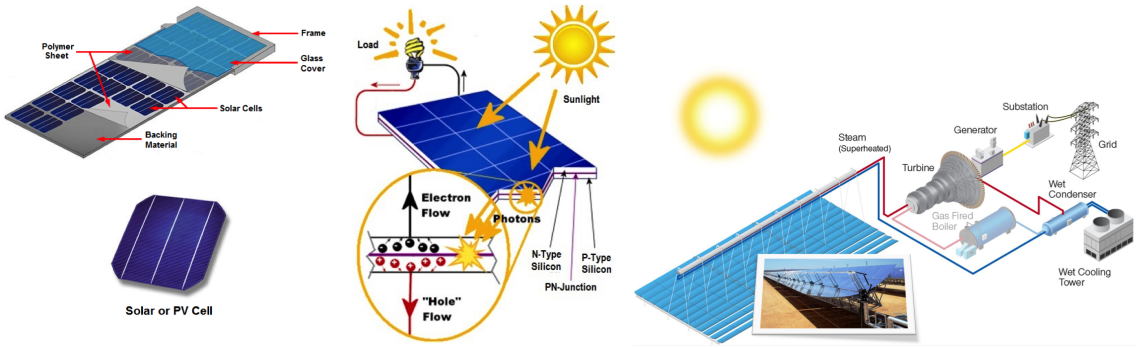

(a) A photovoltaic cell (PV). source: [477]

(b) Solar thermal technology. source: [478, 479]

Figure G.1: Schematic illustrations of prominent solar energy conversion technologies.

up a potential difference across the interface (Figure G.1a) [480–482]. Commercially available Si-based PV modules are priced at $ 300/m² and yield an efficiency of about 10 %. When amortized over a 30-year period, an electricity price of $ 0.35/kWh is required to recover the initial capital. By comparison, the cost of electricity derived from fossil-fuels is only about $ 0.02/kWh, including even the storage and distribution. Widespread commercialization of PVs will therefore require significant improvements to conversion efficiency (from 10 % to at least 24 % for single-crystal Si modules), and dramatic decreases in their total cost (from $ 300/m² to at least $ 100/m²). From a materials science standpoint, this effort requires development or optimization of polycrystalline and nanocrystalline semiconductors (cheaper option) that can separate the photogenerated charge as efficiently as the single-crystal semiconductors (more costly option) [459]. Numerous approaches are currently being pursued, such as thin films, multi junction cells (especially from III-V semiconductors), low or high-concentrating PV, Quantum dots, dye-sensitized cells, organic cells and thermoelectric materials [483–486].

The second method for capturing and converting solar energy is a photoelectrochemical cell (PEC). As opposed to the traditional solid-state approaches of making a junction (as in PVs), these devices replace the phase in contact with the semiconductor[3], by an electrolyte (liquid, gel or organic solid) [481, 488, 489]. In addition to converting solar energy into electricity (termed regenerative cells), these devices can also produce hydrogen (termed, photosynthetic cells [489, 490]), thus providing a promising alternative to conventional carbon-intensive ways of producing hydrogen (steam-reforming of hydrocarbons and coal-gasification). Although this combination of solar energy and electro-

[3]electrodes (anode/cathode) is not necessarily a semiconductor (n-type/p-type), but can also be a metal

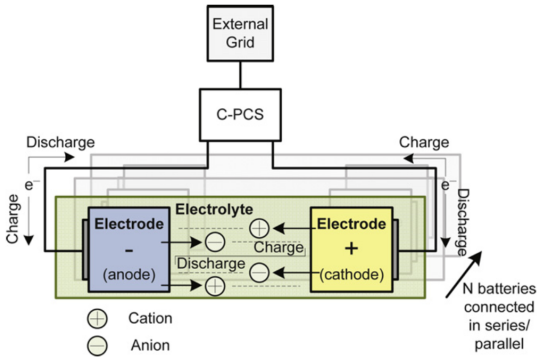

(a) *Battery storage system*: Exchange of ions between two electrodes in forward/reverse directions enables storage/discharge of the electricity to/from the grid.

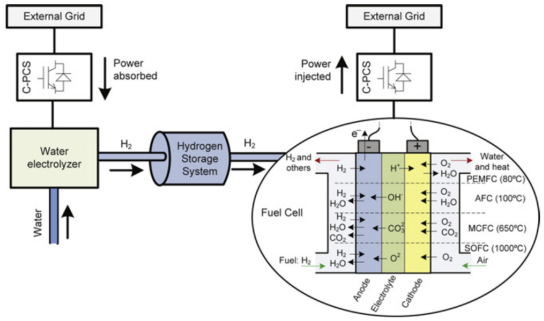

(b) *Regenerative fuel cell system*: Electrical energy from the grid is converted into hydrogen gas, which from the action of fuel cells can be reconverted into electricity as and when required.

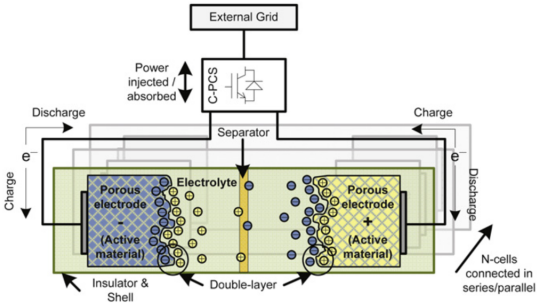

(c) *Supercapacitor*: consists of two porous electrodes in contact with an electrolyte. Exchange of ions charges/discharges the two electrodes, enabling storage/discharge of electricity to/from the grid.

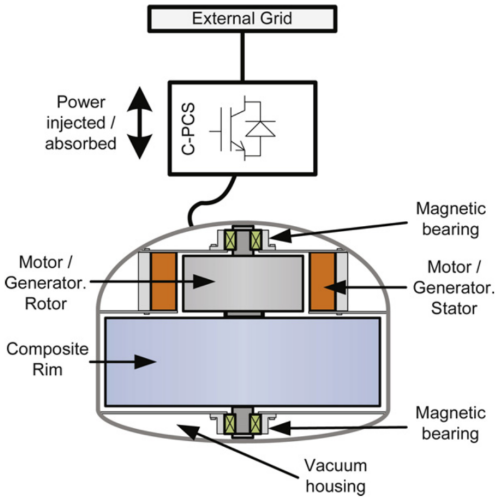

(d) *Flywheel energy storage*: Input electricity is used to rotate the flywheel; when necessary the electricity is regenerated by an electric motor connected to the flywheel.

Figure G.2: Schematic illustrations of prominent energy storage technologies. source: [487]

chemistry makes PECs very attractive, its full potential can only be realized if the key issue concerning the instability of semiconducting materials in close contact with liquids, termed as 'photocorrosion', can be addressed.

Currently, the cheapest method of solar energy capture and conversion is the solar thermal technology (Figure G.1b). It relies on first collecting solar energy to heat a liquid to high temperatures and produce steam, which turns the turbines generating mechanical energy. Finally, the mechanical energy is used to power a generator, which produces electricity [491]. The overall cost of electricity generated from solar-thermal technology is as low as $ 0.10/kWh. Further possibility of integrating capture, conversion, storage and distribution makes this technology a very attractive option that needs to be pursued more vigorously [492]. More research is required towards improving the collection efficiency, and designing new thermochemical cycles, which can enable coversion of the captured energy into many other useful forms, such as the production of a chemical fuel for industries [492, 493].

G.3.1.2 *Energy storage technologies for storing electrical energy*

Once solar energy is converted into usable forms, such as electricity and hydrogen, it requires storage. Notable electrical energy storage technologies include rechargeable batteries (lead-acid, nickel-based, lithium-based, sodium-sulphur, metal-air), supercapacitors (electrochemical double layer (ECDL), pseudo-capacitors, hybrid supercapacitors) and mechanical means (flywheels, pumped hydroelectric storage) [494–496]. The working principle of each technology is briefly noted in Figure G.2. Hydrogen storage technologies will be discussed in more detail later in the Section.

Figure G.3 provides a comparative chart of the energy and power densities achievable using each energy storage technology, source: [494]. A few terminologies need to be first revisited. Energy density (or specific energy, *Wh/kg*) is the measure of the amount of energy that can be stored in a device. Whereas, power density (or specific power, *W/kg*) reflects the amount of work that the device can deliver in a given time, also equivalent to maximum current that can be drawn. Consider a recreation vehicle (RV) for example, which requires two kinds of batteries: one to start the engine (starter battery) and another to run the interior home-setup (home battery). To crank the engine, high power (more work in short time) needs to be delivered, but only for a very short time as the starter motor is engaged for a few seconds. Therefore, the starter battery needs to be of high power density (high energy density is not necessary). On the other hand, the home

battery is expected to deliver its energy for extended period of time, but the current drawn at every instant of time is small. Therefore, the energy density of home battery must be high, but the power density can be low.

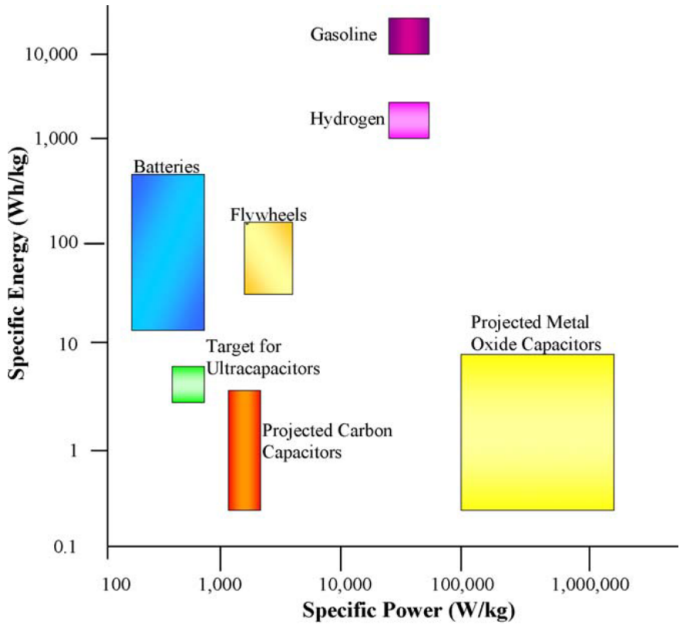

Figure G.3: Comparative chart of achievable energy and power densities with different energy storage technologies. source: [494]

From Figure G.3, it is clear that batteries have the highest energy density (with the exception of hydrogen storage devices), but the lowest power density. Supercapacitors, in particular those based on metal-oxides, can provide very high power densities. Pumped hydroelectric storage is not shown on the chart as it exceeds the scale, but can provide power densities suitable for high power applications (in the order of 100 MW). Flywheels have high power densities compared to batteries and in few cases (composite rotor flywheel technology) even match the energy density offered by batteries. However, the battery technology still remains a cheaper option (Batteries: $50-100/kWh, Flywheel: $400-800/kWh).

The above analysis indicate that batteries are most suitable when a continuous energy supply is of primary importance (such as in laptops and phones). Technologies such as flywheels and supercapacitors are more suited for power storage applications where a very brief power supply, such as in a UPS (uninterrupted power supply) is needed.

Among the many different battery types available in the market (lead-acid, nickel-based, lithium-based, sodium-sulphur, metal-air), the lithium-ion battery (LIB) has kicked off in a big way and has become commercial reality in various portable electronics, electric vehicles, military and aerospace applications [497–502]. Their advantages over other battery types include higher energy density (80-150 *Wh/kg*) and energy efficiency (90-100 %), lower self-discharge rate (5 % maximum per month), longer lifetime (> 1500 cycles) and relatively low maintenance [494]. Given their low power density (500-2000 *W/kg*), applications such as UPS are not yet possible, although further research in that direction is already underway.

The Lithium-ion battery (LIB) is composed of two electrodes (anode, cathode) and an electrolyte (separating the electrodes) (see Figure G.2a). Typically, the cathode is an intercalated lithium compound[4], the anode is graphite or other carbon based material, and the electrolyte is a lithium salt[5] in an organic solvent[6] [503]. During charging, Li ions migrate from cathode to anode, and vice versa during the discharge. Based on the cathode material used different LIB types exist, and each offer a unique chemistry, cost, performance and safety, targeting a specific application. For example, lithium cobalt oxide ($LiCoO_2$) batteries are preferred in handheld electronics, given their high energy densities. Lithium manganese oxide (Li_2MnO_3 or LMO), lithium iron phosphate ($LiFePO_4$) and lithium nickel manganese cobalt oxide ($LiNiMnCoO_2$ or NMC) batteries offer relatively lower energy density (compared to $LiCoO_2$) but longer battery life times and better safety. These batteries are widely used in electric tools, medical equipment and electric powertrains. The NMC cathode in particular, has become a favorite candidate for electric cars [504–506]. Its success is primarily attributed to the synergy resulting from the mixing of Nickel (high specific energy but poor stability) and Manganese (low internal resistance from the spinel structure and low specific energy).

One major disadvantage with LIBs is their flammability [507, 508]. If overheated, they suffer thermal runaway, leading to cell rupture and in extreme cases, explosion. In some cases, even short circuiting has resulted in overheating and fire. Since in most applications multiple cells are always connected together, overheating can spread between the adjacent cells. To reduce these risks, the LIBs need to be fitted with a built-in circuit breaker (current interrupt device (CID)), which regulates charge-discharge current and the temperature. Currently, much of the research on Li-ion batteries is directed towards improving energy density, safety, battery lifetimes, recharging rates and cost-

[4] based on $LiCoO_2$ and $LiMnO_2$
[5] such as, $LiPF_6$, $LiBF_4$, $LiClO_4$
[6] e.g., ethylene/dimethyl/diethyl-carbonates

effectiveness. With the fast-growing market, although scarcity of lithium might appear to be a looming concern, it should be noted that only around 1 % of Li-ion battery is Li by weight; in the future, recycling Li from the batteries is expected to become a standard practice.

G.3.2 *Wind*

Wind is an indirect form of solar energy caused by differential heating of the Earth's surface by the sun, thus is constantly replenished. It is estimated that about 10 million MW of energy is continuously available in the Earth's wind [509]. The kinetic energy stored in the wind is converted into electrical energy using wind turbines. The process involves first aligning the blades in the direction normal to the wind, the rotary blades thus converts wind energy to mechanical energy, which then turns a shaft that is connected to the generator (an induction motor), producing electricity (Figure G.4a).

The maximum achievable efficiency of wind turbines is about 59.3 % (Betz's limit, 1920), but most current turbine technologies operate with an efficiency in the range of 35-45 %. Since the 1980's, remarkable advancements in the areas of aerodynamics, structural dynamics and meteorology have made the technology very reliable, contributing about 5 % annual increase in the energy yield [510]. In areas with sufficiently high wind speeds (12-16 m/s), wind energy has proven to be cost-competitive with fossil-fuel energy (cost of electricity: wind –$ 0.04/kWh, fossil-fuels –$ 0.02/kWh) [511]. It is also the fastest growing renewable energy sector with an annual growth of 27 %[7] [510, 511]. Wind energy now provides about 2.5 % of the global electricity demand. By 2050, about 15-18 % share of the global electricity supply is targeted [512].

Similar to solar energy, the major limitation with wind energy is its variability. Due to variable wind speed based on location, turbulence and the seasonal-diurnal cycles, the power output fluctuates, affecting the quality of the electricity supplied by the grid (e.g., flicker effects, voltage fluctuations etc. . .). Figure G.4b illustrates typical fluctuations in the wind speed and output power over a four-day period (vertical axis indicates percent variation from the average), source: [514]. For this reason, a network of many wind turbines in the form of 'wind farms' are preferred over isolated wind turbines. Here, under ideal conditions the variations in power output will drop by $1/\sqrt{n}$ (n is the number of wind turbines) [510]. These wind farms are set to follow standard grid codes and employ

[7] in terms of the number of worldwide installations

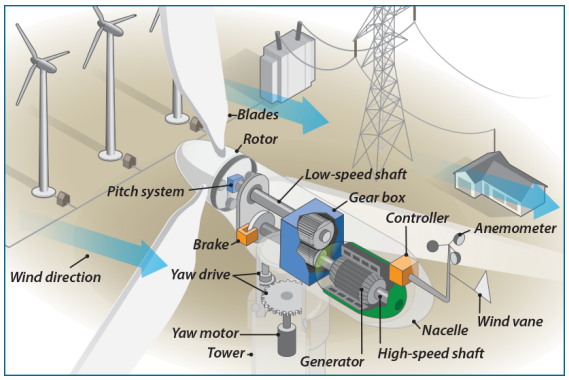

(a) Schematic illustation of a typical wind turbine. source: [513]

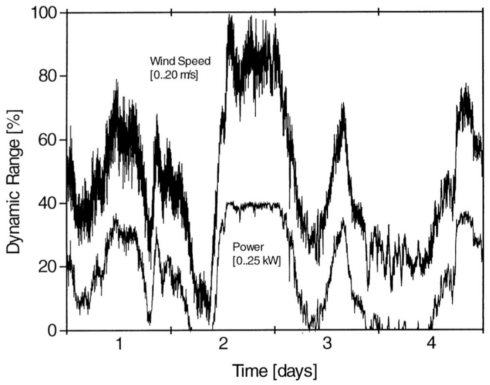

(b) Variability of the wind speed and output wind power with time. source: [514]

Figure G.4: Power generation using wind energy.

energy storage systems (Section G.3.1.2), thus providing better control and reliability over the output power and voltage [487]. In certain regions such as Europe, owing to limited space and high population density on the land, offshore wind farm developments are also being pursued [509, 510]. Studies indicate that the offshore sites can produce higher wind energy compared to onsite sites [510]. For example, Fuglsang *et al* [515] compared a 1.5 MW turbine in an onshore flat terrain and in offshore wind farm, and showed a potential increase in the energy production of 28 % for the offshore site.

G.3.3 *Hydrogen*

Unlike coal, oil or the sun, which are all primary energy sources, hydrogen is a secondary energy source, also called an energy carrier [516, 517]. Since it does not exist in its natural state on the earth, hydrogen must be produced from other sources. Once produced, it can be easily converted into various other forms of energy in an efficient and environmentally friendly way. As an energy carrier, hydrogen can impact a broad range of sectors including stationary/residential systems, transportation and industrial processes [9, 456, 518, 519]. Following are some unique characteristics of hydrogen that makes it an attractive energy carrier:

- *High energy density*
  Hydrogen has one of the highest specific energy density on weight basis. For ex-

ample, the energy contained within 9.5 kg of H_2 is equivalent to that in 25 kg of gasolene [520]. Energy densities of some well known fuels are listed in Table G.1.

- *Clean and environmentally benign when combusted*
  When combusted electrochemically, hydrogen produces electricity without any GHG emissions, the only byproducts are water and some heat. Specific carbon emission (kg C/kg fuel) for hydrogen is zero, whereas that of oil is about 0.84 [517].

- *Multiple production pathways exist*
  Hydrogen can be produced from a number of energy sources (discussed later), both renewable (e.g., solar, wind, biomass) and non-renewable (e.g., natural gas and coal).

- *Ease of transportation*
  It can be easily transported over large distances through pipelines, tankers and rail.

- *Convertibility into other forms of energy*
  Hydrogen can be converted into various other forms of energy suiting the end use, such as electricity, other gases (natural gas blend, synthetic methane) or even directly as a feedstock (in refineries).

In these respects, hydrogen mirrors the appealing attributes of electricity, another most versatile energy carrier that forms the backbone of our current energy system. Hydrogen and electricity form a natural partnership as both the carriers are interconvertible at high efficiencies. They further complement each other with respect to storage characteristics, while hydrogen can store energy indefinitely and at high density, electricity is used at the point of generation and lacks convenient high-density storage. Thus, during the times of seasonal-diurnal fluctuations of renewable electricity, local hydrogen storage and interconversion to electricity can provide reliable power output (see Figure G.2b). To realize these promises however, suitable technologies for hydrogen production, storage, distribution and utilization are required.

Most of the hydrogen energy technologies have already been developed, but only a few of them are competent with the existing technologies. Following is an overview of various technologies used toward hydrogen production, storage, distribution and utilization.

ENERGY CARRIER	STATE OF STORAGE	ENERGY DENSITY BY WEIGHT (kWh/kg)	ENERGY DENSITY BY VOLUME (kWh/L)
Hydrogen	Gas (25 MPa)	33.3	0.64
	Liquid (-253 °C)	33.3	2.36
	Metal hydrides	0.58	3.18
Natural Gas	Gas (25 MPa)	13.9	3.01
	Liquid (-162 °C)	13.9	5.8
LPG	Liquid	12.9	7.5
Methanol	Liquid	5.6	4.42
Gasoline	Liquid	12.7	8.76
Diesel	Liquid	11.6	9.7

Table G.1: Comparison of the energy densities of different energy carriers. source: [519]

G.3.3.1 *Technologies for hydrogen production*

Although hydrogen is the most abundant element in the Universe (~75 % of baryonic mass[8] and > 90 % by number of atoms), pure gaseous hydrogen is scarce in the Earth's atmosphere (0.00005 %). Given their low molecular weight, hydrogen molecules overcome Earth's gravity and rapidly escape into the space (*via* so-called 'Jeans' or the 'hydrodynamic' escape mechanisms) [521]. Any hydrogen found is mostly in the molecular forms such as water and organic compounds. Extraction of gaseous hydrogen from these resources is an energy-intensive process. Currently, 96 % of the total hydrogen produced worldwide is by reforming of fossil fuels (natural gas: 48 %, oil: 30 %, coal: 18 %), and only 4 % is produced by renewable energy sources [11]. But, for a low-carbon future hydrogen must be produced by renewable means only.

Hydrogen production by water splitting is one of the 'green' approaches [519, 522, 523]. This can be achieved by either applying a direct current (as in electrolysers) [524], using sunlight (as in photoelectrochemical cells) [525], using microorganisms (photobiological splitting) [526] or by high-temperature decomposition [527]. In particular, electrolysers provide a conversion efficiency of 70-75 % and would be ideal to work in conjunction with PVs and wind energy. However, since the process requires considerable amounts of electricity, and the renewable means of generating electricity are still expensive, elec-

[8]The baryonic mass refers to all the material in the Universe made up of protons, neutrons and electrons.

trolysis is currently non-viable. Yet, considering the growth rate of PVs and wind energy technologies (discussed in earlier sections), electrolysis can be seen as a promising hydrogen production technology for the future [523].

Other means of producing hydrogen (without CO_2 emission) include use of wind, tidal and biomass. Unfortunately, these methods are not suitable to delivering hydrogen in large quantities that would be required to satisfy the global demands. Additionally, use of nuclear energy (fission and fusion) is also under consideration, but the concerns inherent to nuclear technologies are restraining (Section G.1). For a comprehensive review of these hydrogen production technologies the reader is referred to following articles [511, 528, 529].

G.3.3.2 *Technologies for hydrogen storage*

Hydrogen has a very low volumetric energy density (i.e., energy content by volume), about 3000 times smaller than gasoline at standard temperature and pressure [530]. Under ambient conditions, a 5 *m* diameter vessel would be required to store 5 kg hydrogen (equivalent to 22 litres of petrol). This is certainly very impractical from the most applications' standpoint. The problem can be solved by either storing hydrogen under increased pressure (gas storage), or storing it at extremely low temperatures as a liquid (liquid storage), or storing within solid materials (solid-state storage) [531–533].

Although both gas and liquid storage is widely used in many demonstration vehicles, these are considered to be provisional options only [518]. This is because even at the highest practical pressure (10000 *psi*), compressed H_2 gas requires a large storage space. In the case of liquid hydrogen storage, although it requires relatively lower storage space, about 30-40 % of its energy is lost during liquefaction.

Solid-state storage of hydrogen is a more promising route, which relies on either chemically binding or physically adsorbing hydrogen onto a solid material at high volume densities [534]. In particular, the metal hydrides have shown great promise [535].[9] In this route, the hydrogen molecules split into atomic forms at the solid surface, enters the metallic lattice, and occupy available interstitial sites, forming a stable hydride phase (i.e., hydrogenation). Dehydrogenation process is endothermic, thus when the heat is applied or the pressure is increased, stored hydrogen is released back. Ongoing research in this area aims to find lighter storage materials with higher hydrogen density, and provid-

[9] These include sodium alanates ($NaAlH_4$, Na_3AlH_6), lithium imides (Li_3N), borohydrides ($M^+BH_4^-$, where M is Li, Na or K; B can also be replaced by Al), and magnesium hydrides (MgH_2).

ing reversible H_2 charge/discharge cycle in the temperature range 70-100 °C, at a faster rate [535, 536]. In the recent years, a number of nanostructured materials have shown promising hydrogen storage properties. Notable are carbon nanotubes [537], core-shell nanocomposites [538] and metal-organic frameworks [539].

G.3.3.3 *Technologies for hydrogen distribution*

Unlike the electricity grid, present infrastructure for H_2 distribution is limited. Four options are available for future developments in this sector: gaseous truck transport (compressed hydrogen), liquefied truck transport, pipeline and pumping station networks, and finally, decentralised hydrogen production (methane reforming or electrolysis of water) [9]. Trade-off exists between fixed and variable costs. For instance, while trucks offer the lowest investment cost, variable costs in the longer run are high (from the limited H_2 transferability due to low volumetric density). On the other hand, while pipelines offer low variable cost, the fixed cost (or the initial investment) is high. Since the market for hydrogen is still not mature, the investment risks are high. Therefore, the progress in the hydrogen infrastructure development is sluggish. To survive this so called 'valley of death', support from Governments is crucial, for instance a sizeable demand for hydrogen can be created by subsidizing hydrogen fuel cell vehicles [9].

G.3.3.4 *Technologies for hydrogen utilization*

Various technologies exist for efficiently converting the chemical energy stored in hydrogen into other useful forms. These include hydrogen gas turbines, direct steam generation by hydrogen combustion, catalytic burners by combustion of hydrogen, and 'fuel cells' for electricity generation [511]. The most effective utilization of hydrogen is when its chemical energy is converted into electrical energy by 'fuel cells'. The conversion efficiency in fuel cells can reach up to 60 %, and no CO_2 is emitted in the process [540, 541]. These are also highly versatile devices in their application, the electricity generated can be used to create motion, light or heat. In contrast, the gasolene based internal combustion engines operate with 25 % efficiency and are used exclusively for motion [518].

Fuel cells are electrochemical devices composed of an anode, a cathode and an electrolyte (a non-conductive membrane). Fuel (e.g., H_2) is fed at the anodic site, which decomposes into ions and electrons. Ions migrate to the cathodic site through the membrane, while the electrons pass through an external circuit (thus, generating electricity).

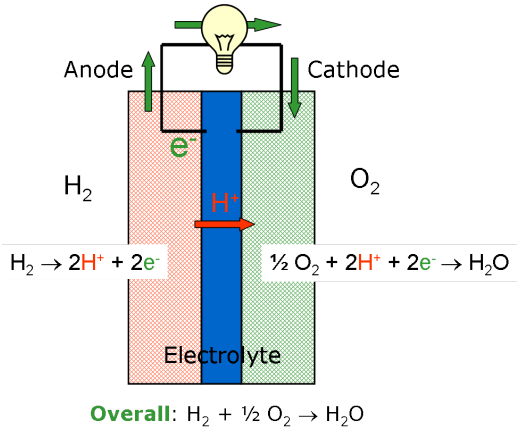

(a) Basic fuel cell construction. source: [542]

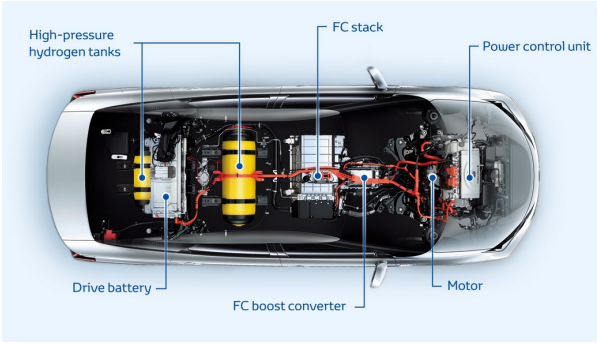

(b) A fuel cell electric vehicle (Toyota Mirai). source: [543]

Figure G.5: Schematic representation of a hydrogen based automotive fuel cell.

FUEL CELL DESIGN	OPERATING TEMPERATURE	ELECTROLYTE USED
Direct Methanol FC	20°C- 90°C	Nafion
PEMFC	30°C- 100°C	Nafion
Alkaline FC	50°C- 200°C	aq. KOH
Phosphoric acid FC	180°C- 250°C	H_3PO_4
Molten Carbonate FC	650°C	Carbonates of Li, Na and K
Solid Oxide FC	500°C- 1000°C	Yttria stabilized Zirconia

Table G.2: Comparison of the characteristics of different fuel cell types.

Recombination of ions and electrons with an oxidant at the cathodic site forms pure water and some heat. Figure G.5 illustrates the basic construction of an automotive fuel cell, and its assembly in the drivetrain of a Toyota Mirai car.

Depending on the membrane used, various different types of fuel cells are available, such as alkaline, polymeric, phosphoric acid, molten carbonate and solid oxide fuel cells [540]. Table G.2 summarises the characteristics of these fuel cell types. The overall reaction is the same in all these cases: combustion of hydrogen to generate electricity, water and heat ($H_2 + 1/2O_2 \longrightarrow H_2O$). Fuel cells operating at low temperatures require catalysts to achieve practical reaction rates at the anode and cathode. A variety of input fuels (methanol, natural gas etc...) can also be combusted in fuel cells, in this way the fuel

cells are intimately but not exclusively linked to the hydrogen. But, the use of hydrogen guarantees cleaner generation of electricity with no emissions.

Notable fuel cell applications are in the stationary/residential systems (cogeneration (heat + power), backup and remote power), the automotive sector (passenger vehicles and trucks), and the industrial sector (for decarbonizing the refining, steel and chemical processes) [544]. In the future low-carbon energy system, a combination of electrolysers (electricity to hydrogen) and fuel cells (hydrogen to electricity) offers a flexible and reliable power output option (Figure G.2b).

Given the broad range of applications, fuel cells are an important technology that needs to be pursued, particularly for a successful realization of hydrogen economy [9]. Remarkable developments are already in progress, for instance within a span of five years (2008–2013) the global market for fuel cells grew by almost 400 % [10], the manufacturing cost of fuel cell electric vehicles has decreased by a staggering 90 % since 2005 [11], and the technology is regarded as one of the key sustainable energy systems by many countries [9]. Commercialization of fuel cells however requires significant reduction in cost (from $ 3000/kW to $ 30/kW), longevity and reliability. This presents materials research challenges related to optimization of electrode materials, electrolyte membranes and the catalysts used [518, 545, 546]. Chapter 2 highlights the challenges and related material progress for the case of polymer electrolyte membrane fuel cells (PEMFCs) which are used in the automotive sector for passenger vehicles. PEMFCs operate at low temperatures (80 °C), provide high power density and can vary their output quickly, thus are well suited for the automotive market as an alternative to fossil-fuel powered internal combustion (IC) engines [8].

Figure G.6 summarizes the cross-cutting relationship between different hydrogen production, storage and utilization technologies.

G.3.3.5 *Hydrogen economy, its opportunities and challenges*

'Hydrogen economy' is a long-term effort to effectively integrate hydrogen and fuel cell technology into the current energy system, which is primarily based on electricity as the primary energy carrier [9, 456, 517]. Essentially two energy distribution systems will be operating, the electric network and the hydrogen network, both well interconnected with suitable energy conversion and storage devices, such that the energy demand and supply is balanced at all times. Transitioning into a hydrogen economy offers a number of attractive opportunities, such as:

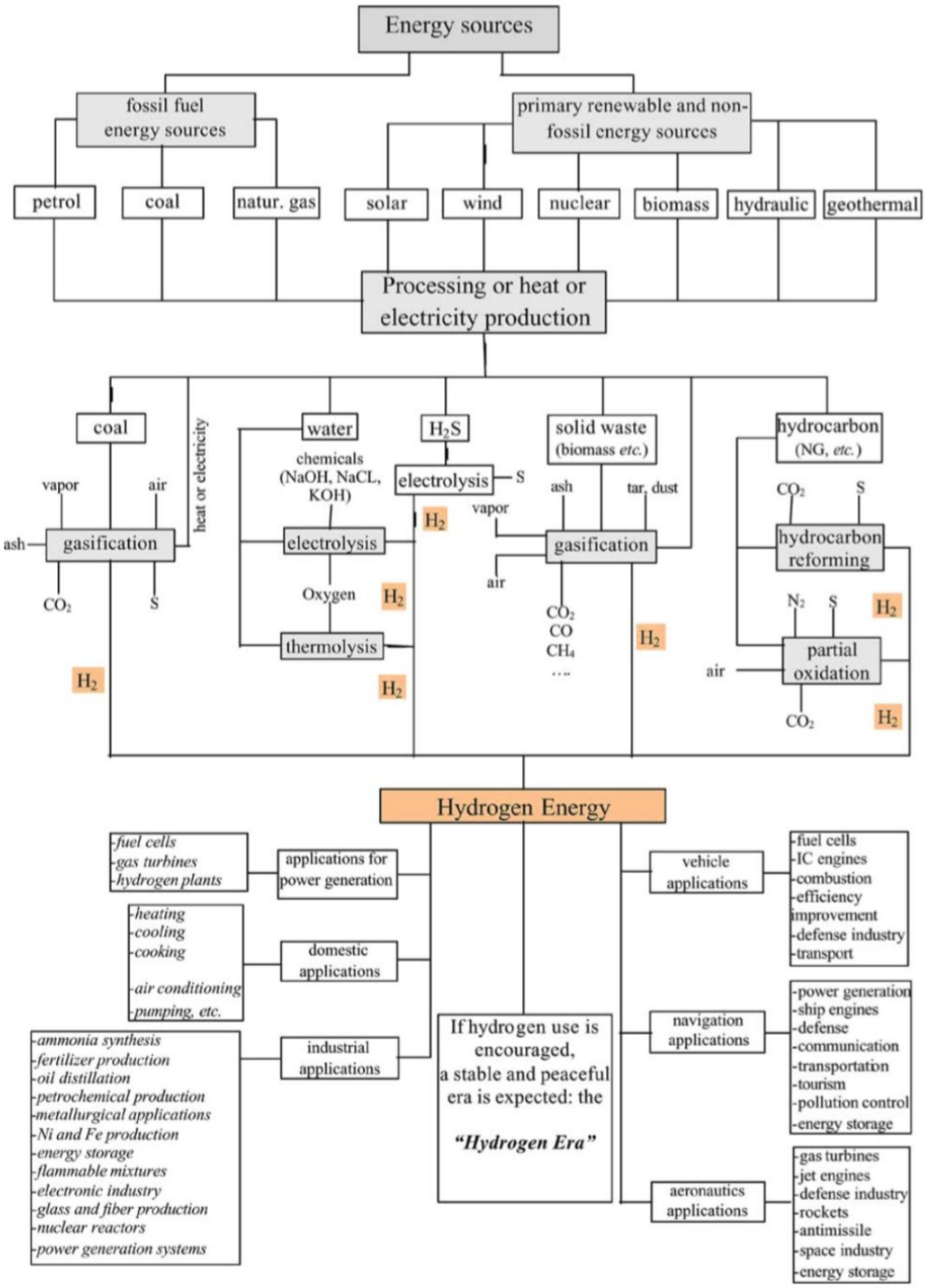

Figure G.6: Cross-cutting relationship between hydrogen production, storage and utilization technologies. source: [517]

- *Reducing global CO_2 emissions*
  Use of hydrogen energy technologies can facilitate significant reductions in the energy-related CO_2 emissions and contribute towards limiting global temperature rise to 2 °C (termed the 2°C scenario (2DS)), thus moving away from the extreme 6 °C scenario (6DS). For instance, deploying even 25 % share of the road transport with fuel cell electric vehicles (FCEVs) by 2050 can contribute up to 10 % of all the cumulative transport-related emission reductions to move from 6DS to 2DS [9].

- *Elimination of foreign dependence for oil*
  Since hydrogen can be produced from various locally available renewable and non-renewable sources, shifting to hydrogen economy can enhance a country's energy security, and also reduce political tensions over fuel sharing such as in the case of oil [518]].

- *Facilitating future low-carbon energy system integration*
  The current energy system based on fossil fuels is highly flexible, efficient and reliable. Given their high energy density (either in solid, liquid or gaseous forms), fossil fuels can store immense amounts of energy, where and when necessary, and also be efficiently transported over large distances. Thus, the supply and demand for electricity in the grid is balanced at all times. In contrast, the low-carbon energy system with high shares of variable renewable energy (VRE: solar, wind, tidal) offers poorer flexibility. Since these energy sources vary spatially and temporally, periods of surplus and deficit in energy supply is inevitable. In such a scenario, hydrogen offers a suite of promising options as outlined below [9].

  – *Power-to-power:* During surplus, excess electricity can be converted into hydrogen (*via* electrolysis of water) and stored in large quantities over long periods, and converted back into electricity as and when required.

  – *Power-to-gas:* During surplus, excess electricity can be converted into hydrogen, that can be in turn be mixed into the natural gas grid, or converted into synthetic methane.

  – *Power-to-fuel:* During surplus, excess electricity can be converted into hydrogen that can be sold as fuel to the transport sector (for use in FCEVs).

  – *Power-to-feedstock:* During surplus, excess electricity can be transformed into hydrogen and then used as a feedstock, for example in refineries.

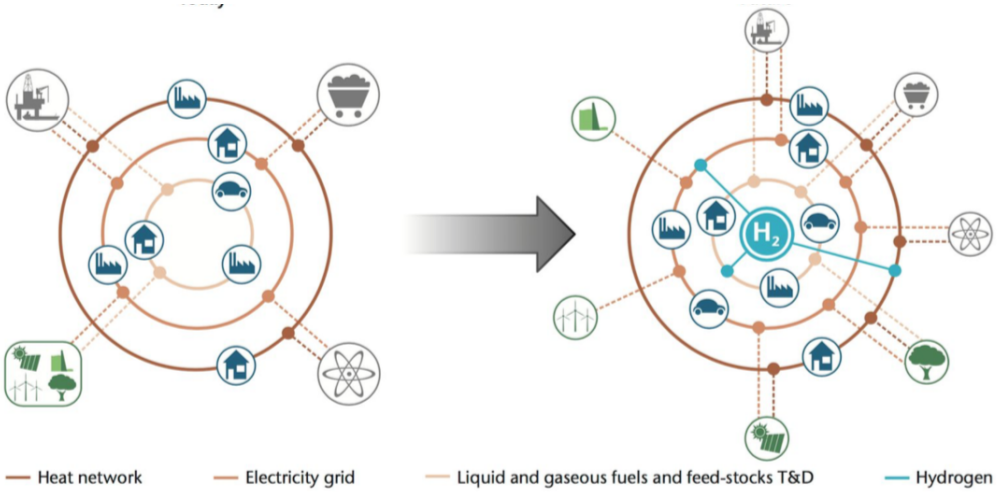

Figure G.7: Illustrations of the present (Left), and the future (Right) energy systems. source: [9]

Despite the undeniable loss of efficiency during these processes (60-70%), an uninterrupted supply of electricity is still guaranteed. Figure G.7 illustrates the energy system today (electricity based) and the projected low-carbon energy system in the future (electricity and hydrogen based) [9].

Considering these attractive economic and environmental opportunities many countries have undertaken major commitments for transitioning into a hydrogen economy [9, 456, 547, 548]. According to the International Energy Agency (IEA), the global public sector expenditure spent towards building hydrogen economy is about $ 1 billion every year. This effort is primarily led by the US, Japan and the EU, accounting for about two thirds of the total expenditure. Their technological roadmaps estimate that transitioning into a mature hydrogen economy would require several decades, led by major developments in the areas of hydrogen production, storage, distribution and utilization. Key technical objectives include:

- Mass production of hydrogen by a CO_2-free route and at a competitive cost
- Development of efficient infrastructure for hydrogen distribution and delivery
- Development of viable storage systems for both stationary and automotive applications
- Reduction of cost for fuel cells and improvements to their performance and lifetimes

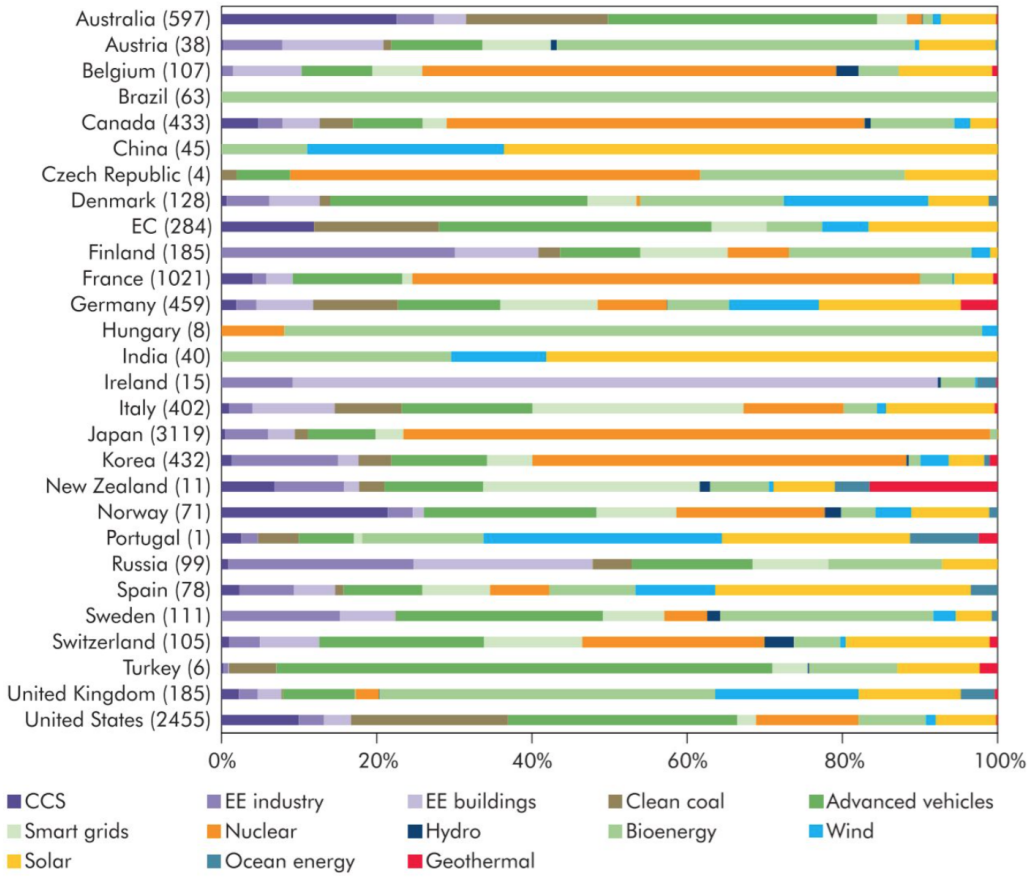

Figure G.8: Annual public-sector spending towards low-carbon technologies (in 2007) (million USD 2008 basis). source: [7]

While a full fledged hydrogen economy encompassing all these developments could be the ultimate goal, a partial implementation of fuel cell technology for use in stationary and automotive applications is a desirable outcome on its own merits [518].

In summary, the present chapter has overviewed key low-carbon energy technologies based on nuclear power, carbon capture and storage, solar, wind and hydrogen. As illustrated in Figure G.8, many countries are actively investing in the research and development of these technologies, although varying in the proportion based on their policy goals and resource availabilities [7]. While the global low-carbon energy research and development needs to be pursued in a much more aggressive manner, current developments provide a good start to future energy revolution.

H

STATEMENT ON THE CHOICE OF MATERIALS

In the chapters discussed in the main thesis, the need for the development of suitable catalysts for the oxygen reduction reaction (ORR) was highlighted (Chapter 2). Subsequently in Chapter 3 the 'alloying' as an effective strategy to improved catalysis on Pt surfaces was presented, which was followed by a detailed review of the recent progress in the development of Pt-alloy nanoparticle catalysts (Chapter 4). Such efforts are imperative for the widespread commercialization of PEMFCs, and as highlighted in Section 3.5, adoption of suitable structural characterization techniques is crucial in order to succeed in this effort. Chapter 6 and Chapter 7 discuss our findings in regards to the structural and compositional characterization of Pt-Fe alloy and Pt-Au nanoparticle alloy systems, studied exclusively with the use of aberration-corrected scanning transmission electron microscopy (previously reviewed in Chapter 5). The choice of these materials is justified from the great interest that they have gathered towards ORR electrocatalysis over the past years. A detailed discussion of these premises and some past works can be found in the Section 6.1 and Section 7.1 for Pt-Fe and Pt-Au systems, respectively. Some notable points can be summarized as below.

The Pt–Fe nanoparticles system has generated a lot of interest, both on the account of its enhanced ORR electrocatalysis [83, 262, 284–288, 366, 367], and also because of the magnetic properties that are deployable in ultrahigh-density information storage [368–372]. The PtFe (L1) ordered phase exhibits a very high uniaxial magnetocrystalline anisotropy along the *c* direction of the crystal structure. The Pt_3Fe ($L1_2$) phase is shown to deliver an enhanced ORR activity from the compressively strained Pt overlayers that encapsulate ordered alloy cores. Therefore, the chemical synthesis of Pt–Fe alloy nanoparticles in these ordered phases has been extensively studied in the past years. To note a few, the reported novel alloy structures include intermetallic Pt–Fe/Pt core shells [157], Pt–Fe–Cu ternary alloy nanoparticles [262], mono-disperse Ni/FePt core shells [373], and face-centered tetragonal (fct) FePt nanoparticles (see Chapter 2) [374].[1]

[1]The reported specific activities for these structures are about 0.55 mA/cm², 0.75 mA/cm², 1.95 mA/cm², and 3.16 mA/cm², respectively.

Bimetallic Au-Pt alloy nanoparticles are a promising class of materials for ORR electrocatalysis [393–399]. Several examples substantiating this were discussed in the literature review presented earlier in Chapter 4. Additionally, the Au-Pt nanoparticles are also being considered for the catalysis of many other reactions, such as H_2 activation [400], CO oxidation [401–403] and Methanol oxidation [393]. One major advantage here is that the combination of two noble metals allows the nanoparticle alloys to remain stable in many gaseous, liquid and electrochemical environments.

It is important to note, however, that the Pt-Fe and Pt-Au systems are probably not very practical options for the fuel cell ORR (see Chapter 4). One major issue with the Pt-Fe system is the leaching of Fe in the fuel cell working environments. In the case of Pt-Au, the use of two expensive noble metals creates an unfavorable burden on the overall fuel cell cost. In this juncture, the present work on these materials should be looked at as a model study for the structural investigation of other current and future catalyst systems. In the Appendix D, we discuss many such examples where the characterization techniques used in the main thesis work were applied to investigate thin film catalyst structures composed of Pt–Au–Co and Pt–Ir–Ni alloys, the novel Pt-nanotubular skeletons, and the Bi-decorated Pt nanowires.

Part VII

REFERENCES

[1] *Key world energy statistics*; International Energy Agency, 2005.

[2] *Climate change: the physical science basis.*; Intergovernmental panel on climate change (IPCC), 2013.

[3] *Key trends in CO2 emissions*; International Energy Agency, 2015.

[4] *OECD environmental outlook to 2050*; OECD, 2011.

[5] Mitchell, F., John *Reviews of Geophysics* **1989**, *27.1*, 115–139.

[6] *World Energy Outlook Executive Summary*; International Energy Agency, 2015.

[7] *Energy Technology Perspectives: Scenarios and Strategies to 2050*; International Energy Agency, 2010.

[8] Wang, Y.; Chen, K.; Mishler, J.; Cho, S.; Adroher, X. *Applied Energy* **2011**, *88*, 981–1007.

[9] *Hydrogen and Fuel Cells Technology Roadmap.*; International Energy Agency, 2015.

[10] *Fuel Cell Technologies Market Report*; US Department of Energy, 2013.

[11] Pollet, B.; Staffell, I.; Shang, J. *Electrochim Acta 84 2012*, 235–249.

[12] Carrette, L.; Friedrich, K.; Stimming, U. *Fuel cells* **2001**, *1*, 5–39.

[13] Wang, Y.; Chen, K. S.; Mishler, J.; Cho, S. C.; Adroher, X. C. *Applied Energy* **2011**, *88*, 981–1007.

[14] Kocha, S. S. *Fuel Cells*; Springer, 2013; pp 473–518.

[15] Cleghorn, S.; Ren, X.; Springer, T.; Wilson, M.; Zawodzinski, C.; Zawodzinski, T.; Gottesfeld, S. *International Journal of Hydrogen Energy* **1997**, *22*, 1137–1144.

[16] Gencoglu, M. T.; Ural, Z. *International Journal of Hydrogen Energy* **2009**, *34*, 5242–5248.

[17] Dyer, C. K. *Journal of Power Sources* **2002**, *106*, 31–34.

[18] *Hydrogen and Fuel Cells Technology Roadmap*; International Energy Agency, 2015.

[19] Pei, P.; Chen, H. *Applied Energy* **2014**, *125*, 60–75.

[20] Chalk, S. G.; Miller, J. F.; Wagner, F. W. *Journal of Power Sources* **2000**, *86*, 40–51.

[21] Wang, J. *Energy* **2015**, *80*, 509–521.

[22] Sopian, K.; Daud, W. R. W. *Renewable Energy* **2006**, *31*, 719–727.

[23] Debe, M. K. *Nature* **2012**, *486*, 43–51.

[24] Steele, B. C.; Heinzel, A. *Nature* **2001**, *414*, 345–352.

[25] Mehta, V.; Cooper, J. S. *Journal of Power Sources* **2003**, *114*, 32–53.

[26] https://www.eere.energy.gov/, 2013 (accessed).

[27] https://www.staff.ncl.ac.uk/prodip.das/modeling.html, 2016 (accessed).

[28] Li, X.; Sabir, I. *International Journal of Hydrogen Energy* **2005**, *30*, 359–371.

[29] *Fuel Cells Fact Sheet*; US Department of Energy (DOE), 2010.

[30] Peighambardoust, S. J.; Rowshanzamir, S.; Amjadi, M. *International Journal of Hydrogen Energy* **2010**, *35*, 9349–9384.

[31] Litster, S.; McLean, G. *Journal of Power Sources* **2004**, *130*, 61–76.

[32] Kim, O.-H.; Cho, Y.-H.; Kang, S. H.; Park, H.-Y.; Kim, M.; Lim, J. W.; Chung, D. Y.; Lee, M. J.; Choe, H.; Sung, Y.-E. *Nature Communications* **2013**, *4*.

[33] Uchida, M.; Park, Y.-C.; Kakinuma, K.; Yano, H.; Tryk, D. A.; Kamino, T.; Uchida, H.; Watanabe, M. *Physical Chemistry Chemical Physics* **2013**, *15*, 11236–11247.

[34] Klingele, M.; Breitwieser, M.; Zengerle, R.; Thiele, S. *Journal of Materials Chemistry A* **2015**, *3*, 11239–11245.

[35] Park, S.; Lee, J.-W.; Popov, B. N. *International Journal of Hydrogen Energy* **2012**, *37*, 5850–5865.

[36] Larminie, J.; Dicks, A.; McDonald, M. S. *Fuel cell systems explained*; J. Wiley Chichester, UK, 2003; Vol. 2.

[37] *Fuel Cell Technologies Market Report*; Department of Energy (DOE), 2013.

[38] De Bruijn, F.; Dam, V.; Janssen, G. *Fuel cells* **2008**, *8*, 3–22.

[39] Wu, J.; Yuan, X. Z.; Martin, J. J.; Wang, H.; Zhang, J.; Shen, J.; Wu, S.; Merida, W. *Journal of Power Sources* **2008**, *184*, 104–119.

[40] *Fuel Cell Technical Team Roadmap*; Department of Energy (DOE), 2013.

[41] Mayrhofer, K.; Strmcnik, D.; Blizanac, B.; Stamenkovic, V.; Arenz, M.; Markovic, N. *Electrochima Acta* **2008**, *53*, 3181–3188.

[42] *Mass Production Cost Estimation for Direct H2 PEM Fuel Cell Systems for Automotive Applications: 2010 Update.*; Department of Energy (DOE), 2010.

[43] Shao, Y.; Yin, G.; Gao, Y. *Journal of Power Sources* **2007**, *171*, 558–566.

[44] Borup, R.; Meyers, J.; Pivovar, B.; Kim, Y. S.; Mukundan, R.; Garland, N.; Myers, D.; Wilson, M.; Garzon, W. D., Fernando; et al, *Chemical reviews* **2007**, *107*, 3904–3951.

[45] Yousfi-Steiner, N.; Moçotéguy, P.; Candusso, D.; Hissel, D. *Journal of Power Sources* **2009**, *194*, 130–145.

[46] Song, D.; Wang, Q.; Liu, Z.; Navessin, T.; Eikerling, M.; Holdcroft, S. *Journal of Power Sources* **2004**, *126*, 104–111.

[47] Bessarabov, D.; Hitchcock, A. *Membrane Technology* **2009**, *2009*, 6–12.

[48] Melo, L. G.; Botton, G.; Hitchcock, A. P. *Microscopy and Microanalysis* **2015**, *21*, 2443–2444.

[49] Cullen, D. A.; Koestner, R.; Kukreja, R.; Liu, Z.; Minko, S.; Trotsenko, O.; Tokarev, A.; Guetaz, L.; Meyer, H.; Parish, C. *Journal of The Electrochemical Society* **2014**, *161*, F1111–F1117.

[50] Wang, C.; Duscher, G.; Paddison, S. J. *RSC Advances* **2015**, *5*, 2368–2373.

[51] Susac, D.; Berejnov, V.; Hitchcock, A. P.; Stumper, J. *ECS Transactions* **2013**, *50*, 405–413.

[52] Hitchcock, A.; Wu, J.; Lee, V.; Appathurai, N.; Tyliszczak, T.; Shiu, H.-W.; Shapiro, D.; Berejnov, V.; Susac, D.; Stumper, J. *Microscopy and Microanalysis* **2016**, *22*, 1290–1291.

[53] Yeager, E. *Journal of Molecular Catalysis* **1986**, *38*, 5–25.

[54] Song, C.; Zhang, J. *PEM fuel cell electrocatalysts and catalyst layers*; Springer, 2008; pp 89–134.

[55] Stonehart, P.; Ross, P. N. *Catalysis Reviews* **1975**, *12*, 1–35.

[56] Markovic, N.; Schmidt, T.; Stamenkovic, V.; Ross, P. *Fuel Cells* **2001**, *1*, 105–116.

[57] Marković, N.; Adžić, R.; Cahan, B.; Yeager, E. *Journal of Electroanalytical Chemistry* **1994**, *377*, 249–259.

[58] Paulus, U.; Wokaun, A.; Scherer, G.; Schmidt, T.; Stamenkovic, V.; Markovic, N. . M.; Ross, P. *Electrochimica Acta* **2002**, *47*, 3787–3798.

[59] Gattrell, M.; MacDougall, B. **2003**,

[60] Wu, J.; Yang, H. *Accounts of chemical research* **2013**, *46*, 1848–1857.

[61] Rossmeisl, J.; Karlberg, G. S.; Jaramillo, T.; Nørskov, J. K. *Faraday discussions* **2009**, *140*, 337–346.

[62] Keith, J. A.; Jerkiewicz, G.; Jacob, T. *ChemPhysChem* **2010**, *11*, 2779–2794.

[63] Hammer, B.; Nørskov, J. K. *Advances in catalysis* **2000**, *45*, 71–129.

[64] Stamenkovic, V.; Mun, B. S.; Mayrhofer, K. J.; Ross, P. N.; Markovic, N. M.; Rossmeisl, J.; Greeley, J.; Nørskov, J. K. *Angewandte Chemie* **2006**, *118*, 2963–2967.

[65] Nørskov, J. K.; Rossmeisl, J.; Logadottir, A.; Lindqvist, L.; Kitchin, J. R.; Bligaard, T.; Jonsson, H. *The Journal of Physical Chemistry B* **2004**, *108*, 17886–17892.

[66] Markovic, N.; Ross, P. N. *Surface Science Reports* **2002**, *45*, 117–229.

[67] Angerstein-Kozlowska, H.; Conway, B.; Sharp, W. *Journal of Electroanalytical Chemistry and Interfacial Electrochemistry* **1973**, *43*, 9–36.

[68] Allen, G. C.; Tucker, P. M.; Capon, A.; Parsons, R. *Journal of Electroanalytical Chemistry and Interfacial Electrochemistry* **1974**, *50*, 335–343.

[69] Hammond, J.; Winograd, N. *Journal of Electroanalytical Chemistry and Interfacial Electrochemistry* **1977**, *78*, 55–69.

[70] Nagy, Z.; You, H. *Electrochimica Acta* **2002**, *47*, 3037–3055.

[71] Chen, Z.; Higgins, D.; Yu, A.; Zhang, L.; Zhang, J. *Energy and Environmental Science* **2011**, *4*, 3167–3192.

[72] Wu, J.; Yang, H. *Accounts of chemical research* **2013**, *46*, 1848–1857.

[73] Greeley, J.; Stephens, I.; Bondarenko, A.; Johansson, T. P.; Hansen, H. A.; Jaramillo, T.; Rossmeisl, J.; Chorkendorff, I.; Nørskov, J. K. *Nature chemistry* **2009**, *1*, 552–556.

[74] Debe, M. K.; Atanasoski, R. T.; Steinbach, A. J. *ECS Transactions* **2011**, *41*, 937–954.

[75] Wang, J. X.; Inada, H.; Wu, L.; Zhu, Y.; Choi, Y.; Liu, P.; Zhou, W.-P.; Adzic, R. R. *Journal of the American Chemical Society* **2009**, *131*, 17298–17302.

[76] Zhang, J.; Lima, F.; Shao, M.; Sasaki, K.; Wang, J.; Hanson, J.; Adzic, R. *The Journal of physical chemistry B* **2005**, *109*, 22701–22704.

[77] Luo, J.; Wang, L.; Mott, D.; Njoki, P. N.; Lin, Y.; He, T.; Xu, Z.; Wanjana, B. N.; Lim, I.; Im, S. *Advanced Materials* **2008**, *20*, 4342–4347.

[78] Gong, K.; Du, F.; Xia, Z.; Durstock, M.; Dai, L. *Science* **2009**, *323*, 760–764.

[79] Li, Y.; Zhou, W.; Wang, H.; Xie, L.; Liang, Y.; Wei, F.; Idrobo, J.-C.; Pennycook, S. J.; Dai, H. *Nature nanotechnology* **2012**, *7*, 394–400.

[80] Brouzgou, A.; Song, S.; Tsiakaras, P. *Applied Catalysis B: Environmental* **2012**, *127*, 371–388.

[81] Chen, C.; Kang, Y.; Huo, Z.; Zhu, Z.; Huang, W.; Xin, H. L.; Snyder, J. D.; Li, D.; Herron, J. A.; Mavrikakis, M. *Science* **2014**, *343*, 1339–1343.

[82] Nilsson, A.; Pettersson, L. G.; Norskov, J. *Chemical bonding at surfaces and interfaces*; Elsevier, 2011.

[83] Stamenkovic, V. R.; Mun, B. S.; Arenz, M.; Mayrhofer, K. J.; Lucas, C. A.; Wang, G.; Ross, P. N.; Markovic, N. M. *Nature materials* **2007**, *6*, 241–247.

[84] Zhang, S.; Yuan, X.-Z.; Hin, J. N. C.; Wang, H.; Friedrich, K. A.; Schulze, M. *Journal of Power Sources* **2009**, *194*, 588–600.

[85] Shao-Horn, Y.; Sheng, W.; Chen, S.; Ferreira, P.; Holby, E.; Morgan, D. *Topics in Catalysis* **2007**, *46*, 285–305.

[86] Chen, S.; Gasteiger, H. A.; Hayakawa, K.; Tada, T.; Shao-Horn, Y. *Journal of the Electrochemical Society* **2010**, *157*, A82–A97.

[87] Ferreira, P.; Shao-Horn, Y.; Morgan, D.; Makharia, R.; Kocha, S.; Gasteiger, H. *Journal of The Electrochemical Society* **2005**, *152*, A2256–A2271.

[88] Yu, Y.; Xin, H.; Hovden, R.; Wang, D.; Mundy, J.; Abruna, H.; Muller, D. *Microscopy and Microanalysis* **2011**, 938–939.

[89] Xin, H.; Mundy, J.; Liu, Z.; Cabezas, R.; Hovden, R.; Kourkoutis, L.; Zhang, J.; Subramanian, N.; Makharia, R.; Wagner, F. *Nano Letters* **2012**, *12*, 490–497.

[90] Carlton, C. E.; Chen, S.; Ferreira, P. J.; Allard, L. F.; Shao-Horn, Y. *The Journal of Physical Chemistry Letters* **2012**, *3*, 161–166.

[91] Prabhudev, S.; Bugnet, M.; Bock, C.; Botton, G. *ACS Nano* **2013**, *7*, 6103–6110.

[92] Bowker, M. *Nature Materials* **2002**, *1*, 205–206.

[93] Voorhees, P. W. *Journal of Statistical Physics* **1985**, *38*, 231–252.

[94] Burlakov, V. *arXiv preprint arXiv:0710.5224* **2007**,

[95] Woehl, T.; Park, C.; Evans, J.; Arslan, I.; Ristenpart, W.; Browning, N. *Nano Letters* **2014**, *14*, 373–378.

[96] Asoro, M.; Kovar, D.; Shao-Horn, Y.; Allard, L.; Ferreira, P. *Nanotechnology* **2009**, *21*, 025701.

[97] Chen, H.; Yu, Y.; Xin, H. L.; Newton, K. A.; Holtz, M. E.; Wang, D.; Muller, D. A.; Abruña, H. D.; DiSalvo, F. J. *Chemistry of Materials* **2013**, *25*, 1436–1442.

[98] Wang, X.; Kumar, R.; Myers, D. J. *Electrochemical and Solid-State Letters* **2006**, *9*, A225–A227.

[99] Stamenkovic, V.; Mun, B.; Mayrhofer, K.; Ross, P.; Markovic, N. *Journal of the American Chemical Society* **2006**, *128*, 8813–8819.

[100] Chen, S.; Ferreira, P.; Sheng, W.; Yabuuchi, N.; Allard, L.; Shao-Horn, Y. *Journal of the American Chemical Society* **2008**, *130*, 13818–13819.

[101] Ball, S. C.; Hudson, S. L.; Theobald, B. R.; Thompsett, D. *ECS Transactions* **2007**, *11*, 1267–1278.

[102] Bonakdarpour, A.; Wenzel, J.; Stevens, D.; Sheng, S.; Monchesky, T.; Löbel, R.; Atanasoski, R.; Schmoeckel, A.; Vernstrom, G.; Debe, M. *Journal of The Electrochemical Society* **2005**, *152*, A61–A72.

[103] Wang, D.; Yu, Y.; Xin, H.; Hovden, R.; Ercius, P.; Mundy, J.; Chen, H.; Richard, J.; Muller, D.; DiSalvo, F. *Nano Letters* **2012**, *12*, 5230–5238.

[104] Strasser, P.; Koh, S.; Yu, C. *ECS Transactions* **2007**, *11*, 167–180.

[105] Strasser, P.; Koh, S.; Greeley, J. *Physical Chemistry Chemical Physics* **2008**, *10*, 3670–3683.

[106] Maass, S.; Finsterwalder, F.; Frank, G.; Hartmann, R.; Merten, C. *Journal of Power Sources* **2008**, *176*, 444–451.

[107] Linse, N. Start/stop phenomena in polymer electrolyte fuel cells. Ph.D. thesis, Diss., Eidgenössische Technische Hochschule ETH Zürich, Nr. 20132, 2012, 2012.

[108] Linse, N.; Scherer, G.; Wokaun, A.; Gubler, L. *Journal of Power Sources* **2012**, *219*, 240–248.

[109] Schulenburg, H.; Schwanitz, B.; Linse, N.; Scherer, G.; Wokaun, A.; Krbanjevic, J.; Manke, I. *The Journal of Physical Chemistry C* **2011**, *115*, 14236–14243.

[110] Zerda, T.; Xu, W.; Zerda, A.; Zhao, Y.; Dreele, R. *Carbon* **2000**, *38*, 355–361.

[111] Linse, N.; Gubler, L.; Scherer, G.; Wokaun, A. *Electrochimica Acta* **2011**, *56*, 7541–7549.

[112] Meier, J. C.; Galeano, C.; Katsounaros, I.; Topalov, A. A.; Kostka, A.; Schüth, F.; Mayrhofer, K. J. *ACS Catalysis* **2012**, *2*, 832–843.

[113] Zana, A.; Speder, J.; Reeler, N. E.; Vosch, T.; Arenz, M. *Electrochimica Acta* **2013**, *114*, 455–461.

[114] Gasteiger, H. A.; Kocha, S. S.; Sompalli, B.; Wagner, F. T. *Applied Catalysis B: Environmental* **2005**, *56*, 9–35.

[115] Shinozaki, K.; Zack, J.; Richards, R.; Pivovar, B.; Kocha, S.; , I. M. *Journal of Electrochemical Society* **2015**, *162*, F1144–F1158.

[116] Severin, K.; Blanchard, G.; Bruening, M. A suite of undergraduate laboratories focused on surface and interface science. A suite of undergraduate laboratories focused on surface and interface science. 1999; pp U309–U309.

[117] Bard, A. J.; Faulkner, L. R.; Leddy, J.; Zoski, C. G. *Electrochemical methods: fundamentals and applications*; Wiley New York, 1980; Vol. 2.

[118] Nicholson, R. *Analytical Chemistry* **1965**, *37*, 1351–1355.

[119] Liu, J. *Journal of electron microscopy* **2005**, *54*, 251–278.

[120] Thomas, J.; Terasaki, O. *Topics in catalysis* **2002**, *21*, 155–159.

[121] Chu, M.-W.; Chen, C. H. *ACS nano* **2013**, *7*, 4700–4707.

[122] Egerton, R. *Topics in catalysis* **2002**, *21*, 185–190.

[123] Gai, P. *Current Opinion in Solid State and Materials Science* **2001**, *5*, 371–380.

[124] Datye, A. *Journal of Catalysis* **2003**, *216*, 144–154.

[125] Kiely, C. *Nature Materials* **2010**, *9*, 296–297.

[126] Crozier, P.; Situ, S.; Pennycook, S.; Nellist, P.; York, N. *Springer New York New* **2011**,

[127] Sanchez, S.; Small, M.; Sivaramakrishnan, S.; Wen, J.; Zuo, J.; Nuzzo, R. *Analytical Chemistry* **2010**, *82*, 2599–2607.

[128] Stroppa, D.; Zagonel, L.; Montoro, L.; Leite, E.; Ramirez, A. *Chem-phys-chem* **2012**, *13*, 437–443.

[129] Thomas, J.; Midgley, P. *Chemical Communications* **2004**, *11*, 1253–1267.

[130] Yang, J.; Small, M.; Grieshaber, R.; Nuzzo, R. *Chemical Society Reviews* **2012**, *41*, 8179–8194.

[131] Yacaman, M.; Ascencio, J.; Tehuacanero, S.; Marin, M. *Topics in catalysis* **2002**, *18*, 167–173.

[132] Ortalan, V.; Uzun, A.; Gates, B. C.; Browning, N. D. *Nature nanotechnology* **2010**, *5*, 843–847.

[133] Mathew, R. J.; Russell, A. E. *Topics in Catalysis* **2000**, *10*, 231–239.

[134] Russell, A.; Rose, A. *Chemical Reviews* **2004**, *104*, 4613–4636.

[135] Russell, A.; Maniguet, S.; Mathew, R.; Yao, J.; Roberts, M.; Thompsett, D. *Journal of Power Sources* **2001**, *96*, 226–232.

[136] Viswanathan, R.; Liu, R.; Smotkin, E. *Review of scientific instruments* **2002**, *73*, 2124–2127.

[137] Bazin, D.; Rehr, J.; Chemistry, B. *The Journal of Physical* **2003**, *107*, 12398–12402.

[138] Singh, J.; Lamberti, C.; van Bokhoven, J. *Chemical Society Reviews* **2010**, *39*, 4754–4766.

[139] Corcoran, C.; Tavassol, H.; Rigsby, M.; Bagus, P.; Wieckowski, A. *Journal of Power Sources* **2010**, *195*, 7856–7879.

[140] Casalongue, H. S.; Kaya, S.; Viswanathan, V.; Miller, D. J.; Friebel, D.; Hansen, H. A.; Nørskov, J. K.; Nilsson, A.; Ogasawara, H. *Nature communications* **2013**, *4*.

[141] Lin, W.; Herzing, A.; Kiely, C.; Wachs, I. *The Journal of Physical Chemistry, C* **2008**, *112*, 5942–5951.

[142] Ross, P. *Electrochimica acta* **1991**, *36*, 2053–2062.

[143] Strasser, P.; Koh, S.; Anniyev, T.; Greeley, J.; More, K.; Yu, C.; Toney, M. *Nature chemistry* **2010**, *2*, 454–460.

[144] Hüfner, S. *Photoelectron spectroscopy: principles and applications*; Springer Science & Business Media, 2013.

[145] Schoegl, R. *Advances in Catalysis* **2009**, *52*, 273–338.

[146] Roth, C.; Martz, N.; Fuess, H. *Physical Chemistry Chemical Physics* **2001**, *3*, 315–319.

[147] Nellist, P. *Science of Microscopy 2007*, 1–53.

[148] Woehl, T.; Park, C.; Evans, J.; Arslan, I.; Ristenpart, W.; Browning, N. *Nano Letters* **2014**, *14*, 373–378.

[149] Sheng, W.; Chen, S.; Vescovo, E.; Shao-Horn, Y. *Journal of Electrochemical Society* **2012**, *159*, B96.

[150] Alloyeau, D.; Bouar, Y.; Oikawa, T.; Langlois, C.; Pravot, G.; Le Loiseau, A.; Ricolleau, C. *Physical Review Letters* **2010**, *105*, 1–4.

[151] Heggen, M.; Oezaslan, M.; Houben, L.; Strasser, P. *The Journal of Physical Chemistry C* **2012**, *116*, 19073–19083.

[152] Sanchez, S.; Small, M.; Zuo, J.; Nuzzo, R. *Journal of American Chemical Society* **2009**, *131*, 8683–8689.

[153] Chang, L.; Barnard, A.; Gontard, L.; Dunin-Borkowski, R. *Nano Letters* **2010**, *10*, 3073–3076.

[154] Lu, N.; Wang, J.; Xie, S.; Brink, J.; McIlwrath, K.; Xia, Y.; Kim, M. *The Journal of Physical Chemistry, C* **2014**, *118*, 28876–28882.

[155] Cui, C.; Gan, L.; Heggen, M.; Rudi, S.; Strasser, P. *Nature Materials* **2013**, *12*, 765–771.

[156] Chen, S.; Sheng, W.; Yabuuchi, N.; Ferreira, P. J.; Allard, L. F.; Shao-Horn, Y. *The Journal of Physical Chemistry C* **2008**, *113*, 1109–1125.

[157] Prabhudev, S.; Bugnet, M.; Bock, C.; Botton, G. A. *ACS Nano* **2013**, *7*, 6103–6110.

[158] Jones, L.; MacArthur, K.; Fauske, V.; van Helvoort, A.; Nellist, P. *Nano letters* **2014**, *14*, 6336–6341.

[159] Gan, L.; Yu, R.; Luo, J.; Cheng, Z.; Zhu, J. *Journal of Physical Chemistry Letters* **2012**, *3*, 934–938.

[160] Monteforte, M.; Kobayashi, S.; Tung, L. D.; Higashimine, K.; Mott, D. M.; Maenosono, S.; Thanh, N. T.; Robinson, I. K. *New Journal of Physics* **2016**, *18*, 033016.

[161] Yankovich, A. B.; Berkels, B.; Dahmen, W.; Binev, P.; Sanchez, S.; Bradley, S.; Li, A.; Szlufarska, I.; Voyles, P. M. *Nature communications* **2014**, *5*.

[162] Ferreira, P. J.; Shao-Horn, Y. *Electrochemical and solid-state letters* **2007**, *10*, B60–B63.

[163] Alloyeau, D.; Langlois, C.; Ricolleau, C.; Le Bouar, Y.; Loiseau, A. *Nanotechnology* **2007**, *18*, 375301.

[164] Alloyeau, D.; Oikawa, T.; Nelayah, J. *Applied Physics* **2012**, *101*, 121920–121924.

[165] Gan, L.; Cui, C.; Heggen, M.; Dionigi, F.; Rudi, S.; Strasser, P. *Science* **2014**, *346*, 1502–1506.

[166] Han, L.; Liu, H.; Cui, P.; Peng, Z.; Zhang, S.; Yang, J. *Scientific reports* **2014**, *4*.

[167] Bernal, S.; Calvino, J.; Cauqui, M.; Gatica, J.; Cartes, C.; Omil, J.; Pintado, J. *Catalysis Today* **2003**, *77*, 385–406.

[168] Alloyeau, D.; Ricolleau, C.; Mottet, C.; Oikawa, T.; Langlois, C.; Le Bouar, Y.; Braidy, N.; Loiseau, A. *Nature materials* **2009**, *8*, 940–946.

[169] Johnston-Peck, A.; Cullen, D.; Tracy, J. *Particles and Particle Systems Characterization* **2013**, *30*, 678–682.

[170] Chan, M.; Chen, L.; Nan, F.; Britten, J.; Bock, C.; Botton, G. *Nanoscale* **2012**, *4*, 7273–7279.

[171] Wittig, J.; Bentley, J.; Allard, L.; Wellons, M.; Lukehart, C. *Microscopy and Microanalysis* **2008**, *14*, 216–217.

[172] Challa, S.; Delariva, A.; Hansen, T.; Helveg, S.; Sehested, J.; Hansen, P.; Garzon, F.; Datye, A. *Journal of American Chemical Society* **2011**, *133*, 20672–20675.

[173] Abruna, H. D.; Chen, H.; Yu, Y.; Xin, H.; Newton, K.; Holtz, M.; Wang, D.; Muller, D.; DiSalvo, F. *Chem Mater* **2013**, *25*, 1436–1442.

[174] Gan, L.; Heggen, M.; Cui, C.; Rudi, S.; Strasser, P. *ECS transactions* **2013**, *58*, 1471–1475.

[175] Deiana, D.; Wagner, J.; Hansen, T. *ECS* **2015**, *66*, 115–127.

[176] Yu, Y.; Xin, H.; Hovden, R.; Wang, D.; Rus, E.; Mundy, J.; Abruna, H.; Muller, D. *Nano Letters* **2012**,

[177] Jeyabharathi, C.; Hodnik, N.; Baldizzone, C.; Meier, J.; Heggen, M.; Phani, K.; Mayrhofer, K. *ChemCatChem* **2013**, *5*, 2627–2635.

[178] Dubau, L.; Lopez-Haro, M.; Castanheira, L.; Durst, J.; Chatenet, M.; Bayle-Guillemaud, P.; Maillard, F. *Applied Environmental and Catalysis, B* **2013**, *142*, 801–808.

[179] Gan, L.; Heggen, M.; Malley, R.; Theobald, B.; Strasser, P. *Nano letters* **2013**, *13*, 1131–1138.

[180] Zecevic, J.; de Jong, K. P.; de Jongh, P. E. *Current Opinion in Solid State and Materials Science* **2013**, *17*, 115–125.

[181] Grothausmann, R.; Zehl, G.; Manke, I.; Fiechter, S.; Bogdanoff, P.; Dorbandt, I.; Kupsch, A.; Lange, A.; Hentschel, M.; Schumacher, G. *Journal of American Chemical Society* **2011**, *133*, 18161–18171.

[182] Koster, A.; Ziese, U.; Verkleij, A.; Janssen, A.; DeJong, K. *The Journal of Physical Chemistry B* **2000**, *104*, 9368–9370.

[183] Weyland, M. *Topics in Catalysis* **2002**, *21*, 175–183.

[184] Midgley, P.; Weyland, M. *Ultramicroscopy* **2003**, *96*, 413–431.

[185] Midgley, P.; Dunin-Borkowski, R. *Nature Materials* **2009**, *8*, 271–280.

[186] Abruna, H. D.; Yu, Y.; Xin, H.; Hovden, R.; Wang, D.; Rus, E.; Mundy, J.; Muller, D. *Nano Letters* **2012**,

[187] Chen, C.; Zhu, C.; White, E.; Chiu, C.; Scott, M.; Regan, B.; Marks, L.; Huang, Y.; Miao, J. *Nature 2013*, 4–9.

[188] Gontard, L.; Dunin-Borkowski, R.; Ozkaya, D. *Journal of Microscopy* **2008**, *232*, 248–259.

[189] Goris, B.; Beenhouwer, J.; De, S.; Backer, A.; Zanaga, D.; Batenburg, K.; Iglesias, A.; Aert, S.; Bals, S.; Sijbers, J. *Nano Letters* **2015**, *15*, 6996–7001.

[190] Allard, L.; Overbury, S.; Bigelow, W.; Katz, M.; Nackashi, D.; Damiano, J. *Microscopy and Microanalysis* **2012**, *18*, 656–666.

[191] Delalande, M.; Guinel, M.; Allard, L.; Delattre, A.; Le, L.; Bris, R.; Samson, Y.; Bayle-Guillemaud, P.; Reiss, P. *The Journal of Physical Chemistry C* **2012**, *116*, 6866–6872.

[192] Prabhudev, S.; Bugnet, M.; Zhu, G.; Bock, C.; Botton, G. *ChemCatChem* **2015**, *7*, 3655–3664.

[193] Chi, M.; Wang, C.; Lei, Y.; Wang, G.; Li, D.; More, K. L.; Lupini, A.; Allard, L. F.; Markovic, N. M.; Stamenkovic, V. R. *Nature communications* **2015**, *6*.

[194] Giorgio, S.; Joao, S.; Nitsche, S.; Chaudanson, D.; Sitja, G.; Henry, C. *Ultramicroscopy* **2006**, *106*, 503–507.

[195] Yoshida, H.; Kuwauchi, Y.; Jinschek, J.; Sun, K.; Tanaka, S.; Kohyama, M.; Takeda, S. *Science* **2012**, *335*, 317–319.

[196] Simonsen, S.; Chorkendorff, I.; Dahl, S.; Skoglundh, M.; Sehested, J.; Helveg, S. *Journal of the American Chemical Society* **2010**, *132*, 7968–7975.

[197] Hansen, T. W.; Wagner, J. B. *ACS Catalysis* **2014**, *4*, 1673–1685.

[198] de Jonge, N.; Ross, F. M. *Nature nanotechnology* **2011**, *6*, 695–704.

[199] Jungjohann, K.; Bliznakov, S.; Sutter, P.; Stach, E.; Sutter, E. *Nano letters* **2013**, *13*, 2964–2970.

[200] Park, J.; Zheng, H.; Lee, W.; Geissler, P.; Rabani, E.; Alivisatos, A. *ACS Nano* **2012**, *6*, 2078–2085.

[201] Holtz, M. E.; Yu, Y.; Abruña, H.; Muller, D. *Microscopy and Microanalysis* **2012**, *18*, 1094–1095.

[202] Zhu, G.; Prabhudev, S.; Yang, J.; Gabardo, C.; Botton, G.; Soleymani, L. *The Journal of Physical Chemistry C* **2014**, *118*, 22111–22119.

[203] Hodnik, N.; Dehm, G.; Mayrhofer, K. *Accounts of Chemical Research* **2016**, *49*, 2015–2022.

[204] Gai, P. *Topics in catalysis* **2002**, *21*, 161–173.

[205] Jinschek, J. *Chemical Communications* **2014**, *50*, 2696–2706.

[206] Binev, P.; Dahmen, W.; DeVore, R.; Lamby, P.; Savu, D.; Sharpley, R.; Springer, U. *In Modeling Nanoscale Imaging in Electron Microscopy* **2012**, 73–126.

[207] Stevens, A.; Kovarik, L.; Yang, H.; Pu, Y.; Carin, L.; Browning, N. *Microscopy and Microanalysis* **2016**, *22*, 560–561.

[208] Carlton, C.; Chen, S.; Ferreira, P.; Allard, L.; Shao-horn, Y. *Journal of Physical Chemistry* **2012**,

[209] Xin, H.; Mundy, J.; Liu, Z.; Cabezas, R.; Hovden, R.; Kourkoutis, L.; Zhang, J.; Subramanian, N.; Makharia, R.; Wagner, F. *Nano Letters* **2012**, *12*, 490–497.

[210] Jarausch, K.; Thomas, P.; Leonard, D.; Twesten, R.; Booth, C.; Four-dimensional, S. *Ultramicroscopy* **2009**, *109*, 326–337.

[211] Genc, A.; Kovarik, L.; Gu, M.; Cheng, H.; Plachinda, P.; Pullan, L.; Wang, C. *Ultramicroscopy* **2013**, *131*, 24–32.

[212] Egerton, R. F. *Electron energy-loss spectroscopy in the electron microscope*; Springer Science & Business Media, 2011.

[213] Botton, G. *Science of Microscopy.* **2007**, 273–405.

[214] Sigle, W. *Annual Reviews of Materials Research Society* **2005**, *35*, 239–314.

[215] Rez, P.; Muller, D. *Annual Reviews of Materials Research Society* **2008**, *38*, 535–558.

[216] Avery, N. R. *Chemical Physics Letters* **1983**, *96*, 371–373.

[217] Steininger, H.; Lehwald, S.; Ibach, H. *Surface Science* **1982**, *123*, 1–17.

[218] Gland, J. L.; Sexton, B. A.; Fisher, G. B. *Surface Science* **1980**, *95*, 587–602.

[219] Durham, P.; Koningsberger, D.; Prins, R. *Wiley&Sons, New York* **1988**, 53.

[220] Bertin, E. *Principles and practice of X-ray spectrometric analysis.*; Springer, 2012.

[221] Teo, B. K. *EXAFS: Basic Principles and Data Analysis*; Springer, 1986; pp 21–33.

[222] Newville, M. *Reviews in Mineralogy and Geochemistry* **2014**, *78*, 33–74.

[223] Frenkel, A.; Yevick, A.; Cooper, C.; Vasic, R. *Annual Review of Analytical Chemistry* **2011**, *4*, 23–39.

[224] Witkowska, A.; Dsoke, S.; Principi, E.; Marassi, R.; Cicco, A.; Albertini, V. *Journal of Power Sources* **2008**, *178*, 603–609.

[225] Principi, E.; Witkowska, A.; Dsoke, S.; Marassi, R.; DiCicco, A. *Physical Chemistry Chemical Physics* **2009**, *11*, 9987–9995.

[226] Gonzalez Ruiz-Camacho, B.; Valenzuela, M.; Huerta, R.; Suarez-Alcantara, K.; Canton, S.; Pola-Albores, F. *International Journal of Hydrogen Energy* **2013**, *38*, 12648–12656.

[227] Witkowska, A.; DiCicco, A.; Principi, E. *Physical Review, B* **2007**, *76*, 104–110.

[228] Frenkel, A.; Hills, C.; Nuzzo, R. *The Journal of Physical Chemistry, B* **2001**, *105*, 2689–12703.

[229] Jia, Q.; Liang, W.; Bates, M.; Mani, P.; Lee, W.; Mukerjee, S. *ACS Nano* **2015**, *9*, 387–400.

[230] Strasser, P.; Koh, S.; Anniyev, T.; Greeley, J.; More, K.; Yu, C.; Liu, Z.; Kaya, S.; Nordlund, D.; Ogasawara, H. *Nature chemistry* **2010**, *2*, 454–460.

[231] Friebel, D.; Miller, D. J.; O?Grady, C. P.; Anniyev, T.; Bargar, J.; Bergmann, U.; Ogasawara, H.; Wikfeldt, K. T.; Pettersson, L. G.; Nilsson, A. *Physical Chemistry Chemical Physics* **2011**, *13*, 262–266.

[232] Allen, P.; Conradson, S.; Wilson, M.; Gottesfeld, S.; Raistrick, I.; Valerio, J.; Lovato, M. *Journal of Electroanalytical Chemistry* **1995**, *384*, 99–103.

[233] Teliska, M.; O'Grady, W.; Ramaker, D. *The Journal of Physical Chemistry B* **2005**, *109*, 8076–8084.

[234] Caldwell, K. M.; Ramaker, D. E.; Jia, Q.; Mukerjee, S.; Ziegelbauer, J. M.; Kukreja, R. S.; Kongkanand, A. *The Journal of Physical Chemistry C* **2014**, *119*, 757–765.

[235] Jia, Q.; Segre, C. U.; Ramaker, D.; Caldwell, K.; Trahan, M.; Mukerjee, S. *Electrochimica Acta* **2013**, *88*, 604–613.

[236] Russell, A. E.; Tessier, B.; Wise, A.; Rose, A.; Price, S. W.; Richardson, P.; Ball, S.; Theobald, B.; Thompsett, D.; Crabb, E. M. *ECS transactions* **2011**, *41*, 55–67.

[237] Kaya, S.; Friebel, D.; Ogasawara, H.; Anniyev, T.; Nilsson, A. *Journal of Electron Spectroscopy and Related Phenomena* **2013**, *190*, 113–124.

[238] Hyman, M. P.; Medlin, J. W. *The Journal of Physical Chemistry C* **2007**, *111*, 17052–17060.

[239] Friebel, D.; Viswanathan, V.; Miller, D. J.; Anniyev, T.; Ogasawara, H.; Larsen, A. H.; O?Grady, C. P.; Nørskov, J. K.; Nilsson, A. *Journal of the American Chemical Society* **2012**, *134*, 9664–9671.

[240] Teliska, M.; Murthi, V. S.; Mukerjee, S.; Ramaker, D. E. *Journal of the Electrochemical Society* **2005**, *152*, A2159–A2169.

[241] Erickson, E. M.; Thorum, M. S.; Vasi, R.; Marinkovi, N. S.; Frenkel, A. I.; Gewirth, A. A.; Nuzzo, R. G. *Journal of the American Chemical Society* **2011**, *134*, 197–200.

[242] Friebel, D.; Miller, D. J.; Nordlund, D.; Ogasawara, H.; Nilsson, A. *Angewandte Chemie International Edition* **2011**, *50*, 10190–10192.

[243] Tuaev, X.; Rudi, S.; Petkov, V.; Hoell, A.; Strasser, P. *ACS Nano* **2013**, *7*, 5666–5674.

[244] Chen, G.; Kuttiyiel, K. A.; Su, D.; Li, M.; Wang, C.-H.; Buceta, D.; Du, C.; Gao, Y.; Yin, G.; Sasaki, K. *Chemistry of Materials* **2016**, *28*, 5274–5281.

[245] de Smit, E.; Swart, I.; Creemer, J. F.; Hoveling, G. H.; Gilles, M. K.; Tyliszczak, T.; Kooyman, P. J.; Zandbergen, H. W.; Morin, C.; Weckhuysen, B. M. *Nature* **2008**, *456*, 222–225.

[246] Egerton, R. F. *Physical principles of electron microscopy: an introduction to TEM, SEM, and AEM*; Springer Science and Business Media, 2006.

[247] Viswanathan, R.; Liu, R.; Smotkin, E. S. *Review of scientific instruments* **2002**, *73*, 2124–2127.

[248] Witkowska, A.; Dsoke, S.; Principi, E.; Marassi, R.; Di Cicco, A.; Albertini, V. R. *Journal of Power Sources* **2008**, *178*, 603–609.

[249] Ishiguro, N.; Saida, T.; Uruga, T.; Nagamatsu, S.-i.; Sekizawa, O.; Nitta, K.; Yamamoto, T.; Ohkoshi, S.-i.; Iwasawa, Y.; Yokoyama, T. *Acs Catalysis* **2012**, *2*, 1319–1330.

[250] Tada, M.; Murata, S.; Asakoka, T.; Hiroshima, K.; Okumura, K.; Tanida, H.; Uruga, T.; Nakanishi, H.; Matsumoto, S.-i.; Inada, Y. *Angewandte Chemie International Edition* **2007**, *46*, 4310–4315.

[251] Mayrhofer, K. J.; Ashton, S. J.; Meier, J. C.; Wiberg, G. K.; Hanzlik, M.; Arenz, M. *Journal of Power Sources* **2008**, *185*, 734–739.

[252] Arán-Ais, R. M.; Yu, Y.; Hovden, R.; Solla-Gullón, J.; Herrero, E.; Feliu, J. M.; Abruña, H. D. *Journal of the American Chemical Society* **2015**, *137*, 14992–14998.

[253] Dubau, L.; Castanheira, L.; Berthomé, G.; Maillard, F. *Electrochimica Acta* **2013**, *110*, 273–281.

[254] Chenna, S.; Crozier, P. A. *ACS Catalysis* **2012**, *2*, 2395–2402.

[255] Takao, S.; Sekizawa, O.; Samjeske, G.; Nagamatsu, S.-i.; Kaneko, T.; Yamamoto, T.; Higashi, K.; Nagasawa, K.; Uruga, T.; Iwasawa, Y. *The journal of Physical Chemistry Letters* **2015**, *6*, 2121–2126.

[256] Shao, M.; Chang, Q.; Dodelet, J.-P.; Chenitz, R. *Chemical reviews* **2016**, *116*, 3594–3657.

[257] Cao, M.; Wu, D.; Cao, R. *ChemCatChem* **2014**, *6*, 26–45.

[258] Antolini, E.; Passos, R.; Ticianelli, E. *Electrochimica Acta* **2002**, *48*, 263–270.

[259] Koh, S.; Toney, M.; Strasser, P. *Electrochimica Acta* **2007**, *52*, 2765–2774.

[260] Mukerjee, S.; Srinivasan, S.; Soriaga, M.; McBreen, J. *Journal of the Electrochemical Society* **1995**, *142*, 1409–1422.

[261] Mani, P.; Srivastava, R.; Strasser, P. *The Journal of Physical Chemistry C* **2008**, *112*, 2770–2778.

[262] Chen, L.; Bock, C.; Mercier, P.; MacDougall, B. *Electrochimica Acta* **2012**, *77*, 212–224.

[263] Gan, L.; Rudi, S.; Cui, C.; Heggen, M.; Strasser, P. *Small* **2016**, *12*, 3189–3196.

[264] Jennings, P.; Pollet, B.; Johnston, R. *Physical Chemistry Chemical Physics* **2012**, *14*, 3134–3139.

[265] Yang, S.; Peng, Z.; Yang, H. *Advanced Functional Materials* **2008**, *18*, 2745–2753.

[266] Ghosh, T.; Zhou, Q.; Gregoire, J.; van Dover, R.; DiSalvo, F. *The Journal of Physical Chemistry C* **2010**, *114*, 12545–12553.

[267] Lim, B.; Jiang, M.; Camargo, P.; Cho, E.; Tao, J.; Lu, X.; Xia, Y. *science* **2009**, *324*, 1302–1305.

[268] Yang, L.; Vukmirovic, M.; Su, D.; Sasaki, K.; Herron, J.; Mavrikakis, M.; Adzic, R. *The Journal of Physical Chemistry C* **2013**, *117*, 1748–1753.

[269] Liu, H.; Ye, F.; Yao, Q.; Cao, H.; Xie, J.; Lee, J. Y.; Yang, J. *Scientific reports* **2014**, *4*.

[270] Yancey, D.; Carino, E.; Crooks, R. *Journal of the American Chemical Society* **2010**, *132*, 10988–10989.

[271] Hwang, S.; Yoo, S.; Jeon, T.; Lee, K.; Lim, T.; Sung, Y.; Kim, S. *Chemical Communications* **2010**, *46*, 8401–8403.

[272] Han, B.; Carlton, C. E.; Suntivich, J.; Xu, Z.; Shao-Horn, Y. *The Journal of Physical Chemistry C* **2015**, *119*, 3971–3978.

[273] Zhang, J.; Vukmirovic, M.; Xu, Y.; Mavrikakis, M.; Adzic, R. *Angewandte Chemie International Edition* **2005**, *44*, 2132–2135.

[274] Tan, X.; Prabhudev, S.; Kohandehghan, A.; Karpuzov, D.; Botton, G.; Mitlin, D. *ACS Catalysis* **2015**, *5*, 1513–1524.

[275] Kang, Y.; Snyder, J.; Chi, M.; Li, D.; More, K.; Markovic, N.; Stamenkovic, V. *Nano Letters* **2014**, *14*, 6361–6367.

[276] Mazumder, V.; Chi, M.; More, K.; Sun, S. *Angewandte Chemie International Edition* **2010**, *49*, 9368–9372.

[277] Wang, C.; Li, D.; Chi, M.; Pearson, J.; Rankin, R.; Greeley, J.; Markovic, N. *The Journal of Physical Chemistry Letters* **2012**, *3*, 1668–1673.

[278] Loukrakpam, R.; Wanjala, B.; Yin, J.; Fang, B.; Luo, J.; Shao, M.; Zhong, C. *ACS catalysis* **2011**, *1*, 562–572.

[279] Wang, C.; der Vliet, D.; More, K.; Zaluzec, N.; Peng, S.; Sun, S.; Paulikas, A. *Nano Letters* **2010**, *1*, 919–926.

[280] Xiong, L.; Manthiram, A. *Journal of the Electrochemical Society* **2005**, *152*.

[281] Beard, B. C.; Ross, P. N. *Journal of the Electrochemical Society* **1990**, *137*, 3368–3374.

[282] Watanabe, M.; Tsurumi, K.; Mizukami, T.; Nakamura, T.; Stonehart, P. *Journal of the Electrochemical Society* **1994**, *141*.

[283] Ghosh, T.; Leonard, B.; Zhou, Q.; DiSalvo, F. *Chemistry of Materials* **2010**, *22*.

[284] He, C.; Zhao, N. *Journal of Materials Chemistry* **2012**, *22*, 1297–1304.

[285] Li, X.; An, L.; Wang, X.; Li, F.; Zou, R.; Xia, D. *Journal of Materials Chemistry* **2012**, *22*, 6047–6052.

[286] Kim, J.; Lee, Y.; Sun, S. *Journal of the American Chemical Society* **2010**, *132*, 4996–4997.

[287] Lee, D. C.; Mikulec, F. V.; Pelaez, J. M.; Koo, B.; Korgel, B. A. *The Journal of Physical Chemistry B* **2006**, *110*, 11160–11166.

[288] Sun, S.; Murray, C.; Weller, D.; Folks, L.; Moser, A. *Science* **2000**, *287*, 1989–1992.

[289] Lebedeva, M. V.; Pierron-Bohnes, V.; Goyhenex, C.; Papaefthimiou, V.; Zafeiratos, S.; Nazmutdinov, R. R.; Da Costa, V.; Acosta, M.; Zosiak, L.; Kozubski, R. *Electrochimica Acta* **2013**, *108*, 605–616.

[290] Ghosh, T.; Leonard, B. M.; Zhou, Q.; DiSalvo, F. J. *Chemistry of Materials* **2010**, *22*, 2190–2202.

[291] Jung, N.; Chung, Y.-H.; Chung, D. Y.; Choi, K.-H.; Park, H.-Y.; Ryu, J.; Lee, S.-Y.; Kim, M.; Sung, Y.-E.; Yoo, S. J. *Physical Chemistry Chemical Physics* **2013**, *15*, 17079–17083.

[292] Hodnik, N.; Jeyabharathi, C.; Meier, J.; Kostka, A.; Phani, K.; Mayrhofer, K. *Physical Chemistry Chemical Physics* **2014**, *16*, 13610–13615.

[293] Zou, L.; Li, J.; Yuan, T.; Zhou, Y.; Li, X.; Yang, H. *Nanoscale* **2014**, *6*, 10686–10692.

[294] Lang, X.-Y.; Han, G.-F.; Xiao, B.-B.; Gu, L.; Yang, Z.-Z.; Wen, Z.; Zhu, Y.-F.; Zhao, M.; Li, J.-C.; Jiang, Q. *Advanced Functional Materials* **2015**, *25*, 230–237.

[295] Miura, A.; Wang, H.; Leonard, B. M.; Abruña, H. D.; DiSalvo, F. J. *Chemistry of Materials* **2009**, *21*, 2661–2667.

[296] Kang, Y.; Pyo, J. B.; Ye, X.; Gordon, T. R.; Murray, C. B. *ACS nano* **2012**, *6*, 5642–5647.

[297] Deng, L.; Hu, W.; Deng, H.; Xiao, S. *The Journal of Physical Chemistry C* **2010**, *114*, 11026–11032.

[298] Ahmadi, M.; Behafarid, F.; Cui, C.; Strasser, P.; Cuenya, B. *Acs Nano* **2013**, *7*, 9195–9204.

[299] Liao, H.; Fisher, A.; Xu, Z. J. *Small* **2015**, *11*, 3221–3246.

[300] Prabhudev, S.; Bugnet, M.; Zhu, G.; Bock, C.; Botton, G. *ChemCatChem* **2015**, *7*, 3655–3664.

[301] Chi, M.; Wang, C.; Lei, Y.; Wang, G.; Li, D.; More, K. L.; Lupini, A.; Allard, L. F.; Markovic, N. M.; Stamenkovic, V. R. *Nature communications* **2015**, *6*.

[302] Marks, L.; Peng, L. *Journal of Physics: Condensed Matter* **2016**, *28*, 053001.

[303] Koh, S.; Strasser, P. *Journal of the American Chemical Society* **2007**, *129*, 12624–12625.

[304] Strasser, P.; Koh, S.; Greeley, J. *Physical Chemistry Chemical Physics* **2008**, *10*, 3670–3683.

[305] Petkov, V.; Wanjala, B.; Loukrakpam, R.; Luo, J.; Yang, L.; Zhong, C.; Shastri, S. *Nano Letters* **2012**, *12*, 4289–4299.

[306] Fernandez, P.; Ocan, P.; Gamez, D.; Rojas, S.; Fuente, J.; Sanza, J.; Fierro, J. *The Journal of Physical Chemistry C* **2007**, *111*, 2913–2923.

[307] Wanjala, B.; Luo, J.; Loukrakpam, R.; Fang, B.; Mott, D.; Njoki, P.; Engelhard, M.; Naslund, H.; Wu, J.; Wang, L. *Chemistry of Materials* **2010**, *22*, 4282–4294.

[308] Peng, Z.; Yang, H. *Journal of the American Chemical Society* **2009**, *131*, 7542–7543.

[309] Luo, J.; Wang, L.; Mott, D.; Njoki, P.; Lin, Y.; He, T.; Zhong, C. *Advanced Materials* **2008**, *20*, 4342–4347.

[310] Ataee-Esfahani, H.; Wang, L.; Nemoto, Y.; Yamauchi, Y. *Chemistry of Materials* **2010**, *22*, 6310–6318.

[311] Peng, Z.; Wu, J.; Yang, H. *Chemistry of Materials* **2010**, *22*, 1098–1106.

[312] Wang, C.; Daimon, H.; Sun, S. *Nano letters* **2009**, *9*, 1493–1496.

[313] Yang, H. *Angewandte Chemie International Edition* **2011**, *50*, 2674–2676.

[314] Westsson, E.; Koper, G. J. *Catalysts* **2014**, *4*, 375–396.

[315] Strasser, P.; Koh, S.; Anniyev, T.; Greeley, J.; More, K.; Yu, C.; Liu, Z.; Kaya, S.; Nordlund, D.; Ogasawara, H. *Nat Chem* **2010**, *2*, 454–460.

[316] Chen, Y.; Liang, Z.; Yang, F.; Liu, Y.; Chen, S. *The Journal of Physical Chemistry C* **2011**, *115*, 24073–24079.

[317] Wang, J.; Inada, H.; Wu, L.; Zhu, Y.; Choi, Y.; Liu, P.; Zhou, W.; Adzic, R. *J American Chemical Society* **2009**, *131*, 17298–17302.

[318] Luo, J.; Wang, L.; Mott, D.; Njoki, P.; Lin, Y.; He, T.; Xu, Z.; Wanjana, B.; Lim, I.; Zhong, C. *Advanced Materials* **2008**, *20*, 4342–4347.

[319] Inaba, M.; Ito, H.; Tsuji, H.; Wada, T.; Banno, M.; Yamada, H.; Saito, M.; Tasaka, A. *ECS Transactions* **2010**, *33*, 231–238.

[320] Guo, S.; Zhang, S.; Sun, S. *Angewandte Chemie International Edition* **2013**, *52*, 8526–8544.

[321] Chen, Y.; Liang, Z.; Yang, F.; Liu, Y.; Chen, S. *The Journal of Physical Chemistry C* **2011**, *115*, 24073–24079.

[322] Zhang, J.; Vukmirovic, M. B.; Xu, Y.; Mavrikakis, M.; Adzic, R. R. *Angewandte Chemie International Edition* **2005**, *44*, 2132–2135.

[323] Inaba, M.; Ito, H.; Tsuji, H.; Wada, T.; Banno, M.; Yamada, H.; Saito, M.; Tasaka, A. *ECS Transactions* **2010**, *33*, 231–238.

[324] Erlebacher, J.; Margetis, D. *Physical review letters* **2014**, *112*, 155505.

[325] Wang, D.; Yu, Y.; Xin, H. L.; Hovden, R.; Ercius, P.; Mundy, J. A.; Chen, H.; Richard, J. H.; Muller, D. A.; DiSalvo, F. J. *Nano letters* **2012**, *12*, 5230–5238.

[326] Wang, J. X.; Inada, H.; Wu, L.; Zhu, Y.; Choi, Y.; Liu, P.; Zhou, W.-P.; Adzic, R. R. *Journal of the American Chemical Society* **2009**, *131*, 17298–17302.

[327] Bian, T.; Zhang, H.; Jiang, Y.; Jin, C.; Wu, J.; Yang, H.; Yang, D. *Nano letters* **2015**, *15*, 7808–7815.

[328] Kuttiyiel, K. A.; Choi, Y.; Sasaki, K.; Su, D.; Hwang, S.-M.; Yim, S.-D.; Yang, T.-H.; Park, G.-G.; Adzic, R. R. *Nano Energy* **2016**,

[329] Wang, W.; Lei, B.; Guo, S. *Advanced Energy Materials* **2016**,

[330] Li, Q.; Wu, L.; Wu, G.; Su, D.; Lv, H.; Zhang, S.; Zhu, W.; Casimir, A.; Zhu, H.; Mendoza-Garcia, A. *Nano letters* **2015**, *15*, 2468–2473.

[331] Liu, H.; Dou, M.; Wang, F.; Liu, J.; Ji, J.; Li, Z. *RSC Advances* **2015**, *5*, 66471–66475.

[332] Ding, X.; Yin, S.; An, K.; Luo, L.; Shi, N.; Qiang, Y.; Pasupathi, S.; Pollet, B. G.; Shen, P. K. *Journal of Materials Chemistry A* **2015**, *3*, 4462–4469.

[333] Tamaki, T.; Minagawa, A.; Arumugam, B.; Kakade, B. A.; Yamaguchi, T. *Journal of Power Sources* **2014**, *271*, 346–353.

[334] Arumugam, B.; Kakade, B. A.; Tamaki, T.; Arao, M.; Imai, H.; Yamaguchi, T. *RSC advances* **2014**, *4*, 27510–27517.

[335] Arumugam, B.; Tamaki, T.; Yamaguchi, T. *ACS applied materials & interfaces* **2015**, *7*, 16311–16321.

[336] Wang, D.; Xin, H. L.; Hovden, R.; Wang, H.; Yu, Y.; Muller, D. A.; DiSalvo, F. J.; Abruña, H. D. *Nature materials* **2013**, *12*, 81–87.

[337] Wang, D.; Yu, Y.; Xin, H. L.; Hovden, R.; Ercius, P.; Mundy, J. A.; Chen, H.; Richard, J. H.; Muller, D. A.; DiSalvo, F. J. *Nano letters* **2012**, *12*, 5230–5238.

[338] Cui, C.; Gan, L.; Heggen, M.; Rudi, S.; Strasser, P. *Nature materials* **2013**, *12*, 765–771.

[339] Zhang, L.; Iyyamperumal, R.; Yancey, D. F.; Crooks, R. M.; Henkelman, G. *ACS nano* **2013**, *7*, 9168–9172.

[340] Wang, L.; Yamauchi, Y. *Chemistry of Materials* **2011**, *23*, 2457–2465.

[341] Sneed, B. T.; Young, A. P.; Jalalpoor, D.; Golden, M. C.; Mao, S.; Jiang, Y.; Wang, Y.; Tsung, C.-K. *ACS nano* **2014**, *8*, 7239–7250.

[342] Wang, L.; Yamauchi, Y. *Journal of the American Chemical Society* **2010**, *132*, 13636–13638.

[343] Fang, P.-P.; Duan, S.; Lin, X.-D.; Anema, J. R.; Li, J.-F.; Buriez, O.; Ding, Y.; Fan, F.-R.; Wu, D.-Y.; Ren, B. *Chemical Science* **2011**, *2*, 531–539.

[344] Colic, V.; Bandarenka, A. S. *ACS Catalysis* **2016**, *6*, 5378–5385.

[345] Weiss, J.; Carpenter, R.; Higgs, A. *Ultramicroscopy* **1991**, *36*, 319–329.

[346] http://zeiss-campus.magnet.fsu.edu/index.html, 2016 (accessed).

[347] Rossouw, C.; Allen, L.; Findlay, S.; Oxley, M. *Ultramicroscopy* **2003**, *96*, 299–312.

[348] Jones, L.; Nellist, P. D. *Microscopy and Microanalysis* **2013**, *19*, 1050–1060.

[349] Dwyer, C.; Etheridge, J. *Ultramicroscopy* **2003**, *96*, 343–360.

[350] Katz-Boon, H.; Rossouw, C. J.; Dwyer, C.; Etheridge, J. *Ultramicroscopy* **2013**, *124*, 61–70.

[351] Haider, M.; Rose, H.; Uhlemann, S.; Kabius, B.; Urban, K. *Journal of Electron Microscopy* **1998**, *47*, 395–405.

[352] Dellby, N.; Krivanek, O. L.; Nellist, P. D.; Batson, P. E.; Lupini, A. R. *Journal of Electron Microscopy* **2001**, *50*, 177–185.

[353] Hosokawa, F.; Sawada, H.; Kondo, Y.; Takayanagi, K.; Suenaga, K. *Japanese Society for Microscopy* **2013**, *62*, 23–41.

[354] Nellist, P.; Dellby, N.; Krivanek, O.; Murfitt, M.; Szilagyi, Z.; Lupini, A.; Pennycook, S. Towards sub-0.5 angstrom beams through aberration corrected STEM. Conference-series, Institute of Physics. 2004; pp 159–164.

[355] Rossouw, D. Electron Energy Loss Spectroscopy of Metallic Nanostructures and Carbon Nanotubes. Ph.D. thesis, McMaster University, 2014.

[356] Rodenburg, J. *Advances in Imaging and Electron Physics* **2008**, *150*, 87–184.

[357] Findlay, S.; Shibata, N.; Sawada, H.; Okunishi, E.; Kondo, Y.; Ikuhara, Y. *Ultramicroscopy* **2010**, *110*, 903–923.

[358] Okunishi, E.; Ishikawa, I.; Sawada, H.; Hosokawa, F.; Hori, M.; Kondo, Y. *Microscopy and Microanalysis* **2009**, *15*, 164–165.

[359] Cowley, J. M. *Applied Physics Letters* **1969**, *15*, 58–59.

[360] Gubbens, A.; Barfels, M.; Trevor, C.; Twesten, R.; Mooney, P.; Thomas, P.; Menon, N.; Kraus, B.; Mao, C.; McGinn, B. *Ultramicroscopy* **2010**, *110*, 962–970.

[361] Damiano, J.; Nackashi, D. P.; Mick, S. E. *Microscopy and Microanalysis* **2008**, *14*, 1332–1333.

[362] Crozier, P. A.; Hansen, T. W. *MRS Bulletin* **2015**, *40*, 38–45.

[363] Zheng, H.; Meng, Y. S.; Zhu, Y. *MRS Bulletin* **2015**, *40*, 12–18.

[364] Yoshida, H.; Kuwauchi, Y.; Jinschek, J. R.; Sun, K.; Tanaka, S.; Kohyama, M.; Shimada, S.; Haruta, M.; Takeda, S. *Science* **2012**, *335*, 317–319.

[365] Noh, K. W.; Liu, Y.; Sun, L.; Dillon, S. J. *Ultramicroscopy* **2012**, *116*, 34–38.

[366] Ammam, M.; Easton, E. B. *Journal of Power Sources* **2013**, *236*, 311–320.

[367] Johnston-Peck, A. C.; Cullen, D. A.; Tracy, J. B. *Particle & Particle Systems Characterization* **2013**, *30*, 678–682.

[368] Sato, K. *Nature materials* **2009**, *8*, 924–925.

[369] Sato, M.; Takahashi, Y.; Fujimoto, S. *Physical review letters* **2009**, *103*, 020401.

[370] Wittig, J.; Bentley, J.; Allard, L.; Wellons, M.; Lukehart, C. *Microscopy and Microanalysis* **2008**, *14*, 216–217.

[371] Liu, C.; Klemmer, T. J.; Shukla, N.; Wu, X.; Weller, D.; Tanase, M.; Laughlin, D. *Journal of Magnetism and Magnetic Materials* **2003**, *266*, 96–101.

[372] Müller, M.; Erhart, P.; Albe, K. *Physical Review B* **2007**, *76*, 155412.

[373] Zhang, S.; Hao, Y.; Su, D.; Doan-Nguyen, V. V.; Wu, Y.; Li, J.; Sun, S.; Murray, C. B. *Journal of the American Chemical Society* **2014**, *136*, 15921–15924.

[374] Li, Q.; Wu, L.; Wu, G.; Su, D.; Lv, H.; Zhang, S.; Zhu, W.; Casimir, A.; Zhu, H.; Mendoza-Garcia, A. *Nano letters* **2015**, *15*, 2468–2473.

[375] Chen, S.; Sheng, W.; Yabuuchi, N.; Ferreira, P. J.; Allard, L. F.; Shao-Horn, Y. *The Journal of Physical Chemistry C* **2008**, *113*, 1109–1125.

[376] Ruban, A.; Skriver, H. L.; Nørskov, J. K. *Physical Review B* **1999**, *59*, 15990.

[377] Stamenkovic, V.; Schmidt, T.; Ross, P.; Markovic, N. *The Journal of Physical Chemistry B* **2002**, *106*, 11970–11979.

[378] Müller, M.; Albe, K. *Physical Review B* **2005**, *72*, 094203.

[379] Yang, B.; Asta, M.; Mryasov, O.; Klemmer, T.; Chantrell, R. *Acta materialia* **2006**, *54*, 4201–4211.

[380] Torres, K.; Thompson, G. *Ultramicroscopy* **2009**, *109*, 606–611.

[381] Han, L.; Wiedwald, U.; Kuerbanjiang, B.; Ziemann, P. *Nanotechnology* **2009**, *20*, 285706.

[382] Chen, L.; Chan, M. C.; Nan, F.; Bock, C.; Botton, G. A.; Mercier, P. H.; MacDougall, B. R. *ChemCatChem* **2013**, *5*, 1449–1460.

[383] Kirkland, E. J. *Advanced computing in electron microscopy*; Springer, 1998; pp 19–39.

[384] Kirkland, E. J. *Ultramicroscopy* **2011**, *111*, 1523–1530.

[385] Kirkland, E. J. *Acta Crystallographica Section A: Foundations and Advances* **2016**, *72*.

[386] Chan, M. C.; Chen, L.; Nan, F.; Britten, J. F.; Bock, C.; Botton, G. A. *Nanoscale* **2012**, *4*, 7273–7279.

[387] Li, X.; An, L.; Wang, X.; Li, F.; Zou, R.; Xia, D. *Journal of Materials Chemistry* **2012**, *22*, 6047–6052.

[388] Ahmadi, M.; Behafarid, F.; Cui, C.; Strasser, P.; Cuenya, B. R. *ACS Nano* **2013**, *7*, 9195–9204.

[389] Delalande, M.; Guinel, M. J.-F.; Allard, L. F.; Delattre, A.; Le Bris, R.; Samson, Y.; Bayle-Guillemaud, P.; Reiss, P. *The Journal of Physical Chemistry C* **2012**, *116*, 6866–6872.

[390] Allard, L. F.; Overbury, S. H.; Bigelow, W. C.; Katz, M. B.; Nackashi, D. P.; Damiano, J. *Microscopy and Microanalysis* **2012**, *18*, 656–666.

[391] Verbeeck, J.; Van Aert, S. *Ultramicroscopy* **2004**, *101*, 207–224.

[392] Prabhudev, S.; Chiang, C.; Chatzidakis, M.; Rossouw, D.; Botton, G. A. *in communication*

[393] Wanjala, B. N.; Luo, J.; Fang, B.; Mott, D.; Zhong, C.-J. *Journal of Materials Chemistry* **2011**, *21*, 4012–4020.

[394] Bian, T.; Zhang, H.; Jiang, Y.; Jin, C.; Wu, J.; Yang, H.; Yang, D. *Nano letters* **2015**, *15*, 7808–7815.

[395] Qu, J.; Liu, H.; Ye, F.; Hu, W.; Yang, J. *International Journal of Hydrogen Energy* **2012**, *37*, 13191–13199.

[396] Ataee-Esfahani, H.; Wang, L.; Nemoto, Y.; Yamauchi, Y. *Chemistry of Materials* **2010**, *22*, 6310–6318.

[397] Kumar, S. S.; Phani, K. *Journal of Power Sources* **2009**, *187*, 19–24.

[398] Zhai, J.; Huang, M.; Dong, S. *Electroanalysis* **2007**, *19*, 506–509.

[399] Luo, J.; Njoki, P. N.; Lin, Y.; Wang, L.; Zhong, C. J. *Electrochemistry communications* **2006**, *8*, 581–587.

[400] Zhou, S.; Jackson, G. S.; Eichhorn, B. *Advanced Functional Materials* **2007**, *17*, 3099–3104.

[401] Suntivich, J.; Xu, Z.; Carlton, C. E.; Kim, J.; Han, B.; Lee, S. W.; Bonnet, N.; Marzari, N.; Allard, L. F.; Gasteiger, H. A. *Journal of the American Chemical Society* **2013**, *135*, 7985–7991.

[402] Doherty, R. P.; Krafft, J.-M.; Méthivier, C.; Casale, S.; Remita, H.; Louis, C.; Thomas, C. *Journal of catalysis* **2012**, *287*, 102–113.

[403] Yamamoto, T. A.; Nakagawa, T.; Seino, S.; Nitani, H. *Applied Catalysis A: General* **2010**, *387*, 195–202.

[404] Xie, W.; Herrmann, C.; Kömpe, K.; Haase, M.; Schlücker, S. *Journal of the American Chemical Society* **2011**, *133*, 19302–19305.

[405] Mourdikoudis, S.; Chirea, M.; Zanaga, D.; Altantzis, T.; Mitrakas, M.; Bals, S.; Liz-Marzán, L. M.; Pérez-Juste, J.; Pastoriza-Santos, I. *Nanoscale* **2015**, *7*, 8739–8747.

[406] Buck, M. R.; Bondi, J. F.; Schaak, R. E. *Nature chemistry* **2012**, *4*, 37–44.

[407] Bradley, M. J.; Read, C. G.; Schaak, R. E. *The Journal of Physical Chemistry C* **2015**, *119*, 8952–8959.

[408] Guo, S.; Li, J.; Dong, S.; Wang, E. *The Journal of Physical Chemistry C* **2010**, *114*, 15337–15342.

[409] Zeng, J.; Yang, J.; Lee, J. Y.; Zhou, W. *The Journal of Physical Chemistry B* **2006**, *110*, 24606–24611.

[410] Banerjee, I.; Kumaran, V.; Santhanam, V. *The Journal of Physical Chemistry C* **2015**, *119*, 5982–5987.

[411] Malis, O.; Radu, M.; Mott, D.; Wanjala, B.; Luo, J.; Zhong, C. *Nanotechnology* **2009**, *20*, 245708.

[412] Yamauchi, Y.; Tonegawa, A.; Komatsu, M.; Wang, H.; Wang, L.; Nemoto, Y.; Suzuki, N.; Kuroda, K. *Journal of the American Chemical society* **2012**, *134*, 5100–5109.

[413] Massalski, T. B.; Okamoto, H.; Subramanian, P.; Kacprzak, L.; Scott, W. W. *Binary alloy phase diagrams*; American Society for Metals Metals Park, OH, 1986; Vol. 1.

[414] Hernández-Fernández, P.; Rojas, S.; Ocón, P.; Gómez de la Fuente, J.; San Fabián, J.; Sanza, J.; Pena, M.; García-García, F.; Terreros, P.; Fierro, J. *The Journal of Physical Chemistry C* **2007**, *111*, 2913–2923.

[415] Mariscal, M.; Oldani, N.; Dassie, S.; Leiva, E. *Faraday discussions* **2008**, *138*, 89–104.

[416] Petkov, V.; Wanjala, B. N.; Loukrakpam, R.; Luo, J.; Yang, L.; Zhong, C.-J.; Shastri, S. *Nano letters* **2012**, *12*, 4289–4299.

[417] Braidy, N.; Purdy, G. R.; Botton, G. A. *Acta Materialia* **2008**, *56*, 5972–5983.

[418] Xiao, S.; Hu, W.; Luo, W.; Wu, Y.; Li, X.; Deng, H. *The European Physical Journal B-Condensed Matter and Complex Systems* **2006**, *54*, 479–484.

[419] Deng, L.; Hu, W.; Deng, H.; Xiao, S. *The Journal of Physical Chemistry C* **2010**, *114*, 11026–11032.

[420] Frens, G. *Nature* **1973**, *241*, 20–22.

[421] Lu, L.; Sun, G.; Zhang, H.; Wang, H.; Xi, S.; Hu, J.; Tian, Z.; Chen, R. *Journal of Materials Chemistry* **2004**, *14*, 1005–1009.

[422] Petrou, M.; Petrou, C. *Image processing: the fundamentals*; John Wiley & Sons, 2010.

[423] Bingham, E.; Hyvärinen, A. *International journal of neural systems* **2000**, *10*, 1–8.

[424] Rossouw, D.; Burdet, P.; de la Peña, F.; Ducati, C.; Knappett, B. R.; Wheatley, A. E.; Midgley, P. A. *Nano letters* **2015**, *15*, 2716–2720.

[425] Rossouw, D.; Krakow, R.; Saghi, Z.; Yeoh, C. S.; Burdet, P.; Leary, R. K.; de la Peña, F.; Ducati, C.; Rae, C. M.; Midgley, P. A. *Acta Materialia* **2016**, *107*, 229–238.

[426] Pedregosa, F.; Varoquaux, G.; Gramfort, A.; Michel, V.; Thirion, B.; Grisel, O.; Blondel, M.; Prettenhofer, P.; Weiss, R.; Dubourg, V. *Journal of Machine Learning Research* **2011**, *12*, 2825–2830.

[427] de la Peña, F.; Burdet, P.; Ostasevicius, T.; Sarahan, M.; Nord, M.; Fauske, V. T.; Taillon, J.; Eljarrat, A.; Mazzucco, S.; Donval, G. Hyperspy: HyperSpy 0.8. 2. 2015.

[428] Yu, R.; Song, H.; Zhang, X.-F.; Yang, P. *The Journal of Physical Chemistry B* **2005**, *109*, 6940–6943.

[429] Tyson, W.; Miller, W. *Surface Science* **1977**, *62*, 267–276.

[430] Chan, C. T.; Bohnen, K. P.; Ho, K. *Physical review letters* **1992**, *69*, 1672.

[431] Rousset, S.; Chiang, S.; Fowler, D.; Chambliss, D. *Physical review letters* **1992**, *69*, 3200.

[432] Chatzidakis, M.; Prabhudev, S.; Saidi, P.; Chiang, C.; Hoyt, J.; Botton, G. A. *in communication*

[433] Paik, C.; Jarvi, T.; Ogrady, W. *Electrochemical and solid-state letters* **2004**, *7*, A82–A84.

[434] Okunishi, E.; Ishikawa, I.; Sawada, H.; Hosokawa, F.; Hori, M.; Kondo, Y. *Microscopy and Microanalysis* **2009**, *15*, 164–165.

[435] Okunishi, E.; Sawada, H.; Kondo, Y. *Micron* **2012**, *43*, 538–544.

[436] Ishikawa, R.; Okunishi, E.; Sawada, H.; Kondo, Y.; Hosokawa, F.; Abe, E. *Nature materials* **2011**, *10*, 278–281.

[437] Oshima, Y.; Sawada, H.; Hosokawa, F.; Okunishi, E.; Kaneyama, T.; Kondo, Y.; Niitaka, S.; Takagi, H.; Tanishiro, Y.; Takayanagi, K. *Journal of electron microscopy* **2010**, *59*, 457–461.

[438] Findlay, S.; Shibata, N.; Sawada, H.; Okunishi, E.; Kondo, Y.; Yamamoto, T.; Ikuhara, Y. *Applied Physics Letters* **2009**, *95*, 191913.

[439] Findlay, S.; Azuma, S.; Shibata, N.; Okunishi, E.; Ikuhara, Y. *Ultramicroscopy* **2011**, *111*, 285–289.

[440] Findlay, S.; Shibata, N.; Sawada, H.; Okunishi, E.; Kondo, Y.; Ikuhara, Y. *Ultramicroscopy* **2010**, *110*, 903–923.

[441] Sasaki, K.; Naohara, H.; Choi, Y.; Cai, Y.; Chen, W.-F.; Liu, P.; Adzic, R. R. *Nature Communications* **2012**, *3*, 1115.

[442] Wang, R.; Higgins, D. C.; Prabhudev, S.; Lee, D. U.; Choi, J.-Y.; Hoque, M. A.; Botton, G. A.; Chen, Z. *Journal of Materials Chemistry A* **2015**, *3*, 12663–12671.

[443] Wang, R.; Higgins, D. C.; Lee, D. U.; Prabhudev, S.; Hassan, F. M.; Chabot, J.-Y.; Botton, G.; et al, *Nano Energy* **2016**, *20*, 57–67.

[444] Ono, L.; Yuan, B.; Heinrich, H.; Cuenya, B. R. *The Journal of Physical Chemistry C* **2010**, *114*, 22119–22133.

[445] Blackstock, J.; Stewart, D.; Li, Z. *Applied Physics A* **2005**, *80*, 1343–1353.

[446] Muller, O.; Roy, R. *Journal of the Less Common Metals* **1968**, *16*, 129–146.

[447] Despres, J.; Elsener, M.; Koebel, M.; Kröcher, O.; Schnyder, B.; Wokaun, A. *Applied Catalysis B: Environmental* **2004**, *50*, 73–82.

[448] Abe, Y.; Kawamura, M.; Sasaki, K. *Japanese journal of applied physics* **1999**, *38*, 2092.

[449] Abe, Y.; Yanagisawa, H.; Sasaki, K. *Japanese journal of applied physics* **1998**, *37*, 4482.

[450] Seriani, N.; Pompe, W.; Ciacchi, L. C. *The Journal of Physical Chemistry B* **2006**, *110*, 14860–14869.

[451] Goeke, R. S.; Datye, A. K. *Topics in Catalysis* **2007**, *46*, 3–9.

[452] Furuya, Y.; Mashio, T.; Ohma, A.; Dale, N.; Oshihara, K.; Jerkiewicz, G. *The Journal of chemical physics* **2014**, *141*, 164705.

[453] Dresselhaus, M.; Thomas, I. *Nature* **2001**, *414*, 332–337.

[454] *International energy agency's interactive sankey diagram*; International Energy Agency http://www.iea.org/Sankey/, 2013.

[455] *World Fossil Fuels Reserves and Expected Consumption (White Paper)*; The Colarado River Commission of Nevada, 2002.

[456] Marbán, T., G.; Valdés-Solís *International Journal of Hydrogen Energy* **2007**, *32*, 1625–1637.

[457] *International Energy Outlook*; US Energy Information Administration, 2016.

[458] Deutch, J.; Moniz, E.; Ansolabehere, S.; Driscoll, M.; Gray, P.; Holdren, J.; Joskow, P.; Lester, R.; Todreas, N. *The future of nuclear power.*; An MIT Interdisciplinary Study (http://web. mit. edu/nuclearpower)., 2003.

[459] Lewis, N.; Nocera, D. *Proceedings of the National Academy of Sciences* **2006**, *103*, 15729–15735.

[460] Zinkle, S.; Was, G. *Acta Materialia* **2013**, *61*, 735–758.

[461] Shrader-Frechette, K. *Nuclear power and public policy: the social and ethical problems of fission technology.*; Springer Science Business Media, 2012.

[462] Wang, Q.; Chen, X. *Renewable and Sustainable Energy Reviews* **2012**, *16*, 2610–2617.

[463] Abu-Khader, M. *Progress in Nuclear Energy* **2009**, *51*, 225–235.

[464] Lee, S.; Saw, S. *Journal of fusion energy* **2011**, *30*, 398–403.

[465] Braams, C.; Stott, P. *Nuclear fusion: half a century of magnetic confinement fusion research.*; CRC Press., 2002.

[466] Metz, D.-O., B; Coninck, H.; Loos, M.; Meyer, L. *Carbon dioxide capture and storage.*; Intergovernmental Panel on Climate Change, DC., 2005.

[467] Cuéllar-Franca, R. M.; Azapagic, A. *Journal of CO2 Utilization* **2015**, *9*, 82–102.

[468] Twidell, J.; Weir, T. *Renewable energy resources*; Routledge, 2015.

[469] Ellabban, O.; Abu-Rub, H.; Blaabjerg, F. *Renewable and Sustainable Energy Reviews* **2014**, *39*, 748–764.

[470] Erdinc, O.; Uzunoglu, M. *Renewable and Sustainable Energy Reviews* **2012**, *16*, 1412–1425.

[471] Manzano-Agugliaro, F.; Alcayde, A.; Montoya, F.; Zapata-Sierra, A.; Gil, C. *Renewable and Sustainable Energy Reviews* **2013**, *18*, 134–143.

[472] U.S. Solar Radiation Resource Maps. http://rredc.nrel.gov/solar/old_data/nsrdb/1961-1990/redbook/atlas/, 2016(accessed).

[473] *Annual Energy Flow*; U.S. Annual Energy Energy Information Administration, 2015.

[474] *Primary Energy Production by Source*; U.S. Energy Information Administration, 2015.

[475] *World Energy Assessment Report: Energy and the Challenge of Sustainability*; United Nations Development Program, 2003.

[476] *Annual Energy Outlook*; Energy Information Administration (US Dept of Energy, Washington, DC)., 2005.

[477] http://www.electricaltechnology.org, 2016 (accessed).

[478] http://www.saarcenergy.org/wp-content/uploads/2016/06/Study-Report1_-Shyam.pdf, 2016 (accessed).

[479] http://www.areva.com/EN/global-offer-725/concentrated-solar-power-renewable-energies-solutions.html, 2016 (accessed).

[480] Kazmerski, L. *Journal of electron spectroscopy and related phenomena* **2005**, *150*, 105–135.

[481] Gratzel, M. *Nature* **2001**, *414*, 338–344.

[482] *Solar Photovoltaic Energy Technology Roadmap*; International Energy Agency, Vol. 2014.

[483] Green, M. *Solar energy* **2004**, *76*, 3–8.

[484] Green, M. *Progress in Photovoltaics Research and Applications* **2001**, *9*, 123–135.

[485] Parida, B.; Iniyan, S.; Goic, R. *Renewable and sustainable energy reviews* **2011**, *15*, 1625–1636.

[486] Green, M.; Ho-Baillie, A.; Snaith, H. *Nature Photonics* **2014**, *8*, 506–514.

[487] Diaz-Gonzalez, S. A. G.-B. O. . V.-R. R., F. *Renewable and Sustainable Energy Reviews* **2012**, *16*, 2154–2171.

[488] Van de Krol, R. *Photoelectrochemical hydrogen production*; Springer, 2012; pp 13–67.

[489] Bard, A.; Fox, M. *Accounts of Chemical Research* **1995**, *28*, 141–145.

[490] Tachibana, Y.; Vayssieres, L.; Durrant, J. *Nature Photonics* **2012**, *6*, 511–518.

[491] Thirugnanasambandam, M.; Iniyan, S.; Goic, R. *Renewable and sustainable energy reviews* **2010**, *14*, 312–322.

[492] *Solar thermal Electricity Technology Roadmap*; International Energy Agency, 2014.

[493] Mills, D. *solar Energy* **2004**, *76*, 19–31.

[494] Hadjipaschalis, I.; Poullikkas, A.; Efthimiou, V. *Renew Sustain Energy Rev 13(6-7)*, 1513–1522.

[495] Ibrahim, H.; Ilinca, A.; Perron, J. *Renewable and sustainable energy reviews* **2008**, *12*, 1221–1250.

[496] Ribeiro, P.; Johnson, B.; Crow, M.; Arsoy, A.; Liu, Y. *Proceedings of the IEEE* **2001**, *89*, 1744–1756.

[497] Dunn, B.; Kamath, H.; Tarascon, J. *Science* **2011**, *334*, 928–935.

[498] Scrosati, B.; Garche, J. *Journal of Power Sources* **2010**, *195*, 2419–2430.

[499] Scrosati, B. *Electrochimica Acta* **2000**, *45*, 2461–2466.

[500] Yoshio, M.; Brodd, R.; Kozawa, A. **2009**,

[501] Aifantis, K.; Hackney, S.; Kumar, R. *High energy density lithium batteries: materials engineering applications.*; John Wiley and Sons., 2010.

[502] Etacheri, V.; Marom, R.; Elazari, R.; Salitra, G.; Aurbach, D. *Energy Environmental Science* **2011**, *4*, 3243–3262.

[503] Nitta, N.; Wu, F.; Lee, J.; Yushin, G. *Materials today* **2015**, *18*, 252–264.

[504] Andre, D.; Kim, S.; Lamp, P.; Lux, S.; Maglia, F.; Paschos, O.; Stiaszny, B. *Journal of Materials Chemistry A* **2015**, *3*, 6709–6732.

[505] Wu, C. *MRS bulletin* **2010**, *35*, 650–651.

[506] Chen, X.; Shen, W.; Vo, T.; Cao, Z.; Kapoor, A. *10th International Power Energy Conference IPEC* **2012**, *2012*, 230–235.

[507] Bandhauer, T.; Garimella, S.; Fuller, T. *Journal of the Electrochemical Society* **2011**, *158*, R1–R25.

[508] Wen, J.; Yu, Y.; Chen, C. *Materials Express* **2012**, *2*, 197–212.

[509] Herbert, G.; Iniyan, S.; Sreevalsan, E.; Rajapandian, S. *Renewable and sustainable energy Reviews* **2007**, *11*, 1117–1145.

[510] Ackermann, T.; Soder, L. *Renewable and sustainable energy reviews* **2000**, *4*, 315–374.

[511] Sherif, S. A.; Barbir, F.; Veziroglu, T. *Solar energy* **2005**, *78*, 647–660.

[512] *Wind energy: Technology Roadmap*; International Energy Agency, 2013; Vol. 25; pp 705–722.

[513] http://www.energy.gov/eere/wind/inside-wind-turbine-0, 2016 (accessed).

[514] Dutton, A.; Bleijs, J.; Dienhart, H.; Falchetta, M.; Hug, W.; Prischich, D.; Ruddell, A. *International Journal of Hydrogen Energy* **2000**, *25*, 705–722.

[515] Fuglsang, P.; Thomsen, K. *Journal of solar energy engineering* **2001**, *123*, 296–303.

[516] Mazloomi, K.; Gomes, C. *Renewable and Sustainable Energy Reviews* **2012**, *16*, 3024–3033.

[517] Midilli, A.; Ay, M.; Dincer, I.; Rosen, M. *Renewable Sustainable Energy Reviews* **2005**, *9*, 255–271.

[518] Crabtree, G.; Dresselhaus, M. *MRS Bulletin* **2008**, *33*, 421–428.

[519] Cipriani, G.; Dio, V.; Genduso, F.; Cascia, D.; Liga, R.; Miceli, R.; Galluzzo, G. *International Journal of Hydrogen Energy* **2014**, *39*, 8482–8494.

[520] Peschka, W. *Springer Science Business Media* **2012**,

[521] Tian, F.; Toon, O.; Pavlov, A.; De, A.; Sterck, H. *Science* **2005**, *308*, 1014.

[522] Holladay, J.; Hu, J.; King, D.; Wang, Y. *Catalysis Today* **2009**, *139*, 244–260.

[523] Turner, J. *Science* **2004**, *305*, 972–974.

[524] Ursua, A.; Gandia, L.; Sanchis, P. *Proceedings of the IEEE* **2012**, *100*, 410–426.

[525] Van de krol, R.; Gratzel, M. *Photoelectrochemical hydrogen production*; Springer NewYork, 2012.

[526] Kapdan, I.; Kargi, F. *Enzyme and microbial technology* **2006**, *38*, 569–582.

[527] Funk, J. *International Journal of Hydrogen Energy* **2001**, *26*, 185–190.

[528] Ni, M.; Leung, D.; Leung, M.; Sumathy, K. *Fuel processing technology* **2006**, *87*, 461–472.

[529] Yildiz, B.; Kazimi, M. *International Journal of Hydrogen Energy* **2006**, *31*, 77–92.

[530] Staffell, I. *The Energy and Fuel Data Sheet*; 2011.

[531] Ross, D. *Vacuum* **2006**, *80*, 1084–1089.

[532] Eberle, U.; Felderhoff, M.; Schueth, F. *Angewandte Chemie International Edition* **2009**, *48*, 6608–6630.

[533] Felderhoff, M.; Weidenthaler, C.; von Helmolt, R.; Eberle, U. *Physical Chemistry Chemical Physics* **2007**, *9*, 2643–2653.

[534] Walker, G. *Solid-state hydrogen storage: materials and chemistry.*; Elsevier., 2008.

[535] Sakintuna, B.; Lamari-Darkrim, F.; Hirscher, M. *International Journal of Hydrogen Energy* **2007**, *32*, 1121–1140.

[536] Schlapbach, L.; Zuttel, A. *Nature* **2001**, *414*, 353–358.

[537] Cheng, H.; Yang, Q.; Liu, C. *Carbon* **2001**, *39*, 1447–1454.

[538] Christian, M.; Aguey-Zinsou, K. *ACS Nano* **2012**, *6*, 7739–7751.

[539] Murray, D. M., LJ; J, R. *Chemical Society Reviews* **2009**, *38*, 1294–1314.

[540] Mekhilef, S. R., S; Safari, A. *Renewable and Sustainable Energy Reviews* **2012**, *16*, 981–989.

[541] Kordesch, K.; Simader, G. *Chemical Reviews* **1995**, *95*, 191–207.

[542] http://addis.caltech.edu/images/, 2016 (accessed).

[543] http://www.toyota-global.com/innovation/environmental_technology/fuelcell_vehicle/, 2016 (accessed).

[544] Carrette, L.; Friedrich, K.; Stimming, U. *Fuel cells* **2001**, *1*, 5–39.

[545] Steele, B.; Heinzel, A. *Nature* **2001**, *414*, 345–352.

[546] Debe, M. *Nature* **2012**, *486*, 43–51.

[547] Neef, H. *Energy* **2009**, *34*, 327–333.

[548] Solomon, B.; Banerjee, A. *Energy policy* **2006**, *34*, 781–792.